Thermal and Microstructure Modeling of Metal Deposition Processes with Application to Ti-6Al-4V

by

Shawn Michael Kelly

Dissertation submitted to the Faculty of the Virginia Polytechnic Institute and State University in partial fulfillment of the requirements for the degree of

DOCTOR OF PHILOSOPHY

in

Materials Science and Engineering

Professor Stephen L. Kampe, Chairman

Dr. Sudarsanam Suresh Babu, Co-Chairman

Professor Alex O. Aning

Professor William T. Reynolds, Jr.

Dr. Stan A. David, FASM

Dr. Leo Christodoulou

12 November 2004

Blacksburg, Virginia

Keywords: titanium alloy, additive manufacturing, metal deposition, near net shape, rapid prototyping, heat treatment, thermal model, microstructure model

Thermal and Microstructure Modeling of Metal Deposition Processes

with Application to Ti-6Al-4V

Shawn Michael Kelly

(ABSTRACT)

Near-net shape processes, such as laser metal deposition (LMD), offer a unique combination of process flexibility, time savings, and reduced cost in producing titanium alloy components. The current challenge in processing titanium alloys using LMD methods is understanding the complex microstructure evolution as a part is fabricated layer by layer. The microstructure is affected by the repeated thermal cycling that occurs during the deposition process, as shown by a series of baseline microstructure experiments. The current work focuses on the characterization, thermal, and microstructural modeling of multilayered Ti-6Al-4V deposits. A thermal model has been developed using finite difference techniques to predict the thermal history of LMD processes. A microstructure model that predicts the α phase fraction and morphology evolution was constructed to quantify the effect of thermal cycling on the as-deposited microstructure evolution. Alpha dissolution and growth are modeled assuming one-dimensional plate dissolution according to a parabolic rate law, and a Johnson-Mehl-Avrami-Kolmorgorov (JMAK) nucleation and growth model, respectively. Alpha morphology (colony-α and basketweave-α) evolution is tracked using a simplistic approach whereby only certain morphologies dissolve and grow above a specified temperature in the $\alpha+\beta$ field.

Characterization of the deposit has shown that a complex microstructure evolves consisting of a two distinct regions: a transient region of undeveloped microstructure and a characteristic layer that is periodically repeated throughout the deposit. The transient region contains a fine basketweave and colony-α morphology. The characteristic layer contains a two phase mixture of $\alpha+\beta$, with the alpha phase exhibits regions of colony-α (layer band) and basketweave-α morphology.

The different regions of microstructural contrast in the deposit are associated with thermal cycling. The thermal model results show that a heat affected zone defined by the beta transus extends approximately 3 layers into the deposit. The phase fraction model predicts the greatest variation in microstructural evolution to occur in a layer *n* after the deposition of layer *n+3*. The results of the morphology model show that increased amounts of colony-α form near the top of a characteristic layer. It follows that a layer band (colony-α region) forms as a result of heating a region of material to a peak temperature just below the beta transus, where a large amount of primary-α dissolves. Upon cooling, colony-α forms intragranularly. The coupled thermal and microstructure models offer a way to quantitatively map microstructure during LMD processing of Ti-6Al-4V.

Acknowledgements

I would like to thank my advisor, Dr. Stephen L. Kampe, for his advice, ever positive support, and guidance. In addition, I am indebted to Dr. S. Suresh Babu, who offered to serve as a mentor and co-advisor during my time at ORNL. His *pro bono* efforts were instrumental in developing me as a scientist. I would also like to thank Dr. Alex Aning, Dr. Bill Reynolds, Dr. Stan David, and Dr. Leo Christodoulou for serving as committee members and commenting on the thesis.

I would also like to acknowledge, Dr. Steven Fishman of ONR, Dr. Kevin Slattery of Boeing, and Dr. Frank Arcella of AeroMet, for providing the opportunity to work on this project. Funding was provided under ONR contracts N00014-98-3-0022 and N00014-00-1-0579. I am also grateful for the financial support provided by Thomas Zacharia of ORNL through the Joint Institute for Computational Sciences (contract number DE-AC05-00OR22725). His support made it possible to broaden my experiences as a graduate student by working at ORNL for the past year and a half. I would also like to thank Dr. Stan David for allowing me to "join" the joining group at ORNL and acknowledge my input on group activities.

I would like to thank my (past) lab mates, K. Knipling, B. Hailer, A. Goff, J. Franklin, and Dr. J. Schultz for, at the very least, making the lab environment an interesting place to work and for providing assistance and discussion on various topics. I am indebted to David Berry, whom has saved me countless hours of time repairing equipment through his technical assistance. I would also like to mention the following people from ORNL who have helped me with various tasks during my time at ORNL: S. Badlani, O. Barabash, N. Evans, Z. Feng, D.A. Frederick, T. Geer, E. Kenik, L. Malone, N. Manning, D. McCoy, A. Payzant, R. Reed, M. Santella, K. Yarborough, and J. Vitek.

I would also like to thank my parents, Tim and Charlene, my brothers, Brian and Stephen, my Grandparents, Nicholas and Madge Notarange, the rest of my family, and my Wife's family for their support and encouragement while I delayed gainful employment for the pursuit of "scientific enlightenment."

Last, but not least, I am grateful for my wife, Chandale, who has supported, encouraged, and most importantly, has loved me unconditionally during a time of late-night trips to the lab, relocation to a new city, and sleepless nights spent writing my thesis.

Table of Contents

Thermal and Microstructure Modeling of Metal Deposition Processes with Application to Ti-6Al-4V i

Acknowledgements iii

Nomenclature xx

Chapter 1: Introduction 1

Laser Metal Deposition Processes 1

Laser Metal Deposition State of the Art 1

Welding: Similarities and Differences to LMD 3

Summary 4

Motivation and Goals 5

Chapter 2: Solid-State Phase Transformations and Microstructure in Ti-6Al-4V 10

Typical Phase Transformations in Ti-6Al-4V 10

Primary Reactions: Cooling through the beta transus 13

General Aspects of Diffusion Controlled $\beta \rightarrow \alpha+\beta$ Reaction 13

Crystallography 13

Composition of Phases 14

Specific Morphologies of the $\beta \rightarrow \alpha+\beta$ reaction 15

Grain boundary allotriomorphs (α_{GB}) 15

Primary Alpha (α_P) Formation 16

Massive Transformation ($\beta \rightarrow \alpha_m$) 19

Martensitic Transformation ($\beta \rightarrow \alpha'$) 20

Reactions upon heating 21

General Aspects of Alpha Dissolution 21

Composition Variation 21

Elevation of the beta transus during non-equilibrium heating 22

Reactions during heating and cooling in the $\alpha + \beta$ phase field 23

Secondary-alpha (α_S) formation during cooling 23

Dissolution of alpha (α_{GB}, α_S and α_P) during heating 25

LMD Thermal Cycles and Microstructure 25

Summary 27

Chapter 3: Developing Baseline Microstructures for Comparison with LMD of Ti-6Al-4V 30

Baseline Microstructure Experiment 30
Samples 30
Procedure 32
Characterization Techniques 34
General 34
Electron backscattered diffraction ("OIM") 34
TEM 36
Results 37
Measured Cooling Rates and Hardness 37
Slow Cooling (0.6K/s) 37
Moderate Cooling (10K/s) 49
Fast Cooling (94K/s) 61
Quench Cooling (>500K/s) 68
Discussion and Summary 76
Effect of Cooling Rate 76
Diffusion Controlled Transformation ($\beta \rightarrow \alpha + \beta$) 76
Diffusionless Transformations ($\beta \rightarrow \alpha_m$ and $\beta \rightarrow \alpha'$) 78
Primary and Secondary Heat Treatment 79
Summary 81

Chapter 4: As-Deposited Microstructure Characterization 83

Experiment 83
Results 87
The Characteristic Layer 87
Microstructure of the Transient Layers 98
Hardness Measurements 102
Composition Measurements 103
EBSD Analyses 106
Discussion 111
Beta Grains 111
Characteristic Layer 111
Nominal Microstructure (Graded Basketweave-α) 111
Layer Bands (Colony-α) 112
Transient Layers 115

Microstructure Evolution Path 116
Microstructure-Property Effects 118
Conclusion 118

Chapter 5: Heat Treatment of LMD Ti-6Al-4V Deposits 121

Introduction and Review of α+β Heat Treatments (Ref.[24]) 121
Experiment 123
Results 123
Summary 126

Chapter 6: Thermal Model 128

Original Thermal Model Description 128
Revisions to Original Thermal Model 132
Verification of the Thermal Model with LENS Experimental Data 132
Mesh Refinement 134
Volumetric Heat Sources 136
Volumetric Heat Source Results for LENS 140
Results 141
Calibration of Input Parameters for LENS 141
Calibration of LaserFormed (LF) Ti-6Al-4V 143
Revised Thermal Model Description for LFv5o-005 146
LFv5o-005 Results 149
Discussion of LFv5o-005 Results 160
Maximum Temperature 160
Cooling Rate 163
Solidification 164
Thermal Model Summary 166
The Model 166
Temperature as a function of time 167
Maximum Temperature 168
Minimum Temperature 168
Heating Rate 169
Cooling Rate 169
Comparison with As-Deposited Microstructure 169

Chapter 7: Microstructure Modeling 170

Background Information on Microstructure Modeling 170

Nucleation and Growth 170
Dissolution 171
Additivity 171
Application of additivity to nucleation and growth 172
Dissolution 174
Computational Tools 175
Obtaining kinetic data and introducing the modeling equations 176
Phase equilibria 176
Reactions During Heating: Alpha Dissolution 179
Isothermal Heating 179
Continuous (Linear) Heating 187
Reactions During Cooling: Alpha Nucleation and Growth 190
Isothermal Cooling 190
Continuous Cooling 195
Modeling phase fraction evolution during heating and cooling 197
Summary of equations and parameters used in the phase fraction model 197
Application to generic linear heating and cooling cycles 198
Application to synchrotron experiments 199
Modeling alpha morphology evolution 201
Application of the phase fraction and morphology model to baseline microstructure experiments 206
Results 206
Discussion 207
Conclusions 208

Chapter 8: Coupling the Thermal and Microstructure Model 210

Introduction 210
Results 210
Modeling phase fraction evolution during LMD thermal cycles 210
Modeling morphology evolution during laser LMD thermal cycles 217
Discussion 222
Comparison of morphology model and as-deposited microstructure 223
Conclusion 226

Chapter 9: Conclusions and Future Work 228

Executive Summary 228
LMD processing of Ti-6Al-4V 228
Baseline microstructures in Ti-6Al-4V 228

As-deposited LMD Ti-6Al-4V microstructure 230
Stability of as-deposited LMD Ti-6Al-4V microstructure 231
Thermal modeling of LMD processes 231
Microstructure model development 232
Coupled thermal and microstructural modeling for LMD of Ti-6Al-4V 233
Conclusion 234
Future Work 235
In depth investigation of microstructure evolution during secondary heat treatments 235
Validation of a massive transformation in Ti-6Al-4V 236
Thermal model improvements 236
Microstructure model improvements 236
Process design for microstructure and property control 237
Chapter 10: Appendices 238
Selected Area Diffraction Indexing Procedure 239
Image Analysis of Last Three Layers 264
Thermal Properties of Ti-6Al-4V 267
Thermal Model Finite Difference Equations 269
Convection Heat Transfer Estimation in LMD Builds 274
Thermal Model Flow Chart 278
DiCTra Simulation Macro 279
Microstructure Model Code 282
Reference 288
Vita 297

List of Figures

Figure 1.1: Illustration of the direction of heat flow in multiple pass welding (a), early in a LMD single line build (b), later in the single line LMD build (c), and during the LMD block build (d). Heat flow for (a) and (b) is generally 2D; heat flow for (c) is 1D; for (d) is "one and half-D." 4

Figure 1.2: Schematic of a coupled process model for metal deposition processes, where thermal and microstructure models are used to control process conditions. Process model figure and microstructure model picture courtesy of AeroMet Corporation. 6

Figure 2.1: Pseudo-binary phase diagram showing the phase variation with vanadium composition (calculated with ThermoCalc). The alloy composition is Ti - 6Al - 3.99V - 0.25Fe - 0.203O - 0.021C - 0.013N 10

Figure 2.2: Schematic of primary heat treatment above the beta transus illustrating complete dissolution of alpha to beta (AB), followed by cooling at different rates to produce martensitic-alpha α' (CD), massive alpha α_m (CE)and primary-alpha α_P and retained beta (CF). 12

Figure 2.3: Schematic of secondary heat treatment confined to a maximum temperature below the beta transus resulting in dissolution of primary-alpha α_P to beta during heating (GH) and subsequent nucleation and growth of secondary-alpha α_S from the dissolved α_P during cooling (IJ). The final microstructure consists of $\alpha_P + \alpha_S + \beta$. 13

Figure 2.4: Schematic illustrating the variation of vanadium composition during the growth of an alpha particle upon cooling assuming local equilibrium at the α/β interface. 15

Figure 2.5: Schematic illustrating the sequence of diffusion controlled phase transformation events occurring during continuous cooling of Ti-6Al-4V through the beta transus. Transformation start curves for allotriomorphic or grain boundary alpha and intragranular alpha are shown. (a) A single beta grain is shown in gray. (b) the first alpha to form is allotriomorphic Widmanstätten alpha at the beta grain boundaries. (c) alpha continues to grow along the beta grain boundaries. (d) primary-alpha begins to nucleate and grow first at the grain boundary alpha as colonies of primary-alpha sideplates and finally with increased undercooling (e), primary-alpha nucleates within the remaining beta in a basketweave morphology. 16

Figure 2.6: BSE micrograph showing the grain boundary alpha (α_{GB}) and primary-alpha (α_P) colony morphologies that form via a diffusion controlled transformation during cooling through the beta transus. The white contrast is the beta phase and the gray contrast is alpha. 17

Figure 2.7: BSE micrograph showing grain boundary (α_{GB}) and primary-alpha (α_P) – colony and basketweave morphologies that form via a diffusion controlled transformation upon cooling through the beta transus. The white contrast is beta and the dark contrast is alpha. 18

Figure 2.8: An example micrograph of martensitic-alpha (α') in Ti-6Al-4V resulting from very rapid cooling rates from above the beta transus. 21

Figure 2.9: Quantitative illustration of the composition profile changes during diffusion controlled alpha dissolution during isothermal (1123K) heat experiments as calculated using numerical diffusion simulation software (DiCTra). The orientation of the alpha and beta phases is shown in the diagram at the top of the plot. .22

Figure 2.10: BSE micrographs illustrating primary- (α_P) and secondary-alpha (α_S) formation during a heat treatment in the two phase field followed by (a) quenching and (b) moderate cooling at 3.2K/s to transform $\beta \rightarrow \alpha_S + \beta$, followed by quenching. Upon quenching, any beta present transforms to alpha-martensite (α'). [Courtesy of S.L. Semiatin, Ref.[39]] 24

Figure 2.11: Phase Transformations possible during LMD of Ti-6Al-4V 26

Figure 2.12: Calculated and experimental phase equilibria in Ti-6Al-4V showing the equilibrium alpha and beta phase fraction illustrating the dissolution temperature T_{DISS}. Experimental data from ternary isothermal sections are also shown (Ref. [62]). Below T_{DISS} the experimental phase fraction remains constant. 27

Figure 3.1: Optical micrographs of as-received (a) and normalized (b-d) microstructures of Ti-6Al-4V samples used in baseline microstructure and thermal simulation experiments. (a) As-received microstructure showing equiaxed alpha grains outlined in beta. Normalized samples showing large prior beta grains (b), and a large fraction of grain boundary nucleated alpha and primary-alpha colonies (c,d). 31

Figure 3.2: A Ti-6Al-4V sample being resistively heated in a Gleeble 1500 thermomechanical simulator. 33

Figure 3.3: Macrostructure of primary (a, T=1373 K) and secondary (b, T = 1198 K) samples cooled at 0.6 K/s. The primary heat treatment produced large colonies primary-alpha, while the addition of the secondary heat treatment produced smaller, secondary-alpha intragranular colonies. 38

Figure 3.4: Optical microstructure of primary (T=1373 K) samples cooled at 0.6 K/s. The primary heat treatment produced large mixture of basketweave (a, b, c) and colony (b, d) primary-alpha. 39

Figure 3.5: Optical microstructure after the secondary heat treatment (T = 1198 K, 0.6K/s) consisting of a mixture of (a) grain boundary nucleated primary-alpha (α_P) colonies and (b) intragranularly nucleated secondary alpha (α_S) colonies. In (a) α_{GB} is indicated by arrows. 40

Figure 3.6: BSE micrographs of primary samples cooled at 0.6 K/s. The microstructure consists of (a) basketweave α_P and (b) intragranularly nucleated α_P colonies with vanadium clearly partitioning to the beta phase. .41

Figure 3.7: BSE micrographs of secondary samples cooled at 0.6 K/s. The microstructure consists of (a-b) α_P and α_S colonies with vanadium clearly partitioning to the beta phase. 41

Figure 3.8: EBSD analysis of the primary heat treatment, 0.6K/s cooling rate. A IQ map (a) showing the microstructure analyzed and (b)a phase map showing the locations where the beta phase was detected in this sample. The beta phase fraction is 0.1%. [BL_01_01_Scan_3] 42

Figure 3.9: EBSD analysis of the primary heat treatment, 0.6K/s cooling rate. (a) Boundary misorientation and (b) an alpha inverse pole figure map. [BL_01_01_Scan_3] 44

Figure 3.10: EBSD analysis of the secondary heat treatment, 0.6K/s cooling rate. An IQ map (a) showing the microstructure analyzed with two different prior beta grains highlighted. A phase map (b) showing the locations where the beta phase was detected in this sample. The beta phase fraction is 0.5%. [BL_01_02_Scan_3] 45

Figure 3.11: EBSD analysis of the secondary heat treatment, 0.6K/s cooling rate. (a) Boundary misorientation and (b) an alpha inverse pole figure map. [BL_01_02_Scan_3] 46

Figure 3.12: TEM bright field and corresponding indexed diffraction pattern from the secondary heat-treated sample cooled at 0.6K/s. (a) BF, alpha colonies (10kx, A02233); (b)SAD, (460mm, A02235) indexed as B=[2 2 -4 3] α-Ti; (c) BF example of the interface between two alpha grains (71kx, A02237) which contains the titanium hydride interface and retained parent β phases. The diffraction pattern (d) obtained from (c) was not able to be indexed as alpha, beta, or the interface phase (FCC, a0=4.45Å). 47

Figure 3.13: Secondary heat-treated sample cooled at 0.6K/s. (a) TEM bright field image (25.5kx, A02412) of two grains within an alpha colony and (b) a plot of the composition versus distance as measured using EDS in microprobe mode across these grains starting with the beta phase in the upper left and moving towards the bottom right corner. (c-d) examples of EDS spectra showing a (c) good fit between the measured and fitted spectra and (d) poor fit between measured and modeled spectra. The spectra is blue, modeled spectra is green, and the residual is yellow. 49

Figure 3.14: Optical microstructure of primary (a,b; T=1373 K) and secondary (c,d; T=1198 K) samples cooled at 10 K/s. The primary microstructure (a,b) is dominated by basketweave α_P with small amounts of colony α_P located at the grain boundaries and intragranularly. The secondary microstructure (c,d) consists of some retained colony α_P at the grain boundary with the majority of the prior beta grains containing basketweave-alpha where α_P and α_S are indistinguishable. 50

Figure 3.15: BSE micrographs of primary samples cooled at 10 K/s. The microstructure consists of (a) prior-beta grain boundary (highlighted) nucleated colonies of α_P with the grain boundary decorated in α_{GB} and (b) intragranular nucleated basketweave α. Again, vanadium partitions to the beta phase 51

Figure 3.16: BSE micrographs of secondary samples cooled at 10 K/s, viewed in BSE mode. The microstructure consists of (a-b) colonies of α and single alpha grains nucleating from prior beta grain boundaries, and (c-d) basketweave alpha. In both types of morphologies, vanadium clearly partitions to the beta phase. In the higher magnification micrographs (b, d), fine structure consisting of primary and secondary alpha outlined in beta is revealed. 52

Figure 3.17: High magnification microstructure of secondary heat treated samples cooled at 10 K/s, viewed in BSE mode. The microstructure consists of primary and secondary nucleated alpha phase, with the fine secondary phase grains appearing between primary α laths. 53

Figure 3.18: EBSD analysis of the primary heat treatment, 10K/s cooling rate. A IQ map (a) showing the microstructure analyzed and (b)a phase map showing the locations where the beta phase was detected in this sample. The beta phase fraction is 0.2%. [BL_02_01_Scan_3] 53

Figure 3.19: EBSD analysis of the primary heat treatment, 10K/s cooling rate. (a) Boundary misorientation and (b) an alpha inverse pole figure map. [BL_02_01_Scan_3] 54

Figure 3.20: EBSD analysis of the secondary heat treatment, 0.6K/s cooling rate. A IQ map (a,c) showing the microstructure analyzed and (b,d) phase map showing the locations where the beta phase was detected in this sample. The beta phase fraction in (b) is 2.1% and (d) is 1.1%. Images (c,d) are from the highlighted region in (a). [(a,b): BL_02_02_Scan_1] [(c,d): BL_02_02_Scan_2] 55

Figure 3.21: EBSD analysis of the secondary heat treatment, 0.6K/s cooling rate. A IQ map (a,c) showing the microstructure analyzed and (b,d) phase map showing the locations where the beta phase was detected in this sample. The beta phase fraction in (b) is 2.1% and (d) is 1.1%. Images (c,d) are from the highlighted region in (a). [(a,b): BL_02_02_Scan_1] [(c,d): BL_02_02_Scan_2] 57

Figure 3.22: TEM (a) bright field and (b) dark field images (13kx, A02401, A02402) and (c) corresponding indexed SAD pattern (460mm, A02399) from the primary heat-treated sample cooled at 10K/s. (a-b) colony of alpha phase indexed (c) as α-Ti with B=[1-1 0 1]. The (1 1 -2 0) reflection is used to form the dark field image in (b). 58

Figure 3.23: TEM bright field and corresponding indexed diffraction pattern from the primary heat-treated sample cooled at 10K/s. (a) BF (210kx, A02405) interface between two alpha grains, with both alpha and beta planes diffracting; (b) SAD pattern (460mm, A02406) indexed as B=[0 0 0 1] α-Ti and B=[0 1 1] Ti-β. 59

Figure 3.24: Primary heat-treated sample cooled at 10K/s. (a) TEM bright field image (13kx A02407) of several alpha grains of a single colony and (b) results of EDS measurements made across two alpha grains (Spots 1-10). The average composition of spots 10-13 measured from a beta grain was Ti – 4.0Al – 15.1V – 1.2 Fe wt.%. 59

Figure 3.25: TEM bright field and corresponding indexed diffraction patterns from the secondary heat-treated sample cooled at 10K/s. (a) BF (6.9kx, A02238)primary ("P") and secondary ("S") alpha grains, (b) BF (22kx, A02239) Beta phase and interface phase(TiH_x) between two secondary alpha grains; (c) BF (25.5kx, A02242) irregular region of β phase; (d) SAD pattern for the micrographs (460mm A02240), indexed as B=[001] β-Ti; 60

Figure 3.26: Optical microstructure of primary samples cooled at 94 K/s. The microstructure consists of (a-c) intragranular α′ and (d) possibly grain boundary nucleated - α_m with intragranular α'. 62

Figure 3.27: BSE micrographs of primary heat treated samples cooled at 94 K/s, viewed in BSE mode. (a-b) a prior beta grain boundary (highlighted) and (c-d) intragranular mixed α′ and α_m has formed. The lack of atomic number contrast is due to negligible partitioning of beta stabilizers during rapid cooling. 63

Figure 3.28: EBSD analysis of the primary heat treatment, 93K/s cooling rate. A IQ map (a) showing the microstructure analyzed with a region of a prior beta grain boundary and (b) a phase map showing the locations where the beta phase was detected in this sample. The beta phase fraction is 0.3%. [BL_03_01_Scan_3] 64

Figure 3.29: EBSD analysis of the primary heat treatment, 93K/s cooling rate. (a) Boundary misorientation and (b) an alpha inverse pole figure map. [BL_03_01_Scan_3] 65

Figure 3.30: TEM bright field and corresponding indexed diffraction patterns from the primary heat-treated sample cooled at 94K/s. (a) BF (44kx, A02303) alpha grains; (b) BF (620kx, A02305) interface between neighboring alpha grains; (c) BF (44kx, A02305), strongly diffracting alpha grains indexed in (d) SAD (460mm, A02307), indexed as B=[3 0 -3 1] α-Ti.....66

Figure 3.31: TEM bright field and corresponding indexed diffraction patterns from the primary heat-treated sample cooled at 94K/s. (a) BF (25kx, A02309) and (b) (135kx, A02310) strongly diffraction regions of alpha showing the defects (stacking faults); (c) SAD (460mm, A02311), indexed as B=[0 0 0 1] α-Ti. 67

Figure 3.32: Optical microstructure after the primary heat treatment (T = 1198 K) and water quenching producing nominal cooling rates of (a) 3400 and (b) 6800 K/s. The microstructure consists primarily of (a, b) α′ with (a) apparent α_m at prior beta grain boundaries. The prior-beta grain boundary is highlighted in (a). 68

Figure 3.33: High magnification microstructure of primary heat treated samples cooled at 6790 K/s, viewed in BSE mode. The microstructure consists of needles of α′ with very little segregation of alloying elements. ..69

Figure 3.34: EBSD analysis of the primary heat treatment, ~3400K/s cooling rate. A IQ map (a) showing the microstructure analyzed with a region of massive-alpha located at a prior beta grain boundary and (b)a phase map showing the locations where the beta phase was detected in this sample. The beta phase fraction is 1.4% a large portion of that fraction from several scratches on the sample. [BL_04_01_2_Scan_3CC].....70

Figure 3.35: EBSD analysis of the primary heat treatment, ~3400K/s cooling rate. (a) Boundary misorientation and (b) an alpha inverse pole figure map. [BL_04_01_2_Scan_3CC] 71

Figure 3.36: EBSD analysis of the primary heat treatment, ~3400K/s cooling rate. A IQ map (a) showing the microstructure analyzed with a region of massive-alpha located at a prior beta grain boundary and (b)a phase map showing the locations where the beta phase was detected in this sample. The beta phase fraction is 6.7%. [BL_04_01_2_Scan_3AA].....72

Figure 3.37: EBSD analysis of the primary heat treatment, ~3400K/s cooling rate. (a) Boundary misorientation and (b) an alpha inverse pole figure map. [BL_04_01_2_Scan_3AA].....73

Figure 3.38: TEM bright field micrographs of the α′ morphology from the primary heat-treated sample quenched at 3400K/s. (a) BF (6.9kx, A02376); (b) BF (6.9kx, A02376); (c) BF (25.5kx, A02361); (d) BF (25.5 kx A02362). 74

Figure 3.39: TEM bright field micrographs of the α′ morphology from the primary heat-treated sample quenched at 3400K/s. (a) BF (25.5 kx A02372)and (b) BF (210kx, A02374): stacking faults; (c) BF (25.5 kx A02368) and (d) BF (210 kx A02370) dislocations.....75

Figure 3.40: TEM bright field micrographs of the α′ morphology and indexed diffraction patterns from the primary heat-treated sample quenched at 3400K/s. (a) BF (55kx A02313) and (b) corresponding SAD (460mm, A02312) indexed as B=[5 -4 -1 6] α-Ti and B=[1 1 1] β-Ti; (c) BF (71kx A02366) and (d) corresponding SAD (460mm, A02367) indexed as B=[1 1 -2 1] α-Ti with double diffraction spots labeled with "X". 76

Figure 3.41: Summary of the effect of cooling rate on different aspects of the beta decomposition process.....81

Figure 4.1: Single line build consisting of 18 layers of Ti-6Al-4V laser deposited onto a substrate of the same material. Laser motion is in the +x direction and layers are added in the +z direction.....84

Figure 4.2: As received profile of a Ti-6Al-4V laser deposit showing the columnar prior beta grains and a periodic banding (layer bands, "LB") at every layer except the last three.....87

Figure 4.3: (a) Optical macrograph of the last 5 deposited layers from the centerline (y) of the as-deposited materials. The macrograph shows the "transient" and "characteristic" layers, with layer bands indicated by arrows. (b-c) backscattered electron micrographs of two regions within the deposit. In the BSE micrographs beta and alpha regions appear white and gray, respectively. In (b), a colony-alpha morphology typical of the layer band is shown. In (c), a basketweave-alpha morphology typical of the

material between layer bands is shown. The layer band and nominal material form a characteristic layer that is repeated during processing. 89

Figure 4.4: TEM (a) BF image, (c) CDF image, and (b,d) corresponding SAD patterns from the bottom the characteristic layer. (a) BF image of the microstructure containing alpha grains, (b)SAD pattern indexed as B=$[1\ 1\ -2\ 3]_{\alpha}$. (c) CDF image of the α/β interface using the $[0\ 1\ 1]_{\beta}$ reflection in (d). (d) SAD pattern indexed as B=$[3\ 1\ -1]_{\beta}$. 91

Figure 4.5: TEM bright-field images (a,b) and SAD pattern (c) from the middle of the characteristic layer. (a) BF image of the microstructure showing a typical morphology containing alpha grains. (b) BF image showing α_{GB} running vertically with α_P nucleating from one side (β_1). The α_P nucleating from the other beta grain (β_2) does not have the same orientation. (c)SAD pattern indexed as B=[1 1 -2 0]-alpha (diffracting conditions for b) 93

Figure 4.6: TEM bright-field images (a,b), and SAD pattern (c) from material just below the layer band. (a) BF image of the microstructure containing alpha grains. (b) BF image of interface between alpha grains for the diffraction conditions (c) shown in the B=$[100]_{\beta}$ SAD pattern. 95

Figure 4.7: TEM (a) BF image, (c) CDF image, and (b,d) corresponding SAD patterns from layer band. (a) BF image of the microstructure containing alpha grains, (b)SAD pattern indexed as B=$[1\ 1\ -2\ 0]_{\alpha}$. (c) CDF image of the α/β interface using the $[1\ -1\ 0]_{\beta}$ reflection in the (d) B=$[1\ 1\ 0]_{\beta}$ SAD pattern. 97

Figure 4.8: Macrograph of the last 5 layers to be deposited illustrating the lack of layer bands in the last three layers deposited. The morphology for regions exhibiting microstructural contrast are labeled. 99

Figure 4.9: Micrographs from the last three layers to be deposited. Regions from the middle of: (a) L16 (n+1) showing fine basketweave and fine packet colony alpha, (b) L17 (n+2) showing fine packet-colonies of alpha with some areas of fine basketweave alpha, and (c) L18 (n+3) exhibiting predominantly fine packet-colonies of alpha. 100

Figure 4.10: Movie of the BSE images taken from the last three layers of the deposit compared with the as-deposited macro structure. (QuickTime, 26.9MB) 101

Figure 4.11: Hardness map over a three layer area with approximate locations of the layer bands indicated. Measurements were made at 100μm intervals. The histogram is also shown, with the average hardness being 366 HV 103

Figure 4.12: (a) Composition profile for the 8.1 mm long traverse that crosses three layer bands. The positions of the layer bands, indicated by the dashed lines, are approximate. (b) Composition profile of the central 9.9 mm long traverse measured from L16 and L17 that does not cross any layer band. The average composition in weight percent is (a) 90.54 Ti, 5.58 Al, and 2.83 V and (b) 88.47 Ti, 5.77 Al, and 2.28 V. 105

Figure 4.13: Alpha and beta phase compositions measured using EDS on samples located within the characteristic layer. The top of the characteristic layer is defined by the layer band and the bottom is "just above the previous layer band". 106

Figure 4.14: EBSD pattern quality maps of the layer band region at (a) "low" and (b-d) "high" resolution. Red pixels indicate the locations where beta was detected (1.8%-β and >1%-β in low and high magnification images). The locations of the high magnification images are for illustrative purposes (high magnification analyses are from different location in the sample). 107

Figure 4.15: EBSD α-IPF maps of the layer band region at (a) "low" and (b-d) "high" magnification. Different colors represent different crystallographic directions of the α grains according to the unit triangle shown above (a). Black pixels are beta phase. The locations of the high magnification images are for illustrative purposes (high mag images are from different location in the sample). 109

Figure 4.16: EBSD Grain Boundary misorientation maps of the layer band region at (a) "low" and (b-d) "high" magnification. Adjacent boundaries with a misorientation >15° are blue. `The locations of the low magnification images are for illustrative purposes (low mag images are from different location in the sample) 110

Figure 4.17: JMatPro-Calculated equilibrium composition of the beta phase for the nominal bulk alloy composition in the as-received deposit. Data points represent compositions from isothermal ternary sections for a nominal Ti-6Al-4V alloy Ref. [62]. 115

Figure 4.18: Schematic evolution of different microstructure morphologies in the observed Ti-6Al-4V deposit. The positions of the maximum depth of melting and beta heating are approximate. Arrows are added to these lines to indicate the position is below layer n. The transient and characteristic layers are shown for the deposition of layer n+4 on layer n. 117

Figure 5.1: Average alpha lath width as a function of cooling rate following a 2-hour solution treatment at 1186K and a 4-hour aging treatment at 811K....122

Figure 5.2: Optical microstructures following STA heat treatment illustrating the (a) nominal basketweave-α and (b) layer band colony-α microstructure morphologies retained....123

Figure 5.3: Optical macrographs of the (a) as-deposited and (b) beta heat treated laser deposited Ti-6Al-4V material. The y-z plane is shown, where z is the direction of added layers and x is the direction of laser travel. (a) Shows the inhomogeneous macrostructure consisting of columnar prior beta grains and a periodic horizontal banding termed layer bands ("LB"). (b) Shows the homogenized macrostructure consisting of equiaxed prior beta grains containing primary-alpha colonies. 124

Figure 5.4: Comparison of as-deposited (a-b) and beta heat treated (c-d) microstructures in laser deposited Ti-6Al-4V. The layer band colony-alpha morphology is shown in (a) and the nominal basketweave alpha morphology is shown in (b). In the beta heat treated microstructures, (a) and (c) are from regions where the layer band and nominal microstructure once existed. 125

Figure 6.1: Schematic of the single line build modeled geometry (left), mesh and applied boundary conditions (right). The shaded region corresponds to the modeled 2-dimensional geometry for an 8-layer model. The nodal mesh has nodes spaced equally at 0.5 mm. The substrate (SUB) is 7 mm thick (z) and each layer (L1, through L8) are 5 mm in height (z). 130

Figure 6.2: Schematic illustrating the original method used to simulate additive layer deposition for a two-layer single line build. The original method assumes that a new layer initially has a constant temperature when added to the deposit....132

Figure 6.3: Comparison of experimental, Rosenthal solution, and Modeled (small and large substrates) results for a LENS 316 stainless steel single line build. 134

Figure 6.4: Refined mesh of LENS deposits used in revised thermal model. Each dot represents a computation point. The grid spacing varies in the substrate in both y and z while remaining constant in the deposited layers, of which 2 are shown here. 136

Figure 6.5: Geometry of the single ($c_1 = c_2$) or double ($c_1 \neq c_2$) ellipsoidal heat sources. Laser travel is in the $x = c_1 - v_{laser} * t$ direction. 138

Figure 6.6: Comparison of the ellipsoidal ($c_1 = c_2 = 1$) and double ellipsoidal ($c_1 = 0.5$, $c_2 = 1.5$) volumetric heat sources at $y = z = 0$. All remaining coefficients are arbitrarily set equal to 1. 140

Figure 6.7: Comparison of Rosenthal, experimental, and modeled (with and without a volumetric heat source for a large substrate) LENS thermal cycles for 316 stainless steel. The modeled and experimental data are taken at the center (y, x) of a layer and at the substrate/first layer interface (z). 141

Figure 6.8: LENS calibration variables and results. The points indicated by a cross are the target experimental values for which the modeled values are compared....142

Figure 6.9: Results of LF Ti-6Al-4V thermal model calibration, showing the affect of beam variables on FZ and HAZ dimensions. The target value is bounded by an ellipse of ± 1 standard deviation. 145

Figure 6.10: Schematic of the deposit geometry and locations of the surface boundary conditions. Node positions (small dots) are shown for the substrate and first deposited layer. 147

Figure 6.11: Comparison of as-deposited and calculated fusion- (FZ) and heat affected- (HAZ) zones using a macrograph from the as-deposited material. The isotherm labels (temperature) are given in units of Kelvin. 150

Figure 6.12: A movie of the two-dimensional (y-z) temperature distribution with time during the deposition of eight layers of material using parameter set LFv50-005. Contours (isotherms) for temperatures of interest are shown. 151

Figure 6.13: Temperature versus time plotted for two positions along the centerline (y=0mm) of the deposit in the first and fifth layers. 153

Figure 6.14: Thermal profiles of the X-Z plane at the centerline of the deposit (y = 0) for the first 40 seconds (corresponding to 101.6 mm of laser travel) of each layer deposition (L1 – L8). The x-position is calculated by multiplying the elapsed time by the laser scan-velocity. The applied energy distribution at (y = 0, z = 21mm) as a function of x-position (time) is illustrated for the first layer deposition (L1). 154

Figure 6.15: Two-dimensional image map of the maximum temperature experienced in the deposit during each layer deposition for parameter set LFv5o-005. Horizontal gridlines indicate the position of each layer, while the isotherms indicate important phase transformation temperatures. 155

Figure 6.16: Predicted sizes of different isotherms for each layer deposition in the depth (from the top of a deposited layer, [*z*]), width (from the centerline, [*y*]), and length, [*x*]. 157

Figure 6.17: Two-dimensional image map of the minimum temperature experienced in the deposit during each layer deposition for parameter set LFv5o-005. Horizontal gridlines indicate the position of each layer. 158

Figure 6.18: Two-dimensional image map of the maximum heating rate experienced in the deposit during each layer deposition for parameter set LFv5o-005. The heating rate is nominally measured over the temperature range $T_{beta} \pm 100K$. Horizontal gridlines indicate the position of each layer. 159

Figure 6.19: Two-dimensional image map of the absolute maximum cooling rate experienced in the deposit during each layer deposition for parameter set LFv5o-005. Two sets of contours are plotted, one for critical cooling rates corresponding to equilibrium and non-equilibrium beta-to-alpha transformation products[28] and maximum temperatures which also determine if these products are possible. After three layers are added, cooling rates are less than 20 K/s. 160

Figure 6.20: Comparison of modeled maximum temperature with the as-deposited macrostructure. The modeled data is taken after the eighth layer addition. The as-deposited macrostructure consists of the last 6 layers added to the deposit, with the layer n representing the characteristic, repeated layer. Layers n+1 through n+3 represent a transient layer. The locations of the characteristic and transient layers are indicated by boxes on the macrograph and modeled data. 162

Figure 6.21: Comparison of the modeled maximum cooling rate with the as-deposited macrostructure, highlighting the transient and characteristic layers of modeled and as-deposited material. 163

Figure 6.22: Comparison of expected beta grain growth directions from the modeled temperature data and as-deposited macrostructure (y-z plane). The arrows indicate the direction of beta growth, which is normal to the liquidus isotherm. 165

Figure 6.23: Schematic of solidification process and the shape of the melt pool required to produce prior beta grains oriented in the direction observed in the as-deposited material. The melt pool is indicated by dashed lines, and the direction of beta grain growth by the arrows. Solidification occurring from the top of the bead will occur if sufficient surface cooling is provided in the form of a shielding gas. 166

Figure 7.1: TTT diagram computed using the kinetics provided by Malinov (Ref.[27]). Isothermal transformation (extent of reaction, ζ_α) curves are shown for 1, 50 and 99 percent, and linear cooling curves (dashed) are shown for the range of Malinov's experiments (0.083 and 0.83 K/s). 174

Figure 7.2: Computed beta fraction as a function of temperature for different linear heating rates (in K/s on the plot). The JMAK kinetic parameters are derived by Elmer *et al*. (Ref. [123]) 175

Figure 7.3: Calculated equilibrium phase fraction for the two-phase alpha (HCP) and beta (BCC) phase field in the as-deposited material. Experimental data is from ternary isothermal sections in Ref. [62]. 177

Figure 7.4: Equilibrium phase fraction curves used in microstructure modeling. The beta transus and dissolution temperatures are 1272.9 and 981.2 K, respectively. At room temperature, the alloy contains 91%-α + 9%-β. Experimental values from Margolin and Farrar, Ref. [62]. 179

Figure 7.5: Diffusion cell used in DiCTra dissolution simulations, with the half-thicknesses of the phases shown. 180

Figure 7.6: Beta interface position and extent of reaction plotted as a function of time for the isothermal DiCTra heating simulations. 181

Figure 7.7: Beta interface and extent of reaction plotted as a function of the root of time. The initial linear portion of the curves is used to determine the slope, which is the isothermal parabolic growth rate. 182

Figure 7.8: Beta interface growth rate, scaled using the steady state beta interface position, plotted as a function of isothermal reaction temperature, with the fitted equation shown, extended to the true beta transus of 1273K. 183

Figure 7.9: Beta fraction evolution determined from Eq. [7.5] as a function of time and (a) isothermal temperature of 1250 K and (b) as a function of temperature. The equilibrium fraction beta at 1250 and 300K are also shown in (a). 185

Figure 7.10: Comparison of DiCTra and dissolution model (Eq. [7.8]) calculations, plotting extent of isothermal alpha dissolution reaction as a function of time for several isothermal temperatures. DiCTra simulations were not performed for 1223 and 1273K. 186

Figure 7.11: Heating TTT diagram showing the extent of the alpha to beta dissolution reaction for a system initially containing a negligible amount of beta. 187

Figure 7.12: Schematic illustrating the evolution reaction during heating ($T_1<T_2<T_3$). Equivalent and actual times are shown on the left and right independent variable axes. 188

Figure 7.13: Modeled evolution of beta fraction during continuous heating. 189

Figure 7.14: Comparison in the dissolution model and experimentally determined beta transus temperatures under different heating rates. Experimental data is from Elmer[123] and Ivasishin[22,58]. 190

Figure 7.15: JMatPro calculated TTT diagrams for primary-alpha nucleation and growth. Curves for grain boundary (GB) nucleated α_{GB} and colony α_P and intragranularly (IG) nucleated basketweave-α_P are shown. 192

Figure 7.16: Kinetic parameter describing alpha nucleation and growth, derived from JMatPro TTT diagrams for the AR-MID composition. 193

Figure 7.17: Modeled TTT diagrams using Eq. [7.12] and Figure 7.16 along with the JMatPro calculated curves for grain boundary (α_{GB} and colony α_P) and intragranular (basketweave-α_P) nucleation and growth in the alloy of AR-MID composition. 194

Figure 7.18: Comparison of modeled TTT start curves with experimental and modeled literature values.[27,29,138,139] 195

Figure 7.19: Modeled continuous cooling curves for various cooling rates. The equilibrium alpha fraction is also indicated. The M_S temperature is from Ref.[140]. 196

Figure 7.20: Alpha fraction plotted as a function of temperature (column 1) and time (column 2) for different heating and cooling rates and peak temperatures as indicated. The equilibrium fraction is shown as a dashed curve in all figures. 199

Figure 7.21: Experimental[141] data measured during time resolved x-ray diffraction experiments compared with data obtained from the phase fraction model and equilibrium phase diagram. 200

Figure 7.22: Schematic illustrating the alpha phase fraction (f_α), colony- ($f_{C\text{-}\alpha}$) and basketweave- ($f_{BW\text{-}\alpha}$) alpha evolution during a primary and secondary heat treatment. 202

Figure 7.23: Modeling the phase fraction and morphology evolution in 0.6 K/s cooling rate baseline microstructure experiment. From top to bottom, thermal cycles, alpha phase fraction (f_α), and fraction colony-α ($f_{C\text{-}\alpha}$). 206

Figure 7.24: Modeling the phase fraction and morphology evolution in 10 K/s cooling rate baseline microstructure experiment. From top to bottom, thermal cycles, alpha phase fraction (f_α), and fraction colony-α ($f_{C\text{-}\alpha}$). 207

Figure 8.1: Temperature and alpha phase fraction evolution with time at two z positions along the centerline (y=0) of the deposit. The positions lie within a layer *n* and experience an additional three thermal cycles (*n+3*), with the *n+3* cycle causing the most variation in the phase fraction evolution path. Gaps in the phase fraction data near 400 and 500 seconds distinguish between 100%-β and 100%-liquid. 212

Figure 8.2: Comparison of modeled and equilibrium alpha fractions as a function of time at a constant position within the deposit. 100%beta and liquid are not distinguished in this plot. 213

Figure 8.3: Alpha phase fraction evolution mapped with z-position and time (independent variables) at constant y-position (centerline, y-0) in the deposit. Beta and liquid are differentiated by the color red and blank space. The fusion and heat affected zones are indicated for layer 4 (L4) and the characteristic layer is indicated for layers 6-8 (L6-L8). 214

Figure 8.4: 2D phase fraction evolution movie. Melting is indicated in the movie by the eroding of the layer. Horizontal gridlines represent the positions of each layer. (QuickTime, 107MB). 216

Figure 8.5: Screen captures from the movie in Figure 8.4 during the last layer deposition at (a) 12.8 and (b) 98.2 seconds after the deposition of the 8th layer. (a) occurs during solidification and (b) is at the completion of the pass. Melting is indicated in the movie by the eroding of the layer as indicated in (a). Horizontal gridlines represent the positions of each layer. 217

Figure 8.6: Colony-alpha ($f_{C\text{-}\alpha}$) evolution at three positions in the fourth layer. The evolution is shown during the deposition of four layers onto the fourth layer (*n* through *n+4*). Gaps in the colony-α fraction curves represent where the alpha phase fraction (f_α) equals zero. 218

Figure 8.7: 2D fraction colony-alpha ($f_{C\text{-}\alpha}$) evolution movie. Melting is indicated in the movie by the eroding of the layer as before. (QuickTime, 152MB). 220

Figure 8.8: The final morphology distribution after the deposition of the 8th layer (interpolated data, 10x resolution). 221

Figure 8.9: Comparison of 2D (y-z) cross sections from the morphology model (left) and as-deposited macrostructure (right). Equivalent regions in the model and as-deposited macrostructure are indicated. 224

Figure 8.10: Comparison of the microstructure within the characteristic layer of the morphology model and as-deposited material. 226

Figure 10.1: Image analysis results showing beta phase fraction, threshold correlation, and threshold value for images taken along the deposit's z-axis beginning (z=0) near the center of the 15th layer (L15) and ending at the top of the 18th layer (L18). Approximate locations of the 15th layer band and the intersection of layers 16 through 18 are indicated. 265

Figure 10.2: BSE micrographs representing the (a) best and (b) worst correlation values of the plot in Figure 10.1. Alpha is dark to medium gray, while beta is white. (a) is located in the fully developed 15th layer (layer *n*) while (b) is located at the interface of the 17th and 18th layer (*n+2* and *n+3*). 266

Figure 10.3: Plot of density as a function of temperature, after Eq.[10.1]; used in the thermal model. 267

Figure 10.4: Plot of thermal conductivity as a function of temperature, after Eq.[10.2]; used in the thermal model. 268

Figure 10.5: Plot of specific heat as a function of temperature, after Eq. [10.3]; used in the thermal model. 268

Figure 10.6: Finite difference control representation illustrating the local node numbering scheme and the location of the variables d_i and A_i. The control volume is indicated by the box. 270

Figure 10.7: Flow chart for the thermal model. 278

List of Tables

Table I: Characteristics of the Beta → Alpha + Beta Transformation 11

Table II: Coefficients for diffusion into beta titanium described by the equation $D(T) = D_0 \exp(-Q / (R\,T))$. Ref [39]. 14

Table III: Measured Cooling Rates and Microhardness Values of Ti-6Al-4V Baseline Microstructure Samples 37

Table IV: Summary of Quantitative Microprobe Analyses 84

Table V: Summary of As-Deposited Macro and Microstructure Measurements 90

Table VI: Summary of Bulk Composition Analyses Made From Different Locations Within the Deposit. [Weight Percent Element] 104

Table VII: Processing parameters used in experimental and modeled LENS comparisons. 133

Table VIII: Thermal model calibration ranges for AeroMet's LaserFormed Ti-6Al-4V 143

Table IX: Processing parameter set for LaserForming thermal model calibration. 144

Table X: Selected values from LF thermal model calibration data meeting the criteria in Figure 6.9 146

Table XI: Constant processing parameters used in the thermal model (Parameter Set LFv5o-005). 148

Table XII: Parameters used in Equation [6.12] to produce FZ and HAZ dimensions similar to those measured in the as received deposit[24]. (Parameter Set LFv5o-005). 149

Table XIII: Alloy Composition in Weight Percent from As-Deposited Material Used in Modeling Experiments 177

Table XIV: Phase amounts and composition for Ti-6Al-4V at 873K (From Ref. [62]) 178

Table XV: Summary of Equations Used to Model Alpha Dissolution and Growth During Non-Isothermal Conditions. 198

Table XVI: Morphology Model Criteria and Nomenclature 205

Table XVII: Summary of Implicit Finite Difference Equations for Different Geometries. 273

Nomenclature

Titanium Metallurgy

Symbol	Definition	Units
α	The alpha hexagonally close packed beta phase of titanium and its alloys. Stable below the beta transus	-
β	The body centered cubic beta phase of titanium and its alloys. Stable above the beta transus	-
$\alpha+\beta$	A two phase mixture, stable below the beta transus.	-
α_P	Primary-alpha, forms during cooling from a peak temperature above the beta transus.	-
α_S	Secondary-alpha; forms during cooling from a peak temperature below the beta transus.	-
α'	Martensitic-α	-
α_m	Massive-α	-
T_{VAP}	Vaporization temperature. For pure Ti, T_{VAP} = 3560K	K
T_{LIQ}	Liquidus temperature. For Ti-6Al-4V, T_{LIQ} = 1923K	K
T_{BETA}	Beta transus temperature. For Ti-6Al-4V, T_{BETA} = 1273K	K
T_{DISS}	Temperature where alpha begins to dissolve into beta. For Ti-6Al-4V, T_{DISS} = 981K	K
M_S	Martensite start temperature. For Ti-6Al-4V, M_S = 848K	K

LMD Terminology

Symbol	Definition	Units
x	Direction of laser travel.	m
y	Direction of the width of a layer.	m
z	Direction of layer addition.	m
SUB	Substrate. Layers are added to the substrate.	-
L1, L2,…,Ln	Layer Number. L1=first layer added, L2 = second layer added on top of L1	-
LB1, LB2,…,LBn	Layer Band number.	-
n, n+1, n+2…	A layer *n* and the deposition of one (*n+1*), two (*n+2*), etc. layers on top of layer *n*.	-

Thermal Model		
Symbol	**Definition**	**Units**
m	A global node number.	
$P, p+1$	Time steps.	
t	Real time.	s
Δt	Time increment. $\Delta t = t^{p+1}-t^{p}$.	s
$T(m,p)$	Temperature as a function of node position and time.	K
$k(T)$	Thermal conductivity as a function of temperature.	W/(m K)
$C_p(T)$	Specific heat as a function of temperature.	J/(kg K)
$\rho(T)$	Density as a function of temperature	kg/m^3
T_{laser}	In the original thermal model, the temperature of a newly deposited layer.	K
t_{dwell}	In the original thermal model, the time a newly deposited layer is held at $T_{laser.}$	S
l	Length of the part in the x-direction.	M
T_{melt}	In the original thermal model, the melt temperature of the alloy.	K
Δx	Finite thickness (x) of the two-dimensional area (y-z) being modeled.	M
v_{laser}	Scan velocity of the laser heat source in the +x direction.	m/s
T_{base}, T_{sub}	The temperature of the substrate.	K
t_{pass}	Time needed for the laser to deposit a single layer if moving at v_{laser}.	S
P	Beam power at target	W
$P(x,y)$	A surface heat flux due to laser irradiation	W
r_b	Beam radius	m
$Q(y,z,t)$	Three dimensional ellipsoidal distribution of heat	W
Q_0	Beam power	W
σ	Defines where the beam power is 5% of the Q_0 value, $\sigma = 2.99$	-
a	Beam radius in the y-direction for an ellipsoidal distribution of heat.	m
b	Beam radius in the z-direction for an ellipsoidal distribution of heat.	m
c	Beam radius in the x-direction for a single ellipsoidal distribution of heat.	m
c_1, c_2	Beam width in the x-direction in front (c_1) and behind (c_2) the center of beam for a double ellipsoidal distribution of heat.	m
f_1, f_2	Fraction of heat in front (f_1) and behind (f_2) the center of a beam for a double ellipsoidal distribution of heat.	-
α	The process efficiency, or amount of laser energy absorbed in the deposit.	-
Q_{melt}	Energy used to heat a volume of material to the melting point.	W

z_0	z-offset of the focal point of the laser beam (in the z-direction, thickness of a layer). z_0 = 0: beam focused on the top of the new layer	m
h_{sub}, $h_{surface}$	Convective heat transfer coefficient on the substrate and surface of the deposit	W/(m^2 K)
T_∞	Temperature of the convective cooling medium	K

Microstructure Model

Symbol	Definition	Units
ζ	Extent of reaction.	-
n	Geometric term describing the site of a reaction. Avrami exponent.	-
$k(T)$	Kinetic function describing a reaction (phase transformation)	s$^{1/n}$
t	Time	s
$f_{eq,\alpha}(T)$, $f_{eq,\beta}(T)$	The equilibrium phase fraction of alpha and beta, as a function of temperature.	-
B	Modeling plate growth, B is the plate half-thickness	M
$\alpha_{1,H}$	One-dimensional parabolic thickening rate on heating (H)	m/s$^{0.5}$
$B_{SS,\beta}(T)$	Steady state β-plate half-thickness at an isothermal temperature	M
$\alpha_{1,H,SS}(T)$	One-dimensional steady-state parabolic thickening rate on heating (H)	s$^{-0.5}$
f_α(t,T), f_β(t,T)	Alpha and beta phase fraction evolution with time and temperature	-
t^*	Equivalent time for an amount of material transformed at a temperature T_i to transform at temperature T_{i+1}	s
t_{crit}	Time for the extent of reaction to equal 1	s
$t^*_{D,i}$	Equivalent time during α dissolution (D) for a time step i.	s
$t^*_{G,i}$	Equivalent time during α growth (G) for a time step i.	s
$f_{\alpha,i}$	Phase fraction α at time step i.	-
T_i	Temperature at time step i.	K
$f_{C\text{-}\alpha}$	Fraction colony-α. Morphology fraction.	-
$f_{BW\text{-}\alpha}$	Fraction basketweave-α. Morphology fraction.	-
T_{IG}	Temperature below which colony-α ceases to form and intragranularly nucleated basketweave begins to form. T_{IG} = 1100K	K
Subscript FD	Final amount of a phase or morphology following dissolution. e.g. $f_{BW\text{-}\alpha,FD}$	-
Subscript FG	Final amount of a phase or morphology following growth. e.g. $f_{C\text{-}\alpha,FG}$	-

Chapter 1: Introduction

Laser Metal Deposition Processes

Laser Metal Deposition State of the Art

Laser metal deposition (LMD) processes have drawn much attention lately because of their ability to form small quantities of functional prototypes and structural parts at significantly reduced cost to the buyer.[1] Several commercialized LMD processes exist, including Laser Engineered Net Shaping (LENS*)[2], Directed Light Fabrication (DLF**)[3], and Laser Additive Manufacturing (LAM***).[4] All LMD processes are similar in that a three dimensional part in a CAD file is sliced into layers which in turn define laser scan trajectories. A high power laser is used to heat and melt metal powder, which solidifies to form a fully dense layer. The addition of multiple layers will produce a three dimensional fully dense part having a net or near-net shape. In the current work, the common titanium alloy, Ti-6Al-4V, is deposited to form a near net shape single line build using the LAM process, which employs an 18 kW CO_2 laser and can deposit material at a rate of 0.9 to 4.5 kg hr^{-1}.[1]

Early papers on the laser deposition of titanium primarily reported results from the initial development of these processes and to advocate these processes to industry. As a result, the papers mainly dealt with the initial measurements of material properties, the apparent quality of the parts produced, and the potential economic advantages of the process;[4-6] however, the evolution and understanding of microstructure was largely neglected.

Recently, Kobryn, *et al*.[7-9] have explored the effect of process parameters on the build characteristics (porosity, build height) and microstructural features (prior beta grain width) of laser deposited Ti-6Al-4V using the LENS process (0.5 – 1.2 kW Nd-YAG laser), and a process similar to LAM developed by the Applied Research Lab (Penn State, 14 kW CO_2 laser). These deposits were multilayer builds. Ti-6Al-4V is a common two-phase (HCP-α + BCC-β) heat-treatable alloy which forms with a variety of microstructures dependent upon the conditions employed upon cooling from the high temperature β form of the alloy. The use of the Nd:YAG

* LENS is a trademark of Sandia National Laboratory and the US Department of Energy
** DLF is a trademark of Los Alamos National Laboratory and the US Department of Energy
*** LAM is a trademark of AeroMet Corporation, Eden Prairie, MN

laser resulted in a fine Widmanstätten two-phase microstructure and discontinuous α at prior beta grain boundaries, indicating a rapid cooling rate. The microstructure of material deposited with the CO_2 laser had a coarser Widmanstätten morphology with continuous α at prior beta grains, indicating a slower cooling rate. Slow cooling rates will result from conditions of high incident energy (high power setting and low translation speed); conversely, low laser power and high velocity result in fast cooling rates. Layer bands, visible as periodic layers of differential optical contrast, were also observed in their results[7,9,10] and described by the authors as being due to a sudden change in the number of equiaxed α particles in the Nd:YAG builds, and due to a change in the coarseness of the Widmanstätten structure in the CO_2 builds. The authors associated the presence of the layer bands to dynamic variations in the heat affected zone with each new layer that is deposited. No further analysis or proof of this explanation was given. The layer band morphology has also been observed by Kelly *et al*.[11]. Goodwin *et al*.[12] who noted that with increased laser power, the entire microstructure attains the colony morphology characteristic of the layer band.

Microstructural evolution in laser metal deposition (LMD) builds is inherently complex. Without knowledge of the thermal history developed during the build process, analysis of the resultant microstructure becomes difficult. Recent research on understanding the microstructural evolution in LMD builds from a thermal standpoint has been performed on builds of H13 tool steel[13,14], P20 tool steel[15], and 316 stainless steel[16,17]. Investigation of H13 builds used experimental thermocouple data to obtain a thermal history at a given location within the build, and utilized equilibrium phase diagrams to describe the microstructural evolution in the deposit. The work performed on stainless steel has examined the shape and thermal profile of the laser induced melt pool and resulting solidification behavior. Vasinota, *et al*.[18] have also investigated the effect of process parameters on the solidification behavior in laser engineered net shaping (LENS) builds.

Limited work has been performed to understand the microstructural evolution in LMD Ti-6Al-4V processes through thermal modeling. Kobryn *et al*.[8,9] have performed focused experiments to deduce the microstructural evolution in LMD Ti-6Al-4V. To this end, single pass laser glazes (no metal deposition, just laser heating) and finite element method (FEM) simulations of single pass laser glazes were made at different levels of incident energy and the heat affected and fusion

zones of the experimental glazes compared with the thermal histories predicted from the FEM results. While the results of the thermal model are useful and interesting, they are not encompassing of LMD processes as they do not consider the deposition of multiple layers of material. The characteristics of the thermal profile and the microstructure will undoubtedly change as multiple layers are added.

Welding: Similarities and Differences to LMD

One of the obvious questions raised about this research is the similarity to work already completed in the modeling of welding, in particular multiple pass welding. In multiple pass welding, two pieces of metal are joined using multiple passes of the heat source with addition of material with each pass. The multiple passes are necessary to fill the gap between the two pieces or to create a fully penetrating weld when two thick pieces are being joined. As a result, the underlying material experiences a number of thermal cycles that can result in a complex microstructure, just as in LMD. It must be conceded that LMD and welding, specifically, multiple pass welding are similar for the first few passes of the laser in a single line build. The similarity is a result of the two dimensional heat flow (in the plane normal to the direction of laser motion) caused by the presence of the substrate or pieces to be joined (Figure 1.1a-b). However, as more layers are added in a single line build fashion (Figure 1.1c) heat flow becomes increasingly one-dimensional. For the deposition of multiple tracks and layers (Figure 1.1d) heat flow remains essentially two dimensional. Thus, in order to accurately determine microstructure, a new thermal model must be (and has been) developed to capture the additive nature, variation in heat flow dimension, and geometry inherent with LMD processes.

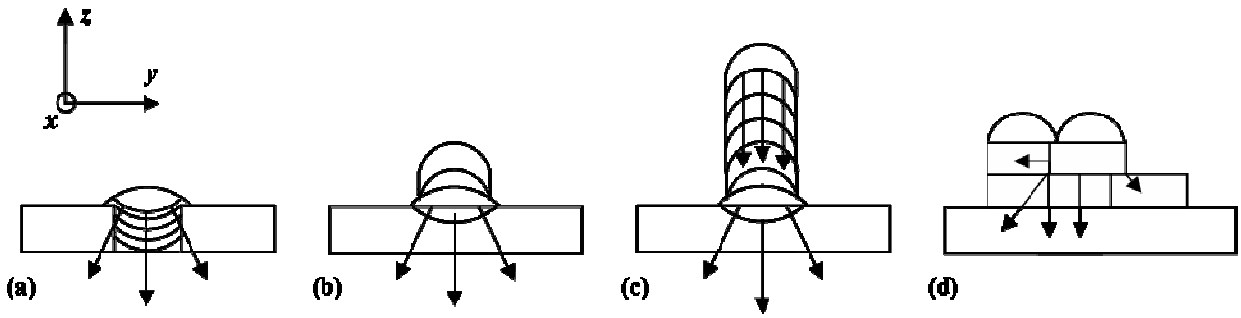

Figure 1.1: Illustration of the direction of heat flow in multiple pass welding (a), early in a LMD single line build (b), later in the single line LMD build (c), and during the LMD block build (d). Heat flow for (a) and (b) is generally 2D; heat flow for (c) is 1D; for (d) is "one and half-D."

The macrostructure of multiple pass weldements is similar to that observed in LMD of Ti-6Al-4V, namely the presence of columnar prior beta grains grown epitaxially from bead to bead.[19] The microstructure of single pass laser welded Ti-6Al-4V consists of diffusional and martensitic alpha as confirmed by optical and transmission electron microscopy.[20]

There has been some progress in modeling weld microstructures in titanium and its alloys. Shah, *et al.*[21,22] have modeled the thermal and microstructure behavior in single pass Ti-6Al-4V welds. The thermal model is based on the Rosenthal[23] point source solution and considers temperature independent thermal properties. The microstructure model considers the phase transformations occurring during a single thermal cycle on cooling from a peak temperature above the beta transus. Characteristic equations for each microstructural feature were integrated over the thermal cycle. Controlled simulation of the thermal cycle was performed using a thermal simulator (similar to Gleeble). The resultant microstructures of the thermal simulation experiments were relatively similar to those calculated, with some discrepancies noted in the beta grain size at high peak temperatures and the fraction of alpha phase. It should be noted that only colony alpha morphology was considered. Other forms and combinations of the alpha phase morphologies (colony + basketweave) were not considered.

Summary

The LMD process is still in its infancy. While much work has been performed to advocate the use of LMD to industry, little work has been performed to understand the evolution of microstructure. This understanding is necessary before further success of the process can be realized. LMD is similar to welding processes, in particular, multiple pass welding; however, differences arise in the heat transfer dimensionality when multiple layers are added to a build.

Here, heat flow become increasingly one dimensional, which actually simplifies the evolution of microstructure; however, if the build geometry changes to a block-type build, heat flow becomes increasingly two dimensional. Thus, the existing thermal models for welding are not sufficient to handle changes in geometry associated with LMD processes. While the description of microstructure evolution in Ti-6Al-4V is not directly related to geometry, it is related to the thermal cycling present in LMD. Therefore, the evolution of Ti-6Al-4V microstructures over multiple thermal cycles must be considered if such models are to be compatible with LMD processes.

Motivation and Goals

LMD processes have the potential to reduce the cost of short production runs or prototype parts, produce parts containing functionally graded or position sensitive microstructures, and in the future, see deployment in space-based processing. In order for any of these potential markets to be realized, understanding of the microstructural evolution during processing is a must. Trial and error experiments are one way to define optimized processing conditions, but these experiments can drive-up the cost of production to the buyer. Since LMD uses a heat source to fuse new layers to a deposit, microstructure is affected primarily by temperature. Thermal cycling can result in many different phase transformations taking place at different positions in the build, resulting in a complex microstructural development path. Knowing how microstructural evolution and process management interact creates an opportunity to control microstructure during a laser build process as a means to eliminate inhomogenieties in the microstructure, to predictively map microstructural variations, and/or to produce functionally-graded or position-optimized microstructures. Thus a process model can be envisioned that considers the temperature and its effect on microstructure, as shown in Figure 1.2. The proposed microstructure model could be extended to other processing techniques and materials, provided processing conditions (thermal history) and kinetic parameters describing the basic microstructure evolution are known.

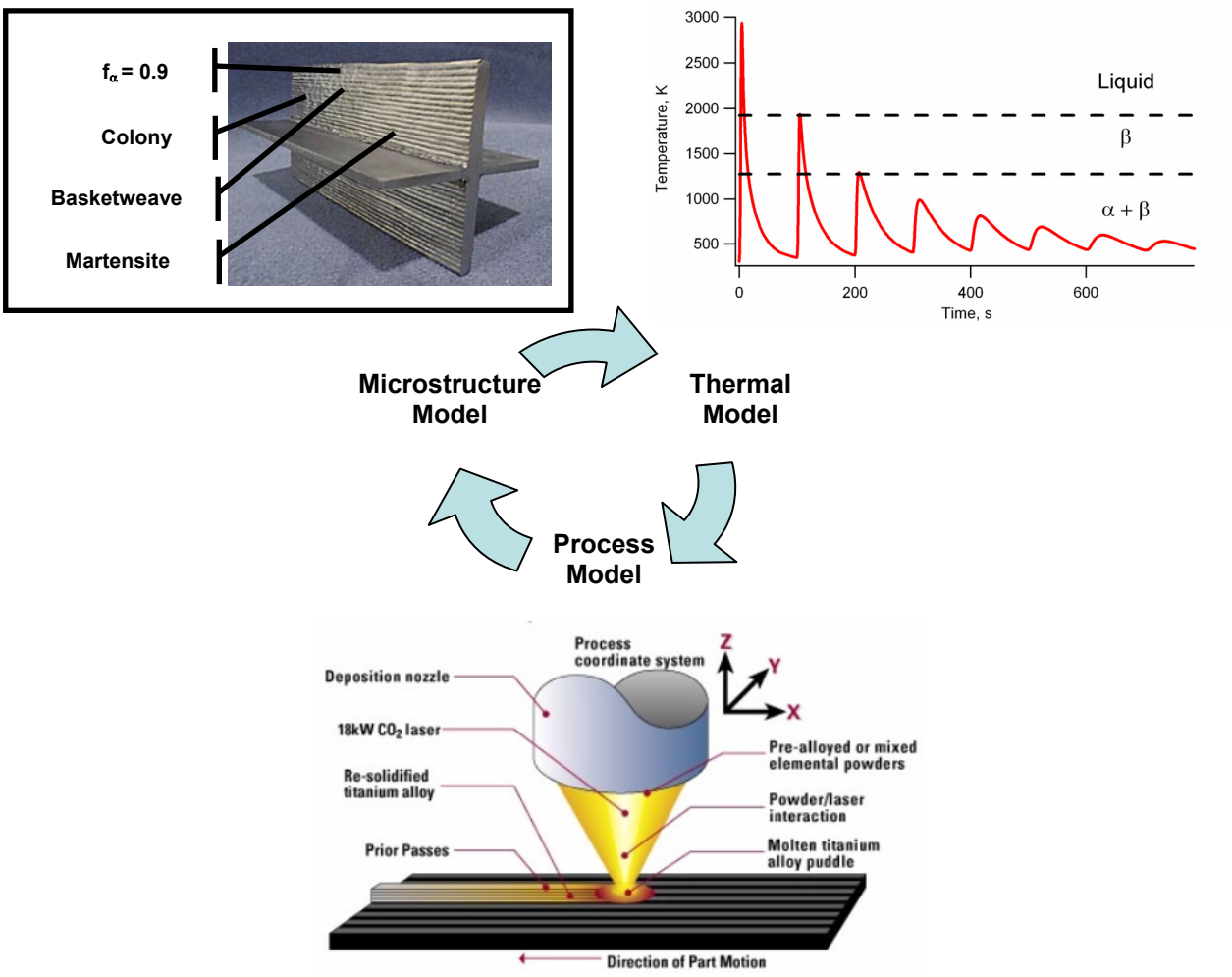

Figure 1.2: Schematic of a coupled process model for metal deposition processes, where thermal and microstructure models are used to control process conditions. Process model figure and microstructure model picture courtesy of AeroMet Corporation.

The research described in this thesis builds upon previous work involving LMD of the titanium alloy, Ti-6Al-4V.[24-26] Previous work with LMD of Ti-6Al-4V has involved characterization of the as-deposited microstructure using optical microscopy, electron microprobe, and hardness measurements to develop a hypothesis for the evolution path. In addition a thermal model was developed to model the thermal history during metal deposition processes. The current research supplements the preliminary characterization and thermal modeling efforts, and is outlined below. The broad questions which will be addressed in each chapter of this thesis are as follows:

- Chapter 2: *What are the possible solid-state transformations that may take place during laser metal deposition of Ti-6Al-4V?* The possible solid state phase transformations taking place during LMD of Ti-6Al-4V are reviewed and related nomenclature defined.

- Chapter 3: *What are the characteristics of the previously defined microstructures?* A series of experiments are performed on Ti-6Al-4V samples in order to establish "baseline microstructures" produced under controlled thermal cycles having different peak temperatures and cooling rates. Characterization of these microstructures is also performed using several different techniques. Optical microscopy is used to give an overview of the microstructure. Scanning electron microscopy in backscattered electron mode is used to indicate the extent of solute partitioning occurring. Electron backscattered diffraction is used to show crystallographic characteristics. Finally, transmission electron microscopy investigates the substructure of the microstructure.

- Chapter 4: *What are the microstructural features of as-deposited Ti-6Al-4V?* The microstructure of as-deposited Ti-6Al-4V produced using AeroMet Corporation's LAM process is characterized using the methods in Chapter 3. Based on the observed macro- and microstructure, a theory for the spatial and temporal evolution of microstructure in the deposit is developed.

- Chapter 5: *What happens to the as-deposited microstructure during different heat treatments?* In order to obtain a microstructurally homogeneous deposit, heat treatments must be performed on the as-deposited parts. Two heat treatments are investigated where the sample is heated into the two phase ($\alpha+\beta$) and into the single phase (β) fields. The results of the heat treatment study reinforce the current theory for microstructure evolution.

- Chapter 6: *What is the thermal history of the as-deposited material currently under observation?* The original[24,26] thermal model results are compared with experimental (thermocouple) data for a similar LMD process. Based on this comparison, it is concluded that a more accurate representation of the laser heat source and deposit geometry are needed. As a result, an improved thermal model is developed employing the same numerical methods as in the original model, but incorporating a different heat source and more appropriate boundary conditions. Since processing conditions for the current deposit are unknown, a calibration of the processing parameters was performed based on the as-deposited microstructure. The resulting calibrated processing conditions

are then used to produce a thermal history for the as-deposited material under investigation.

- Chapter 7: *How does thermal cycling effect microstructure evolution?* A microstructural model is proposed that considers two main transformations occurring during the deposition process. They are nucleation and growth of alpha from the beta phase that occurs upon cooling, and subsequent dissolution of the alpha phase upon heating. These microstructural transformations will be modeled using the principle of additivity applied to the theoretical equations that describe their isothermal evolution. The kinetic parameters describing these transformations are derived. Alpha dissolution kinetics are derived based on the assumption that the movement of the alpha/beta interface is similar to the thinning of an alpha plate by diffusion controlled dissolution. Alpha nucleation and growth parameters are based on Johnson-Mehl-Avrami nucleation and growth theory; kinetics are obtained from available time-temperature transformation diagrams. Both alpha phase fraction and morphology models are developed. The model is compared to recent time resolved x-ray diffraction experiments and the baseline microstructure experiments (Chapter 3).

- Chapter 8: *How does microstructure evolve during laser metal deposition of Ti-6Al-4V using the thermal model results?* The microstructure model is applied to the thermal model results. The predicted microstructure evolution is then compared with the theory developed in Chapter 4.

The near term goals of this research are:

- Establish baseline microstructures that can be compared to laser deposited Ti-6Al-4V in order to better understand the effect of thermal cycling on microstructure evolution.

- Complete the characterization of the as-deposited material using the scanning electron microscope, electron backscattered diffraction techniques and the transmission electron microscope. These techniques will aid in determining the micro-variation of alloying elements within individual alpha grains of the deposit. In addition, these techniques will be used to determine if non-equilibrium (martensite) transformations are present.

- Improve the thermal model by using a more accurate heat input and boundary conditions. Compare the thermal model results with experimental data for a similar (LENS) process. Back-calculate processing conditions based location of the fusion and heat affected zones of the substrate.

- Develop a microstructure model that tracks alpha phase fraction and morphology during thermal cycling as a way to predict microstructure during LMD processing of Ti-6Al-4V.

The long term goals for this research include:

- Developing a database whereby knowing LMD processing conditions, the microstructure can be predicted real-time, and thus controlled by tailoring the processing conditions.

- Examine other unconventional processing techniques such as laser surface alloying of *in situ* composite coatings and fabrication of bulk intermetallic parts using metal deposition processes.

Chapter 2: Solid-State Phase Transformations and Microstructure in Ti-6Al-4V

Typical Phase Transformations in Ti-6Al-4V

In alpha-beta titanium alloys such as Ti-6Al-4V, the body centered cubic (BCC) beta (β) phase transforms to a hexagonally close packed (HCP) alpha (α) phase upon cooling through the beta transus. At room temperature in this alloy, the beta-to-alpha transformation is not complete, resulting in approximately 10% by volume beta phase. In a typical Ti-6Al-4V alloy, the beta transus temperature is approximately 1273 K (1000°C). This temperature is greatly affected by interstitial impurities, especially oxygen.[27] A pseudo binary phase diagram showing the effect of vanadium composition on phase stability in a Ti-6Al-4V alloy is shown in Figure 2.1.

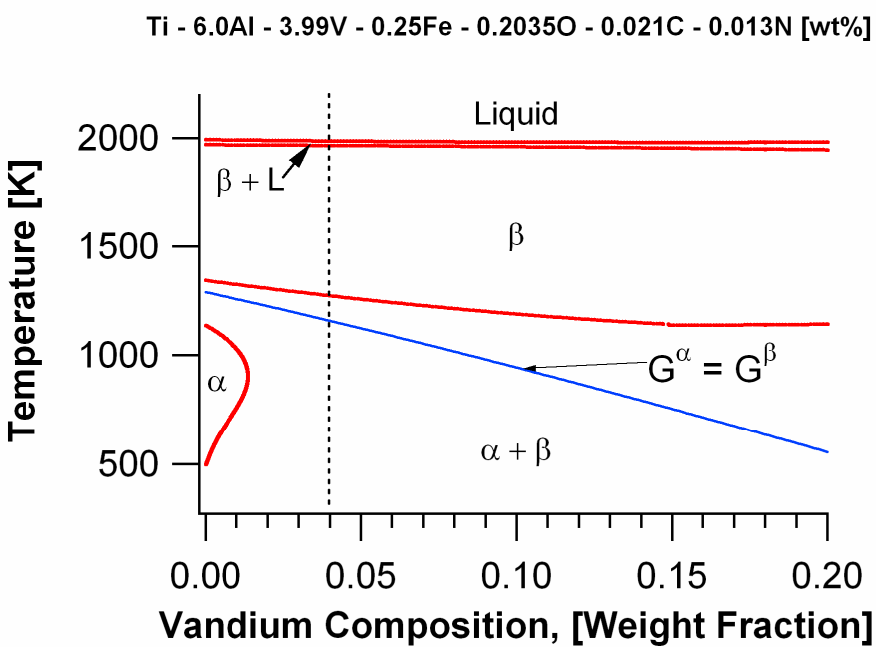

Figure 2.1: Pseudo-binary phase diagram showing the phase variation with vanadium composition (calculated with ThermoCalc). The alloy composition is Ti - 6Al - 3.99V - 0.25Fe - 0.203O - 0.021C - 0.013N

The beta phase may transform into a variety of alpha phase morphologies as it cools through the beta transus in Ti-6Al-4V. The α morphologies include diffusion-controlled allotriomorphic and Widmanstätten alpha, massive (α_m), and martensitic (α') alpha. Typical cooling rates for these transformation products have recently been studied[28] and can be found in Table I.

Table I: Characteristics of the Beta → Alpha + Beta Transformation

Transformation Product	Cooling Rate, K/s	Start Temperature
Allotriomorphic (α_{GB})	CR < 20	1243-1273K
Widmanstätten (α)	CR < 20	~1173K,Ref.[29]; ~1223K,Ref.[30]
Massive (α_m)	20< CR <410	1243-1273K
Martensitic (α')	CR >410	M_S = 848K

Typical phase transformations during a heating and cooling thermal cycle involving a peak temperature above the beta transus are schematically shown in Figure 2.2. In Figure 2.2 the **AB** leg represents heating above the beta transus which leads to complete dissolution of the alpha phase. The **CD** and **CE** legs represent decomposition of beta upon rapid cooling to non-equilibrium products α' and α_m. A diffusional transformation of beta to a two phase structure consisting of primary-alpha (α_P) and beta is shown by **CF**. Heat treatments following the **A-B-C-F** temperature-time profile are called "primary" treatments forming primary-alpha microstructures.

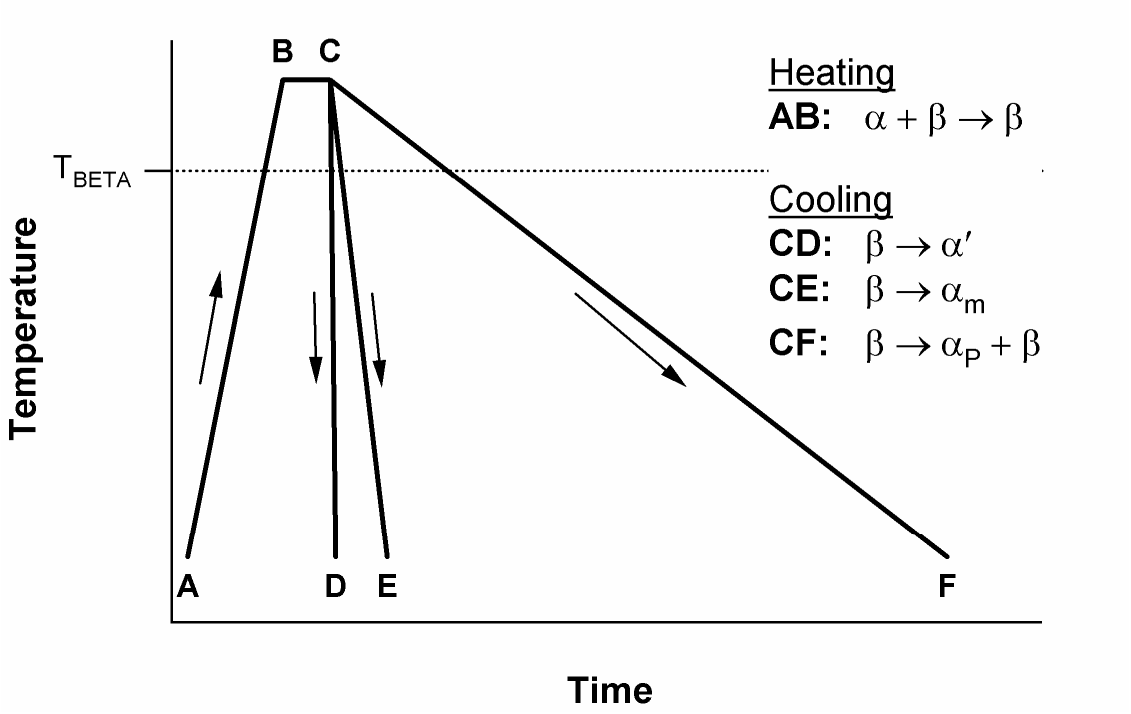

Figure 2.2: Schematic of primary heat treatment above the beta transus illustrating complete dissolution of alpha to beta (AB), followed by cooling at different rates to produce martensitic-alpha α′ (CD), massive alpha α_m (CE)and primary-alpha α_P and retained beta (CF).

Figure 2.3 schematically illustrates the reactions taking place during a secondary heat treatment where heating and cooling occurs below the beta transus. In Figure 2.3, **GH** represents primary-alpha dissolution, where the pre-existing alpha phase (in this case α_P) dissolves into beta resulting in a mixture of α_P and β. During cooling, **IJ**, the newly formed regions of β decomposes into secondary-alpha (α_S), resulting in a mixture of retained beta, primary- and secondary-alpha. Primary alpha forms upon cooling from a temperature above the beta transus and secondary alpha forms upon heating and cooling in the two phase region. Even though the massive and martensitic reactions are not shown in Figure 2.5, the products may form during cooling in a secondary heat treatment provided the maximum temperatures are above the T_0 temperature and the cooling rates are sufficient. The T_0 temperature is where the α and β phases have the same Gibbs free energy. Below the T_0 temperature, the free energy of the alloy is lowered if the product assumes the massive or martensitic alpha phase.

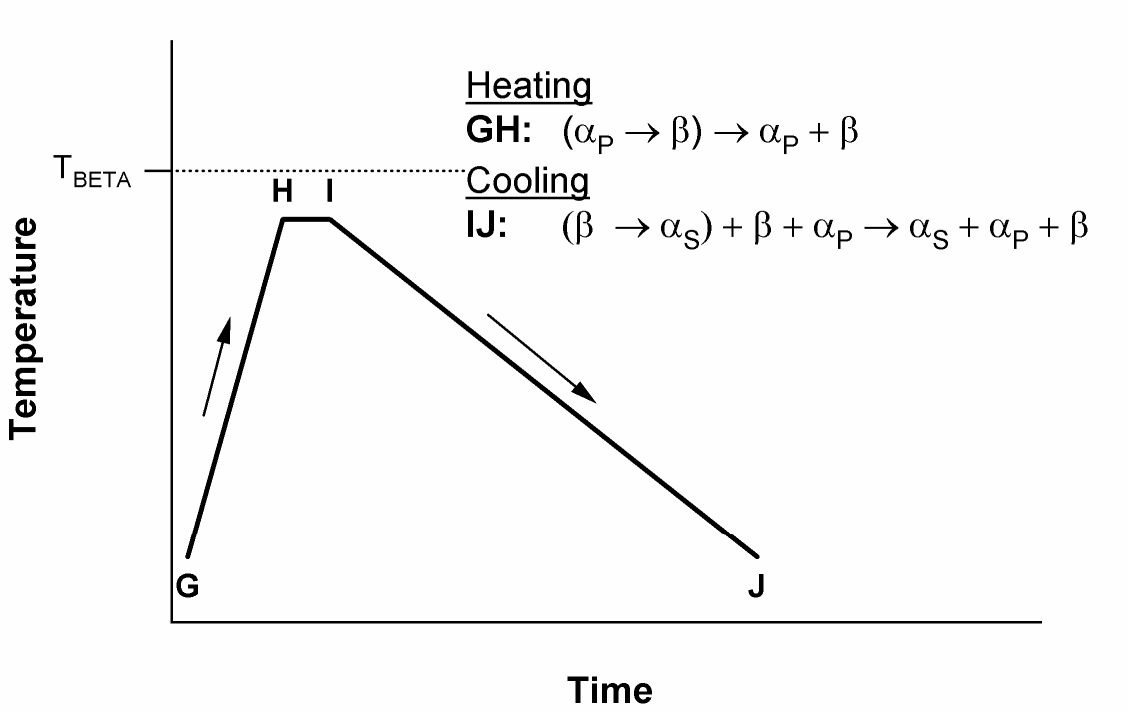

Figure 2.3: Schematic of secondary heat treatment confined to a maximum temperature below the beta transus resulting in dissolution of primary-alpha α_P to beta during heating (GH) and subsequent nucleation and growth of secondary-alpha α_S from the dissolved α_P during cooling (IJ). The final microstructure consists of $\alpha_P + \alpha_S + \beta$.

Each of the different reactions that form during primary and secondary heat treatment will be discussed below in relation to the alpha phase morphologies that may form.

Primary Reactions: Cooling through the beta transus

General Aspects of Diffusion Controlled β→α+β Reaction

Crystallography

Ti-6Al-4V is a two phase, α+β alloy at room temperature under slow to moderate cooling conditions. Alpha that forms from the high temperature stable beta phase nucleates and grows such that the basal plane of the phase, $\{0001\}_\alpha$, is parallel to the $\{110\}_\beta$ plane of the β phase and the $<\bar{1}11>_\beta \parallel <11\bar{2}0>_\alpha$.[31] This is known as the Burgers orientation relationship.[32] As a result, the α phase that forms assumes a needle, lath, lamellar, or plate morphology often referred to as acicular alpha having a high aspect ratio(10:1)[33]. The α/β interface lies close to the $\{10\bar{1}0\}_\alpha$ prismatic planes of the α phase and the $\{110\}_\beta$ planes of the beta phase. The overall α+β morphology, where the product phase is related to the parent phase by a crystallographic

relationship and the product grains attain a plate shape, is known as the Widmanstätten morphology. It will be shown below that the Widmanstätten morphology can take two forms: colony and basketweave alpha. In addition, the Widmanstätten alpha that forms during cooling through the beta transus (leg **CF** in Figure 2.2) is called primary-alpha (α_P) and alpha that forms after heating in the two phase region (leg **GHIJ** in Figure 2.3) is called secondary-alpha (α_S).

Composition of Phases

Vanadium is a beta-stabilizer, meaning it will partition to the beta phase during α growth. In addition, the intrinsic vanadium diffusivity[34] is 75 to 95% (at 1273 and 973K, respectively) that of aluminum impurity* diffusivity[36] in beta-titanium, as shown in Table II. The interface between the alpha and beta grain becomes enriched in vanadium and thus stabilized. Thus, the nucleation and growth of the alpha phase is mainly dependent on the diffusion of vanadium into the beta phase[37,38], which diffuses slower than aluminum. As illustrated in Figure 2.4, as the alpha precipitate grows it is depleted of vanadium, raising the interface vanadium concentration ($C_{V,\alpha/\beta}$) above the bulk beta phase composition ($C_{V,\beta}$) as vanadium is transported into the beta phase. The *widening* of the alpha particle continues until $C_{V,\beta} = C_{V,\alpha/\beta}$; however, the particle continues to *lengthen* by growing into fresh beta of composition $C_{V,\beta}$. In this manner, a plate or needle like shape to the alpha grains is attained.

Table II: Coefficients for diffusion into beta titanium described by the equation $D(T) = D_0 \exp(-Q / (R T))$. Ref [39].

Element	D_0 [$\mu m^2/s$]	Q/R [K]	Type	Ref
Ti	$2.0*10^4$	15000	Intrinsic	[34]
V	$1.0*10^5$	17460	Intrinsic	[34]
Al	$1.2*10^5$	18040	Impurity*	[36]

* Impurity diffusion occurs in dilute substitutional alloys where the solvent and solute share the same lattice sites and vacancies.[35]

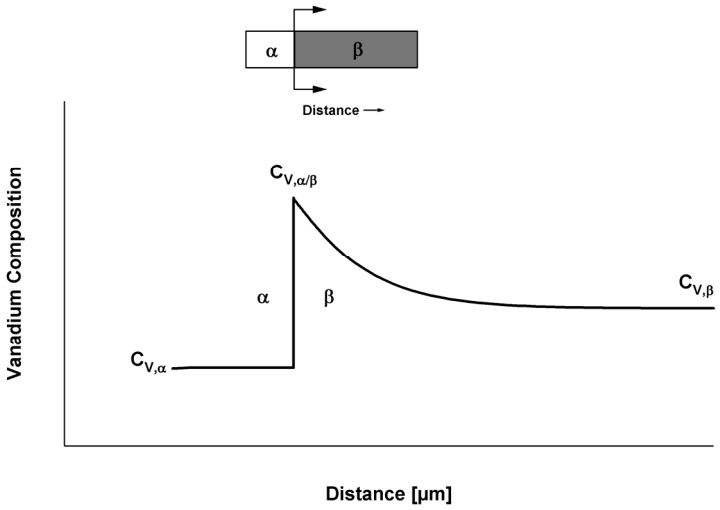

Figure 2.4: Schematic illustrating the variation of vanadium composition during the growth of an alpha particle upon cooling assuming local equilibrium at the α/β interface.

Specific Morphologies of the β→ α+β reaction

Grain boundary allotriomorphs (α_{GB})

The sequence of nucleation and growth events that occur upon cooling through the beta transus (leg **CF** in Figure 2.2) is schematically shown in the continuous cooling transformation (CCT) diagram in Figure 2.5. Shown in the CCT diagram are the start-of-transformation curves for allotriomorphic or "grain boundary" alpha and intragranular alpha. Upon cooling through the beta transus, the first alpha to nucleate is allotriomorphic or "grain boundary" alpha because of its location on the beta grain boundaries. While this is the first alpha to form upon cooling through the beta transus, it is not typically called primary-alpha, instead it will be called grain boundary alpha (α_{GB}). Eventually, the beta grain boundaries will be completely decorated by the grain boundary alpha, either as a continuous or discontinuous fashion, the latter due to faster cooling or greater amounts of beta stabilizer[40] in the alloy. Grain boundary alpha will typically[40,41] exhibit a Burgers orientation relationship with one of the beta grains with which the alpha forms from. An example of grain boundary alpha is shown in Figure 2.6.

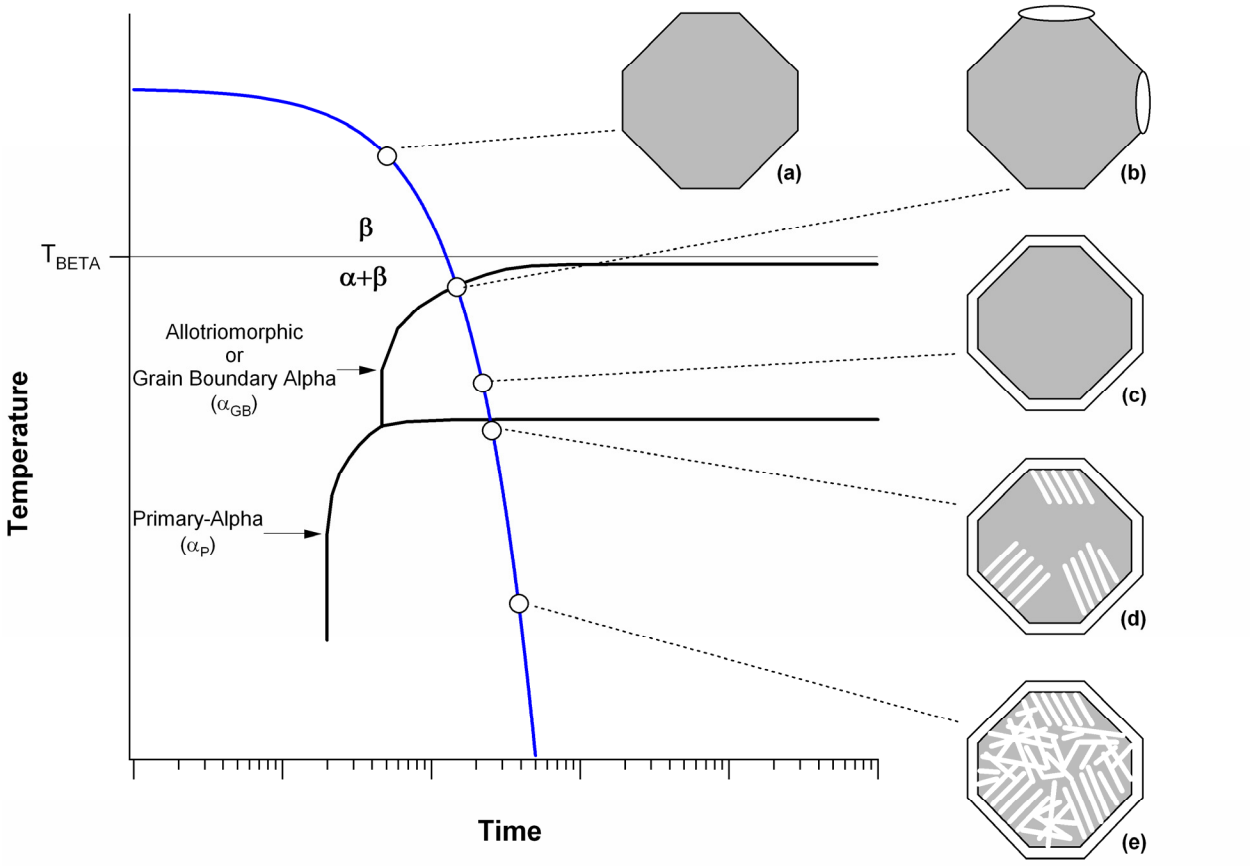

Figure 2.5: Schematic illustrating the sequence of diffusion controlled phase transformation events occurring during continuous cooling of Ti-6Al-4V through the beta transus. Transformation start curves for allotriomorphic or grain boundary alpha and intragranular alpha are shown. (a) A single beta grain is shown in gray. (b) the first alpha to form is allotriomorphic Widmanstätten alpha at the beta grain boundaries. (c) alpha continues to grow along the beta grain boundaries. (d) primary-alpha begins to nucleate and grow first at the grain boundary alpha as colonies of primary-alpha sideplates and finally with increased undercooling (e), primary-alpha nucleates within the remaining beta in a basketweave morphology.

Primary Alpha (α_P) Formation

Colony-α_P Morphology

With further undercooling, primary-alpha sideplates or colonies begin to grow from the grain boundary alpha (Figure 2.5d) into the parent beta grain with which a rational Burgers orientation exists; i.e., these primary-alpha colonies are a variant of Widmanstätten alpha.[41] The individual alpha grains have a high aspect ratio (not equiaxed) and tend to form in colonies where several of the alpha plates will be aligned parallel to one another due to the favorable orientations present at the beta grain boundary. The interface between the grain boundary alpha and primary-alpha sideplate tend to have a low angle grain boundary.[42] An example of the α_{GB} and α_P-colony morphologies are shown in the BSE micrograph of Figure 2.6.

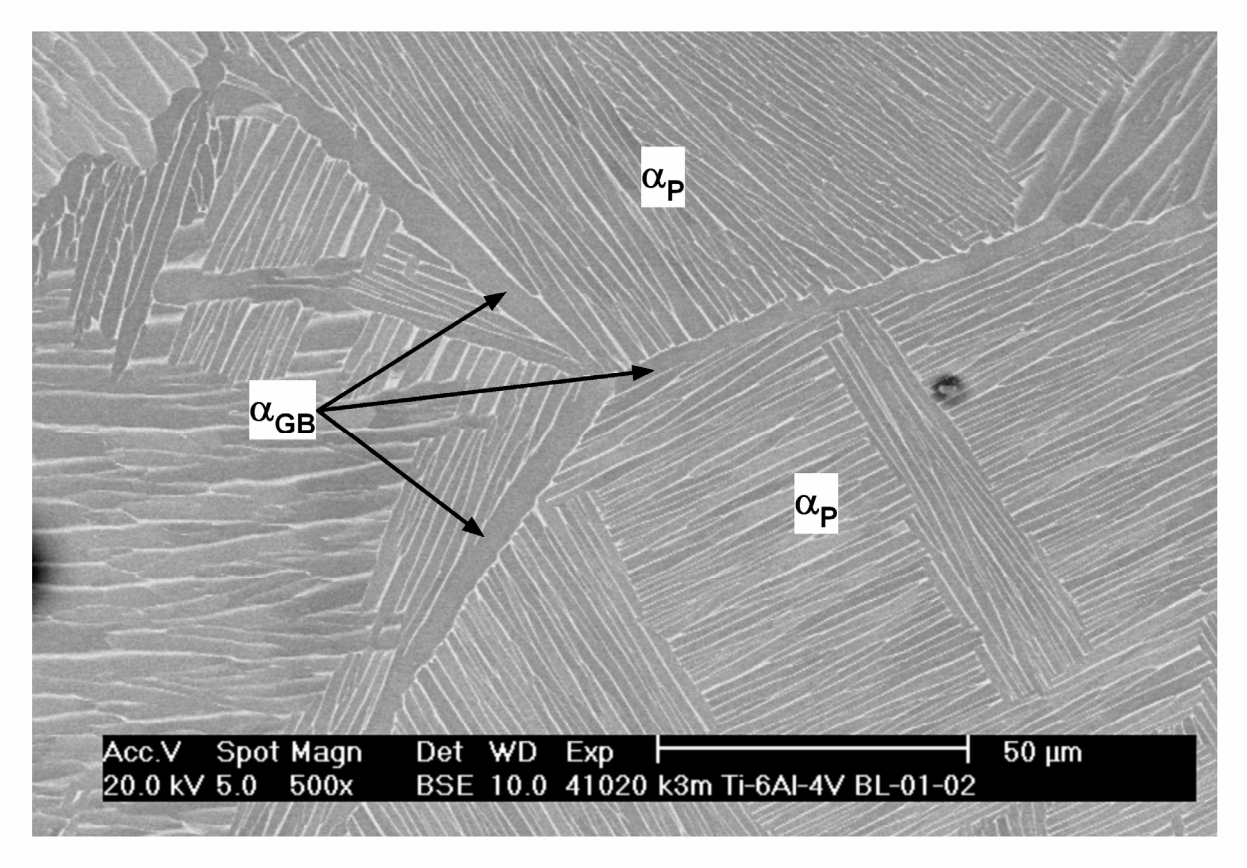

Figure 2.6: BSE micrograph showing the grain boundary alpha (α_{GB}) and primary-alpha (α_P) colony morphologies that form via a diffusion controlled transformation during cooling through the beta transus. The white contrast is the beta phase and the gray contrast is alpha.

Basketweave α_P morphology

The last Widmanstätten alpha (Figure 2.5e) forms within the remaining beta in a pseudo-random (1 of 12 crystallographic variants) fashion because the driving force to form alpha is high at increased undercooling causing the alpha grains to nucleate in the remaining beta. This alpha morphology is referred to as primary-basketweave alpha. An example of α_{GB} and α_P - colonies and -basketweave are shown in Figure 2.7.

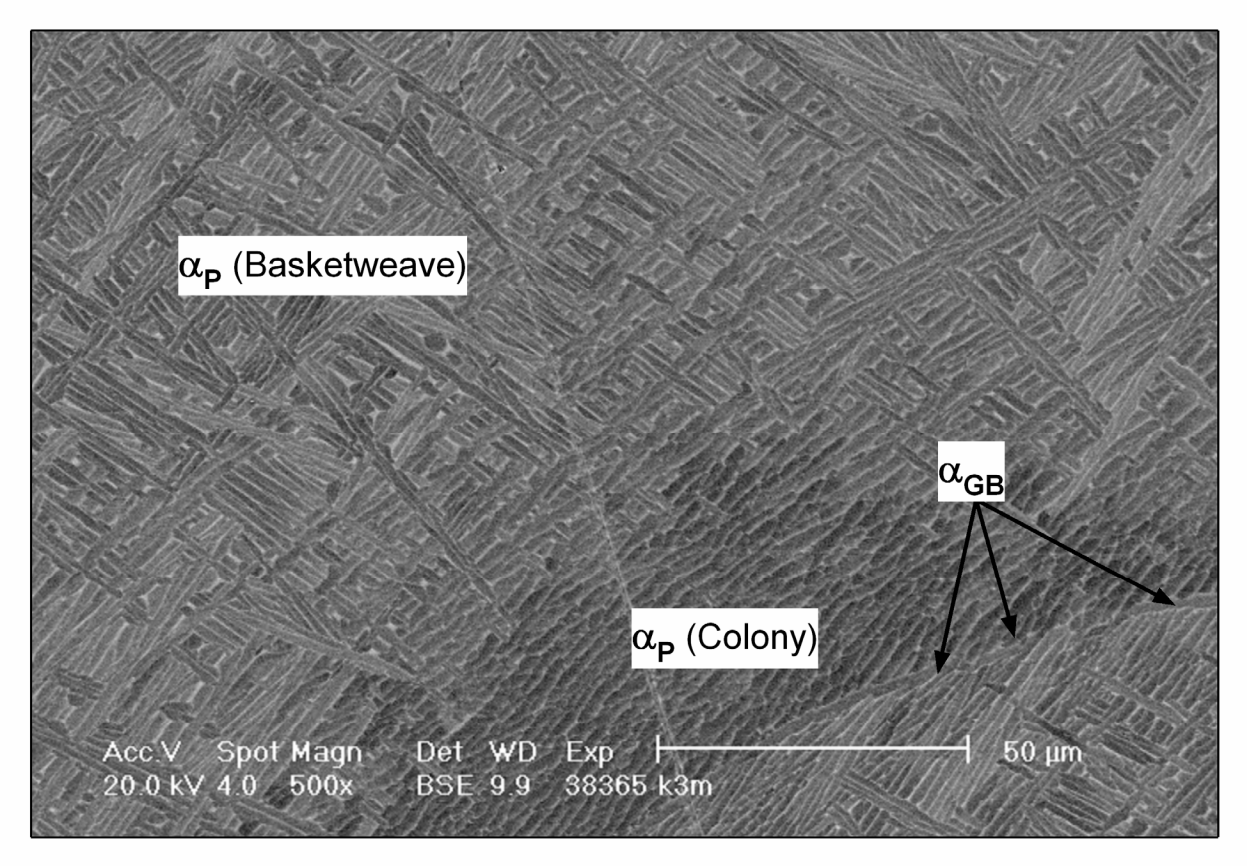

Figure 2.7: BSE micrograph showing grain boundary (α_{GB}) and primary-alpha (α_P) – colony and basketweave morphologies that form via a diffusion controlled transformation upon cooling through the beta transus. The white contrast is beta and the dark contrast is alpha.

The tendency to form a basketweave morphology increases with cooling rate. With slow cooling rates, the growth of the Widmanstätten sideplates will consume the available beta before the undercooling becomes high enough for basketweave formation. Similarly, smaller beta grain sizes will tend to have more colony alpha than basketweave. Lastly, heavily beta stabilized alloys will tend to have more basketweave present since less undercooling is required in these alloys.[43]

Discussion of the Colony and Basketweave α_P Morphologies

A colony is defined as two or more neighboring alpha grains that are parallel to one another. In this sense, a true basketweave structure has a colony density of 1, while 6 parallel alpha grains would represent a colony density of 6. There is often a distribution of small colonies and single alpha grains within a given micrograph; very rarely will you find a completely "random" structure of individually oriented alpha grains. Because of this, ascribing a definition of colony

or basketweave to a microstructure is somewhat subjective and depends on the overall microstructure.

It should be noted that while the nucleation of primary-alpha on α_{GB} is clear, the actual nucleation sites of intragranular alpha such as basketweave alpha is unclear due to difficulties in the interpretation of two-dimensional micrographs. It is conceivable that primary alpha nucleates solely at a prior beta grain boundary. The eventual interpenetration of these grains at the center of a prior beta grain might, in two dimensions, appear as alpha grains that have nucleated homogeneously (or heterogeneously at some defect) at the center of the beta grain thus resembling a basketweave type structure. Serial sectioning microscopy techniques would be necessary to truly understand the 3D structure of two-phase titanium alloys.

Massive Transformation ($\beta \rightarrow \alpha_m$)

The existence of the massive transformation product was originally discussed in relation to Ti-X (X: Ag, Au, or Si) alloys[44-46] and recently studied in Ti-6Al-4V.[28] The massive ($\beta \rightarrow \alpha_m$) transformation is possible in Ti-6Al-4V at moderate cooling rates and is competitive with diffusional and martensitic transformations at low and high cooling rates within the overall cooling rate region where α_m may form. The massive transformation is composition invariant, meaning that the composition of α_m will be the same as the parent β phase. In order for this to occur, the T_0 temperature must be sufficiently low to restrict the growth of diffusional α.[44] The growth mechanism of a massive transformation requires thermally activated migration of individual atoms over small distances and across an incoherent interface.[47] Fuhrahara has shown that partial coherency can be expected in the massive transformation.[48] Massive products have been shown to preferentially nucleate at β grain boundaries at the highest cooling rates followed by martensitic plates adjacent to the prior beta grain boundary, and finally at individual martensite plates within the prior beta grain.[28] The α_m phase appears as an irregular shaped grain boundary precipitate. Massalski describes the massive transformation morphology to be "patchy."[49] TEM studies indicate that α_m has a blocky morphology, a heavily dislocated substructure, and a HCP crystal structure identical to the martensite formed at higher cooling rates.[44]

Martensitic Transformation ($\beta \rightarrow \alpha'$)

Upon rapid cooling from above the T_0 temperature, β may decompose by a diffusionless process to martensitic-alpha, α'. The orientation relationship for the $\beta \rightarrow \alpha'$ transformation has also been determined to be that of the characteristic Burgers orientation as was described for nucleation and growth of the α phase: $(110)_\beta \parallel (0001)_{\alpha'}$ and $<\bar{1}11>_\beta \parallel$ to $<11\bar{2}0>_{\alpha'}$, the habit plane is determined to be either $(334)_\beta$ or $(344)_\beta$.[50] Ahmed and Rack[28] determined that the martensitic transformation in Ti-6Al-4V forms at cooling rates greater than 410 K/s, while Gil, *et al.*[38] observed a fully martensitic microstructure at cooling rates of 5.1 K/s. Ahmed and Rack measured the cooling rate at 900°C while Gil, et al. state that the cooling phase was furnace controlled or constant. Gil's cooling rate seems a bit low.

The α' plates form as long orthogonally oriented acicular grains with a substructure consisting of dislocations, stacking faults and some twins on $(1011)_\alpha$. An example optical micrograph of α' formation at a prior beta grain boundary is illustrated in Figure 2.8. Complete decomposition of α' to equilibrium α occurs on heating above approximately 973K.[51] Below this temperature, the decomposition of α' is incomplete due to slow diffusion.

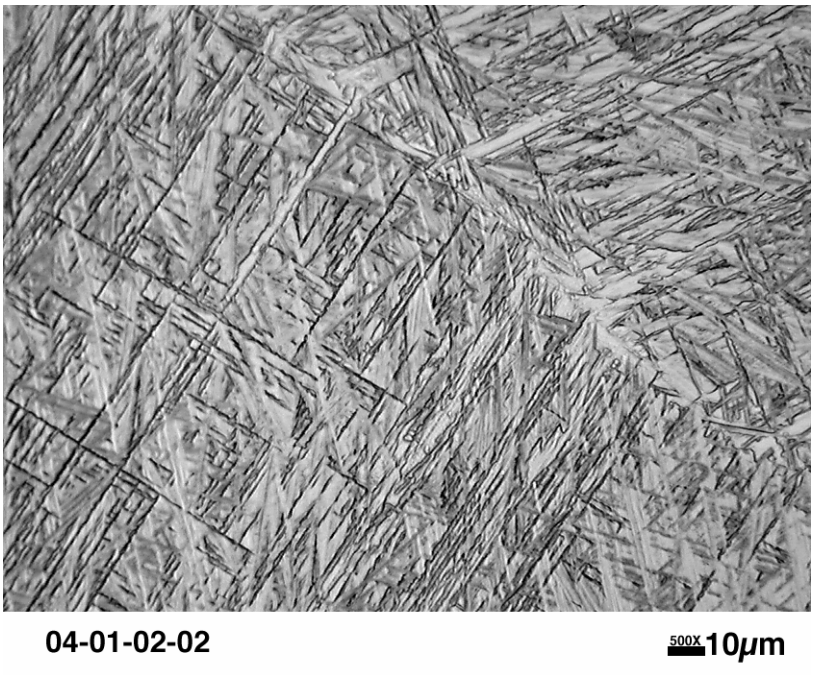

Figure 2.8: An example micrograph of martensitic-alpha (α′) in Ti-6Al-4V resulting from very rapid cooling rates from above the beta transus.

Reactions upon heating

General Aspects of Alpha Dissolution

Comparatively much less work has been done on examining dissolution of alpha phase during heating (e.g. leg EF in Figure 2.2). The alpha dissolution reaction occurs by movement of the alpha beta interface, which is caused by the transport of beta stabilizing elements across the interface.[52,53] In this sense alpha dissolution can be thought of as diffusion controlled beta growth. Most of the work has focused on the shift in the completion of the $(\alpha+\beta)\rightarrow\beta$ to temperatures greater than the beta transus.

Composition Variation

Figure 2.9 schematically illustrates the aluminum and vanadium composition profiles during diffusion controlled dissolution of the alpha phase. The curves represent simulated isothermal heating experiments for an initial (t=0) temperature of 873K and an isothermal hold temperature of 1123K. The calculation was performed using numerical diffusion simulation software (DiCTra)[54,55] and the composition profiles were obtained at different times in the dissolution process. At the initial time (t=0), the composition is α (6.0Al - 2.2V) and β (2.2Al – 26.8V),

where beta appears to the left of the interface in Figure 2.9. At the isothermal hold temperature (1123K, t=1000s) the equilibrium composition is α (6.4Al – 1.6V) and β (5.4Al – 8V). The movement of the α/β interface is captured at an intermediate time of 1 second. The movement of the α/β interface occurs by transport of vanadium from beta to alpha, thereby reducing the bulk vanadium composition in beta and allowing it to grow into the alpha phase. Concomitantly, aluminum must diffuse from alpha to beta in order to maintain a mass balance at the moving interface. Clearly, a much larger amount of vanadium must be redistributed during heating; therefore the alpha dissolution rate is primarily controlled by vanadium diffusion.

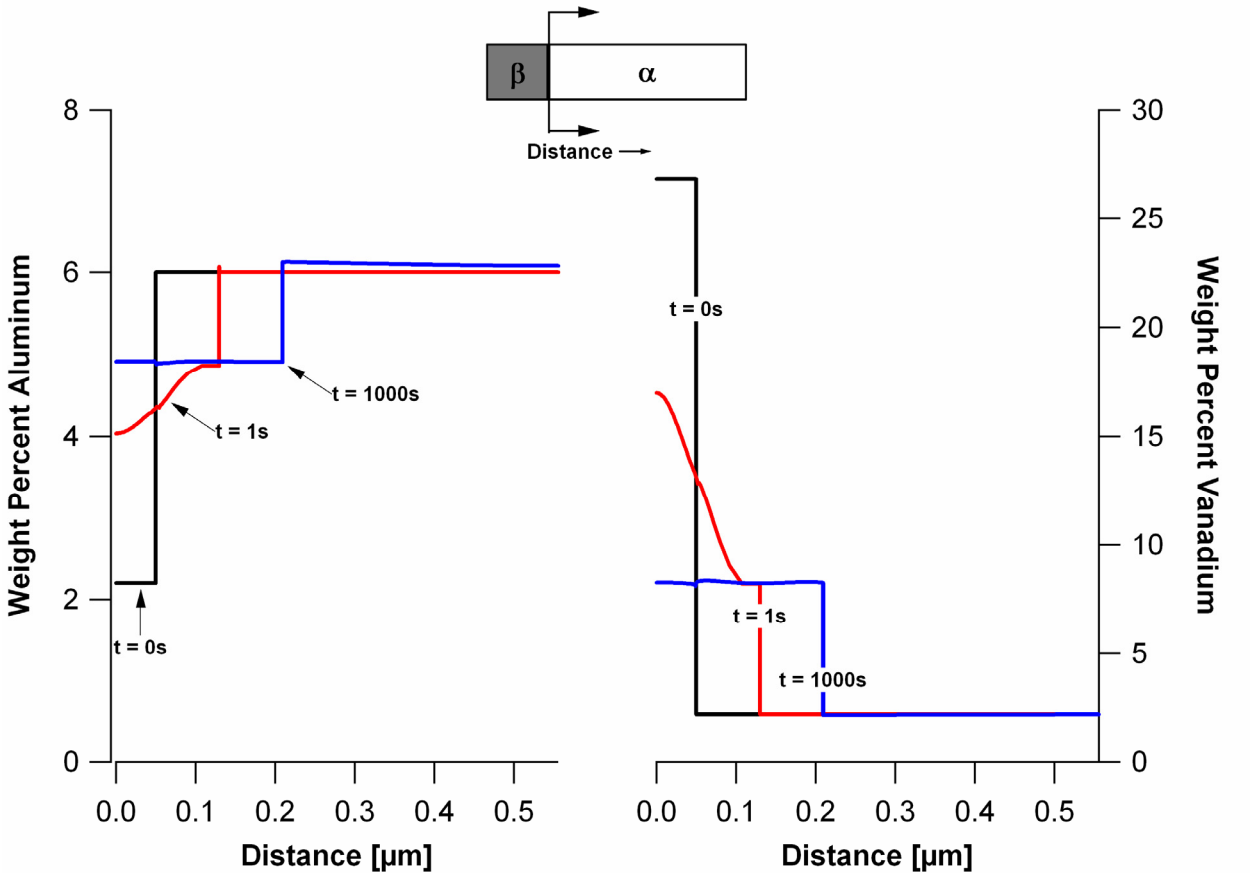

Figure 2.9: Quantitative illustration of the composition profile changes during diffusion controlled alpha dissolution during isothermal (1123K) heat experiments as calculated using numerical diffusion simulation software (DiCTra). The orientation of the alpha and beta phases is shown in the diagram at the top of the plot.

Elevation of the beta transus during non-equilibrium heating

Under equilibrium conditions, the (α+β)→β reaction is expected to complete at the beta transus; however, Ivasishin *et al.* [52,56] have shown that a heating rate of 20, 50, and 100K/s raised the

effective beta transus by approximately 30, 55, 70 K, respectively. Using a diffusion model and dilatometric measurements, Szklinarz also showed that under high heating rates, a superheat above the beta transus would be required in order for the necessary diffusion (homogenization of the beta phase) to occur.[53] Details of either experiment are not presented in the paper. Elmer, *et al*.[57] has shown using spatially-resolved x-ray diffraction (SRXRD) that during welding of Ti-6Al-4V, the α/β transition requires, on average, 169±25.7K of superheat of the beta transus (1213K for the composition studied) under an average heating rate of 42.7 K/s. Shah, *et al.*[22] have determined (based on the data of Ivasishin[58]) that the increase in the beta transus temperature, ΔT_β, depends on the thickness of the alpha lamella or equiaxed α grains, d_α, heating rate, φ and the maximum heating rate where $\Delta T_\beta=0$, $\varphi_0 = 0.19$ K/s according to Equation [2.1].

$$\Delta T_\beta = 6.87 d_\alpha \log\left(\frac{\varphi}{\varphi_0}\right) \qquad [2.1]$$

The heating rate has been shown to decrease the overall β grain boundary kinetics, leading to smaller beta grain sizes at a given temperature for increased heating rates for initially fine prior beta grained material. Rapid thermal heat treatment has been used as a method of austenite grain refinement in coarse grained steels; however, in coarse grained α+β alloys, grain refinement does not take place under rapid heating. This is because the α+β→β transition occurs by movement of the α/β interface until only the parent β phase exists; nucleation of new β regions does not occur.[52] Nucleation of beta within alpha would be necessary in order for grain refinement to occur. In addition, during rapid heat treatment, compositional inhomogeneities may exist due to the insufficient time to redistribute alloying elements.

Reactions during heating and cooling in the α + β phase field

Secondary-alpha (α_S) formation during cooling

We now examine the morphologies that form during cooling from a peak temperature in the two phase field (secondary heat treatment). If the dissolution reaction is not complete it becomes necessary to distinguish primary-alpha from the alpha that will form upon cooling during the sub-transus thermal cycle (leg FG in Figure 2.2). Designated as secondary-alpha (α_S), this alpha phase nucleates and grows into the beta phase and can have similar morphological forms to that

of primary-alpha: colony and basketweave depending on the thermal cycle. An example of α_S formation is illustrated in the BSE micrographs of Figure 2.10a-b obtained after heat treatment of an initially equiaxed $\alpha+\beta$ structure in the two phase field. The sample in Figure 2.10a was quenched before α_S forms, leaving β to transform to α' and the preexisting α_P. In Figure 2.10b, the β present is allowed to transform in a diffusion controlled manner to α_S before quenching to transform remaining β to α'. The α_S is present in a colony morphology that appears to nucleate both from existing α_P and intragranularly in β.

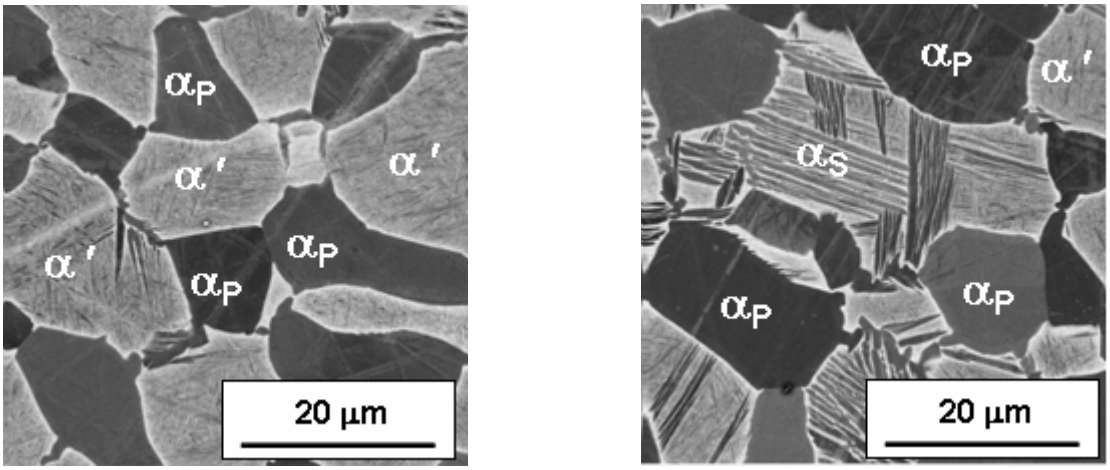

(a) (b)

Figure 2.10: BSE micrographs illustrating primary- (α_P) and secondary-alpha (α_S) formation during a heat treatment in the two phase field followed by (a) quenching and (b) moderate cooling at 3.2K/s to transform $\beta \rightarrow \alpha_S + \beta$, followed by quenching. Upon quenching, any beta present transforms to alpha-martensite (α'). [Courtesy of S.L. Semiatin, Ref.[39]]

Recently, Semiatin, *et al.*[39] have examined the microstructure evolution during heat treatment of Ti-6Al-4V. In their results it was found that secondary alpha begins to form in a temperature range of 1088 to 1173 K, with lower start temperatures observed with increasing cooling rate and decreasing maximum temperature in the two phase field. It should be noted that these experiments were performed on samples of Ti-6Al-4V containing equiaxed globular primary-alpha and beta, which is distinctly different than the cast structures in LMD Ti-6Al-4V; however, it allows for easily distinguishing between primary and secondary alpha forms since the primary alpha is equiaxed and the secondary alpha forms in a colony or basketweave morphology.

Semiatin *et al.* point out that secondary-alpha formation may occur by heterogeneous or homogeneous nucleation.[39] The work of Gil *et al.* [38] and Malinov *et al.*[29] suggest that primary and secondary alpha form homogenously. Semiatin *et al.* conclude that high

supersaturation of the beta matrix with vanadium led to secondary-alpha formation.[39] It is currently unclear what types of heterogeneous nucleation sites intragranular primary alpha and secondary alpha form from, though one likely assumption would be dislocations with the beta phase. It is possible that with high undercooling homogeneous nucleation will take place. Evidence also exists for sympathetic nucleation[59,60] in titanium alloys, where a precipitate crystal forms at an the interphase boundary of another crystal of the same phase. In this sense existing α crystals act as nucleation sites for additional α formation, and the reaction proceeds auto-catalytically.

Dissolution of alpha (α_{GB}, α_S and α_P) during heating

The final question that must be answered is what happened to α_{GB}, α_P, and α_S during heating into the two phase field? The dissolution of the α phase upon heating has been discussed by Sha and Guo,[61] who determined using differential scanning calorimetry (DSC) that secondary- followed by primary-alpha dissolve during heating. This conclusion was made based on the assumption that primary alpha has formed at a higher temperature than the secondary product, and thus upon heating will not begin to dissolve until the temperature where it was formed is reached. That is to say, α_{GB} and α_P are more stable structures than α_S.

There are many questions left unanswered as to what happens to certain morphologies during dissolution. The baseline microstructure experiments performed in this thesis will help elucidate what morphologies might dissolve first during reheating into the two phase field.

LMD Thermal Cycles and Microstructure

Thermal cycling in LMD due to the addition of multiple layers of material with a high power heat source plays an important role in microstructural development. A typical LMD thermal history is shown in Figure 2.11 with different phase transformations for Ti-6Al-4V taking place. These include diffusional, massive, martensitic, and growth of beta grains. The **AB** leg represents rapid heating above the beta transus, which may delay the time and temperature where alpha dissolution will be completed. The **BC** and **CD** legs represent decomposition of beta upon rapid cooling to non-equilibrium products and the reversion of these products to beta upon heating again through the beta transus. A diffusional transformation of beta to a two phase structure consisting Widmanstätten alpha and beta is shown in **DE**. The Widmanstätten alpha

structure after **DE** will consist of grain-boundary (α_{GB}) and primary-alpha (α_P). The α_P will have a morphological mixture of colony- and basketweave α_P depending on cooling rate. **EF** represents primary-alpha dissolution whereby the α_P morphologies that formed during **DE** will dissolve into the beta phase. When cooling begins (**FG**) secondary-alpha (α_S) will form from the beta present resulting in a mixture of retained beta, primary and secondary-alpha. The morphology of the remaining α_P will be unchanged from point **E** forward, while the α_S morphology will depend on peak temperature and cooling rate. The resulting α_S morphology could be colony or basketweave-α_S.

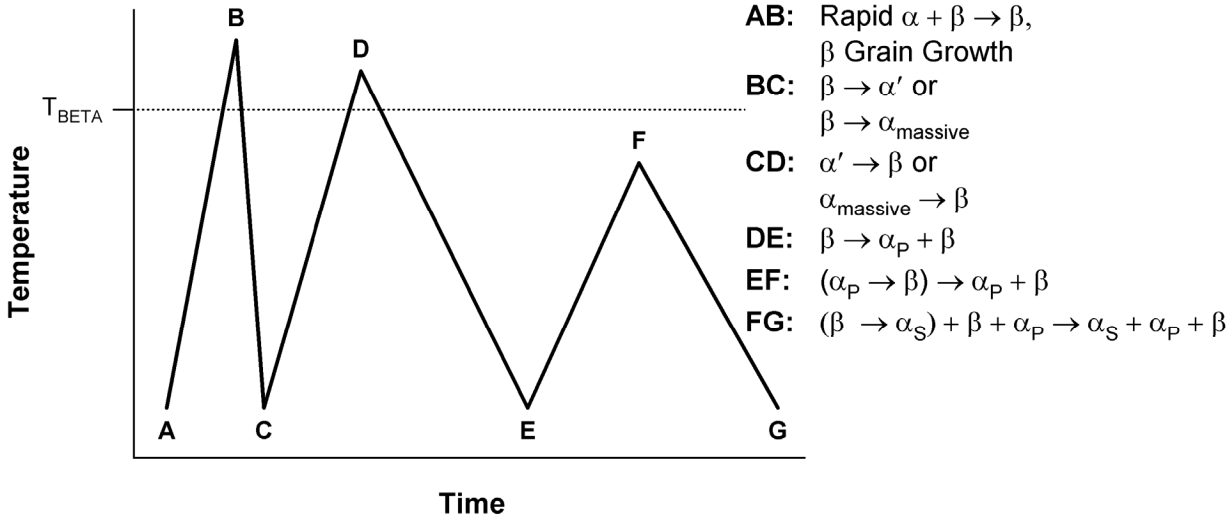

Figure 2.11: Phase Transformations possible during LMD of Ti-6Al-4V

It should be noted that of the thermal cycles shown illustrated Figure 2.11, **ABC** and **CDE** represent primary thermal cycles while **EFG** represent a secondary thermal cycles. An additional thermal cycle could be added to the schematic illustrating that if the peak temperature is below a certain temperature, no further changes in microstructure will occur. This temperature is known as the dissolution temperature T_{DISS} and is illustrated in Figure 2.12. Below T_{DISS} the experimental equilibrium fraction of alpha and beta remain constant at approximately 0.91 and 0.09, respectively. Clearly, the greatest microstructural changes will occur within a range of temperatures between T_{DISS} and T_{BETA}, which corresponds to a "secondary" thermal cycle. Both primary and secondary thermal cycles will play a role in microstructural development in LMD as will be shown in the next chapter.

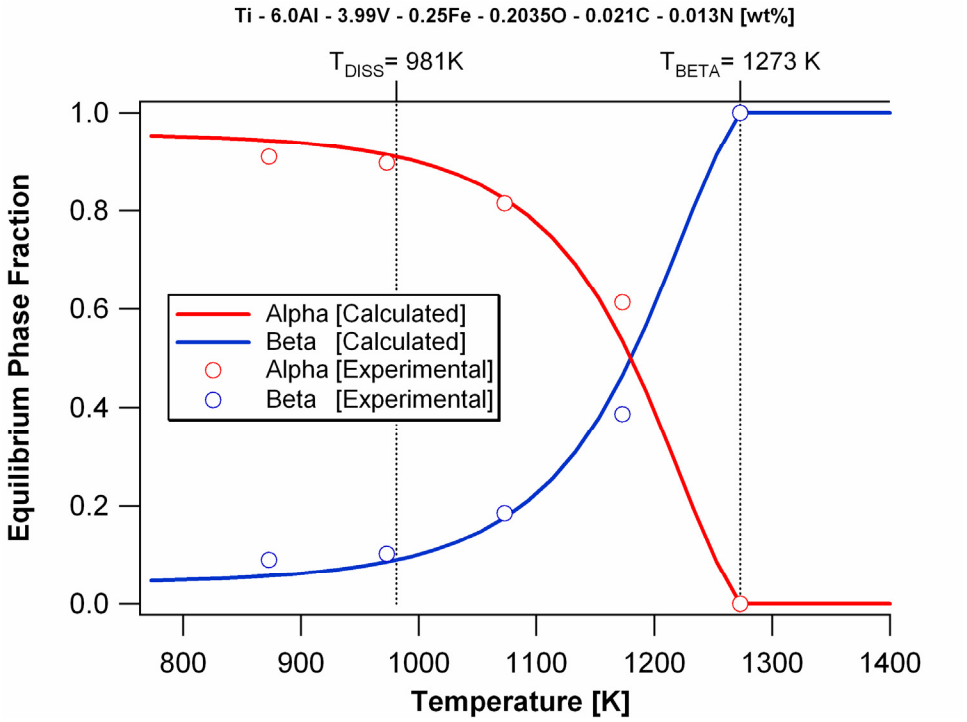

Figure 2.12: Calculated and experimental phase equilibria in Ti-6Al-4V showing the equilibrium alpha and beta phase fraction illustrating the dissolution temperature T_{DISS}. Experimental data from ternary isothermal sections are also shown (Ref. [62]). Below T_{DISS} the experimental phase fraction remains constant.

Summary

The pertinent characteristics of solid state phase transformations possible during laser deposition of Ti-6Al-4V are summarized below.

- Slow to moderate cooling (<20K/s) through the beta transus will result in a nucleation and diffusion controlled growth of alpha forms. Alpha nucleates first at prior beta grain boundaries as α_{GB} followed by growth of primary-α (α_P) sideplates. The α_P sideplates tend to form in a colony morphology under slow cooling rates, with the colony density (number of parallel alpha grains per colony) decreasing with increased cooling rates. Eventually with increased undercooling, the α_P laths appear to form intragranularly in a basketweave morphology. In general, all α to form exhibits a Burgers orientation relationship with the parent beta grain. Plate-like morphologies that have this orientation relationship are called Widmanstätten alpha. Diffusion controlled growth of the alpha phase is limited by vanadium diffusion. Diffusion rates, on average, of vanadium are lower than that of aluminum in BCC titanium.

- Under fast ($20 < CR < 410$ K/s) and quench ($CR > 410$K/s) cooling from above the beta transus, massive alpha (α_m) and martensitic alpha (α') may form from the beta phase, respectively. α_m appears at grain boundaries while α' appears intragranularly as orthogonally oriented plates. α' exhibits the same Burgers orientation relationship with β as its diffusion-controlled counterpart.

- Heating through the $\alpha+\beta$ phase field at moderate to fast rates will produce an effective elevation in the beta transus, where alpha has completely dissolved into beta. Heating rates reported in the literature vary, but range from 0.1 to 10 K/s. Alpha dissolves into beta via movement of the α/β interface, i.e., a diffusion controlled process and no nucleation of beta within alpha grains has been observed. The effective elevation in the finish of the $\alpha+\beta \rightarrow \beta$ transformation is a result of sluggish vanadium diffusion.

- During cooling from a maximum temperature is in the $\alpha+\beta$ phase field, secondary-alpha (α_S) will form under slow to moderate cooling rates (CR<20K/s), in similar morphologies as α_P within regions of dissolved beta. The formation of α_S will play an important role in understanding the microstructure evolution in LMD Ti-6Al-4V.

- It speculated that during heating in the two phase field, α_P followed by α_{GB} will dissolve due to the potential variation in composition within these morphologies.

- The dissolution temperature (T_{DISS} = 981K) and the beta transus (T_{BETA} = 1273K) will define the region of greatest microstructural change, where the dissolution of α_P and subsequent growth of α_S occur.

Chapter 3: Developing Baseline Microstructures for Comparison with LMD of Ti-6Al-4V

The purpose of this chapter is to provide a more quantitative basis for identifying typical LMD microstructures using a variety of characterization techniques, including optical microscopy, scanning electron microscopy (SEM), transmission electron microscopy (TEM), and electron backscattered diffraction (EBSD). These microstructures will be produced under controlled thermal cycles. The controlled thermal cycles chosen in these "baseline" experiments will explore the microstructure produced by primary and secondary thermal treatments under different cooling rates.

Baseline Microstructure Experiment

A series of controlled heating and cooling experiments have been conducted to produce microstructures in Ti-6Al-4V that can be compared to those in LMD Ti-6Al-4V. A thermomechanical simulator was used to produce the controlled heating and cooling rates in the Ti-6Al-4V samples. The samples had been heat treated in the beta phase field (normalized) to produce a cast-like microstructure consisting of large prior beta grains, grain-boundary nucleated alpha and primary-alpha colonies. The baseline microstructures were produced using primary- and secondary- heat treatments which correspond to heating to maximum temperatures in the β and $\alpha+\beta$ phase fields, respectively. The microstructures are analyzed using optical metallography, backscattered electron imaging on the SEM, TEM, and finally EBSD.

Samples

Samples used in the thermomechanical simulator consisted of Ti-6Al-4V bar, 11 mm long and 6.35 mm in diameter. The as-received condition, shown in Figure 3.1a, consists of equiaxed alpha grains in a beta matrix produced during thermomechanically processing into bar. The samples were normalized by heat treating under vacuum at 1450 K for 30 minutes followed by a furnace cool to room temperature. The resulting macrostructure, shown in Figure 3.1b, consists of coarse prior beta grains, approximately 1165 ± 230 μm in diameter. A primary-alpha (α_P) colony microstructure was produced with the prior beta grain boundaries decorated by α_{GB} as shown in Figure 3.1c-d.

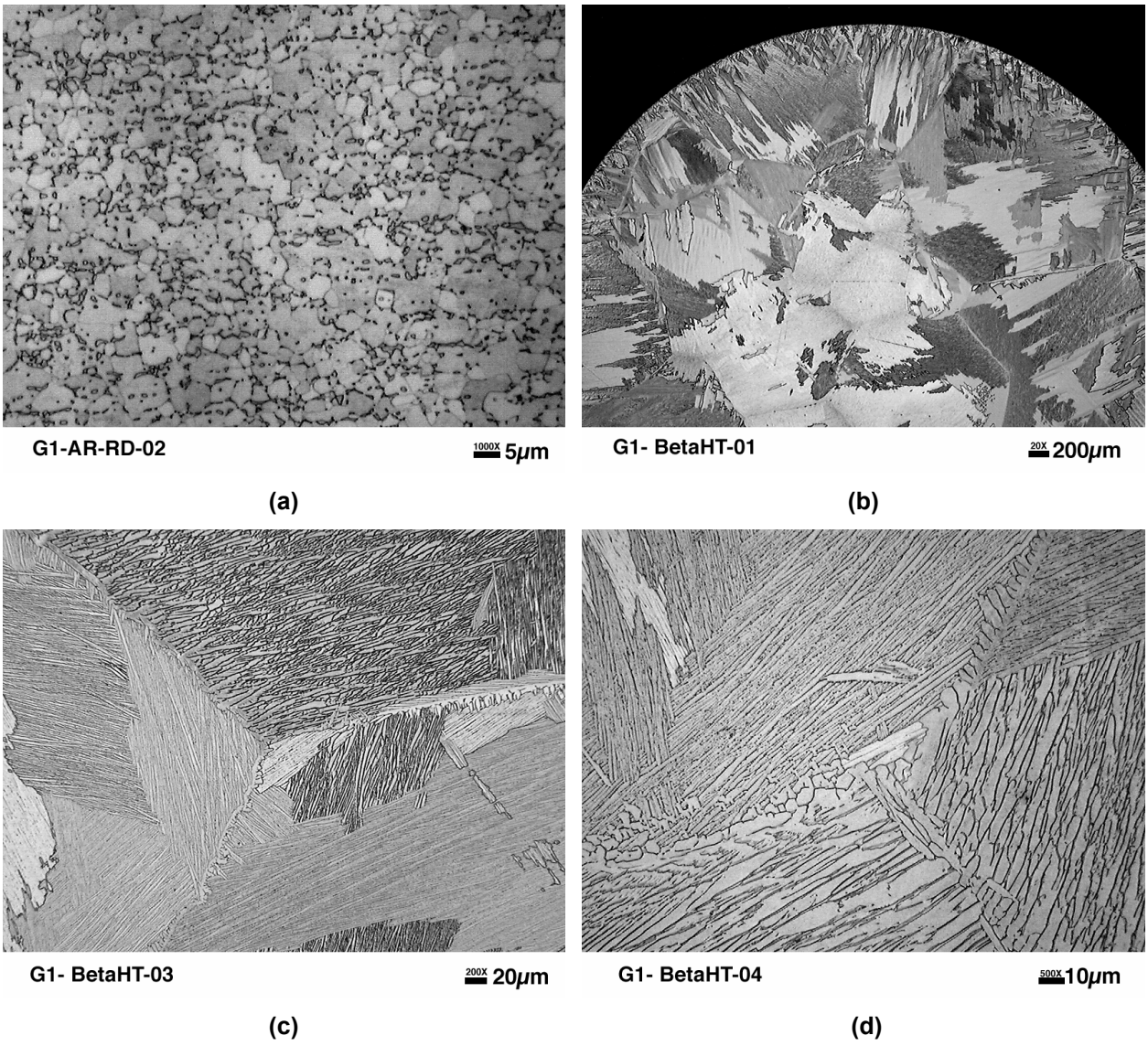

Figure 3.1: Optical micrographs of as-received (a) and normalized (b-d) microstructures of Ti-6Al-4V samples used in baseline microstructure and thermal simulation experiments. (a) As-received microstructure showing equiaxed alpha grains outlined in beta. Normalized samples showing large prior beta grains (b), and a large fraction of grain boundary nucleated alpha and primary-alpha colonies (c,d).

The purpose of the normalization heat treatment was to produce significantly larger equiaxed prior beta grains to simulate the prior beta grain size observed in laser deposited material. According to the work of Semiatin, *et al*.[63,64] under isothermal conditions (30 minutes at 1450 K) and a starting beta grain size of 1μm, we would expect a prior beta grain size of approximately 1150 μm, while for non isothermal heating and cooling to 1450 K (no hold) from the beta transus at a rate of 1°C/s, a prior beta grain size of 900μm would be expected.

Procedure

In order to determine a standard microstructure for diffusion-controlled and non-equilibrium beta transformation products in Ti-6Al-4V, a series of experiments have been performed on the Gleeble 1500 thermomechanical simulator (Dynamic Systems, Inc. Poestenkill, NY). The Gleeble utilizes resistive heating to produce controlled rapid heating and cooling rates in a controlled atmosphere. Figure 3.2 shows a typical Gleeble set-up using the quench spray head. The temperature of the sample is measured using fine diameter (250μm) Type-K thermocouple (Pt – Pt-13%Rh) that has been percussion welded at the mid-span of the sample. To achieve the rapid cooling rates a quench apparatus is placed near the mid-span of the sample. The water cooled copper jaws hold the sample in place during heating and transfer the current to the sample. A contact dilatometer (not shown) may be attached to the sample at mid span to measure the dilatation caused by temperature changes and phase transformations.

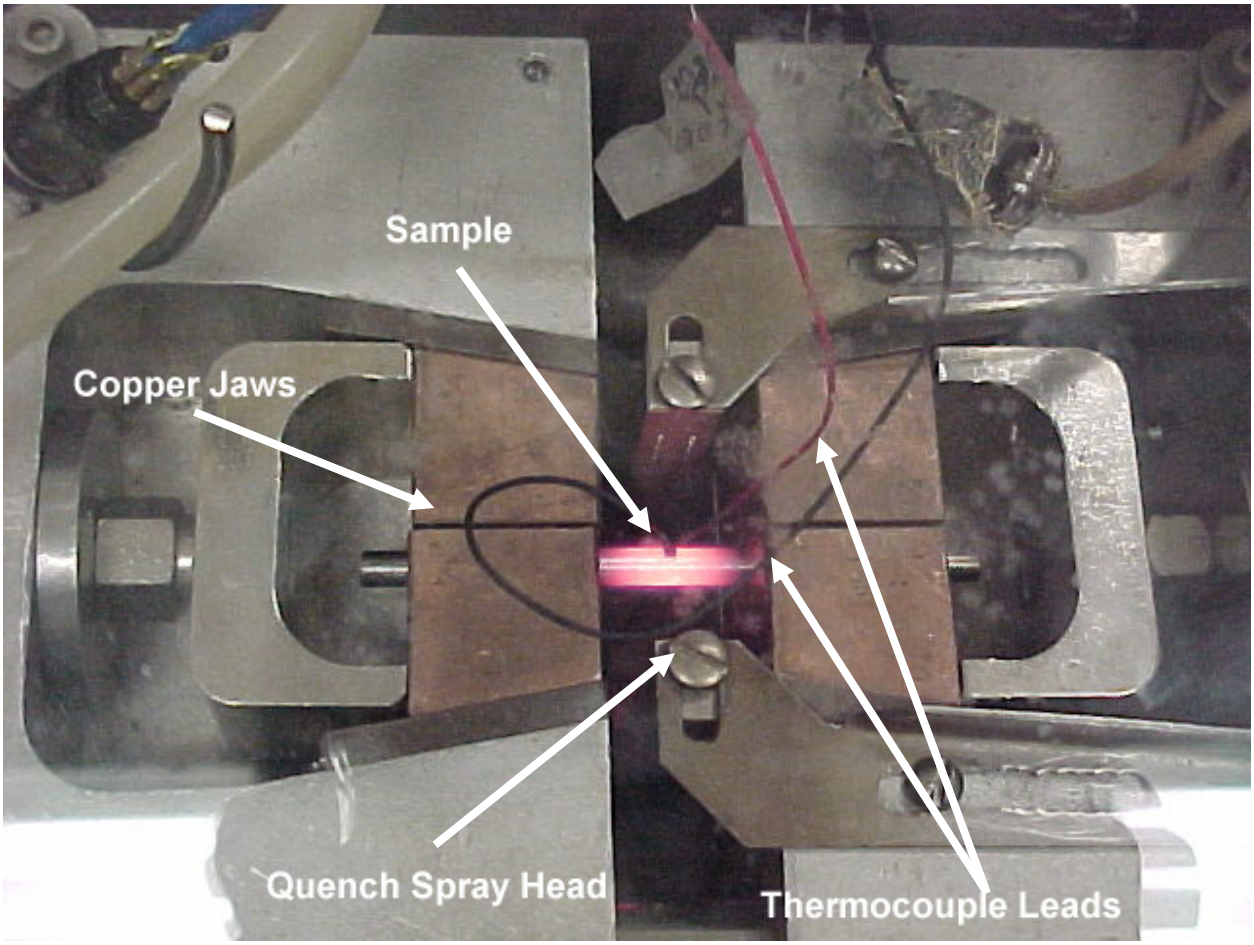

Figure 3.2: A Ti-6Al-4V sample being resistively heated in a Gleeble 1500 thermomechanical simulator.

The samples used in these experiments are the normalized samples described above. In the following experiments, large beta grain sizes allow for the observation of other beta transformation products such as intragranular primary- and secondary-alpha, not just grain boundary nucleated primary-alpha phase, which would be the case if an as-received or fine beta grain size were used.

The heating schedule used was a 2.5K/s heating rate to 1373K (T_{beta} + 105 K), hold at this temperature for 10 minutes, followed by cooling to room temperature at rates of 0.6, 10, 100, and >500 K/s. The slowest two cooling rates favor diffusion controlled $\beta \rightarrow \alpha+\beta$ transformation microstructures, while the fastest cooling rates should produce non-equilibrium beta transformation products, specifically $\alpha'+\alpha_{massive}$ and α'.[28] During the heating and hold at 1373 K segments of the thermal cycle, the sample was under vacuum (~10^{-4} Torr). During the cooling segment of the thermal cycle, the vacuum was maintained for cooling rates less than 10 K/s. For

the 100 and 500 K/s cooling rates, helium and water were used, respectively. The change in the diameter of the sample was measured throughout the experiment using a contact dilatometer for each sample except the 500 K/s samples, where the dilatometer interferes with the quench spray; however, this data is not presented here.

Two sets of samples underwent the 0.6, 10, and 500K/s cooling rate primary heat treatment. The second set underwent an additional sub-transus secondary heat treatment to investigate the effect of heating the primary-alpha microstructures high into the two phase region. These samples were held at 1198 K (T_{beta} – 70 K) for 10 minutes and cooled at the same rates and atmospheres as before.

Characterization Techniques

General

Optical samples were sectioned parallel to the diameter of the sample near the mid-span where the thermocouple was attached. The optical samples were ground and polished using standard metallographic techniques and etched using a solution of 5% HF and water for approximately 10 seconds. Optical samples were examined using a Leica MEF3 metallograph. The optical samples were also examined on an FEI XL30 field emission gun scanning electron microscope (SEM) with electron backscattered diffraction (EBSD) capabilities. SEM samples were observed after removing the previous etch (optical metallography) using a colloidal silica final polish (for 2 minutes). In addition, Vickers microhardness measurements were made using a load of 300 g and an indent time of 15 seconds on a Leco M-400-H2. Five indents were made on each polished and etched optical metallographic sample.

Electron backscattered diffraction ("OIM")

The purpose of the electron backscattered diffraction analyses (EBSD) performed in the SEM was to establish an understanding of the crystallographic development of the different morphologies present, to illustrate crystallographic relationships between the alpha and beta phases, and to reveal crystallographic information about the non-equilibrium phases that form during the more rapid cooling heat treatments.

Being a rather new technique, at least in the fully automated form, only a few experiments have been performed on titanium alloys using EBSD. Seward, *et al*. examined the $\alpha \rightarrow \beta$ transformation in commercially pure titanium using EBSD techniques.[65] It was determined that during heating above the beta transus†, beta appears both intragranularly and at the α/α grain boundaries as allotriomorphs, with the beta phase having the Burgers orientation relationship with the alpha phase. Based on the observed surface relief, intragranular plates and allotriomorphic types of beta phase were found to form via a military and civilian transformation, respectively. At the completion of the transformation, the intragranular beta phase is consumed by the allotriomorphic beta phase due to surface energy differences in the two shapes.

Banerjee, *et al*. used metal deposition techniques (LENS™) to produce a compositionally graded Ti-8Al-*x*V alloy and used EBSD to characterize the grain boundary orientation relationships.[40] The grain boundaries in the deposit are very large and due to the composition grading, a single beta grain boundary can extend through a large composition gradient. The orientation relationship between these large beta grains with a graded composition and the alpha grain boundary allotriomorphs (α_{GB}) and primary alpha (α_P) sideplates were examined in EBSD. It was determined that most of the α_{GB} precipitates exhibit a Burgers orientation relationship with the parent β phase. In addition, the α_{GB} was not continuous (having the same orientation) along the boundary. Instead, alternating α_{GB} precipitates sharing the basal plane formed; however, the $<11\bar{2}0>$ directions are parallel to two different $<111>$ directions on the same $\{011\}$ planes of the beta grain obeying the Burgers orientation relationship, leading to two types of α_{GB} precipitates.

The data for the EBSD analysis of the baseline microstructure experiments will be presented in several graphical forms and each will be briefly described here for the primary heat-treatment 0.6 K/s sample. An image of the microstructure can be obtained by mapping the quality of the EBSD pattern, or "image quality" obtained at each measured point. The image quality (IQ) parameter is defined as the sum of the Hough transform peaks obtained, and as a result the IQ is related to the material and its condition. Factors such as strain, different phases, orientation, and

† Recall that pure titanium is single phase alpha below 873K and single phase beta above.

different elements will effect the EBSD pattern that is acquired. Increased strain, for example, has been shown to produce lower quality patterns and as a result can be used to locate regions of massive or martensitic products in steels that are otherwise difficult to detect in optical microscopy.[66] In addition, experimental parameters dealing with the microscope (voltage) and acquisition (camera brightness/contrast, gain, exposure) all effect the quality of the EBSD pattern obtained. As a result, it is unrealistic to infer a quantitative measure from IQ, instead it is useful for comparing an image to the orientation data obtained.

TEM

TEM samples were sectioned parallel to the diameter of the sample near the mid-span where the thermocouple was attached. Discs (3-mm diameter) were cut from the center of the sample using an electro-discharge machining (EDM) apparatus. The 3-mm discs were ground from a starting thickness of 150 to 200 μm to 75 μm using in order 600-grit, 40-μm, 15-μm, 5-μm, 2400-grit, and 4000grit abrasive discs. The 2400 and 4000-grit discs gave a "mirror" finish to the 3mm samples. Next, the samples were dimple-ground from one side to a ~10 μm thickness at the center of the disc. The diamond pastes used for dimple grinding were in order 6, 3, and 0.5μm with a mineral oil lapping fluid and lastly an Al_2O_3 suspension polish. Perforation of the discs was performed on a Tenupol-3 twin jet electropolishing apparatus using a solution of 600ml methanol, 335ml 2-butoxyethanol, 60ml perchloric, and 5ml glycerin at temperatures below -40°C and a voltage between 10 and 20V. Times for perforation ranged from 30s to 3 minutes. A perforation detection sensitivity of 5-7 was used, with 10 being the most sensitive setting. The best results were obtained at higher temperatures (-15°C); however, this is in the regime where titanium hydride phase forms at the alpha beta interface (interface phase).[67-70]

Samples were examined on the FEI Tecnai 20 (200kV) TEM. The TEM was used to investigate the morphology, crystal structure, and limited composition measurements of the two phase microstructure in each of the baseline microstructure samples, except the primary-slow cooled heat treatment (bad sample). Selected area diffraction (SAD) patterns were indexed using the aid of a program written in *Mathematica* using the locations of the diffracted spots and the angles between them. (See Appendix: Selected Area Diffraction Indexing Procedure).

Results

The results are presented in the following manner. First the measured cooling rates and hardness are presented. This is followed by examination of the effect of cooling rate and primary and secondary thermal treatment using optical microscopy, SEM in backscattered electron imaging mode, EBSD, and TEM.

Measured Cooling Rates and Hardness

The measured cooling rate and average hardness of each sample is shown in Table III. There is a general trend towards increasing hardness for increased cooling rate; however, no specific conclusion may be drawn due to difficulty in measuring the cooling rate during the water quench. Two of the three water-quenched samples (Sample 04-01-1 and -4) melted due to an over-correction by the temperature controller during the quench phase of the thermal program. During the quench phase of the third sample (04-01-2), the quench hose became dislodged before the sample had completely cooled to room temperature, resulting in the sample cooling from 1373 K at 3400 K/s to 673 K and then air cooling to room temperature.

Table III: Measured Cooling Rates and Microhardness Values of Ti-6Al-4V Baseline Microstructure Samples

Sample	01-01	01-02	02-01	02-02	03-01	04-01-1	04-01-2	04-01-4
Primary HT Cooling Rate, K/s	0.6	0.6	10	10	94	>500	3400	6790
Secondary HT Cooling Rate, K/s	-	0.6	-	10	-	-	-	-
Average HV_{300}	305±14	328±53	314±23	332±18	351±8	408±14	335±25	369±15

Slow Cooling (0.6K/s)

The macrostructure of the primary and secondary heat-treated samples with the slowest cooling rate (0.6K/s) are shown in Figure 3.3a-b. In the primary sample, Figure 3.3a, several rather large prior beta grains are present in the center of the sample. These grains are comprised of rather large regions of macrostructural contrast. It is typical for Ti-6Al-4V that differences in macrostructural contrast corresponds to similar microstructure morphologies at the micro-level. In the secondary sample, Figure 3.3b, it is difficult to distinguish individual prior beta grains,

though their size should be identical to the primary sample since sub-beta transus heating does not affect the prior beta grain size. Clearly the regions of optical contrast are much smaller in the secondary sample.

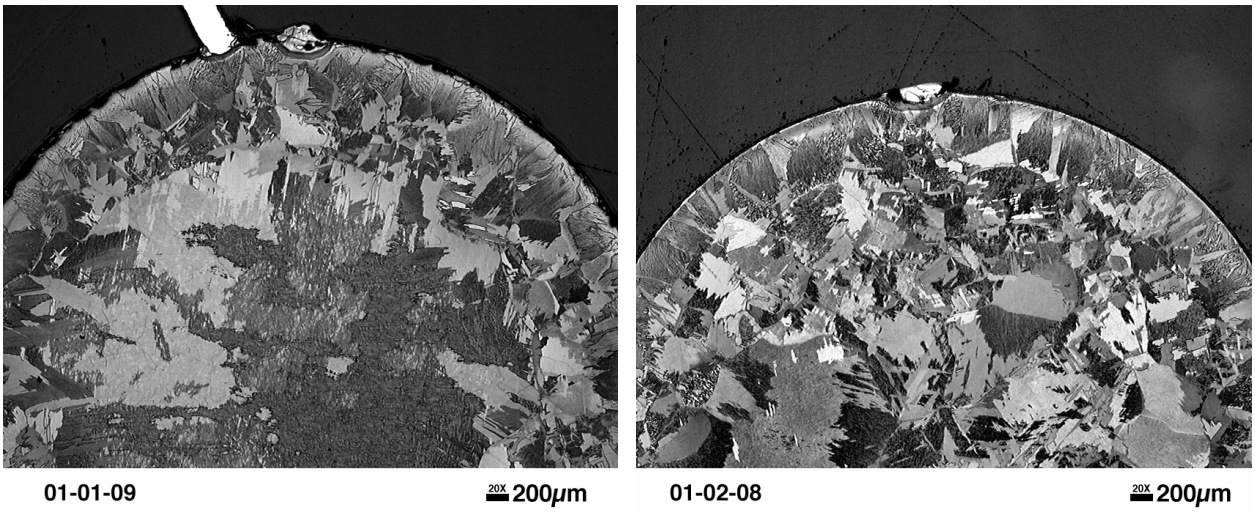

Figure 3.3: Macrostructure of primary (a, T=1373 K) and secondary (b, T = 1198 K) samples cooled at 0.6 K/s. The primary heat treatment produced large colonies primary-alpha, while the addition of the secondary heat treatment produced smaller, secondary-alpha intragranular colonies.

At the microstructural level, the morphology of the optical contrast in Figure 3.3 becomes more apparent. Figure 3.4 shows different microstructural morphologies present in the primary heat treated sample cooled at 0.6 K/s. The aforementioned regions of optical contrast contain α_P in both colony and basketweave morphologies. The presence of α_P colonies is expected due to the slow cooling rates used; however it is somewhat surprising to see α_P in a basketweave arrangement at such slow cooling rates. This may be a result of the large prior beta grains being used which allow for sufficient time/undercooling for α_P to nucleate intragranularly in the basketweave arrangement.

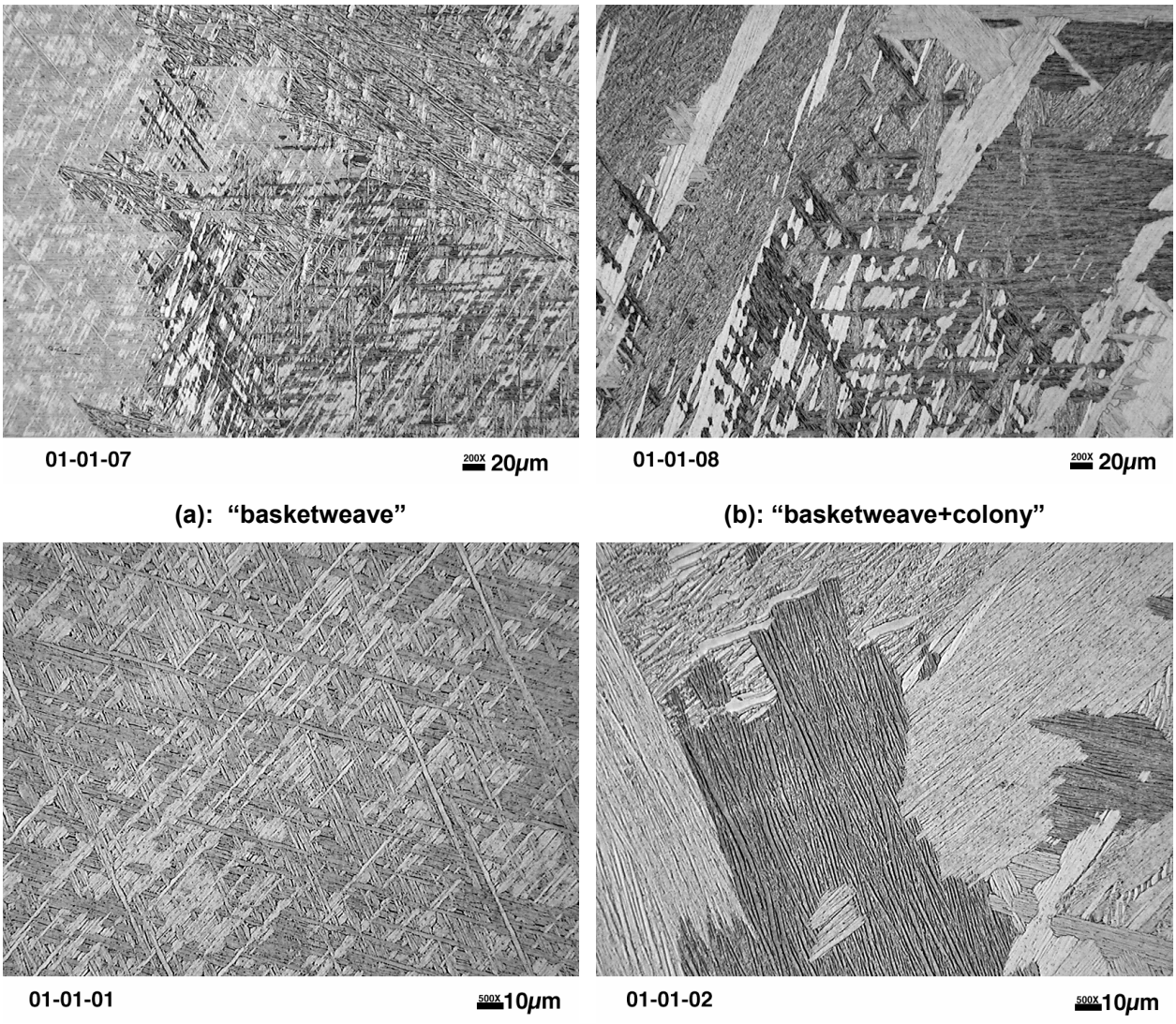

Figure 3.4: Optical microstructure of primary (T=1373 K) samples cooled at 0.6 K/s. The primary heat treatment produced large mixture of basketweave (a, b, c) and colony (b, d) primary-alpha.

The microstructure after the secondary heat treatment and the slowest cooling rate is shown in Figure 3.5 and is comprised mainly of colony α_P that has nucleated at prior beta grain boundaries and α_S that has nucleated intragranularly, as indicated. Note the lack of α_P or α_S in a basketweave morphology, indicating that it preferentially dissolves during the secondary-heat treatment, leaving intragranularly nucleated α_S colonies.

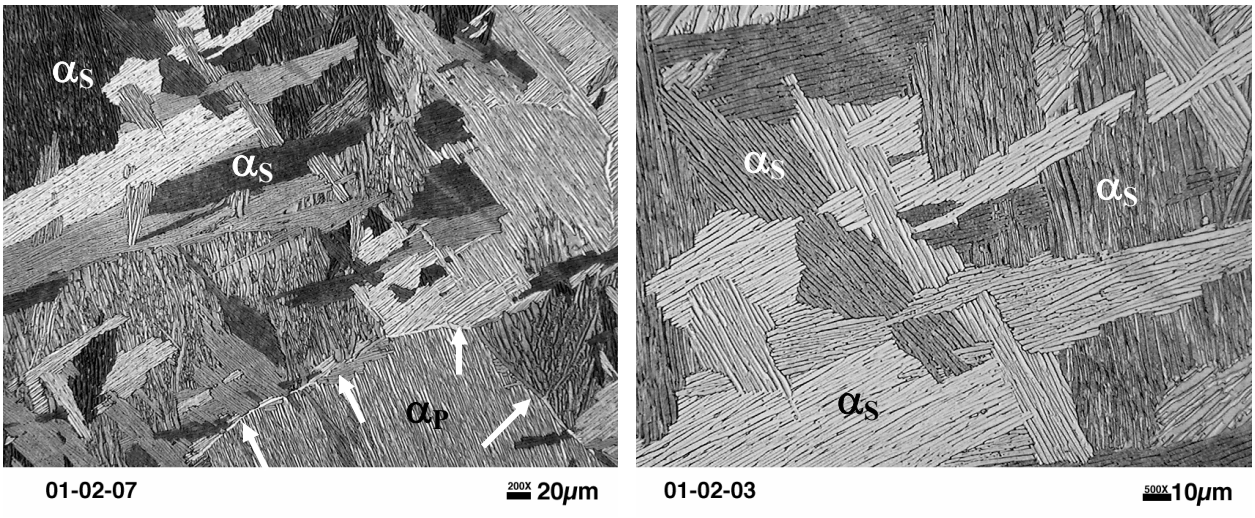

Figure 3.5: Optical microstructure after the secondary heat treatment (T = 1198 K, 0.6K/s) consisting of a mixture of (a) grain boundary nucleated primary-alpha (α_P) colonies and (b) intragranularly nucleated secondary alpha (α_S) colonies. In (a) α_{GB} is indicated by arrows.

Examination of the baseline microstructure samples in the SEM was done using the backscattered electron (BSE) mode to qualitatively reveal the distribution of alloying elements between the alpha and beta phases. Figure 3.6 shows the phase contrast due to the distribution of alloying elements in the primary heat treated sample cooled at 0.6 K/s. Vanadium, having a higher atomic number than aluminum, partitions to the beta phase producing lighter (white) shading in BSE mode. The retained beta matrix is very fine between the α_P grains.

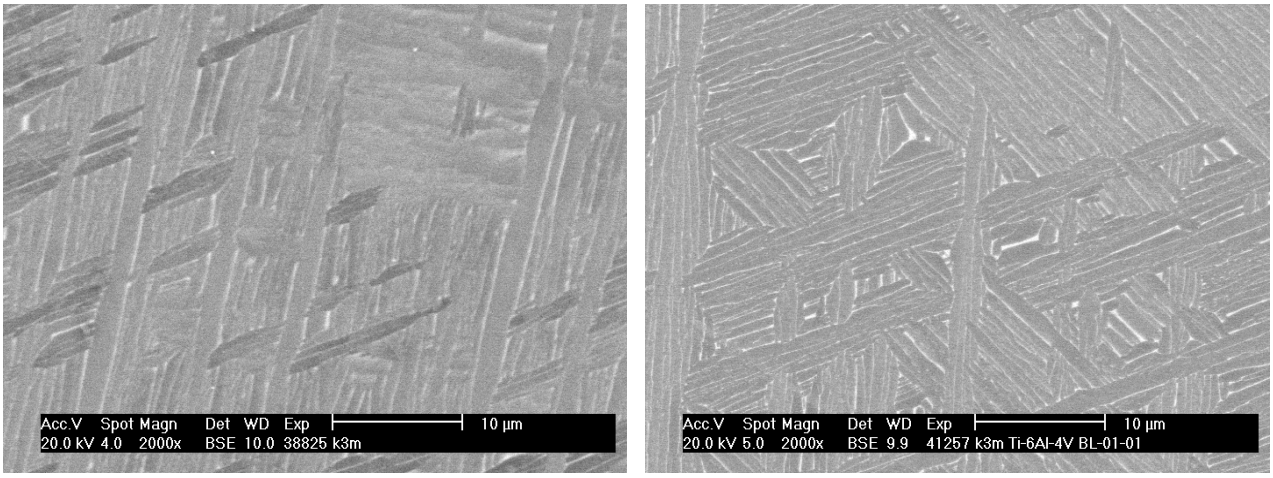

(a) Primary **(b) Primary**

Figure 3.6: BSE micrographs of primary samples cooled at 0.6 K/s. The microstructure consists of (a) basketweave α_P and (b) intragranularly nucleated α_P colonies with vanadium clearly partitioning to the beta phase.

The colony structure produced by the secondary heat treatment and slow cooling consists of regions of alpha outlined in beta phase that is enriched in vanadium as illustrated in Figure 3.7.

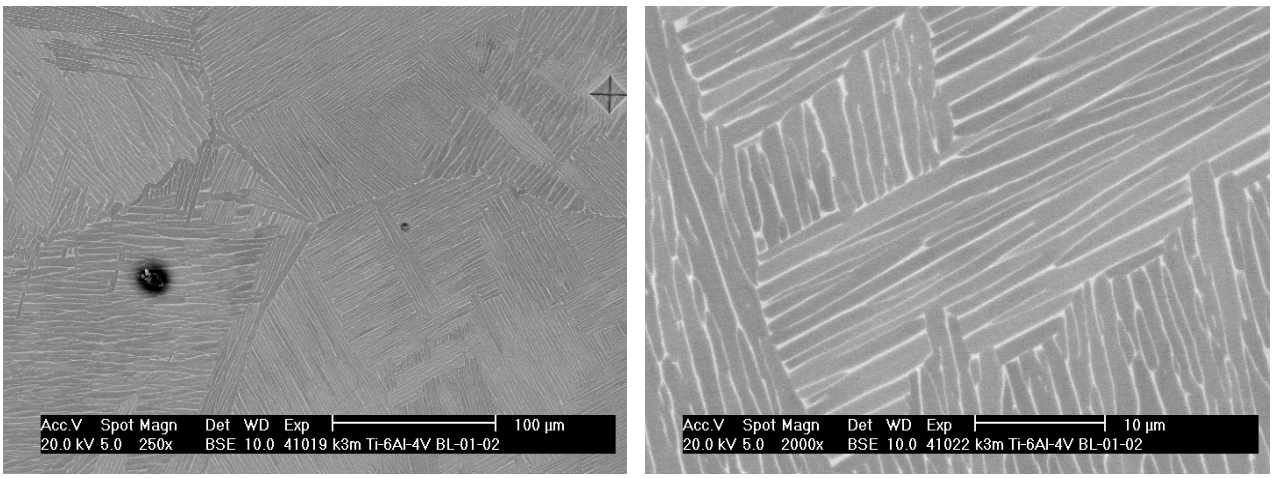

(a) Secondary **(b) Secondary**

Figure 3.7: BSE micrographs of secondary samples cooled at 0.6 K/s. The microstructure consists of (a-b) α_P and α_S colonies with vanadium clearly partitioning to the beta phase.

An IQ map for the primary heat-treatment 0.6 K/s cooling rate sample is shown in Figure 3.8a. First, note the scale of the image, where the marker indicates that 90µm is equivalent to 100 steps. This simply means points were measured at 0.9µm intervals. In Figure 3.8a, the IQ ranges from 15 (black pixels) to 64 (white pixels), where the poorest image quality is observed in the scratches on the surface of the sample. The microstructure that is revealed consists of a mixture of colony and basketweave α_P morphologies. At the boundaries of individual α grains

and colonies there is a region of poor IQ present at the grain interfaces. The poor pattern quality in these regions is due to overlap of the beam spot with two different phases or crystallographic orientation giving arise to multiple EBSD patterns that must be indexed. In this case the analysis software cannot differentiate one pattern or the other, thus to the computer, the pattern quality is poor.

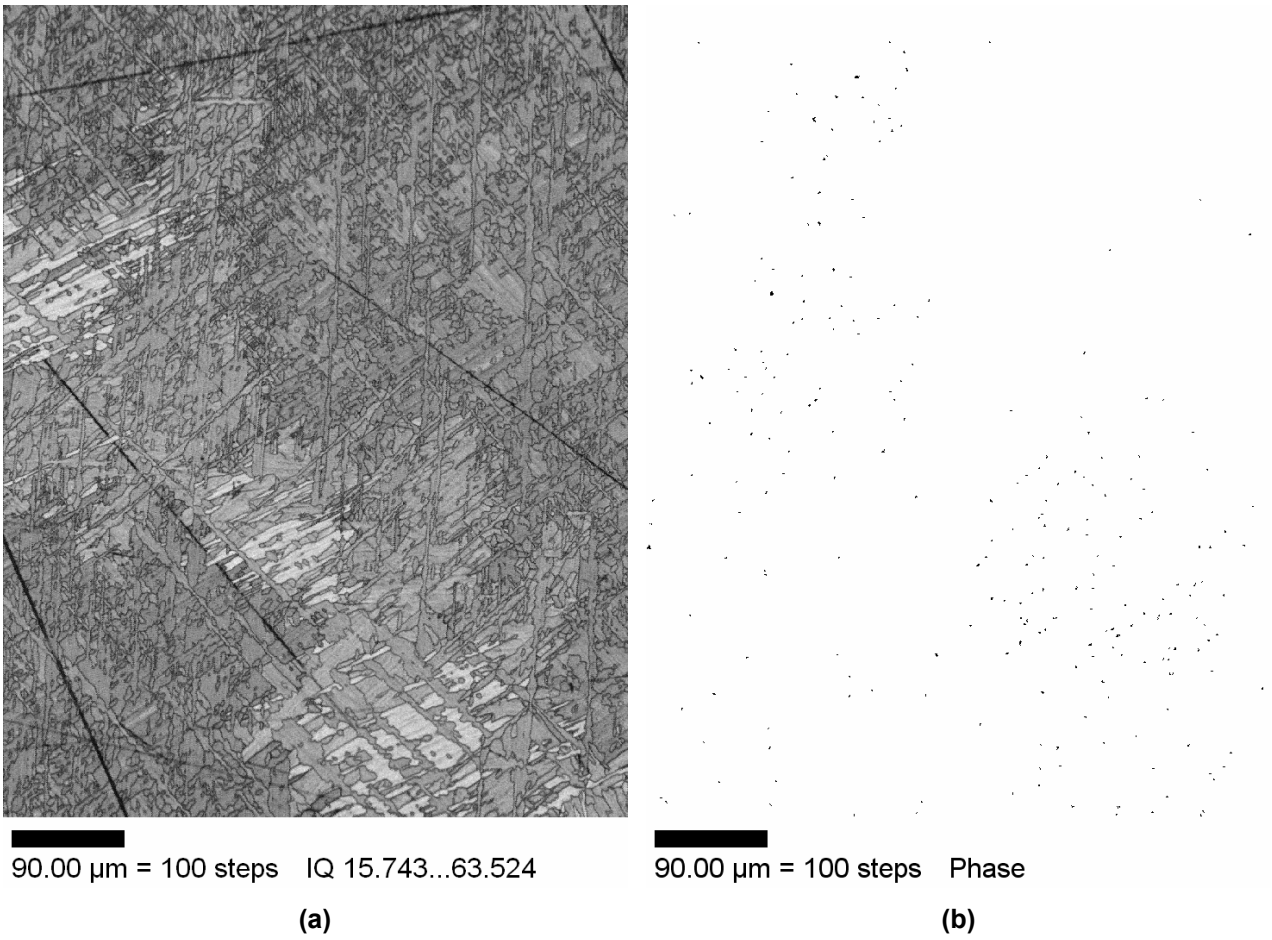

Figure 3.8: EBSD analysis of the primary heat treatment, 0.6K/s cooling rate. A IQ map (a) showing the microstructure analyzed and (b)a phase map showing the locations where the beta phase was detected in this sample. The beta phase fraction is 0.1%. [BL_01_01_Scan_3]

In Figure 3.8b the beta phase is mapped over the analyzed region, giving an area fraction of 0.1% beta. Clearly, the software/technique has difficulty in detecting the beta phase since it is present on such a fine scale (see the backscattered images, Figure 3.6). When the beta phase is detected, there is no apparent pattern or correlation to the actual microstructure. This indicates that EBSD could not be used as a method to measure phase fraction in alloys where the physical dimensions of the phase are on the order of the beam dimensions. It should be noted that a finer scan

resolution was attempted with little or no improvement in detecting the beta phase consistently. As will be seen in the TEM results, the beta phase thickness is submicron, meaning that a finer step size (<<0.9μm) using a fine diameter beam analysis steps would be necessary for sufficient resolution of the beta phase.

The misorientation at each analysis point can also be mapped as illustrated in Figure 3.9a. Boundaries can be defined in several ways, but here the rotation angle boundary misorientation is plotted. The misorientation angle is the minimum rotation angle (out of all symmetrically equivalent possibilities - based on the axis/angle description of orientation) required to bring two lattices into coincidence.[71] Plotted in Figure 3.9a are boundaries of varying levels of misorientation: <10°, 10-15°, and >15°. The microstructure is dominated by high angle boundaries, which are present between individual and colonies of alpha grains. The alpha grains within colonies are oriented in a similar crystallographic orientation.

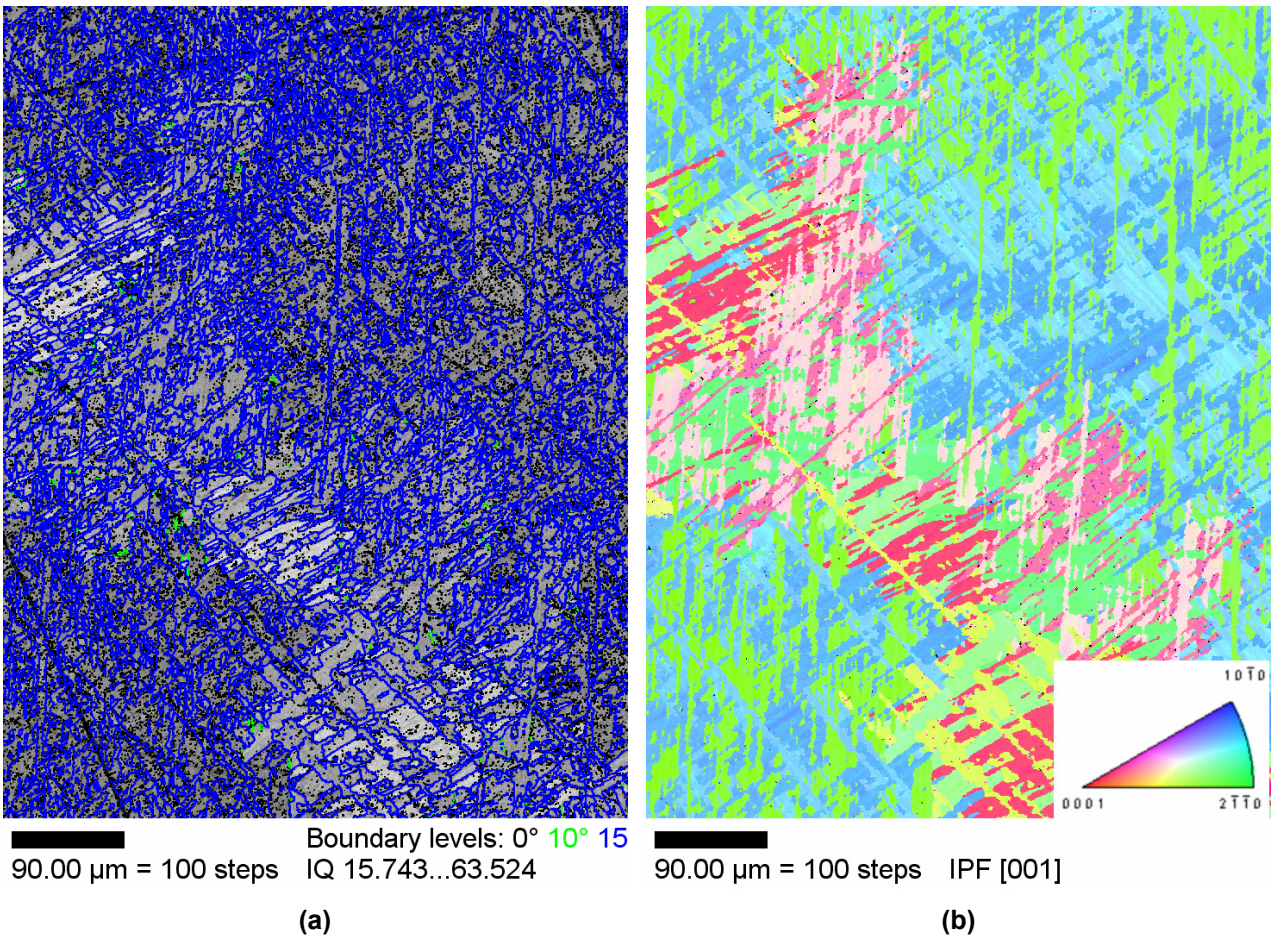

Figure 3.9: EBSD analysis of the primary heat treatment, 0.6K/s cooling rate. (a) Boundary misorientation and (b) an alpha inverse pole figure map. [BL_01_01_Scan_3]

Figure 3.9b shows an inverse pole figure map of the alpha phase, color coding the different orientation of each analysis point according to the HCP unit triangle. About 8 different variants out of the 12 possible Burgers variants are observed in Figure 3.9b. Similarly oriented α_P grains can be thought to have originated from a beta grain of unique orientation.

The results of the EBSD analysis of the 0.6K/s secondary heat treatment sample are shown in Figure 3.10 and Figure 3.11. The microstructure analyzed consists of three prior beta grains each containing a colony alpha morphology, with the fraction of beta phase detected to be 0.5% (Figure 3.10a-b).

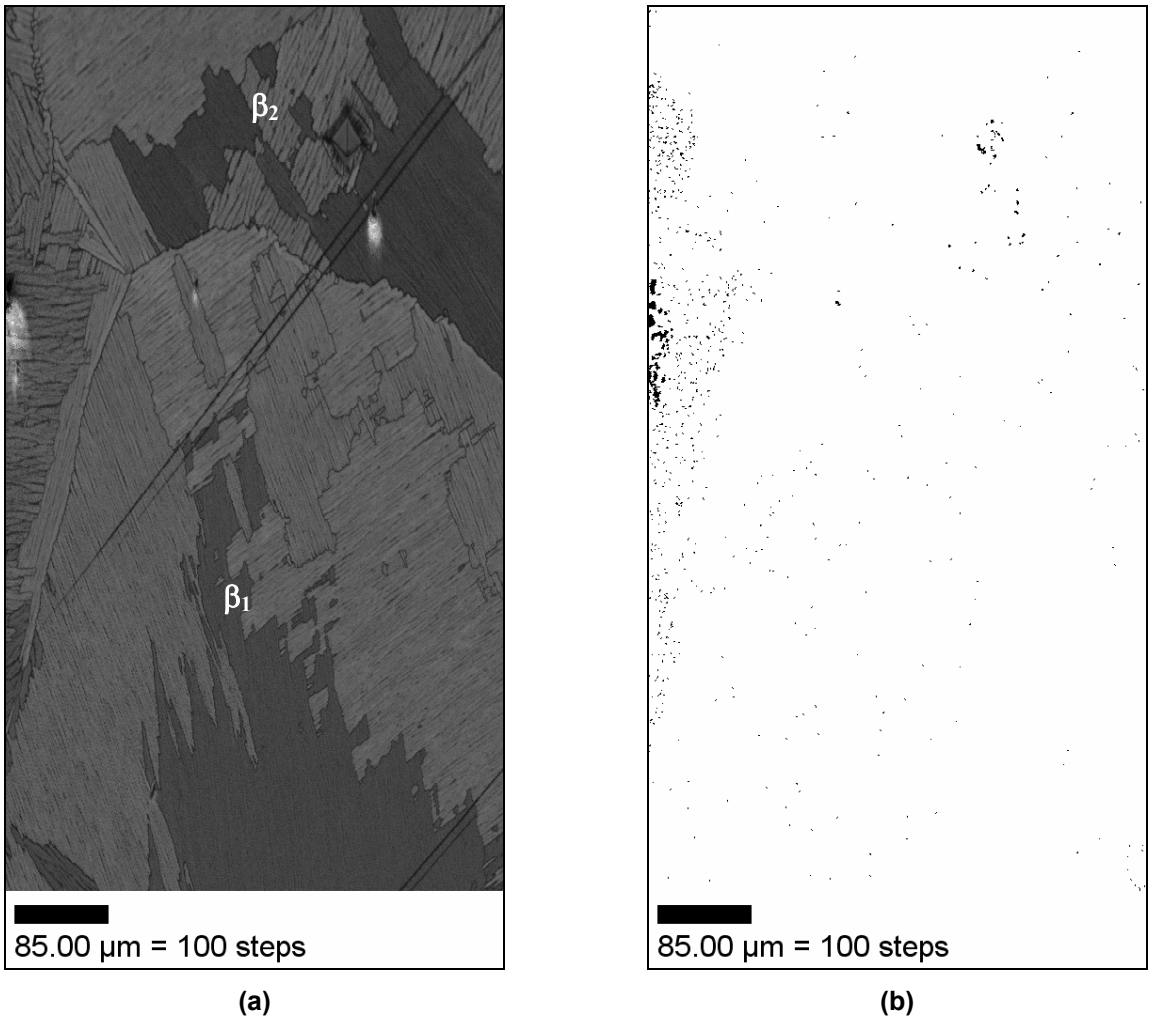

Figure 3.10: EBSD analysis of the secondary heat treatment, 0.6K/s cooling rate. An IQ map (a) showing the microstructure analyzed with two different prior beta grains highlighted. A phase map (b) showing the locations where the beta phase was detected in this sample. The beta phase fraction is 0.5%. [BL_01_02_Scan_3]

The plot of boundary misorientation (Figure 3.11a) indicates that most colonies are separated by high angle grain boundaries (>15°) while low angle grain (<5°) boundaries exist within the colony. Note that the colony at the bottom center of the image contains high angle grain boundaries. One possible explanation for this deviation is the IQ map (Figure 3.10a) indicates that this region is of a rather low image quality and as a result the software had difficulty in correctly indexing the EBSD patterns; however, other regions are equally as poor, yet are not as dominated by high angle boundaries. In Figure 3.11b the orientation of the high angle grain boundary containing colony is near the center of the unit triangle with apparent variations in the orientation within the colony, suggesting that two colonies of different orientation may be intersecting in this region.

Figure 3.11b clearly shows that α_P colonies that form at α_{GB} have the same crystallographic orientation, e.g. the [0001] (red) orientation, while the other irrational side of the α_{GB} forms with a different orientation. It is also interesting to note that in Figure 3.10a the prior beta grain marked "β_1" contains several colonies of α_P and α_S of different orientation; however, in Figure 3.11b the intragranular colonies have the same crystallographic orientation.

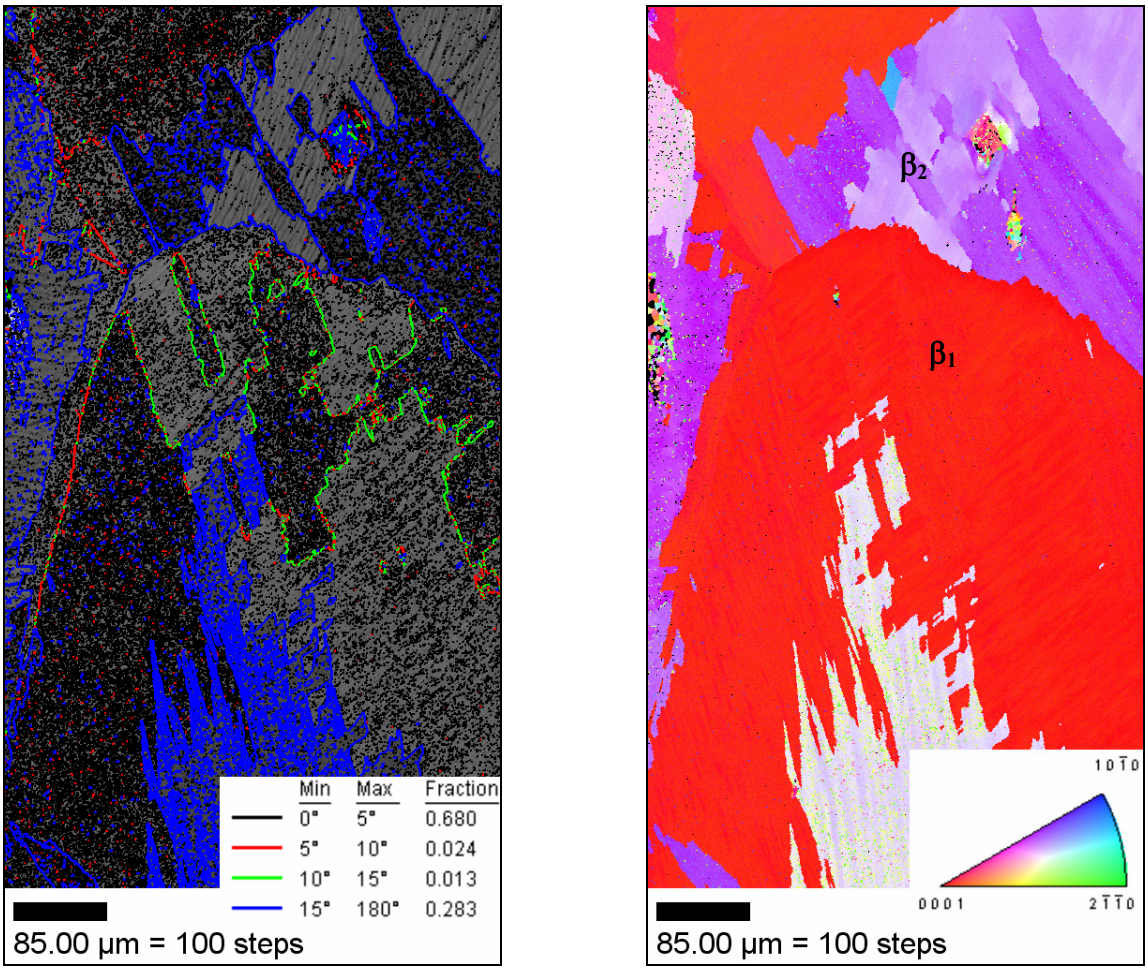

Figure 3.11: EBSD analysis of the secondary heat treatment, 0.6K/s cooling rate. (a) Boundary misorientation and (b) an alpha inverse pole figure map. [BL_01_02_Scan_3]

Bright field images and corresponding indexed diffraction patterns for the secondary heat treatment sample cooled at 0.6 K/s are shown in Figure 3.12a-d. Several α grains of a single colony are shown in Figure 3.12a and the interface between two alpha grains is shown in Figure 3.12c. Due to the local nature of TEM sample preparation, it is difficult to distinguish between α_P and α_S in these micrographs. The α grains are separated by a region of interface phase

(probably TiH_x) resulting from the electropolishing procedure[69] and β phase is found at the center of the α grains. The thickness of the beta phase is approximately 220 nm, and the alpha grains are relatively free of dislocations and stacking faults. The diffraction pattern in Figure 3.12d was not able to be indexed; however it most likely represents diffraction from the interface phase.

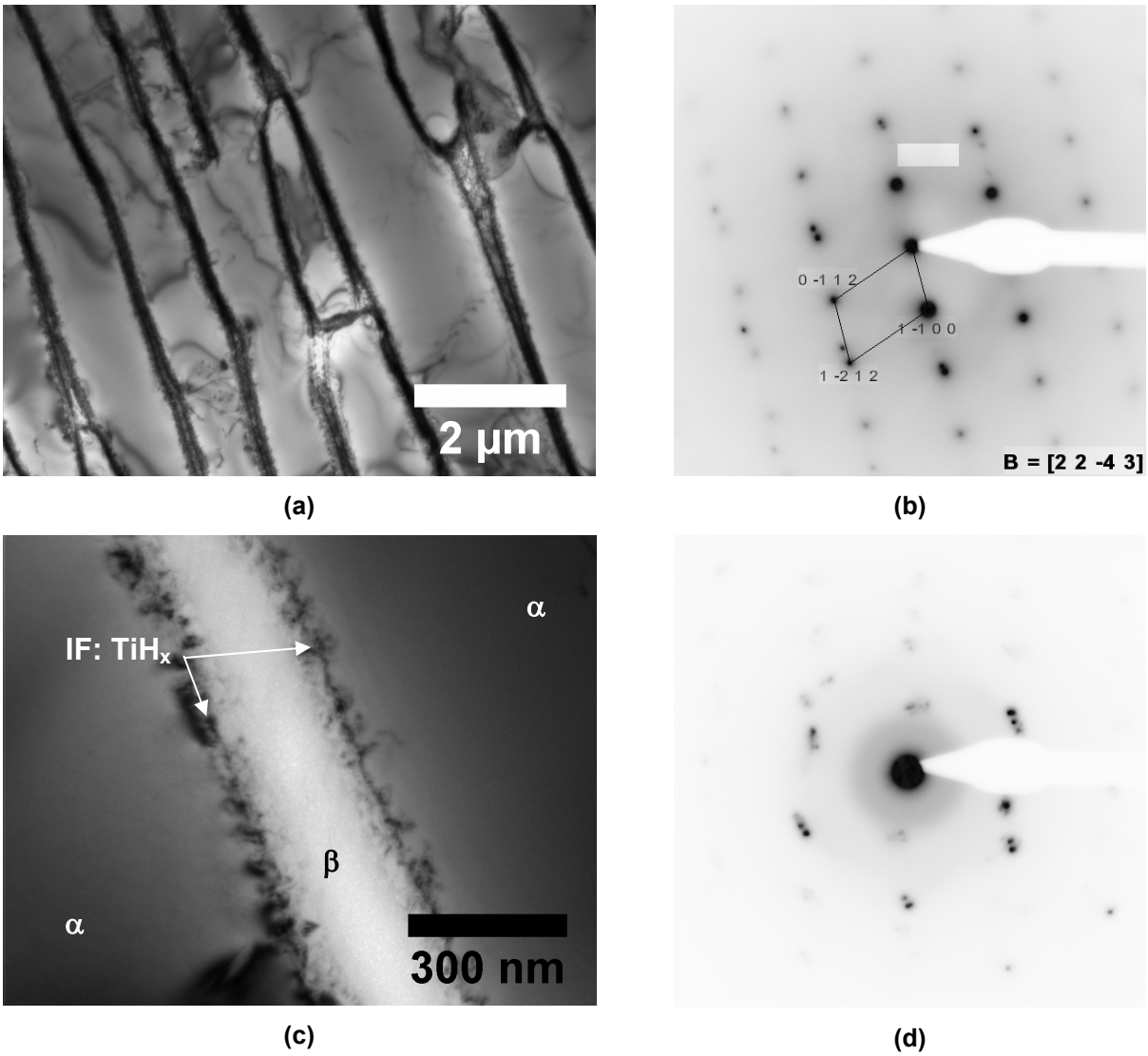

Figure 3.12: TEM bright field and corresponding indexed diffraction pattern from the secondary heat-treated sample cooled at 0.6K/s. (a) BF, alpha colonies (10kx, A02233); (b)SAD, (460mm, A02235) indexed as B=[2 2 -4 3] α-Ti; (c) BF example of the interface between two alpha grains (71kx, A02237) which contains the titanium hydride interface and retained parent β phases. The diffraction pattern (d) obtained from (c) was not able to be indexed as alpha, beta, or the interface phase (FCC, a0=4.45Å).

Energy dispersive spectroscopy (EDS) measurements were made across two alpha grains and their corresponding beta grain boundaries as shown in Figure 3.13a-b. Problems arose in

obtaining accurate composition measurements due to the overlap of the Ti-K_β and V-K_α peaks in the EDS spectra as shown in Figure 3.13c-d. A poor fit is indicated by a residual (yellow curve) that is not symmetric about zero intensity. Note the wide variation of Ti and V, with an increase in Ti accompanied by a decrease in V, due to the overlap of the aforementioned peaks in the spectra. The aluminum composition is much more behaved, remaining relatively constant through the α phase and decreasing slightly in the β phase. In addition, Fe, present in small amounts in this alloy, tends to segregate to the β phase since it is a β-stabilizing element like V.

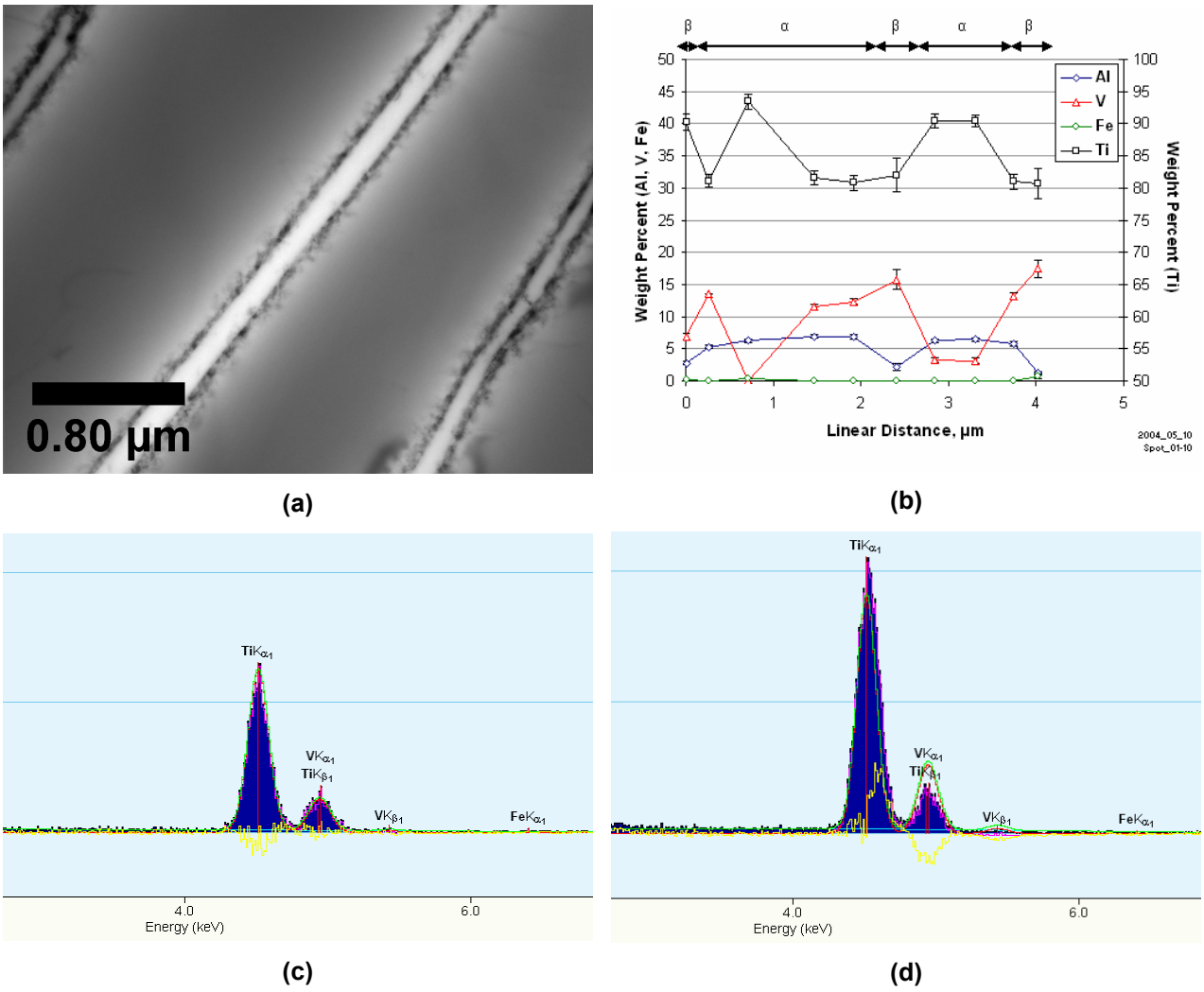

Figure 3.13: Secondary heat-treated sample cooled at 0.6K/s. (a) TEM bright field image (25.5kx, A02412) of two grains within an alpha colony and (b) a plot of the composition versus distance as measured using EDS in microprobe mode across these grains starting with the beta phase in the upper left and moving towards the bottom right corner. (c-d) examples of EDS spectra showing a (c) good fit between the measured and fitted spectra and (d) poor fit between measured and modeled spectra. The spectra is blue, modeled spectra is green, and the residual is yellow.

Moderate Cooling (10K/s)

The microstructures produced after the primary and secondary thermal treatments and 10 K/s cooling rate are illustrated in Figure 3.14. The primary heat treatment (Figure 3.14a-b) microstructure is comprised of small colonies of α_P nucleated at prior beta grain boundaries, with the interior of the prior beta grains dominated by basketweave α_P. The individual α_P grains, especially those nucleating from the grain boundary are very long and fine (high aspect ratio), following the primary heat treatment. After the secondary heat treatment (Figure 3.14c-d), the basketweave structure is retained is maintained. It difficult to distinguish between α_P and α_S in

these predominantly basketweave morphologies, with the exception of the long α_P colonies emanating from a prior beta grain boundary in Figure 3.14c.

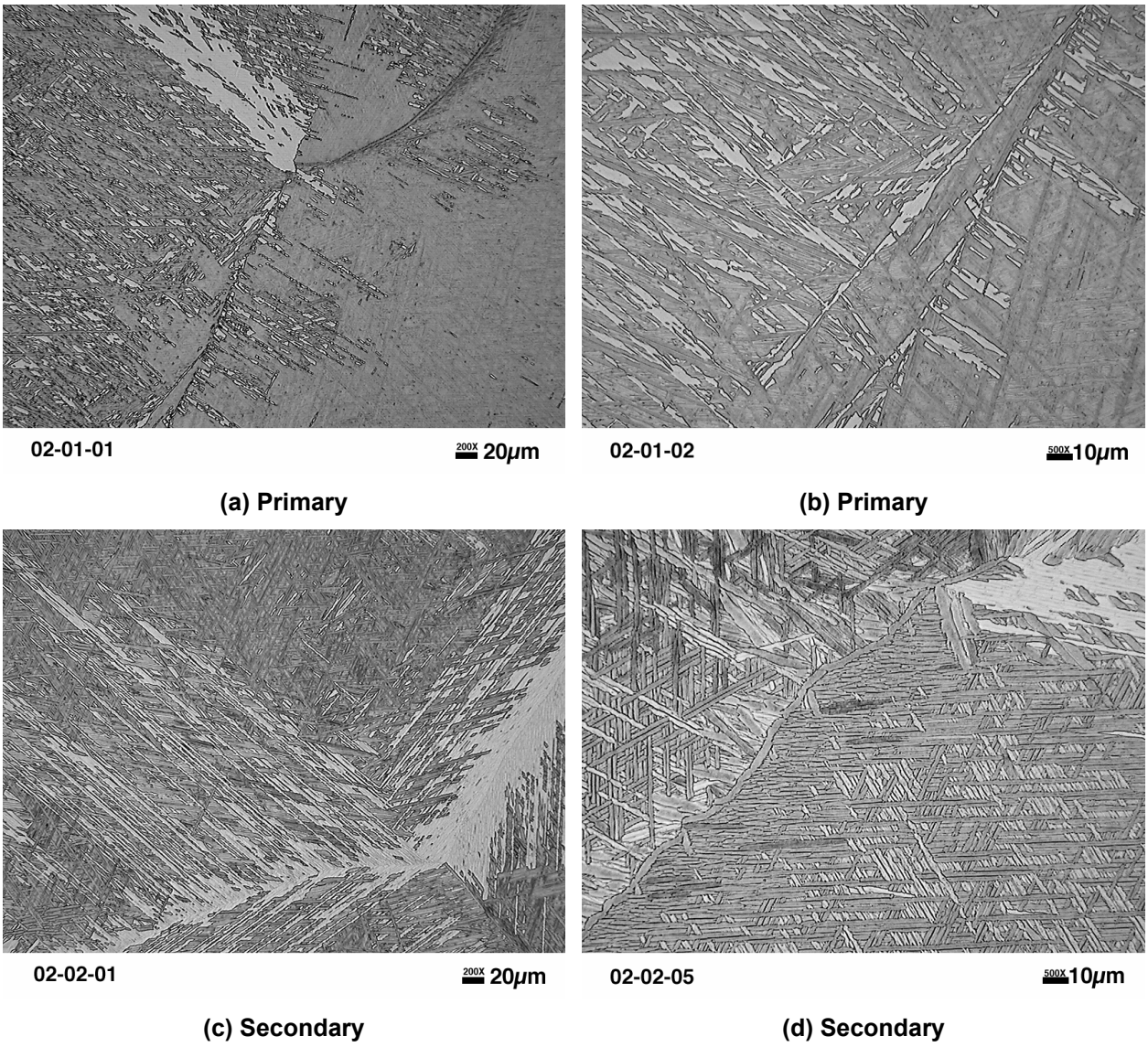

Figure 3.14: Optical microstructure of primary (a,b; T=1373 K) and secondary (c,d; T=1198 K) samples cooled at 10 K/s. The primary microstructure (a,b) is dominated by basketweave α_P with small amounts of colony α_P located at the grain boundaries and intragranularly. The secondary microstructure (c,d) consists of some retained colony α_P at the grain boundary with the majority of the prior beta grains containing basketweave-alpha where α_P and α_S are indistinguishable.

Increasing the cooling rate reduces the thickness of the alpha grains in the primary-heat treated sample as shown in Figure 3.15. The beta phase continues to be enriched in vanadium, however the beta phase is much finer as compared to the slower cooled primary heat treatment (Figure 3.6).

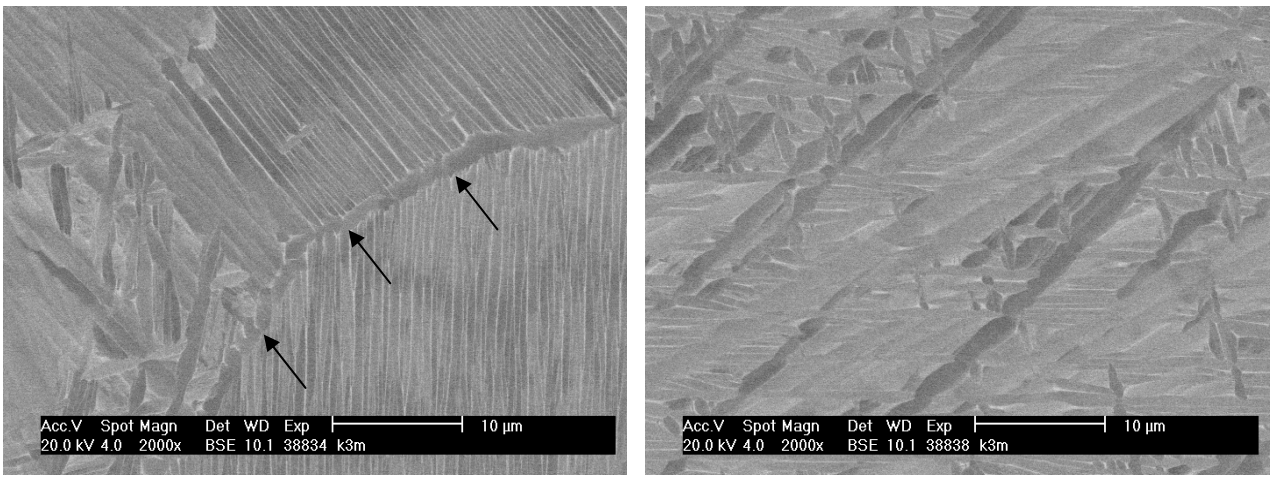

(a) Primary **(b) Primary**

Figure 3.15: BSE micrographs of primary samples cooled at 10 K/s. The microstructure consists of (a) prior-beta grain boundary (highlighted) nucleated colonies of α_P with the grain boundary decorated in α_{GB} and (b) intragranular nucleated basketweave α. Again, vanadium partitions to the beta phase

The effect of the secondary heat treatment on the microstructure becomes clearer during the faster cooling rate used in the 10K/s samples (Figure 3.16 and Figure 3.17). With the faster cooling rate, less time is available for the dissolved alpha grains to reassume their original morphology (e.g. by movement of the primary alpha grain boundaries). Instead, when cooling begins, alpha grains are forced to nucleate between the primary alpha grains that did not dissolve during the heating and isothermal holding period of the heat treatment. Primary-alpha grains are most easily distinguished due to their origination at the prior beta grain boundary as in Figure 3.16a. It is also notable that the β phase is more easily distinguished after the secondary heat treatment. This indicates that during cooling after a primary heat treatment insufficient time is allowed for significant partitioning of vanadium to the beta phase, leading to microstructures with little contrast in both the 0.6K/s and 10 K/s samples.

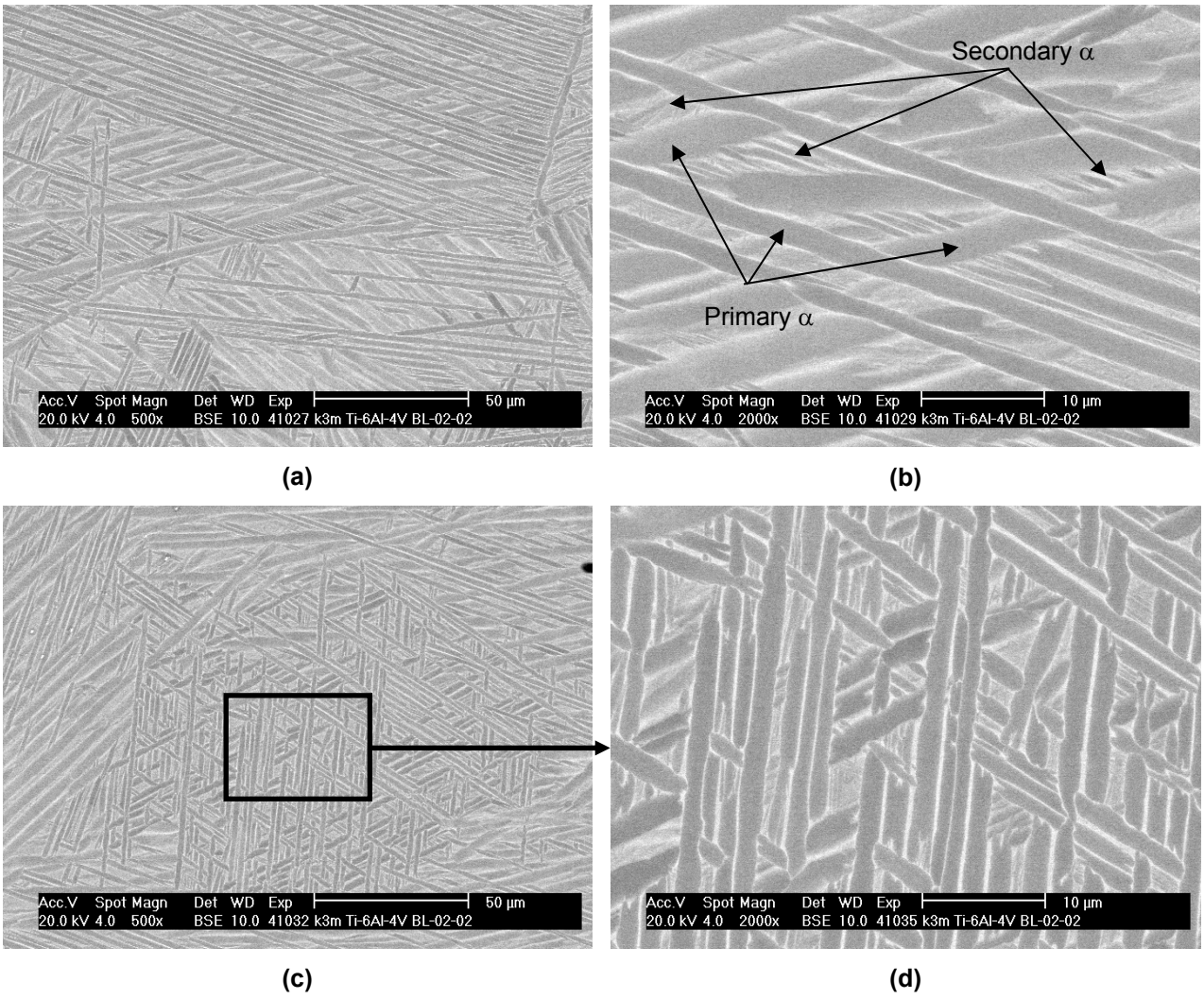

(a) **(b)**

(c) **(d)**

Figure 3.16: BSE micrographs of secondary samples cooled at 10 K/s, viewed in BSE mode. The microstructure consists of (a-b) colonies of α and single alpha grains nucleating from prior beta grain boundaries, and (c-d) basketweave alpha. In both types of morphologies, vanadium clearly partitions to the beta phase. In the higher magnification micrographs (b, d), fine structure consisting of primary and secondary alpha outlined in beta is revealed.

The primary and secondary alpha grains are more clearly observed in the high magnification micrographs of Figure 3.17, where the α_S grain width is on the order of 0.1μm.

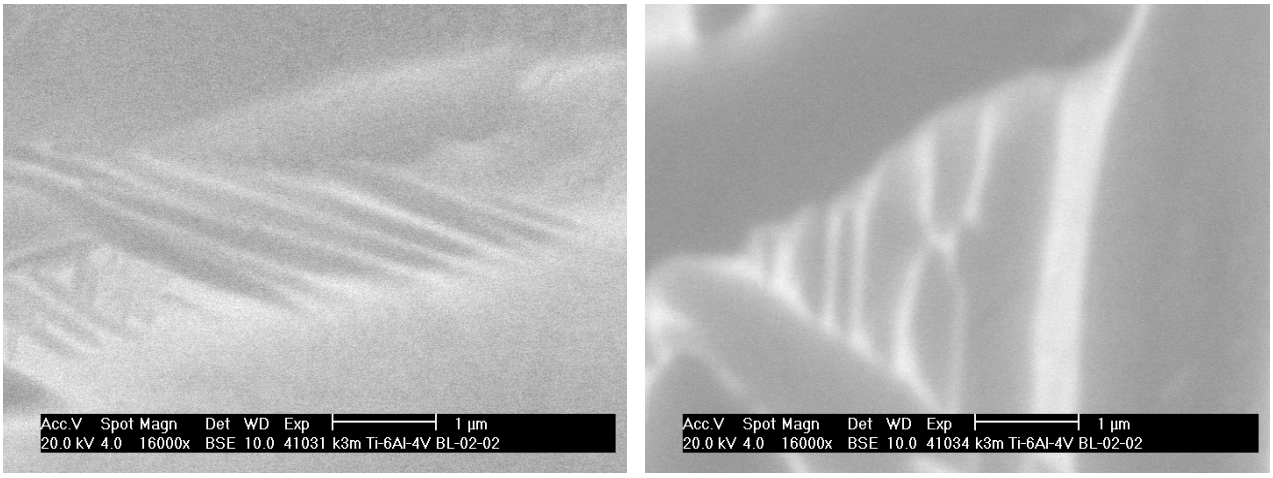

(a) **(b)**

Figure 3.17: High magnification microstructure of secondary heat treated samples cooled at 10 K/s, viewed in BSE mode. The microstructure consists of primary and secondary nucleated alpha phase, with the fine secondary phase grains appearing between primary α laths.

The basketweave microstructure is observed in the EBSD analysis in Figure 3.18 and Figure 3.19. The beta phase was not easily detected and was measured to be 0.2%.

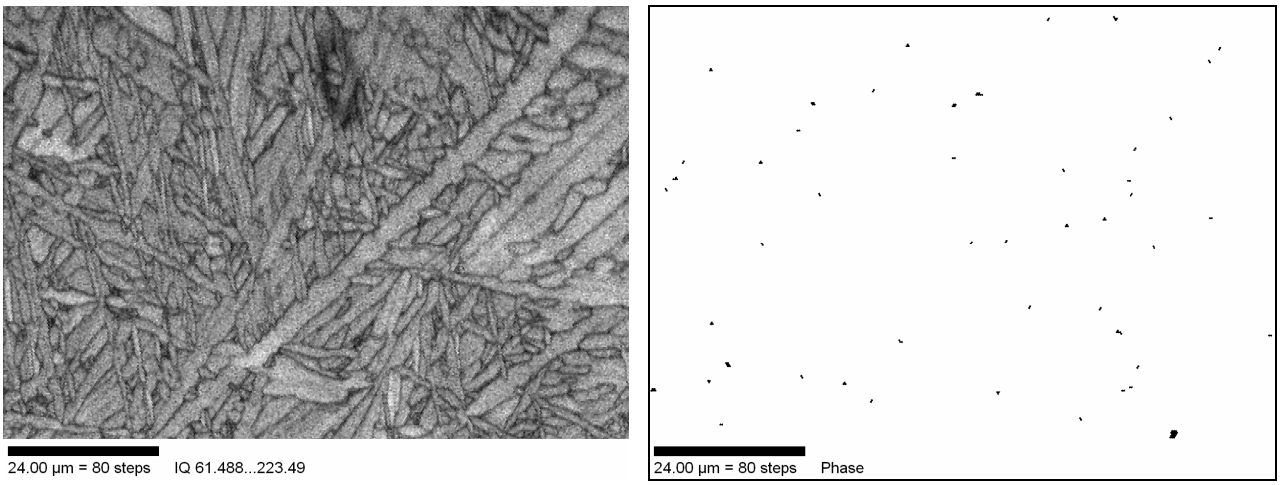

(a) **(b)**

Figure 3.18: EBSD analysis of the primary heat treatment, 10K/s cooling rate. A IQ map (a) showing the microstructure analyzed and (b)a phase map showing the locations where the beta phase was detected in this sample. The beta phase fraction is 0.2%. [BL_02_01_Scan_3]

The boundaries between the basketweave alpha grains are high angle boundaries as shown in Figure 3.19a, with the orientations of the individual alpha grains shown in Figure 3.19b.

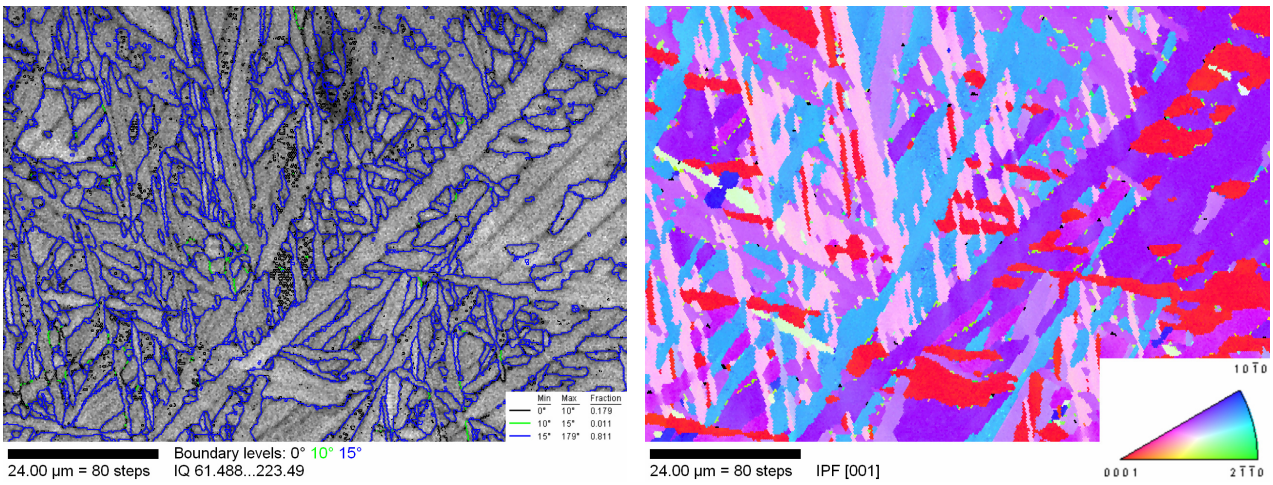

Figure 3.19: EBSD analysis of the primary heat treatment, 10K/s cooling rate. (a) Boundary misorientation and (b) an alpha inverse pole figure map. [BL_02_01_Scan_3]

Figure 3.20 and Figure 3.21 show the EBSD results from the 10K/s secondary heat treatment, which results in a basketweave morphology. Two different scans are shown in Figure 3.20 and Figure 3.21; a relatively lower magnification scan performed at 0.9µm steps and a higher magnification scan using 0.4µm steps. The primary- and secondary-alpha grains were easily resolved in BSE mode of the SEM (Figure 3.16c-d); however, the EBSD analysis does not provide such fine detail. The amount of beta phase detected is higher than any of the samples previously mentioned at 2.1% for the lower magnification scan. This could be attributed to the presence of the secondary-alpha which is outlined in beta, giving a greater amount of beta that will be diffracted from when the beam interacts with this region. Also recall that after the secondary heat treatment, the beta phase appears to be further stabilized as indicated in the BSE micrographs by better Z contrast.

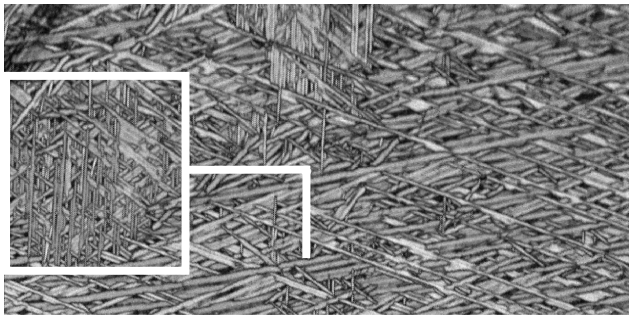

(a)

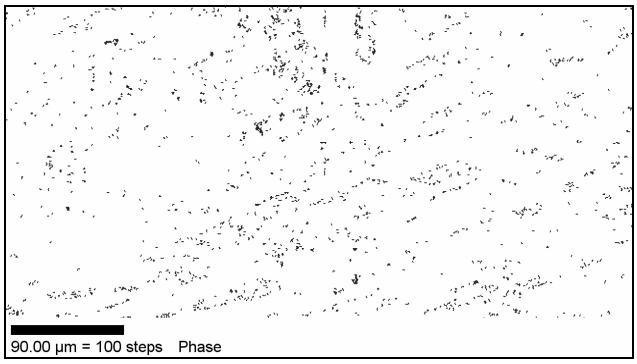

(b)

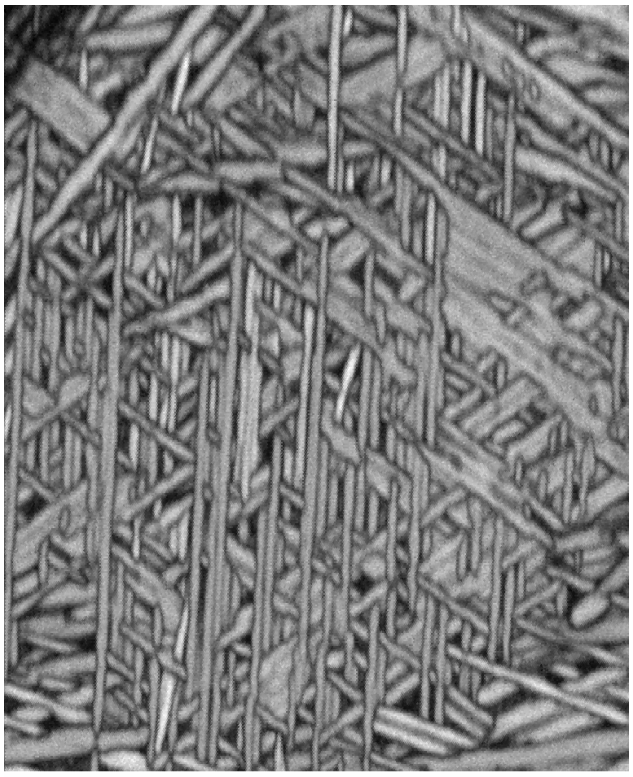

(c)

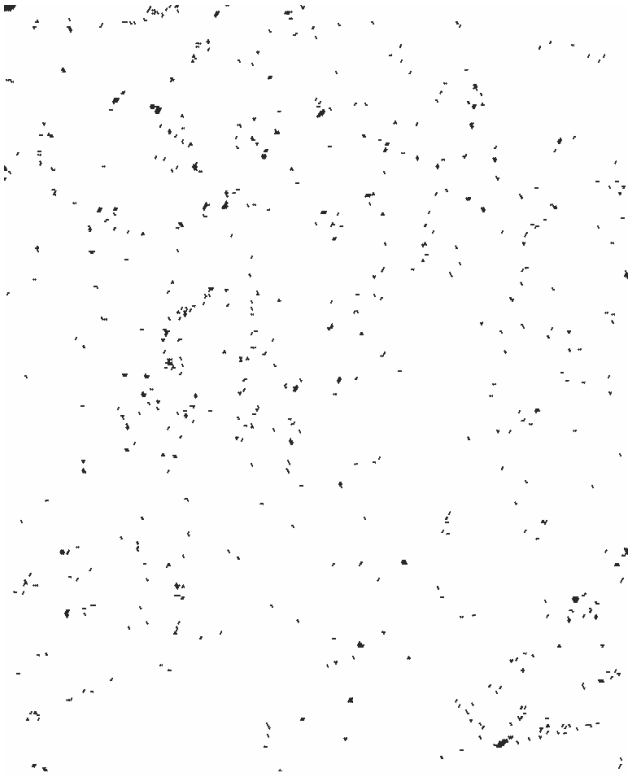

(d)

Figure 3.20: EBSD analysis of the secondary heat treatment, 0.6K/s cooling rate. A IQ map (a,c) showing the microstructure analyzed and (b,d) phase map showing the locations where the beta phase was detected in this sample. The beta phase fraction in (b) is 2.1% and (d) is 1.1%. Images (c,d) are from the highlighted region in (a). [(a,b): BL_02_02_Scan_1] [(c,d): BL_02_02_Scan_2]

The boundary misorientation continues to be dominated by high angle boundaries as shown in Figure 3.21a,c. The alpha inverse pole figure maps (Figure 3.21b,d) are interesting in that they show the presence of (0001)-oriented grain boundary nucleated alpha plates that extend well into the prior beta grain. The grain boundary nucleated alpha phase in Figure 3.16a are the same

grains analyzed in Figure 3.21b,d. The high magnification region exhibits very few grains of the (0001) orientation. There are two possible reasons for this region of dissimilar orientation in Figure 3.20-Figure 3.21: (1) this large region dissolved during the secondary heat treatment or, (2) this region nucleated from a different location on the prior beta grain e.g. errors in interpretation of a 2-dimensional micrograph. The first case is proposed because during the secondary heat treatment, this region may have completely dissolved to beta before retransforming to alpha of a different orientation upon cooling. Without the knowledge of the 3-dimensional microstructure the resolving he origin of this region becomes difficult.

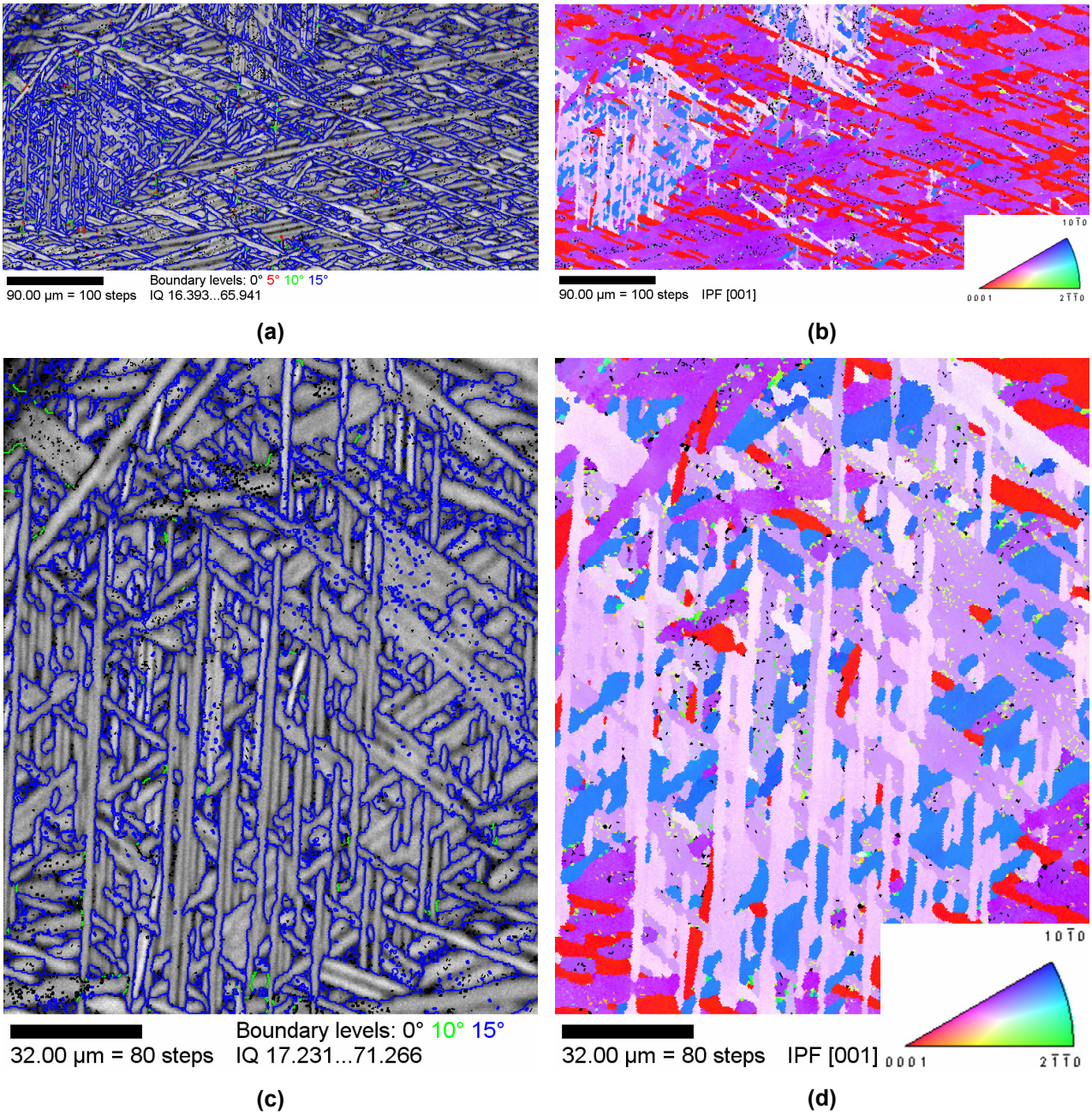

Figure 3.21: EBSD analysis of the secondary heat treatment, 0.6K/s cooling rate. A IQ map (a,c) showing the microstructure analyzed and (b,d) phase map showing the locations where the beta phase was detected in this sample. The beta phase fraction in (b) is 2.1% and (d) is 1.1%. Images (c,d) are from the highlighted region in (a). [(a,b): BL_02_02_Scan_1] [(c,d): BL_02_02_Scan_2]

TEM micrographs and indexed diffraction patterns from the 10K/s primary heat-treatment are shown in Figure 3.22 and Figure 3.23. A strongly diffracting colony is shown in bright and dark field mode in Figure 3.22a-b. The alpha grains comprising the colonies tend to show more imperfections/dislocations, indicating that dislocation density increases with cooling rate (compare Figure 3.12a with Figure 3.24a).

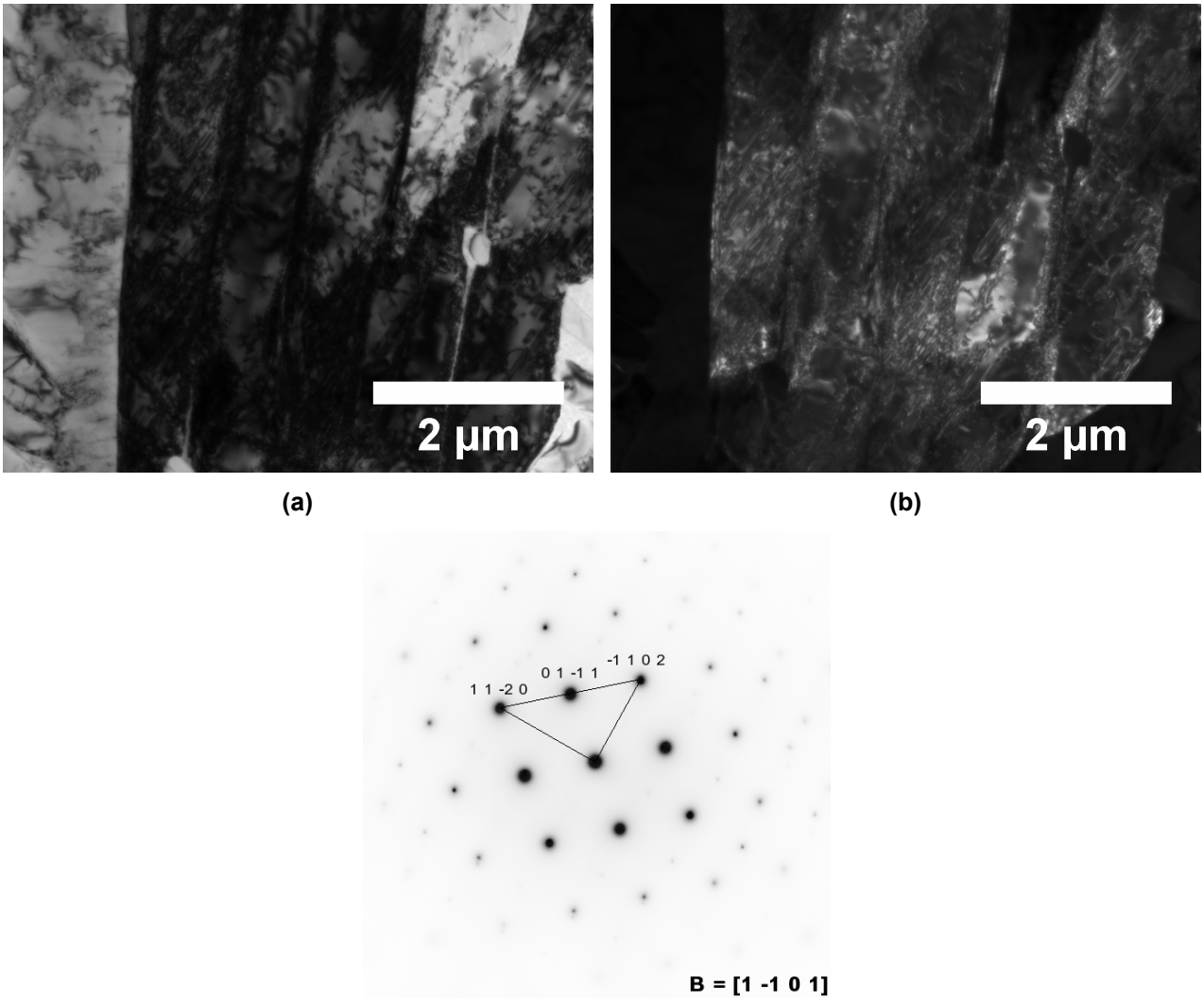

Figure 3.22: TEM (a) bright field and (b) dark field images (13kx, A02401, A02402) and (c) corresponding indexed SAD pattern (460mm, A02399) from the primary heat-treated sample cooled at 10K/s. (a-b) colony of alpha phase indexed (c) as α-Ti with B=[1-1 0 1]. The (1 1 -2 0) reflection is used to form the dark field image in (b).

Figure 3.23 shows a bright field micrograph and corresponding diffraction pattern of the interface between two strongly diffracting α grains and the strongly diffracting parent β phase.

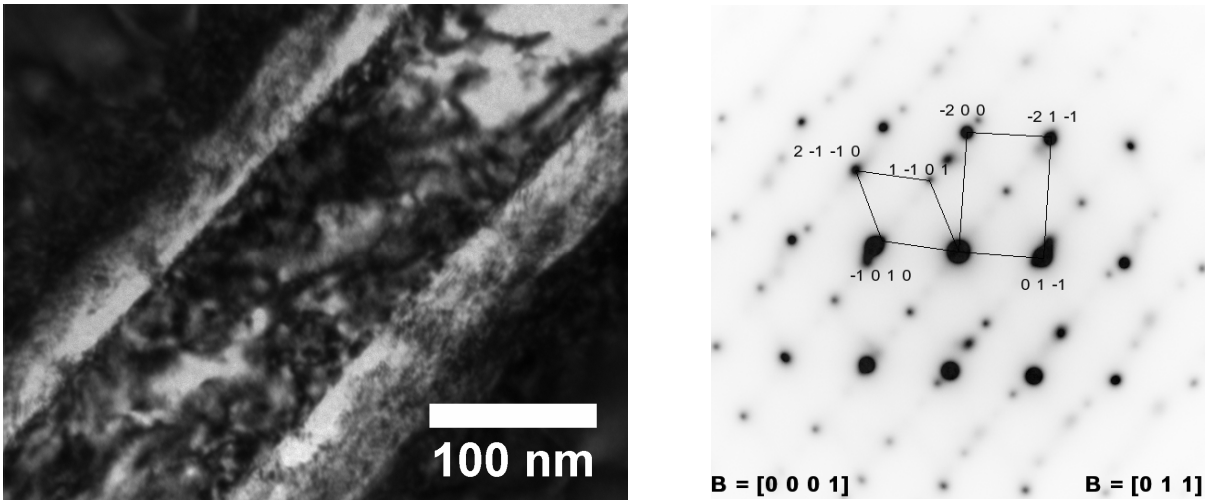

(a) (b)

Figure 3.23: TEM bright field and corresponding indexed diffraction pattern from the primary heat-treated sample cooled at 10K/s. (a) BF (210kx, A02405) interface between two alpha grains, with both alpha and beta planes diffracting; (b) SAD pattern (460mm, A02406) indexed as B=[0 0 0 1] α-Ti and B=[0 1 1] Ti-β.

Figure 3.24 shows the results of EDS analysis across two alpha grains and along a beta grain boundary. Again, difficulties arose in distinguishing between the Ti and V compositions in the peak fitting procedure; however, aluminum composition remained constant across the alpha grain before decreasing as the beta grain was traversed.

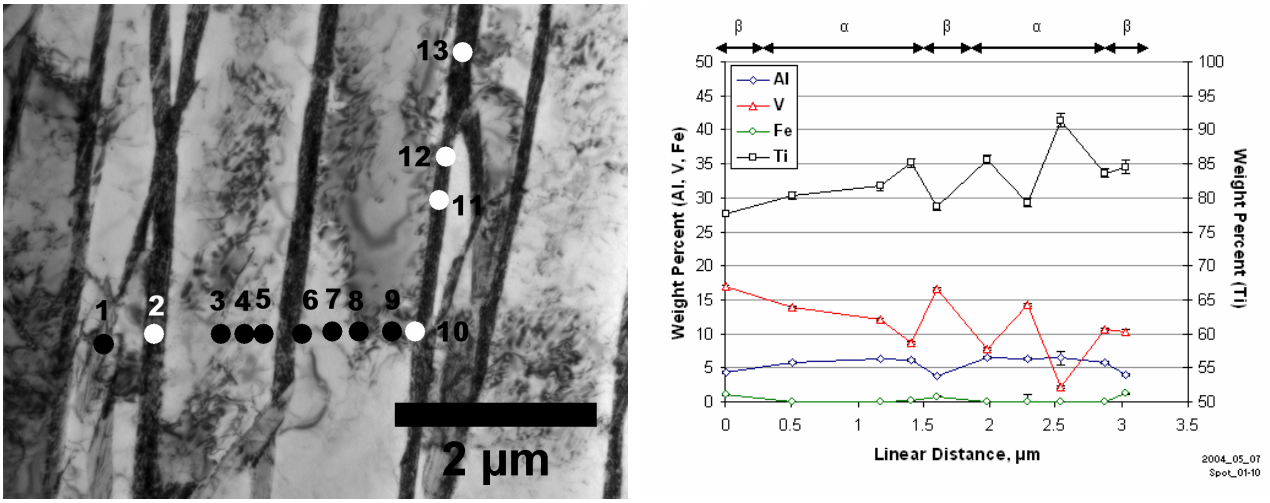

(a) (b)

Figure 3.24: Primary heat-treated sample cooled at 10K/s. (a) TEM bright field image (13kx A02407) of several alpha grains of a single colony and (b) results of EDS measurements made across two alpha grains (Spots 1-10). The average composition of spots 10-13 measured from a beta grain was Ti – 4.0Al – 15.1V – 1.2 Fe wt.%.

Bright field TEM micrographs and diffraction patterns from the secondary heat treatment cooled at 10K/s are shown in Figure 3.25a-d. Secondary alpha grains and the retained beta phase are

revealed in Figure 3.25a-b. The secondary alpha grains grow between primary alpha grains in the region of dissolved alpha. Though not shown, the grains in these images were indexed to be alpha-Ti, while the interface between these grains was indexed as beta-Ti as in Figure 3.25d.

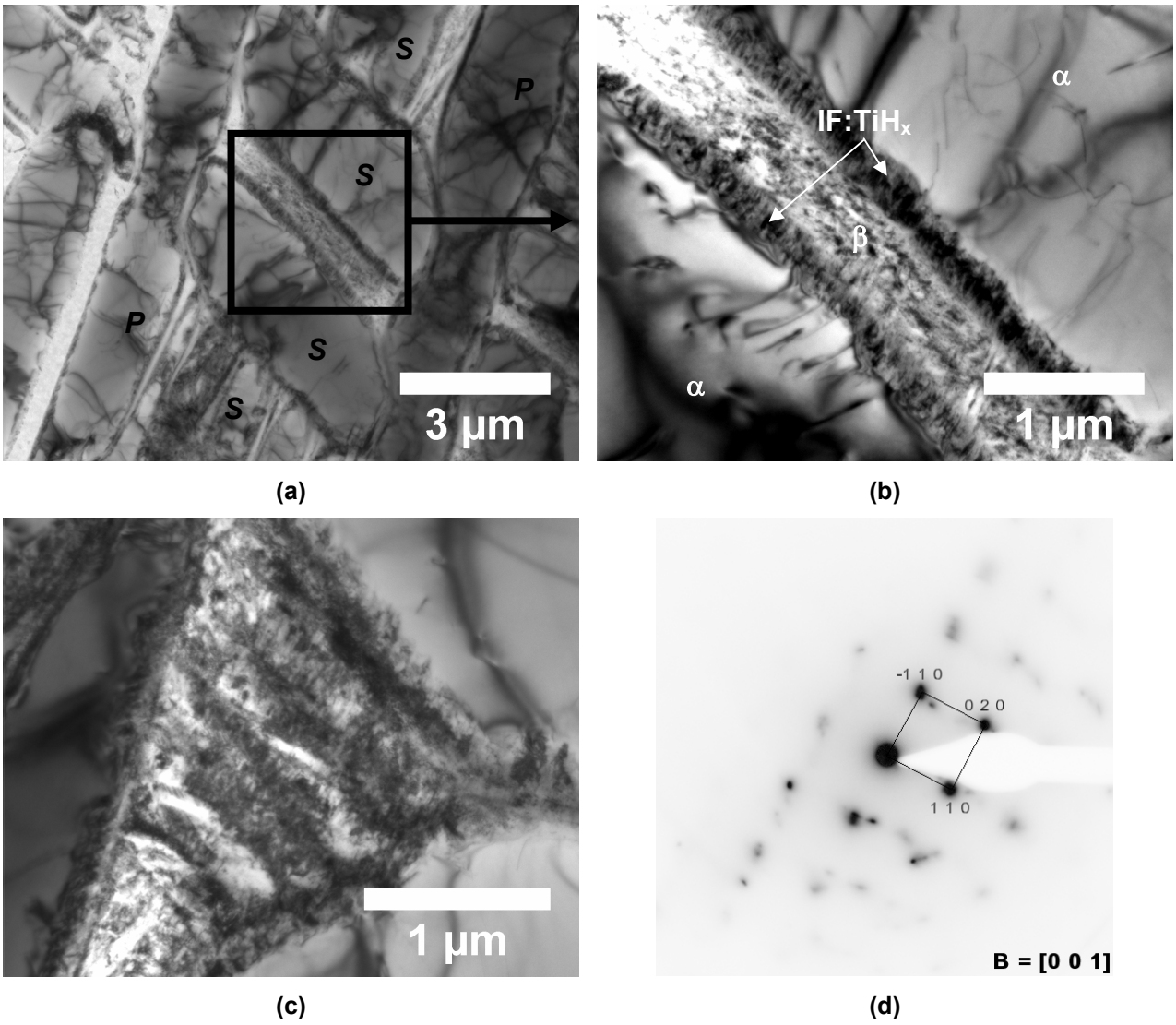

Figure 3.25: TEM bright field and corresponding indexed diffraction patterns from the secondary heat-treated sample cooled at 10K/s. (a) BF (6.9kx, A02238)primary ("P") and secondary ("S") alpha grains, (b) BF (22kx, A02239) Beta phase and interface phase(TiH_x) between two secondary alpha grains; (c) BF (25.5kx, A02242) irregular region of β phase; (d) SAD pattern for the micrographs (460mm A02240), indexed as B=[001] β-Ti;

It should be noted that the particular interface shown in Figure 3.25b is rather thick (0.9µm) as compared to other interfaces (Figure 3.12c) measured to be 200-300nm thick. This indicates that the alpha grains in Figure 3.25c are secondary alpha grains while those in Figure 3.12c are most primary. As with the primary heat treated sample at the 10K/s cooling rate, the number of

crystal imperfections appears to have increased in this sample as compared with the slow cooled samples. EDS measurements were not made on this sample or any of the remaining samples.

Fast Cooling (94K/s)

Figure 3.26a-d shows the microstructure after cooling at 94 K/s during the primary heat treatment. A secondary heat treatment was not performed on these samples. The majority of the microstructure consists of thin needles of alpha-martensite (α') that is distinctly different than the equilibrium transformation products observed in Figure 3.4 through Figure 3.14. The prior beta grain boundary, indicated in Figure 3.26d appears to be decorated in massive alpha. Ahmed states that in addition to prior beta grain boundaries, α_m may also form at individual α' plates,[28] but this fine detail cannot be resolved using the optical microscope.

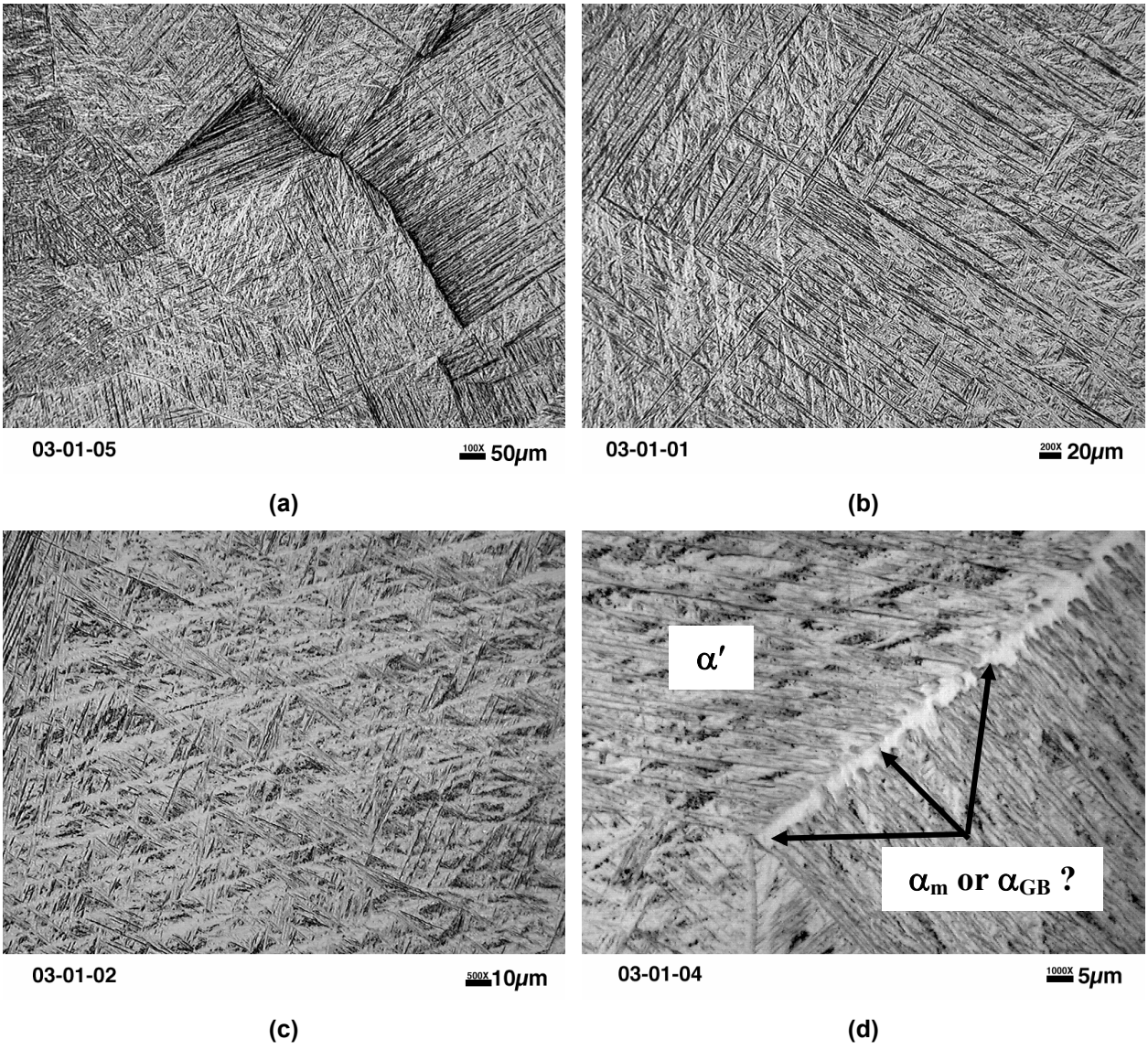

Figure 3.26: Optical microstructure of primary samples cooled at 94 K/s. The microstructure consists of (a-c) intragranular α′ and (d) possibly grain boundary nucleated - α_m with intragranular α'.

The effect of a much faster cooling rate on the partitioning of vanadium to the beta phase is illustrated in Figure 3.27 for the primary sample cooled at 94 K/s. The microstructure consists of α′ with a lack of partitioning of alloying elements during the rapid cooling, resulting in a relatively "flat" contrasted image. The unresolved precipitate that forms at prior beta grain boundaries is illustrated in Figure 3.27a-b; however, due to the relatively low magnification (fine scale of the transformation products) and lack of atomic contrast, it is difficult to locate massive alpha within the prior beta grains (Figure 3.27c-d). Most contrast in this image is due to electron channeling or preferred orientation contrast and perhaps minute variations in the surface profile.

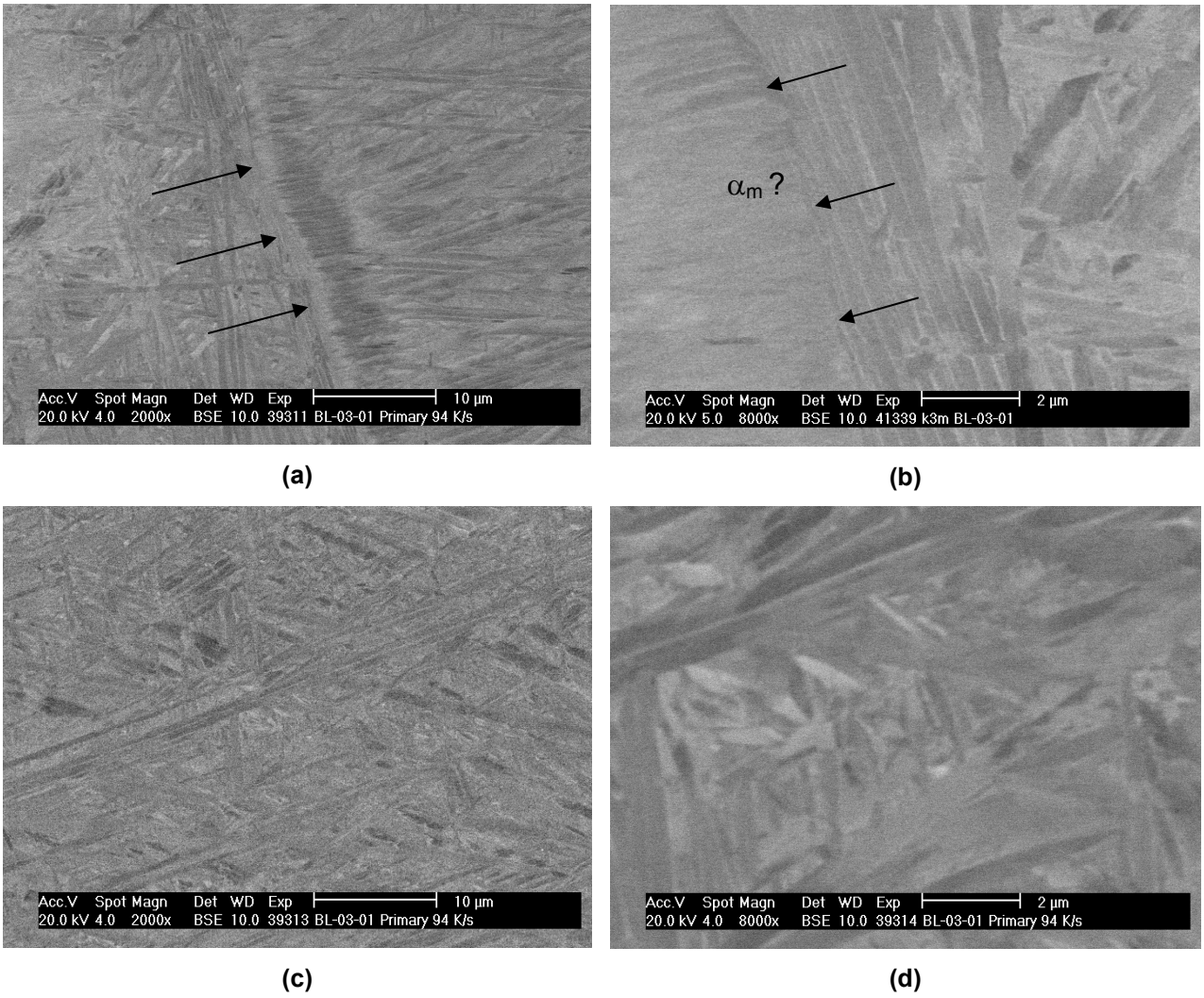

Figure 3.27: BSE micrographs of primary heat treated samples cooled at 94 K/s, viewed in BSE mode. (a-b) a prior beta grain boundary (highlighted) and (c-d) intragranular mixed α′ and α_m has formed. The lack of atomic number contrast is due to negligible partitioning of beta stabilizers during rapid cooling.

Figure 3.28a shows an IQ map of a prior beta grain boundary. It is interesting to note that the grain boundary region has a relatively higher IQ than the surrounding matrix grains, which from the previous micrographs appear to be needles of alpha-martensite (α′). The martensite would be associated with grains of higher internal strain and would therefore degrade the quality of the EBSD image obtained at these analysis points. The amount beta phase detected is 0.3%.

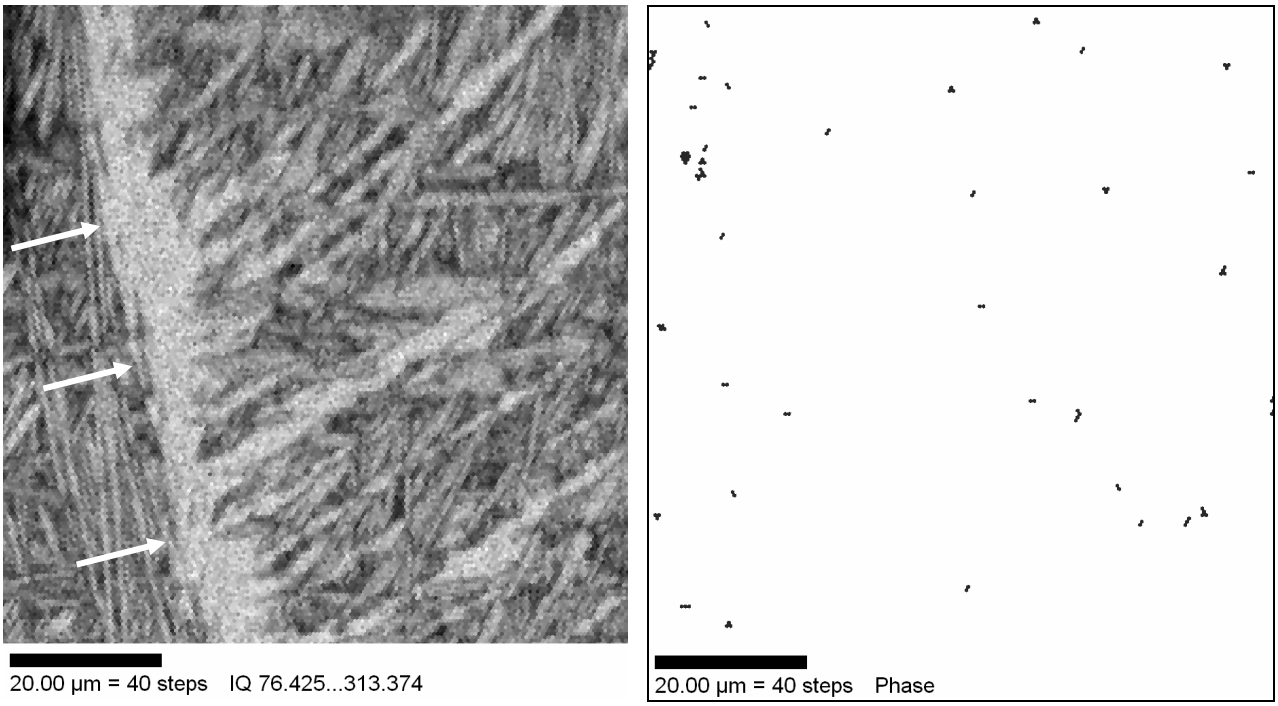

Figure 3.28: EBSD analysis of the primary heat treatment, 93K/s cooling rate. A IQ map (a) showing the microstructure analyzed with a region of a prior beta grain boundary and (b) a phase map showing the locations where the beta phase was detected in this sample. The beta phase fraction is 0.3%. [BL_03_01_Scan_3]

The boundary misorientation and alpha grain orientation map within the 93 K/s sample is shown in Figure 3.29a-b. Clearly the intragranular α' grains are separated by high angle boundaries while there are additional high angle boundaries within the unresolved grain boundary precipitate. The orientation of the internal high angle boundaries within the precipitate are near the center of the unit triangle IPF for alpha-titanium.

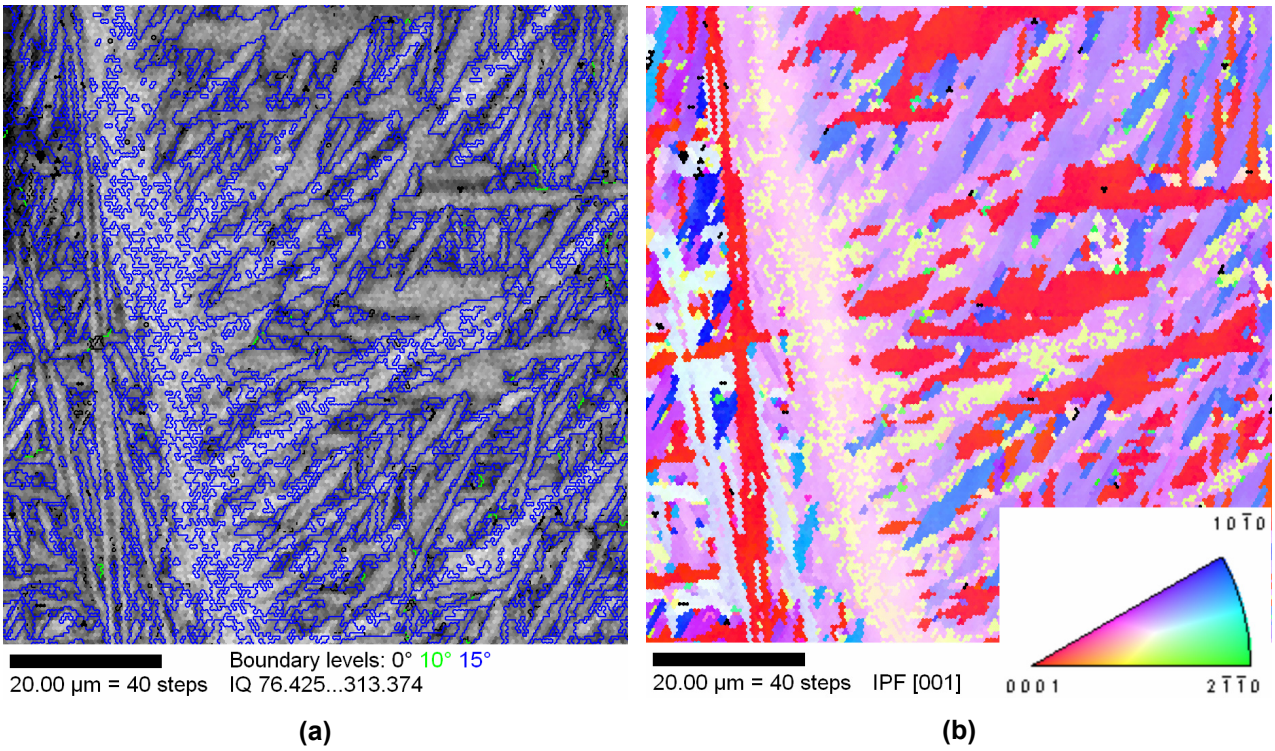

Figure 3.29: EBSD analysis of the primary heat treatment, 93K/s cooling rate. (a) Boundary misorientation and (b) an alpha inverse pole figure map. [BL_03_01_Scan_3]

Figure 3.30 and Figure 3.31 show the microstructure and indexed diffraction patterns from the sample receiving a primary heat treatment and cooled at 94 K/s. The grains in the micrographs are indexed as α-Ti; however, the interface between alpha grains is very fine, measured to be ~ 10nm. The alpha grains have an increased number of imperfections as shown in Figure 3.31 where there appear to be stacking faults present. Plichta, *et al*. noted that in binary titanium samples quenched to produce α_m and α' that the massive samples contained a random arrangement of dislocations and the α_m grains were often of irregular size.[44]

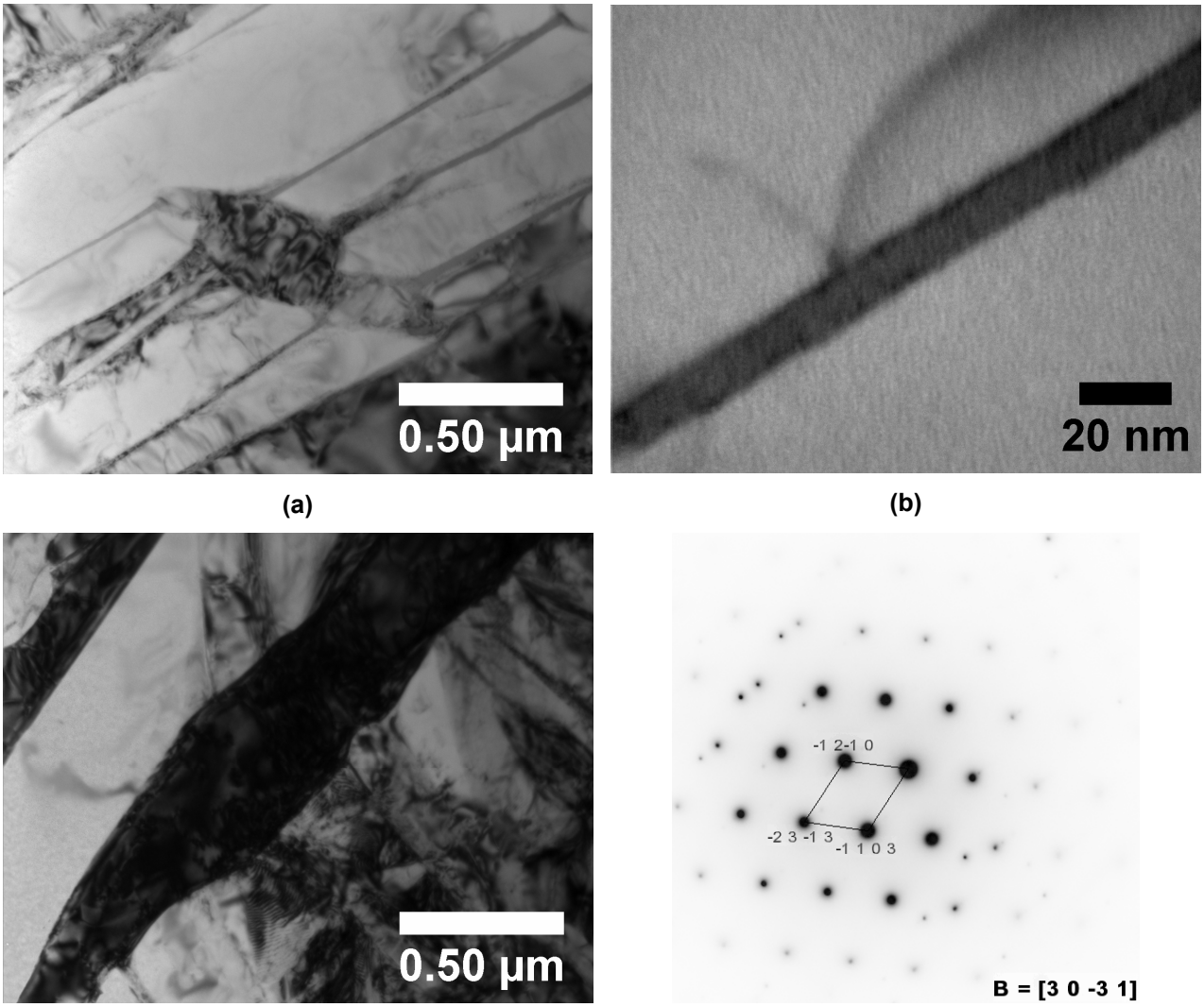

Figure 3.30: TEM bright field and corresponding indexed diffraction patterns from the primary heat-treated sample cooled at 94K/s. (a) BF (44kx, A02303) alpha grains; (b) BF (620kx, A02305) interface between neighboring alpha grains; (c) BF (44kx, A02305), strongly diffracting alpha grains indexed in (d) SAD (460mm, A02307), indexed as B=[3 0 -3 1] α-Ti.

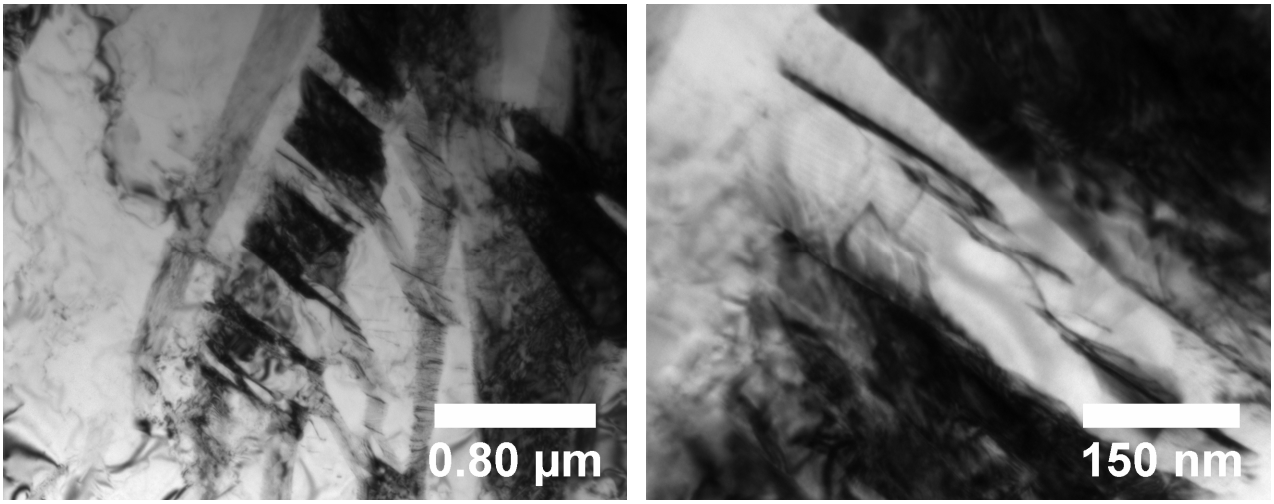

(a) (b)

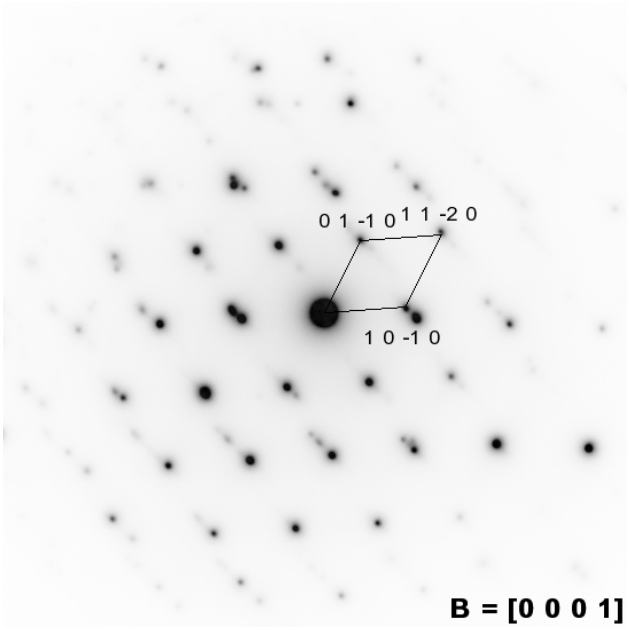

(c)

Figure 3.31: TEM bright field and corresponding indexed diffraction patterns from the primary heat-treated sample cooled at 94K/s. (a) BF (25kx, A02309) and (b) (135kx, A02310) strongly diffraction regions of alpha showing the defects (stacking faults); (c) SAD (460mm, A02311), indexed as B=[0 0 0 1] α-Ti.

Ahmed and Rack, investigated α_m and α' formation in Ti-6Al-4V, found that the α_m grains were indexed as α-Ti, and appeared at prior beta grain boundaries, adjacent to martensite plates, and at individual martensite plates.[28] Furthermore, it was found that the α_m grains had a heavily dislocated substructure. Composition analyses would need to be performed to further support the conclusion that the grains in Figure 3.30 and Figure 3.31 are indeed α_m. The precipitate does

show similar characteristics to allotriomorphic alpha. In the meantime, we will leave the issue if the grain boundary precipitate unresolved.

Quench Cooling (>500K/s)

Water quenching from the primary heat treatment temperature produces a predominately martensitic microstructure as shown in the micrographs of Figure 3.32.

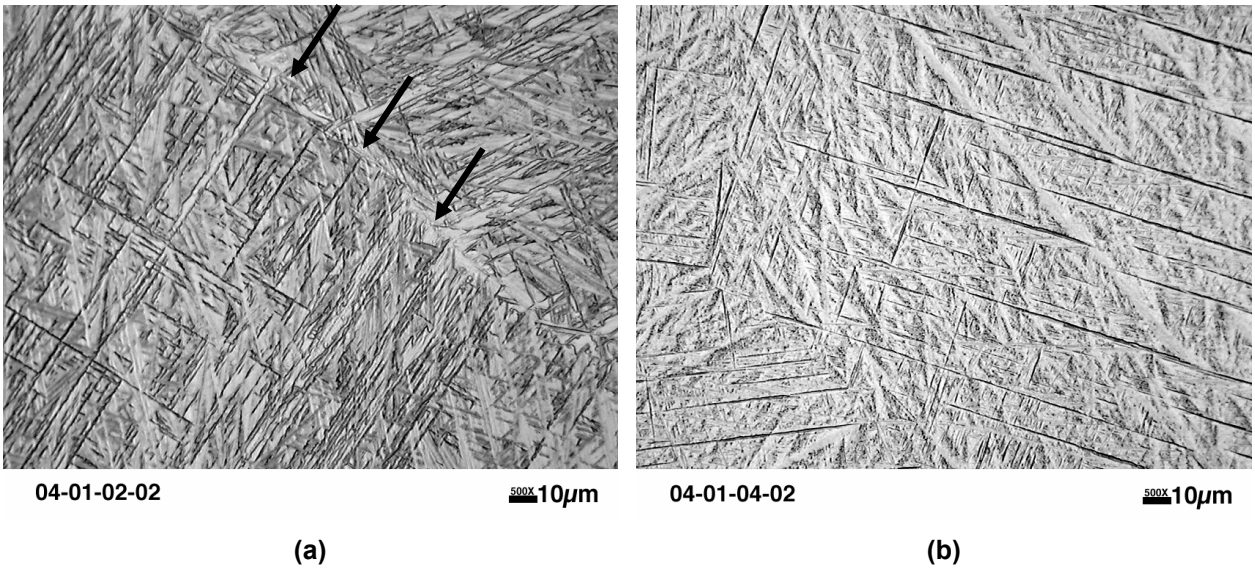

Figure 3.32: Optical microstructure after the primary heat treatment (T = 1198 K) and water quenching producing nominal cooling rates of (a) 3400 and (b) 6800 K/s. The microstructure consists primarily of (a, b) α′ with (a) apparent α_m at prior beta grain boundaries. The prior-beta grain boundary is highlighted in (a).

During water quenching, the backscattered electron micrographs become increasingly devoid of contrast due to the presence of α′ and absence of the vanadium rich beta phase. Figure 3.33 shows high magnification BSE micrographs of the α′ microstructure.

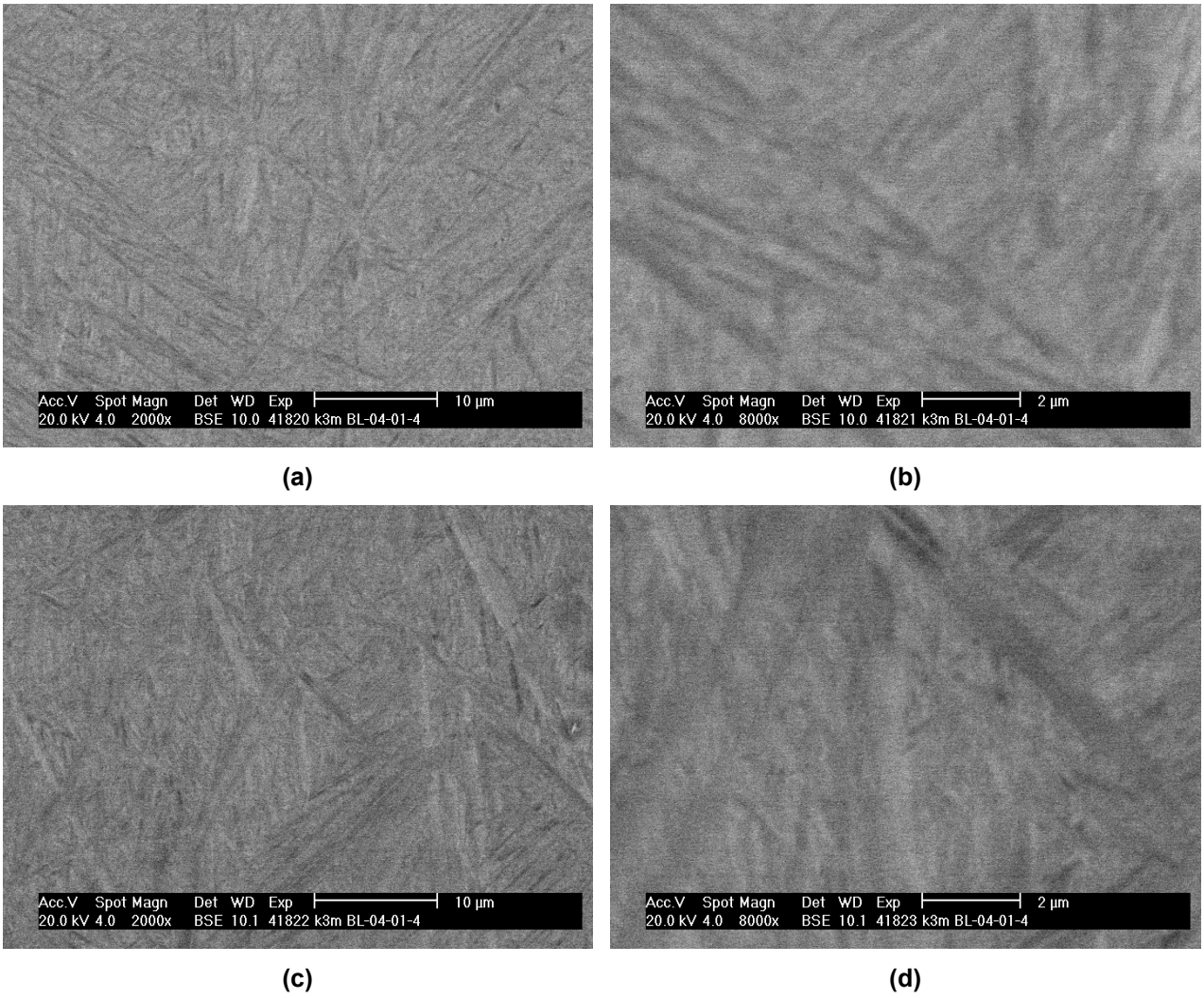

Figure 3.33: High magnification microstructure of primary heat treated samples cooled at 6790 K/s, viewed in BSE mode. The microstructure consists of needles of α′ with very little segregation of alloying elements.

Examining the rapidly quenched (3400K/s) samples in Figure 3.34 and Figure 3.35, an irregular precipitate (possibly α_m or α_{GB}) is again observed at a prior beta grain boundary with this region essentially absent of beta phase. The overall IQ is rather poor due to the retained strain in the martensitic transformation.

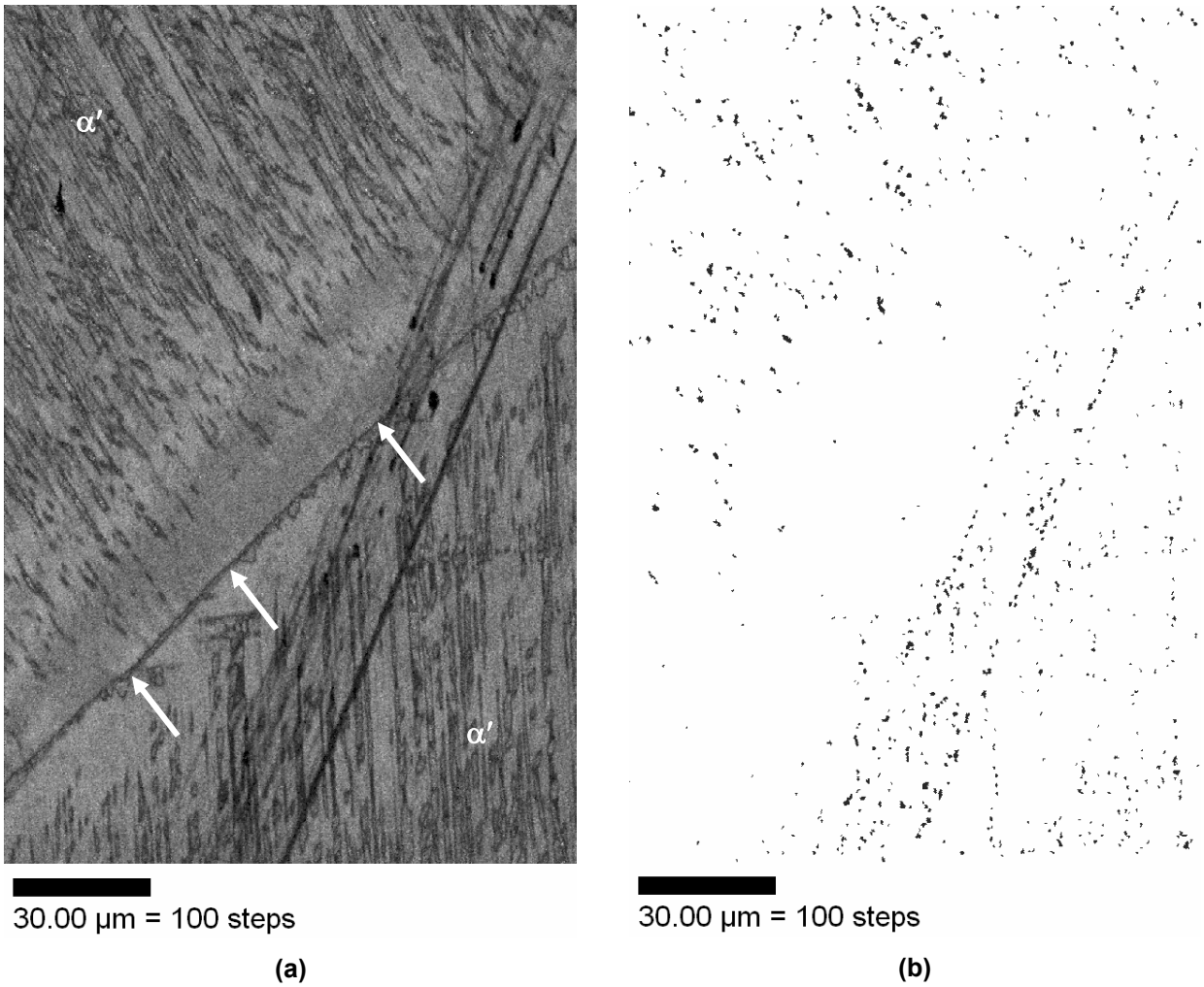

Figure 3.34: EBSD analysis of the primary heat treatment, ~3400K/s cooling rate. A IQ map (a) showing the microstructure analyzed with a region of massive-alpha located at a prior beta grain boundary and (b)a phase map showing the locations where the beta phase was detected in this sample. The beta phase fraction is 1.4% a large portion of that fraction from several scratches on the sample. [BL_04_01_2_Scan_3CC]

The prior beta grain boundary precipitate is of a single orientation (0001), similar to a colony as shown in Figure 3.35b. The prior beta grain boundary is decorated by low angle boundaries, while the α′ grains are separated by high angle boundaries.

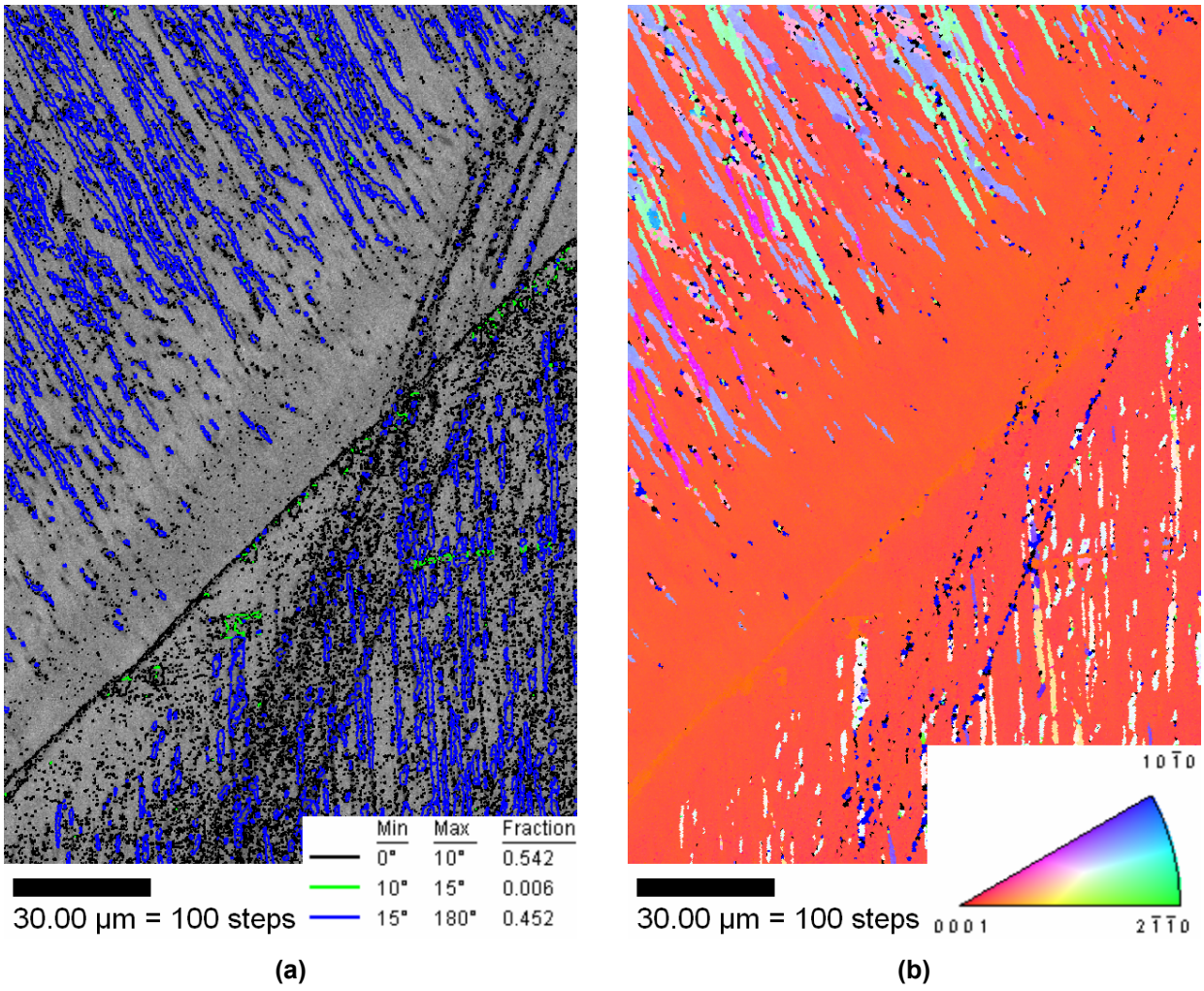

Figure 3.35: EBSD analysis of the primary heat treatment, ~3400K/s cooling rate. (a) Boundary misorientation and (b) an alpha inverse pole figure map. [BL_04_01_2_Scan_3CC]

An additional scan of an interior region of the prior beta grain is shown in Figure 3.36 and Figure 3.37 for the 3400K/s sample. The IQ map is dark, indicating that the relative image quality was poor, due to the strains associated with the α′ formation. In addition, there is a large fraction of beta phase present at 6.7%, which is unlikely for a sample that is quenched. The high fraction of beta phase is probably due to incorrectly indexed analysis points. Approximately 90% of the points indexed as beta phase had a confidence index (a measure of the quality of pattern fitting) less than 0.1. For FCC materials, a CI < 0.1 indicates a poor fit between the EBSD pattern and the indexed pattern.[71] The poor quality of the EBSD analysis in the martensitic and to some extent the massive samples are due to the fine scale and associated strain of the microstructures (as will be seen in the TEM section).

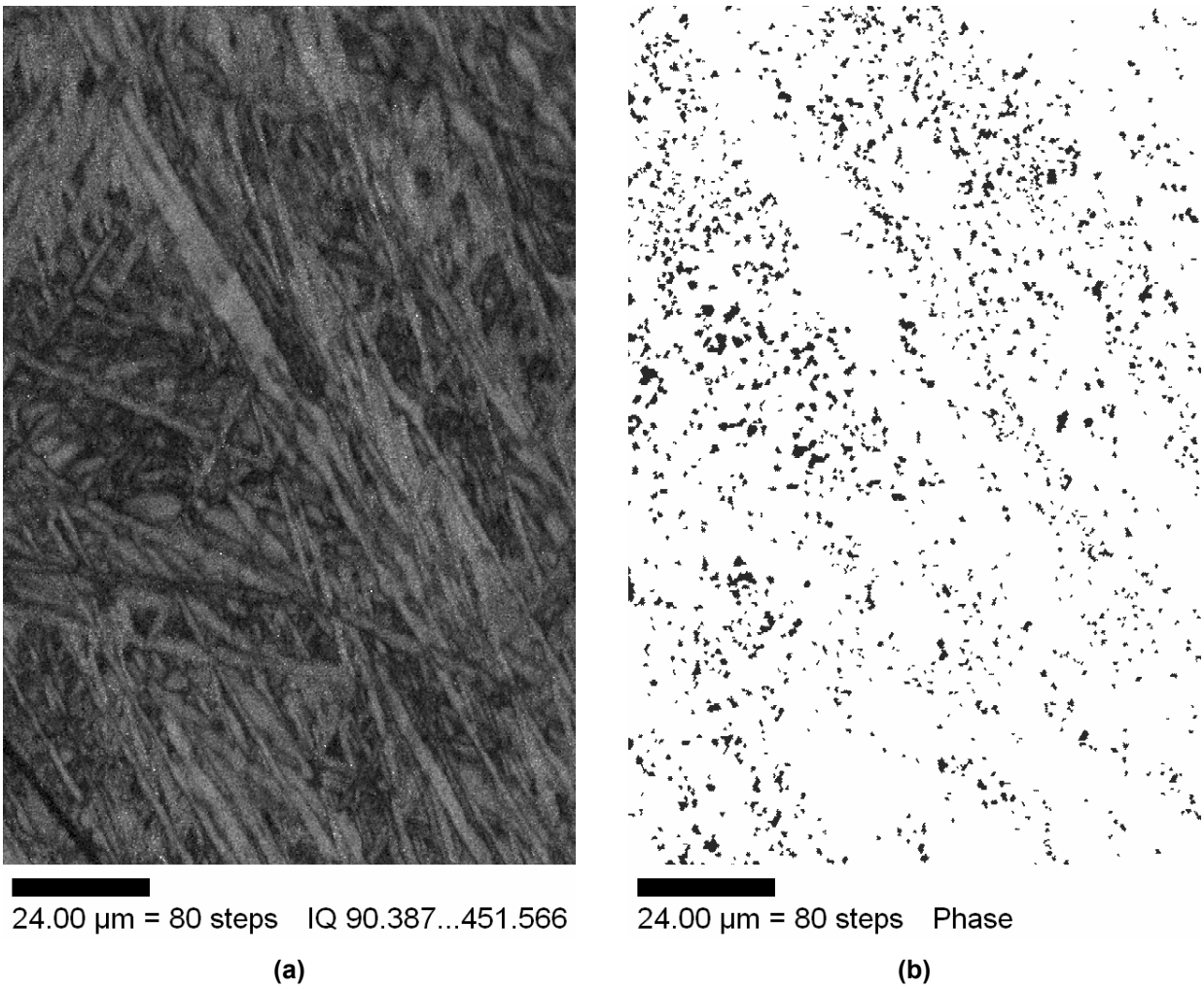

Figure 3.36: EBSD analysis of the primary heat treatment, ~3400K/s cooling rate. A IQ map (a) showing the microstructure analyzed with a region of massive-alpha located at a prior beta grain boundary and (b)a phase map showing the locations where the beta phase was detected in this sample. The beta phase fraction is 6.7%. [BL_04_01_2_Scan_3AA]

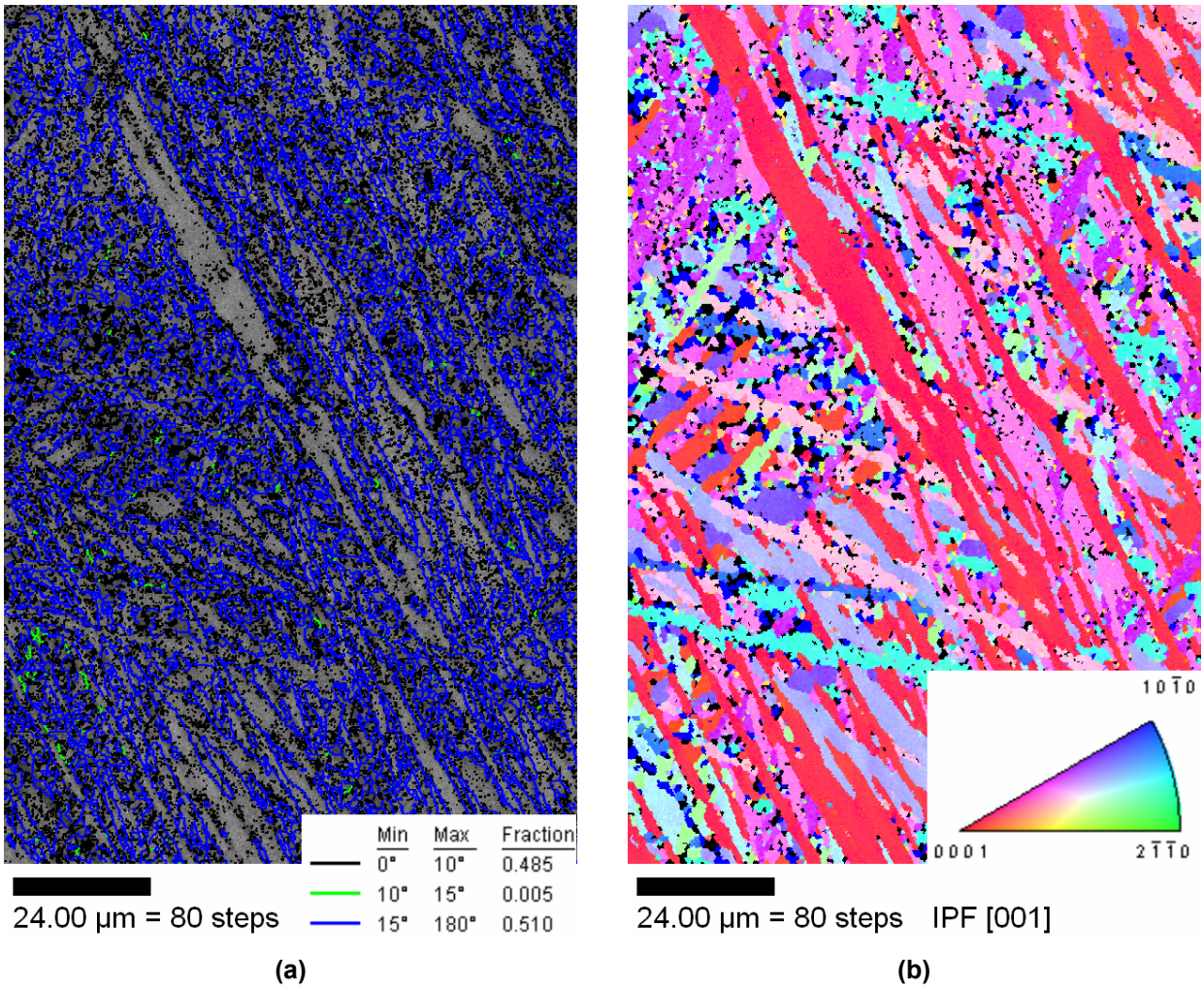

Figure 3.37: EBSD analysis of the primary heat treatment, ~3400K/s cooling rate. (a) Boundary misorientation and (b) an alpha inverse pole figure map. [BL_04_01_2_Scan_3AA]

Examination of the rapidly quenched samples in the TEM reveals a heavily dislocated and faulted arrangement of α′ as seen in Figure 3.38 and Figure 3.39. Figure 3.40 shows that the α′ grains can be indexed as α-Ti and in Figure 3.40a-b β-Ti is detected. Unfortunately a dark field image was not taken to locate the β phase in this micrograph.

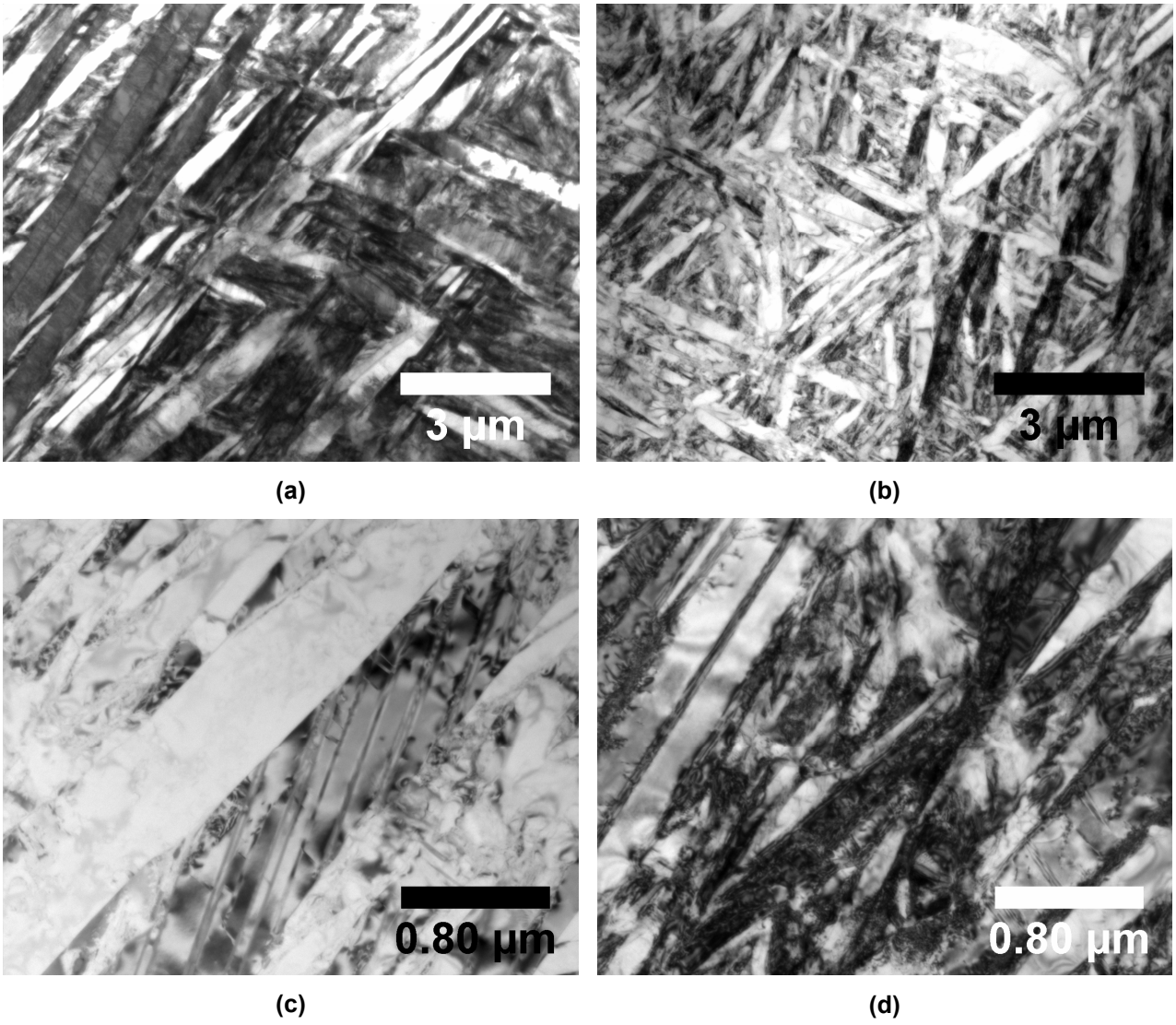

Figure 3.38: TEM bright field micrographs of the α′ morphology from the primary heat-treated sample quenched at 3400K/s. (a) BF (6.9kx, A02376); (b) BF (6.9kx, A02376); (c) BF (25.5kx, A02361); (d) BF (25.5 kx A02362).

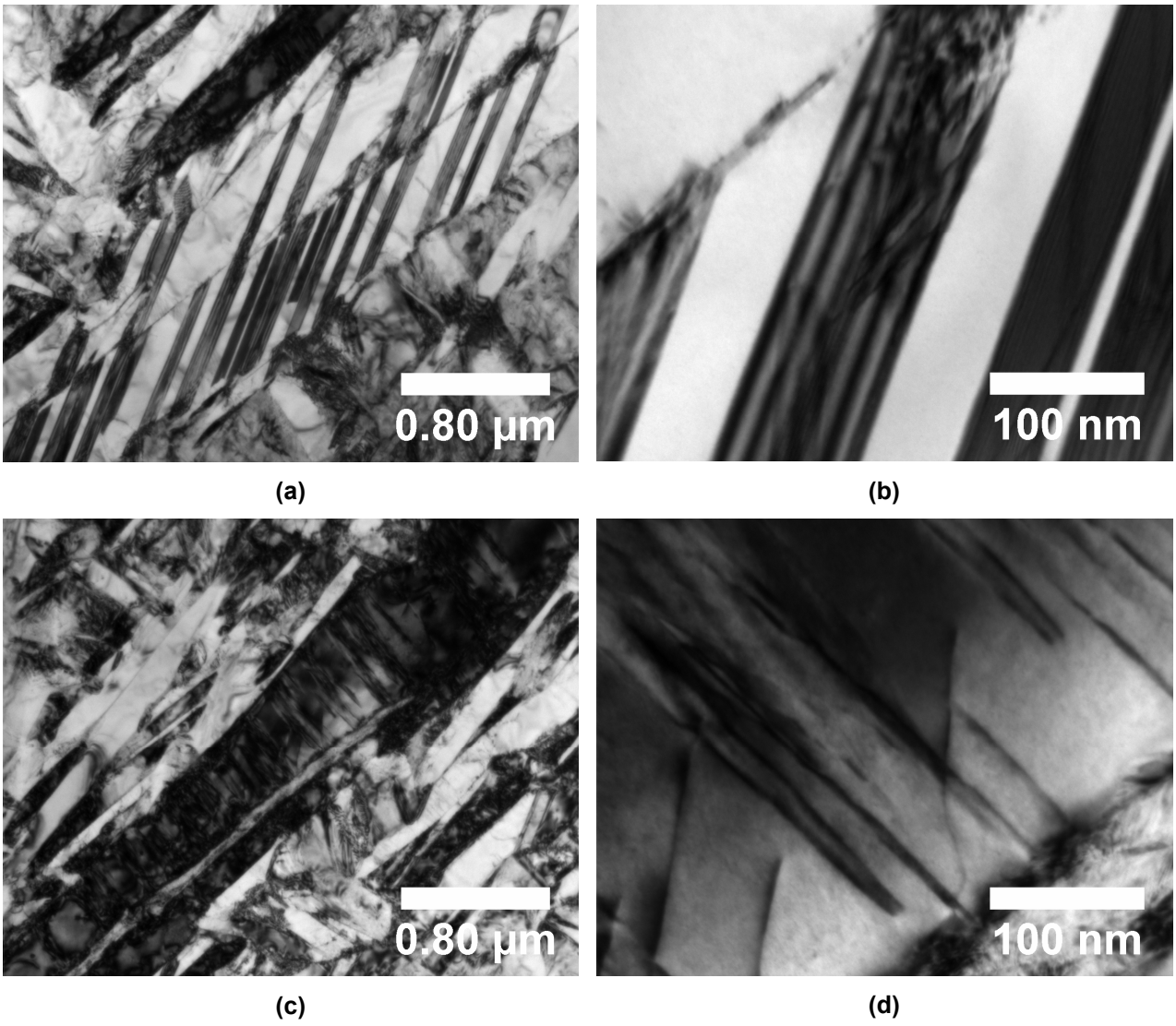

Figure 3.39: TEM bright field micrographs of the α′ morphology from the primary heat-treated sample quenched at 3400K/s. (a) BF (25.5 kx A02372)and (b) BF (210kx, A02374): stacking faults; (c) BF (25.5 kx A02368) and (d) BF (210 kx A02370) dislocations.

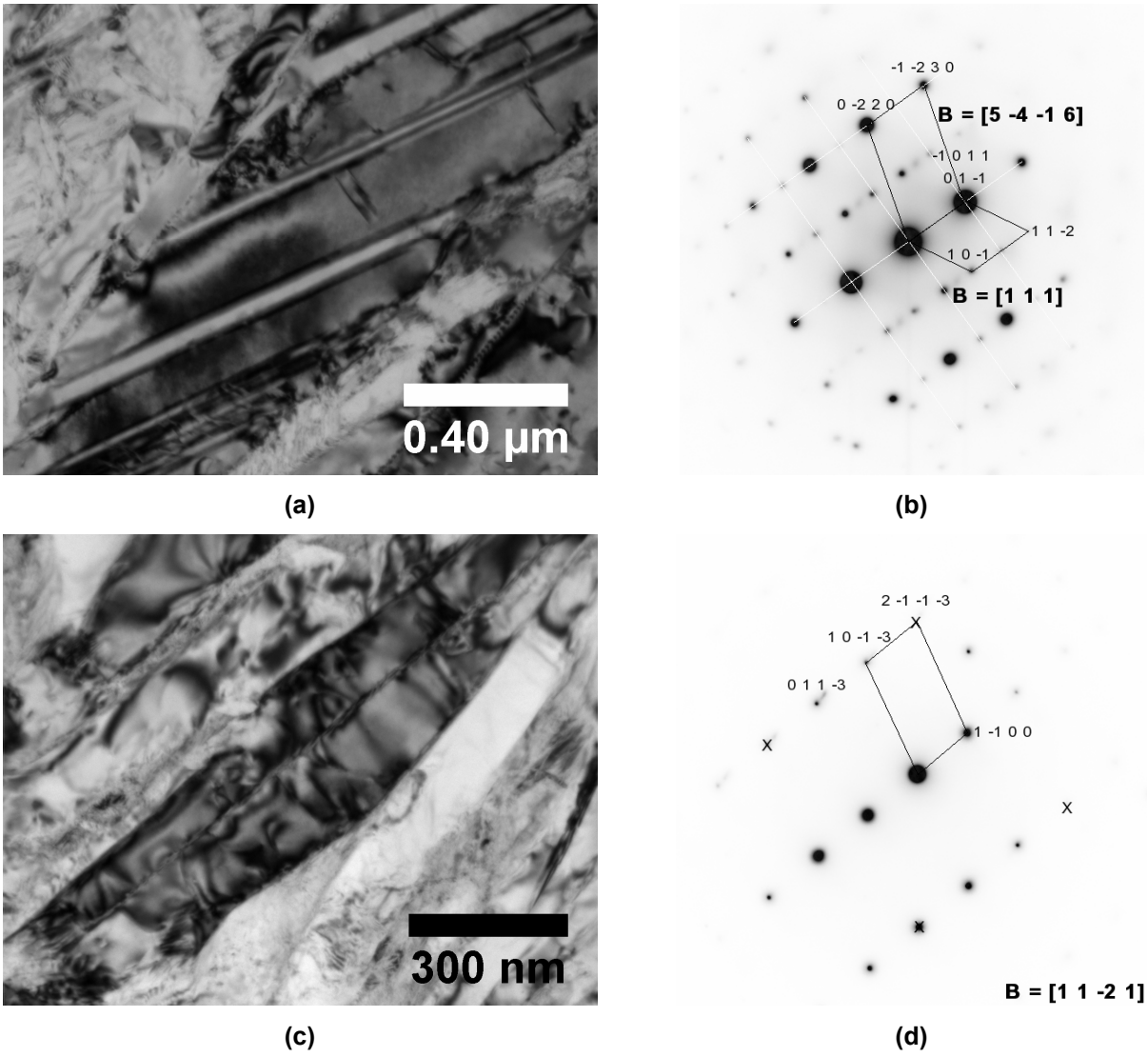

Figure 3.40: TEM bright field micrographs of the α′ morphology and indexed diffraction patterns from the primary heat-treated sample quenched at 3400K/s. (a) BF (55kx A02313) and (b) corresponding SAD (460mm, A02312) indexed as B=[5 -4 -1 6] α-Ti and B=[1 1 1] β-Ti; (c) BF (71kx A02366) and (d) corresponding SAD (460mm, A02367) indexed as B=[1 1 -2 1] α-Ti with double diffraction spots labeled with "X".

Discussion and Summary

Effect of Cooling Rate

Diffusion Controlled Transformation (β→α + β)

For cooling rates less than 10K/s, beta decomposes into alpha[‡] via a diffusion controlled reaction (β→α+β), in agreement with the results of Ahmed and Rack.[28] The aspect ratio of the alpha

[‡] In the discussion of cooling rate effects, distinction between α_P and α_S will not be made.

grains increased with cooling rate, as did the amount of basketweave-α appearing in the microstructure. With regards to the α aspect ratio, increasing cooling rate resulted in thinner and longer α grains. Slower cooling rates produced higher quantities of colony α, with a mixture of colony and basketweave α at 0.6K/s and a predominately basketweave-α morphology at 10K/s. These observations are typical, according to the review by Chestnutt *et al*.[43] Both the higher aspect ratio and the increased amount of basketweave-α at increased cooling rates can be attributed to the increase in driving force for nucleation and a decrease in diffusion rates with faster cooling. More α grains of different Burgers variants will nucleate at these higher rates, resulting in the basketweave morphology, while the amount of diffusion that takes place to widen the α laths is decreased resulting in thinner α grains.

Backscattered electron imaging of the α + β structure revealed that the higher atomic number elements, namely vanadium, partition to the beta phase as expected, resulting in a clear demarcation of two-phase microstructure. There was little difference in phase contrast between the 0.6 and 10K/s cooling rates for a primary *or* secondary treatment.

Electron backscattered diffraction confirmed that the individual alpha grains of a colony are oriented in the same crystallographic direction, and as a result, are separated by low angle grain boundaries (differing in orientation by less than 5°). Neighboring alpha grains of different orientation, e.g. basketweave-α, have higher angle boundaries between them (>15°). It will be noted here that due to the small amount of retained β in the microstructure, the EBSD analyses had an extremely difficult time "locating" beta and accurate phase fraction amounts could not be determined. As a result, the region between adjacent alpha grains produced poorer quality patterns, due to overlap of the electron beam with α and β phases.

The TEM analyses on the 0.6 and 10K/s samples revealed the tendency for an increase in the number of defects (mainly dislocations) within the alpha grain. The remainder of the TEM and EDS observations are cooling rate independent for cooling rates less than 10K/s. β grains contained a very fine sub-structure, and their thickness was on the order of 100 to 300 nm. The α/β interface was plagued by the presence of TiH_x contamination[69] from electropolishing despite careful preparation. Energy dispersive spectroscopy (EDS) measurements made across

alpha and beta grains confirmed that β contains less aluminum than α and that this is independent of cooling rate. Difficulty in distinguishing between the Ti-K_β and V-K_α peaks in the EDS spectra lead to inconsistencies in the amounts of each element measured, though, the qualitative trend was higher amounts of V in β as expected.

Diffusionless Transformations ($\beta \rightarrow \alpha_m$ and $\beta \rightarrow \alpha'$)

For the "fast" (94K/s) and "quench" (>500 K/s) cooling rates beta decomposes to a mixture of α' and an unresolved prior beta grain boundary precipitate, possibly α_m or α_{GB}, in agreement with Ahmed and Rack;[28] however, selected area diffraction patterns collected in the TEM revealed the presence of β even at these high cooling rates indicating an incomplete transformation of $\beta \rightarrow \alpha'$. An irregular precipitate was observed in optical micrographs to form at some prior beta grain boundaries, different from α_{GB} observed at slower cooling rates. The precipitate was not "massive" in the sense that a large area of the beta grain is overtaken as is typically observed.[49] Currently, the exact nature of this precipitate is unresolved; further compositional measurements are needed to confirm the composition-invariant nature of the transformation. Martensitic-alpha was found to form at prior beta grain boundaries and intragranularly as high aspect ratio needles. The optical micrographs revealed a tendency for the α' grains to be oriented orthogonally.

Backscattered electron imaging of the non-equilibrium transformation products resulted in images of limited contrast as compared to the slower cooling rate samples. This indicates the decreasing tendency for vanadium to partition upon cooling through the beta transus as cooling rate increases, resulting in the formation non-equilibrium products. The poor contrast could also be associated with strain. Despite the poor BSE image contrast, a very fine substructure became apparent.

Electron backscattered diffraction analyses of "fast" cooled samples indicated that the diffraction patterns from precipitate formed at prior beta grain boundaries was of better quality than the intragranular phase (α') and that these patterns were indexed as α (HCP). Though many factors affect pattern quality, the lack of strain associated with a massive transformation as compared to a martensitic transformation could be an explanation for improved diffraction patterns. The EBSD analyses also revealed that precipitate at prior beta grain boundaries contains high angle

(>15°) boundaries within the region. Individual α' grains were also separated by high angle boundaries without internal low or high angle boundaries. EBSD analyses of the water quenched samples resulted in images of poor pattern quality due to the associated strain with α'.

TEM was used to obtain high magnification images of the fine microstructure in the non-equilibrium samples. EDS measurements were not performed on either the 94K/s or (>500K/s) samples. This measurement would be required for proof of the massive transformation which is composition invariant. The sample at 94K/s contained grains of α' and possibly α_m that were much finer than the 0.6 and 10K/s samples. The α grains could be indexed as HCP, though no beta SAD patterns could be obtained partly because the interface between grain was very fine on the order of 10nm in some cases. The substructure of the α' (or α_m) grains varied from heavily dislocated to no dislocations, grain to grain.

TEM analyses of the quenched sample revealed a disordered arrangement of fine α' grains having a variation in substructure. Some α' grains were heavily dislocated, others were not. Likewise, stacking faults were observed in some grains while neighboring grains were not faulted. α' grains were indexed as HCP. Interestingly, beta was indexed in one diffraction pattern indicating that even at these high cooling rates beta is retained albeit in small quantities.

Altogether, the "diffusionless" samples produced using fast and quench cooling were distinctly different from samples cooled at slow and moderate rates in all characterization techniques used. The exception being that all alpha products could be indexed as HCP using SAD. As a result, distinction between diffusion-controlled and diffusion-less products in LMD should be straightforward using the characterization techniques demonstrated in this chapter.

Primary and Secondary Heat Treatment

During slow cooling (0.6K/s), the primary heat treatment produces a wide variety of basketweave and colony α_P morphologies, while the secondary heat treatment produces a mixture of colony- α_P and α_S and very little basketweave-alpha. The α_S colonies are found intragranularly, while α_P colonies remain at the prior beta grain boundary. There is indication that intragranular basketweave α_P grains preferentially dissolved during the secondary heat treatment leaving intragranular colony-α_S. Indisputable evidence does not exist as to the

nucleation site of the colony-α_S due to the errors associated with interpreting 3-dimensional microstructures from 2-dimensionsal micrographs. The EBSD analyses lend proof to the dissolution argument where the colony α_P clearly has the same orientation as α_{GB} it nucleates from. It should be noted that at the secondary heat treatment temperature of 1198K, the equilibrium phase fraction is 40% α and 60% β. Thus upon cooling the potential exists for a final microstructure consisting of 40% α_P + 50% α_S +10% β. That is, an equal amount of α_P and α_S may be present in the microstructure.

Under moderate cooling (10K/s) the primary heat treated samples contain basketweave α_P nucleated at prior beta grain boundaries and intragranularly. Some colony-α_P containing fine α_P grains is found at the grain boundaries. After the secondary heat treatment, the α_P grains nucleated at prior beta grain boundaries remain (confirmed by EBSD) with the apparent formation of fine α_S grains between the α_P grains. The thickness of the α_S grains is less than 1 μm as observed in backscattered electron imaging and TEM. TEM results indicated that secondary heat treated samples had lesser amounts of defects within individual alpha grains.

The backscattered electron images of the secondary heat treatment samples cooled at 0.6 and 10K/s had much greater phase contrast than the secondary samples, indicating that during the secondary heat treatment, further vanadium diffusion to the beta phase occurred.

In the 10K/s secondary heat treated sample two regions were investigated using EBSD that apparently had either dissolved during the heat treatment or had nucleated from other sides of the parent beta grain. These regions where shown to contain different alpha variants from the surrounding α_P grains. Evidence does not exist to rule out dissolution of this region and subsequent growth of α_S of a different orientation variant or perhaps this is a result of looking at a two dimensional image of a three-dimensional microstructure.

Further experimentation should be performed to elucidate what morphologies dissolve and form during secondary heat treatments. This would be achieved by performing similar primary heat treatments as in this investigation, followed by secondary heat treatments of different temperatures in the two phase field. During these secondary heat treatments, α_P would dissolve during heating. Upon cooling, the sample could be quenched or allowed to cool slowly and then

quenched, so that the amount of alpha dissolved and formed would be demarcated by the presence of α′.

Summary

The baseline microstructure results show that cooling rates of orders of magnitude in difference can result in different beta decomposition products, morphologies, and substructures as summarized in Figure 3.41.

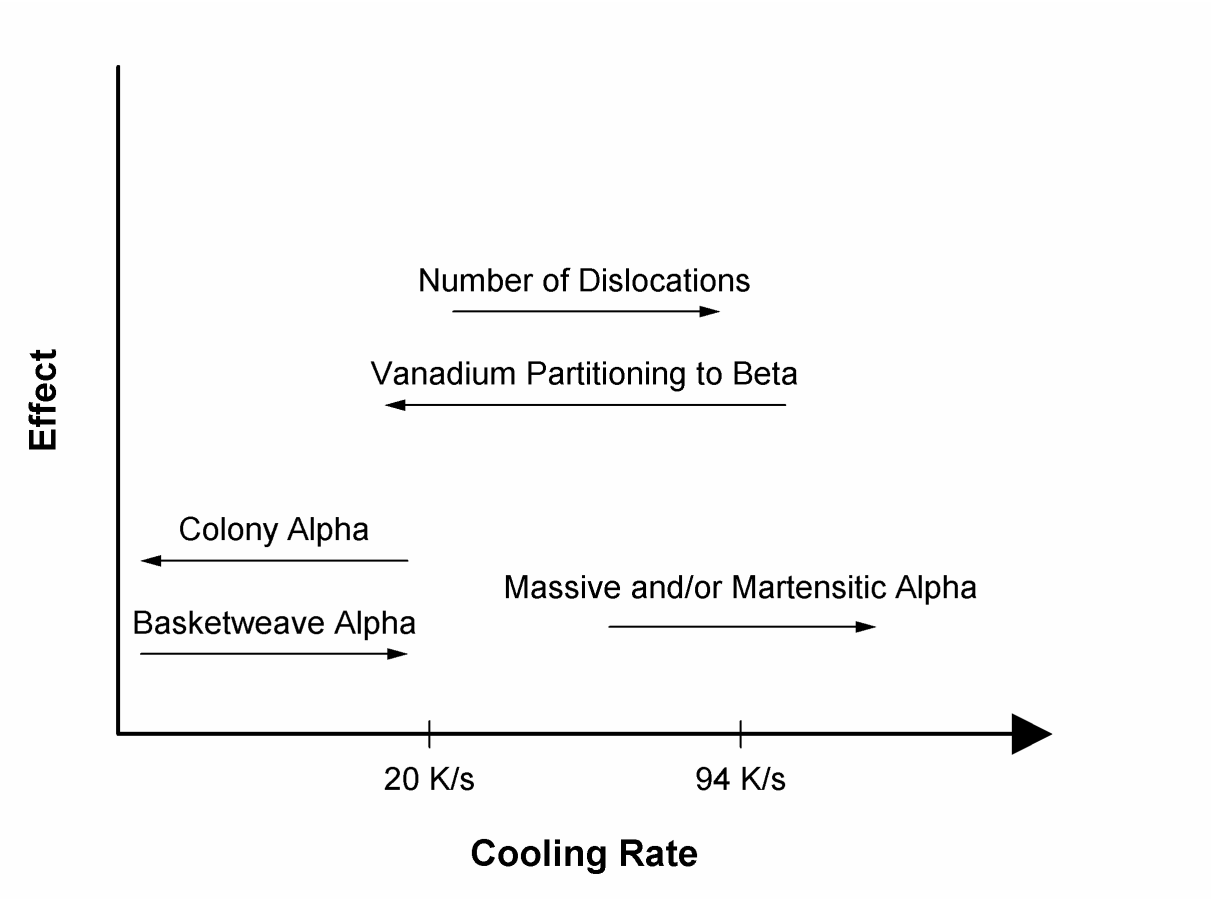

Figure 3.41: Summary of the effect of cooling rate on different aspects of the beta decomposition process.

More important to the understanding of LMD-Ti-6Al-4V microstructure are the effects of thermal cycling into the β and α+β phase fields. The differences in the primary and secondary heat treatments correspond to the formation of primary-(α_P) and secondary-alpha (α_S) morphologies, respectively. Primary alpha generally appears at the prior beta grain boundary, though with faster cooling rate it is proposed that intragranular nucleation may occur. The nucleation sites of α_S remain unresolved, but arguments have been presented for both

intragranular nucleation from dissolved regions or interpenetration of grains nucleated from other sides of the prior beta grain. The effect of different peak temperatures on the amount and morphology of α_S has not been explored, and further experimentation should be performed to resolve the location of α_S nucleation.

The following thought experiment will underscore the potential effect of primary and secondary thermal cycles on microstructure. If a primary treatment with a cooling rate of 10K/s were performed, a microstructure of basketweave α_P would be expected. If a secondary treatment with 0.6K/s cooling rate were performed on this sample the resulting α_S should have a colony morphology. The final microstructure will contain colony α_S in a "matrix" of basketweave α_P; a very similar microstructure to that observed in LMD Ti-6Al-4V. The next chapter will examine LMD Ti-6Al-4V microstructure, where the potential effect of primary and secondary heat treatment will become clear.

Chapter 4: As-Deposited Microstructure Characterization

LMD-Ti-6Al-4V as-deposited microstructures are characterized using optical microscopy, SEM operating in back-scattered election imaging mode, TEM, EBSD, EDS, electron microprobe, and hardness measurements. The results are used to hypothesize a microstructure evolution path during laser deposition.

Experiment

Laser deposited, Ti – 6wt.% Al – 4 wt.% V, "rib-on-web" builds examined herein were fabricated by AeroMet Corporation (Eden Prairie, MN) using their Laser Additive Manufacturing (LAM) process. Typical processing conditions for the LMD of Ti-6Al-4V include a laser power of 11kW (CO_2), laser velocity of 2.54 mm/s, and a mass deposition rate of 0.936 kg/hr.[72] No post forming consolidation is used.

Eighteen layers (individually denoted hereafter as L1 through L18) of Ti-6Al-4V were deposited on a 7 mm thick Ti-6Al-4V substrate that was previously mill-annealed at 700-730 °C for 2 hours. Each deposited layer was about 6 mm thick; however, due to overlap and remelting of the layer due to the addition of a subsequent layer, each ripple seen in Figure 4.1 is about 3 mm thick. A layer is defined as the distance between cusps created by the intersection of the concave portion of each layer. The coordinate system indicated in Figure 4.1, where *x* is the direction of laser travel, *z* is the direction of layer addition, and *y* defines the width of a layer, is used throughout the thesis. All characterization was performed on samples taken from the *y*-*z* plane.

Samples were removed from the deposit, polished using standard metallographic techniques, and etched such that the macro and microstructures of the indicated y-z plane of the deposit were revealed. A 5 vol.% hydrofluoric acid (HF) in deionized water solution was used as the etchant. Samples were submersed in the etchant for approximately 10 seconds, rinsed in a beaker of deionized water, and then dried.

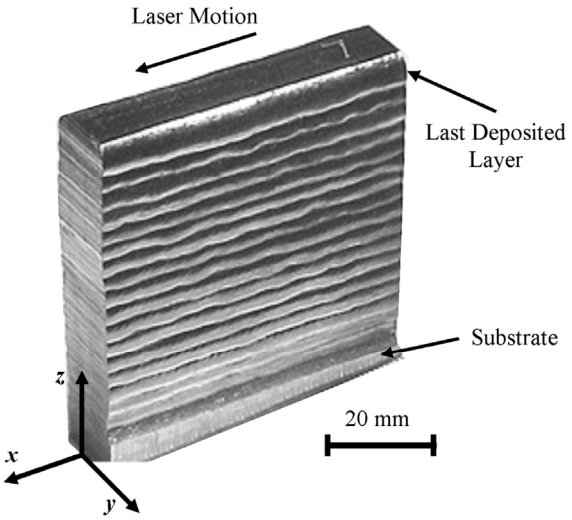

Figure 4.1: Single line build consisting of 18 layers of Ti-6Al-4V laser deposited onto a substrate of the same material. Laser motion is in the +x direction and layers are added in the +z direction.

A Cameca SX-50 Microprobe Analyzer was used to map the composition of the as received deposit. Polished and etched samples were used. A beam current of 20.1 nA and an acceleration voltage of 15 kV were used. Line scans intersecting zero, one, and two layers were performed in order to obtain a quantitative variation of aluminum, vanadium, and titanium in the as-deposited material. The scan length, step distance, beam dimensions, and number of analyses performed per scan varied according to Table IV. Calibration of aluminum, vanadium, and titanium x-ray intensities were based on primary standards of kyanite (Al_2SiO_5), $YbVO_4$, and TiO_2, respectively. Aluminum, vanadium, and titanium were detected on thallium acid phthalate (TAP), lithium fluoride (LiF), and penta-erithrytol (PET) crystals, respectively.

Table IV: Summary of Quantitative Microprobe Analyses

Feature Analyzed	Scan Length, *z*	Step Distance, Δz	Beam Dimensions	Number of Analyses
Layer Band	8.1 mm	50 μm	5x4 μm	163
	1.6 mm	20 μm	5x4 μm	80 x 3
Top of Part (Absent of Layer Band)	9.9	100 μm	10x8μm	100 x 3

A single as-deposited polished sample containing the last 6 layers of the deposit was examined on an FEI XL30 field emission gun (FEG) scanning electron microscope (SEM) with electron backscattered diffraction (EBSD) capabilities. A colloidal silica final polish (for 2 minutes) was

used to remove the metallographic etch. Typically the SEM was operated in backscattered electron mode using a voltage of 20kV, with the images generated from both atomic and height contrast. SEM samples were mounted to aluminum SEM stubs using silver paste.

The samples for TEM were obtained by sectioning a region from the center of the deposit into four regions that, under the optical microscope, exhibit different microstructural features. Sectioning was performed using a diamond wafering blade, and the rough cut rectangular prisms measured approximately 15mm wide (*y*), 4mm long (*x*), and 0.2mm thick (*z*). The starting samples were oriented such that the flat surface is parallel to the *x*-*y* plane and their thickness in the *z*-direction of Figure 4.1. The microstructure varies greatly in the *z*-direction, so by sectioning normal to the *z* direction, there is a better chance of getting a sample with the microstructural features of interest in the center of the TEM sample. Discs (3-mm diameter) were cut using an electro-discharge machining (EDM) apparatus.

The 3-mm discs were ground from a starting thickness of 150 to 200 μm to 75 μm using 600-grit, 40-μm, 15-μm, 5-μm, 2400-, and 4000-grit abrasive discs. The 2400- and 4000-grit discs gave a "mirror" finish to the 3mm samples. Next, the samples were dimple-ground from one side to a 10 μm thickness at the center of the disc. The diamond pastes used for dimple grinding were 6, 3, and 0.5μm with a mineral oil lapping fluid and lastly an Al_2O_3 suspension polish. Perforation of the discs was performed on a Tenupol-3 twin jet electropolishing apparatus using a solution of 600ml methanol, 335ml 2-butoxyethanol, 60ml perchloric, and 5ml glycerin at temperatures below -40°C and a voltage between 10 and 20V. Times for perforation ranged from 30s to 3 minutes. A perforation light detection sensitivity of 5-7 was used, with 10 being the most sensitive setting. The best results were obtained at higher temperatures (-15°C); however, this is in the regime where titanium hydride phase forms at the alpha beta interface (interface phase, as noted in Chapter 3).[67-70]

Samples were examined on the FEI Tecnai 20 (200kV) TEM. The TEM was used to investigate the morphology, crystal structure, and limited composition measurements of the two phase microstructure in each of the baseline microstructure samples, except the primary-slow cooled heat treatment (bad sample). Selected area diffraction (SAD) patterns were indexed using the aid

of a program written in *Mathematica* using the locations of the diffracted spots and the angles between them. (See Appendix: Selected Area Diffraction Indexing Procedure).

Results

Laser deposited Ti-6Al-4V exhibits a unique as-formed macrostructure (Figure 4.2), which contains large columnar prior β-grains (1.39 ± 0.80 mm wide) and, with the exception of the last three deposited layers (L16 – L18), the appearance of regularly spaced layer bands.[73] The last three layers of the deposit are not fully developed in relation to the underlying material and define a transient region. The region defined by the layer bands is defined as a characteristic layer as shown in Figure 4.3a. Prior beta grain boundaries are continuous across the layer band and multiple layers. The bands appear near the concave cusp of each deposited layer. The bands are spaced evenly throughout the deposit, 2.9 ± 0.5 mm apart and have a thickness of 166 ± 29 μm. No porosity was observed in the deposit.

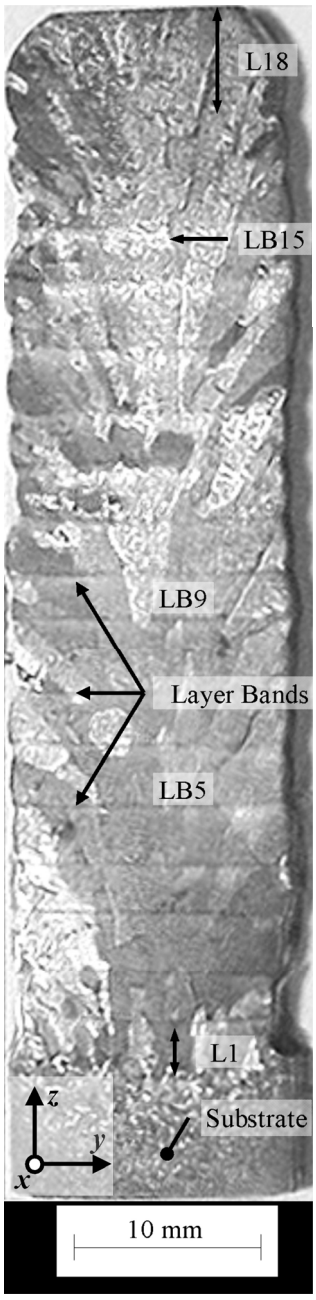

Figure 4.2: As received profile of a Ti-6Al-4V laser deposit showing the columnar prior beta grains and a periodic banding (layer bands, "LB") at every layer except the last three

The Characteristic Layer

The microstructure between the layer bands (Figure 4.3c) consists of basketweave α laths outlined in retained β with continuous α at prior-β grain boundaries.[24] Within the layer bands, the microstructure (Figure 4.3b) exhibits larger colonies of α that have apparently formed intragranularly. The average α individual alpha lath width between the layer bands varies from 0.9 μm just above a layer band to 1.8 μm just below the next layer band as measured from optical micrographs. Thus, a characteristic layer is defined by the regions containing a scale-graded basketweave-colony-alpha morphologies as indicated in Figure 4.3a.

Table V shows the results of quantitative metallographic measurements obtained from the fully-developed as-deposited macro and microstructural features. These features appear to be

characteristic of the majority of the build, i.e., for the layers comprising the substrate through L15.

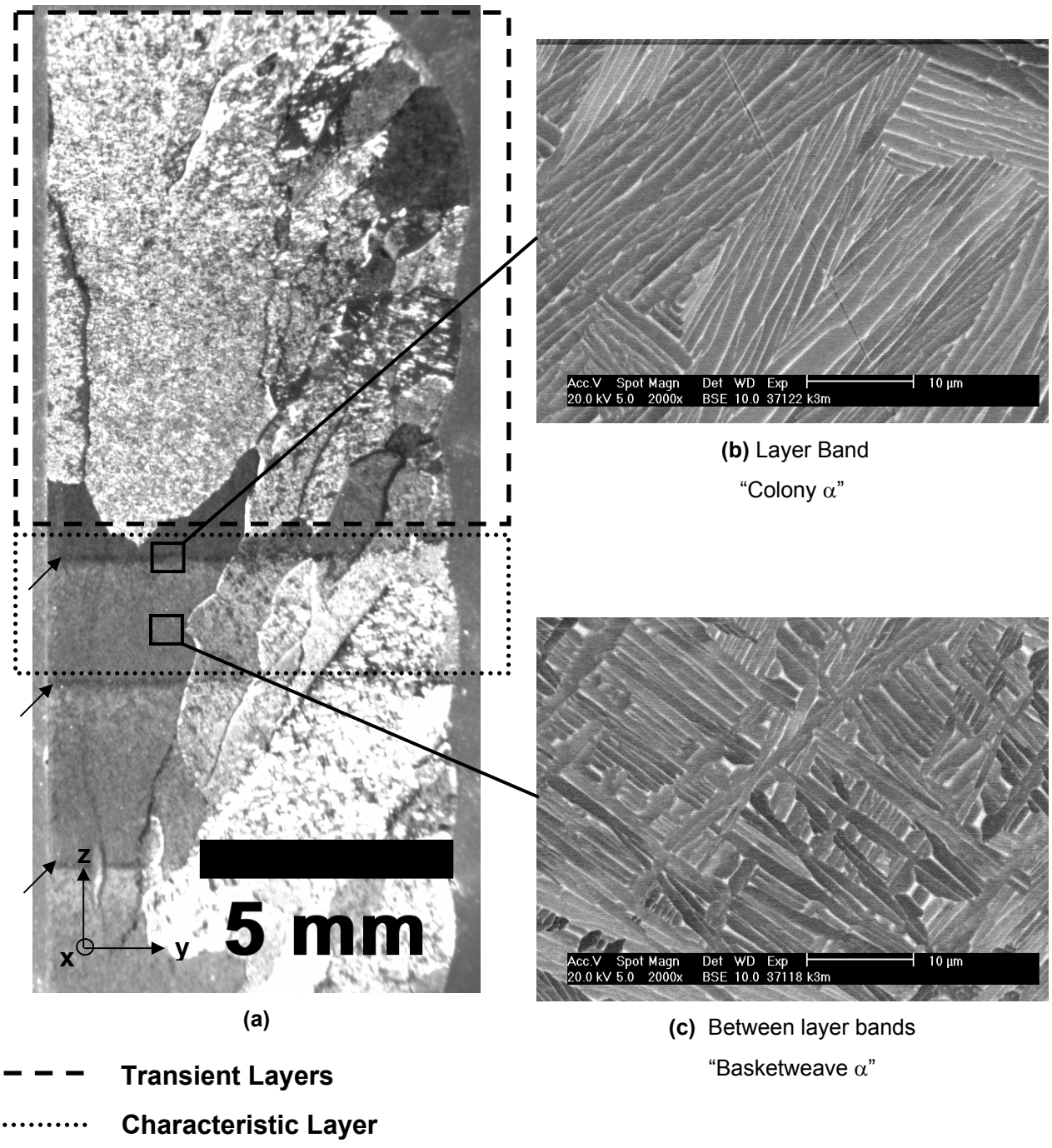

Figure 4.3: (a) Optical macrograph of the last 5 deposited layers from the centerline (y) of the as-deposited materials. The macrograph shows the "transient" and "characteristic" layers, with layer bands indicated by arrows. (b-c) backscattered electron micrographs of two regions within the deposit. In the BSE micrographs beta and alpha regions appear white and gray, respectively. In (b), a colony-alpha morphology typical of the layer band is shown. In (c), a basketweave-alpha morphology typical of the material between layer bands is shown. The layer band and nominal material form a characteristic layer that is repeated during processing.

Table V: Summary of As-Deposited Macro and Microstructure Measurements.

Feature		Average ± St. Dev.
Fusion Zone Depth (Substrate)		1.05 ± 0.22 mm
Heat Affected Zone Depth (Substrate)		4.48 ± 1.43 mm
Prior Beta Grain Width (Deposit)		1.39 ± 0.81 mm
Layer Band	Spacing	2.94 ± 0.49 mm
	Width	165.75 ± 28.52 μm
	Colony Width	13.19 ± 7.17 μm
Alpha Lath Width	Entire Deposit	1.12 ± 0.52 μm
	Bottom of Layer	0.92 ± 0.38 μm
	Middle of Layer	1.01 ± 0.33 μm
	Top of Layer	1.57 ± 0.59 μm
	Last 3 Deposited Layers (L16 – L18)	0.90 ± 0.38 μm
Vickers Micro Hardness	Layer Band	347 ± 13 HV_{300gf}
	Between Layer Bands	351 ± 21 HV_{300gf}

TEM observations of the as-deposited material are shown for positions within the characteristic layer are shown in Figure 4.4 through Figure 4.7. In these figures, the "(a)" images represent typical morphologies taken at the same magnification (4.4kx). All selected area diffraction (SAD) patterns were taken using a camera length of 460mm.

The material at the bottom of the characteristic layer, just above a layer band, is shown in Figure 4.4. The morphology shows some colony alpha; however the number of parallel alpha grains in a colony is low (Figure 4.4a). Dislocations appear in some of the α grains. Both alpha and beta could be indexed in these micrographs (Figure 4.4b,d). The centered dark field (CDF) image (Figure 4.4c) shows the $[011]_{\beta}$ planes strongly diffracting. The beta phase appears dislocated or contaminated by the interface phase (TiH_x) The average width of the alpha and beta phases are 0.83 μm and 0.11 μm, respectively, giving an estimated phase fraction of 88%-α + 12%-β.

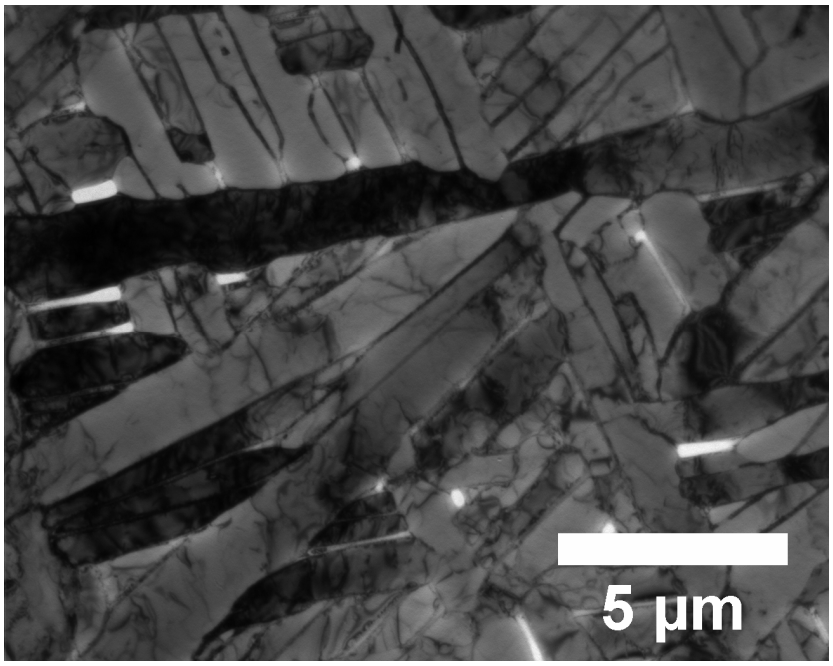

(a) A02679, 4.4kx

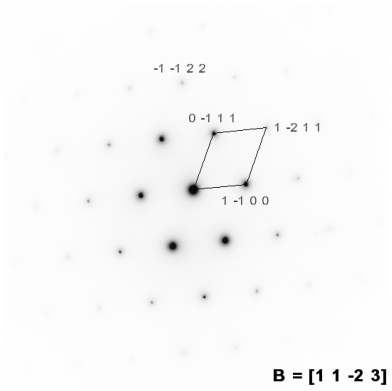

(b)A02680

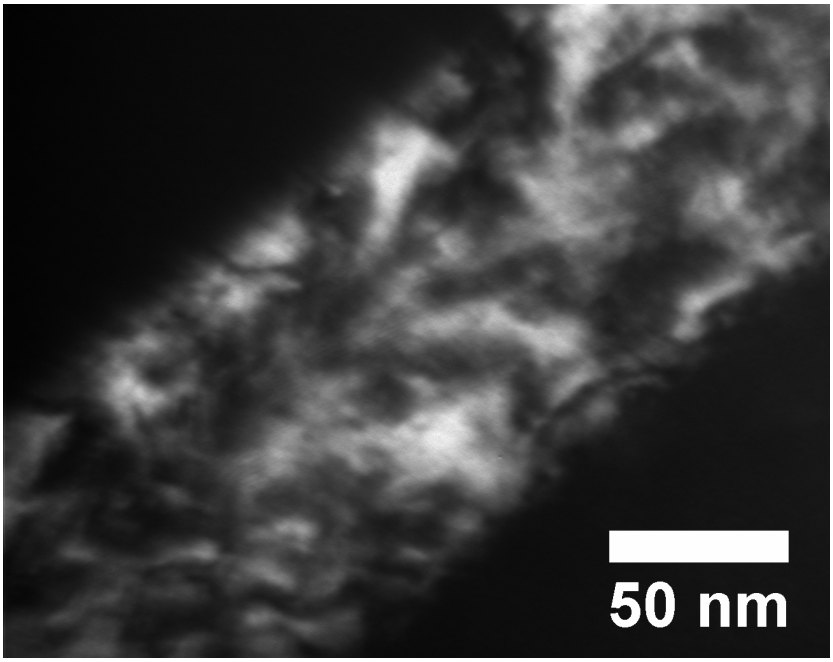

(c) A02678, 350kx

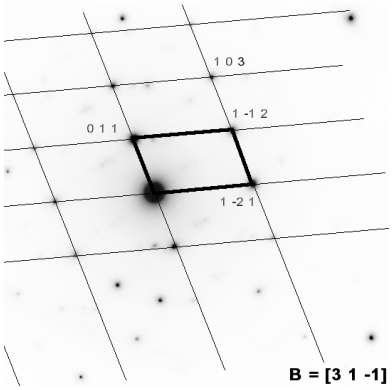

(d)A02671

Figure 4.4: TEM (a) BF image, (c) CDF image, and (b,d) corresponding SAD patterns from the bottom the characteristic layer. (a) BF image of the microstructure containing alpha grains, (b)SAD pattern indexed as B=[1 1 -2 3]$_\alpha$. (c) CDF image of the α/β interface using the [0 1 1]$_\beta$ reflection in (d). (d) SAD pattern indexed as B=[3 1 -1]$_\beta$.

TEM observations from the material at the center of the characteristic layer are shown in Figure 4.5. The alpha morphology generally appears to be basketweave (Figure 4.5a) and free of dislocations. This foil intersected a prior beta grain boundary, as shown in Figure 4.5b. The α_P

sideplates nucleate and grow from one side of α_{GB} designated β_1. The α_P grains in the other prior beta grain, β_2, are not oriented in the same direction as those in β_1. Figure 4.5b illustrates a colony morphology forming from the grain boundary where approximately 16 alpha grains are parallel (α_P,β_1 grain). Both α (Figure 4.5c) and β (not shown) could be indexed. The average width of the alpha and beta phases are 0.93 μm and 0.11 μm, respectively, giving an estimated phase fraction about of 90%-α + 10%-β

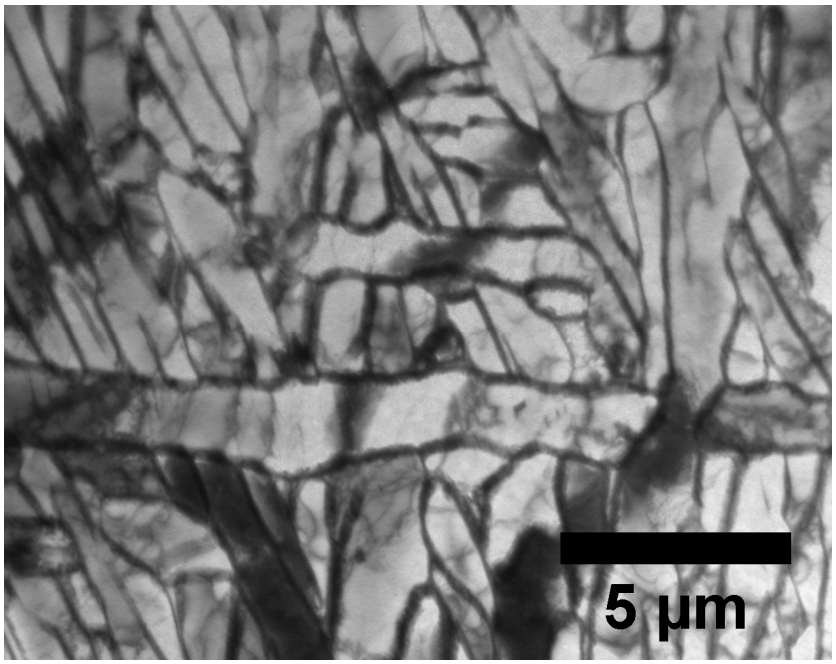

(a) A02652_S_4_4, scaled to 4.4kx, original 3.1kx

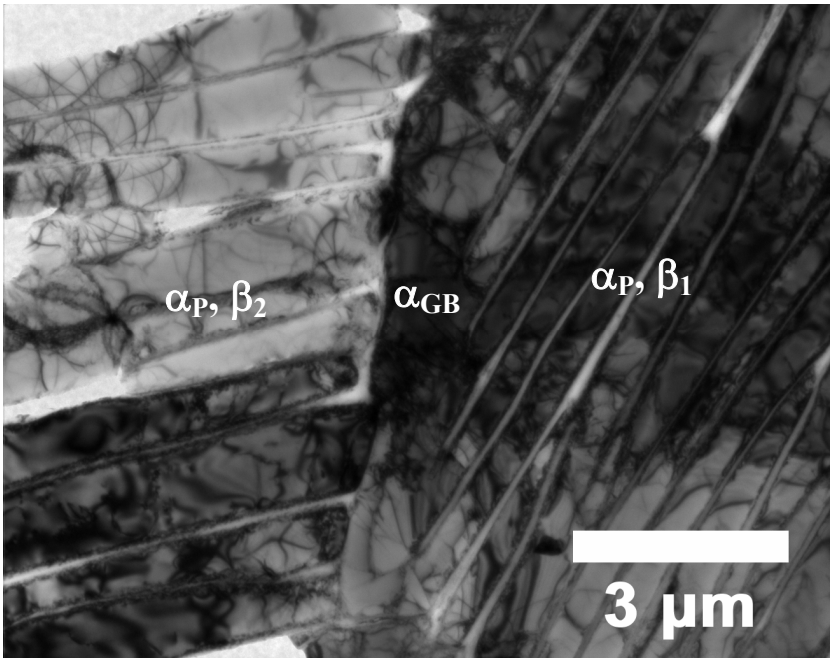

(b) A02639, 6.9kx

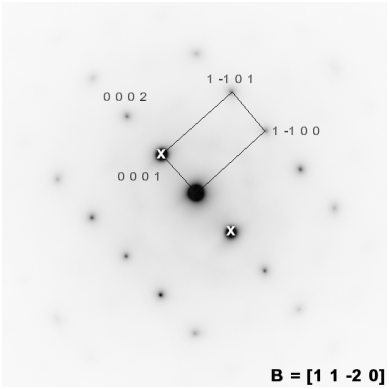

(c)A02637

Figure 4.5: TEM bright-field images (a,b) and SAD pattern (c) from the middle of the characteristic layer. (a) BF image of the microstructure showing a typical morphology containing alpha grains. (b) BF image showing α_{GB} running vertically with α_P nucleating from one side (β_1). The α_P nucleating from the other beta grain (β_2) does not have the same orientation. (c)SAD pattern indexed as B=[1 1 -2 0]-alpha (diffracting conditions for b).

The material just below a layer band is shown in Figure 4.6. One distinction from previous images is that the α grains appear larger. The average width of the alpha and beta phases are

1.11 μm and 0.1 μm, respectively, giving an estimated phase fraction about of 92%-α + 8%-β. The morphology shows some small colonies (few parallel α grains) with the α grains containing few dislocations. The α/β interface (Figure 4.6b) shows the β and interface phase strongly diffracting. An SAD pattern from β is shown in Figure 4.6c. The α phase could be indexed as well.

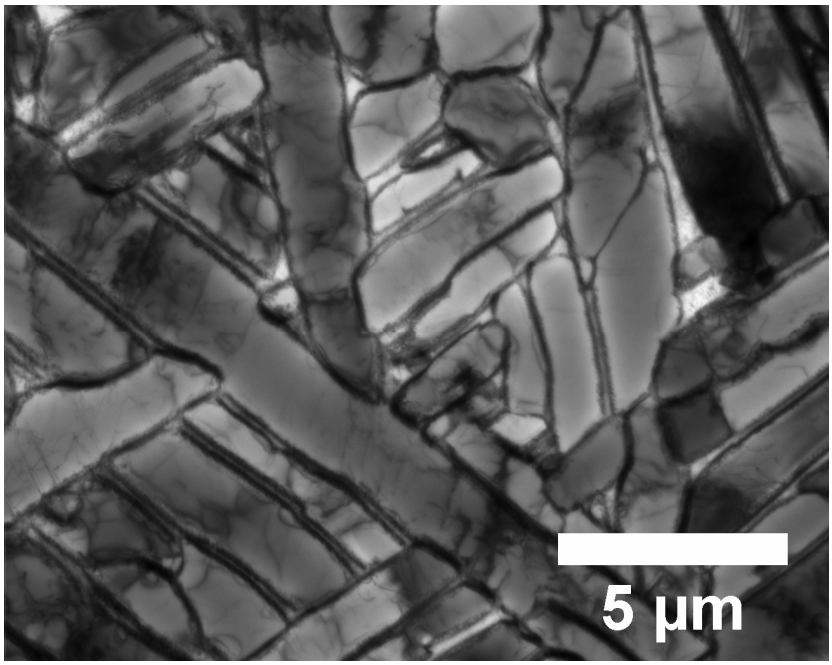

(a) A02501 4.4kx

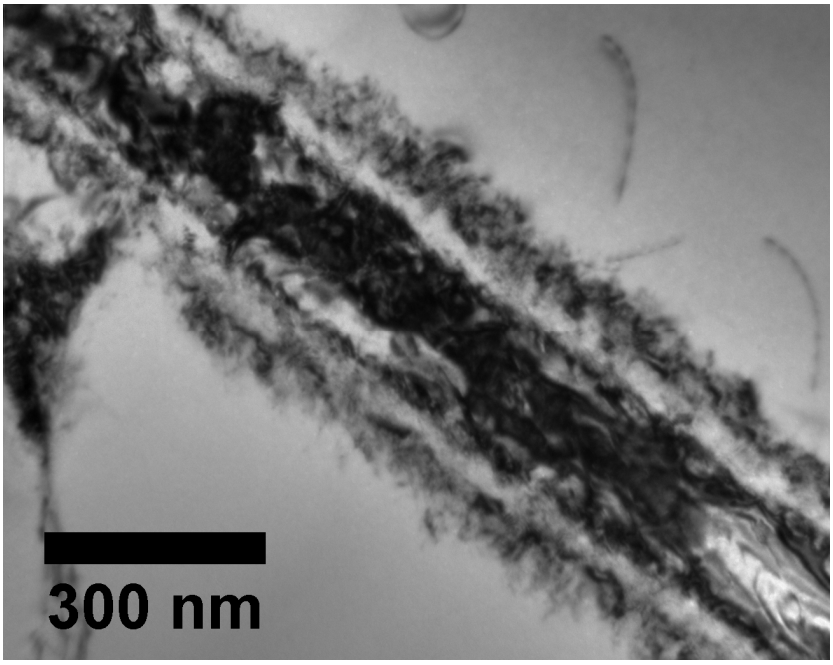

(b) A02494, 71kx

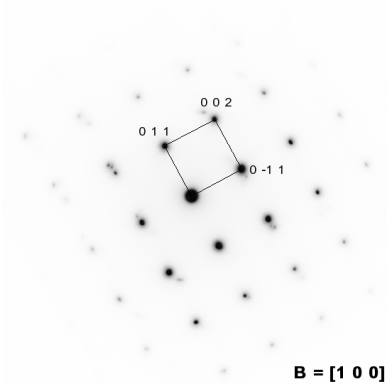

(c)A02493, Lλ=191

Figure 4.6: TEM bright-field images (a,b), and SAD pattern (c) from material just below the layer band. (a) BF image of the microstructure containing alpha grains. (b) BF image of interface between alpha grains for the diffraction conditions (c) shown in the B=[100]$_\beta$ SAD pattern.

TEM observations of the layer band material are shown in Figure 4.7. Many parallel alpha laths of a single colony are shown in Figure 4.7a with the SAD pattern of the strongly diffracting central colony in Figure 4.7b. A CDF image of the beta phase is shown in Figure 4.7c. The

average width of the alpha and beta phases are 0.91 μm and 0.08 μm, respectively, giving an estimated phase fraction about of 90%-α + 10%-β.

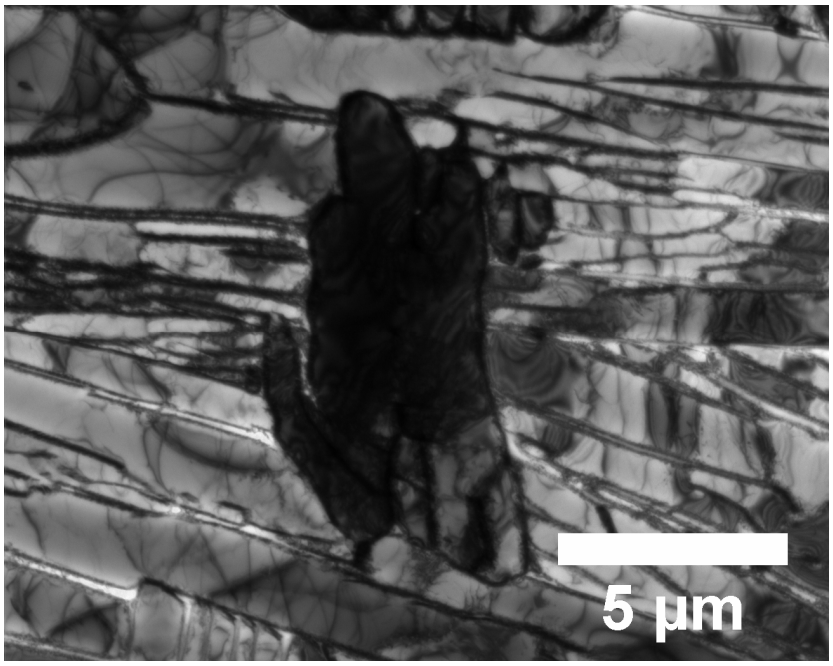

(a) A02465, 4.4kx

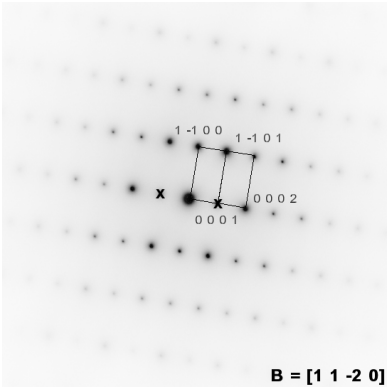

(b)A02466

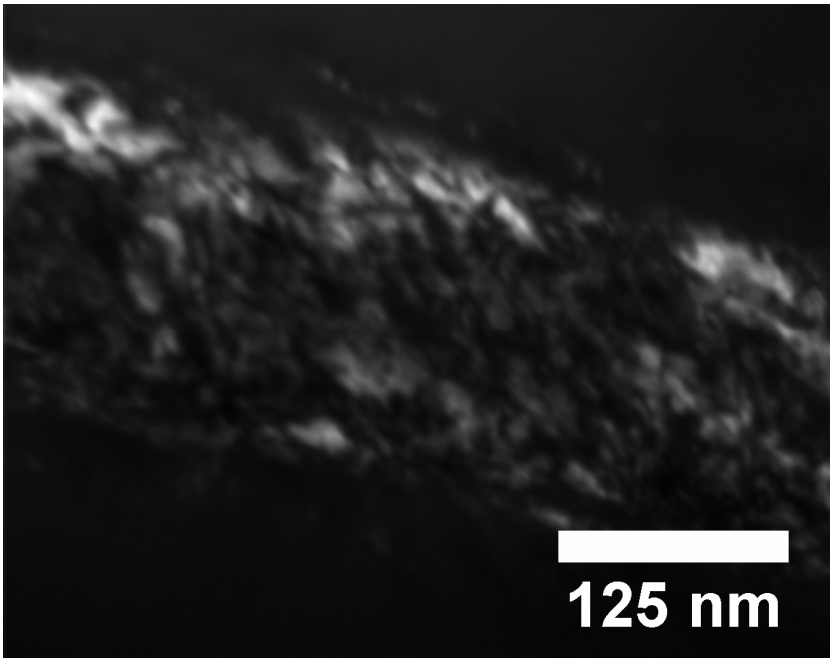

(c) A02480, 175kx

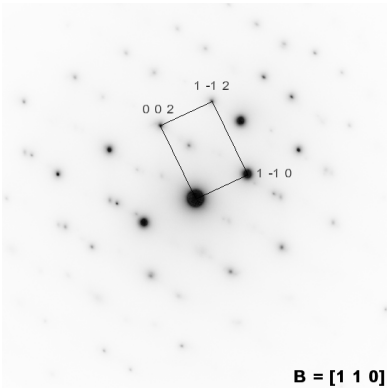

(d)A02477

Figure 4.7: TEM (a) BF image, (c) CDF image, and (b,d) corresponding SAD patterns from layer band. (a) BF image of the microstructure containing alpha grains, (b)SAD pattern indexed as B=[1 1 -2 0]$_\alpha$. (c) CDF image of the α/β interface using the [1 -1 0]$_\beta$ reflection in the (d) B=[1 1 0]$_\beta$ SAD pattern.

Microstructure of the Transient Layers

The morphology of the last three layers deposited vary relative to the fully-developed microstructure, and is schematically mapped in Figure 4.8. These transient layers have experienced incomplete thermal histories relative to previous layers (characteristic layers), and can be used to capture the intermediate development and evolution of the layer band and gradient alpha morphologies observed in the fully developed underlying layers. L15 was the last deposited layer to exhibit both the gradient alpha and layer band morphologies. Examination of the last four layers that have been deposited indicates that the microstructure changes from a fine basketweave (L16) morphology to a fine packet-colony alpha structure (L18). The alpha lath width in the fine colonies was less than 1 μm. Representative optical micrographs from L16 through L18 can be observed in Figure 4.9.

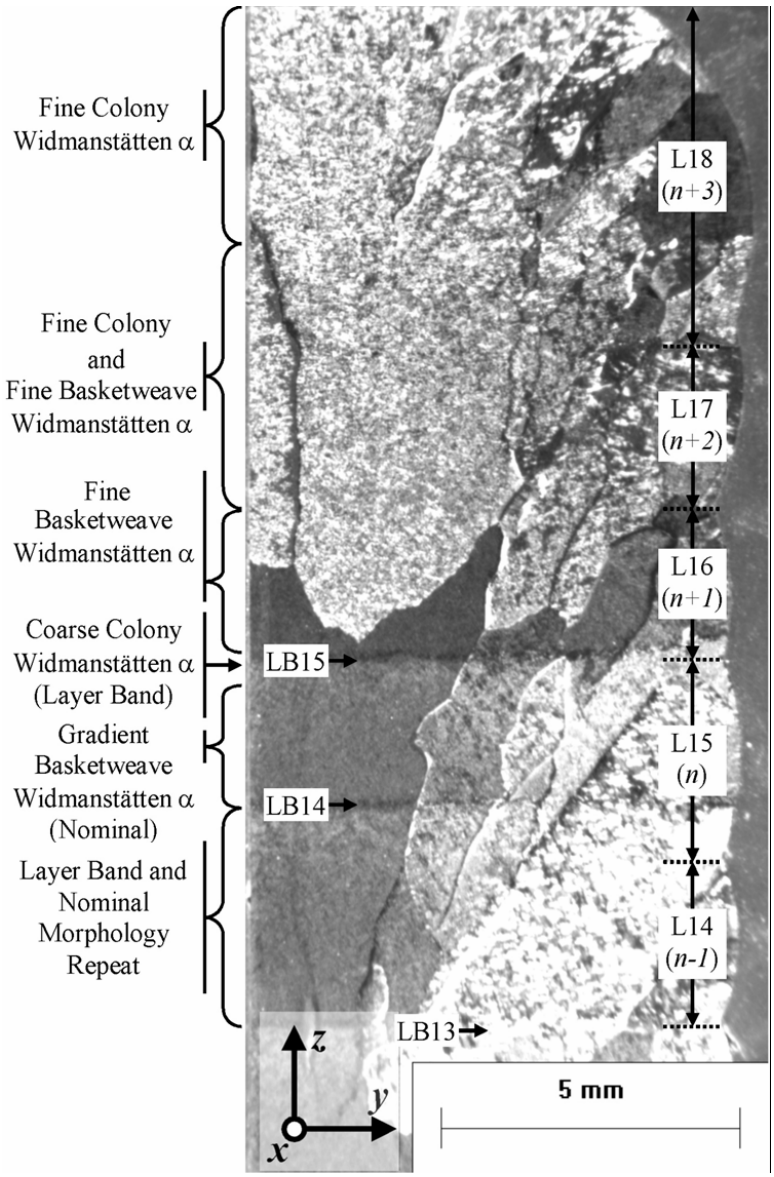

Figure 4.8: Macrograph of the last 5 layers to be deposited illustrating the lack of layer bands in the last three layers deposited. The morphology for regions exhibiting microstructural contrast are labeled.

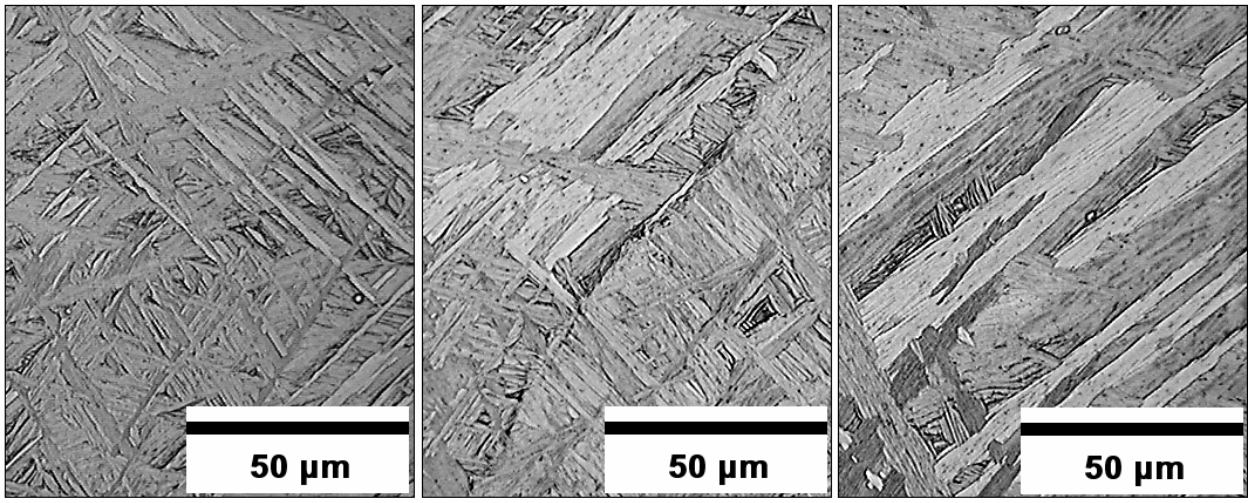

Figure 4.9: Micrographs from the last three layers to be deposited. Regions from the middle of: (a) L16 (n+1) showing fine basketweave and fine packet colony alpha, (b) L17 (n+2) showing fine packet-colonies of alpha with some areas of fine basketweave alpha, and (c) L18 (n+3) exhibiting predominantly fine packet-colonies of alpha.

In order to better understand the microstructure morphology and to quantitatively determine the fraction of alpha and beta phase, several backscattered electron (BSE) micrographs were taken along the last four layers of the as-deposited material and complied into a movie (Figure 4.10). The location of each BSE frame and the calculated phase fraction is shown. A brief description of the image analysis results can be found in the Appendix (Image Analysis of Last Three Layers). This movie clearly shows the different morphologies present within layers 15 through 18 (*n* through *n+3*) including the last layer band, LB15. In layer 15, a basketweave structure is observed that transitions to a packet colony morphology at layer band 15. The morphology of L16 begins as a fine basketweave before transitioning to a fine colony morphology. The fine colony morphology continues into layer 17 and 18. In layers 16 through 18, the contrast of the images decreases with increasing z-position, indicating that partitioning of vanadium to the beta phase is less than in the 15th layer. The apparent lack of vanadium partitioning to the beta phase leads to a much finer packet colony structure.

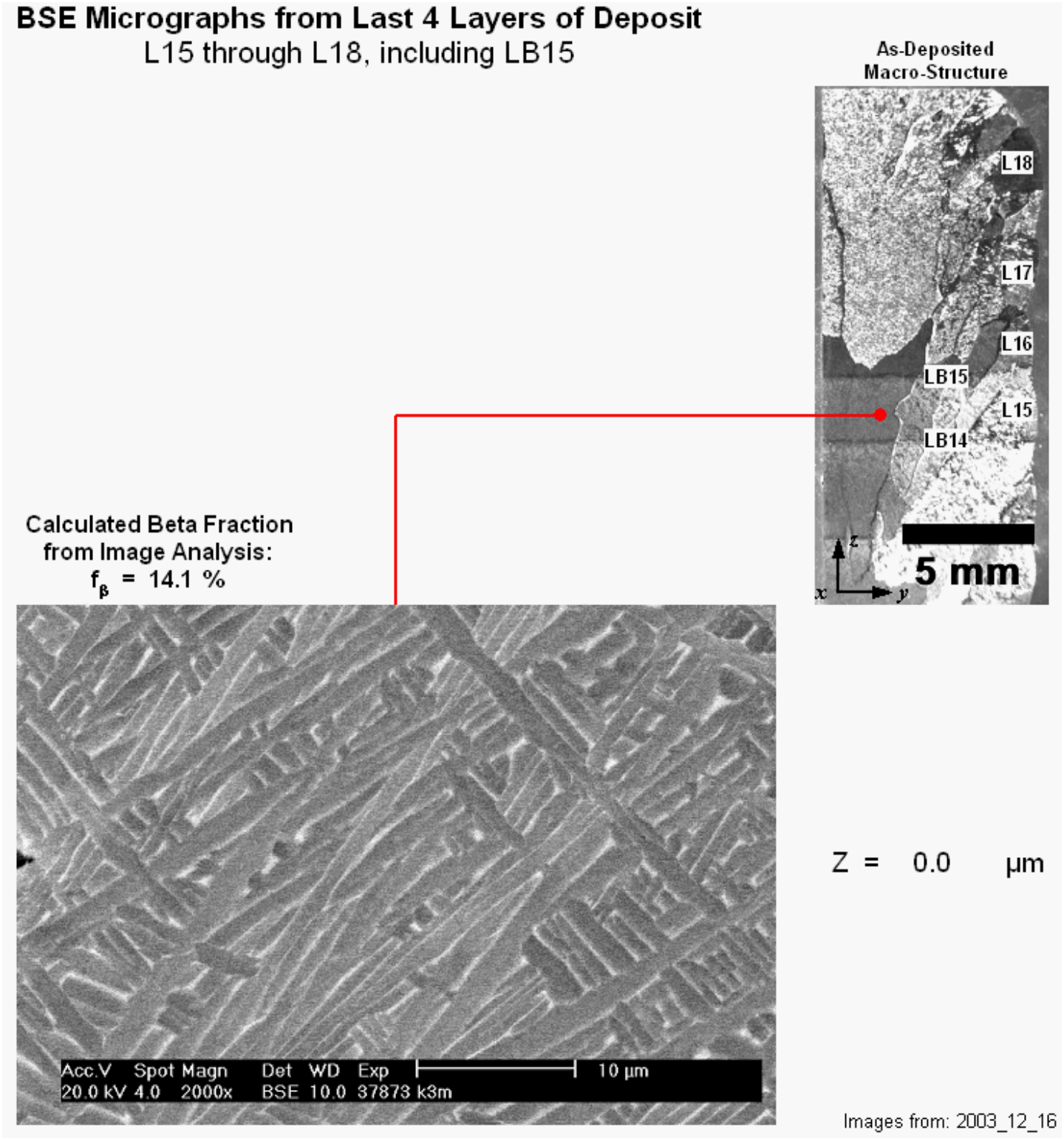

Figure 4.10: Movie of the BSE images taken from the last three layers of the deposit compared with the as-deposited macro structure. (QuickTime, 26.9MB)

Hardness Measurements

Vickers hardness measurements were employed to determine if the layer band microstructure results in a difference in mechanical properties. The results are shown in

Table V for macro and microhardness measurements made both on and off of a layer band. The results indicate no discernable or statistically significant differences in hardness as one moves from inter- through intra-banded material. In addition, a microhardness map was made over a three layer area, and no variations in hardness were observed as shown in Figure 4.11. The average hardness value was 366 HV with a Gaussian distribution observed.

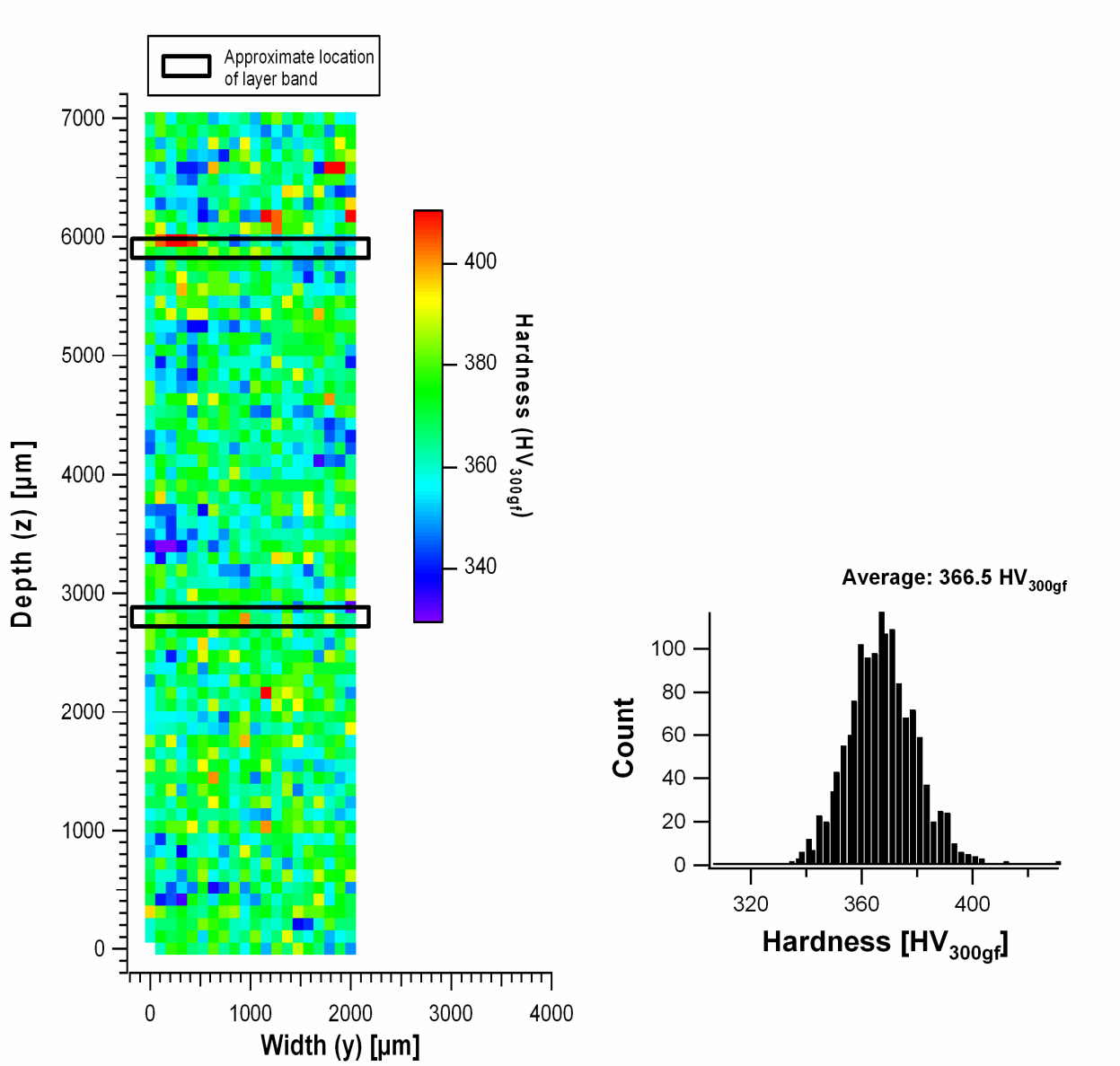

Figure 4.11: Hardness map over a three layer area with approximate locations of the layer bands indicated. Measurements were made at 100µm intervals. The histogram is also shown, with the average hardness being 366 HV.

Composition Measurements

Bulk compositional analysis (Luvak Inc., Boylston, MA) of the elements Al, V, Fe, O, C, and N were performed on 2 samples taken from the middle and top (L18) of the deposit. In addition, oxygen was measured from separate samples containing predominantly layer band (colony-α) and layer (basketweave-α) material. The results are shown in Table VI and indicate that the measured composition is within acceptable limits[74] for this alloy and is in agreement with previously published compositions for this alloy and build method.[5] Also, it can be concluded

that the layer band does not necessarily have a higher oxygen content. The "middle of deposit" composition will be designated AR-MID and will be used in the microstructure modeling efforts.

Table VI: Summary of Bulk Composition Analyses Made From Different Locations Within the Deposit. [Weight Percent Element]

Location	Al	V	Fe	O	C	N
Top of Deposit	6.09	4.08	0.27	0.2015	0.030	0.012
Middle of Deposit	6.00	3.99	0.25	0.2035	0.021	0.013
Layer Band	-	-	-	0.221	-	-
Between Layer Bands	-	-	-	0.206	-	-
ASTM-B367-93 Ref. [74]	5.5 - 6.75	3.5 - 4.5	0.4 max	0.25 max	0.10 max	0.05 max

Quantitative compositional analyses were made at various *z*-positions in the as-deposited material to determine if segregation of alloying elements could be responsible for the layer band contrast, as has been observed in fusion welds of Ti-6Al-4V.[75] Traverses were made across layer band(s) and across the last three layers in the deposit where layer bands are absent. A nominal alloy composition of 90.4 wt.% Ti, 5.6 wt.% Al, and 2.8 wt.% V was obtained. Figure 4.12(a) shows no systematic variation in the composition of the deposit across three layer bands. Figure 4.12(b) shows a slight decrease in the amount of titanium present in the last two deposited layers. Significant scatter is observed in the titanium and vanadium composition profiles due to the difficulty in distinguishing between these two elements (V-K_α and Ti-K_β peaks overlap); however, in all of the analyses, the scatter in the aluminum composition was low. Thus, the aluminum composition was used as a benchmark for the conclusion that a compositional gradient is not present within the deposit.

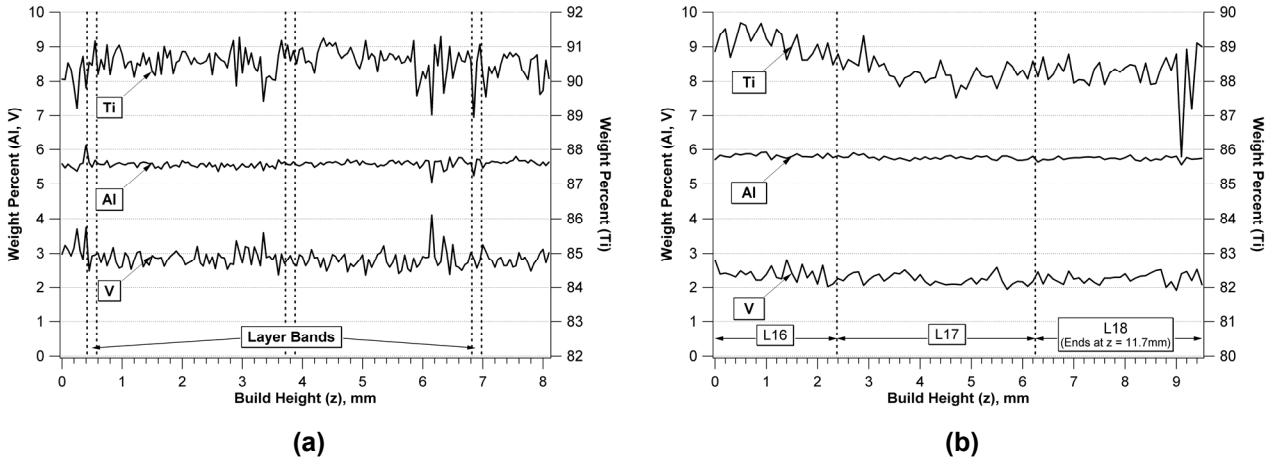

Figure 4.12: (a) Composition profile for the 8.1 mm long traverse that crosses three layer bands. The positions of the layer bands, indicated by the dashed lines, are approximate. (b) Composition profile of the central 9.9 mm long traverse measured from L16 and L17 that does not cross any layer band. The average composition in weight percent is (a) 90.54 Ti, 5.58 Al, and 2.83 V and (b) 88.47 Ti, 5.77 Al, and 2.28 V.

Energy dispersive spectroscopy (EDS) measurements made in the TEM of the alpha and beta phases at different locations within the characteristic layer are shown in Figure 4.13a-b. These measurements were made to asses the local composition variation within the characteristic layer. The alpha composition measurements shown in Figure 4.13a represent the averages for approximately 8 individual measurements from the alpha grain for each sample (just above a layer band, middle of layer, just below a layer band and the layer band). The beta composition measurements, Figure 4.13b, are "averages" from 2-3 measurements. There is little variation in the alpha composition as a function of position within the characteristic layer, whereas in the beta composition, vanadium decreases and titanium increases as the layer band is approached. It should be noted that difficulties were experienced in constantly distinguishing between the Ti-K_β and V-K_α peaks in the EDS spectra due to overlap. This results in errors in the amount of Ti and V measured.

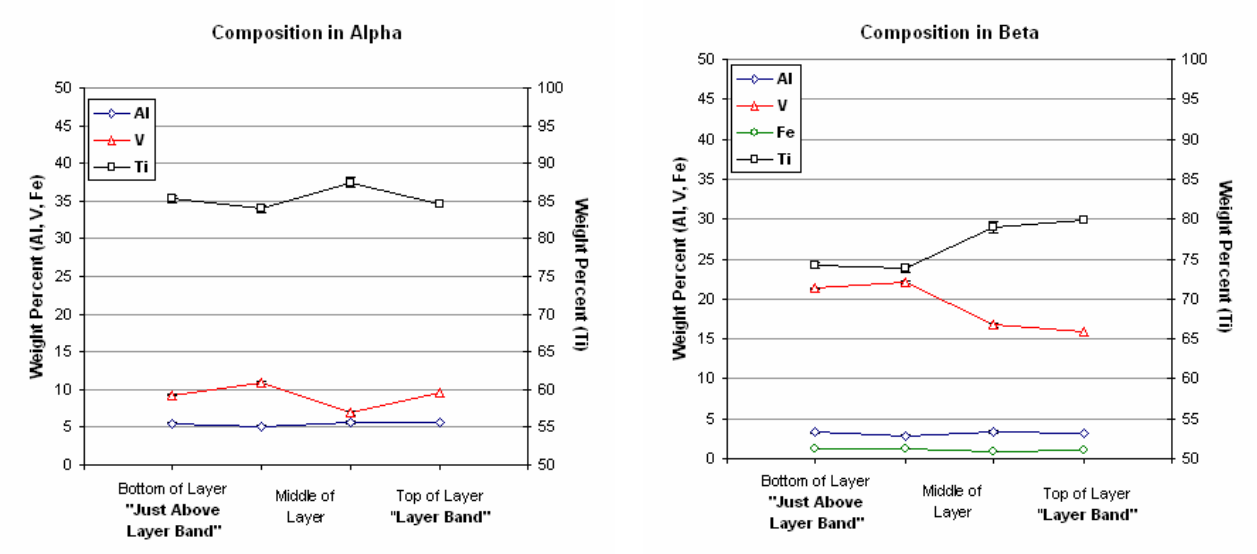

Figure 4.13: Alpha and beta phase compositions measured using EDS on samples located within the characteristic layer. The top of the characteristic layer is defined by the layer band and the bottom is "just above the previous layer band".

EBSD Analyses

EBSD analyses made on the as-deposited material in the location of a layer band are shown in Figure 4.14 through Figure 4.16. In each figure, the "(a)" image is a large scan traversing a section of layer band while the "b-d" images represent higher resolution scans made (b) above a layer band, (c) within the layer band and (d) below the layer band. It should be noted that the analyzed regions of the (a) and (b-d) images are from different locations within the same sample (different y locations). The images of Figure 4.14 are maps shaded according to the quality of the EBSD pattern obtained ("pattern quality"), where poor patterns are shaded black and excellent patterns white. Regions of poor quality are located between grains, especially those grains of different orientation, hence colonies appear as a single grain as in Figure 4.14c. In addition, poor quality can also be attributed to regions of crystalline distortion, i.e. strain and dislocations. The variations in the pattern quality maps appear evenly distributed throughout the y and z directions. Also appearing in the pattern quality maps are locations where beta was detected as indicated by the red pixels. The location and detection of the beta phase is inconsistent even for the high resolution scans made at 0.1 and 0.15 μm steps. The resulting fractions of beta are less than 1%.

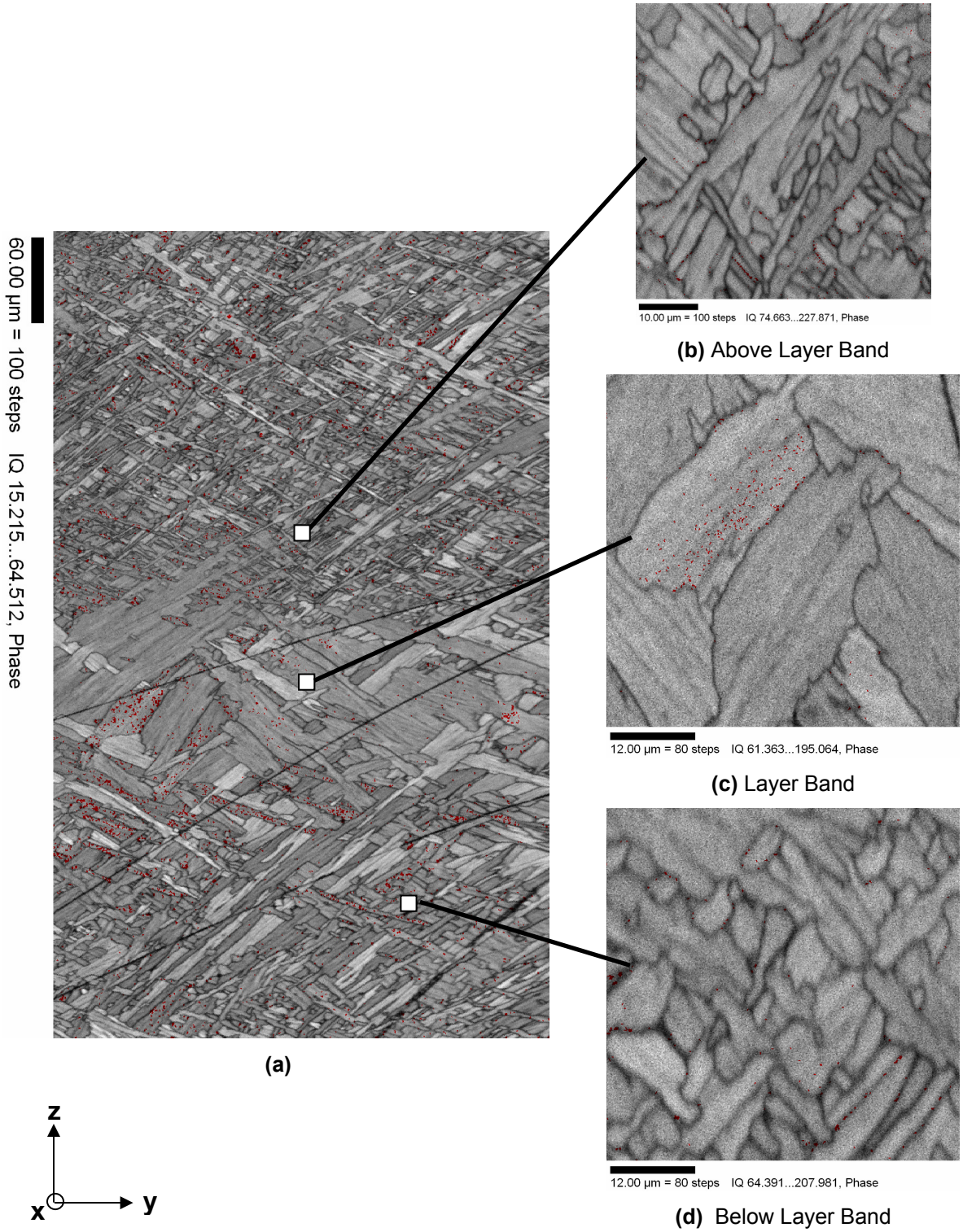

Figure 4.14: EBSD pattern quality maps of the layer band region at (a) "low" and (b-d) "high" resolution. Red pixels indicate the locations where beta was detected (1.8%-β and >1%-β in low and high magnification images). The locations of the high magnification images are for illustrative purposes (high magnification analyses are from different location in the sample).

Figure 4.15 shows a map of the different orientations of the α grains with each point colored according to an automatically color coded unit triangle of the inverse pole figure. For example red indicates a <0001> orientation while blue represents a <10-10> orientation. Colonies of α are represented by a single color as observed in the layer band regions. The distribution of the different orientations also appears to be uniform.

Figure 4.16 shows the variation in the misorientation between and within α grains, best seen in the high resolution images (b-d). Between individual α grains and α colonies, the boundaries are high angle (>15°, blue). Within individual α grains and α colonies there is little misorientation between grains.

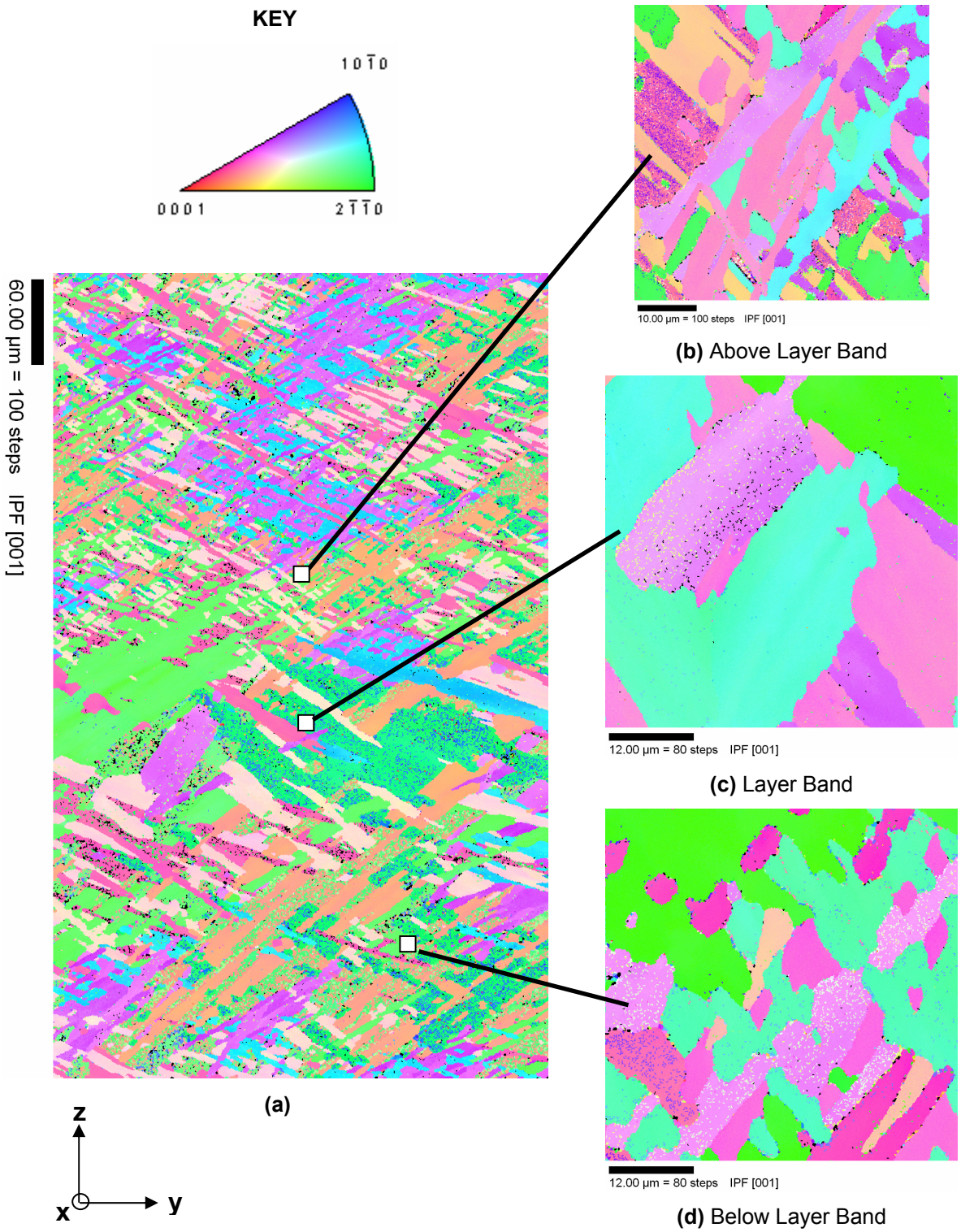

Figure 4.15: EBSD α-IPF maps of the layer band region at (a) "low" and (b-d) "high" magnification. Different colors represent different crystallographic directions of the α grains according to the unit triangle shown above (a). Black pixels are beta phase. The locations of the high magnification images are for illustrative purposes (high mag images are from different location in the sample).

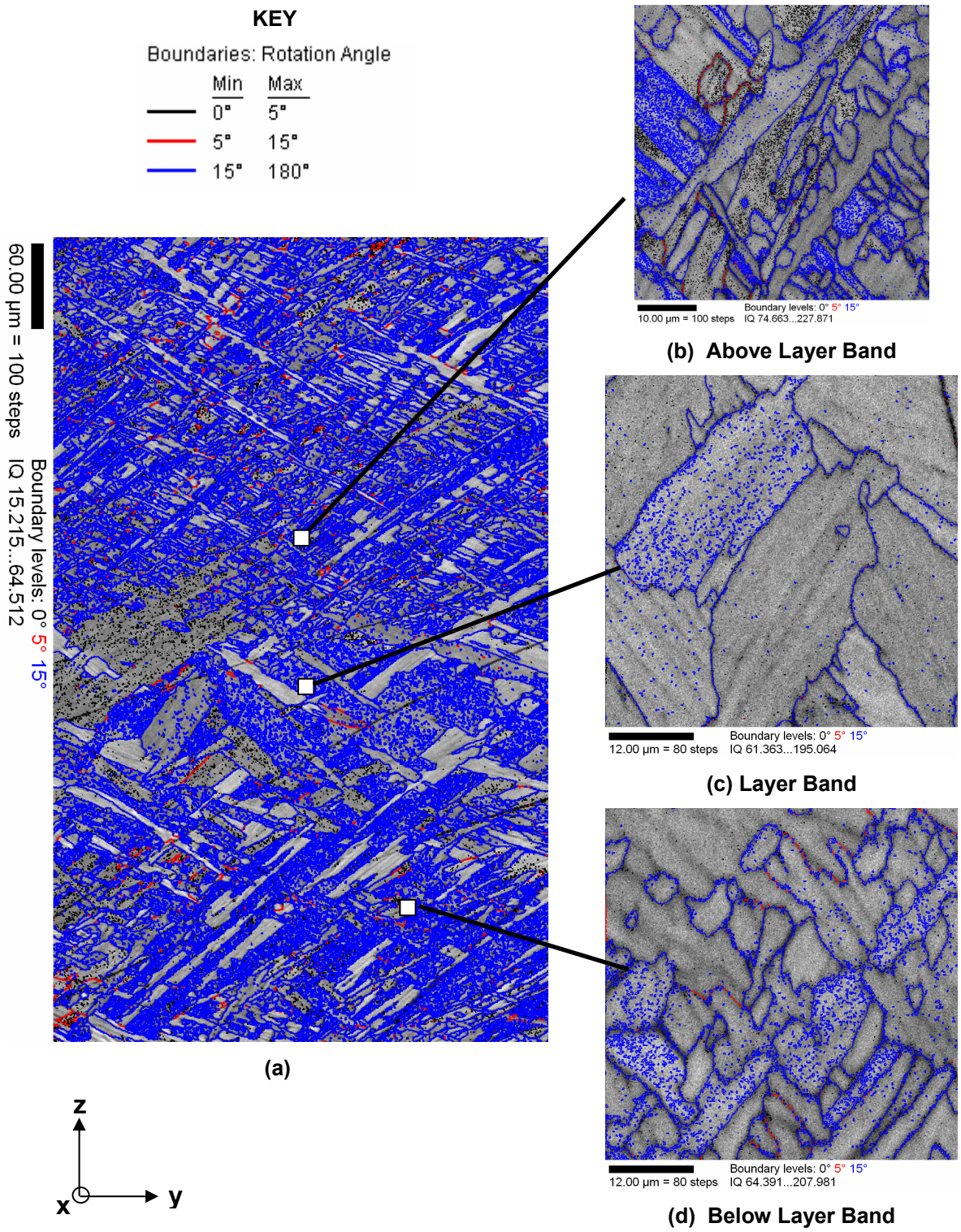

Figure 4.16: EBSD Grain Boundary misorientation maps of the layer band region at (a) "low" and (b-d) "high" magnification. Adjacent boundaries with a misorientation >15° are blue. `The locations of the low magnification images are for illustrative purposes (low mag images are from different location in the sample).

Discussion

Beta Grains

It was observed that the prior beta grains in the deposit are columnar in nature, oriented nearly perpendicular to the substrate in the *y*-*z* plane, and slightly tilted in the direction of laser motion in the *x*-*z* plane. The prior beta grains also grow across multiple deposited layers. Initial solidification of the columnar grains occurs epitaxially from the grains in the base metal, or previously deposited layers, due to similarities in the composition and surface energies of the metal. This allows for the columnar grains to continue growing across multiple layers. The columnar nature of the prior beta grains is typical for high-energy processes, such as welding and laser deposition of thick layers. Upon cooling from the melt, the growing grains align themselves with the steepest temperature gradients.[76] In LMD of a single line of material, heat flows nearly perpendicular to the substrate in both the *y* and *x* directions. There is a slight bias of the prior beta grains in the +*x* direction, or the direction of laser motion, due to the moving heat source. Fully equiaxed beta grain morphologies can be eliminated by decreasing the thermal gradient (dT/dz) and increasing the solidification rate (dz/dt)[8-10,77,78].

Characteristic Layer

Nominal Microstructure (Graded Basketweave-α)

The microstructural morphology observed between layer bands (nominal microstructure) is basketweave-α. It is known that increasing cooling rates from the β phase field, increasing the amount of β stabilizer (V in the case of Ti-6Al-4V), and decreasing the β excursion temperature and time will favor formation of the basketweave-, as opposed to a colony-α morphology.[43] The width of the individual α laths is smallest just above a layer band (e.g., LB1) and largest just below the next layer band (e.g., LB2). The gradient in α lath width is present between every layer band in the deposit and just above the last layer band observed. An analysis of variance (ANOVA) and Student's t-test of the data verifies that there is statistical difference between the mean width of the individual alpha laths measured at the bottom, middle, and top of a layer.

Compositional gradients and/or thermal effects are two of the most likely reasons why such a gradient in the microstructure would exist. There was no systematic variation in the bulk

composition between layer bands as determined using the electron microprobe. According to the EDS measurements there was a slight decrease in the local beta phase vanadium composition as the layer band was approached which could lead to a transition to a colony morphology.[43] The local variation in beta phase composition appears to be a result of different amounts of equilibration that occurs during heating into the two phase field, and is less likely due to macro/micro segregation during solidification. Thus, it can be concluded that the gradient in the individual α lath size is due to thermal effects, specifically peak heating temperature and cooling rate from the peak temperature. Higher temperatures result in larger grains while faster cooling rates result in finer grains. These effects are actually competing since typically higher peak temperatures lead to faster cooling rates. If time is considered, an argument could be made that larger alpha grains are a result of longer times at or above a certain temperature within the α+β phase field. Knowledge of the thermal history of the build will clarify whether time, temperature, or cooling rate are responsible for the gradient in α lath size for the LMD process.

Layer Bands (Colony-α)

Within the layer bands, a colony-α morphology is exhibited, in contrast to the basketweave-α morphology within the nominal microstructure. The colony or packet size, layer band thickness, and inter-band spacing remains essentially constant throughout the build, indicating that the origin of the layer banding is constant and periodic through the course of the building process. Furthermore, TEM and EBSD investigations did not reveal any differences in substructure or orientation. Furthermore, these investigations did not exhibit any of the characteristics of the non-equilibrium transformation products, such as α′ or α_m as observed in Chapter 3. It was stated above that the basketweave morphology will tend to form with increasing cooling rate from the β phase field, increasing the amount of β stabilizer (V in the case of Ti-6Al-4V), and/or decreasing the β excursion temperature and time.[43] Based on these effects, three theories can be proposed to account for the formation of the layer bands; these include oxidation, macro/microsegregation of alloying constituents, and thermal cycling effects.

In titanium alloys, the α phase is stabilized by oxygen interstitials and subsequently embrittles the alloy at high levels.[79] It is conceivable that the surface of each freshly deposited layer could dissolve oxygen, resulting in a region that was α stabilized. As the next layer is deposited, the

"α-case" of the previous layer would be "buried" into the microstructure thus providing the optical contrast observed. However, such oxygen-rich regions effects can be ruled out as a cause of the layer band for several reasons. First, the hardness both on and off of the layer band were statistically (ANOVA and Student's t-test) similar suggesting the absence of an embrittling α-cased region. Further, the deposition of the alloy is conducted in a nominally-inert atmosphere; the surface was free of discoloration or discernable evidence of high temperature oxidation.

A second conceivable explanation for the formation of the layer bands is macrosegregation of solute in the solidifying material. Macrosegregation is defined as segregation that extends over several grain diameters. The type of macrosegregation that is described most often in literature on fusion welding is termed transverse solute banding.[80,81] The bands normally appear as curvilinear contours on the polished and etched surfaces of fusion weldments. These bands are attributed to thermal variations in the weld pool, which periodically change the solid-liquid interface velocity.[82] Electron microprobe studies have shown that in titanium alloys, transverse solute banding is a result of vanadium and aluminum segregation.[83] Quantitative electron microprobe composition analyses performed on the LMD Ti-6Al-4V deposit revealed no systematic variation in the bulk aluminum composition as a layer band was traversed. According to Ref. [43], we would expect to observe an increase in the aluminum concentration or a decrease in vanadium concentration as a layer band was traversed. In addition, if the layer band was a result of a solidification effect, one would expect to observe the banding in the last deposited layer. Bulk solute segregation during solidification (macrosegregation) effects have ruled out as a cause of the layer band formation.

The third hypothesis for the presence of layer bands in the LMD material is due to the multiple thermal cycles that a fixed point sees during the build of the part. Specifically, the effect of thermal cycling on local composition variations and microstructure will be discussed. The analysis of Kobryn *et al*.[9,78] agrees in that the macroscopic banding is a result of a new heat affected zone being formed; however, no further analysis of the microstructure evolution is given. Based on the current results, the formation of layer bands is similar to what was proposed above for the presence of a gradient in the α lath width. It is reasonable to assume that there exists a specific combination of peak temperature, time at peak temperature, and cooling rate that lead to the formation of the colony (layer band) morphology over the basketweave

(nominal) morphology. It is also known that the layer bands remain present in the material if subsequent heat treatments are conducted at least 87K below beta transus (see Chapter 5)[24], indicating that the characteristic layer is was last heated within the $\alpha + \beta$ phase field. Specifically, the results are consistent with heating above a temperature where a large region of alpha dissolves followed by subsequent growth of α_S. The colony-α of the layer band appear to nucleate intragranularly, supporting the theory that they forms as a result of heating to a peak temperature high in the $\alpha+\beta$ phase field.

The EDS measurements from the layer band suggest that the vanadium composition in beta was 5wt.% less than just above the previous layer band, i.e., a greater amount of vanadium partitions to the beta phase at the bottom of a characteristic layer. The aluminum composition in α and β remained constant throughout the characteristic layer. Depletion of vanadium composition in beta can be associated with heating high into the $\alpha+\beta$ phase field or into the single β phase field, where the phase composition is near the bulk alloy composition. Examining the equilibrium composition of the beta phase (Figure 4.17), at temperatures above 1200K the beta phase composition is nearly that of the nominal alloy composition (6Al-4V). Thus cooling from this regime at sufficient rates would produce little vanadium partitioning. The EDS results suggest that the layer band (colony-α) forms during heating high into the $\alpha+\beta$ or β phase fields; however, confidence in the amounts of vanadium calculated are low due to problems associated with distinguishing between the Ti-K_β and V-K_α peaks in the EDS spectrum. The effect of thermal cycles on the microstructure (and composition) will be further investigated in the thermal and microstructure modeling chapters.

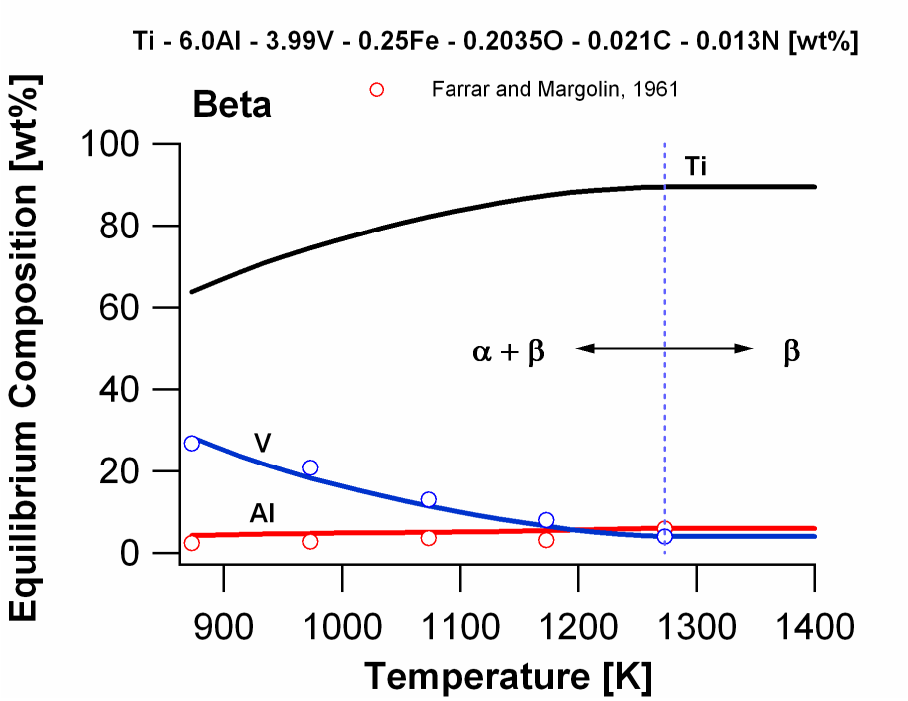

Figure 4.17: JMatPro-Calculated equilibrium composition of the beta phase for the nominal bulk alloy composition in the as-received deposit. Data points represent compositions from isothermal ternary sections for a nominal Ti-6Al-4V alloy Ref. [62].

Lastly, it should be noted that α' and α_m were not observed in the characteristic layer. This conclusion is based on the results of Chapter 3 using the same techniques used to characterize the as-deposited microstructure.

Transient Layers

In the as-deposited results, electron microprobe analyses performed in the transient region of the deposit (Figure 4.12b) indicate that macrosegregation is not present. This suggests a newly formed layer solidifies with a homogeneous distribution of alloying elements.

The baseline microstructure experiments further support the claim that a characteristic layer forms during heating in the two phase field whereas the transient layers always see peak temperatures into the β phase field. Primary heat treatment resulted in a lack of vanadium partitioning to beta, observed as a lack of contrast in BSE images from Chapter 3(Figure 3.6, Figure 3.7, Figure 3.15, and Figure 3.16). A similar lack of contrast was observed in the series of BSE images taken from the transient region of the deposit (Figure 4.10). The characteristic layer exhibits much greater BSE contrast than the transient region. This suggests the transient

region last experiences heating in the β phase field, while the characteristic layer experiences heating in the α+β phase field.

The microstructures present in the transient region appear to be diffusion controlled transformation products, namely a very fine basketweave and colony-α morphology. These fine structures result from heating above the beta transus and faster cooling (relative to the characteristic layer). From optical microscopy and the BSE images, there are no observed α′ or α_m non-equilibrium phases in the transient layers.

Microstructure Evolution Path

We can gain some insight as to when the characteristic layer forms (i.e., what layer deposition is responsible for their formation) through clues in the as-deposited microstructure. First, the layer band traverses prior beta grains and grain boundaries, suggesting that the formation of the layer band occurs as a result of a solid-state transformation. Second, the last several layers of as-deposited material (L15-L18) have left a record as to what phase transformations have taken place in order to form the characteristic layer.

Once steady state is established by the build process, the four most recent layers are distinct. These are identified as *n* through *n+3* in the manner illustrated in Figure 4.9 where characteristic layer, *n*, is established to be that where the layer banding and gradient alpha morphology appear within the same layer. The hypothesized evolution of the different microstructure morphologies is schematically shown in Figure 4.18. When layer *n* is deposited, it cools relatively quickly from the molten state to form a fine colony-α morphology in layer *n* as observed in L18 (Figure 4.9).

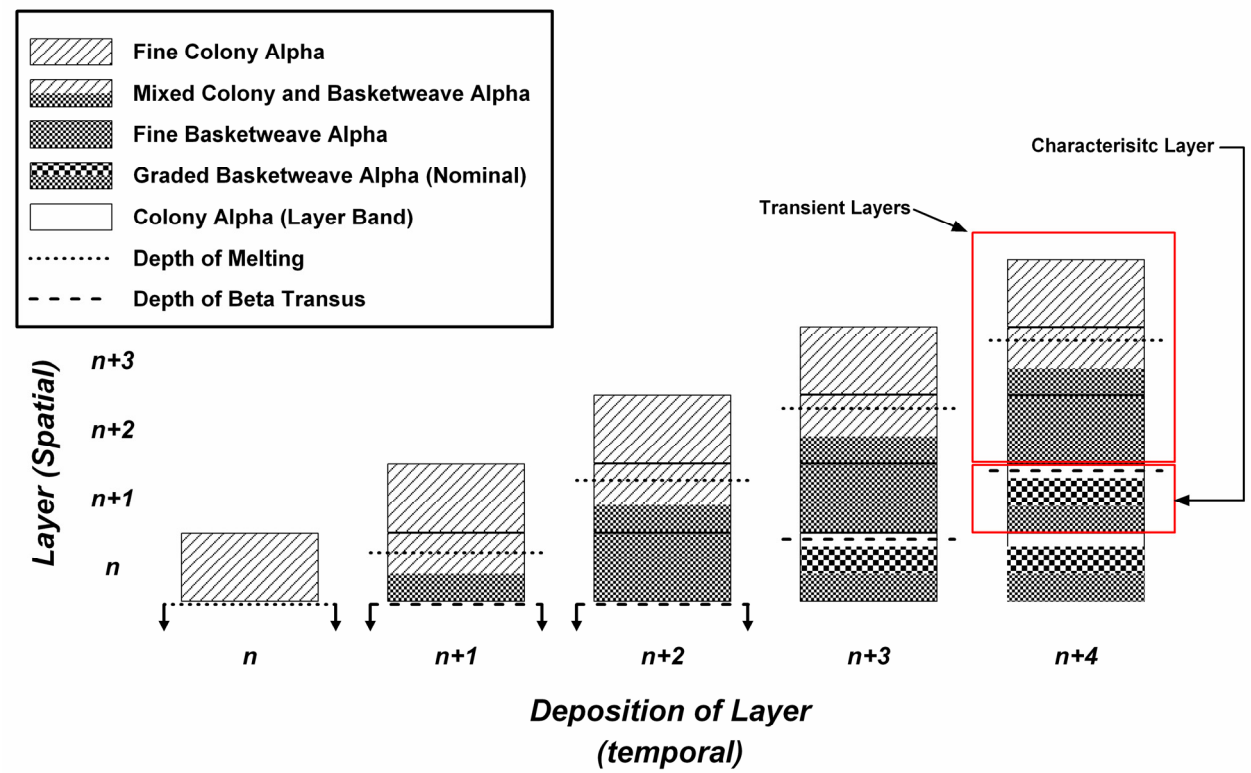

Figure 4.18: Schematic evolution of different microstructure morphologies in the observed Ti-6Al-4V deposit. The positions of the maximum depth of melting and beta heating are approximate. Arrows are added to these lines to indicate the position is below layer n. The transient and characteristic layers are shown for the deposition of layer n+4 on layer n.

The next layer, *n+1*, is deposited on top of *n*, remelting a portion of layer *n* and heating the remaining portion high into the β phase field. This heating is followed by rapid cooling leading to a fine basketweave α morphology with a dispersed fine colony morphology, as observed in L17 (Figure 4.9). Layer *n+2* is deposited on top of *n* and *n+1*, again causing heating of layer *n* into the β phase field, but for a lesser peak temperature, period of time above the beta transus, and cooling rates than previously experienced. The result is a basketweave-α morphology. Upon deposition of *n+3*, only a narrow region near the top of layer *n* will see an excursion high into the α+β phase field followed by a slow cooling rate to form the colony morphology, i.e. a layer band is formed. The material below the layer band does not see a thermal cycle that is of sufficient temperature or time produce the colony morphology. Instead, the previously existing fine basketweave morphology in layer *n* caused by the deposition of layer *n+2* is transformed into a graded basketweave morphology due to a gradient in peak temperatures and cooling rates experienced. With further layer depositions (e.g. *n+4*) the peak temperatures will not be sufficient to produce significant changes in the microstructure, and the graded basketweave and

layer band morphologies developed during the prior 3 thermal excursions will be retained. Based on microstructural observations made within the last four deposited layers, the characteristic layer, comprised of the gradient alpha and layer band morphologies, forms in layer *n* due to the deposition of layer *n+3*.

Microstructure-Property Effects

The colony, basketweave, and columnar beta grain morphologies observed in laser deposited Ti-6Al-4V will have different effects on the mechanical properties of the deposit. This has been reviewed in Ref [24], but important aspects are summarized here. Colonies act as single microstructural units because of the similar grain orientations and define an effective slip length[84] of an advancing crack. This was observed in the EBSD grain boundary misorientation map (Figure 4.16). Large colonies tend to degrade strength and ductility (Hall-Petch relationship)[85,86]; however, they create a more tortuous crack path[87], enhancing toughness. On the other hand, basketweave morphologies increase strength and ductility while degrading toughness.[84,88] Large beta grains tend to enhance creep and fracture toughness, while degrading strength, ductility and fatigue properties.[89] It would seem that these variations in microstructure produce variations in the mechanical properties. Most of the available data for laser deposited Ti-6Al-4V is from heat-treated samples or experiments were microstructure variations are not shown.[90] In general, the mechanical properties of laser-deposited Ti-6Al-4V are reported to be on par with acceptable (Mil-Handbook) limits.[5] The evolution of microstructure is worth investigating in order to produce functionally graded parts in the future.

Conclusion

The laser deposition of multiple layers of the titanium alloy Ti-6Al-4V results in unique macro and microstructural morphologies that could have both beneficial and adverse effects on mechanical properties. The macrostructure exhibits columnar prior beta grains oriented perpendicular to the substrate approximately 1.4 mm in width that have grown across multiple layers as a result of epitaxial growth from the substrate and/or previously deposited layers. The deposit exhibits two regions of macro-and microstructural contrast. The last three layers are in a undeveloped “transient” state. A “characteristic layer” is found in the fourth most recent layer and is repeated in the underlying material. The characteristic layer contains a distinct

microstructural morphology, defined as a layer band. The layer bands are a band of material approximately 165μm thick exhibiting a colony α morphology. The microstructure between layer bands is basketweave α outlined in retained β phase and exhibits a gradient in the α lath width between layer bands. The layer bands are present for every layer except the last three layers to be deposited. Layer bands traverse prior beta grains and grain boundaries, and do not change as a result of sub-beta transus heating indicating their formation occurs after multiple layers have been deposited. The layer bands have the same hardness as the surrounding material. There are no variations in substructure or orientation associated with the layer band or basketweave morphologies. Furthermore, α' and α_m were not observed in the deposit. Variations in the degree of beta phase partitioning were observed in the layer band region as well as the transient layers and are attributed to thermal cycling. Regions where vanadium did not partition strongly to the beta phase are associated with heating high into the α+β and/or β phase fields. Thermal effects are responsible for the formation of the gradient and layer band morphologies.

Generally, the basketweave alpha morphology forms in a layer *n* during a relatively high temperature excursion into the beta phase field followed by a rapid cool to below the beta transus. The layer band forms with a sequential pass of the heat source when a narrow region of layer *n* experiences heating near the beta transus of a critical time, temperature and cooling rate to form the colony morphology, while the underlying basketweave material is heated into the two-phase field and cooled slowly, producing a graded basketweave morphology, where regions closer to the layer band exhibit thicker individual alpha laths due to a particular combination of cooling rate and peak temperature within the two phase region. The addition of subsequent layers does not produce a thermal cycle sufficient to alter the microstructure in layer *n*. Thus, it is theorized for the build observed in the current work that the basketweave morphology forms in a layer, *n*, after the deposition of layer *n+2* while the layer band and scale-graded basketweave-α morphology forms after the deposition of layer *n+3*. Furthermore, the characteristic layer is found in layer *n*, and below (e.g., *n-1*, *n-2*,…). The layers *n+1* through *n+3* define the transient layers.

Thermal cycling in the $\alpha+\beta$ phase field will produce varying amounts of alpha dissolution and subsequent growth of α_S and possible variations in local phase compositions, leading to the greatest variation in microstructure.

Chapter 5: Heat Treatment of LMD Ti-6Al-4V Deposits

The present chapter reviews α+β heat treatments and reports on β heat treatments performed on the as-deposited material. The results are discussed in relation to the postulated microstructural evolution sequence.

Introduction and Review of α+β Heat Treatments (Ref.[24])

Inhomogeneities in the macro and microstructure are both an advantage and disadvantage to LMD. If the process can be accurately controlled, these microstructural differences could be used to tailor the properties in appropriate regions in the build; however, significant work in this area remains for a truly functionally-graded material to be realized.[91] Traditionally, microstructural control of Ti-6Al-4V would be obtained through thermomechanical processing[84]; however, that is not an option because the parts are net or near net shape and one main purpose of LMD is to bypass conventional forming techniques. In the meantime, heat treatment of LMD parts must be used as a secondary way of modifying the microstructure to acceptable conditions.

Solution treat and age (STA) experiments have been performed on LMD Ti-6Al-4V material,[24] the results of which are summarized here. The solution treatment is used to revert a desired amount of alpha to beta by heating high in the α+β phase field followed by cooling at a sufficient rate to retain increased amounts of beta at room temperature.[92] The aging treatment, then converts the retained beta to fine alpha precipitates, increasing the tensile and possibly fatigue strength.[92]

The STA treatments were performed for Boeing who later performed mechanical testing on the samples as part of their validation process for LMD Ti-6Al-4V. As-deposited samples were heated to 1186 K, held for 2-hours and cooled at rates ranging from 0.005 to 11.8 K/s, followed by a four-hour aging treatment at 811K followed by a furnace cool. The microstructure was observed after the aging treatment. Increasing cooling rates decreased the overall individual alpha lath width (Figure 5.1) but had no other effect on microstructure. After the STA heat treatment, the gradient in the individual alpha lath width was homogenized leaving a basketweave-α morphology (Figure 5.2a). The layer band colony-α morphology remained

(Figure 5.2b). This indicates that at 1186K, the amount of alpha dissolution is insufficient to alter the colony morphology. According to the equilibrium phase diagram at this temperature (Figure 2.12) there should be 53% β at 1186K meaning that about half of the alpha phase initially present should dissolve. Subsequent α_S formation during cooling from the solution temperature is not observed in the optical microscope. Homogenizing the gradient in α grain width suggests that the solution-temperature was sufficient to homogenize any local composition gradients present, resulting in a uniform alpha lath thickness. Even though the microstructure was not observed before the aging treatment at 811K, little change in morphology would be expected since the aging temperature is 170K less than where the equilibrium phase diagram predicts alpha dissolution will occur.

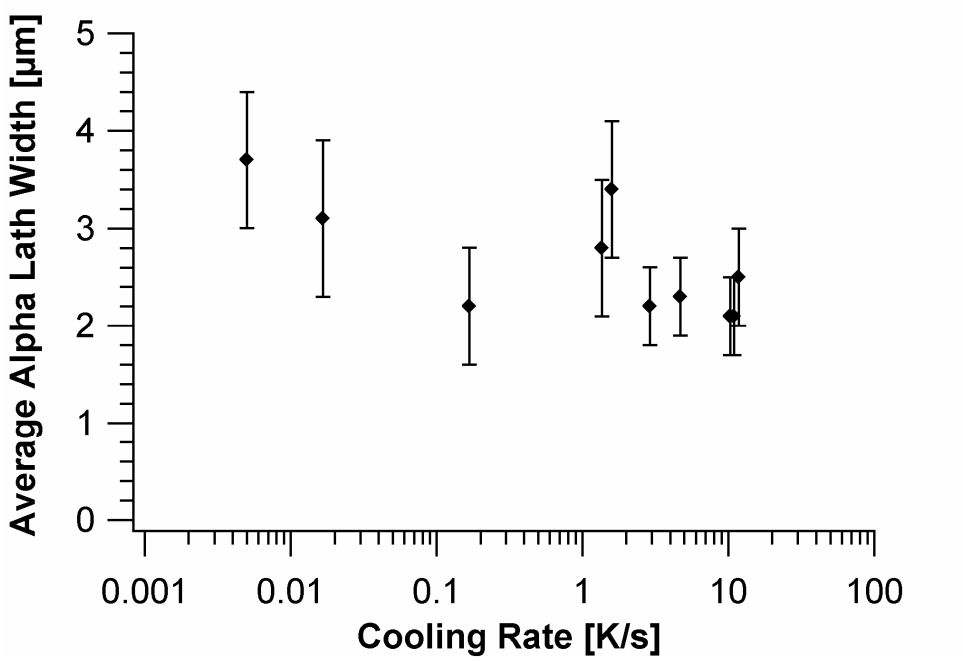

Figure 5.1: Average alpha lath width as a function of cooling rate following a 2-hour solution treatment at 1186K and a 4-hour aging treatment at 811K.

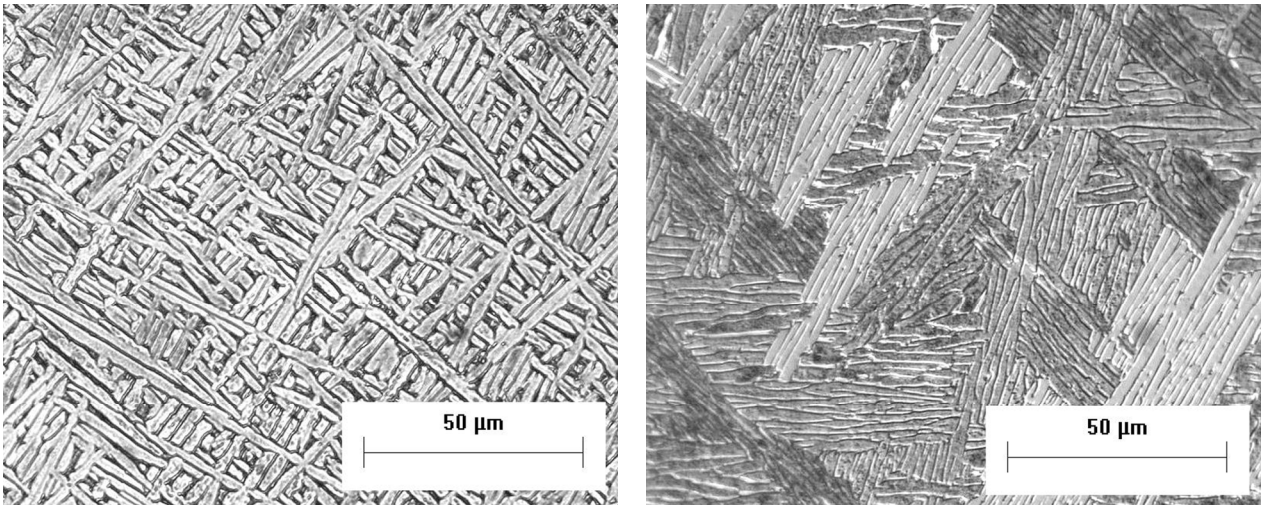

(a) Nominal **(b) Layer Band**

Figure 5.2: Optical microstructures following STA heat treatment illustrating the (a) nominal basketweave-α and (b) layer band colony-α microstructure morphologies retained.

Experiment

Laser deposited, Ti – 6wt.% Al – 4 wt.% V, "rib-on-web" builds examined herein were fabricated by AeroMet Corporation (Eden Prairie, MN) using their Laser Additive Manufacturing (LAM) process.[4] The polished and etched (water, 5%HF) as-deposited sample (Figure 5.3a) was used in this heat treatment study. Several layer bands in this sample were marked using microhardness indents prior to heat treatment. The sample was wrapped in Ta foil and vacuum encapsulated in a quartz tube. Heat treatments were performed in a tube furnace operating at 1473 K, 200K above the beta transus for this alloy. The sample was held at this temperature for 2 hours and furnace cooled. Following heat treatment the sample was lightly polished using colloidal silica and etched. Visual examination of the microstructure was performed on an FEI XL30 FEG SEM operating in backscattered electron mode at 20 kV.

Results

Figure 5.3 illustrates the before (a) and after (b) macrostructure of the beta heat treated sample. Clearly, the layer bands and columnar beta grain structure have been eliminated and replaced with equiaxed prior beta grains. Figure 5.4 compares the before (a-b) and after (c-d) microstructure of the layer band and nominal morphology. The microstructure of the beta heat treated sample consists entirely of colony alpha phase outlined in untransformed beta,

eliminating the gradient in alpha grain size of the basketweave morphology and the discontinuity in the microstructure encountered at the layer bands.

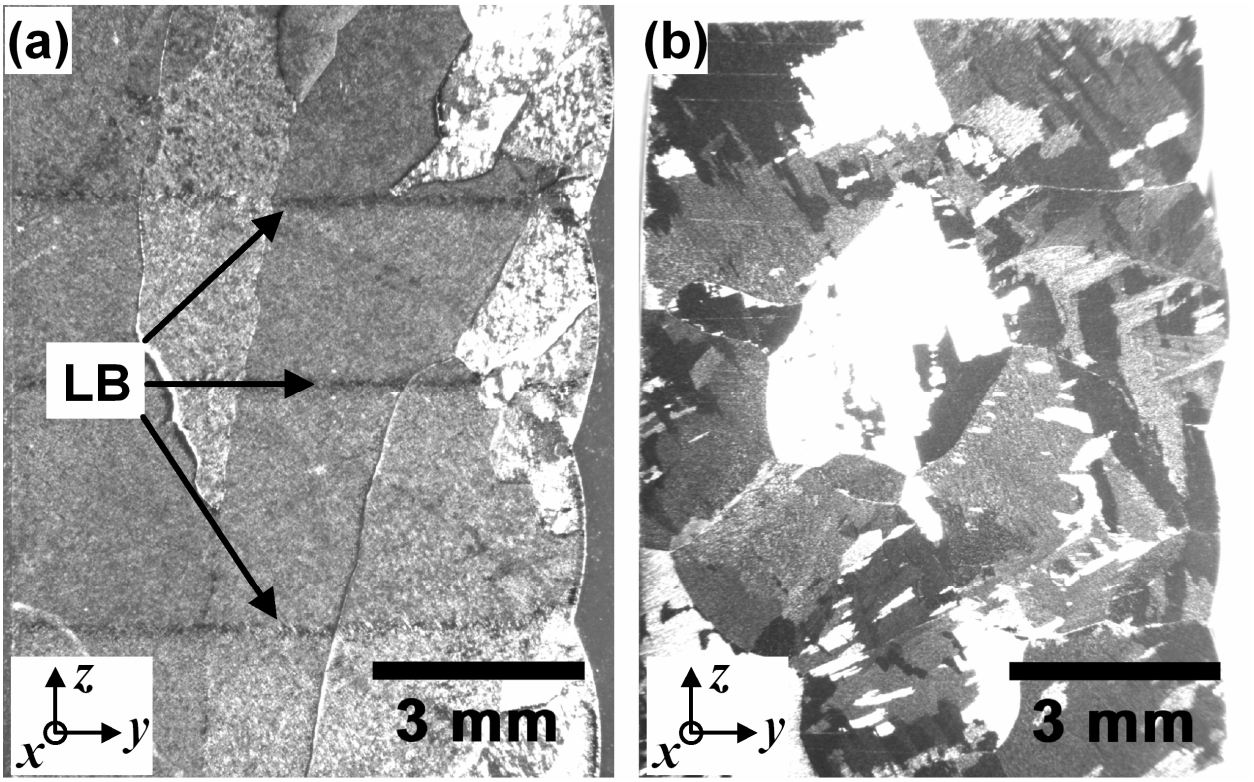

Figure 5.3: Optical macrographs of the (a) as-deposited and (b) beta heat treated laser deposited Ti-6Al-4V material. The y-z plane is shown, where z is the direction of added layers and x is the direction of laser travel. (a) Shows the inhomogeneous macrostructure consisting of columnar prior beta grains and a periodic horizontal banding termed layer bands ("LB"). (b) Shows the homogenized macrostructure consisting of equiaxed prior beta grains containing primary-alpha colonies.

The layer bands present in the as deposited material were unaffected by heat treatment within the $\alpha+\beta$ phase field[24], while the beta treatment produced a colony-primary alpha morphology, similar to that observed in the as-deposited layer band region, throughout the entire sample. Heating above the beta transus at slow heating rates tends to homogenize the microstructure and upon cooling through the beta transus, new primary-alpha (α_P) laths will have a morphology dictated primarily by cooling rate as shown in the Baseline Microstructure Experiments, (Chapter 3). α_P laths first nucleate at the beta grain boundaries and grow inward, with faster cooling rates producing multiple α_P lath variants (basketweave) and slower cooling rates producing colonies of similarly aligned α_P laths.

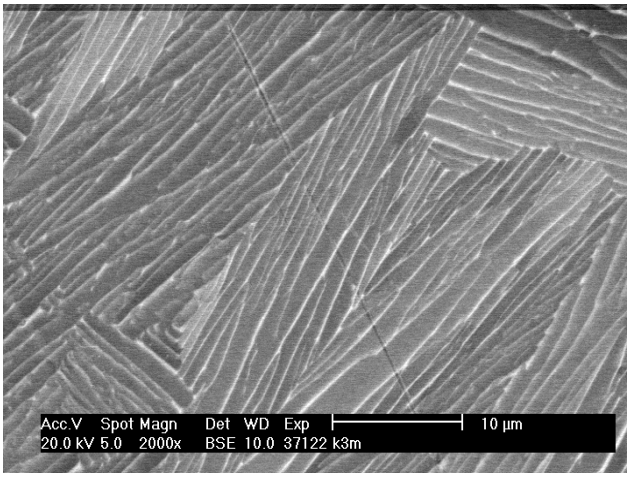

(a) $\alpha+\beta$ Heat Treated, Layer Band Region

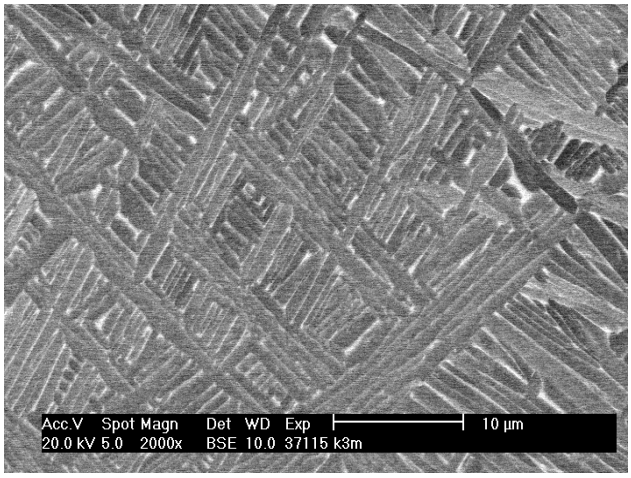

(b) $\alpha+\beta$ Heat Treated, Nominal Region

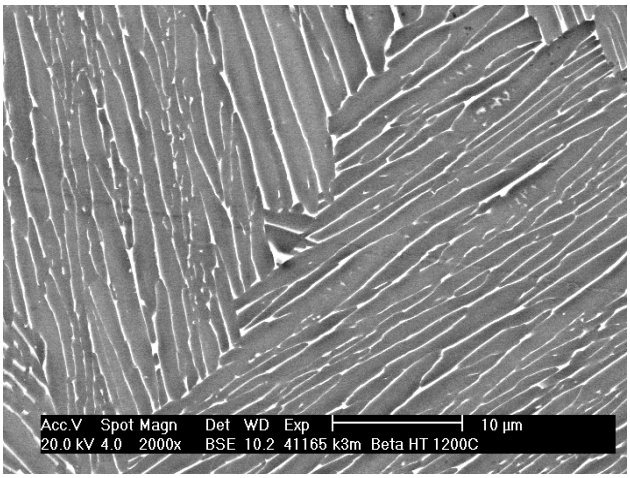

(c) β Heat Treated, Layer Band Region

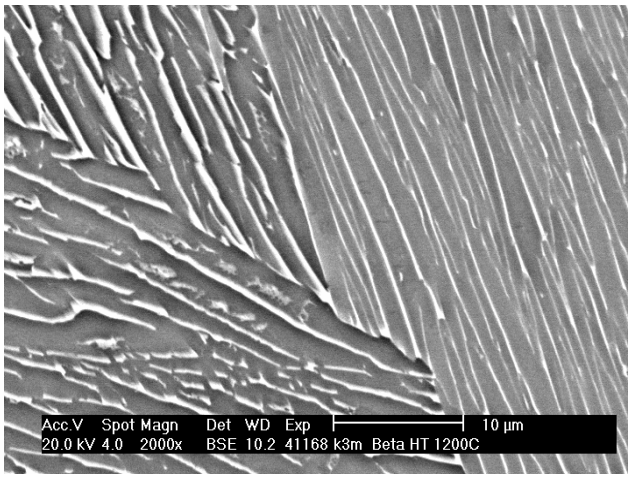

(d) β Heat Treated, Nominal Region

Figure 5.4: Comparison of as-deposited (a-b) and beta heat treated (c-d) microstructures in laser deposited Ti-6Al-4V. The layer band colony-alpha morphology is shown in (a) and the nominal basketweave alpha morphology is shown in (b). In the beta heat treated microstructures, (a) and (c) are from regions where the layer band and nominal microstructure once existed.

The colony alpha observed after the beta heat treatment is α_P while in the as-deposited layer band the colony-α appears to be secondary-alpha (α_S). Had the layer band formed as a result of heating above the beta transus, the material above it would be similar because the maximum temperature would be also be above the beta transus; however, just above a layer band a fine basketweave morphology is observed. A few degrees temperature difference above the beta transus would not introduce any observable changes in the cooled microstructure as the starting composition will be the same. As observed in the baseline microstructure experiments (Chapter 3) the cooling rates would have to be significantly (order of magnitude) different to produce observable changes in the α_P morphology. The cooling rate determines the time available for

diffusion to occur and faster cooling rates will increase the driving force for nucleation, leading to a basketweave-α_P morphology at high cooling rates. It was postulated that heating high into the $\alpha+\beta$ phase field will produce the greatest microstructural change. From these results it can be concluded that the layer band forms during heating to a temperature high in the $\alpha+\beta$ phase field, sufficient to dissolve a large amount of alpha so that when cooled a new α_S morphology forms. Heating at lower temperatures does not cause sufficient α dissolution to occur to produce morphological changes, e.g. α_S formation. Heating above the beta transus will result in similar α_P microstructures provided the cooling rates are not significantly different.

Summary

After a 2-hour solution treatment in the $\alpha+\beta$ phase field (1186K) and a 4-hour aging treatment the layer band remains and the gradient in the α width is eliminated. Increasing cooling rate from the solution temperature resulted in finer α grains. This indicates that the layer band forms as a result of heating above 1186K. Heating 200K above the beta transus to a temperature of 1473K, homogenized the entire microstructure, eliminating the layer band and basketweave structure and replacing it with a colony-α_P morphology. From these results it can be concluded that the layer band forms during heating high into the $\alpha+\beta$ phase field (at least above 1186K) to a temperature sufficient dissolve a large amount of alpha so that when cooled a new morphology forms (α_S).

At this point in this thesis the following has been postulated about the microstructure evolution of the as-deposited material:

- The characteristic layer forms in a layer *n* after the deposition of *n*+3 layers on top. The 3 layers above *n* are in a transient microstructural state.

- During the *n+2* thermal cycle basketweave-α_P morphology is produced in the characteristic layer during heating above the beta transus.

- During the *n+3* cycle, the characteristic layer is heated into the $\alpha+\beta$ phase field resulting in the greatest microstructural change. The layer band forms at the top of the characteristic layer due to heating high in the two phase field, at least greater than 1186K.

The graded basketweave results from heating to lesser temperatures in the α+β phase field.

- The colony-α in the layer band is secondary alpha, while the graded basketweave is primary α that has a grain size primarily determined by peak temperature, though cooling rate could also produce a variation in α grain size.

- In order for the above assumptions to hold true, cooling rate must not vary significantly during the *n+2* layer deposition and the maximum temperature must increase with z-position in the deposit. The thermal model section will quantify the temperature distribution in the deposit.

Chapter 6: Thermal Model

This chapter will describe the thermal model developed to obtain the thermal history of laser metal deposition processes. The original thermal model had undergone significant revisions since being first introduced in Ref.[24,26]. The original thermal model will be briefly described, followed by a verification of the model with experimental data for the LENS process. Revisions and reasoning behind these revisions will then be given. The model will then be calibrated for LENS™ and LaserForming™ metal deposition processes. Finally, results will be presented for the revised thermal model using the calibrated LaserForming™ processing conditions. These results will be discussed in relation to the as-deposited microstructure.

Original Thermal Model Description[§]

The thermal model calculates the two-dimensional transient temperature distribution as a result of multiple layer depositions of the titanium alloy Ti-6Al-4V during a single line build. A numerical solution to the two-dimensional transient heat conduction equation is obtained using implicit (backwards-difference) finite-difference techniques.[93] The results presented herein are computed using the implicit finite difference scheme. Explicit (forwards-difference) and Crank-Nicolson schemes were also constructed; however, the implicit scheme maintained a comfortable median between required computational power and accuracy. Temperature dependent thermophysical properties were incorporated within the model. The thermal model was programmed using the software package, MATHEMATICA, by Wolfram.[94] Further details of the modeling scheme may be obtained from Ref. [24,26].

In the implicit method, a system of equations that describes the temperature, $T(m, p)$, of each node, m, at a time step, p, within the build is solved simultaneously to give the temperature profile at the next time step, $T(m, p+1)$. In this method, the temperature of each node is dependent upon the temperatures of surrounding nodes at the new time step (See Appendix: Thermal Model Finite Difference Equations). Temperature dependent properties are incorporated into the temperature calculation at the next time step ($p+1$) by extrapolating the thermal properties using the known temperatures from previous time steps (e.g., p, $p-1$) as shown in Eq. [6.1] for thermal conductivity, $k(m, p+1)$.[93]

[§] The original thermal model description is taken from Reference [26]

$$k(m,p+1) \cong k(T(m,p)) + (T(m,p) - T(m,p-1)) \cdot \left(\frac{\partial k}{\partial T} \right) \Bigg|_{T=T(m,p)} \qquad [6.1]$$

Recommended values of Ti-6Al-4V temperature dependent thermal properties (density, thermal conductivity, and specific heat) and phase transition temperatures have recently been published[95] and are used in the model (See Appendix: Thermal Properties of Ti-6Al-4V). The beta transus ($\alpha+\beta \leftrightarrow \beta$), and melting ($\beta \leftrightarrow$ L) temperatures are reported to be 1268K (995°C) and 1923 K (1650°C), respectively. Including the discontinuities in the thermal property functions effects changes in the temperature profile as the beta transus and liquidus temperatures are traversed due to the increased energy associated with overcoming these phase transitions. While this is not a preferred method of solving phase change problems, it offers a simple way of considering change of phase that gives accurate results if the time steps are kept small.

Initial versions of the thermal model[24] utilized the symmetry in the "single line build" geometry to reduce computational time; however, the current model has been modified to accept multiple passes (tracks) of the laser in a layer, making the build asymmetric. In this paper the entire cross section of the single line build is modeled as illustrated in Figure 6.1. The simplifying assumptions made in the model include: heat flow in the *y*-*z* plane is transient, heat flow in the *x* direction is steady-state and ignored, a constant temperature is maintained at the base (y, $z = 0$) and sides ($y = \pm$ 10mm, z) of the substrate, and convective cooling occurs on the outer surface of the build. Figure 6.1 illustrates these boundary conditions and introduces a labeling convention, "L*n*". For example, "SUB" refers to the substrate; "L1" refers to the first deposited layer; etc. The laser travels in the +*x* direction, and adds a new layer by stepping in the +*z* direction.

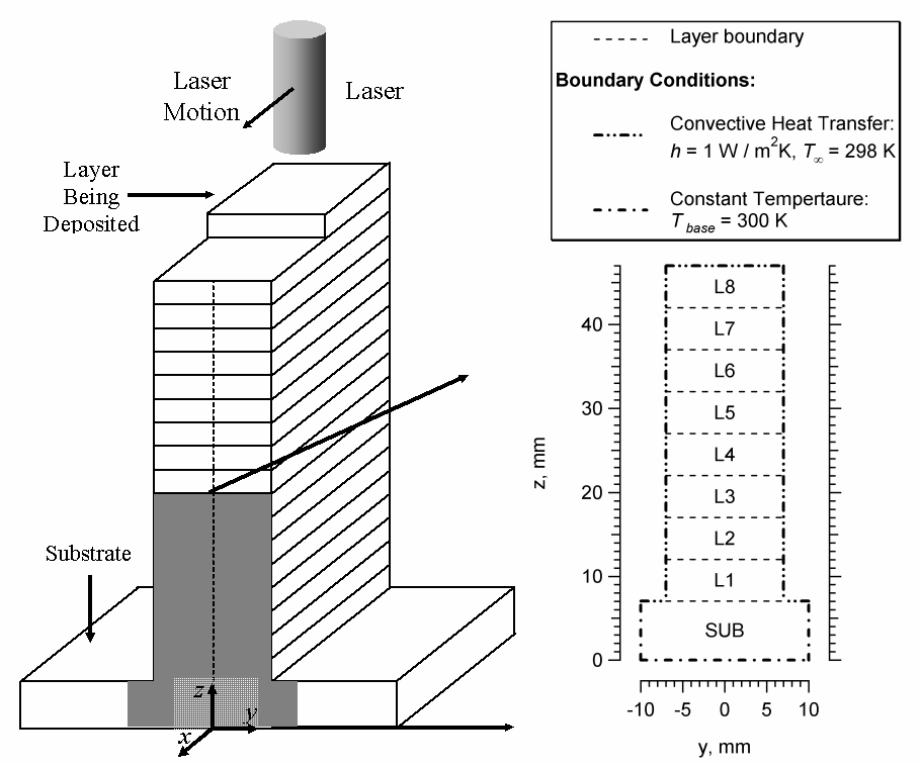

Figure 6.1: Schematic of the single line build modeled geometry (left), mesh and applied boundary conditions (right). The shaded region corresponds to the modeled 2-dimensional geometry for an 8-layer model. The nodal mesh has nodes spaced equally at 0.5 mm. The substrate (SUB) is 7 mm thick (*z*) and each layer (L1, through L8) are 5 mm in height (*z*).

Modeling the deposition process was simplified by first assuming that as the laser moves away from the origin in the x direction, heat is no longer input into the two dimensional plane being modeled. This 2-dimensional plane is assumed to have a finite thickness relative to the direction of laser motion, Δx, which allows for the correct amount of heat to be input into the build for a given laser scan speed. Heat is input (deposited) into the build at a fixed x position by assuming that when the laser is overhead, heating occurs, and when the laser moves away, cooling occurs as illustrated in Figure 6.2. Initially at $t = 0$, only the substrate (SUB) is present, having a uniform temperature T_{base}. At time $t = t_1$, a new layer is "birthed" or deposited having a constant temperature, T_{laser}, that is a factor f of the melting temperature, Eq. [6.2]

$$T_{laser} = (1 + f)T_{melt} \qquad [6.2]$$

The new layer is held at T_{laser} for a "dwell time" (e.g., $0 < t \leq t_{dwell}$ for layer 1 (L1)), that is calculated from the laser scan speed, v_{laser}, and the finite thickness of the y-z plane, Δx, according to Eq. [6.3]. The laser scan speed can be specified or calculated from Eq. [6.4].

$$t_{dwell} = \frac{\Delta x}{v_{laser}} \quad [6.3]$$

$$v_{laser} = \frac{l}{t_{pass}} \quad [6.4]$$

The dwell time simulates the period of time that the laser is passing over the finite thickness, Δx. For $t > t_{dwell}$, there is no heat input into the build and the part is allowed to cool primarily by heat flow through the substrate (dictated by the constant temperature of the substrate at $z = 0$) and secondarily through convective cooling on the outside of the build. The part is allowed to cool for an interpass time (frequency of layer addition), t_{pass}, which is calculated from v_{laser} and the build length, l, according to Eq. [6.4]. When $t = t_{pass} + \Delta t$, a second layer is deposited on top of the first, and the process is repeated. Solutions to the transient heat conduction equation are obtained at every time increment, Δt and stored to a file. A flow chart for the thermal model may be seen in the Appendix: Thermal Model Flow Chart.

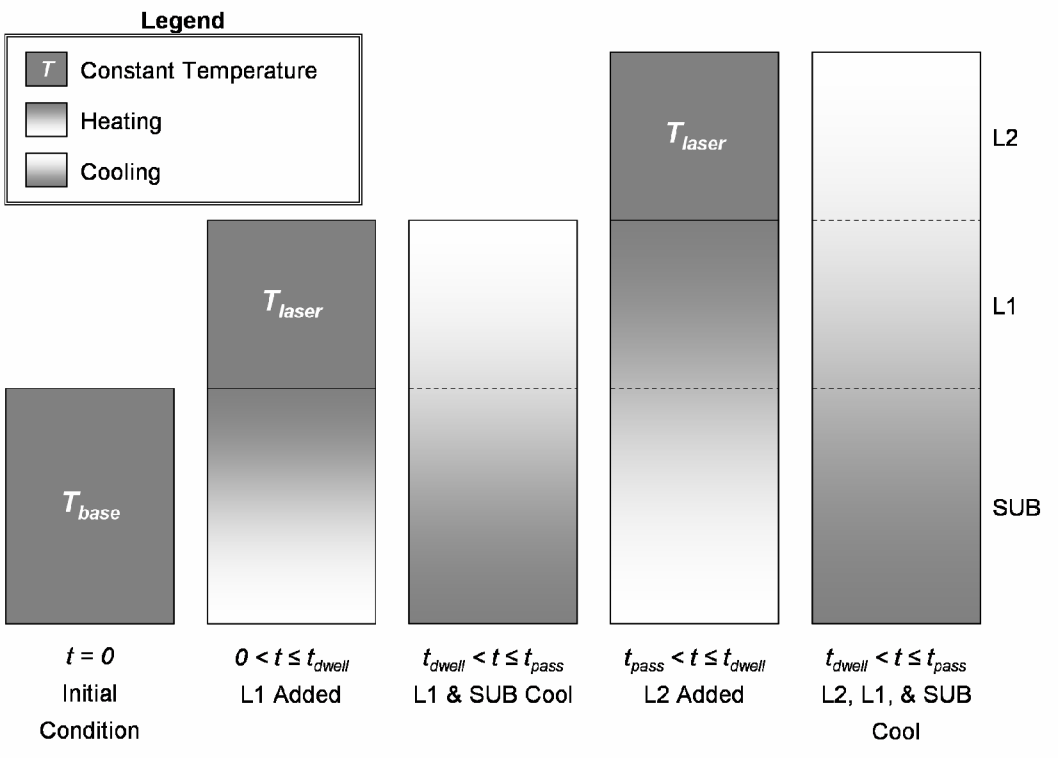

Figure 6.2: Schematic illustrating the original method used to simulate additive layer deposition for a two-layer single line build. The original method assumes that a new layer initially has a constant temperature when added to the deposit.

Revisions to Original Thermal Model

Verification of the Thermal Model with LENS Experimental Data

An attempt has been made to verify the results of the thermal model with experimental data provided by Michelle Griffith at Sandia National Laboratory for 316-stainless steel single line builds fabricated using the LENS™ process.[96] The data was obtained via a thermocouple near the intersection of the substrate and first layer. The processing conditions used in the LENS 316SS build process and the thermal model are listed in Table VII. The laser speed, interpass time, and layer dimensions are the same throughout; however, the maximum temperature of the experimental data is not known due to the resolution of the thermocouple acquisition (the acquisition rate was approximately 10Hz). A maximum temperature of 1875K was chosen as the constant temperature of a new layer in the modeled deposit, the value being approximately 150° greater than the melting point for 316SS[2], and being an average temperature of the melt pool as reported by Hofmeister.[17,95] A comparison of the thermal model and experimental data, shown in Figure 6.3, indicated that the trend in the temperature versus time curve is correct; however,

the modeled cooling rates are much faster than that observed experimentally. In addition, the well known analytical solution for a moving heat source problem developed by Rosenthal[23] is shown in Figure 6.3. The results of Rosenthal solution indicate that some of the assumptions made in the thermal model are oversimplified. This could be a substrate boundary condition effect or an insufficient amount of heat being input during the deposition process. Both of these possible inaccuracies in the model will be discussed below and corrected. It should be noted that the Rosenthal solution could not be readily applied to model repetitive thermal cycling because it requires as an initial condition that the temperature of the body be constant, which in general would not be the case in LMD.

Table VII: Processing parameters used in experimental and modeled LENS comparisons.

	Beam Power P_0, W	**Beam Radius r_b, mm**	**Laser Scan Speed v_{laser}, mm/s**	**t_{pass}, s**	**Maximum Temperature, K**	**Substrate Dimensions((y × z), mm**	**Layer Dimensions (y × z), mm**
Measured	450	0.250	7.493	5.084	~1800		
Thermal Model (Small Substrate)	-	-	7.493	5.084	1875 (t_{dwell} = 0.133 s)	1.1 x 0.7	0.4 x 0.25
Thermal Model (Large Substrate)	-	-	7.493	5.084	1875 (t_{dwell} = 0.133 s)	12 x 6	0.4 x 0.25

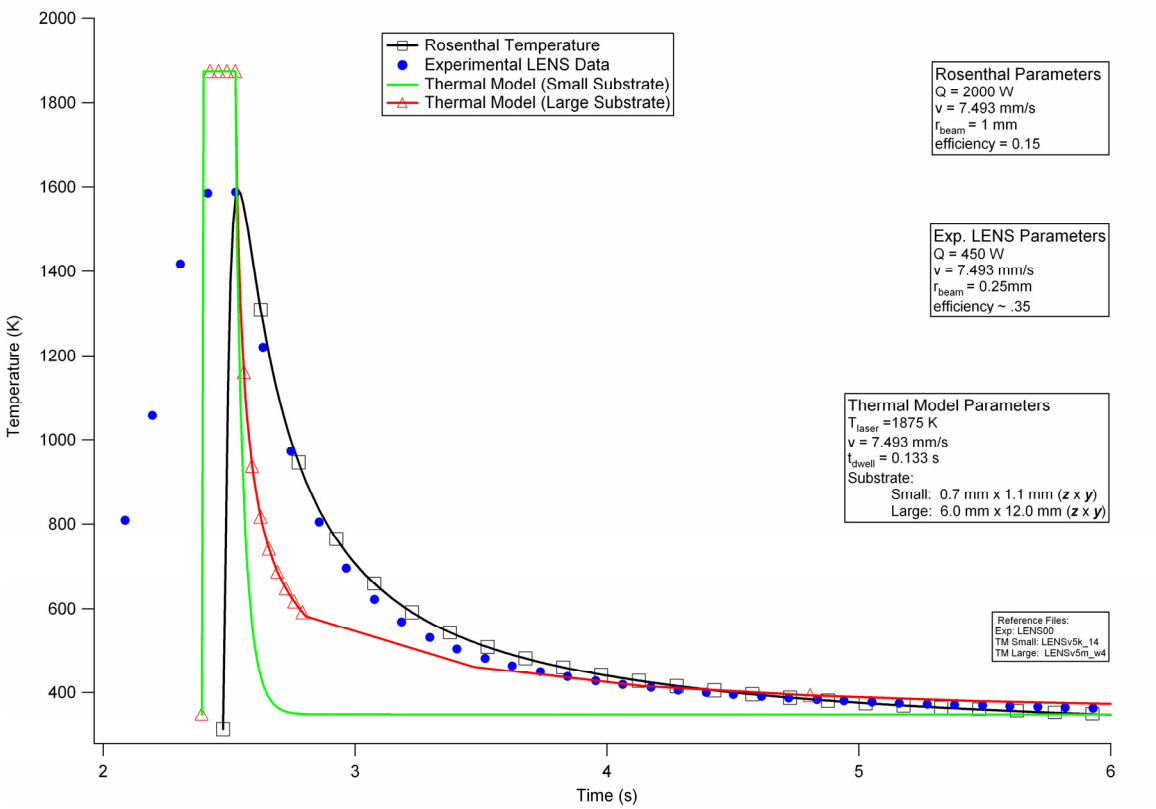

Figure 6.3: Comparison of experimental, Rosenthal solution, and Modeled (small and large substrates) results for a LENS 316 stainless steel single line build.

Mesh Refinement

Recall that the computational grid used in the original thermal model is set to be a constant value. Because the LENS process is about two orders of magnitude smaller in scale as compared to AeroMet's LAM process, this dictates that a much finer grid spacing be used in the LENS models (0.05mm for LENS vs. 1 mm for LAM) in order to obtain a sufficient number of computation points within a layer. The substrate thickness is approximately the same in both build processes, but because of the fine grid spacing used in the LENS models, it becomes inefficient to model the entire substrate with a constant grid size.

The thermal model code was modified to vary the substrate grid spacing in both the y and z directions, with finer grid spacing being found nearest the deposited layer. Underneath a deposited layer, the grid spacing was left constant in order to simplify the meshing scheme. With the additional flexibility of variable grid spacing, the finite difference equations were generalized such that each surrounding node could be a different distance from the central node. The new finite difference equations are listed in the Appendix: Thermal Model Finite Difference

Equations. A refined mesh is shown in Figure 6.4 for a two layer single line build (symmetrical about y = 0). The results of using a larger substrate when modeling the LENS process are also shown in Figure 6.3. Clearly, increasing the substrate size leads to slower cooling rates in the deposit. The improvement in the thermal model that accompanies the change in the substrate size is mainly due to increasing the distance between the substrate boundary conditions and the heat source. In the previous version of the thermal model, the close proximity of the constant-temperature boundary condition forced the rapid cooling of the part. Increasing this distance more closely resembles the semi-infinite slab condition that was intended for the substrate boundary. The Rosenthal solution also assumes a semi-infinite boundary condition.

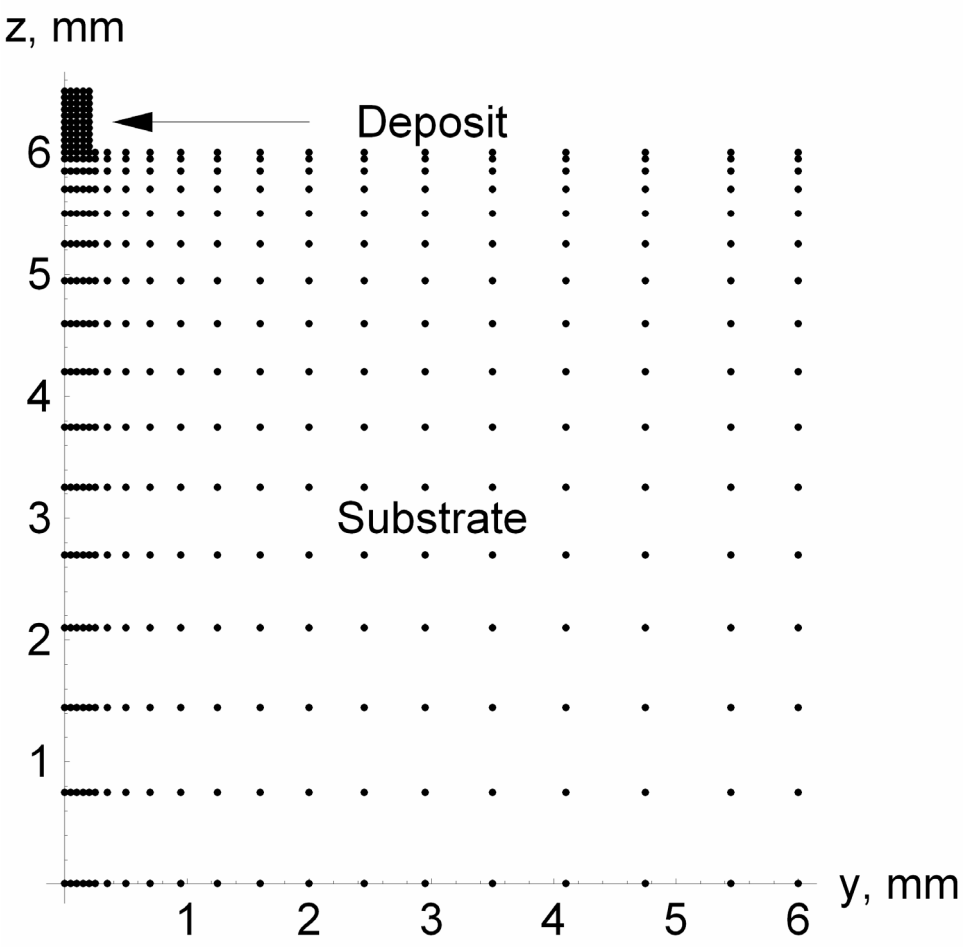

Figure 6.4: Refined mesh of LENS deposits used in revised thermal model. Each dot represents a computation point. The grid spacing varies in the substrate in both y and z while remaining constant in the deposited layers, of which 2 are shown here.

Volumetric Heat Sources

Reexamination of Figure 6.3 indicates that the heating rate of the experimental LENS data is much slower than that observed in the thermal model data. This is due to the way heat is applied to the deposit in the thermal model. Recall that previous versions of the thermal model assumed that when a new layer is deposited, the layer is prescribed a temperature at or above the melting point, and held at this temperature for a period of time equivalent to the time required for the laser/heat source to pass the particular x-position in the build being modeled. Clearly, this method of modeling heat-input was an underestimate of the actual build conditions.

To remedy this inaccuracy in the model, a distributed heat source was used. In processes where a high intensity heat source is used, the distribution of heat is typically considered to be Gaussian. The distribution may occur over the surface of the conducting medium or through a volume of material. A surface distribution of heat, such as that used by Mazumder[97] and Ashby[98] have been used for laser processing (welding and surface hardening) of materials. Equation [6.5] defines this distribution of power from a laser beam of radius, r_b, defined where the power falls to $1/e^2$ of the total power, P_{max}. Here the x and y directions lie in the plane perpendicular to the beam direction (z), and the resultant power density has units of power per unit area.

$$P(x,y) = \frac{P_{\max}}{r_b^2 \pi} \exp\left(- \frac{2\left(x^2 + y^2\right)}{r_b^2} \right) \qquad [6.5]$$

When there is appreciable melting in the heated area, a more accurate representation of the heat distribution would occur over a volume as opposed to a surface area. This is a result of convection and or keyholing in the melt pool. Goldak,[99] has defined a three-dimensional double ellipsoidal distribution of heat in the melt pool that more accurately describes the thermal cycle than when a surface distribution of heat was used. The energy induced by laser heating can be calculated for any y, z, and time**, according to Equation [6.6]. The parameters a, b, and c_i describe the semi-axes of the ellipsoid, specifically where the beam intensity falls to approximately 0.05 of the intensity at the center of the beam, which defines the variable σ = 2.99.

$$Q(y,z,t) = Q_0 \exp\left(- \sigma \left(\frac{y^2}{a^2} + \frac{z^2}{b^2} + \frac{\left(c - v_{laser} t\right)^2}{c^2} \right) \right) \qquad [6.6]$$

Figure 6.5 schematically illustrates the geometry of a single ($c_1 = c_2$) or double ($c_1 \neq c_2$) ellipsoidal heat source.

** The x axis can be transformed into a time axis by $x = c - v_{laser}\, t$

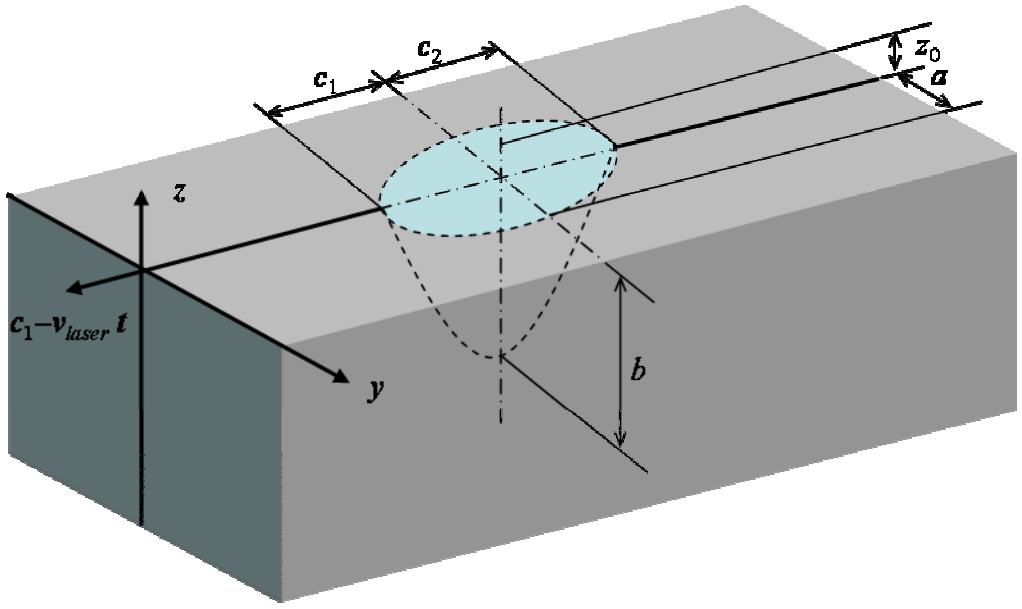

Figure 6.5: Geometry of the single ($c_1 = c_2$) or double ($c_1 \neq c_2$) ellipsoidal heat sources. Laser travel is in the $x = c_1 - v_{laser} * t$ direction.

We are interested in finding the total heat input into the deposit, Q_{in}, thus integrating Equation [6.6] over the domain: ($y \in(-\infty,\infty)$, $z \in(0, \infty)$, $t \in(-\infty,\infty)$), yields Q_{in} as a function of Q_0 as in Equation [6.7].

$$Q_{in} = \int_0^{\infty}\int_{-\infty}^{\infty}\int_{-\infty}^{\infty} Q_0 \exp\left(-\sigma\left(\frac{y^2}{a^2}+\frac{z^2}{b^2}+\frac{\left(c-v_{laser}t\right)^2}{c^2}\right)\right)dtdydz$$
$$Q_0 = \frac{2\sigma\sqrt{\sigma}Q_{in}}{abc\pi^{3/2}} \qquad [6.7]$$

The coefficient Q_{in} represents the total energy delivered to the deposit and is defined by the beam power (P), coupling efficiency of the beam and deposit material (α), and a heating and melting correction (Q_{melt}), as described by Equation [6.8].

$$Q_{in} = P \cdot \alpha - Q_{melt} \qquad [6.8]$$

The melt correction contains two terms, energy used to heat a volume of deposited powder to the melting point (specific heat, $\rho C_p(T_{melt} - T_0)$) and above (latent heat, L), as shown in Equation [6.9]. The volume of deposited material is defined by the beam radius (r_b), the melt depth or the depth of a new layer (z_0), and the laser scan speed (v_{laser}).

$$Q_{melt} = 2r_b z_0 v_{laser} \rho\left(L + C_p\left(T_{melt} - T_0\right)\right) \qquad [6.9]$$

The latent heat correction was first introduced by Ashby[98] and revised by Hu[100] as a means to incorporate energy absorbed during melting without having to solve the moving interface problem associated with the melting process. The specific heat correction is also included because we assume when the powder is deposited, it has already been heated to the melting point during its travel through the beam. This would not be applicable to preplaced powder processes.

The power distribution described by Equations [6.6] through [6.9] can be further modified to match experimental melt pool shapes by defining the fraction of heat distributed to the front (f_1) and rear (f_2) quadrants of the melt pool, such that $f_1+f_2 = 2$, as shown in Equation [6.10].

$$Q(y,z,t) = \begin{cases} f_1 \dfrac{2\sigma\sqrt{\sigma}Q_{in}}{abc_1\pi^{3/2}} \exp\left(-\sigma\left(\dfrac{y^2}{a^2} + \dfrac{z^2}{b^2} + \dfrac{\left(c_1 - v_{laser}t\right)^2}{c_1^{\,2}}\right)\right) & t \le c_1 v_{laser} \\ f_2 \dfrac{2\sigma\sqrt{\sigma}Q_{in}}{abc_2\pi^{3/2}} \exp\left(-\sigma\left(\dfrac{y^2}{a^2} + \dfrac{z^2}{b^2} + \dfrac{\left(c_1 - v_{laser}t\right)^2}{c_2^{\,2}}\right)\right) & t > c_1 v_{laser} \end{cases} \qquad [6.10]$$

Thus, if $f_1 \neq f_2$, there will be two semi-axes, c_1 and c_2, defining the front and rear quadrant. Goldak does not specifically define how f_i and c_i are related, but in order for Equation [6.10] to be continuous at $t = c_1 / v_{laser}$, Equation [6.11] must be true:

$$f_i = \frac{c_i}{c_1 + c_2} \qquad [6.11]$$

Figure 6.6 compares Equation [6.11] for the ellipsoidal ($c_1 = c_2$) and double ellipsoidal ($c_1 \neq c_2$) cases. An additional variable, the z-offset (z_0), can also be used to determine the penetration depth, or focal point of the heat source, into the deposit. It is incorporated into Equation [6.11] by replacing z with $z - z_0$.

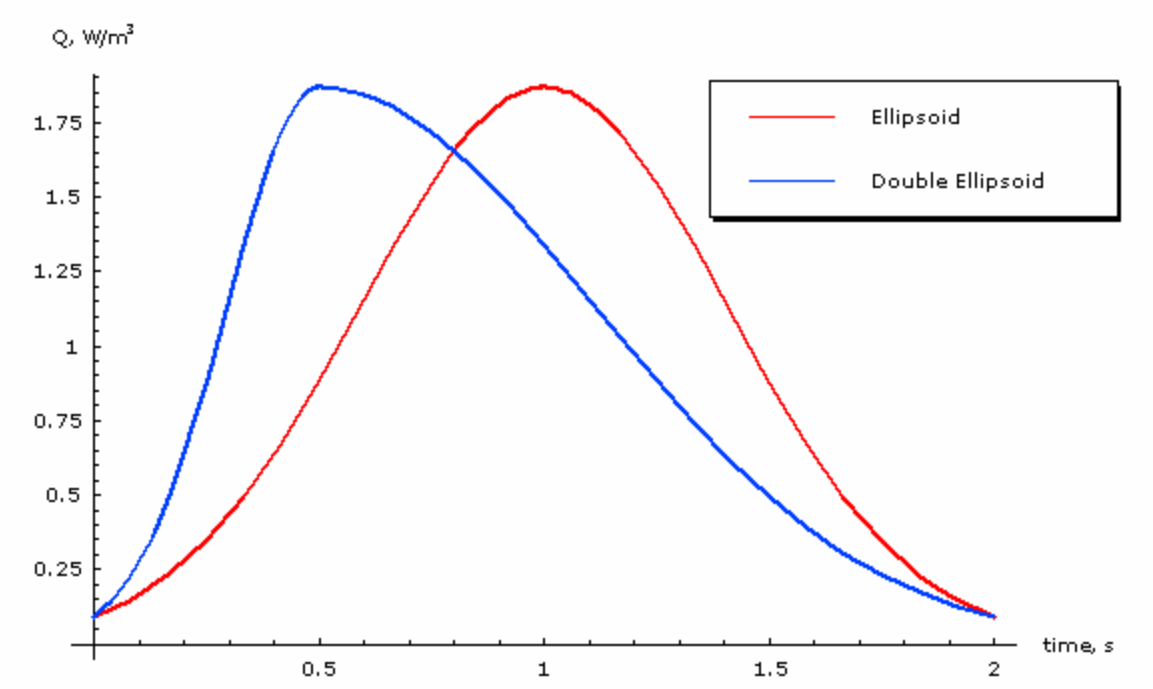

Figure 6.6: Comparison of the ellipsoidal ($c_1 = c_2 = 1$) and double ellipsoidal ($c_1 = 0.5$, $c_2 = 1.5$) volumetric heat sources at $y = z = 0$. All remaining coefficients are arbitrarily set equal to 1.

Integrating the volumetric heat source into the finite difference model is straightforward. At the starting time for a new layer deposition, the additional nodes for the new layer are included into the mesh, having a temperature equivalent to the initial temperature of the substrate (T_{sub}). During the first time step of a new layer, all nodes in the deposit experience some additional heat input according to Equation [6.10], where the variables y, z, and t are determined by the node position and time step. The finite difference equations are solved as they normally would, with the exception that there is an additional heat input term during the dwell time of the laser.

Volumetric Heat Source Results for LENS

When a volumetric heat source is used in the thermal model, a more accurate thermal cycle is observed, as shown in Figure 6.7 for a LENS deposit of 316 stainless steel. The processing parameters used were $a = b = c_1 = c_2 = 0.5$mm, with a and c_i being the radii of the beam as reported by Griffith. The z-offset (z_0) is set equal to 1 deposited layer depth, that is, the beam is focused on the previously deposited layer. The distributed power, Q_{in}, is approximately 151 W, which is the delivered power assuming a absorption efficiency of α=35%[101] for a P=450 W beam heating 316SS and a "melt" correction of 6.35 W. Temperature dependent thermal properties for 316SS were used.[95]

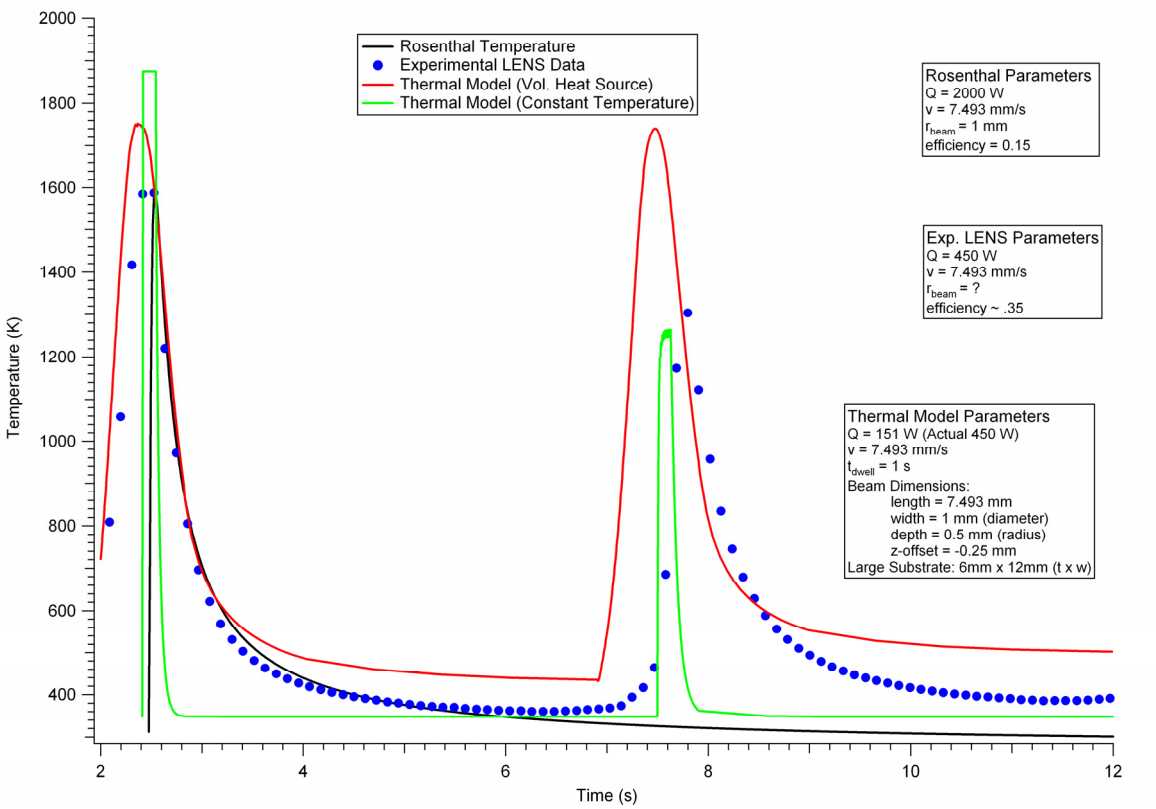

Figure 6.7: Comparison of Rosenthal, experimental, and modeled (with and without a volumetric heat source for a large substrate) LENS thermal cycles for 316 stainless steel. The modeled and experimental data are taken at the center (y, x) of a layer and at the substrate/first layer interface (z).

Results

Calibration of Input Parameters for LENS

An attempt was made to calibrate the variables describing the beam with measured characteristics of the first thermal cycle from the data provided by Ensz and Griffith[96]. The target thermal cycle values, namely maximum temperature, cooling rate from 1500 to 1000K and melt pool length were measured to be approximately 2000K, -2806 K/s, and 0.75 mm for the experimental LENS data. The processing conditions specific to the experimental data included a laser power of 450 W, laser speed of 7.493 mm/s, and approximate layer width and height of 0.4 and 0.25mm, respectively. The following additional conditions imposed: substrate width and height of 12 and 6mm, substrate and ambient temperature of 310 K, convective heat transfer coefficients on the build[101] and substrate of 10^3 and 10^{12} W/m^{2}K, respectively. For the aforementioned processing parameters, the maximum temperature calculated at the bottom of the substrate (z = 0 mm) does not change when substrate convective heat transfer coefficients greater

than 10^{12} W/m^{2}K are applied, thus the substrate convective heat transfer coefficient (10^{12} W/m^{2}K) is equivalent to a semi-infinite boundary condition. The beam characteristics that were varied included the heat source semi-axes, z-offset, and process efficiency (α), with these variables listed in Figure 6.8.

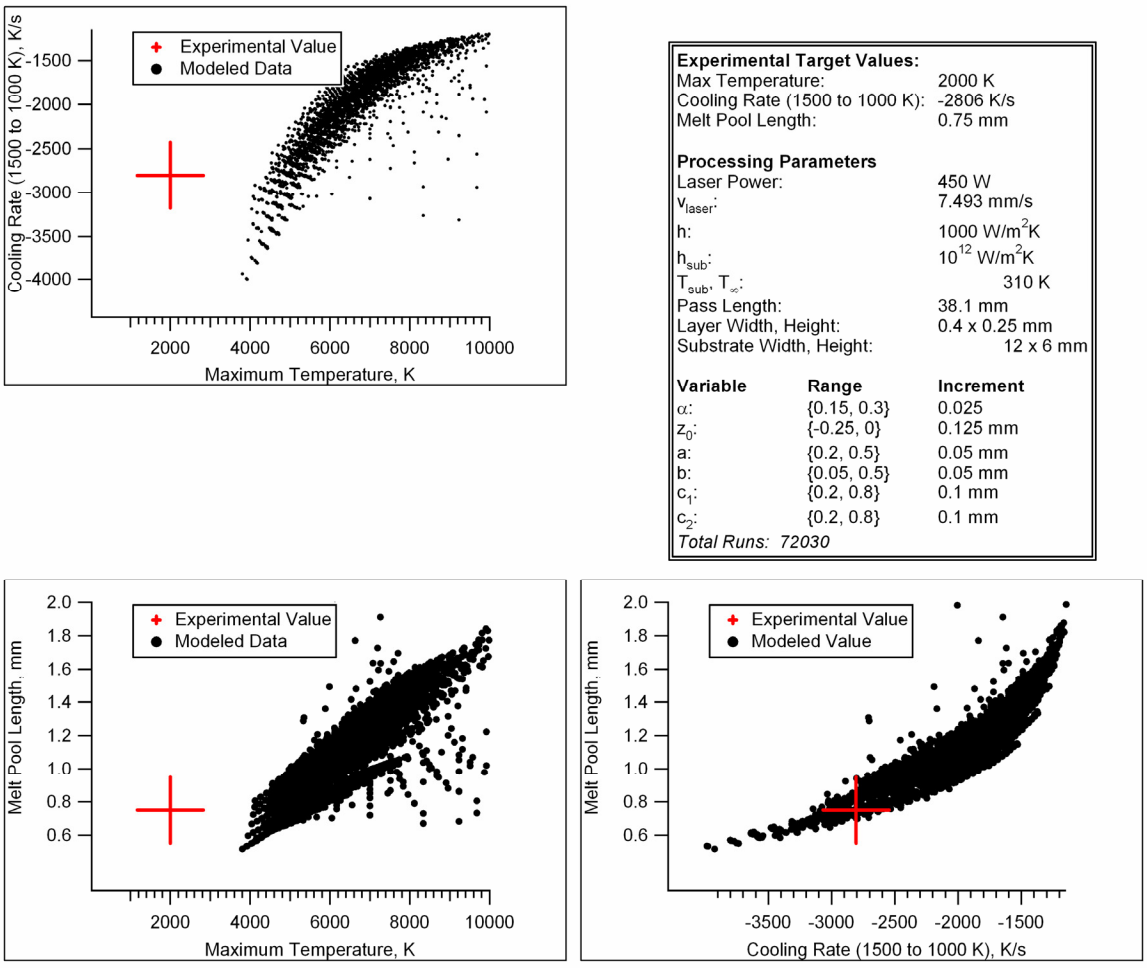

Figure 6.8: LENS calibration variables and results. The points indicated by a cross are the target experimental values for which the modeled values are compared.

Figure 6.8 shows the results of the LENS calibration experiment, showing that while the melt pool length and cooling rate between 1500 and 1000K could be matched with the thermal model, the maximum temperature did not compare well with the target experimental values. This is most likely due to errors in using thermocouples to measure such high temperatures in such a rapid time frame.

Calibration of LaserFormed (LF) Ti-6Al-4V

In order to calibrate the thermal model for AeroMet's Laser Formed (LF) Ti-6Al-4V deposits, we must rely on the as-deposited microstructure, specifically the positions of the fusion (FZ) and heat affected zones (HAZ) in the substrate, listed in Table VIII, as a reference to obtain potential beam characteristics.

Table VIII: Thermal model calibration ranges for AeroMet's LaserFormed Ti-6Al-4V

Fusion Zone Depth	Fusion Zone Width	Heat Affected Zone Depth	Heat Affected Zone Width
1.05 ± 0.22 mm	1 ± 1 mm	4.48 ± 1.43 mm	2 ± 1 mm

Processing conditions for the build under investigation are unfortunately unknown; however, E. Whitney[72] of the Applied Research Laboratory at Penn State has provided estimated build conditions for LMD of Ti-6Al-4V, specifically, laser powers between 11 and 13.5 kW and laser speeds of 2.54 mm/s. The processing parameters used in the calibration experiments are listed in Table IX. The determination of the surface convective heat flux coefficient is shown in the Appendix: Convection Heat Transfer Estimation in LMD Builds. There was no observed difference in the maximum and substrate temperatures at the point ($y = 0$, $z = 0$) for models with substrate convection coefficients (h_{sub}) greater than 10^{10} W/m^2 K, hence the substrate convection coefficient approximates a semi-infinite boundary. It should be noted that the substrate thickness is 9 mm thicker (z) than in the LMD Ti-6Al-4V deposits examined. A larger substrate was chosen in the model because it is likely that during the build process, the substrate (a Ti-6Al-4V plate) sitting on a larger heat sink or is somehow actively cooled. If a smaller substrate were used, problems may arise with too rapid cooling as observed in initial models of the LENS deposits. This was due to the close proximity of the semi infinite or constant temperature boundary condition to the heat source.

Table IX: Processing parameter set for LaserForming thermal model calibration.

Laser Power, P	Laser Velocity, v_{laser}	Part Length, l	T_{base}, T_{sub}	$h_{surface}$	h_{sub}	Layer: width[††] x height	Substrate: width x height
13 kW	2.54 mm/s	250 mm	310 K	200 W/m^2K	10^{10} W/m^2K	15 x 5 mm	38 x 16 mm

Figure 6.9 shows how varying the process efficiency semi-axes of the volumetric heat source and affects the FZ and HAZ dimensions. The ranges and increments of the varied parameters are listed in Figure 6.9, and Table X shows values meeting the criteria for FZ width and HAZ depth, the two most important criteria. The FZ width should be greater than 0, as measured from the edge of a layer to its position in the substrate, to ensure a good mechanical bond with the previous layer. The HAZ should be correctly modeled for reliable input to the microstructure model. In addition, both of these regions are easily measured. The assumption is made that the fusion zone width must be at least the width of a layer, while the HAZ depth is easily determined by the increase in beta grain size in the substrate. As such, these two criteria will be used foremost to determine appropriate processing conditions.

[††] Widths shown (y) are full widths of the layer and substrate; the model uses symmetry in the y-dimension so ½ widths are used in the model.

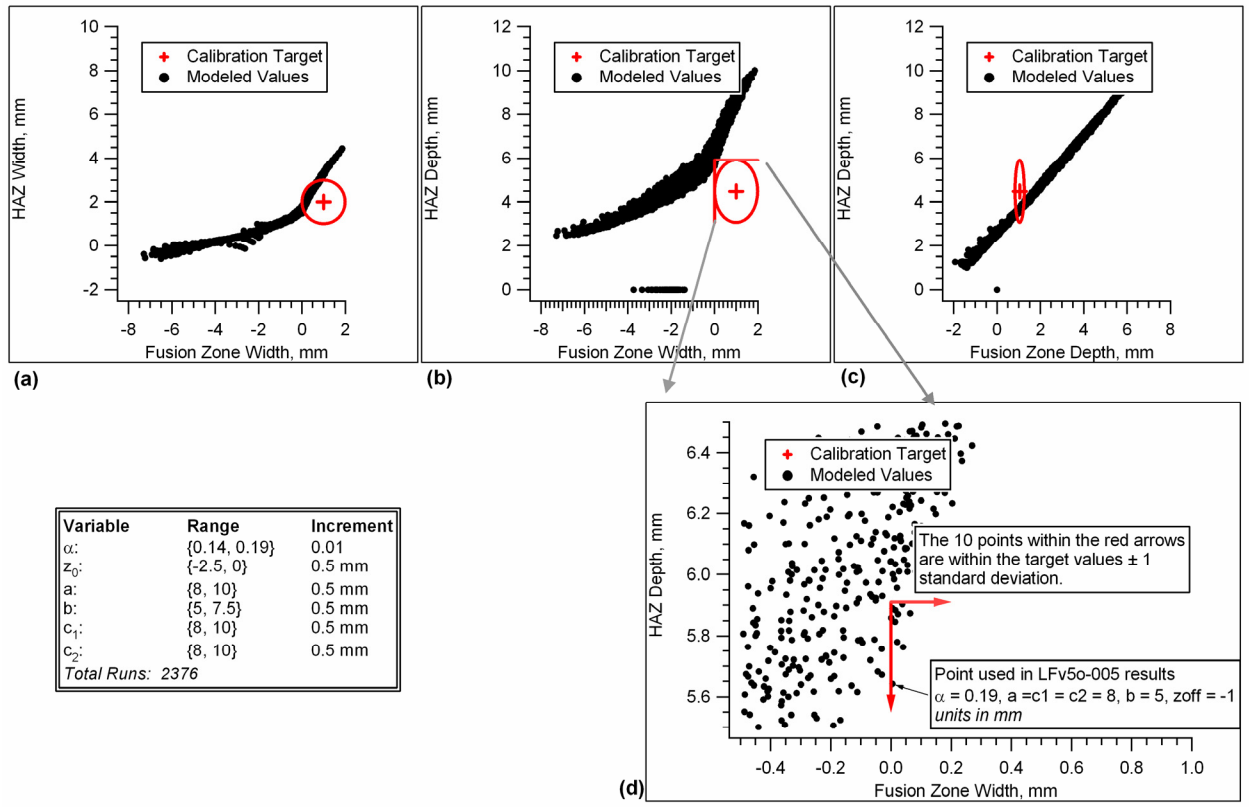

Figure 6.9: Results of LF Ti-6Al-4V thermal model calibration, showing the affect of beam variables on FZ and HAZ dimensions. The target value is bounded by an ellipse of ± 1 standard deviation.

It is clear from Figure 6.9d that only a few data points meet the HAZ depth and FZ width criteria at the upper and lower bounds, respectively. The point with the lowest HAZ depth meeting the HAZ and FZ criteria is indicated in Figure 6.9d and Table X (in red text, hereafter referred to as parameter set LFv5o-005). The point represents a beam of uniform radius ($a = c_1 = c_2 = 8$mm), a beam depth (b) of 5mm (equivalent to the layer thickness) and a z-offset of -1.0mm. The beam efficiency is 0.19, which is comparable to the absorption of energy from a CO_2 laser in Ti-6Al-4V reported to be 0.14 by Wieting and Schriempf.[102] One could make the argument that process efficiency would be increased if powder is being fed into the beam due to the increased scattering of the beam energy. These beam conditions will be used in the planned thermal simulation experiments.

Table X: Selected values from LF thermal model calibration data meeting the criteria in Figure 6.9

α	a, mm	b, mm	c_1, mm	c_2, mm	z_{off}, mm	Tmax, K	CR, K/s	Melt Pool Length, mm	FZ Depth, mm	HAZ Depth, mm	FZ Width, mm	HAZ Width, mm	ΔT from T_{sub} at (y=0, z=0)
0.16	8.0	5.0	8.0	8.0	-2.0	2917	-34.8	9.63	2.98	5.88	0.015	1.57	15.5
0.18	8.5	5.5	8.5	8.5	-2.0	2917	-35.3	9.32	2.96	5.86	0.001	1.56	15.4
0.16	7.5	5.0	7.5	7.5	-1.5	2879	-34.8	9.78	2.94	5.87	0.023	1.58	15.5
0.18	8.0	5.5	8.0	8.0	-1.5	2916	-35.0	9.67	2.99	5.90	0.038	1.61	15.6
0.19	8.5	5.0	8.5	8.5	-1.5	2898	-35.3	9.25	2.82	5.76	0.041	1.58	15.2
0.17	7.0	5.5	7.0	7.0	-1.0	2831	-35.2	9.96	2.95	5.89	0.005	1.57	15.5
0.18	7.5	5.0	7.5	7.5	-1.0	2879	-35.0	9.82	2.92	5.87	0.064	1.64	15.5
0.19	8.0	5.0	8.0	8.0	-1.0	2836	-35.5	9.07	2.69	5.64	0.005	1.49	14.8
0.18	6.5	5.0	6.5	6.5	-0.5	2776	-35.1	10.02	2.85	5.85	0.013	1.58	15.4
0.19	7.0	5.0	7.0	7.0	-0.5	2801	-35.1	9.73	2.81	5.78	0.020	1.56	15.2

Revised Thermal Model Description for LFv5o-005[‡‡]

The thermal model utilizes the two-dimensional implicit finite difference method[93] to find a solution to the heat conduction equation at finite time steps during the course of the deposition process. The thermal model has been improved from prior versions[24,26] to include a flexible computation domain and a volumetric heat source. An example of the computation domain and applied boundary conditions are illustrated in Figure 6.10. Heat flow is assumed to occur in the *y*-*z* directions and not the *x* (direction of laser travel) which means the assumption is made that the temperature distribution is in a quasi-steady state in the *x* dimension, a common assumption known to produce good predictive accuracy.[104] The additive nature of the LMD process is captured by adding a new layer to the computation domain after each pass of the heat source. The laser scan velocity, v_{laser}, and part length, l, are used to determine the frequency of layer addition. The node points (points where temperature is calculated) are distributed evenly within a layer and increased in size in the substrate for computational efficiency. Convective heat transfer due to the carrier gas (argon) used to deliver the metal powder to the deposit is assumed to occur on the outer surface of the substrate and deposit, and is defined by the heat transfer coefficient, h_{sub} and $h_{surface}$, and fluid temperature, T_∞ = 310 K. On the sides and bottom of the

[‡‡] The revised thermal model description is taken from the Experiment>Thermal Model section in Ref.[103]. Parts are somewhat redundant from earlier sections, but are retained here for coherency.

substrate, a fictitious heat transfer coefficient, h_{sub}=10^{10} (W/m^{2}K), is used to approximate a semi-infinite boundary condition. Symmetry of the deposit is utilized and as such, an adiabatic (heat flux, q =0) boundary condition is applied at all z positions corresponding to y = 0.

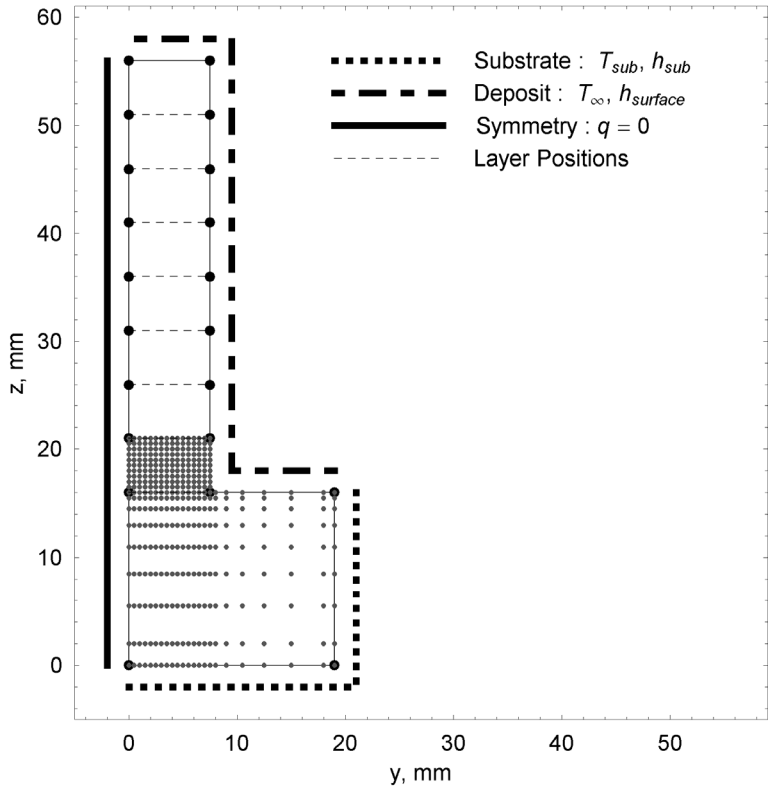

Figure 6.10: Schematic of the deposit geometry and locations of the surface boundary conditions. Node positions (small dots) are shown for the substrate and first deposited layer.

The laser heat source is modeled using a double ellipsoidal distribution of laser power that moves through the deposit with each time step, and can be calculated for any y, z, and time, according to Equation [6.12].[99] A volumetric heat source was chosen over a surface heat flux because of the appreciable amount of melting that occurs during deposition. The parameters a, b, and c_i describe the semi-axes of the ellipsoid, specifically where the beam intensity falls to approximately 0.05 of the intensity at the center of the beam, which defines the variable σ = 2.99. The beam power delivered to the surface is $Q_{in} = P^*\alpha$, where P is the measured beam power and α is coupling efficiency of the beam and material. The heat source distribution is adjusted for the front (i=1) and rear (i=2) of the ellipsoid using the coefficient $f_i = c_i / (c_1 + c_2)$. Replacing z with $z - z_0$ in Equation [6.12] adds an additional parameter (z_0) that can be used to vary the penetration depth or focal point of the heat source. The heat source is applied to all

nodes in the deposit; however, the energy input at distances greater than the semi-axes is minimal.

$$Q(y,z,t)=\begin{cases} f_1\dfrac{2\sigma\sqrt{\sigma}Q_{in}}{abc_1\pi^{3/2}}\exp\left(-\sigma\left(\dfrac{y^2}{a^2}+\dfrac{z^2}{b^2}+\dfrac{(c_1-v_{laser}t)^2}{c_1^{\,2}}\right)\right) & t\le c_1 v_{laser} \\ f_2\dfrac{2\sigma\sqrt{\sigma}Q_{in}}{abc_2\pi^{3/2}}\exp\left(-\sigma\left(\dfrac{y^2}{a^2}+\dfrac{z^2}{b^2}+\dfrac{(c_1-v_{laser}t)^2}{c_2^{\,2}}\right)\right) & t> c_1 v_{laser} \end{cases} \quad [6.12]$$

The thermal properties[95] of Ti-6Al-4V are assumed to vary with temperature (See Appendix: Thermal Properties of Ti-6Al-4V).

Unfortunately, the processing parameters for the as-deposited material under investigation are unknown; However, using estimates[72] of laser power and scan speed for LMD of Ti-6Al-4V and the dimensions of the deposit under investigation, it is possible to obtain parameters for Equation [6.12] that produce the measured microstructure characteristics in the deposit, specifically the dimensions of the heat affected zone (HAZ) and fusion zone(FZ). Table XI shows fixed process parameters while Table XII shows optimized parameters for Equation [6.12] that produce FZ and HAZ dimensions similar to those measured in the as-deposited material (from the center of the first deposited layer/substrate interface (y = 0, z = 16 mm)). The parameters (hereafter referred to as "LFv5o-005") contained in Table XI and Table XII will be used to generate the thermal data for an eight layer deposit that will be coupled with the microstructure model to determine microstructure evolution.

Table XI: Constant processing parameters used in the thermal model (Parameter Set LFv5o-005).

Laser Power, *P*	Laser Velocity, v_{laser}	Part Length, *l*	T_{base}, T_{sub}	$h_{surface}$	h_{sub}	Layer: width x height	Substrate: width x height
13 kW	2.54 mm/s	250 mm	310 K	200 W/m^{2}K	10^{10} W/m^{2}K	15 x 5 mm	38 x 16 mm

Table XII: Parameters used in Equation [6.12] to produce FZ and HAZ dimensions similar to those measured in the as received deposit[24]. (Parameter Set LFv5o-005).

α	a, mm	b, mm	c_1, mm	c_2, mm	z_0, mm	FZ Depth, mm (measured)	HAZ Depth, mm (measured)	FZ Width, mm (measured)	HAZ Width, mm (measured)
0.19	8.0	5.0	8.0	8.0	-1.0	2.69 (1.05 ± 0.22)	5.64 (4.48 ± 1.43)	7.505 (8.5 ± 1)	8.99 (9.5 ± 1)

LFv5o-005 Results

The results of the "calibrated" parameter set (highlighted in Table X, and shown in condensed form in Table XI and Table XII), hereafter referred to as LFv5o-005, are presented in the following section in plots of temperature versus time, maximum and minimum temperature, and maximum heating and cooling rates.

First, a comparison is made between the as-deposited and calibrated heat-affected and fusion zones as shown in Figure 6.11. The heat affected zone (HAZ), defined by the maximum depth of heating above the beta transus is defined by the region of beta grain growth. The fusion zone (FZ) is less obvious, but is defined as the location where the prior beta grains become columnar in nature. The width of the FZ and depth of the HAZ match fairly well, whereas the depth of melting and the width of the HAZ differ by several millimeters.

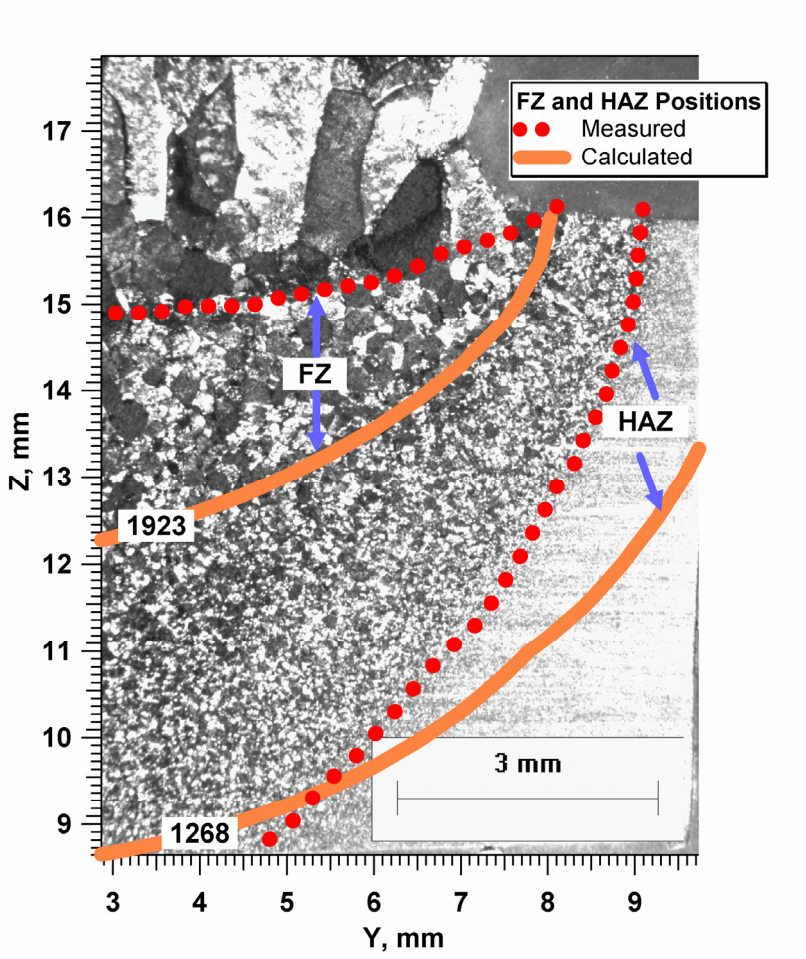

Figure 6.11: Comparison of as-deposited and calculated fusion- (FZ) and heat affected- (HAZ) zones using a macrograph from the as-deposited material. The isotherm labels (temperature) are given in units of Kelvin.

A movie of the two dimensional (*y*-*z*) modeled temperature distribution in the deposit has been created and will aid in the understanding of the subsequent plots. Contours (isotherms) are plotted for the vaporization (T_{VAP}), liquidus (T_{LIQ}), beta transus (T_{BETA}), alpha dissolution (T_{DISS}), and the martensite-start (M_S) temperatures.

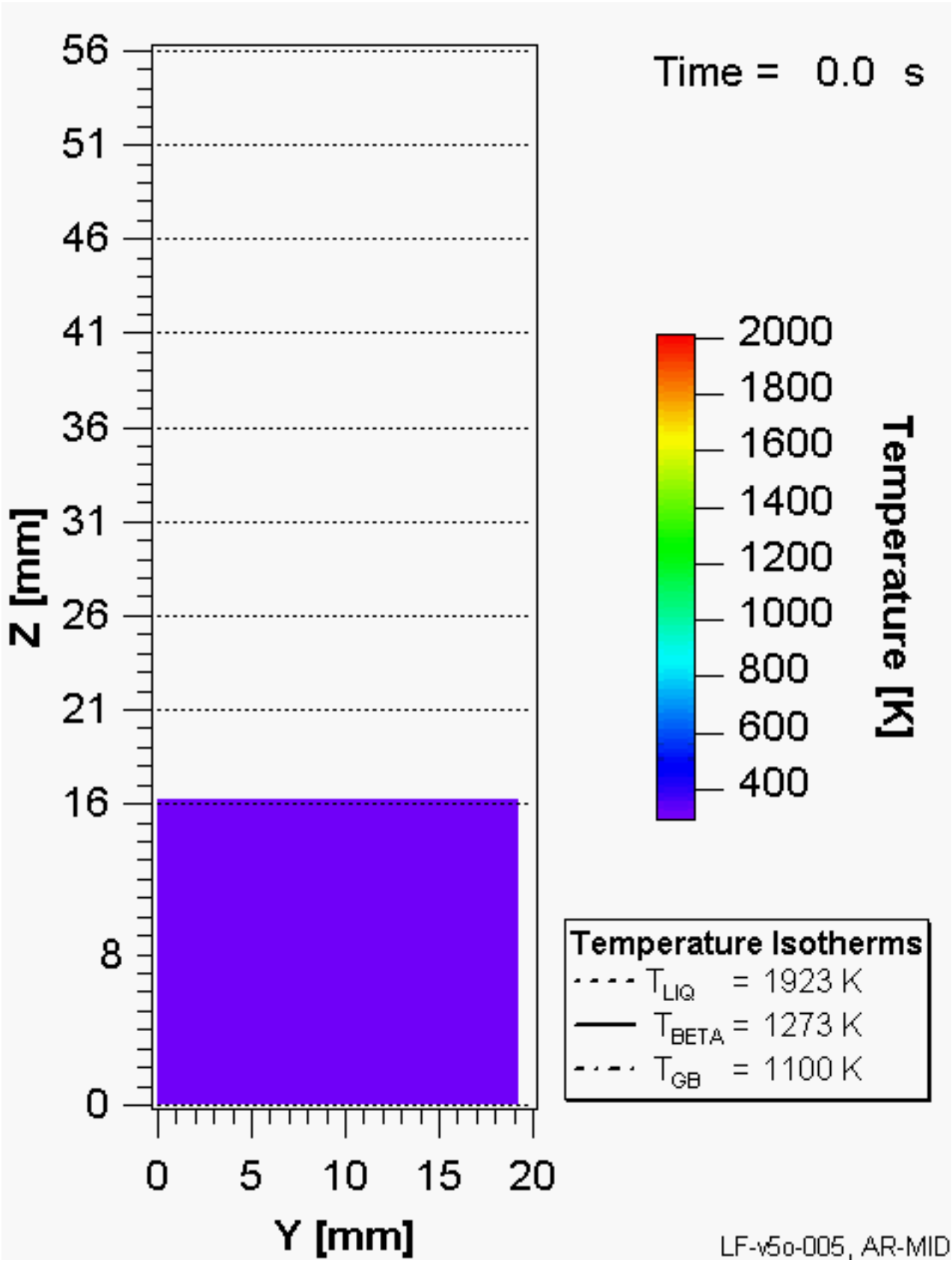

Figure 6.12: A movie of the two-dimensional (y-z) temperature distribution with time during the deposition of eight layers of material using parameter set LFv50-005. Contours (isotherms) for temperatures of interest are shown.

The variation of temperature with time for positions at the top and bottom of the first (L1) and fifth (L5) layer deposited is shown in Figure 6.13. The calculations indicate that during the initial layer deposition, the entire layer sees temperatures well above the liquidus with some regions above the vaporization temperature of pure titanium (3560K), before cooling to nearly room temperature. During the deposition of the second layer, nearly the entire first layer is remelted, while during the third layer deposition, only the very top of L1 is remelted. The most significant microstructural change is predicted to occur during the deposition of the fourth layer, where a region near the top of the layer experiences temperatures above the beta transus (1268 K), while the lower portion of the layer remains in the two phase region. As for the deposition of the fifth layer (L5), shown in Figure 6.13, the peak temperatures and extent of remelting are similar to those described for L1, with the most noticeable difference being a reduction in the thermal gradient (dT/dz) at the peak temperatures. It is also observed that during the deposition of the fourth layer onto L5 (eighth layer on L1) that the top and bottom portions of L5 are heated into the single (β) and two phase regions ($\alpha+\beta$), respectively.

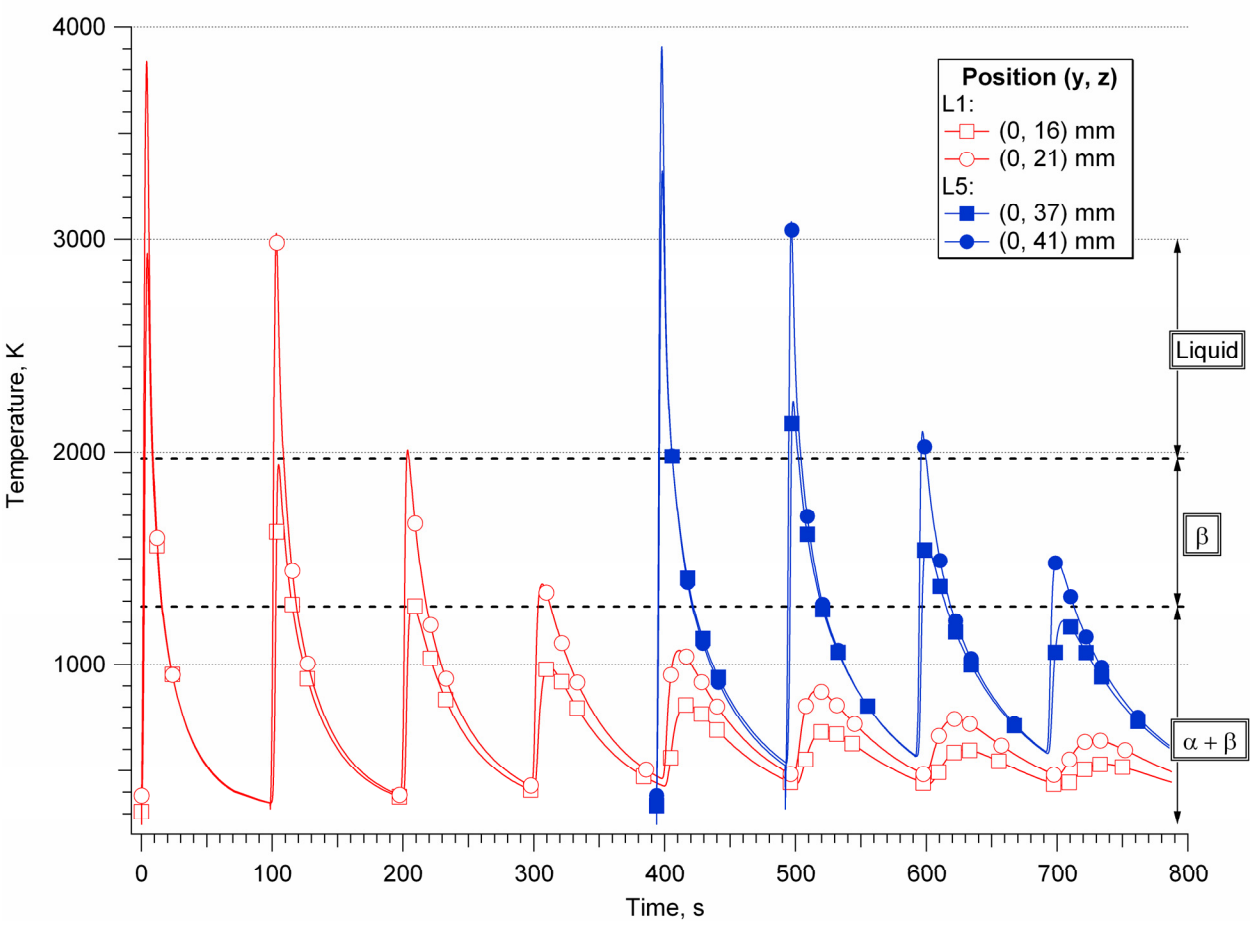

Figure 6.13: Temperature versus time plotted for two positions along the centerline (y=0mm) of the deposit in the first and fifth layers.

Figure 6.14 shows the X-Z temperature profile along the centerline (y = 0) of the deposit for each layer deposition. The x-axis was not explicitly modeled, but it can be depicted by multiplying the (elapsed) time value by the laser scan velocity, assuming heat flow in the *x* is direction is negligible. Each profile in Figure 6.14 represents the first 40 seconds (corresponding to 101.6 mm of laser travel) of each layer deposition. Also shown in Figure 6.14 is the distribution of laser power at the surface of L1 (z = 21, *y* = 0). The length of the beam is 16 mm (c_1 = c_2 = 8mm), leading to a melt pool with a length of approximately 30 mm and a plasma region approximately 5 mm in diameter for the first layer deposited. As additional layers are added, the depth and length of the melt pool increases, while the dimensions of the plasma region remain relatively constant. In addition to the vaporization and melt temperatures, additional contours of microstructural importance, including the beta transus (T_{BETA}), alpha dissolution temperature (T_{DISS}), and martensite start temperature (M_S) are also shown.

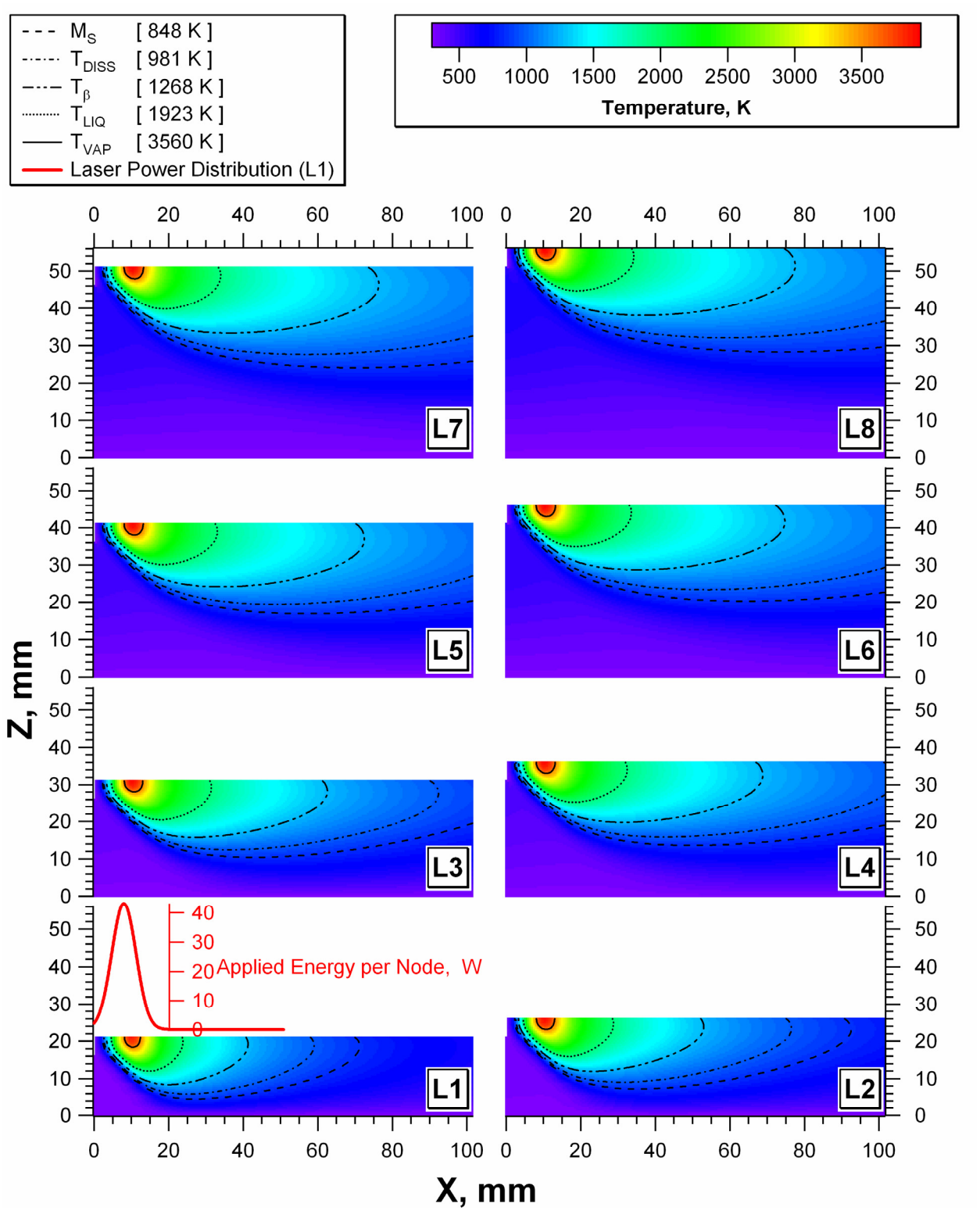

Figure 6.14: Thermal profiles of the X-Z plane at the centerline of the deposit (y = 0) for the first 40 seconds (corresponding to 101.6 mm of laser travel) of each layer deposition (L1 – L8). The x-position is calculated by multiplying the elapsed time by the laser scan-velocity. The applied energy distribution at (y = 0, z = 21mm) as a function of x-position (time) is illustrated for the first layer deposition (L1).

Figure 6.15 shows the maximum temperature for each layer deposition in the form of a two-dimensional image of the deposit. Recall that the deposit is symmetrical so that only the +*y*-z dimension is shown. On these plots are contours indicating important temperatures that will affect the microstructure, namely the vaporization, melting, beta transus, alpha dissolution, and martensite start temperatures. Figure 6.15 shows two distinct conduction modes occurring during the deposition process. For the first three layers deposited, heat is conducted in both the +y and –z directions out of the substrate, forming curved maximum temperature contours. After the fourth layer deposition, heat is conducted mainly in the -z direction through previously deposited layers, leading to nearly linear maximum temperature contours. A minor component of the deposited energy is conducted through the surface of the deposit (+y) via convection.

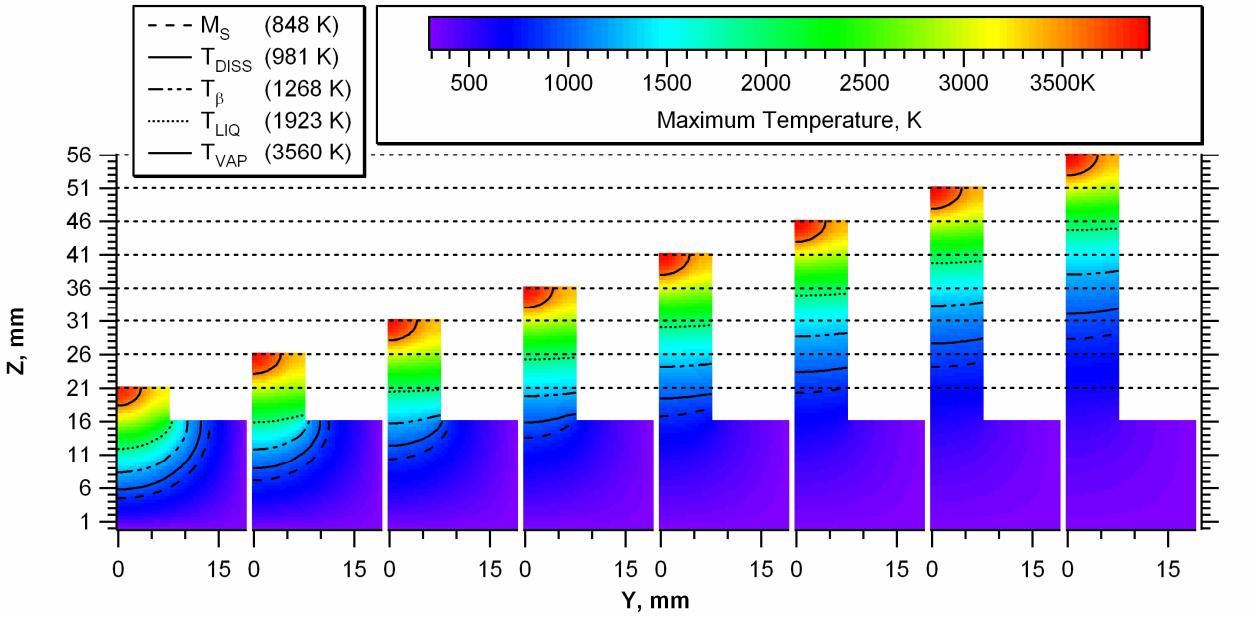

Figure 6.15: Two-dimensional image map of the maximum temperature experienced in the deposit during each layer deposition for parameter set LFv5o-005. Horizontal gridlines indicate the position of each layer, while the isotherms indicate important phase transformation temperatures.

The two maximum temperature contours yet to be discussed are the alpha dissolution temperature, T_{DISS} = 981K, and martensite start temperature, M_S = 848K. The alpha dissolution temperature represents the beginning of alpha dissolution into beta under equilibrium heating conditions, and as such represents a "dissolution"-heat-affected zone (D-HAZ). If the material is heated to a peak temperature below T_{DISS} and cooled slowly, there will be no change in the observed microstructure, unless the cooling rates are sufficient to transform the remaining beta phase to martensite.

Figure 6.16 quantitatively shows the sizes of the plasma, liquidus, and beta transus regions as each layer is added to the deposit. The depth [z] of an isotherm is measured from the top of a layer to the minimum in the isotherm. The width [y] is measured from the centerline (y=0), and is only shown for the vapor isotherm since all other isotherms are as wide as a layer at their maximum. The length [x] is measured from Figure 6.14, and is the maximum length of the particular isotherm, typically found near the top of the last deposited layer. The dimensions of these isotherms remain relatively constant throughout the build process, with the greatest increases being observed in the first three deposited layers. The ratio of width to depth of the plasma region remains constant at 1.4. This is similar to the ratio of the width (*a*) to depth (*b*) [*a*/*b*=1.6] of the distributed heat source. The depth and width of melting (fusion zone) during the first layer deposition extends approximately 4mm deep into the substrate and extends the entire width of the first deposited layer. The fusion zone dimensions, especially the width are in-line with the observed fusion zone dimensions in the as-deposited microstructure. The dimensions of the beta transus isotherm are also in agreement with those measured in the as-deposited material. The beta transus contour represents a beta-heat affected zone (β-HAZ), where above this temperature all previous microstructure with the exception of beta grain size is erased.

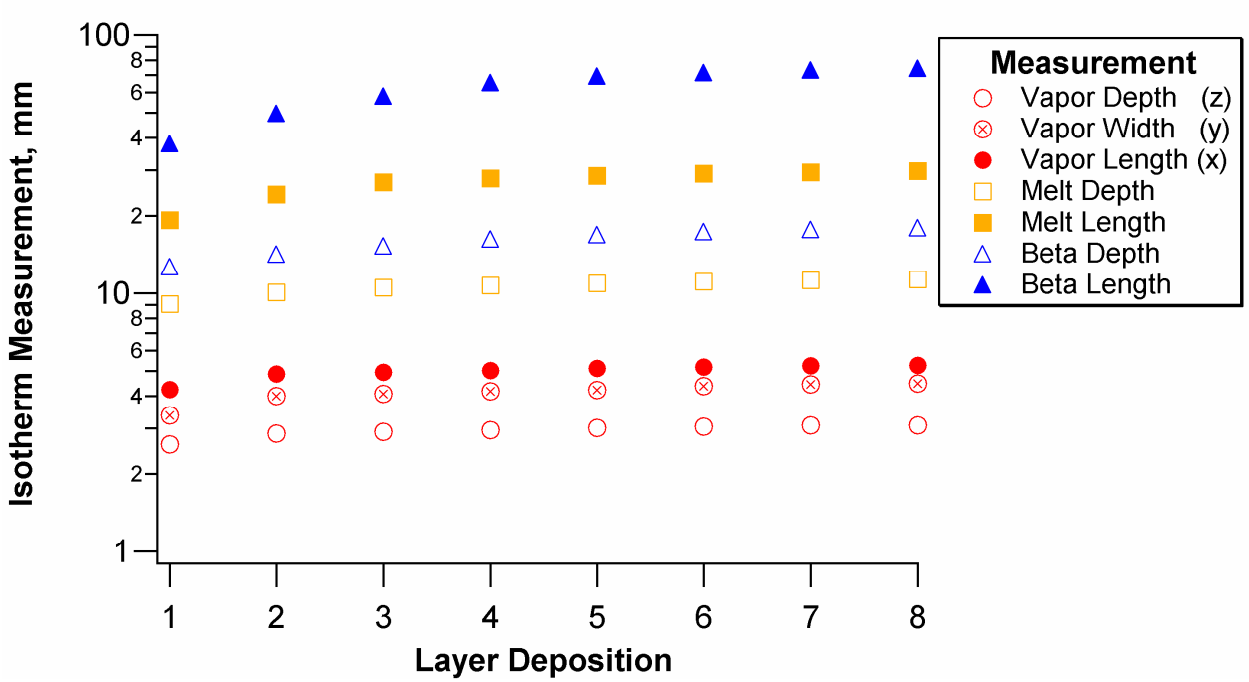

Figure 6.16: Predicted sizes of different isotherms for each layer deposition in the depth (from the top of a deposited layer, [*z*]), width (from the centerline, [*y*]), and length, [*x*].

After the third deposited layer, the dimensions, shape and spacing of the maximum temperatures remain relatively constant. The depth of melting is nominally 2 deposited layers (10mm), the beta transus or β-HAZ extends 3.5 deposited layers (17.5mm), the D-HAZ extends 4.5 deposited layers (22.5mm)) and the M_S approximately 5.5 deposited layers (27.5). This means that a layer deposition will potentially affect the microstructure 5 layers deep or 27.5mm, and this dimension remains relatively constant after 3 layers are added. Thus each deposition thermal cycle has the ability to affect microstructure changes in a large amount of material.

Figure 6.17 shows a two dimensional image map of the minimum temperatures experienced during each layer deposition. As additional layers are added, the minimum temperature is increased. After three layers are added, the minimum temperature distribution in the substrate remains constant, while in the deposit the minimum temperature increases. Also note the minimum temperature predicted at the very top of each layer for layers 2 through 7 (e.g. z = 26, 31, 36, …51 mm), is near 310 K, while the remainder of a new layer is much greater than this temperature. This anomalously low minimum temperature is an artifact of the addition of a new layer, which is why the last layer does not exhibit a very low minimum temperature at z=56mm. When a new layer is added to the deposit, it initially has a constant temperature of T_{base} and is rapidly heated using the distributed heat source. The anomalous minimum temperature reflects

the initial temp of a newly deposited layer, which is assumed to arrive at the heat source in powder form.

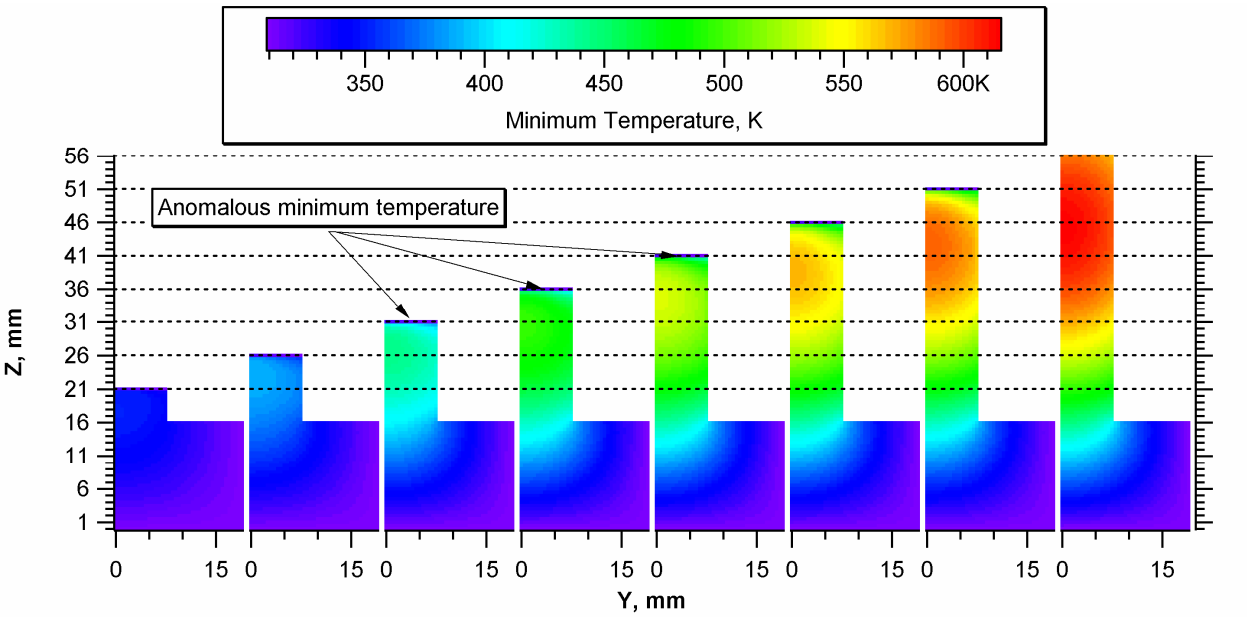

Figure 6.17: Two-dimensional image map of the minimum temperature experienced in the deposit during each layer deposition for parameter set LFv5o-005. Horizontal gridlines indicate the position of each layer.

Figure 6.18 shows a two-dimensional image map of the maximum heating rate experienced during each layer deposition. The maximum heating rate is nominally calculated over the temperature range $T_{beta} \pm 100K$. Heating rates between 900 and 1140 K/s are experienced in a newly deposited layer. The underlying material experiences slower heating rates, ranging from 200 to 800 K/s for maximum temperatures greater than T_{beta}. The distribution of heating rates remains constant after the first three layers are deposited.

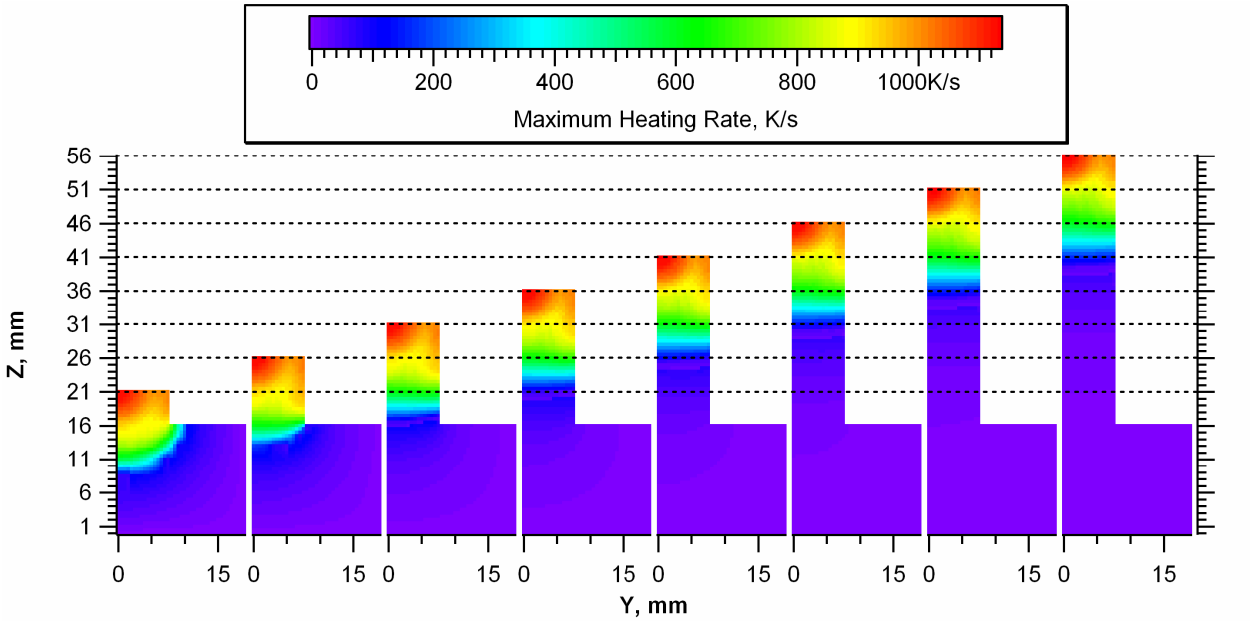

Figure 6.18: Two-dimensional image map of the maximum heating rate experienced in the deposit during each layer deposition for parameter set LFv5o-005. The heating rate is nominally measured over the temperature range T_{beta} ± 100K. Horizontal gridlines indicate the position of each layer.

A two-dimensional image map of the maximum cooling rate achieved during each layer deposition is shown in Figure 6.19. The calculation of the maximum cooling rate is dependent on the maximum temperature achieved for a particular layer deposition. Nominally, the cooling rate is calculated over the temperature range between the M_S and T_{beta} temperatures. Cooling rates are greatest in the newly deposited layer and during the first three layer depositions, thereafter, the cooling rates decrease as multiple layers are added to the deposit. Ahmed and Rack[28] state that cooling rates greater than 20 K/s have the potential to produce a mixture of massive and martensitic transformation products ($\beta \rightarrow \alpha_m + \alpha'$) upon cooling through the beta transus, while slower cooling rates will produce a diffusion controlled transformation ($\beta \rightarrow \alpha + \beta$). For cooling rates greater than 410 K/s, a fully martensitic transformation ($\beta \rightarrow \alpha'$) would be expected.

The critical cooling rates for diffusion-controlled and non-equilibrium transformations are indicated in Figure 6.19 by thick contour lines. The thinner contour lines represent critical temperatures associated with these cooling rates. As such, the mixed massive and martensitic transformation would be expected in the first deposited layer and a large portion of the substrate. For the next two layers deposited, the mixed massive and martensitic morphology would continue to form in the newly deposited layers (2 and 3) and the underlying material. During the

deposition of layers 4 onwards, cooling rates are less than 20K/s and equilibrium transformation products would be expected. The cooling rates in layers 4 through eight remain relatively constant between 5 and 15 K/s. We would expect very little microstructure variation due to cooling rate in the last four deposited layers; however, the difference in maximum temperature over a layer thickness is greater than the difference in cooling rate and will have a much more significant effect on the microstructure produced.

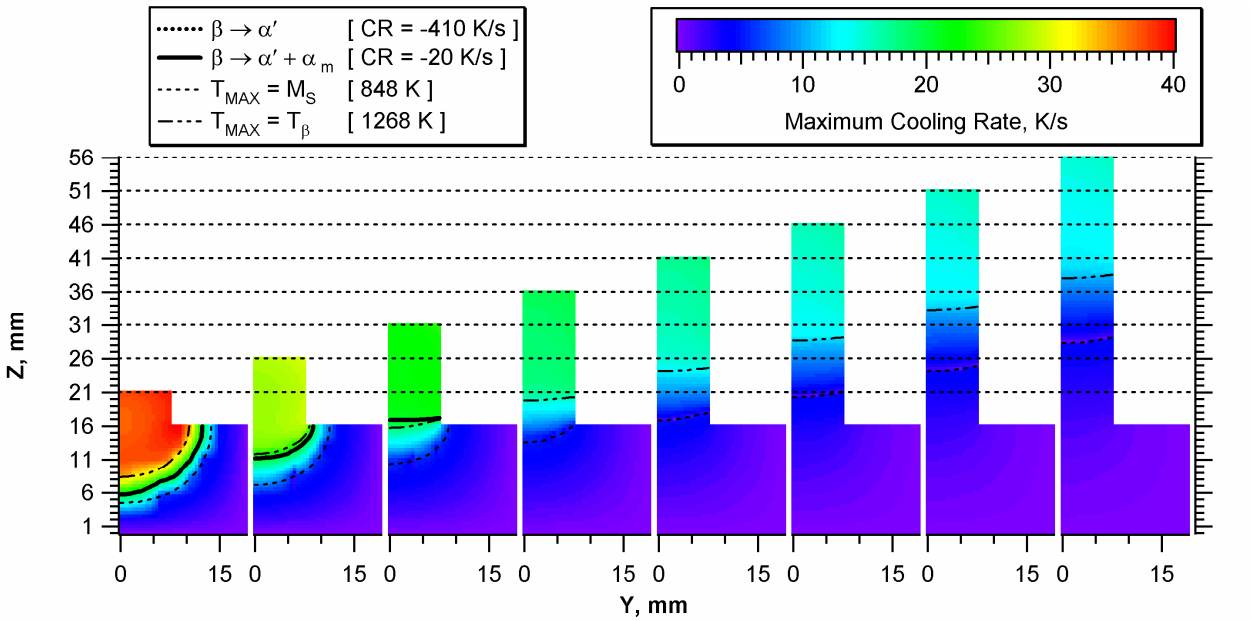

Figure 6.19: Two-dimensional image map of the absolute maximum cooling rate experienced in the deposit during each layer deposition for parameter set LFv5o-005. Two sets of contours are plotted, one for critical cooling rates corresponding to equilibrium and non-equilibrium beta-to-alpha transformation products[28] and maximum temperatures which also determine if these products are possible. After three layers are added, cooling rates are less than 20 K/s.

Discussion of LFv5o-005 Results

Maximum Temperature

The purpose of developing the thermal model was to relate the obtained thermal output to the observed microstructure and to use the output as input to a microstructure model. In the as-deposited microstructure it was observed that the last 3 layers to be deposited (*n+1*, *n+2*, *n+3*) are comprised of a transient microstructure and the underlying layer, *n*, contains the greatest microstructural contrast. Layers below *n* (i.e. *n-1*, *n-2*…) are microstructurally similar to layer *n* and are thus unaffected by the deposition of the last three layers. Layer *n* is known as the characteristic layer, which is periodically repeated in the deposit.

Figure 6.20 examines the modeled maximum temperature during the eighth layer deposition and compares these results with the as-deposited macro-structure from the last 6 layers of the deposit. The characteristic layer, *n*, and the transient layers (*n+1* to *n+3*) of the as deposited macro-structure are highlighted. The isotherms representing the beta transus and dissolution temperatures are indicated in the thermal model data. In Chapters 2 and 3 the importance of primary and secondary heat treatment on microstructure evolution was shown. The material heated above the beta transus will form as primary-alpha, while the material heated below the beta transus will contain secondary and primary alpha when cooled. As a result, the region bracketed by these isotherms is where the greatest microstructural change will occur. Recall from Figure 6.16 that the position of the isotherms becomes constant after the third deposited layer and during each layer addition, the position of these isotherms is incremented by a constant distance with each additional layer (see Figure 6.15). Clearly the region bounded by the isotherms is also periodic. For this reason, the characteristic layer is a result of the heating between these two isotherms and is indicated by a box in Figure 6.20. The box is joined by dashed lines to the characteristic layer box for the as-deposited macrostructure.

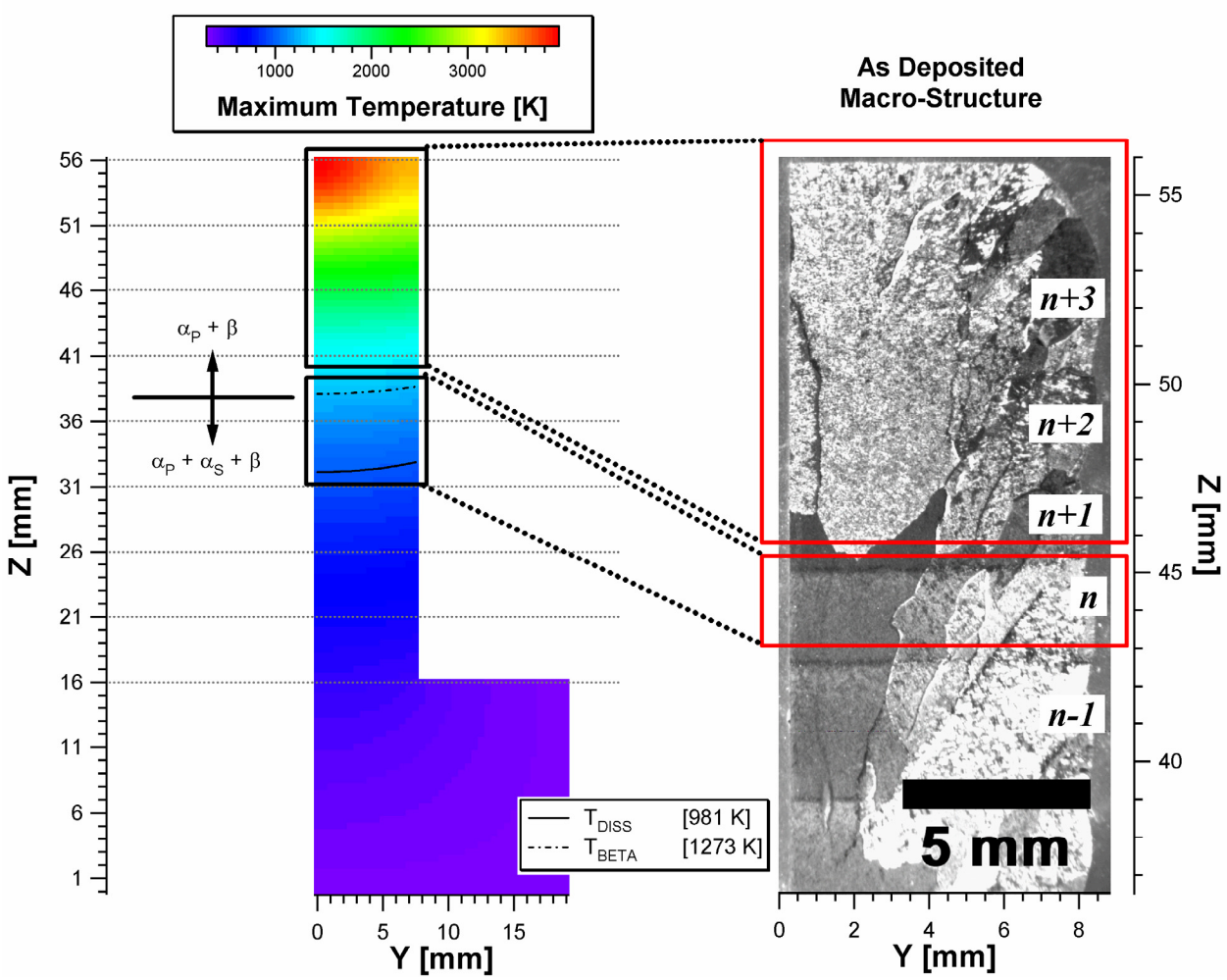

Figure 6.20: Comparison of modeled maximum temperature with the as-deposited macrostructure. The modeled data is taken after the eighth layer addition. The as-deposited macrostructure consists of the last 6 layers added to the deposit, with the layer n representing the characteristic, repeated layer. Layers n+1 through n+3 represent a transient layer. The locations of the characteristic and transient layers are indicated by boxes on the macrograph and modeled data.

The transient region located above the characteristic layer is also highlighted and joined to the same region in the as-deposited microstructure. The modeled transient region encompasses the last 3.5 modeled layers (5mm per layer), similar to the as-deposited macrostructure which encompasses three deposited layers. The modeled characteristic layer is approximately 1 layer, (the distance between the beta transus and dissolution isotherms is 6mm), also similar to the as-deposited macrostructure. At this point it should be noted that in the model, 5mm layers were used, however, in the actual deposit, the exact size of a deposited layer varies from layer to layer, as does the size of the characteristic layer. The important comparison between the as-deposited macrostructure and the modeled deposit is that the number of thermal cycles (layer additions) responsible for the characteristic layer to develop is similar.

Cooling Rate

Figure 6.21 examines the maximum cooling rate in relation to the as-deposited microstructure. The cooling rate in the characteristic layer region is predicted to vary only 4.1K/s through the thickness of the layer. The maximum temperature experienced in this region is varies 292 K, suggesting that maximum temperature will have a more significant effect on the resulting microstructures.

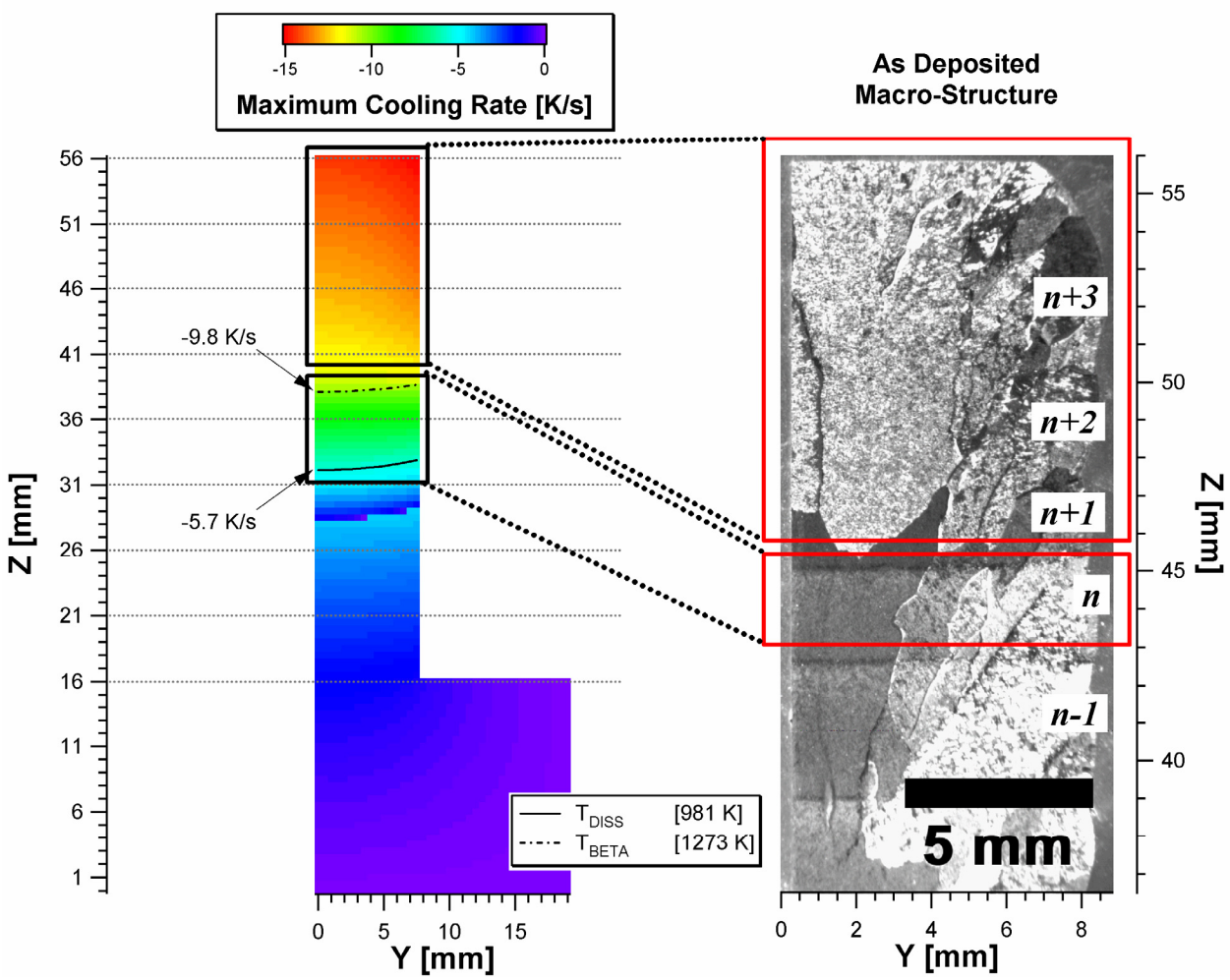

Figure 6.21: Comparison of the modeled maximum cooling rate with the as-deposited macrostructure, highlighting the transient and characteristic layers of modeled and as-deposited material.

The characteristic layer contains a region that essentially receives a secondary heat treatment, i.e. peak temperatures are between T_{DISS} and T_{BETA}. The predicted cooling rate from this secondary-heat treatment is between 5.7 and 9.8K/s. In the baseline microstructure results (Chapter 3), a secondary-heat treatment at 1198K with a 10K/s cooling rate resulted in a basketweave-α_S

morphology with some α_P growing from the prior beta grain boundary. The microstructure within the characteristic layer should therefore contain predominantly basketweave-α_S based on the predicted thermal cycles and baseline microstructure results. The as-deposited microstructure characteristic layer contains basketweave α (nominal microstructure), but it also contains colony-α within the layer band. If equal weights are given to the thermal model and baseline microstructure results, then heating to higher peak temperatures in the $\alpha+\beta$ phase field must result in a change of morphology for cooling rates on the order of 10K/s. This theory will be explored in the microstructure modeling chapters.

Solidification

Solidification is not the primary emphasis of this thesis, but it offers some validation of the thermal model with the as-deposited results. During solidification, beta grains will align themselves parallel to the steepest temperature gradients. A columnar structure forms provided the solidification front is moving at a sufficiently slow rate (faster rates will produce equiaxed grains). A comparison of the beta grain growth alignment expected from he modeled data is shown with the familiar as-deposited macrograph from the last 6 layers added to the deposit. Two time instances are plotted for the modeled temperature, along with the liquidus isotherm. Both times are after the eighth layer has been added. At the first time value (t=696.4s), the liquidus is nearly parallel to *y*-plane; therefore, the beta grains will be oriented parallel to the z-plane as shown by the arrows. This case is very similar to the center of the as-deposited material, where beta grains are oriented perpendicular to the substrate in the y-z plane. Eight seconds later, the modeled liquidus isotherm becomes elliptical. The beta grains then will grow inward, towards the center of the molten region; however, the as-deposited macrostructure suggest the beta grains are oriented outward (though the grains on the upper right corner of the as deposited material may grow inward or outward, this is not known).

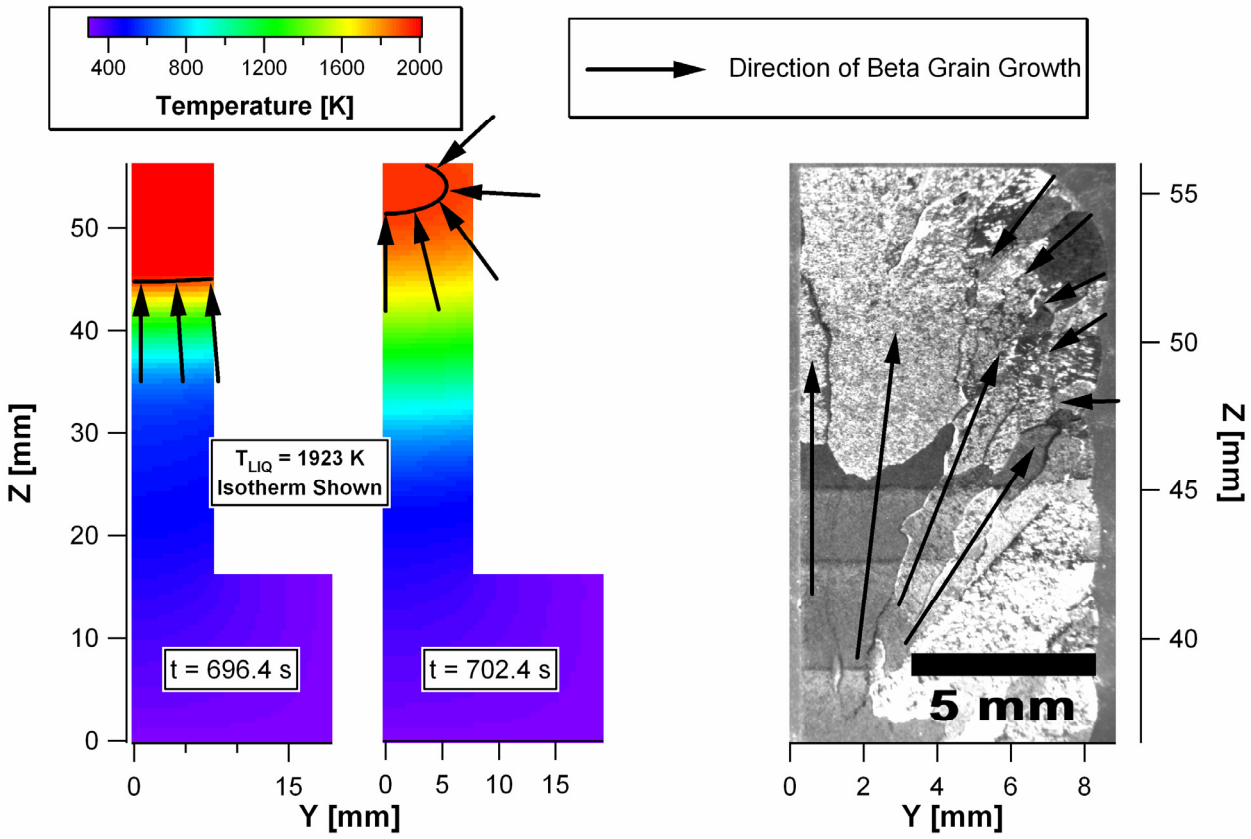

Figure 6.22: Comparison of expected beta grain growth directions from the modeled temperature data and as-deposited macrostructure (y-z plane). The arrows indicate the direction of beta growth, which is normal to the liquidus isotherm.

Figure 6.23 schematically illustrates the shape and movement of the solid-liquid boundary necessary to produce the beta grain orientation shown in the macrograph of Figure 6.22. In Figure 6.23a beta grains start to grow and the solid liquid interface must have the shape shown in order for beta grains to grow outward. This shape may be due to the bead shape of the previous layer. It may be a result of rapid heat extraction through the center of the deposit as compared to the surface, though the former theory appears more likely. Figure 6.23b-c illustrates that at some point the surface of the freshly deposited layer may begin to solidify due to convective cooling at the surface enhanced by the presence of a shielding gas. The growth of the solid-liquid interface at the top of a layer will be much smaller than at the bottom due to higher heat transfer rates by conduction. In Figure 6.23d the solidification process is complete and the orientation of the final beta grains shown. Within the bulk of the deposit, large columnar beta grains would be expected and near the surface, smaller equiaxed grains would be expected.

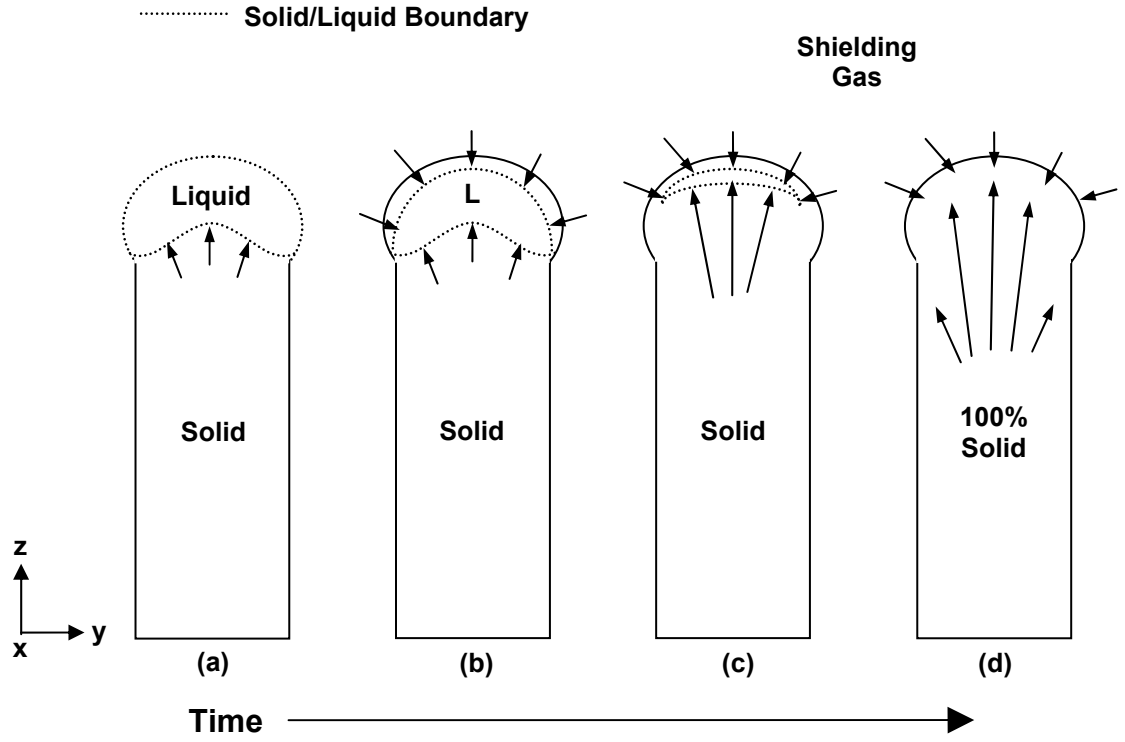

Figure 6.23: Schematic of solidification process and the shape of the melt pool required to produce prior beta grains oriented in the direction observed in the as-deposited material. The melt pool is indicated by dashed lines, and the direction of beta grain growth by the arrows. Solidification occurring from the top of the bead will occur if sufficient surface cooling is provided in the form of a shielding gas.

For more focused experiments on solidification during laser deposition of Ti-6Al-4V, see the work of Kobryn[8-10] and Klingbeil and Bontha[77] whose research focuses on predicting solidification rates and beta grain morphology. Klingbeil and Bontha have determined through single pass thermal modeling that at very high incident energies (30kW) an equiaxed beta grain morphology would be found at the surface and a columnar structure deeper in the layer. Their work complements this thesis nicely.

Thermal Model Summary

The Model

The original[24,26] thermal model was compared with experimental temperature data from LENS™ 316-SS deposits and it was determined restrictive boundary conditions placed on the substrate and oversimplification of the way heat was input into the deposit (new layer has a constant temperature) lead to unlikely high cooling rates. To correct these shortcomings, a three-dimensional volumetric double-ellipsoidal heat source was used to model heat input into the

deposit. Additionally, the size of the substrate was increased, necessitating a variable grid spacing to improve computational efficiency (an eight layer model runs in less than 2 hours on a 2.8GHz PC with 2GB of RAM). A more accurate representation of convection at the surface and substrate was added. Calibration of the heat source dimensions and process efficiency yielded more agreeable results with the LENS™ experimental data; however, the Rosenthal analytical solution still yields very good agreement with experimental data. The calibrated model and experimental results matched for the melt pool length and cooling rate, but not maximum temperature.

Exact processing conditions for the as-deposited microstructure are unknown, necessitating estimation. The model heat source parameters were calibrated for AeroMet's LaserForming™ process using the as-deposited microstructure, specifically the depth and width of the fusion and heat affected (beta transus). The modeled and as-deposited heat affected zone depth and fusion zone width matched well. The modeled fusion zone depth was about 3mm greater than that observed in the deposit. The calibrated parameter set (LFv5o-005) will be used in the microstructure modeling efforts.

Temperature as a function of time

- During the deposition of a layer of material by a high power distributed heat source, multiple phase transitions occur, including heating above the beta transus, melting, and vaporization.

- The three most recent layers added to the deposit will experience heating above the beta transus (a primary heat treatment or thermal cycle) while the fourth most recent layer experiences heating above the alpha dissolution temperature, but below the beta transus (a secondary heat treatment or thermal cycle). In other words layer *n* experiences a secondary heat treatment, while layers *n+1* through *n+3* experience primary thermal treatments. The material below layer *n* (e.g. *n-1*) will not experience sufficient heating to produce microstructural changes and have a similar microstructure to layer *n*.

Maximum Temperature

- After the first three layers are deposited, the heat affected zone extends approximately 4 layers in the –z direction. The size, shape, and temperature distribution of the heat affected zone remain relatively constant after three layers have been deposited.

- As layers are added to the substrate, heat flow becomes one dimensional, conducting in the –z direction, with a small component in the +y direction due to convection. One dimensional heat flow will result in thermally induced microstructural changes that are oriented parallel to the isotherms. The thermal model and microstructure model are in agreement with regards to heat flow direction. The layer bands in the as-deposited material are oriented parallel to the substrate, indicating that they may form as a result of the thermal cycling during deposition.

- The characteristic layer is defined by the position of the beta transus and dissolution temperature isotherms, where varying amounts of secondary alpha will form leading to the greatest changes in microstructure. The maximum depth of the characteristic layer extends 4 layers deep into the deposit. In the as-deposited the characteristic layer containing the layer band (colony-α_S) and nominal (graded basketweave-α_P) microstructure appear in the fourth layer from the top of the deposit. By definition, the transient layer in the model and as-deposited microstructure also agree.

Minimum Temperature

- The minimum temperature experienced in the deposit increases as multiple layers are added. The increase in minimum temperature is due to a shift in the mode of conduction from 2D during the first three layers to 1D in the remaining layer due to a constant laser power and movement of the heat source away from the large heat sink in the substrate. The continuous increase in minimum temperature indicates that the actual deposit may have been fabricated with a decreasing power as the source moves from the substrate, as this increase would affect microstructure greatly if raised above the beta transus.

Heating Rate

- The maximum heating rate is experienced in a newly deposited layer near the heat source. Heating rates greater than 1000K/s can be expected near the heat source. The effect of rapid heating on microstructure development will be explored in the microstructure modeling section.

Cooling Rate

- Modeled cooling rates with the first three layer depositions are greater than in the last 4 due to the transition from a 2D conduction near the substrate to 1D conduction in the "wall." Cooling rates (and peak temperatures $T_{MAX} > M_S$) in the predicted within the first three layers are sufficient to produce non-equilibrium decomposition of beta to a martensitic and massive alpha morphology. After three layers are added to the substrate, predicted cooling rates are less than 20K/s and diffusion-controlled transformation products would be expected.

- Within the characteristic layer (bounded by the dissolution and beta transus isotherms) the cooling rate varies 4 K/s over a distance of 5mm, while peak temperature varies nearly 300K. Larger changes in microstructure in the as-deposited microstructure are a result of peak temperature experienced rather than cooling rate.

Comparison with As-Deposited Microstructure

The calculated position of the beta transus and dissolution isotherms predict the formation of the characteristic layer in a layer *n* after the deposition of layer *n+3*, in agreement with the as-deposited microstructure. The effect of the combination of primary ($T > T_{BETA}$) and secondary ($T_{BETA} > T > T_{DISS}$) thermal cycles on microstructure will be discussed further as a more quantitative analysis of microstructure evolution is made. The thermal cycles calculated from the thermal model can be used as input to the microstructural modeling efforts. Now that we have accurate thermal cycles for the process we can use this information in a model that will quantitatively predict microstructure evolution.

Chapter 7: Microstructure Modeling

The model for describing microstructure evolution during laser deposition of Ti-6Al-4V will be developed in this chapter. The kinetics of alpha phase formation and its morphology will be examined. This chapter will briefly introduce some of the tools available to model microstructure and the commercial software used to aid in the modeling calculations. Then, sub-models for alpha dissolution and growth will be derived. Lastly, the results of the microstructure model will be compared with recent experimental results and the baseline microstructure experiments appearing in Chapter 3. Chapter 8 will apply the microstructure model to the thermal model predicted thermal history.

Background Information on Microstructure Modeling

According to Grong, *et. al.*[105] microstructural variables include, in order of scale, grain size, volume fraction of grains of different types, solid fraction during solidification, second phase particles (intermetallic phases, dispersoids, precipitates), and deformation substructures (subgrain size, dislocation density, subboundary misorientation). A microstructure variable must be, in principle, a physically measurable quantity. In the current work, microstructure is defined as alpha phase fraction.

The evolution of alpha phase fraction will be modeled during alpha dissolution and alpha nucleation and growth. The former generally occurs during heating, with the latter generally forming on cooling. A more exact requirement for the growth or dissolution of a phase would be, if the actual fraction of a phase is less than the equilibrium value, growth will occur; likewise if the actual fraction of a phase is greater than equilibrium, dissolution will occur.

Nucleation and Growth

The modeling of nucleation and growth type phase transformations where the parent and product phases are both solid is typically accomplished through the Johnson-Mehl[106]-Avrami[107-109]-Kolmorgorov[110] (JMAK) equation (Equation [7.1]) which describes the evolution of the extent of reaction, ζ, of the product phase with time. The function $k(T)$ describes the kinetics (nucleation and growth rates) and is strongly dependent on temperature, while n describes the nucleation/growth mechanism of transformation taking place and is independent of temperature.

$$\zeta = 1 - \exp\left(-k(T)t^n\right) \qquad [7.1]$$

The JMAK equation was derived under the ideal conditions of isothermal transformation, proportional or decreasing nucleation and growth rates, and the assumption of site saturation, or all nuclei appear at the same time.

Dissolution

The dissolution of alpha occurs by diffusion controlled movement of the α/β interface and no nucleation of the beta phase within alpha grains. [52,53,58] Dissolution will be modeled assuming that the beta phase grows into alpha. Both phases will be assumed to be plates, and grow in one dimension (normal to the longest dimension). Assuming the beta phase grows under diffusion controlled conditions, the growth rate may be determined assuming a parabolic growth rate. The parabolic thickening rate can be determined by solving the diffusion problem and plotting the interface position as a function of $t^{1/2}$. Two assumptions are made: (1) soft impingement of the diffusion field and (2) Gibbs-Thompson effects due to curvature of the interface are ignored.[111]

Additivity

The aforementioned methods for describing alpha nucleation and growth and alpha dissolution are developed for isothermal heat treatments. In other words, the methods are theoretical tools for predicting time-temperature transformation (TTT) diagrams. In order to apply the above methods to non-isothermal treatments, such as the LMD thermal cycles created in Chapter 6, one must integrate the kinetic equations over the thermal cycle. The principle of additivity is applied to accomplish this task: to predict microstructure evolution for non-isothermal heat treatments based on isothermal experiments.

Christian has presented the basic definition of additivity in his classic text.[111] An additive reaction is one with which a given amount of transformation can be reached by adding the fractions of the time to reach this stage isothermally until the sum reaches unity, as shown in Eq. [7.2]. Here, $t_i(T)$ is the isothermal time to reach an amount of transformation ζ_i and t is the time to ζ_i for the non-isothermal reaction. In this sense t_i is a real time and $t_i(T)$ is an equivalent time.

$$\int_0^t \frac{dt}{t_i(T)} = 1 \qquad [7.2]$$

Avrami[107,108] first described an isokinetic reaction as one where (considering a nucleation and growth reaction), the nucleation and growth rates are proportional, i.e., they have the same temperature variation and be described by a single ("iso") kinetic equation; however, this is rarely observed. Cahn[112] proposed a more general definition of an isokinetic reaction. Grong *et al*.[105] recently reviewed a generalized form of the additivity approach to modeling, with a focus on applications in heat treatment and welding.

Application of additivity to nucleation and growth

In order to apply additivity to model nucleation and growth, the reaction must be isokinetic. If early site saturation is assumed to occur during nucleation and the growth rate is purely a function of temperature, the reaction will still be isokinetic only if the number of nuclei are independent of temperature. This requires that the starting grain size for the isothermal transformation data and the calculated non-isothermal transformation be equivalent if the transformation mechanism is grain boundary nucleation. Christian also states that additivity principles will hold at large degrees of undercooling where composition remains approximately constant.

Beyond the initial definition and application of the additivity principles to nucleation and growth reactions, improvements in the theory and acceptable application have been discussed recently. A constant nucleation to growth rate ratio and fulfillment of the site saturation conditions were not observed in the austenite to pearlite transformation in eutectoid plain carbon steel. This resulted in a modification Cahn's[113] early site saturation criteria to include an effective site saturation.[114] Recent articles by Zhu and Lowe[115,116] caution application of the additivity principle when trying to model nucleation despite the relatively small errors that are produced. Lusk and Jou[117] have stated that use of the geometric parameter, n, as a function of temperature is inappropriate as well as revising a statement previously made by Cahn[112] that all rate-independent (or general isokinetic) reactions are additive. Instances where this statement does not always hold were identified through mathematical derivations. Critical validation and improvement of the principles of additivity continue to be the subject of theoretical research. For example, Reti[118] has developed a non-linear extension of the additivity rule that uses weighting functions to consider the rate of temperature change on the rate of non-isothermal transformation.

Despite these restrictions, the principles of additivity have been successfully applied to the JMAK equation for diffusion controlled transformations in a number of alloys and different processing conditions, including continuous cooling of Ti-6Al-4V.[27] Malinov, *et al.*[27] used the differential scanning calorimeter (DSC) to study the beta to alpha phase transformation in Ti-6Al-4V as a function of cooling rate (0.083K/s to 0.83K/s). The DSC curves (T vs. heat flow) are use to determine the fraction of beta transformed to alpha. JMAK theory is used to describe the transformation of beta to alpha, and kinetic parameters are obtained. For the alloy studied, the start and finish of the $\beta \rightarrow \alpha+\beta$ transformation occurs at 1243K and between 1133-1093K, respectively. The value obtained for n describes nucleation of the α phase from β grain boundaries after site saturation[47] and is assumed to be constant for the entire transformation.

The data Malinov developed is useful for the range of cooling rates over which the kinetic function was derived. A typical TTT diagram will have a "C" shaped transformation curve, where the "nose" of the curve is the temperature where maximum diffusion and nucleation rates are occurring, leading to fastest transformation (shortest time to form α). At high temperatures, diffusion rates are fast and nucleation rates are slow while at low temperatures, nucleation rates (driving force for nucleation) are fast and diffusion is slow, leading to the "C" shaped behavior. The TTT diagram constructed based on Malinov's data, shown in Figure 7.1, does not have the typical "C" shape or nose where diffusion and nucleation rate are at a maximum. Malinov's calculated kinetic function, $k(T)$, goes to infinity with increased undercooling because cooling rates faster than 0.83K/s were not examined. This means that diffusion limitations at increased undercooling do not come into play. Because LMD can have a variety of cooling rates (predicted to range from 1 to 100K/s) for which data does not exist, kinetic data for cooling needs to be determined from available TTT diagrams that cover a wide range of cooling conditions.

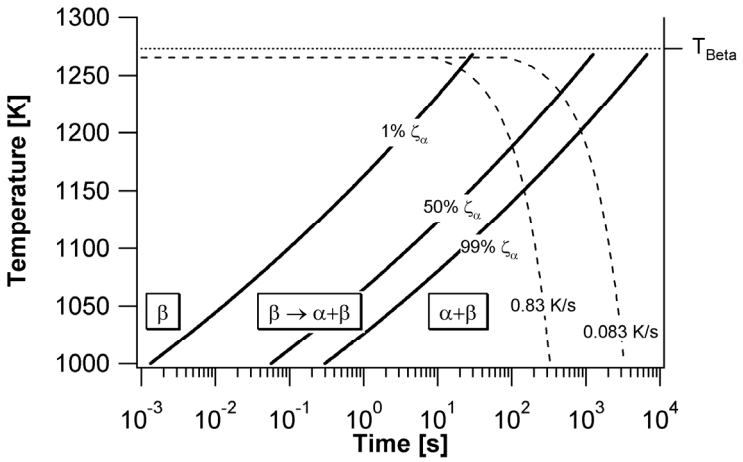

Figure 7.1: TTT diagram computed using the kinetics provided by Malinov (Ref.[27]). Isothermal transformation (extent of reaction, ζ_α) curves are shown for 1, 50 and 99 percent, and linear cooling curves (dashed) are shown for the range of Malinov's experiments (0.083 and 0.83 K/s).

A potential drawback to the additivity approach is the variance of kinetic parameters with the starting microstructure, i.e., parent phase grain size and inhomogeneities in the chemical composition. In this case experimental data is necessary for different starting conditions. In addition, Grong states that both diffusion controlled growth and dissolution of single particles satisfy the additivity condition as long as soft impingement (or overlapping diffusion fields) can be ignored.[119] The issues of soft impingement, grain size, and chemical inhomogeneities can be corrected by simply using an analytical approach (e.g., Fick's Second Law) to model diffusion controlled transformations.[105,120] The microstructural feature of interest is modeled in a local domain (diffusion cell). The volume fraction of a product phase is determined by the movement of the parent/product interface with time. The heat affected zone microstructural evolution during welding processes has been modeled this way for hypoeutectoid[98] and hypereutectoid[121] steels, and duplex stainless steels.[120,122]

In order to model nucleation and growth of the alpha phase during cooling this research will utilize the JMA approach, and a function describing the kinetic parameter $k(T)$ will be determined from available TTT diagrams. Complete data does exist in JMA form for nucleation and growth of Ti-6Al-4V alloys.

Dissolution

Considerably much less work has gone into the examination of applying additivity principles to diffusion controlled dissolution. Two notable cases are mentioned here. Hemmer and Grong

have modeled the dissolution of austenite in duplex stainless steels during welding.[120,122] They modeled dissolution of austenite by integrating Fick's first law over the weld thermal cycle. JMAK kinetics were derived by Elmer *et al.*[123] based on experimental time-resolved x-ray diffraction measurements during welding of Ti-6Al-4V. When applying the resulting kinetic parameters to continuous heating models, it is predicted that melting will occur before complete dissolution of the alpha phase. This is shown in Figure 7.2, where for heating rates greater than 100K/s melting occurs before the equilibrium beta fraction (1.0) is reached. The derived JMAK kinetic parameter that described the nucleation mechanism, *n*, has a value equal to 4. According to Christian, this suggests an increasing nucleation rate during discontinuous precipitation, polymorphic changes, or interface controlled growth.[111]

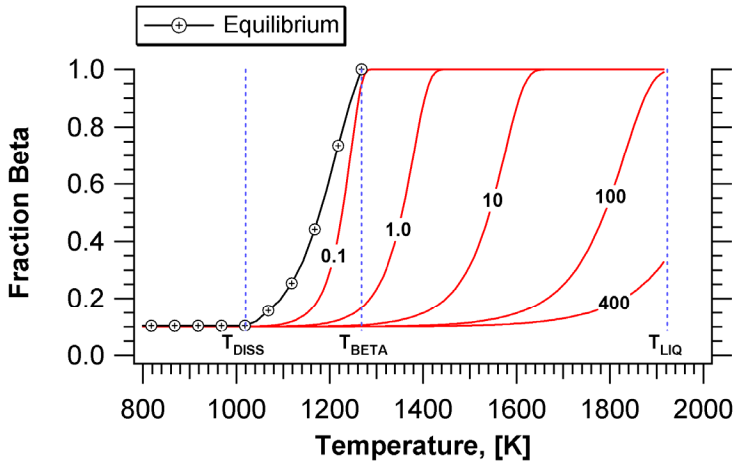

Figure 7.2: Computed beta fraction as a function of temperature for different linear heating rates (in K/s on the plot). The JMAK kinetic parameters are derived by Elmer *et al.* (Ref. [123])

In the current work, a simplistic approach to modeling the diffusion controlled dissolution of alpha has been chosen. This involves determining the diffusion controlled dissolution rate of the alpha phase using diffusion controlled transformation software. The parabolic thickening rate of the beta phase is derived from a series of modeled isothermal heat treatments, as described below.

Computational Tools

Using the available computational tools, ThermoCalc[124] and DiCTra,[54] a thermodynamic and kinetic approach to modeling diffusion controlled transformations can be achieved. The ThermoCalc method uses thermodynamic models to describe the Gibbs free energy as a function of composition, temperature, and pressure. Thermodynamic model parameters are obtained from

optimized experimental data. These parameters are contained in general (e.g., solid solution) and specific alloy-class (e.g., titanium alloys[125]) databases. DiCTra is based on the numerical solution of multiple component diffusion equations. The domain used is a diffusion cell that describes the local microstructure involved. A local equilibrium at the diffusing interface is assumed. The diffusion flux of a species is related to the chemical potential gradient and mobilities of the diffusing species. Coupling of thermodynamic and kinetic solutions is achieved by linking the two programs. Haidemenopoulos[126] used the aforementioned methods to model the rapid dissolution of pearlite and ferrite to austenite in a hypoeutectoid steel during laser hardening.

An additional tool used in the current work is JMatPro[127-129] which simulates material properties for different alloy compositions. JMatPro uses the same databases as ThermoCalc. As such, it can perform some of the similar thermodynamic simulations as ThermoCalc with the addition of calculating TTT diagrams, thermophysical, and mechanical properties as a function of alloy composition. TTT diagrams are based on JMA kinetics. Thermodynamic calculations are used to determine the nucleation parameters. Databases are queried for appropriate growth parameters. Lastly, there is some internal calibration to experimental values for specific alloy compositions.

Obtaining kinetic data and introducing the modeling equations

Phase equilibria

The measured[§§] bulk composition of the as-deposited material is shown in Table XIII. An examination of the phase equilibria for the composition measured in the middle of the deposit was made using the computational thermodynamic software, ThermoCalc Classic, v.P[130] and the associated titanium alloy database (TiDAT, v. 2)[125,131]. In addition, JMatPro v3.0[127] was used to calculate time-temperature-transformation (TTT) diagrams. The aforementioned titanium alloy database was also used in the JMatPro calculations. The TiDAT database allows for the effect of interstitial elements, namely oxygen, on the phase stability of titanium alloys.

[§§] Bulk composition measured by Luvak, Inc. Boylston, MA.

Table XIII: Alloy Composition in Weight Percent from As-Deposited Material Used in Modeling Experiments

Location	Al	V	Fe	O	C	N
Middle of Deposit	6.00	3.99	0.25	0.2035	0.021	0.013

Figure 7.3 shows the calculated equilibrium phase fraction as a function of temperature in the two-phase alpha and beta phase field for the alloy composition measured in the middle of the deposit. The beta transus is calculated to be T_{BETA}=1272.9K (1000°C), which is in agreement with literature values[132] for this alloy (1269±14K, 996±14°C). The dissolution temperature, T_{DISS}, is currently defined to be the temperature below which no microstructural changes will occur under diffusional transformation conditions. In Figure 7.3, T_{DISS} is calculated to be approximately 981K, corresponding to where the fraction alpha changes 1% between this temperature and room temperature. The room temperature fraction of alpha is calculated by ThermoCalc to be 96.2%; however, it is generally accepted that Ti-6Al-4V contains roughly 91%-α at room temperature.

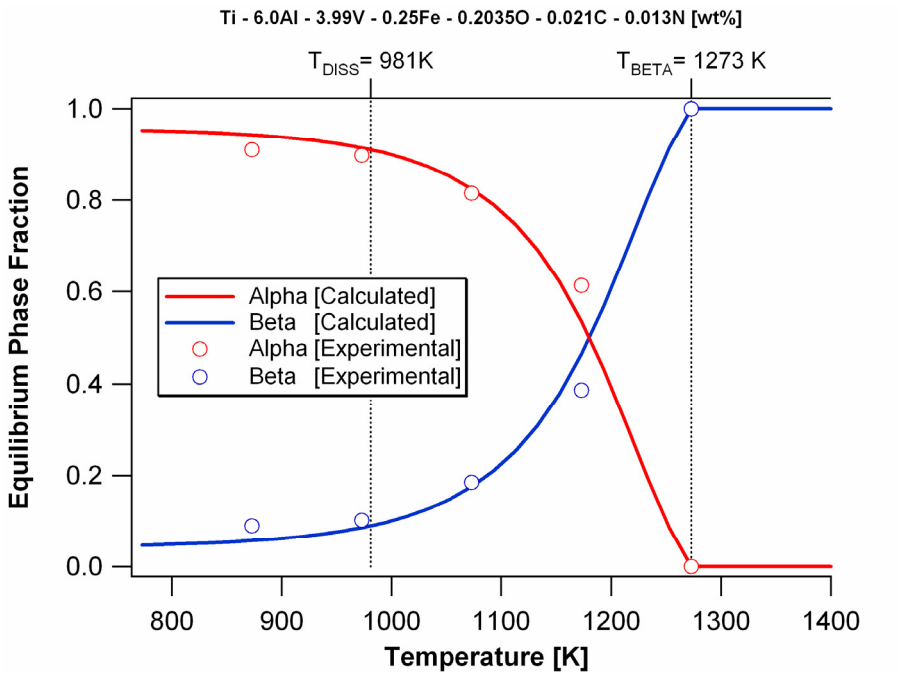

Figure 7.3: Calculated equilibrium phase fraction for the two-phase alpha (HCP) and beta (BCC) phase field in the as-deposited material. Experimental data is from ternary isothermal sections in Ref. [62].

Because ThermoCalc (computational thermodynamics) assumes an infinite time for equilibrium to occur, it predicts an equilibrium composition of beta that contains nearly 100% vanadium at

room temperature and an equilibrium fraction of only 3% beta. It is generally accepted that Ti-6Al-4V alloys contains around 10% beta at room temperature and from the as-deposited measurements the composition of vanadium is around 20%. Thus determination of the room temperature near-equilibrium conditions of the alpha and beta phases must be done from experimentally determined phase diagrams. Using the lowest isothermal section available[62] the phase fraction and composition for the Ti-6Al-4V alloy are determined and shown in Table XIV.

Table XIV: Phase amounts and composition for Ti-6Al-4V at 873K (From Ref. [62])

Phase	Phase Amount [%]	Aluminum [wt. %]	Vanadium [wt. %]
Alpha	91	6.0	2.2
Beta	9	2.4	26.8

In the microstructure model, the room temperature alpha/beta fraction will be assumed to be that reported in Table XIV: 91%-α and 9%-β. Thus, Figure 7.3 is modified slightly, with the alpha and beta fractions forced to 91% and 9% below a temperature of T_{DISS} = 981.2K as shown in Figure 7.4. The curves $f_{eq,\alpha}$ and $f_{eq,\beta}$ represent the equilibrium alpha and beta fractions as a function of temperature.

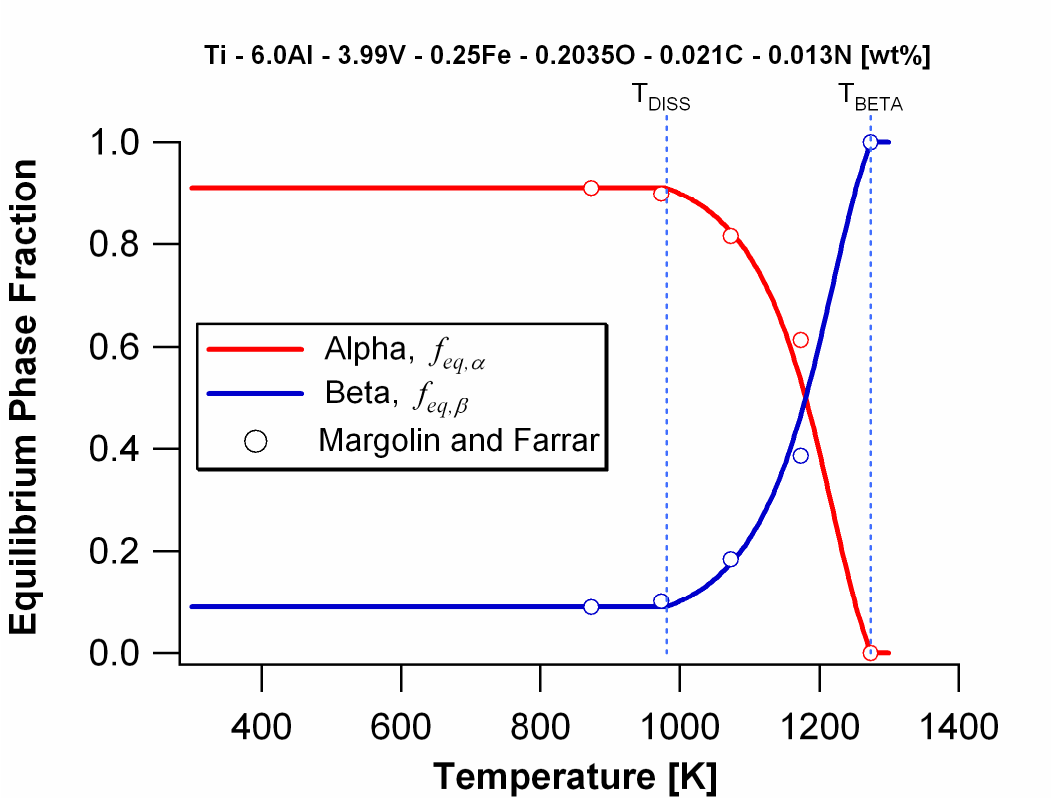

Figure 7.4: Equilibrium phase fraction curves used in microstructure modeling. The beta transus and dissolution temperatures are 1272.9 and 981.2 K, respectively. At room temperature, the alloy contains 91%-α + 9%-β. Experimental values from Margolin and Farrar, Ref. [62].

Reactions During Heating: Alpha Dissolution

Isothermal Heating

Simulating diffusion controlled transformations during heating allows for the determination of the isothermal growth rate. The method used to determine the isothermal growth rate is analogous to experimentally determining a TTT diagram for heating. The isothermal growth rate may then be used to determine the non-isothermal dissolution of alpha that occurs during heating, by using the rules of additivity. Note that dissolution of alpha is equivalent to growth of the beta phase (equations will be derived for the growth of beta and then converted to alpha fraction during the model calculations). A diffusion cell is set-up to represent the room temperature alpha and beta phase composition and fraction that is typically found in Ti-6Al-4V (91%-α, 9%-β). From these measurements we set up a diffusion cell in DiCTra to represent the room temperature alpha and beta phases. We assume the beta thickness is approximately 100μm, after TEM observations of the as-deposited material, and assume this represents a beta

fraction of 9%. The appropriate alpha size for the phase amounts shown in Table XIV is then determined. The diffusion cell is shown in Figure 7.5; note that half-thicknesses of the alpha and beta phases are used in the model. A linear grid of 1 nm spacing is used for both the alpha and beta phase is used in the simulation. Initially, the composition across each cell is assumed to be constant, according to Table XIV.

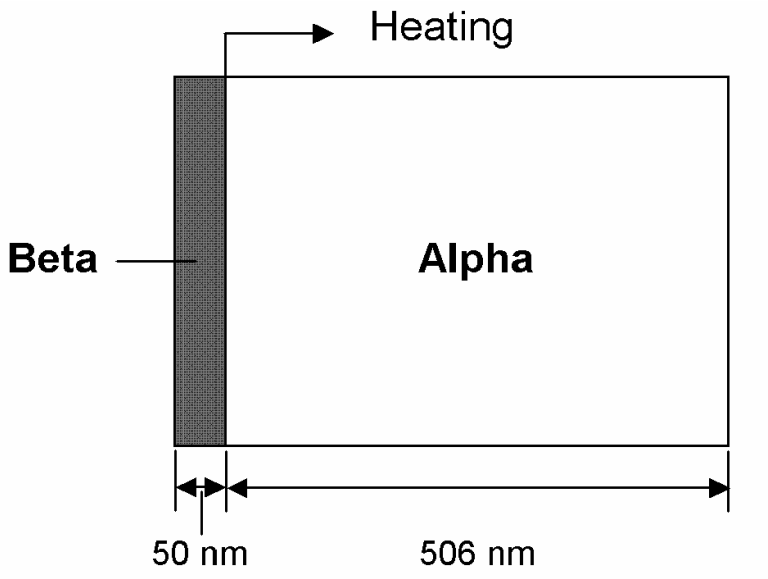

Figure 7.5: Diffusion cell used in DiCTra dissolution simulations, with the half-thicknesses of the phases shown.

For all simulations, the ThermoCalc solid solution (SSOL2)[133,134] and DiCTra mobility-2 (MOB2)[135] databases are used. The solid solution database predicts a beta transus of 1214.9K, which is 58K less than what is actually observed in this alloy (1272.9K). This discrepancy is a result of the solid solution database not considering the effect of oxygen on the alpha phase stability. In addition, the mobility database does not consider the diffusion of oxygen, and therefore, the more appropriate ThermoCalc titanium database (TiDAT) cannot be used, which does consider the effects of oxygen and hence would predict the correct beta transus. This necessitates extrapolating the isothermal growth rates to temperatures above 1213K so that the more accurate information may be used in the microstructure model.

First, simulated isothermal heat treatments are performed on the diffusion cell in Figure 7.5 of composition in Table XIV for a time of one hour. The isothermal temperatures ranged from 873K to 1213K with experiments performed at increments of 50K. An initial time step of 1E-9 seconds and a minimum time step of 1E-5 seconds were found to work well in all of the

simulations. The simulations were performed and the beta interface position as a function of time exported for further analysis. An example DiCTra script (macro file) can be found in the Appendix: DiCTra Simulation Macro.

The results of the isothermal heating experiments are shown in Figure 7.6, plotted as beta interface position as a function of time. Clearly with increasing isothermal temperature, the growth rate (slope) increases. In addition, temperatures greater than 1200 K will lead to nearly complete dissolution of the alpha phase.

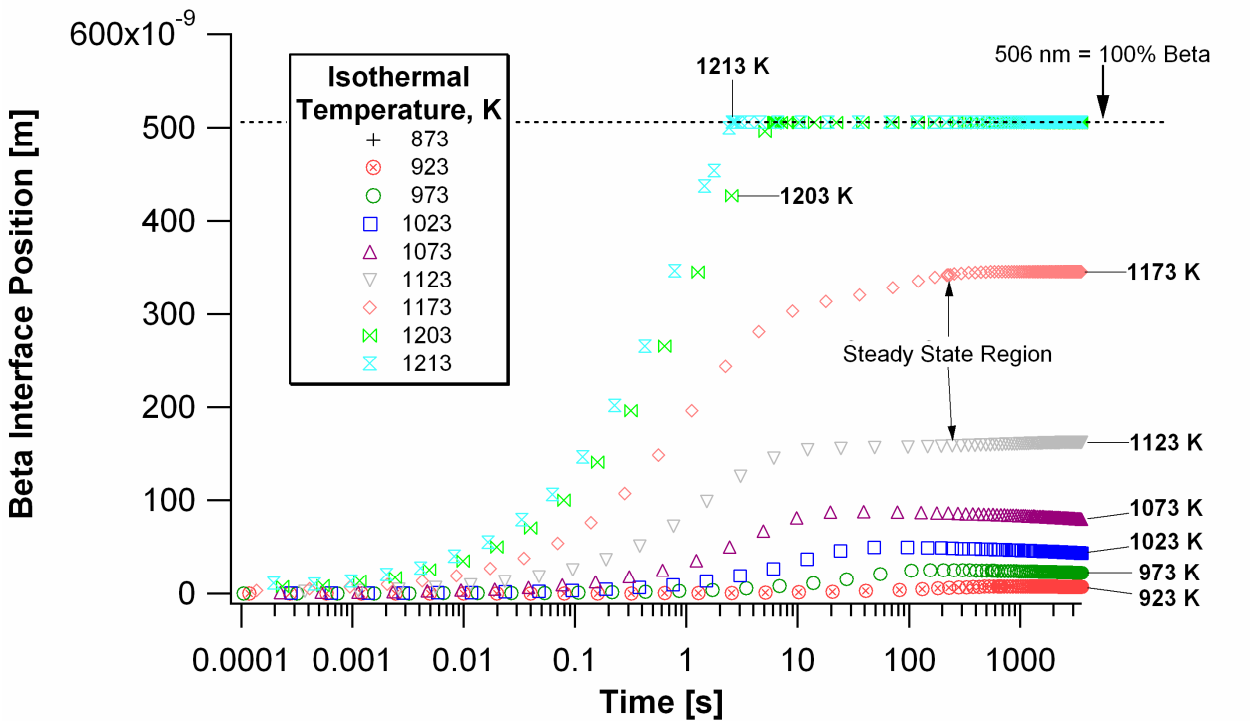

Figure 7.6: Beta interface position and extent of reaction plotted as a function of time for the isothermal DiCTra heating simulations.

The diffusion cell is modeling one dimensional plate growth, since we assume there is no nucleation of new beta phases during heating, thus the reaction takes place by diffusion controlled movement of the alpha/beta interfaces. As described by Whelan[136], isothermal plate growth can be modeled using Eq. [7.3], where B is the plate-half thickness, $\Omega = 2\ (C_i - C_0)\ /\ (C_p - C_i)$ is the supersaturation coefficient and D is the diffusivity. The composition (C) subscripts, p, i, and 0 refer to the plate, interface and matrix compositions, respectively. The plate and matrix refer to the alpha and beta phase, respectively.

$$B = B_0 - \frac{\Omega}{\sqrt{\pi}}\sqrt{Dt} \qquad [7.3]$$

If we plot the beta interface position as a function of $t^{1/2}$, as in Figure 7.7, we can use the slope to define the parabolic growth rate, $\alpha_{1,H}$ as a function of isothermal temperature. The initial linear portion of the beta interface as a function of $t^{1/2}$ was used to determine the slope. At intermediate isothermal temperatures, this may be an overestimate of the actual growth rate, noting the decreased slope of the curves after the initial linear portion.

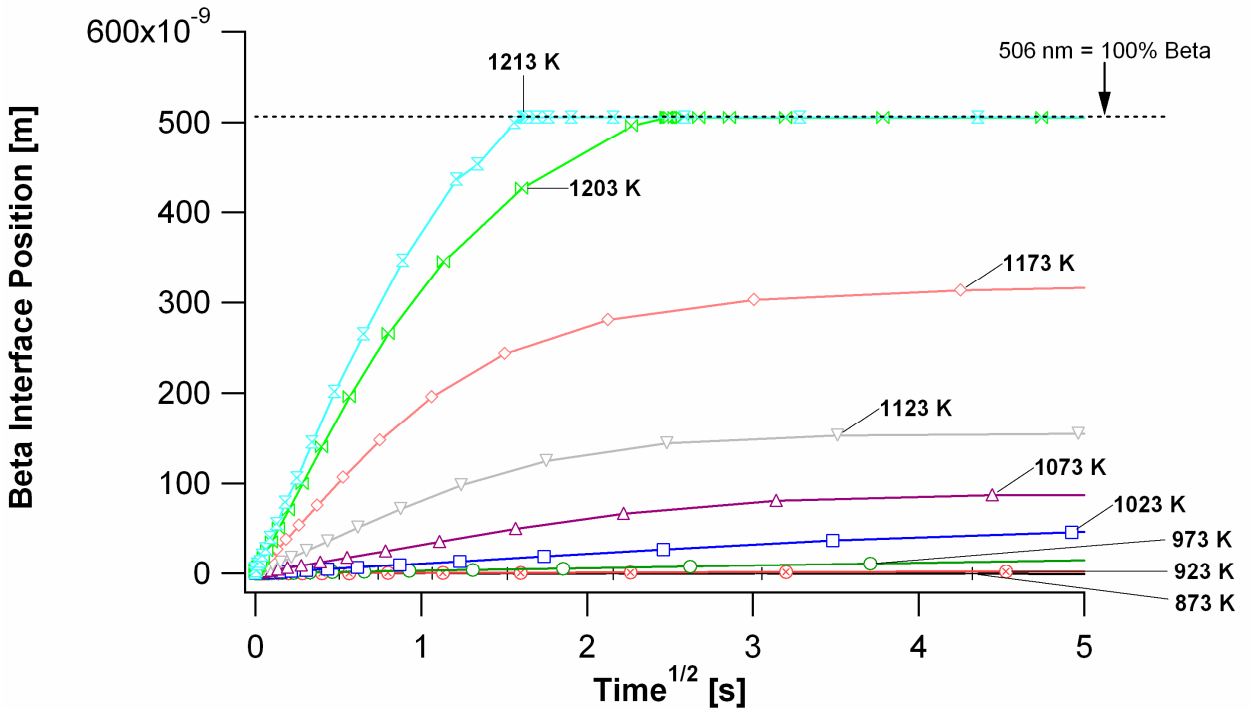

Figure 7.7: Beta interface and extent of reaction plotted as a function of the root of time. The initial linear portion of the curves is used to determine the slope, which is the isothermal parabolic growth rate.

Equation [1] must be modified slightly so that it can be used in the model. If we assume that the initial thickness of the beta particle is zero, and divide by the steady state size of the beta phase, $B_{SS,\beta}$, we can track the extent of the beta to alpha reaction, according to Eq. [7.4]. The steady state position of the beta interface at each isothermal temperature, indicated in Figure 7.6, is used to scale the position of the interface and parabolic growth rate to an "extent of reaction", or ζ. The extent of reaction is zero initially, and 1 when the thickness equals the steady state position of the interface, i.e., equilibrium has been obtained.

$$\zeta_\beta = \frac{B}{B_{SS,\beta}(T)} = \frac{\alpha_{1,H}(T)}{B_{SS,\beta}(T)} t^{1/2} = \alpha_{1,H,SS}(T) t^{1/2} \qquad [7.4]$$

The scaled individual parabolic growth rates are then plotted as a function of temperature and fit to a power law, $\alpha_{1,H,SS}(T)$, as shown in Figure 7.8. The parabolic thickening rate, $\alpha_{1,H,SS}(T)$, combines the diffusivity and supersaturation parameters in Eq. [7.3] into one parameter that is a function of isothermal temperature. In addition the parabolic thickening rate has been extrapolated in Figure 7.8 to account for true beta transus in this alloy, T_{BETA}=1273K.

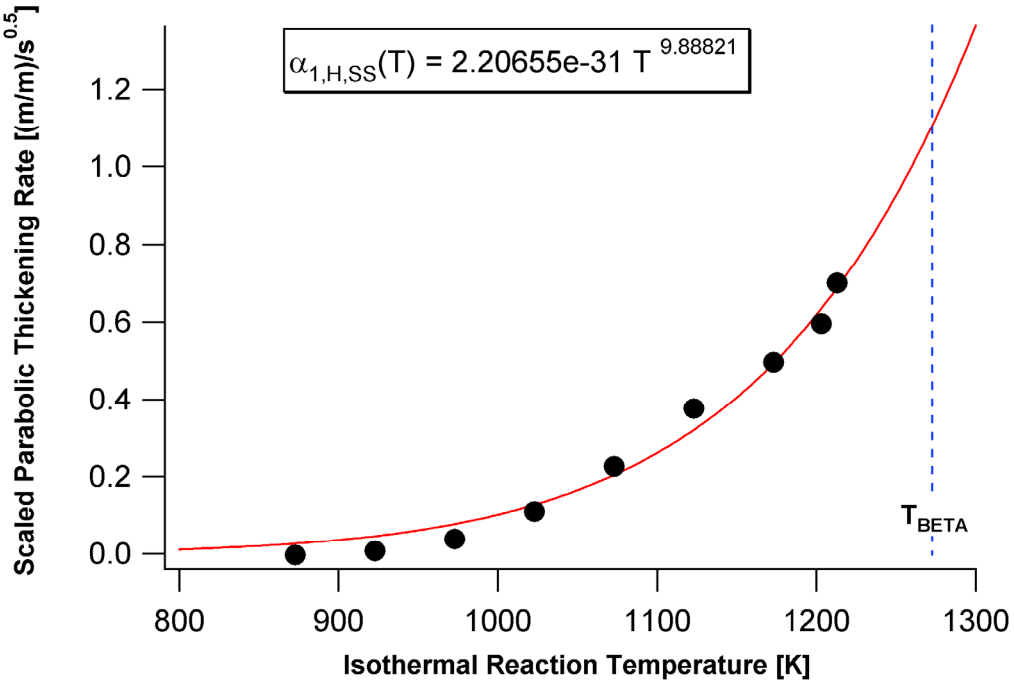

Figure 7.8: Beta interface growth rate, scaled using the steady state beta interface position, plotted as a function of isothermal reaction temperature, with the fitted equation shown, extended to the true beta transus of 1273K.

The extent of reaction is still insufficient to describe the dissolution reaction in terms of the beta phase fraction. Equation [7.4] is scaled using the equilibrium phase diagram fraction, $f_{eq,\beta}$ (Figure 7.4), of beta obtained from ThermoCalc using the TiDAT database and the AR-MID composition. The beta fraction is fit to a linear interpolation function in Mathematica, $f_{eq,\beta}(T)$, so that it may be used in the model. Equation [7.5] represents the evolution of the beta phase fraction, f_β, as a function of time and isothermal temperature.

$$f_\beta(t,T) = f_{eq,\beta}(T)\zeta_\beta(t,T) \qquad [7.5]$$

Equation [7.5] must be modified to account for starting phase fractions not equal to zero. Equation [7.6] introduces an equivalent time, t^*, representing the time required to transform the beta fraction at the initial temperature, $f_\beta(0,T_0)$, to the equilibrium amount at the current isothermal temperature, $f_{\beta,eq}(T_i)$. Equation [7.6] is determined by Eq. [7.5] evaluated at $f_\beta(0,T_0)$, for time.

$$t^* = \left(\frac{f_\beta(0,T_0)}{f_{\beta,eq}(T_i)\alpha_{1,H,SS}(T_i)} \right)^2 \qquad [7.6]$$

In addition, a critical time, t_{crit}, is introduced in Eq. [7.7] to determine when the reaction is complete ($\zeta_\beta = 1$), since the equation does not consider impingement.

$$t_{crit} = \left(\alpha_{1,H,SS}(T_i)\right)^{-2} - t^* \qquad [7.7]$$

We can now complete the definition for the extent of beta transformation as described in Eq. [7.8]

$$\zeta_\beta = \begin{cases} \dfrac{f_\beta(0,T_0)}{f_{\beta,eq}(T_0)} & t = 0 \\ \dfrac{f_\beta(t,T_i)}{f_{\beta,eq}(T_i)} = \alpha_{1,H,SS}(T_i)(t+t^*)^{1/2} & 0 < t \le t^* \\ 1 & t \ge t_{crit} \end{cases} \qquad [7.8]$$

A modeled isothermal transformation according to Eq. [7.8] is plotted Figure 7.9a, where for a room temperature starting fraction of 9% beta and an isothermal temperature of 1250K, equilibrium is achieved in about 1 second. The variation in beta fraction as a function of time and isothermal temperatures may be visualized in Figure 7.9b for a starting fraction at room temperature. Clearly at temperatures high in the beta phase field, the reaction is predicted to proceed rapidly to attain the equilibrium fraction at the specific isothermal temperature. The equilibrium fraction is indicated by the horizontal lines of constant beta fraction on the surface of the plot. At temperatures less than 1030 K, there is little change in the beta fraction from the starting room temperature fraction.

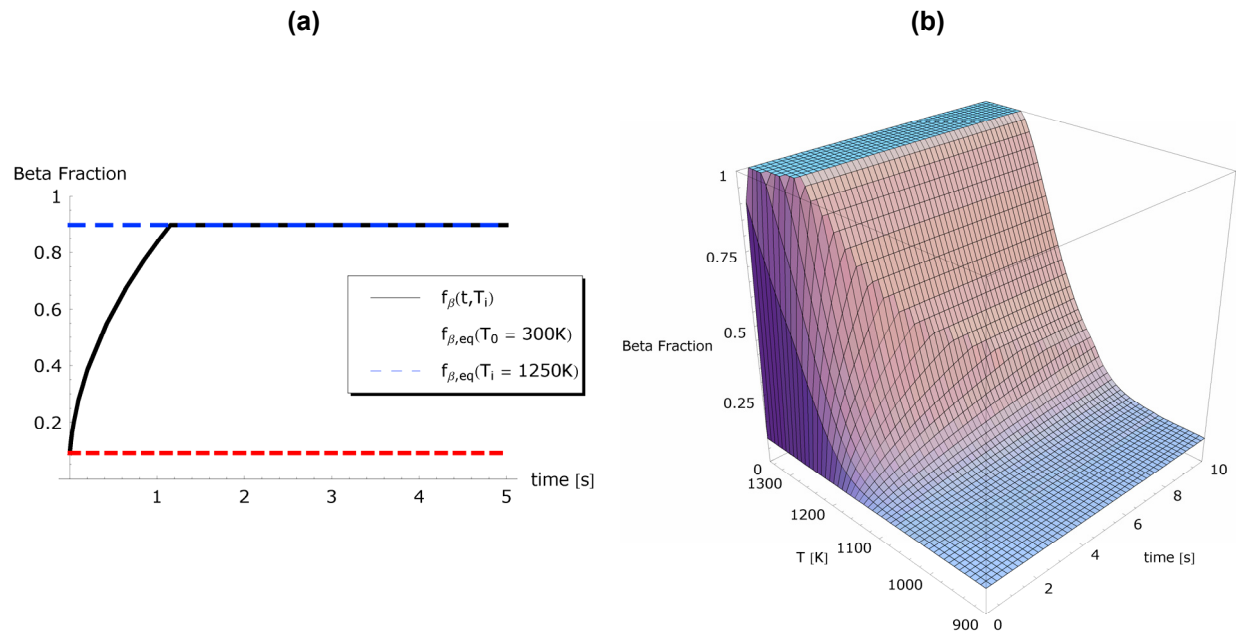

Figure 7.9: Beta fraction evolution determined from Eq. [7.5] as a function of time and (a) isothermal temperature of 1250 K and (b) as a function of temperature. The equilibrium fraction beta at 1250 and 300K are also shown in (a).

Figure 7.10 compares the extent of isothermal alpha dissolution reaction calculated using the dissolution model with the DiCTra calculations. A reasonable comparison is observed, especially at higher temperatures.

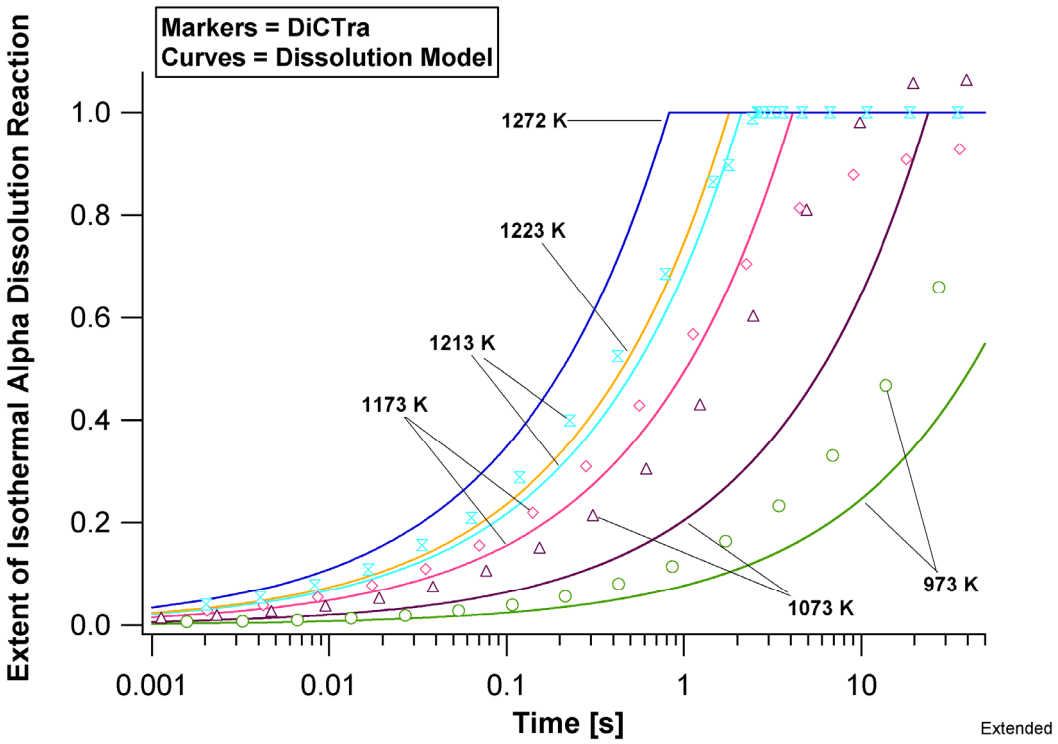

Figure 7.10: Comparison of DiCTra and dissolution model (Eq. [7.8]) calculations, plotting extent of isothermal alpha dissolution reaction as a function of time for several isothermal temperatures. DiCTra simulations were not performed for 1223 and 1273K.

Figure 7.11 shows a predicted (Eq.[7.8]) heating time-temperature-transformation diagram illustrating the extent of the alpha dissolution reaction assuming the initial amount of beta is negligible. This illustrates that during rapid up-quenching of an alpha/beta system, the dissolution reaction will proceed to completion rapidly, where as kinetic data from Elmer[123] suggests that the reaction proceeds about 1000 times slower. In this work, time-resolved x-ray diffraction techniques were used to measure the amount of beta present during spot welding of Ti-6Al-4V; however, JMA kinetic parameters were obtained using modeled temperature data, possibly leading to errors in their calculation. In addition, it is possible that oxygen contamination could stabilize the alpha phase leading to the perceived delay in complete transformation. Since alpha dissolution reaction involves only movement of the alpha/beta interface, the reaction should proceed quite rapidly as the temperature increases because of the increase in diffusion rates at elevated temperatures.

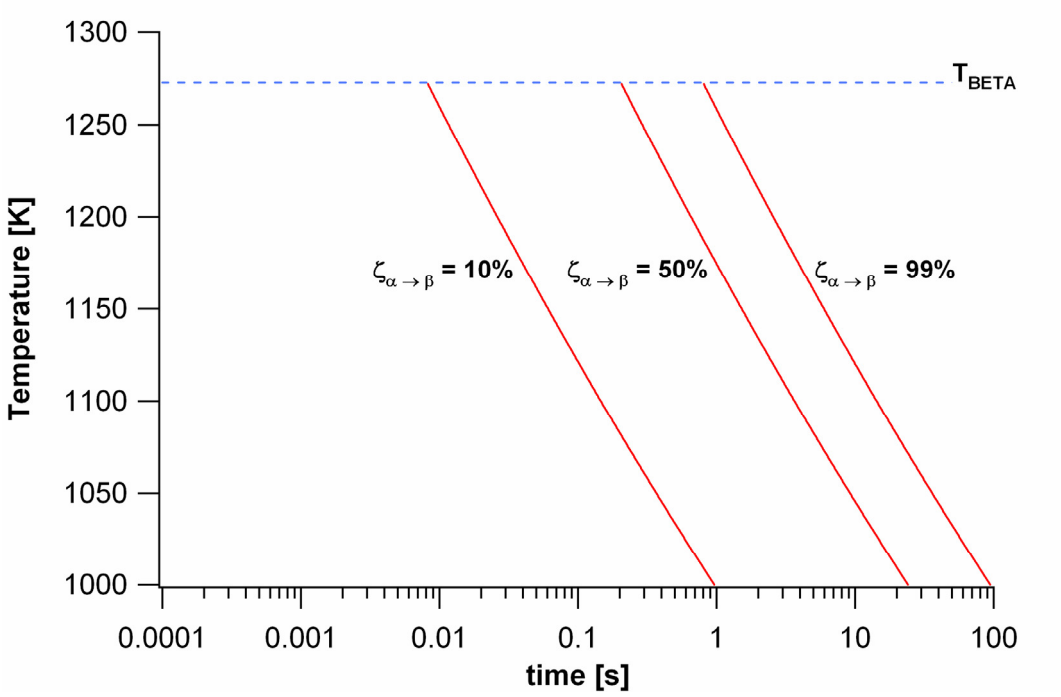

Figure 7.11: Heating TTT diagram showing the extent of the alpha to beta dissolution reaction for a system initially containing a negligible amount of beta.

Continuous (Linear) Heating

We are now at a position to extend the isothermal dissolution model to model continuous heating using a similar framework as outlined in Eqs. [7.6]-[7.8] for isothermal heating. Within this framework, the sum of the fraction evolved during many isothermal steps is used determine the overall evolution path. The fraction of beta, f_{i-1}, is known (by calculation or as an initial value) at the previous time step, t_{i-1}, and at a temperature, T_{i-1}. We need to calculate the fraction evolved during the next time step, t_i, and corresponding temperature, T_i. To do this, we first need to calculate an equivalent time t_i* at temperature T_i to develop the fraction evolved during the preceding time step (i-1) as shown in Eq. [7.9]. When $i=1$, Eq. [7.9] utilizes the initial fraction of alpha, f_0 at an initial temperature, T_0.

$$t_i^* = \left(\frac{f_{i-1}(t_{i-1}, T_{i-1})}{f_{\beta,eq}(T_i)\alpha_{1,H,SS}(T_i)} \right)^2 \qquad [7.9]$$

The fraction evolving during the ith time step is defined by Eq. [7.10], so long as the extent of reaction is less than 1, as defined by t_{crit} in Eq. [7.7]. The time increment Δt is equivalent to $t_i - t_{i-1}$.

$$\zeta_{\beta,i} = \frac{f_\beta(t_i, T_i)}{f_{\beta,eq}(T_i)} = \alpha_{1,H,SS}(T_i)(\Delta t + t_i^*)^{1/2} \qquad [7.10]$$

The process of calculating t^* followed by $\zeta_{\beta,i}$ is repeated until the dissolution reaction is complete. This is schematically shown in Figure 7.12 for a linear heating curve divided into three time steps, where $T_1<T_2<T_3$. During the initial time step, the reaction proceeds along **OA**, following the T_1 curve with the total fraction evolved at **A** being calculated by Eq. [7.10]. At the second time step, the temperature is increased to T_2, at which time an equivalent time (t_2^*) at this temperature is calculated and the reaction allowed to proceed along **BC**. At **C**, the temperature is increased to T_3, and similar calculations are made. The evolution of the reaction proceeds along the path **OA-BC-DE**. It is in this additive manner that a non-isothermal heat treatment may be modeled. [111]

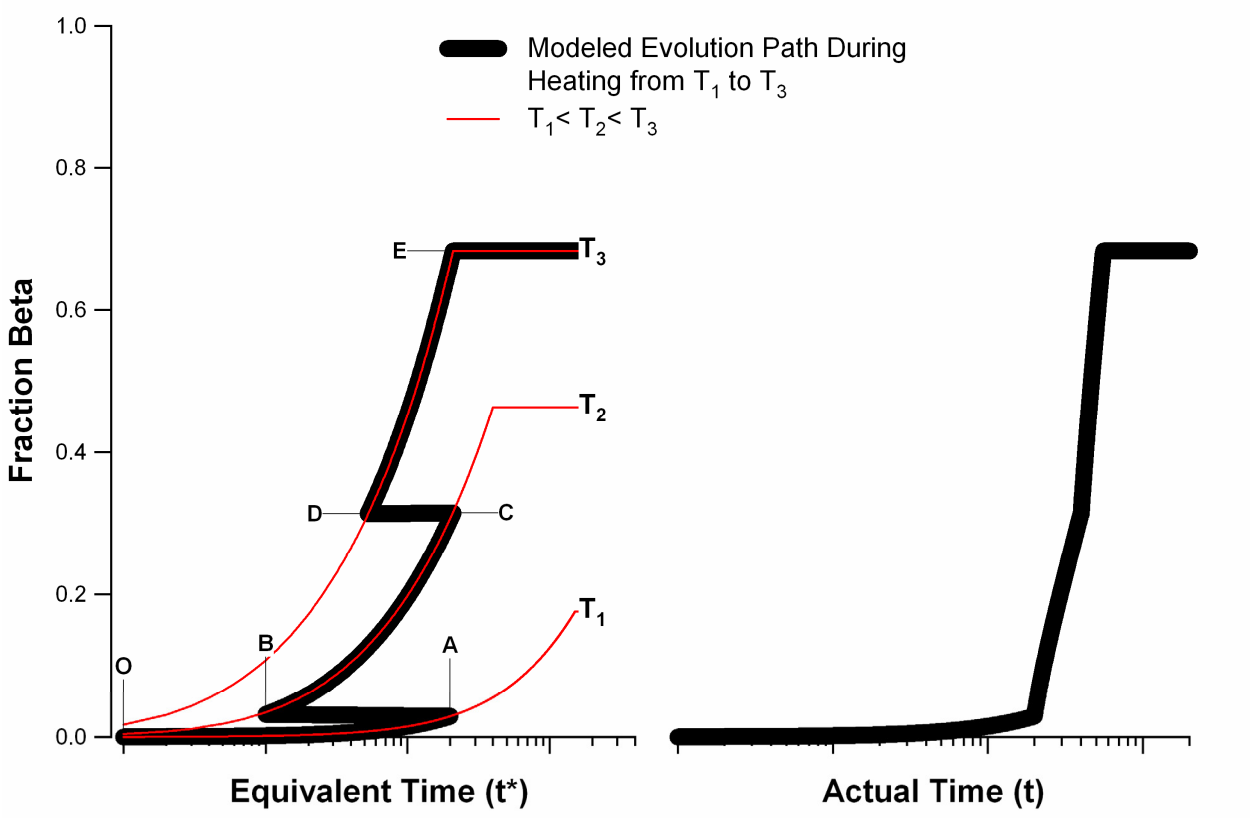

Figure 7.12: Schematic illustrating the evolution reaction during heating ($T_1<T_2<T_3$). Equivalent and actual times are shown on the left and right independent variable axes.

Figure 7.13 shows the application of Eq. [7.10] to continuous linear heating from 300 to 1400 K at rates ranging from 0.1 to 400 K/s. In the current model, elevation in the beta transus is observed for heating rates greater than 25K/s. At the 400K/s heating rate, a superheat of

approximately 112 K is required for complete transformation from a starting fraction equivalent to the room temperature beta fraction. Superheating[53,58] above the beta transus has been observed in titanium alloys [52], where rapid thermal treatment was attempted to be used as a beta grain refiner.

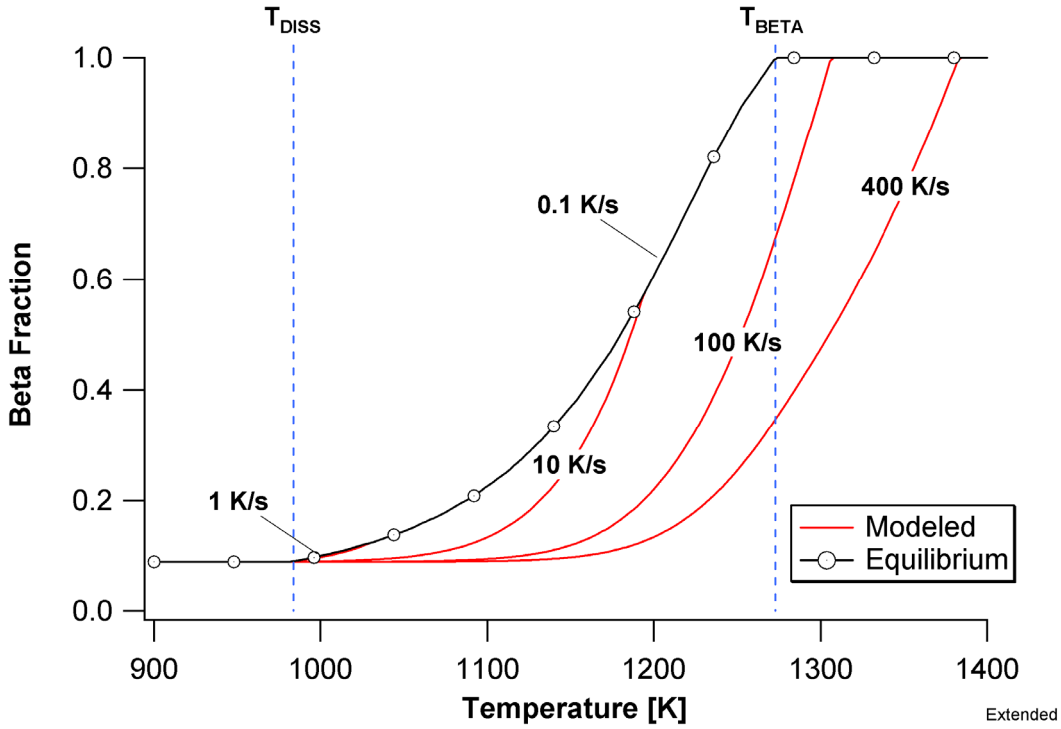

Figure 7.13: Modeled evolution of beta fraction during continuous heating.

A comparison of the elevation in beta transus determined from the current model and experimentally by Ivasishin[22,58] and Elmer[123] for various heating rates is shown in Figure 7.14. The amount of beta transus elevation calculated in the dissolution model is of the same order of magnitude as Ivasishin's data; however, Elmer's data predicts significantly higher transus values, most likely due to oxygen pickup (stabilizes the alpha phase) during testing or errors in the modeled thermal cycles used to predict the kinetics.

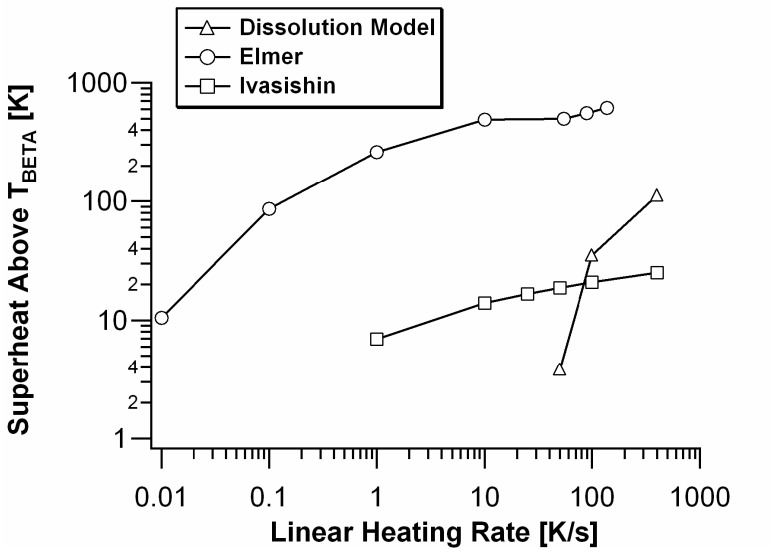

Figure 7.14: Comparison in the dissolution model and experimentally determined beta transus temperatures under different heating rates. Experimental data is from Elmer[123] and Ivasishin[22,58].

Reactions During Cooling: Alpha Nucleation and Growth

Isothermal Cooling

Upon cooling through the beta transus, primary-alpha (α_P) nucleates and grows first at prior beta grain boundaries as grain boundary alpha (α_{GB}), followed by growth of α_P sideplates or colonies from the α_{GB} and lastly at high undercooling intragranularly as basketweave α_P. For simplicity, these three morphological variants of α_P are considered as one, being modeled using a single JMA equation. One assumption that we must make is that the growing particles are spheres, instead of laths, plates or needles as is actually observed, and that their growth is controlled by long range diffusion. The kinetics of a reaction where spheres are growing due to long range diffusion have been described by Christian[111](Section 58), where the volume, v_τ, of a sphere nucleated during time τ, is described by Eq. [7.11]

$$v_\tau = \left(\frac{4\pi}{3}\right) r^3 = \left(\frac{4\pi}{3}\right)\left(\alpha_{3,C}\sqrt{D(t-\tau)}\right)^3 \qquad (t > \tau) \qquad [7.11]$$

The extent of a reaction is given by Eq. [7.12], which now includes the supersaturation term and considers impingement of randomly placed particles, where the kinetic parameter, $k(T)$ is given by Eq. [7.13] and contains the growth rate ($\alpha_{3,C}$) and nucleation rate per unit volume, I_V. The Avrami exponent, n, has a value of 5/2, representing all shapes growing from small dimensions

at a constant nucleation rate.[111] Equation [7.14] describes the extent of reaction as a function of temperature and time.

$$\zeta = 1 - \exp\left[-\Omega \int_0^t v_t I_V dt \right] \quad [7.12]$$

$$k(T) = \frac{8\pi}{15} \Omega I_V \left(\alpha_{3,C}(T) \right)^3 \quad [7.13]$$

$$\zeta = 1 - \exp[-k(T) t^n] \quad [7.14]$$

TTT diagrams exist for this alloy upon cooling, whereas for heating we had to rely on DiCTra to derive growth rates. We could (and have) also derive growth rates simulating the nucleation and growth of alpha phase during cooling, but the effect of interstitial elements, namely oxygen, cannot yet be modeled in DiCTra, leading to erroneous beta transus temperatures. The TTT diagram calculated by JMatPro[127,129] for the composition Ti - 6.0Al - 3.99V - 0.25Fe - 0.2035O - 0.021C - 0.013N [wt%] (labeled "AR-MID") is shown in Figure 7.15.

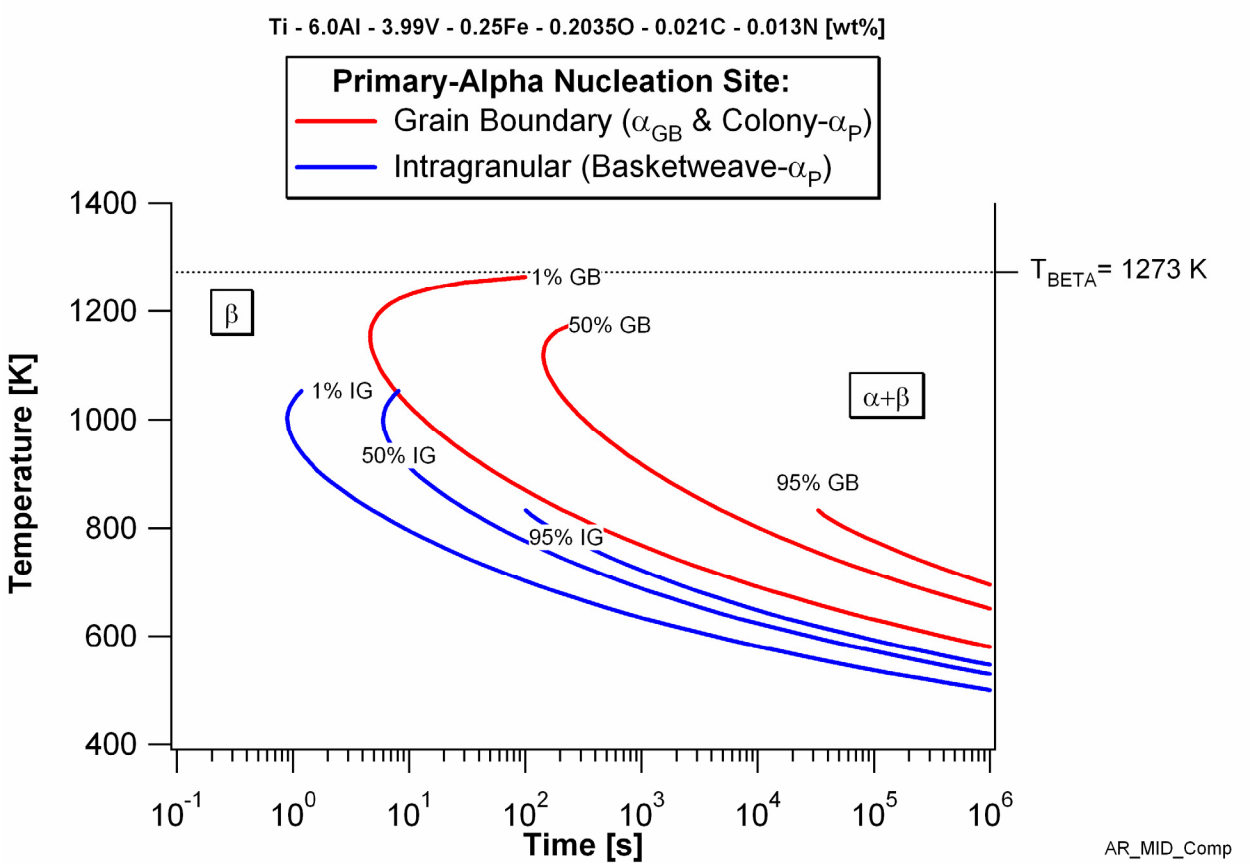

Figure 7.15: JMatPro calculated TTT diagrams for primary-alpha nucleation and growth. Curves for grain boundary (GB) nucleated α_{GB} and colony α_P and intragranularly (IG) nucleated basketweave-α_P are shown.

First, JMatPro considers the formation of alpha at prior beta grain boundaries (α_{GB} and colony-α_P sideplates) and intragranular (basketweave-α_P) nucleation sites. Recall that primary-alpha forms during cooling through the beta transus. In general terms, Saunders explains that JMatPro uses JMA kinetic equations, similar to Eq. [7.12]-[7.14], with variations in $k(T)$ and the Avrami exponent, n for the different morphologies.[127] The only specificities given are that nuclei densities consistent with formation at grain boundaries and dislocation sites are utilized for the grain boundary nucleated and basketweave morphologies.[137] As a result, each morphology is apparently defined by its own JMA equation, the grain boundary nucleated variant occurring at higher temperatures and a slower reaction time and the intragranular variant occurring at lower temperatures and faster incubation times. By decreasing I_V and/or n the time for a given extent of reaction will be delayed. In our current model, a single JMA equation describing both morphology variants is assumed, with an Avrami exponent of n=5/2.

Determination of a function for the kinetic term, $k(T)$, is rather straightforward using TTT diagrams generated in JMatPro. A single equation describing both grain boundary and intragranular nucleated primary-alpha morphologies is sought. The TTT curves provide an extent of reaction ($\beta \rightarrow \alpha_P$) at an isothermal temperature; therefore, solving $\zeta(T_i) = 0.01$ (Eq. [7.12]) for $k(T_i)$ will result in a kinetic parameter that is a function of temperature as shown in Figure 7.16. $k(T_i)$ was derived using the 1% JMatPro predicted TTT curves for grain boundary nucleated alpha for temperatures above 1100K. Below 1100K the 1% curve for intragranular nucleation was used. This function is rather complex due to the combining of two morphological α_P variant into one function. A linear interpolation function created in Mathematica is utilized in the modeling scheme. The peak in $k(T)$ near 1000K represents the greatest growth rate before approaching zero at temperatures near the beta transus and below 800K.

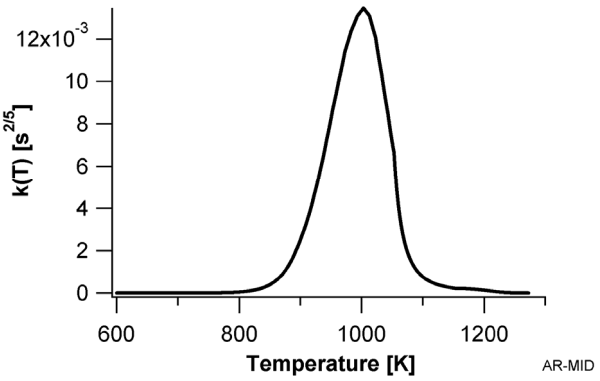

Figure 7.16: Kinetic parameter describing alpha nucleation and growth, derived from JMatPro TTT diagrams for the AR-MID composition.

The resulting modeled TTT diagram for 1 and 95% extent of transformation using the interpolating function defined by Figure 7.16 and Eq. [7.12] is shown in Figure 7.17 along with the JMatPro[127,129] predicted transformation curves from which the fitted kinetic function was derived. As can be seen in the modeled curve in Figure 7.17, $k(T)$ was determined using the 1% reaction curved for both the grain boundary and intragranular nucleation curves. An excellent fit is obtained for the 1% curve, while at 95% there is poor fit to the Widmanstätten curve and a fair fit to the basketweave curve. These differences could be due to variations in the Avrami exponent used in the JMatPro calculations; in the modeled calculation, n remained constant at 2.5.

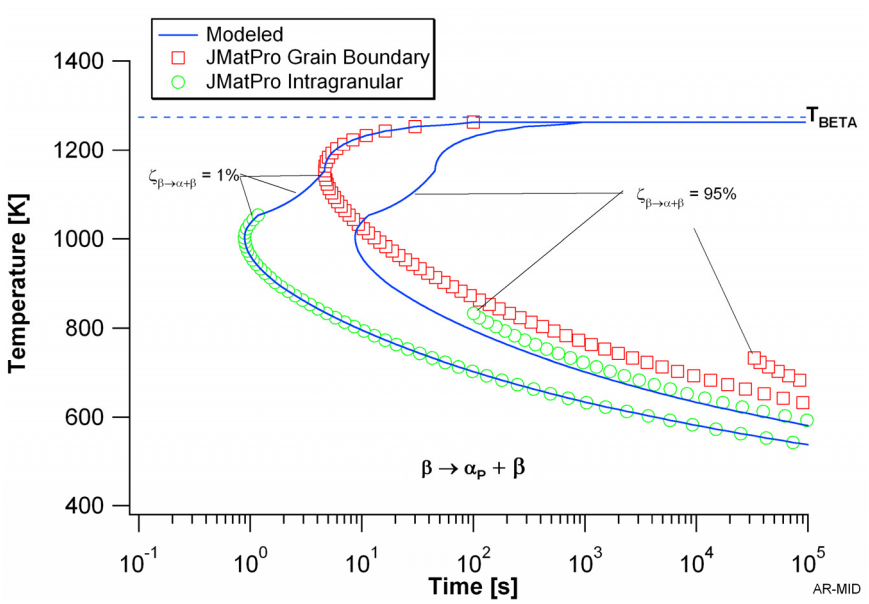

Figure 7.17: Modeled TTT diagrams using Eq. [7.12] and Figure 7.16 along with the JMatPro calculated curves for grain boundary (α_{GB} and colony α_P) and intragranular (basketweave-α_P) nucleation and growth in the alloy of AR-MID composition.

Figure 7.18 compares the calculated TTT start curves with other modeled and experimentally determined curves from the literature.[27,29,138,139] The experimental data lies over several time decades, indicating the variance in results that would be expected in using this approach. The JMatPro data lies with the range of experimental measurements.

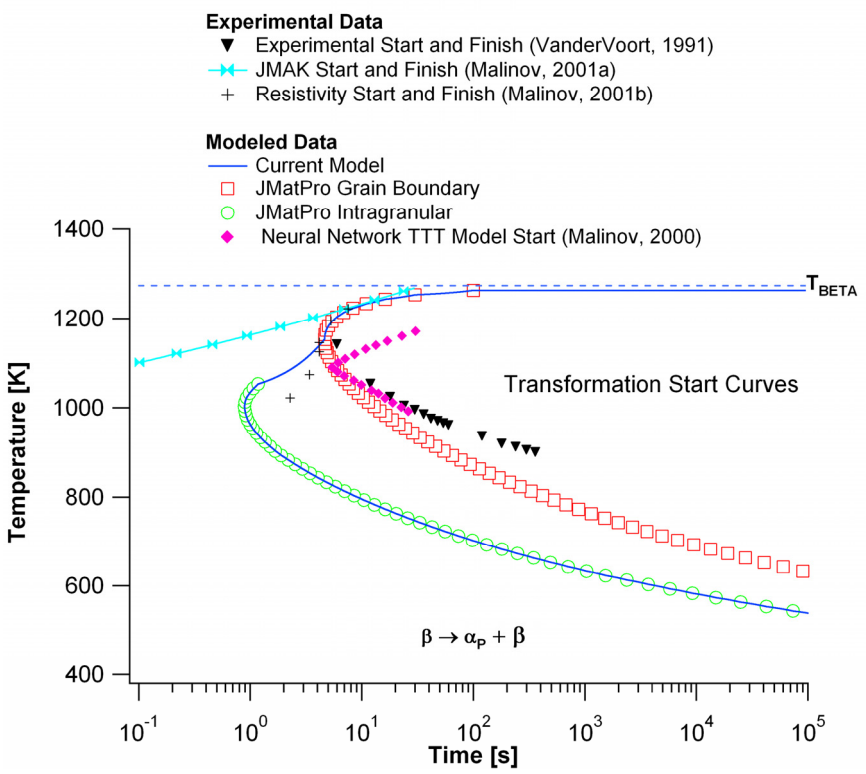

Figure 7.18: Comparison of modeled TTT start curves with experimental and modeled literature values.[27,29,138,139]

Continuous Cooling

Using the principles of additivity discussed previously for heating, the JMA model for isothermal nucleation and growth can be extended to consider nonisothermal growth. The cooling curve is first discritized into many isothermal time steps. Equation [7.14] is then used to determine the extent of reaction that proceeds during the initial time step. Next, an equivalent temperature, $t_{C,i}$*, is calculated according to Eq. [7.15] for the ith time step. A value of n=5/2 and the fitted equation for $k(T)$ were used.

$$t^*_{C,i} = \left(\frac{\ln(1-\zeta_{i-1})}{-k(T_i)} \right)^{1/n} \qquad [7.15]$$

The alpha fraction is determined by multiplying the extent of reaction (Eq.[7.14]) by the equilibrium phase composition: $f_\alpha(T_i) = \zeta_i * f_{\alpha,eq}(T_i)$.

Results of the nonisothermal cooling calculations are shown in Figure 7.19 for cooling rates ranging form 0.1 K/s to 400 K/s. Even at very slow cooling rates, there is an initial deviation from the equilibrium alpha fraction before attaining the room temperature equilibrium fraction.

The end result at cooling rates less than approximately 1 K/s is agreement with the experimental results of Malinov[27], who showed that for cooling rates less than 0.83K/s, a completely diffusion controlled transformation would be achieved. At 20K/s there is approximately 2% metastable beta present. With increased cooling rates, the fraction of metastable beta increases rapidly. At 400K/s, the alpha transformation has been completely suppressed. Any metastable beta present below M_S will transform to massive and or martensitic alpha.

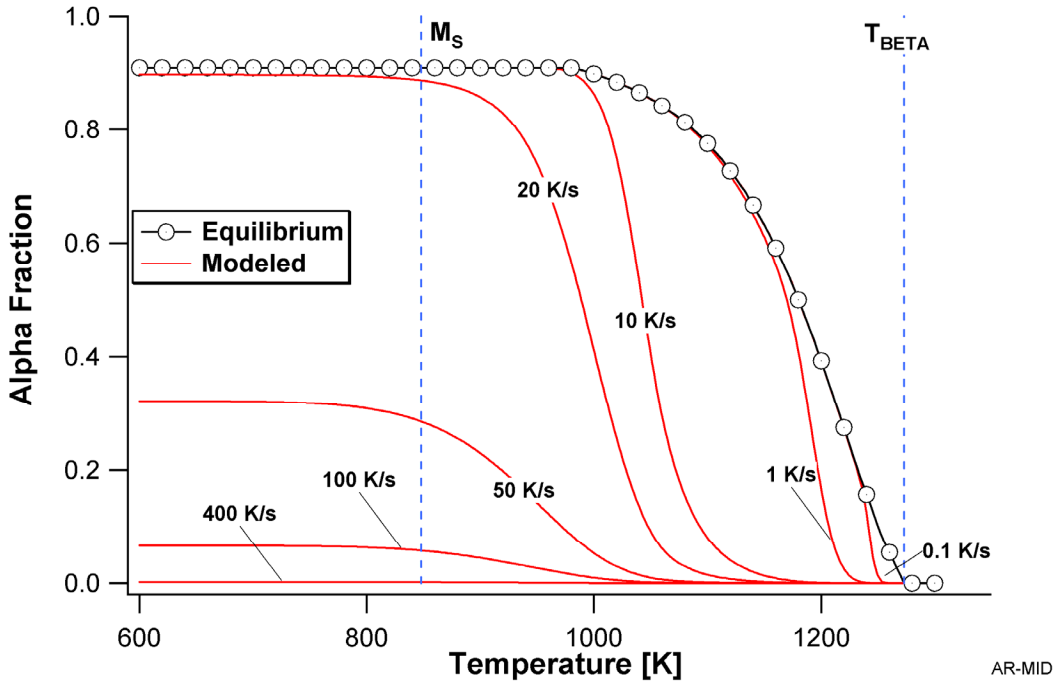

Figure 7.19: Modeled continuous cooling curves for various cooling rates. The equilibrium alpha fraction is also indicated. The M_S temperature is from Ref.[140].

At cooling rates greater than 20 K/s, the current model never attains the room temperature equilibrium value (91% α, 9% β), in agreement with the experimental results of Ahmed and Rack[28] who have shown that diffusion controlled transformations will persist for cooling rates less than 20K/s cooling rates. For cooling rates greater than 20K/s the amount of alpha continues to decrease with increasing cooling rate, indicating metastable beta. In addition, results presented in this thesis reinforce Ahmed and Rack's data by showing diffusion controlled transformation at 10K/s cooling rates. It should be noted that the using the kinetics obtained when the effect of interstitial elements (AR-MID composition) on the phase equilibria was necessary to match the result of Ahmed and Rack at cooling rates in the range of 8-20K/s. If interstitial element effects on phase equilibria not considered (a Ti-6Al-3.99V composition) in

the calculation of the JMatPro TTT calculated $k(T)$, the resulting microstructure model would begin forming metastable beta at 8K/s.

Modeling phase fraction evolution during heating and cooling

Summary of equations and parameters used in the phase fraction model

Now consider a thermal cycle where alpha dissolution and alpha growth occur during heating and cooling, respectively. The thermal cycle has been discretized into many small time steps, defined by T_i and t_i. The equilibrium phase diagram fraction of alpha determines the appropriate sub model (dissolution or growth) that is used for the ith time step. The model will utilize the guidelines in Eq. [7.16], where $f_{\alpha,eq}$ and $f_{\alpha,i}$ are the equilibrium and current alpha fractions. The appropriate sub model is chosen based on the equilibrium and current α fractions for the current temperature and time step (i).

$$\begin{array}{ll} f_{\alpha,i} > f_{\alpha,eq} & \text{Alpha Dissolution} \\ f_{\alpha,i} < f_{\alpha,eq} & \text{Alpha Growth} \\ f_{\alpha,i} = f_{\alpha,eq} & \text{Equilibrium} \end{array} \qquad [7.16]$$

Alpha dissolution is described by Eqs. [7.9]-[7.10] and alpha growth is described by Eqs. [7.12]-[7.15]. The equations used to model alpha dissolution and growth are summarized in Table XV, along with the associated coefficients and references to pertinent equations and figures. The subscript i refers to the current time step, i-1 refers to the previous time step, D refers to dissolution, and G refers to growth. The variable ζ refers to the extent of reaction. The flow of the phase fraction model calculations begins by checking the alpha fraction against the equilibrium fraction (Column 2 in Table XV) for the current (i^{th}) temperature and time step. Based on whether dissolution or growth is occurring, the appropriate equations in Column 3 are evaluated for the current temperature and time step. The phase fraction of alpha ($f_{\alpha,i}$) is stored for each time step. This process is repeated each time step in the entire thermal cycle. It should be noted that the calculations are currently performed separate from the thermal model. The Mathematica code to model phase fraction evolution is shown in the Appendix: Microstructure Model Code.

Table XV: Summary of Equations Used to Model Alpha Dissolution and Growth During Non-Isothermal Conditions.

Reaction	Equilibrium Criteria	Equation	Equation/Figure Reference Number
Alpha Dissolution	$f_\alpha > f_{\alpha,eq}$	$\alpha_{1,D,SS}(T_i) = a(T_i)^b$ $a = 2.21*10^{-31} \quad [K \cdot s^{-1/2}]$ $b = 9.89$	Figure 7.8
		$t^*_{D,i} = \left(\frac{f_{\beta,i-1}}{f_{\beta,eq}(T_i)\alpha_{1,D,SS}(T_i)} \right)^2$	Eq. [7.9]
		$t_{D,i,crit} = (\alpha_{1,D,SS}(T_i))^{-2}$	Eq. [7.7]
		$\zeta_{\beta,i} = \begin{cases} \alpha_{1,D,SS}(T_i)\left(\Delta t_{(i)-(i-1)} + t^*_{D,i}\right)^{1/2} & 0 < \Delta t_{(i)-(i-1)} + t^*_{D,i} \le t_{D,i,crit} \\ 1 & \Delta t_{(i)-(i-1)} + t^*_{D,i} > t_{D,i,crit} \end{cases}$ $f_{\alpha,i} = 1 - f_{\beta,i} = 1 - f_{\beta,eq}(T_i)\zeta_{\beta,i}$	Eqs. [7.8], [7.10]
Alpha Growth	$f_\alpha < f_{\alpha,eq}$	$k(T_i) \equiv InterpolatingFunction(T_i)$	Figure 7.16, Eq.[7.13]
		$t^*_{G,i} = \left(\frac{\ln\left(1 - \frac{f_{\alpha,i-1}}{f_{\alpha,eq}(T_i)}\right)}{-k(T_i)} \right)^{1/n}$	Eq. [7.15]
		$\zeta_{\alpha,i} = 1 - \exp\left[-k(T_i)\left(\Delta t_{(i)-(i-1)} + t^*_{G,i}\right)^n\right]$ $f_{\alpha,i} = f_{\alpha,eq}(T_i)\zeta_{\alpha,i}$ $n = 5/2$	Eq. [7.14]
Equilibrium	$f_\alpha = f_{\alpha,eq}$	Ti - 6.0Al - 3.99V - 0.25Fe - 0.2035O - 0.021C - 0.013N [wt%] Phase Diagram at T_i	Figure 7.4

Application to generic linear heating and cooling cycles

The modeled results for linear heating and cooling cycles are shown in Figure 7.20, for different heating and cooling rates and peak temperatures. According to Eq. [7.16], when the alpha fraction is greater than equilibrium, dissolution is occurring and when the alpha fraction is less than equilibrium, growth is occurring. The intersection of the equilibrium curve with the

modeled curve near the peak temperature is where equilibrium has been attained and alpha dissolution ceases and growth begins.

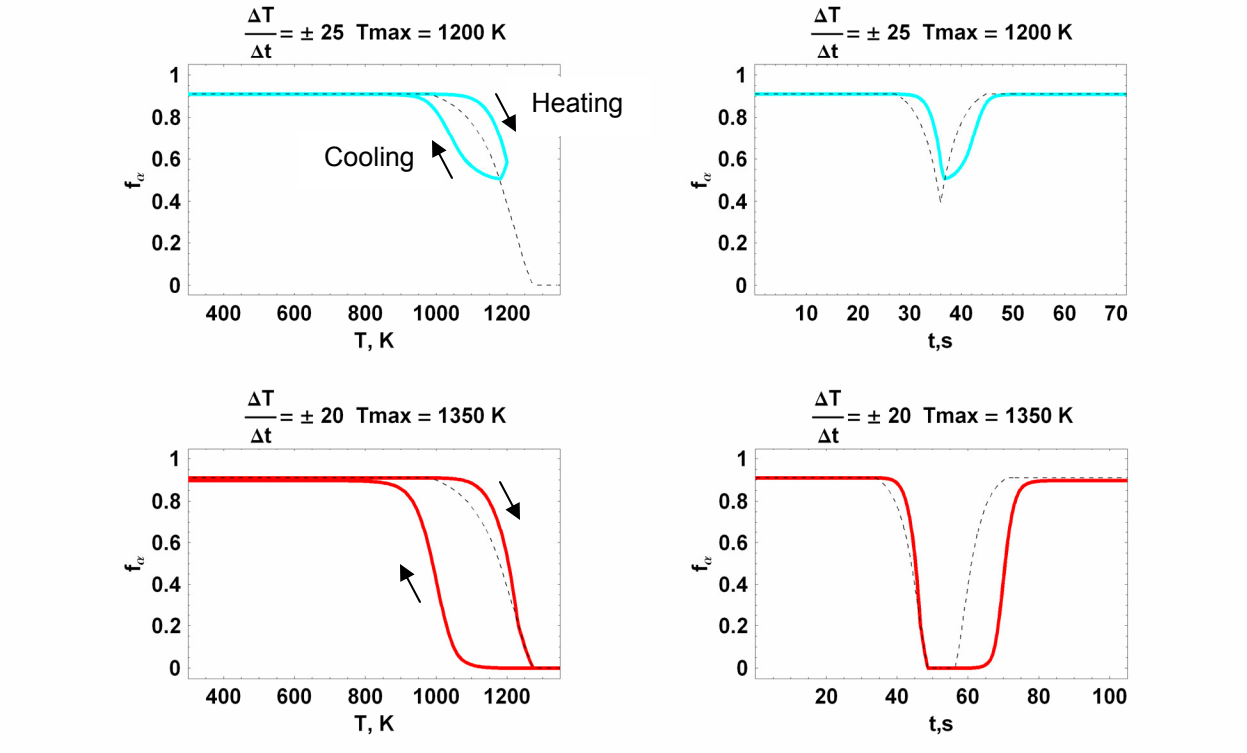

Figure 7.20: Alpha fraction plotted as a function of temperature (column 1) and time (column 2) for different heating and cooling rates and peak temperatures as indicated. The equilibrium fraction is shown as a dashed curve in all figures.

For a peak temperature of 1200K and heating and cooling rates of 25K/s, about 50% alpha is present at the maximum temperature, about 10% less than equilibrium would predict. Note from the f-t curve, the point where equilibrium is attained and dissolution stops is a few seconds after the peak temperature (as indicated by the sharp peak in the equilibrium curve). That is, during initial cooling the alpha dissolution is still occurring, since equilibrium has not been attained. In both cases, there is no metastable beta present after cooling to room temperature.

Application to synchrotron experiments

Recently, experiments have been performed to accurately measure the volume fraction of alpha and beta present during thermal cycling above and below the beta transus.[141] In these experiments, thermal cycling at heating and cooling rates of 20 K/s were performed to temperatures ranging from 873 to 1373 K. Resistance heating (similar to a Gleeble

thermomechanical simulator) was used to heat the sample in an inert chamber while synchrotron radiation (Advanced Photon Source, Argonne National Laboratory) was used to produce diffraction patterns, recorded at 3 second intervals. The resulting phase amounts can be calculated. When the same thermal cycles are used as input to the current phase fraction model, there is good agreement between the model and experiment, as shown in Figure 7.21.

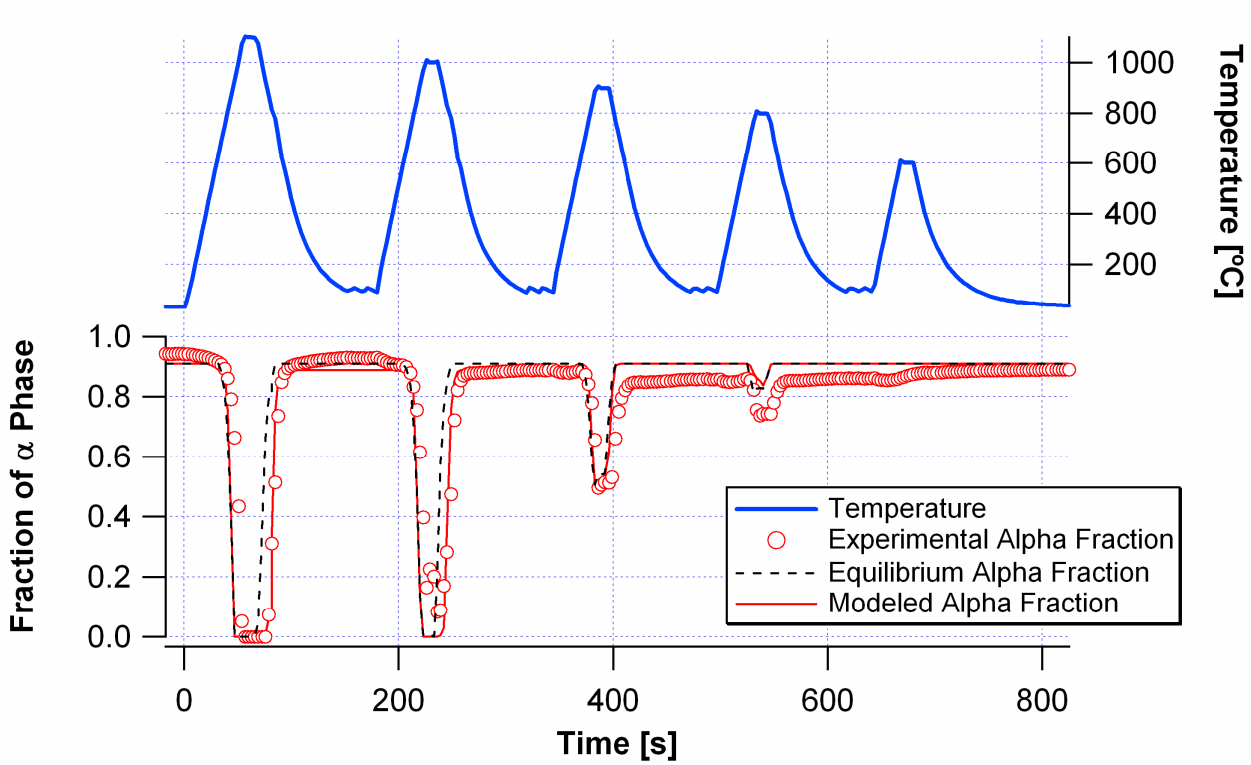

Figure 7.21: Experimental[141] data measured during time resolved x-ray diffraction experiments compared with data obtained from the phase fraction model and equilibrium phase diagram.

The exceptions to the agreement occur during the 2nd cycle, and the residual beta that is retained after repeated thermal cycling (best seen after 400s). During the second cycle, the model predicts a complete transformation to beta, while the experimental data shows about 10% alpha remaining, despite being at the beta transus temperature (1000°C). From the third cycle onward, the experiment predicts about 15% beta after cooling below 873 K, while the model predicts 10% beta. Both of these differences can be explained in terms of retained vanadium in the beta phase.[141] If vanadium diffusion is sluggish in the alpha phase at these heating and cooling rates, it would explain the retained beta at room temperature because the beta phase is stabilized and therefore more of it remains at room temperature. At elevated temperatures, specifically during the second pass in Figure 7.21, the same argument would mean that the alpha phase is depleted

in vanadium and hence alpha stabilized, meaning that a complete transformation to beta would happen slower relative to equilibrium heating and cooling. The current model does not take into account composition variations during thermal cycling, yet there is still good agreement with experimental data.

Modeling alpha morphology evolution

The information in the previous section shows how alpha phase fraction evolves with time. The morphology model examines the different alpha morphologies that evolve during thermal cycling. Reexamination of the TTT diagram for alpha growth (Figure 7.15) indicates that if isothermal holding takes place above 1100K, only grain boundary nucleated alpha will form. This temperature, T_{IG}=1100K, is the temperature below which both intragranularly nucleated alpha forms. The assumption is made for the kinetics describing grain boundary nucleated reactions, the fraction of α_{GB} (outlines prior beta grain boundaries) is negligible and the dominant morphology above T_{IG} is colony-α. Below T_{IG}, the driving force for nucleation is high and nucleation occurs intragranularly typically forming the basketweave-α morphology. The morphology model considers any alpha formed above T_{IG} to form as colony-α ($f_{C\text{-}\alpha}$) and below, basketweave-α ($f_{BW\text{-}\alpha}$). The total amount of these two morphologies at a temperature, T_i, must equal the fraction alpha at the temperature, $f_\alpha(T_i)$, according to Eq.[7.17].

$$f_\alpha(T_i) = f_{C-\alpha}(T_i) + f_{BW-\alpha}(T_i) \qquad [7.17]$$

The morphology evolution is illustrated in a simple example. Consider a sample that receives a primary and secondary heat treatment as schematically shown in Figure 7.22. Upon cooling through the beta transus 10% alpha forms before the temperature drops below T_{IG}. The alpha morphology at T_{IG} will be: $f_{C\text{-}\alpha}$ = 10% and $f_{BW\text{-}\alpha}$ = 0% (point **B**). Upon cooling to room temperature the alpha morphology will be $f_{C\text{-}\alpha}$ = 10% and $f_{BW\text{-}\alpha}$ = 80%, with the overall phase fraction being f_α = 90% and f_β = 10% (point **C**). Equations [7.18]-[7.20] describe the morphology evolution above and below T_{IG} during alpha growth. The subscript "*FD*" refers to a "final" amount when the transition from alpha "dissolution" to growth occurred. The subscript "*FG*" refers to the "final" amount of a morphology when the transition from "growth" to dissolution occurs.

$$\left.\begin{aligned} f_{C-\alpha}(T_i) &= f_{C-\alpha,FD} + \left(f_\alpha(T_i) - f_{\alpha,FD}\right) \\ f_{BW-\alpha}(T_i) &= f_{BW-\alpha,FD} \end{aligned}\right\} \quad T_i > T_{IG} \qquad [7.18]$$

$$f_{C-\alpha,FG} = f_{C-\alpha}(T_{IG})\Big\} \quad T_i = T_{IG} \qquad [7.19]$$

$$\left.\begin{aligned} f_{C-\alpha}(T_i) &= f_{C-\alpha,FG} \\ f_{BW-\alpha}(T_i) &= f_\alpha(T_i) - f_{C-\alpha,FG} \end{aligned}\right\} \quad T_i < T_{IG} \qquad [7.20]$$

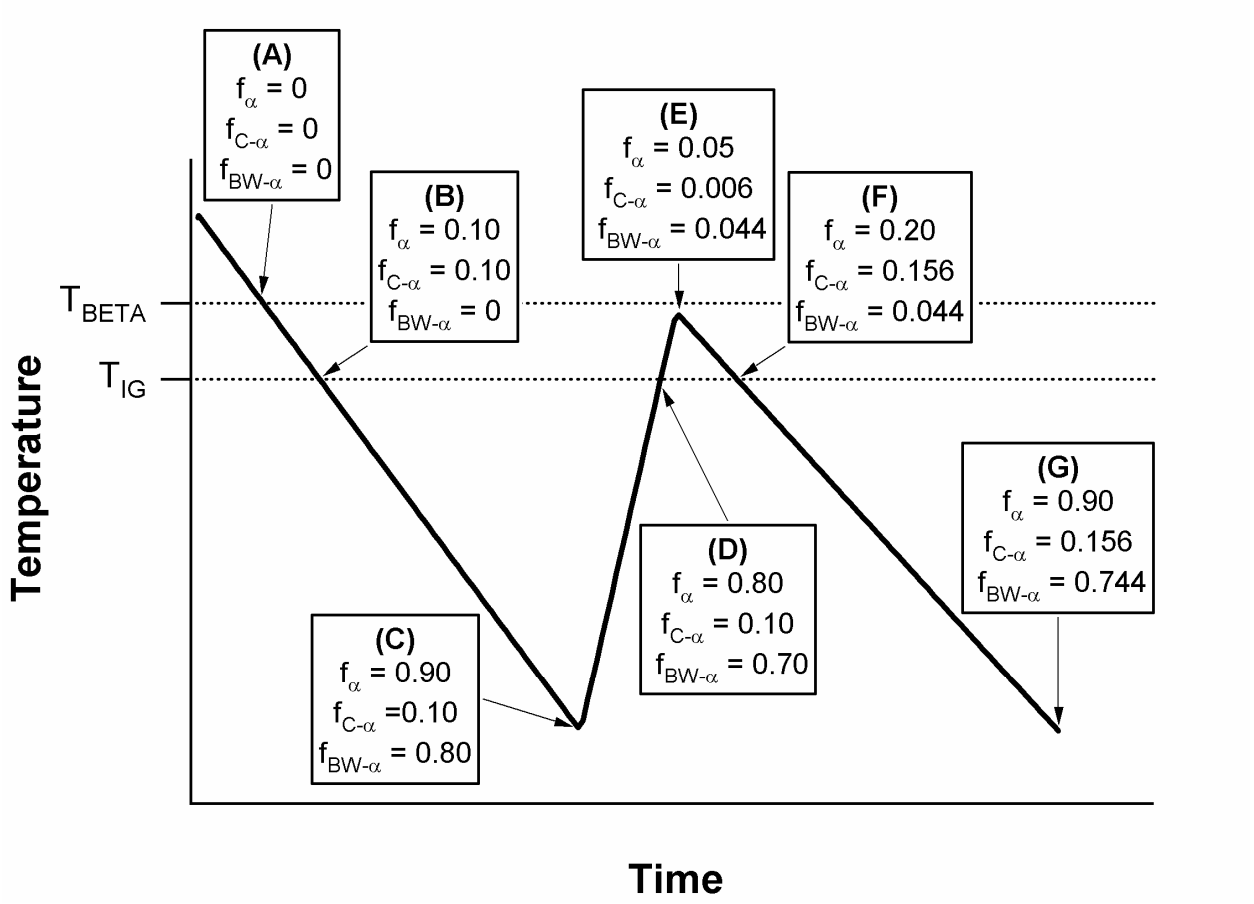

Figure 7.22: Schematic illustrating the alpha phase fraction (f_α), colony- ($f_{C-\alpha}$) and basketweave- ($f_{BW-\alpha}$) alpha evolution during a primary and secondary heat treatment.

During alpha dissolution below T_{IG}, it is assumed that only basketweave dissolves, with $f_{C-\alpha}$ remaining constant, equivalent to the value when T_{IG} was last intersected during growth, $f_{C-\alpha,FG}$, where the subscript "*FG*" means "final" value during "growth." Morphology dissolution below T_{IG} is described by Eq. [7.21].

$$\left.\begin{aligned} f_{C-\alpha}(T_i) &= f_{C-\alpha,FG} \\ f_{BW-\alpha}(T_i) &= f_\alpha(T_i) - f_{C-\alpha,FG} \end{aligned}\right\} \quad T_i < T_{IG} \qquad [7.21]$$

Above T_{IG}, both basketweave- and any existing colony-α dissolve in the same proportion such that when the alpha fraction is zero, the amount of basketweave- and colony-α is also zero. Morphology dissolution above T_{IG} is described by Eq. [7.22].

$$\left.\begin{aligned} f_{C-\alpha}(T_i) &= \frac{f_{C-\alpha}(T_{IG})}{f_{\alpha}(T_{IG})} * f_{\alpha}(T_i) \\ f_{BW-\alpha}(T_i) &= \frac{f_{BW-\alpha}(T_{IG})}{f_{\alpha}(T_{IG})} * f_{\alpha}(T_i) \end{aligned}\right\} \quad T_i \geq T_{IG} \qquad [7.22]$$

where,

$$f_{C-\alpha}(T_{IG}) = f_{C-\alpha,FG}$$

$$f_{BW-\alpha}(T_{IG}) = f_{\alpha}(T_{IG}) - f_{C-\alpha,FG}$$

Continuing with the example in Figure 7.22 above, at the start of dissolution ($T=T_{DISS}$) the alpha morphology consists of 10% colony-α and 80% basketweave-α (point **C**). At $T=T_{IG}$, the alpha-fraction is f_{α} = 80%, and the morphology fractions will be $f_{C\text{-}\alpha}$=10% and $f_{BW\text{-}\alpha}$=70%, i.e., 10% of the basketweave-α has dissolved (point **D**). Further heating to just below the beta transus yields an f_{α}=5%. Since both morphologies are assumed to dissolve in the same proportion, at the peak temperature there will be $f_{C\text{-}\alpha}$ = 0.6% and $f_{BW\text{-}\alpha}$=4.4% (point **E**).

Once alpha growth begins again, $f_{BW\text{-}\alpha,FD}$ and $f_{C\text{-}\alpha,FD}$ is set. When alpha growth begins during cooling from a peak temperature above T_{IG} the only alpha to form is colony-α, the fraction described by Eq.[7.18]. At $T=T_{IG}$ assume f_{α} = 20%, then there will be $f_{C\text{-}\alpha}$=15.6% and $f_{BW\text{-}\alpha}$=4.4% (point **F**). Upon cooling to room temperature f_{α} = 90% and growth of the colony-α has ceased, leading to an overall alpha morphology of $f_{C\text{-}\alpha}$=15.6% and $f_{BW\text{-}\alpha}$=74.4% (point **G**) as described by Eq. [7.21].

It has been assumed that during a thermal cycle above T_{IG} any alpha to form does so intragranularly even though the kinetics (k(T)) were derived (TTT diagram) for grain boundary nucleated colonies.

The criteria used to determine the fraction of colony alpha ($f_{C\text{-}\alpha}$) present during thermal cycling and associated nomenclature are summarized in Table XVI. The calculation proceeds by first evaluating the equilibrium criteria, Column 2, then the temperature criteria, Column 3. The

alpha morphology equations are then evaluated in column 4. The code for the morphology model may be found in the Appendix: Microstructure Model Code.

Table XVI: Morphology Model Criteria and Nomenclature

Reaction	Equilibrium Criteria	Temperature Criteria	Equation
Alpha Dissolution	$f_\alpha(T_i) > f_{\alpha,eq}(T_i)$	$T_i < T_{IG}$	$f_{C-\alpha}(T_i) = f_{C-\alpha,FG}$
		$T_i \geq T_{IG}$	$f_{C-\alpha}(T_i) = \frac{f_{C-\alpha}(T_{IG})}{f_\alpha(T_{IG})} * f_\alpha(T_i)$ where, $f_{C-\alpha}(T_{IG}) = f_{C-\alpha,FG}$
Alpha Growth	$f_\alpha(T_i) < f_{\alpha,eq}(T_i)$	$T_i > T_{IG}$	$f_{C-\alpha}(T_i) = f_{C-\alpha,FD} + \left(f_\alpha(T_i) - f_{\alpha,FD}\right)$
		$T_i = T_{IG}$	$f_{C-\alpha,FG} = f_{C-\alpha}(T_{IG})$
		$T_i < T_{IG}$	$f_{C-\alpha}(T_i) = f_{C-\alpha,FG}$
Equilibrium	$f_\alpha(T_i) = f_{\alpha,eq}(T_i)$	If previous reaction was Alpha Growth: $f_{C-\alpha}(T_i) = f_{C-\alpha,FG}$	
		If previous reaction was Alpha Dissolution: $f_{C-\alpha}(T_i) = f_{C-\alpha,FD}$	

Nomenclature		
Variable	$f_\alpha(T_i)$	Fraction alpha at the current (i^{th}) time step, and T_i
	$f_{\alpha,eq}(T_i)$	Equilibrium Alpha fraction determined from alloy phase diagram at T_i
	T_i	Temperature at the current time step.
	T_{IG}	Lower temperature for colony-α formation, 1100K
	$f_{C-\alpha}(T_i)$	Fraction colony-α at the current time step
	$f_{BW-\alpha}(T_i) = f_\alpha(T_i) - f_{GB-\alpha}(T_i)$	Fraction basketweave-α at the current time step
Subscripts	*G*	A colony-α fraction during alpha growth
	D	A colony-α fraction during alpha dissolution
	S	The starting morphology or phase fraction
	F	The final morphology or phase fraction

Application of the phase fraction and morphology model to baseline microstructure experiments

Results

The baseline microstructure experiments (Chapter 3) were performed under known heating and cooling conditions, so comparison between the two can lead to a better idea of how good the morphology model is. Recall that these experiments consisted of a primary heat treatment at 1373 K (T_{BETA}+100K) followed by controlled linear cooling and a secondary sub-transus heat treatment at 1198K (T_{IG}+98K). The thermal cycles, alpha phase fraction, and fraction grain boundary alpha are shown in Figure 7.23 and Figure 7.24 for the 0.6K/s and 10K/s cooling rates. The starting alpha and morphology fractions are 91%-α and 91%-$f_{C\text{-}\alpha}$, respectively. The starting alpha morphology is entirely colony-α based on the initial alpha microstructure.

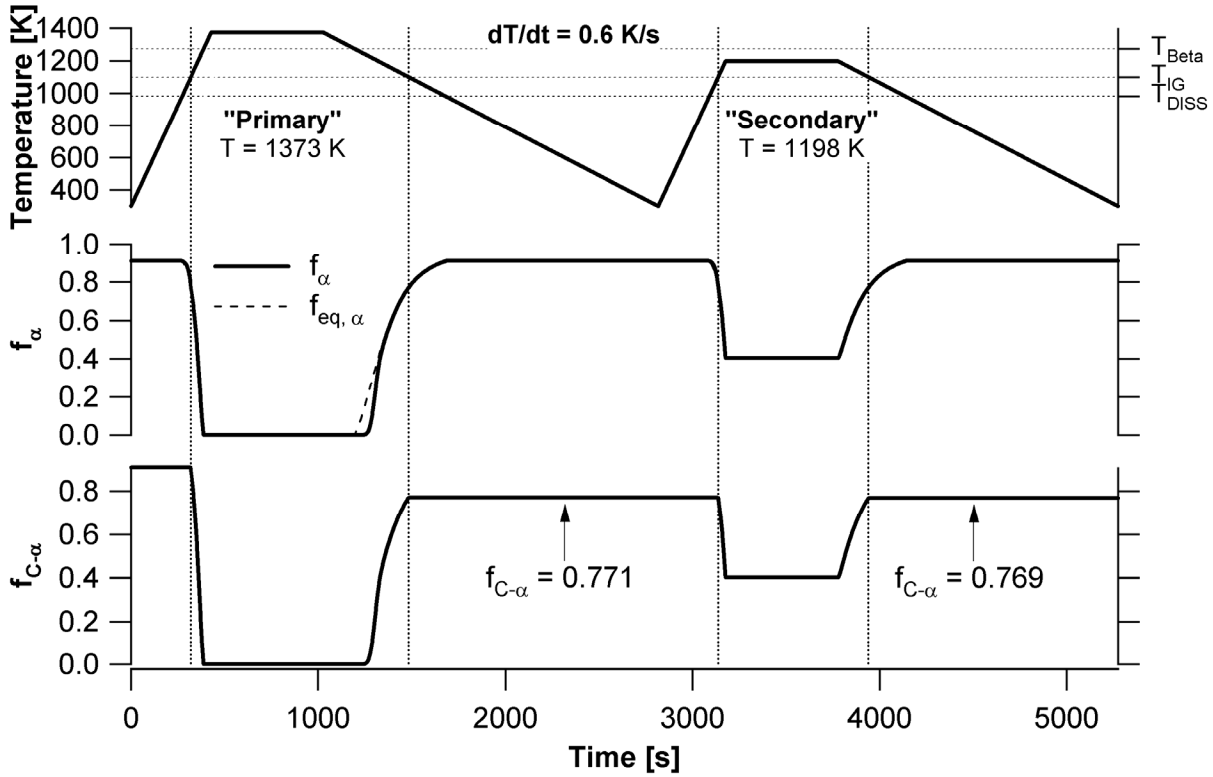

Figure 7.23: Modeling the phase fraction and morphology evolution in 0.6 K/s cooling rate baseline microstructure experiment. From top to bottom, thermal cycles, alpha phase fraction (f_α), and fraction colony-α ($f_{C\text{-}\alpha}$).

For the 0.6 K/s cooling rate the alpha phase fraction (f_α) returns to the room temperature fraction of 91%-α and 9%-β after both primary and secondary treatments. For all but a small period

during cooling from the primary treatment, the alpha fraction closely follows the equilibrium value ($f_{\alpha,eq}$). In the 0.6 K/s modeled morphology, $f_{C\text{-}\alpha}$ is predicted to be 77.1% and 76.9% after the primary and secondary heat treatments.

At a faster 10K/s cooling rate (Figure 7.24), $f_{C\text{-}\alpha}$ decreases to 8% after the primary heat treatment due to less time spent above T_{IG}. After the secondary heat treatment at 10K/s, the amount of grain boundary alpha is more than doubled to a predicted value of 22%.

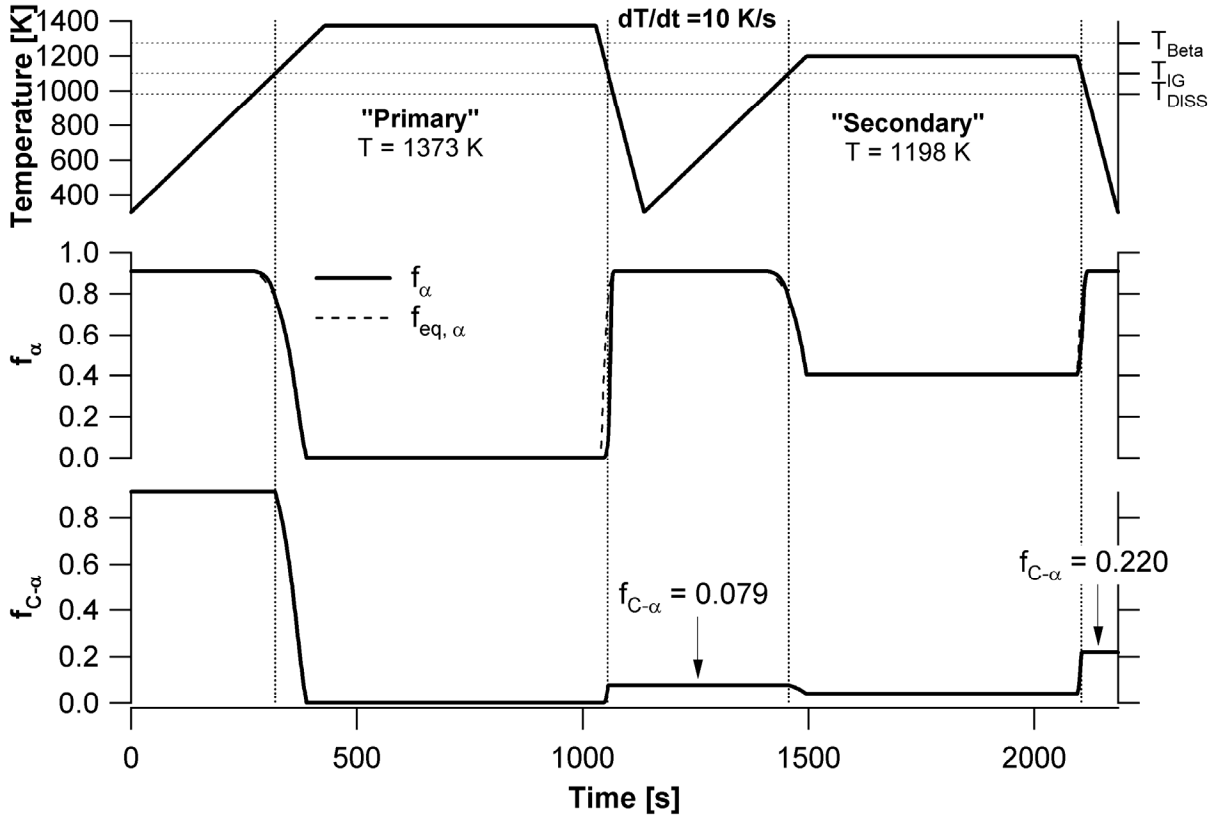

Figure 7.24: Modeling the phase fraction and morphology evolution in 10 K/s cooling rate baseline microstructure experiment. From top to bottom, thermal cycles, alpha phase fraction (f_α), and fraction colony-α ($f_{C\text{-}\alpha}$).

Discussion

The results of modeling the baseline microstructure suggest that for the slow 0.6K/s cooling rate, the amounts of $f_{C\text{-}\alpha}$ should be similar after both heat treatments containing 77% colony alpha and about 14% basketweave-α. In the real samples, the primary heat treatment contained a mixture of basketweave- and grain boundary nucleated colony-α_P. After the secondary heat treatment, the microstructure consisted of primary and secondary colony alpha, with the secondary colony-

α_P appearing intragranularly. There was little to no basketweave-α observed in the secondary sample.

The modeled results for the 10K/s suggest that the microstructure before and after the secondary heat treatment should be again be similar, with predominately a basketweave microstructure ($f_{BW\text{-}\alpha}$=0.831 and 0.69). There will be slightly greater amounts of colony-α after the secondary heat treatment. In the actual microstructure, both primary and secondary heat treatment microstructures contain primarily an alpha basketweave microstructure with some grain boundary nucleated colony-α.

While the actual quantities of the colony and basketweave-alpha morphologies may not match the actual samples, qualitatively, the model does a reasonable job at determining the dominant morphology in the deposit. The assumption has been made that kinetics for dissolution and growth are the same during cooling from above and below the beta transus. A more rigorous approach that adjusts the kinetic parameter ($k(T)$) or the Avrami exponent (n) may lead to more accurate results. In addition the dissolution model assumes that both morphologies dissolve at the same rate. Further experimental work on dissolution of alpha would be needed to adjust this.

Conclusions

A simplistic model has been developed to model the dissolution and growth of the alpha phase during thermal cycling. For the dissolution model, DiCTra simulations were performed to determine a parabolic dissolution rate of alpha during heating. This model assumed that alpha dissolves by a diffusion controlled process. The alpha nucleation and growth model followed a JMA approach where the JMA kinetic parameter k(T) was fit to a modeled TTT diagram for the bulk alloy composition. The TTT diagram considered the formation of alpha at two sites: grain boundaries and intragranularly. The corresponding morphologies being grain boundary nucleated allotriomorphic- and colony-alpha and intragranularly nucleated basketweave-alpha. The evolution of alpha phase fraction was examined for linear heating and cooling cycles. During cooling at rates greater than 20K/s non-equilibrium products would be expected to form, in agreement with literature. During heating at rates greater than 25K/s the alpha phase is still stable above the equilibrium transus temperature. At a heating rate of 500 K/s about 100K of superheat is required for complete alpha dissolution, of the same order of magnitude of the

reported literature values. Comparison of the phase fraction model with recent experimental data for thermal cycling of Ti-6Al-4V yielded reasonable comparison.

A morphology model was developed to determine the morphologies of the alpha phase that form. The model assumes that during cooling above the temperature (T_{IG}) where intragranular nucleation starts, only colony-α forms. Below T_{IG} only basketweave alpha grows. During dissolution below T_{IG} only basketweave dissolves. Above T_{IG} both colony- and basketweave-α dissolve in equal proportions. The resulting morphology evolution was compared to the baseline microstructure experiments for primary and secondary heat treatments where 0.6 and 10K/s cooling rates were used. For the 0.6K/s primary and secondary heat treatments the model predicted a final alpha morphology consisting of 77% colony-α and 14% basketweave-α. The actual samples did not contain any basketweave-α after the secondary heat treatment. For the 10K/s primary and secondary heat treatments, the final alpha morphology was predicted to contain 22% colony-α and 69% basketweave-α. The actual samples contained very little colony-α except at grain boundaries (primary-α). Overall, the model does a good job at predicting the dominant alpha morphology present which should be sufficient to illustrate the effect of thermal cycling on the as-deposited microstructure in Ti-6Al-4V. Further improvements to the morphology model kinetics would be useful in making it a more quantitative model.

Chapter 8: Coupling the Thermal and Microstructure Model

Introduction

In this section, we will show how both the alpha phase fraction and morphology (colony-α) evolve during thermal cycling experienced during laser metal deposition. The phase fraction and morphology equations will be used in conjunction with the LFv5o-005 thermal model results, to describe the microstructure evolution. The goal is to relate this evolution to microstructural features observed in the as-deposited material.

In the thermal model results, it was observed that after the third layer is deposited a heat affected zone develops that extends approximately 4 layers into the deposit. With each additional layer deposition the heat affected zone increments 1 layer in the positive z direction, which in theory should result in an evolution of microstructure that is periodic, as observed in the as-deposited material. The periodic characteristic layer containing the graded basketweave and layer-band (colony α) is designated layer *n* and forms during the deposition of layer *n+3*. The last three layers (*n+1 – n+3*) consist of a microstructure that is uniquely different from *n*, *n*-1,...*n-j* and define the heat-affected-zone microstructure in the deposit. Layers below *n*, e.g. *n-1* are unaffected by thermal cycles after layer *n+2*. Hence the results of the microstructure model will focus on the phase fraction and morphological evolution in the last 5 layers of material, which will provide evidence that the characteristic microstructure in layer *n* develops during the deposition of layer *n+3* and remains unaltered by the deposition of layer *n+4*. In addition, a two dimensional movie of both phase and morphology fraction evolution will be shown and compared with the as-deposited microstructure

Results

Modeling phase fraction evolution during LMD thermal cycles

The discussion of the phase fraction evolution begins with the last five layers to be added in the modeled deposit. These are layers 4 through 8, where layer 4 can be thought of as layer "*n*" and layer eight would be layer "*n+4*". In Figure 8.1, the alpha phase fraction evolution with time is

shown at two z-positions along the centerline (y=0) of the deposit, within layer 4 or layer *n*. The thermal cycles these two points experience are also shown. A phase fraction amount of zero corresponds to 100% β, except when β transforms to liquid, which is indicated in Figure 8.1 by a gap in the alpha fraction curve (This occurs near 300 and 400 seconds). In all instances, alpha transforms completely to beta before melting.

During the first three thermal cycles (*n* through *n+2*), temperatures above the beta transus are experienced by both z-positions. The alpha phase fraction evolution path is essentially equivalent at both positions during the first 3 thermal cycles. During heating, alpha dissolves rapidly to beta before melting due to the high heating rates. Upon cooling, equivalent amounts of alpha form. The final amount of alpha after the deposition of each layer *n* through *n+2* is the room temperature fraction (91% α, 9% beta).

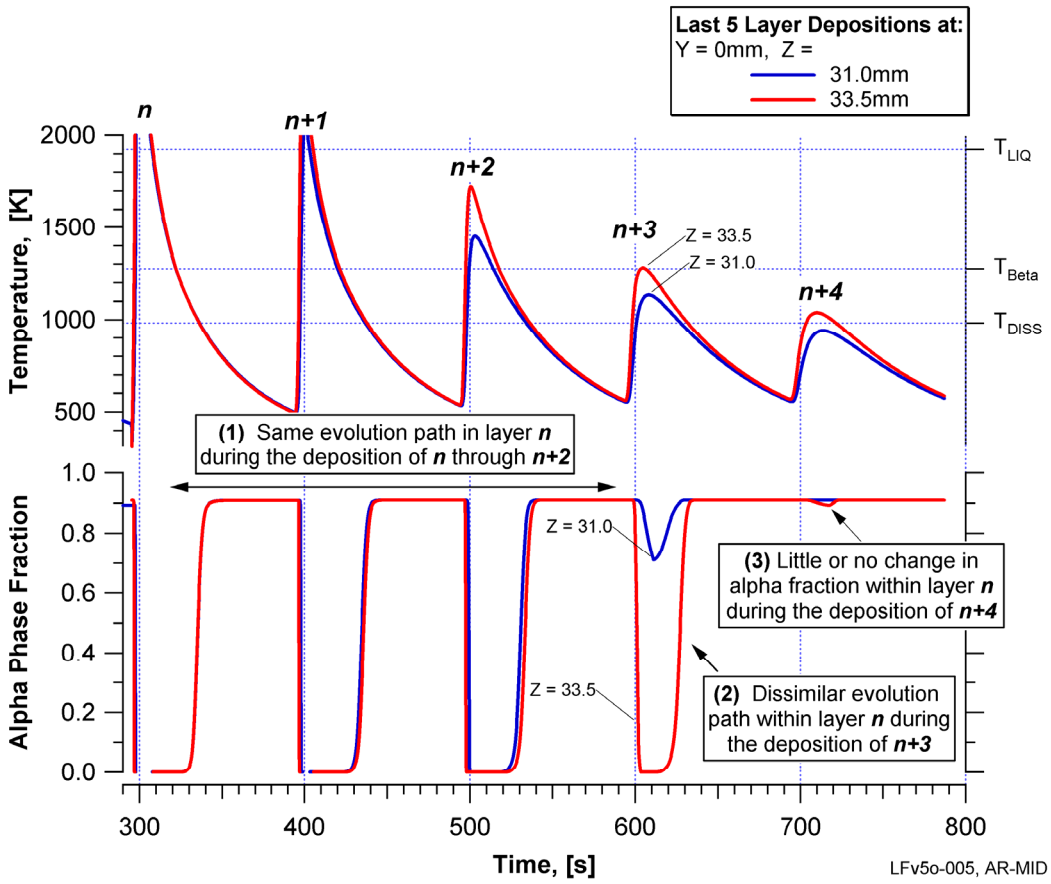

Figure 8.1: Temperature and alpha phase fraction evolution with time at two z positions along the centerline (y=0) of the deposit. The positions lie within a layer *n* and experience an additional three thermal cycles (*n+3*), with the *n+3* cycle causing the most variation in the phase fraction evolution path. Gaps in the phase fraction data near 400 and 500 seconds distinguish between 100%-β and 100%-liquid.

During the thermal cycle caused by the deposition of *n+3*, the greater z-position experiences a temperature above the beta transus and alpha dissolves completely. The lower z-position is heated high into the two phase (α+β) field and as a result, only 20% of the alpha dissolves during the deposition of layer *n+3*. As result, a significant change in the evolution path is observed, though the final amount of alpha is the same for both positions: 91%-α, 9%-β. Further thermal cycles, i.e., the deposition of *n+4*, will be insufficient to produce changes in the alpha fraction with time since the temperatures will be below the dissolution start temperature (T_{DISS} = 981K).

It is also noteworthy that during heating, the modeled fraction typically follows the equilibrium alpha fraction and during cooling there is a slight deviation from equilibrium, as shown in Figure 8.2. The delay on cooling is due to the incubation time necessary to nucleate and grow alpha from the beta phase, whereas on heating no nucleation occurs leading to a much faster reaction.

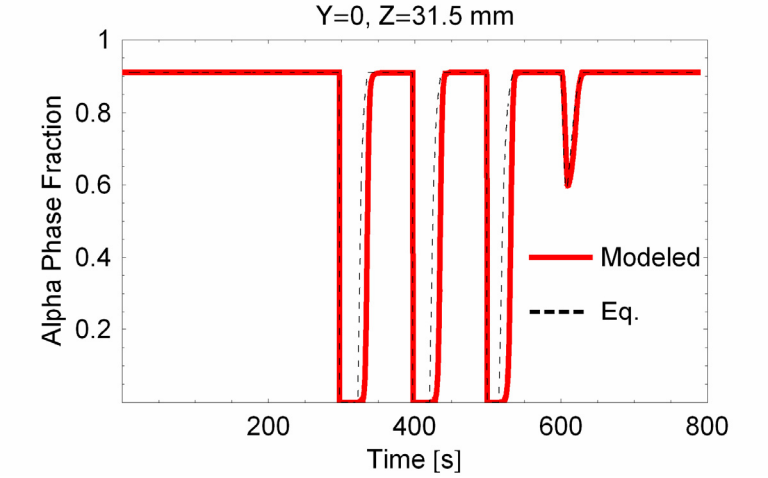

Figure 8.2: Comparison of modeled and equilibrium alpha fractions as a function of time at a constant position within the deposit. 100%beta and liquid are not distinguished in this plot.

Figure 8.1 clearly shows that the greatest deviation in evolution path will occur in layer *n* after the deposition of layer *n+3* and will remain essentially unchanged thereafter. Figure 8.3 looks at the phase fraction evolution along the centerline of the deposit with time $f_\alpha\,(y=0,\ z,\ t)$ for each layer deposition (L1-L8). Both *z*-position and time are independent variables in Figure 8.3 and the *y*-position is held constant. The phase fraction variation in z is "scanned" with time. The "steps" in Figure 8.3 are due to the addition of a new layer to the deposit. Figure 8.3 shows a phase fraction map, with red indicating 100%-beta and purple indicating 91%-alpha. Again, liquid is differentiated from beta by blank space, as indicated.

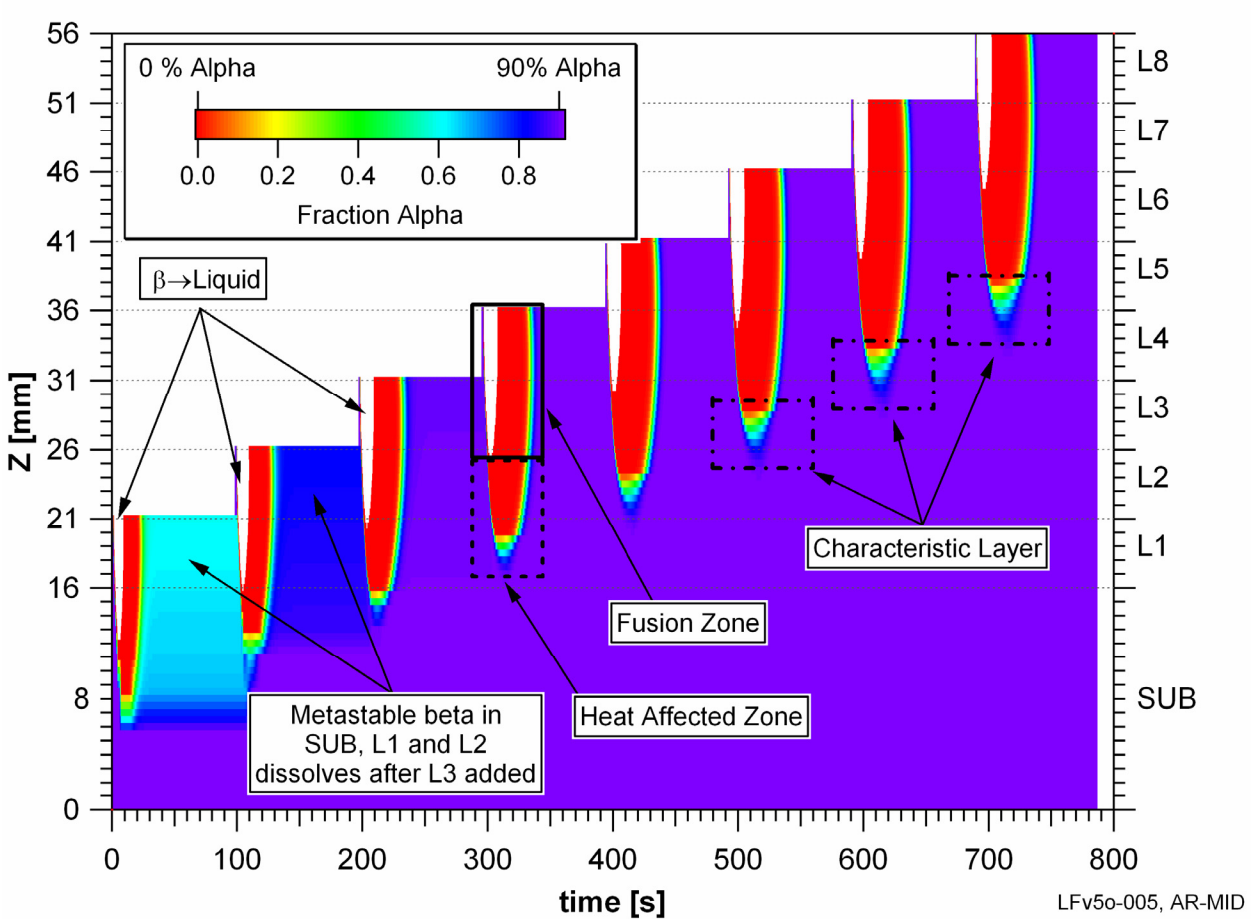

Figure 8.3: Alpha phase fraction evolution mapped with z-position and time (independent variables) at constant y-position (centerline, y-0) in the deposit. Beta and liquid are differentiated by the color red and blank space. The fusion and heat affected zones are indicated for layer 4 (L4) and the characteristic layer is indicated for layers 6-8 (L6-L8).

The thermal model data indicate that the greatest cooling rates are experienced in layers 1 through three because of their proximity to the substrate, which can conduct heat away in two dimensions. The relatively high cooling rates in this region result in metastable beta being present in the substrate, first and second layers. The metastable beta present in these regions will be in the form of alpha martensite, though the model does not explicitly account for this morphology. The metastable beta transforms completely to the room temperature alpha fraction after additional thermal cycles from the deposition of the second and third layers. Thereafter, the room temperature fraction is attained during cooling because cooling rates have been reduced due to a change in the dimension of heat transfer. In the substrate there is 2D heat transfer resulting in faster cooling rates, whereas when more layers are added heat transfer becomes 1D, reducing cooling rates.

The heat-affected-zone is indicated in Figure 8.3 for layer 4 by the dashed box. It is clearly seen that the heat affected zones in layers 5 through 8 are of equivalent size (z) and time to that in layer 4. In addition, the characteristic layer or the greatest deviation in phase fraction evolution path is also indicated by the dash-dot boxes for layers 6-8. Again, the size of this region is similar for each layer addition. Figure 8.3 clearly shows that the evolution of phase fraction along the centerline of the deposit is periodic and the regions defining the evolution are incremented in the positive z-direction by one layer.

For electronic versions of this thesis, the phase fraction evolution with time across the entire 2D deposit may be examined in the form of a movie (Figure 8.4). For paper-based versions the screen captures for two times during the deposition of the last (eighth) layer are shown in Figure 8.5a-b.

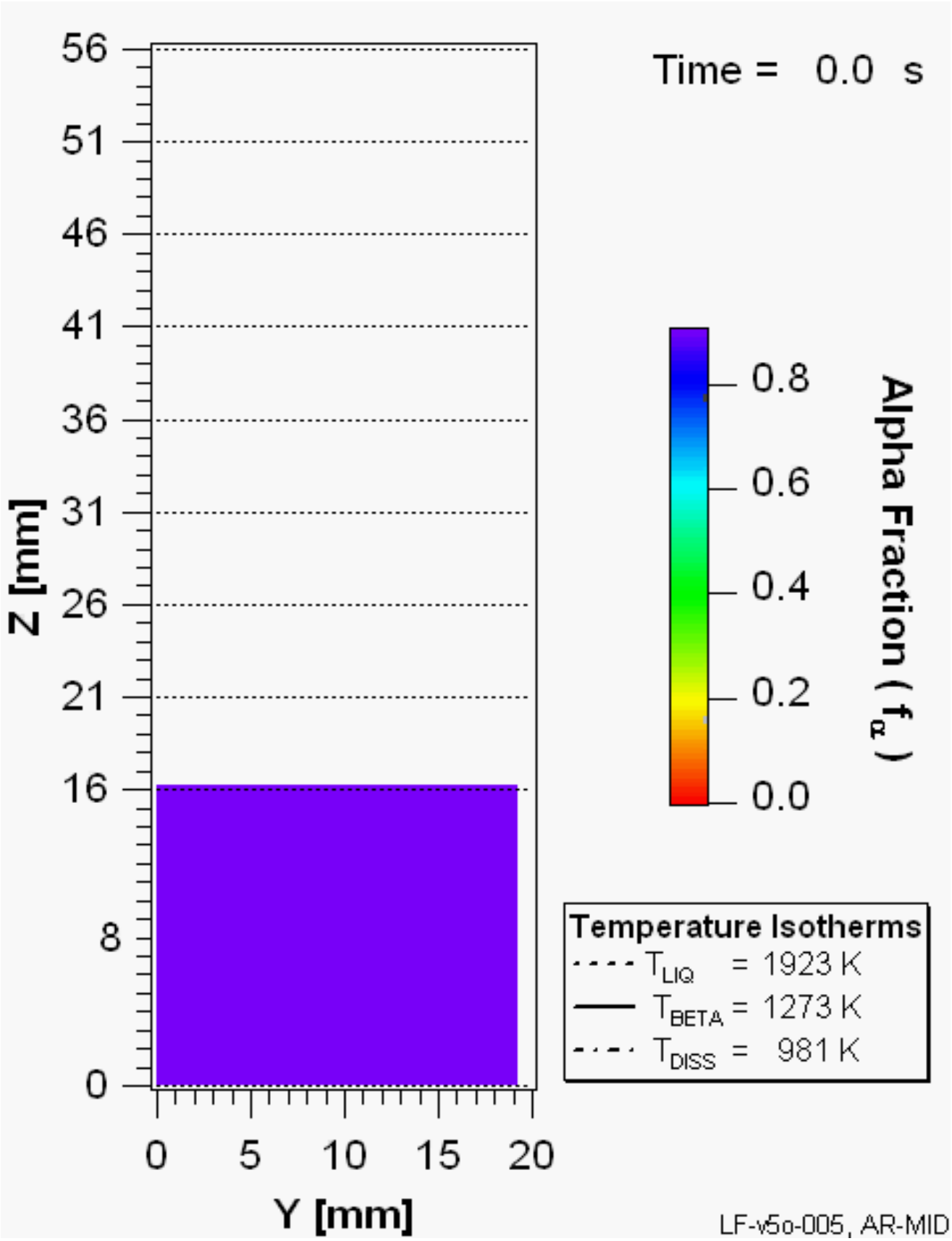

Figure 8.4: 2D phase fraction evolution movie. Melting is indicated in the movie by the eroding of the layer. Horizontal gridlines represent the positions of each layer. (QuickTime, 107MB).

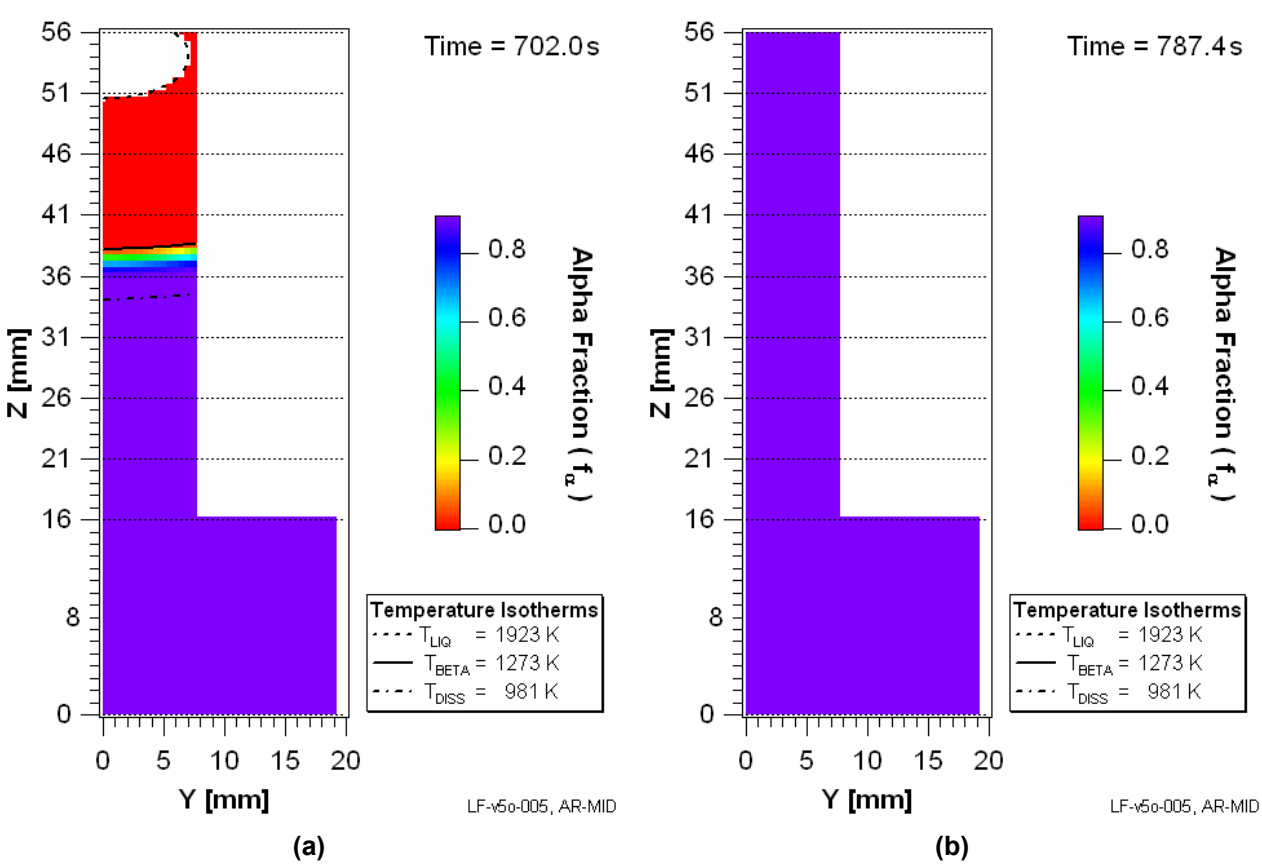

Figure 8.5: Screen captures from the movie in Figure 8.4 during the last layer deposition at (a) 12.8 and (b) 98.2 seconds after the deposition of the 8th layer. (a) occurs during solidification and (b) is at the completion of the pass. Melting is indicated in the movie by the eroding of the layer as indicated in (a). Horizontal gridlines represent the positions of each layer.

The purpose of Figure 8.5a is to illustrate how melting is accounted for in movie and to also illustrate that the variation in phase fraction at an instant in time is nearly parallel to the substrate, due to the ~1D heat flow, as indicated by the isotherms. As viewed in the movie (Figure 8.4) the only 2D variation in the phase fraction is observed in and near the substrate, where heat flow is 2D. Figure 8.5b is featureless, indicating that at the completion of the deposit, the phase fraction of alpha and beta is homogeneous, at 91%-α and 9%β.

Modeling morphology evolution during laser LMD thermal cycles

The results of the morphology model are shown in Figure 8.6 for three positions in the fourth layer. The thermal cycles and colony alpha fraction ($f_{C\text{-}\alpha}$) evolution are shown for the deposition of 4 layers on top of layer four. In other words, the z-positions lie within a layer *n* and Figure 8.6

shows the morphology evolution during the deposition of *n* through *n+4*. Gaps in the $f_{C\text{-}\alpha}$ curves indicate the alpha fraction (f_α) is equal to zero (complete α dissolution).

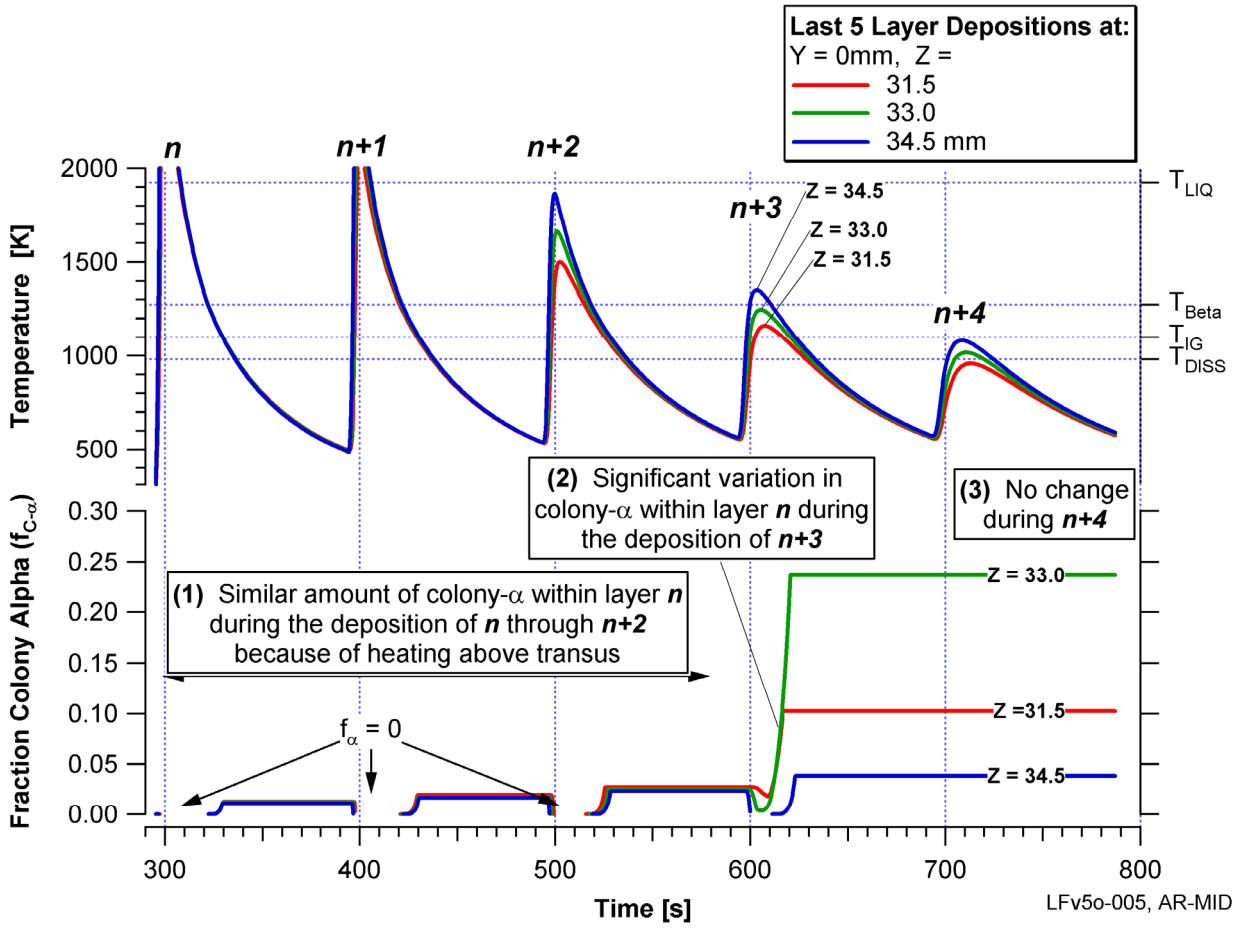

Figure 8.6: Colony-alpha ($f_{C\text{-}\alpha}$) evolution at three positions in the fourth layer. The evolution is shown during the deposition of four layers onto the fourth layer (*n* through *n+4*). Gaps in the colony-α fraction curves represent where the alpha phase fraction (f_α) equals zero.

During the deposition of *n* through *n+2* alpha at the z-positions completely dissolves into beta, resulting in similar amounts of colony-alpha forming during the alpha nucleation and growth stage of each thermal cycle. Recall that in the phase fraction results (Figure 8.1), the evolution of alpha phase fraction was similar over these first three thermal cycles as well. The $f_{C\text{-}\alpha}$ that forms is less than 5%, with the remaining amount being basketweave alpha. In addition the alpha that forms during the first three cycles is primary-alpha.

In Figure 8.6, the most significant change in $f_{C\text{-}\alpha}$ occurs during the *n+3* layer addition with the amount of colony alpha becoming highly z-position sensitive. At z=31.5mm, the amount of

colony alpha present has doubled to near 10%. At z=33.0 there is about five times more colony alpha than during the previous three passes. The colony alpha that forms at these two positions during the n+3 layer addition will be secondary-alpha since the maximum temperature was below the beta transus. Likewise, the material at z=34.5mm will be primary alpha since it experienced a maximum temperature above T_{BETA} during the *n+3* layer addition. The remaining alpha morphology fraction will consist of basketweave alpha (e.g. $f_\alpha = f_{C\text{-}\alpha} + f_{BW\text{-}\alpha}$). During the *n+4* layer addition, the thermal cycles are insufficient to produce changes in the amount of colony or basketweave alpha that has previously formed, thus the variation of $f_{C\text{-}\alpha}$ within layer n is retained.

One final point to retain from Figure 8.6 is that of the three z-positions plotted, Z=33.0mm has the highest and Z=34.5mm has the lowest amount of $f_{C\text{-}\alpha}$ of the three positions. Correspondingly, the gradient ($df_{C\text{-}\alpha}/dz$) above the location of maximum $f_{C\text{-}\alpha}$ is greater than below; therefore, the transition in $f_{C\text{-}\alpha}$ will be gradual below the maximum value within layer n followed by a sharp transition to significantly lower amounts of $f_{C\text{-}\alpha}$ just above the maximum. The lowest amount of $f_{C\text{-}\alpha}$ at Z=34.5 is a result of complete alpha dissolution prior to cooling. At the lower z-positions (Z=31.5 and 33.0mm), a small amount of $f_{C\text{-}\alpha}$ dissolves during the heating leg of the *n+3* thermal cycle, however, complete dissolution does not occur. The *n+3* thermal cycle for these z-positions is high in the two phase field above T_{IG}, resulting in a large fraction of $f_{C\text{-}\alpha}$ upon cooling.

A movie has been constructed showing the two dimensional (y-z) evolution of colony-alpha with time during the deposition of eight layers as seen in Figure 8.7. The final morphology distribution is shown in Figure 8.8. Melting is again indicated by the apparent eroding of the newly deposited layers, however, no distinction is made between $f_\alpha = 0$ and $f_{C\text{-}\alpha} = 0$ in Figure 8.7.

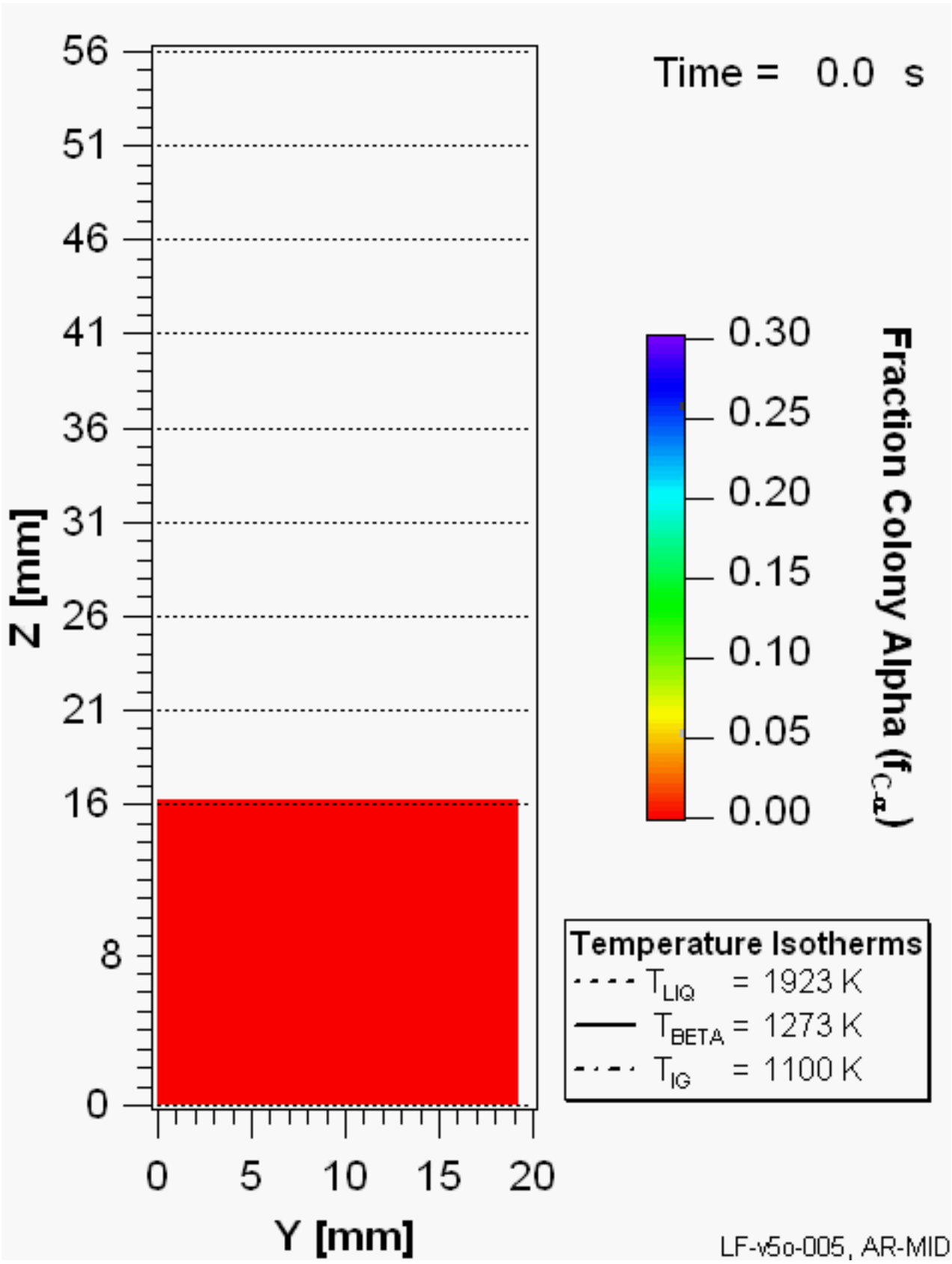

Figure 8.7: 2D fraction colony-alpha ($f_{C-\alpha}$) evolution movie. Melting is indicated in the movie by the eroding of the layer as before. (QuickTime, 152MB).

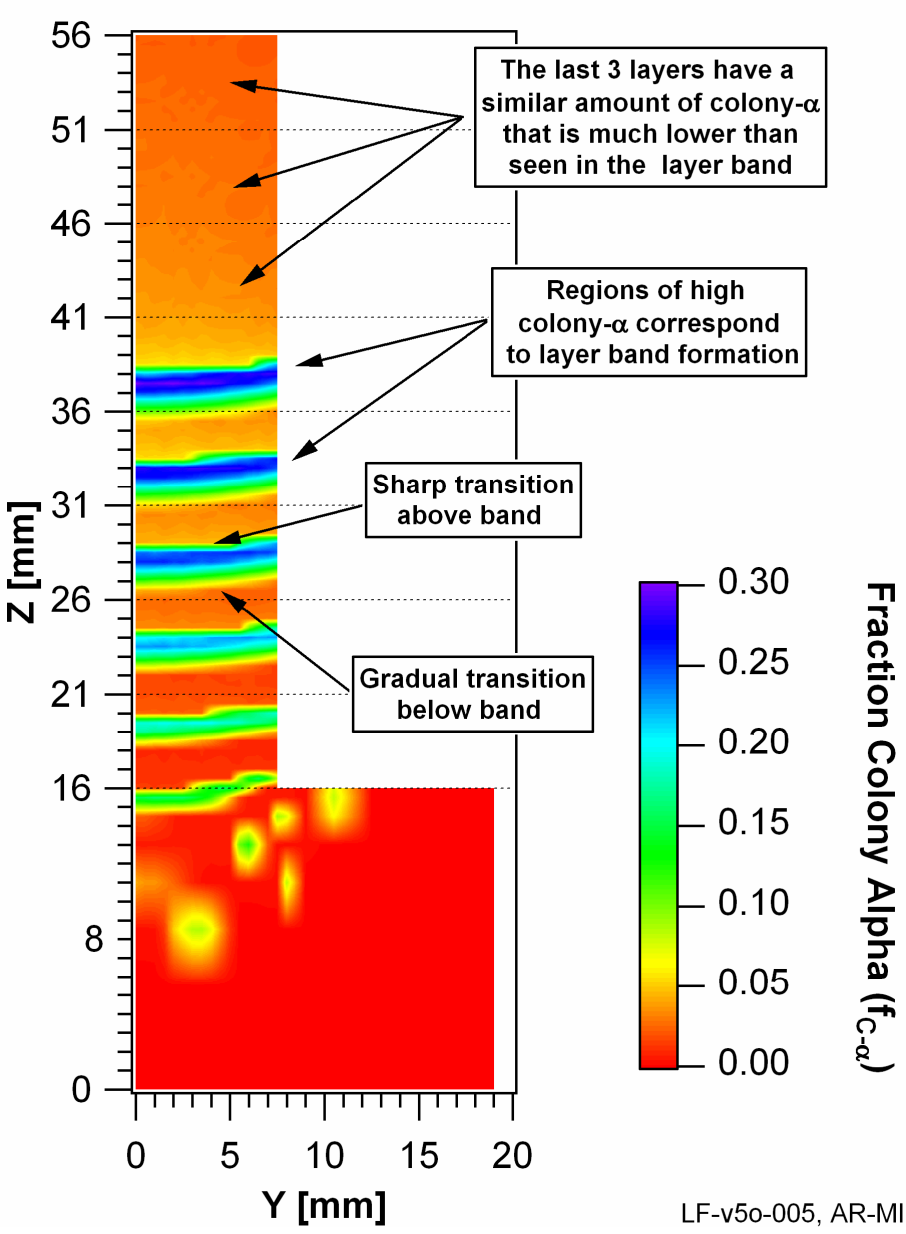

Figure 8.8: The final morphology distribution after the deposition of the 8th layer (interpolated data, 10x resolution).

Figure 8.8 clearly shows a periodic variation in the amount of colony-alpha present in the final deposit. This variation is present in each layer except the last three layers deposited. In these last layers, the alpha phase morphology would be near 90% basketweave alpha (f_{α} =0.91, $f_{C\text{-}\alpha} \approx 0$, $f_{BW\text{-}\alpha} \approx 0.91$. Both of these results are in good agreement with the as-deposited results, where the 3 most recent layers to be deposited consisted primarily of basketweave and fine-colony alpha.

In addition, Figure 8.8 shows that the fourth most recent layer (36 < Z <41mm) is the last layer to contain the periodic variation in colony-alpha, thereby representing a characteristic layer that is periodically repeated through the deposit. In the as-deposited structure, the characteristic layer contained a layer band consisting of colony alpha and a region below the layer band consisting of a basketweave morphology with a variation in the individual alpha lath size. In Figure 8.8, the regions of higher colony alpha correspond to the packet-colony morphology observed in the as-deposited layer band. This conclusion is drawn based on the assumption that the kinetics for grain boundary nucleated colony-alpha formation is equivalent to the kinetics for intragranular colony alpha.

Discussion

Upon cooling through the beta transus alpha forms as colonies of alpha extending from the prior beta grain boundaries. If the beta transus is not crossed (heating and cooling within the two phase field) and the temperature is above T_{IG}, it is assumed alpha will again tend to form in the colony morphology, but not necessarily at grain boundaries (intragranular colony). This assumption is somewhat verified in Chapter 3 (Figure 3.4 and Figure 3.5), which shows that during a primary heat treatment above the beta transus and a cooling rate of 0.6K/s the microstructure is a mixture of basketweave and colony alpha. During a secondary heat treatment at 1198K, the microstructure is dominated by colony alpha nucleated at grain boundaries and intragranularly.

The cooling rate at the Z=33.0mm position in Figure 8.6 producing the largest fraction of $f_{C\text{-}\alpha}$ is approximately 10K/s; however, the experimental baseline microstructure results at this cooling rate produced a basketweave and grain boundary colony morphology where very little packet colony was observed. In defense of this apparent contradiction in model and experiment, the maximum temperature at Z=33mm is 1248K while in the experiment, the peak temperature was 1198K. The greater temperature in the modeled data should lead to further colony formation; however, more focused experiments of the type in the Baseline Microstructure chapter are needed within the temperature range (T_{IG}, T_{BETA}) to further support the claim that packet-colony formation occurs in this range.

Comparison of morphology model and as-deposited microstructure

The similarities between the morphology model and as-deposited macro-structure are illustrated in Figure 8.9 and important conclusions summarized below.

- The last three layers of the as-deposited material and morphology model represent a transient or undeveloped macro-structure in that no layer bands are observed. In the morphology model, the microstructure within the last three layers consists of a constant amount of basketweave alpha (very low colony-alpha), while in the as-deposited microstructure a transition from fine basketweave to fine colony is made over the last three deposited layers.

- The characteristic layer or layer containing the periodic microstructure forms just below the last three deposited layers in both the model and as-deposited microstructure. In other words, a characteristic layer forms in layer n after the deposition of layer n+3. In the morphology model, the characteristic layer contains regions of high and low amounts of colony-alpha, which correspond to the layer band (colony alpha) and nominal (graded basketweave) morphologies in the as-deposited material.

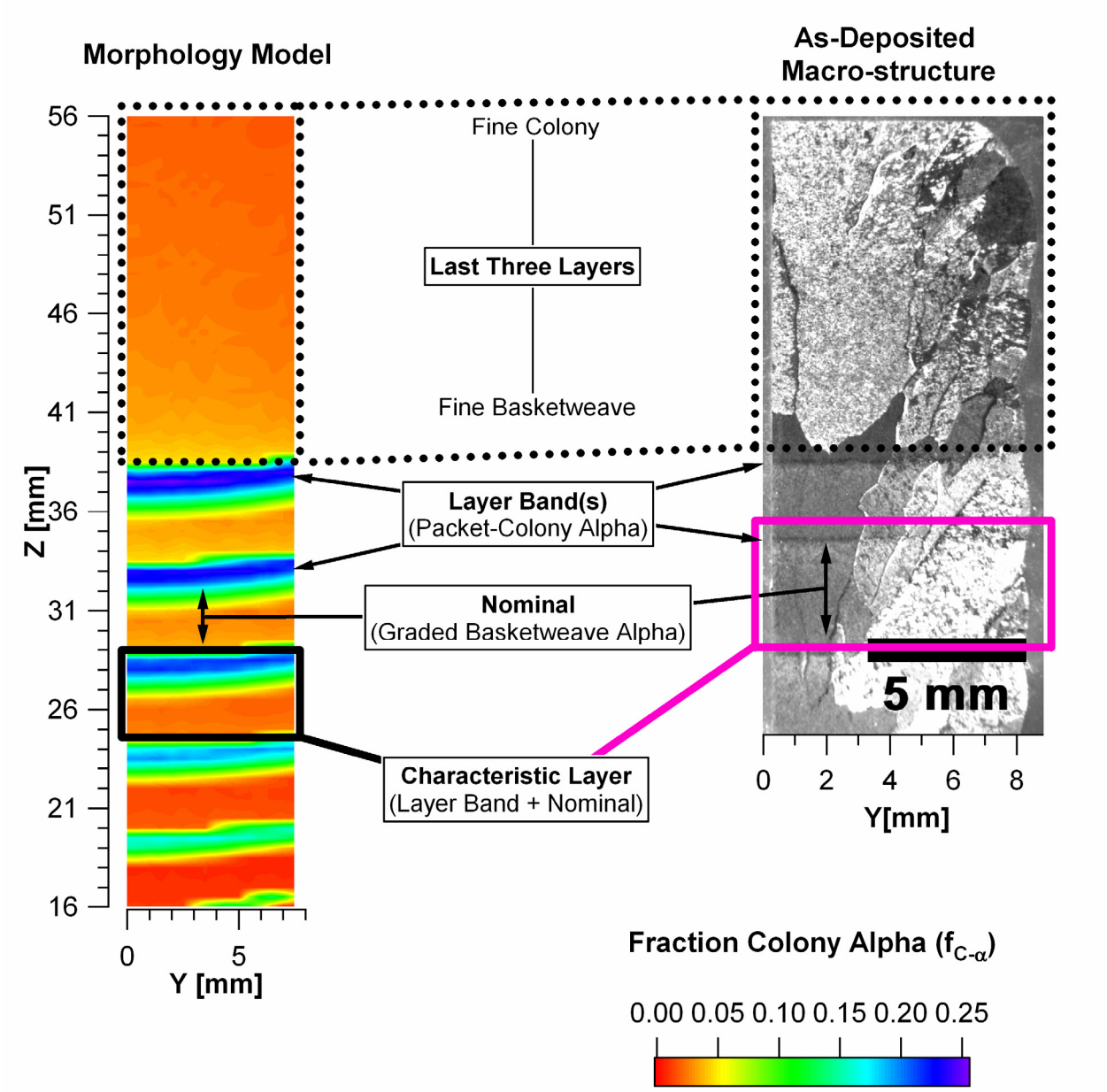

Figure 8.9: Comparison of 2D (y-z) cross sections from the morphology model (left) and as-deposited macrostructure (right). Equivalent regions in the model and as-deposited macrostructure are indicated.

The similarities between the morphology model and as-deposited microstructure within the characteristic layer are illustrated in Figure 8.10 and important conclusions summarized below.

- Higher fractions of colony-alpha correspond to the colony morphology of the layer bands. This is based on the assumption that during a thermal cycle in the two phase field, growth of colony alpha above T_{IG} occurs by similar kinetics as would occur during

cooling through the beta transus. The maximum amount of colony-α observed in the model is neat 25%, whereas in the as-deposited material, the layer band is 100% colony-α. This discrepancy most likely comes from applying kinetics for primary-thermal treatments (where nucleation occurs) to secondary-thermal treatments where the need for nucleation is decreased. In the TTT diagram, a secondary thermal cycle will shift the transformation curves to the left, increasing the amount of colony alpha that would form. In addition, Figure 7.18 shows the variance in experimental TTT curves indicating the difficulty in determining exact kinetics. Furthermore, the TTT diagram calculated by JMatPro (which the current model is based on) utilizes hypothesized variables for nucleation site and mechanism that are fit to produce realistic values. Clearly, better kinetic parameters for alpha nucleation and growth are needed for the secondary thermal cycle.

- Regions of low or zero colony-alpha, found between the layer bands, correspond to high amounts of basketweave in both the morphology model and as-deposited microstructure.

- It is suggested that the gradients in the grain boundary or basketweave fraction can be related to the transition from a graded-basketweave to layer band morphology. Steeper gradients would indicate an abrupt transition, while gentle gradients indicate a gradual transition. In the model and as-deposited microstructure, steeper gradients are found above the layer band, while gradual gradients are found below. The material above the layer band is heated above the beta transus.

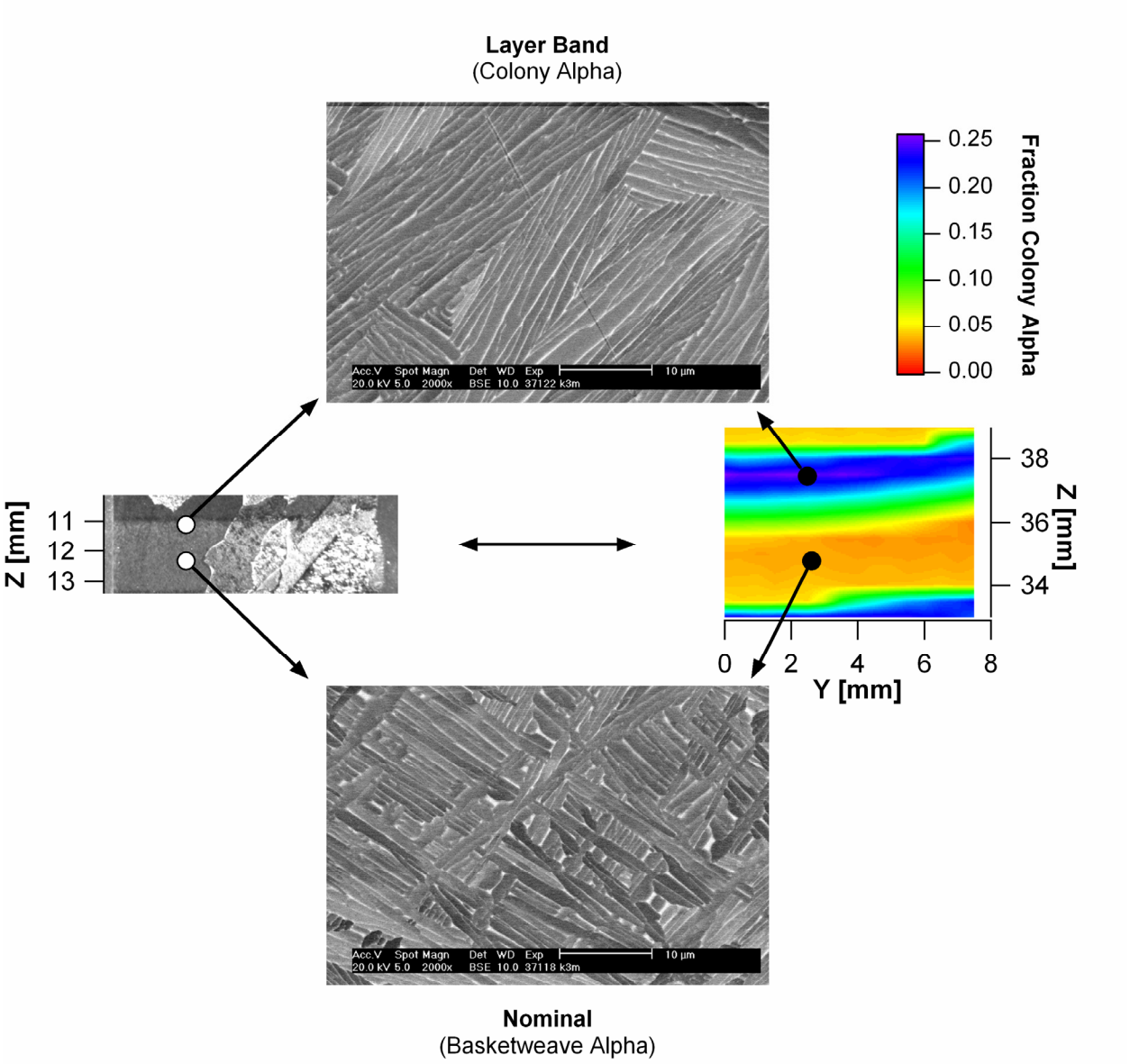

Figure 8.10: Comparison of the microstructure within the characteristic layer of the morphology model and as-deposited material.

Conclusion

The thermal model results were used as input to the phase fraction and morphology evolution models, resulting in a predicted microstructure that is qualitatively similar to the as-deposited microstructure. The phase fraction model predicts a near equilibrium evolution with the greatest spatial (z) variation in the maximum alpha fraction during the *n+3* thermal cycle, corresponding to heating into the α+β phase field. The phase fraction evolution paths for the deposition of

layers *n* through *n+2* are similar, while the deposition of *n+4* leads to no change in the phase fraction. The phase fraction results reinforced the theory that the as-deposited characteristic layer forms after the deposition of layer *n+3* onto layer *n*. In addition, the phase fraction results suggest that non-equilibrium products will not appear after three layers are added.

The morphology model illustrated the periodic nature of the characteristic layer, repeating during the deposition of multiple layers of material. The modeled characteristic layer contained relatively high amounts of colony alpha at the top of the layer and high amounts of basketweave at the bottom of the layer, in agreement to the as-deposited microstructure. The transition from basketweave to a colony-α morphology below the layer band is much more gradual than above the layer band where the transition is sharp.

Above the characteristic layer there are three layers of predominately basketweave-α representing the transient layers in the as-deposited microstructure.

When coupled with the thermal model results, the position of the characteristic and transient layers, and number of thermal cycles to produce these layers is in excellent agreement with the as-deposited microstructure.

The microstructure model has proven that a greater amount of colony alpha (e.g. layer band) forms during a high temperature thermal cycle into the α+β phase field. While an exact quantitative match between model and experiment was not obtained, the microstructure model is useful as an engineering tool to aid in LMD process development.

Chapter 9: Conclusions and Future Work

Executive Summary

LMD processing of Ti-6Al-4V

Laser metal deposition (LMD) processes have drawn much attention lately because of their ability to form small quantities of functional prototypes and structural parts at significantly reduced cost to the buyer. LMD is of particular interest to produce aerospace components of titanium alloys, particularly Ti-6Al-4V, because of the potential cost savings. The microstructural evolution of LMD Ti-6Al-4V has been investigated using materials characterization techniques, and through thermal and microstructure modeling. The laser deposits consist of 18 layers of Ti-6Al-4V produced using a commercial additive manufacturing process (AeroMet Corporation's laser additive manufacturing (LAM™) process). An alternative to conventional forging processes, LAM utilizes a high power CO_2 laser to heat and melt metal powder. The laser is scanned or rastered to produce a two-dimensional layer (*x*-*y* plane), then incremented vertically (*z*-direction) to add additional layers, thereby forming a near-net shape three-dimensional part. Due to the additive nature of the process and thermal cycling associated with a high power heat source, the resulting microstructure evolution is very complex. Understanding of the microstructural evolution in metal deposition processes will aid in the reduction of trial-and-error methods of defining processing conditions and lead to the *in situ* fabrication of designed microstructures and functionally graded materials.

Baseline microstructures in Ti-6Al-4V

In order to better understand the solid-state microstructure evolution during thermal cycling of Ti-6Al-4V, a series of "baseline" microstructure experiments were performed on samples of the alloy using controlled heating and cooling rates. These experiments consisted of primary- and secondary- thermal treatments resulting in the formation of primary- and secondary-alpha transformation products, respectively. Primary-alpha (α_P) forms during cooling through the beta transus temperature (1000°C, 1273K) while secondary-alpha (α_S) forms from β during heating and cooling in the two phase α+β phase field. The peak temperatures for the primary and secondary heat treatments were 1373K (T_{BETA}+100K) and 1198K (T_{BETA}-75K), respectively.

Cooling rates ranging from 0.6 K/s to >500K/s were used to produce both diffusion controlled ($\beta \rightarrow \alpha+\beta$) and diffusionless ($\beta \rightarrow \alpha' + \alpha_m$) transformation products. The samples were characterized using optical microscopy, scanning electron microscopy (SEM) in backscattered electron mode (BSE), electron backscattered diffraction (EBSD), and transmission electron microscopy (TEM). Cooling rates less than 10K/s were shown to produce diffusion controlled transformations of β to α. The alpha and beta phases exhibited good phase contrast in the BSE-SEM with the vanadium phase partitioning to the beta phase. The alpha grains were generally dislocation free, and could be detected using EBSD. The beta phase could not be easily detected in EBSD due to strain or insufficient resolution.

At the 0.6K/s cooling rate a microstructure consisting of colony-α_P and α_S was produced during the primary and secondary treatments, respectively. The colonies contain several α grains oriented parallel to one another separated by low angle (<5°) grain boundaries. During primary heat treatment, α colonies form first at the prior beta grain boundaries. The nucleation sites of the colonies formed during the secondary heat treatments could not be resolved, though it is assumed they form intragranularly.

After the primary heat-treatment cooled at 10K/s, the microstructure consists of predominately basketweave-α_P with some colony-α_P located at prior beta grain boundaries. After the secondary heat treatment cooled at 10 K/s, α_S forms between primary alpha grains as a very fine phase, less than 1 μm in width. Secondary heat treatments at both 0.6 and 10K/s resulted in enhanced partitioning of vanadium to the beta phase as indicated by much better α / β phase contrast in BSE micrographs. Enhanced partitioning is a result of heating in the two phase field where vanadium has additional time to partition to the beta phase. Increasing the cooling rate from 0.6 to 10K/s changed the alpha morphology from colony-α to basketweaveα. Likewise, a difference in primary and secondary heat treatment also produces changes in the microstructure in the form of primary and secondary-alpha phases.

Cooling from above the beta transus at a rate of 94K/s resulted in β decomposition to martensitic-alpha (α') and an precipitate at the prior beta grain boundary that could not be accurately identified (massive-alpha or fine allotriomorphic alpha). The martensitic phase appears as high aspect ratio intragranular needles. α' exhibits little partitioning of alloying

elements, is highly dislocated, and resulted in poor EBSD contrast due to strain. The prior beta grain boundary precipitate generally is irregularly shaped. Water quenching produced a microstructure that was entirely martensitic in nature.

As-deposited LMD Ti-6Al-4V microstructure

The as-deposited LMD macro- and microstructure has been characterized using optical microscopy, SEM in BSE mode, EBSD, TEM, EDS, electron microprobe, and hardness measurements. The macrostructure exhibits columnar prior beta grains oriented perpendicular to the substrate approximately 1.4 mm in width that have grown across multiple layers as a result of epitaxial growth from the substrate and/or previously deposited layers. The as-deposited macrostructure can be divided into two distinct regions. Those layers containing an undeveloped microstructure are labeled "transient layers" and comprise the last three layers of the deposit. The fully developed microstructure, labeled a "characteristic layer", is found in the fourth most recent layer of the deposit and periodically repeated below.

The characteristic layer contains a macroscopic banding, termed a "layer band" at the top of the layer and a "nominal" microstructure below. The layer band is 165μm thick and consists of a colony-α_S morphology. The microstructure between layer bands is basketweave-α_S outlined in retained β phase and exhibits a gradient in the α lath width between layer bands. The layer bands traverse prior beta grains and grain boundaries, indicating their formation occurs after multiple layers have been deposited during a solid state transformation. The layer bands have the same hardness as the surrounding material. There are no variations in substructure or orientation associated with the layer band or basketweave morphologies. Furthermore, α′ and α_m were not observed in the deposit. Variations in the degree of vanadium partitioning to the beta phase were observed in the layer band region as well as the transient layers. The variation was observed as lack of contrast in BSE images and an apparent decrease in the beta phase vanadium composition measured using EDS. Regions where vanadium did not partition strongly to the beta phase are associated with heating high into the α+β and/or β phase fields.

Thermal effects are responsible for the formation of the gradient and layer band morphologies. The transient layers experience heating into the beta phase field, while the characteristic layer forms during heating into the α+β phase field. It is hypothesized that the characteristic layer

forms in a layer *n* due to the deposition of layer *n+3*. Depositing additional layers (i.e. *n+4*, *n+5*…) to the deposit do not alter the microstructure in layer *n*.

Stability of as-deposited LMD Ti-6Al-4V microstructure

Heat treatments performed on the as-deposited material quantify the temperature range where the layer band morphology forms. After a 2-hour solution treatment in the $\alpha+\beta$ phase field (1186K) and a 4-hour aging treatment (811 K) the layer band remains and the gradient in the α width is eliminated. Increasing cooling rate from the solution temperature resulted in finer α grains in the samples. Heating well above the beta transus homogenized the entire microstructure, eliminating the layer band and basketweave structure and replacing it with a colony-α_P morphology. This indicates that the layer band forms as a result of heating above 1186K. From these results it can be concluded that the layer band forms during heating a region of the deposit high into the $\alpha+\beta$ phase field (at least above 1186K) to a temperature sufficient dissolve a large amount of alpha so that when cooled a new morphology forms (colony-α_S).

Thermal modeling of LMD processes

In order to quantify the thermal cycling that occurs during LMD processes a thermal model was developed using implicit finite difference methods. Heat input was modeled using a double ellipsoidal volumetric distribution of heat. An attempt to verify the model was made using experimental data for LENS^{TM} processing of 316-stainless steel; a fair agreement was obtained. Processing conditions for the as-deposited Ti-6Al-4V material were unknown, necessitating calibration of the model against the as-deposited microstructure. The results of calibrated process conditions indicate that after four layers are added, the characteristics of the thermal cycle (maximum temperature, cooling rate, heating rate, size of the heat affected zone) reach a steady state due to a change in the heat flow conditions from 2-D near the substrate to 1-D as the wall forms.

The three most recent layers added to the deposit are predicted to experience heating above the beta transus (a primary heat treatment or thermal cycle) while the fourth most recent layer experiences heating above the alpha dissolution temperature, but below the beta transus (a secondary heat treatment or thermal cycle). In other words layer *n* experiences a secondary heat treatment, while layers *n+1* through *n+3* experience primary thermal treatments. The material

below layer *n* (e.g. *n-1*) will not experience sufficient heating to produce microstructural changes and have a similar microstructure to layer *n*. This is in agreement with the hypothesis made regarding the evolution of as-deposited microstructure. Within the 5mm-thick characteristic layer, the variation in peak temperature (~300K) is much greater than variation in cooling rate (4K/s); therefore, peak temperature will have a much greater affect on microstructure than cooling rate.

Microstructure model development

The effect of thermal history on microstructure is quantified using a microstructure model that determines the α phase fraction and α-morphology evolution during thermal cycling. The phase fraction model consists of two sub–models that are invoked for alpha dissolution and alpha nucleation and growth. Dissolution occurs when the current phase fraction is greater than equilibrium and growth occurs when the current phase fraction is less than equilibrium.

For dissolution of the alpha phase, the parabolic thinning rate is obtained through a series of isothermal "heating" simulations using diffusion controlled transformation software (DiCTra). The parabolic thinning rate is used to describe the kinetics of the alpha thinning process. A JMAK model was used to describe the growth of alpha from beta. The kinetic data for the JMAK model was obtained from a TTT diagram calculated using the computational thermodynamic and materials modeling software, JMatPro.

Both the alpha dissolution and nucleation/growth models are based on kinetic parameters derived for isothermal treatments. These kinetic parameters can be extended to non-isothermal treatments using the principle of additivity where non-isothermal microstructure evolution is described as the sum of many small isothermal steps. The phase fraction model results were compared to recent time-resolved x-ray diffraction experiments and a good match between experiment and model was obtained.

The TTT diagram considered the formation of alpha at two sites: grain boundaries and intragranularly. Grain boundary nucleation predominately occurs above T_{IG}=1100K and intragranular nucleation occurs below 1100K. The corresponding morphologies being grain boundary nucleated allotriomorphic- and colony-alpha and intragranularly nucleated basketweave-alpha. Based on the different morphologies described in the TTT diagram, a

simplistic model was developed to track the evolution of colony and basketweave alpha formation. Above T_{IG}, any alpha that forms does so in a colony-alpha morphology. Likewise, below T_{IG}, any additional alpha to form does so as basketweave-alpha. During alpha dissolution below T_{IG} only basketweave dissolves, while above T_{IG} both basketweave and colony-alpha dissolve at equal rates. The morphology model assumes that during a secondary-thermal cycle (maximum temperature in the $\alpha+\beta$ phase field) nucleation of colony-alpha can occur intragranularly (even though the kinetics are for plate growth at a grain boundary). In addition, the dissolution of basketweave- and colony-α_S and α_P follow the same kinetic parameter.

The resulting morphology evolution was compared to the baseline microstructure experiments for primary and secondary heat treatments where 0.6 and 10K/s cooling rates were used. For the 0.6K/s primary and secondary heat treatments the model predicted a final alpha morphology consisting of 77% colony-α and 14% basketweave-α. The actual samples did not contain any basketweave-α after the secondary heat treatment. For the 10K/s primary and secondary heat treatments, the final alpha morphology was predicted to contain 22% colony-α and 69% basketweave-α. The actual samples contained very little colony-α except at grain boundaries. Overall, the model does a good job at predicting the dominant alpha morphology present which should be sufficient to illustrate the effect of thermal cycling on the as-deposited microstructure in Ti-6Al-4V.

Coupled thermal and microstructural modeling for LMD of Ti-6Al-4V

The thermal model results for LMD of Ti-6Al-4V were used as input to the phase fraction and morphology evolution models, resulting in a predicted microstructure that is qualitatively similar to the as-deposited microstructure. The phase fraction model predicts a near equilibrium evolution with the greatest spatial (z) variation in the maximum alpha fraction during the *n+3* thermal cycle, corresponding to heating into the $\alpha+\beta$ phase field. The phase fraction evolution paths for the deposition of layers *n* through *n+2* are similar, while the deposition of *n+4* leads to no change in the phase fraction. The phase fraction results reinforced the theory that the as-deposited characteristic layer forms after the deposition of layer *n+3* onto layer *n*. In addition, the phase fraction results suggest that non-equilibrium products (α' and α_m) will not appear after three layers are added.

The morphology model illustrates the periodic nature of the characteristic layer that is repeated during the deposition of multiple layers of material. The modeled characteristic layer contained relatively high amounts of colony alpha at the top of the layer and high amounts of basketweave at the bottom of the layer, in agreement to the as-deposited microstructure. The transition from basketweave to a colony-α morphology below the layer band is much more gradual than above the layer band where the transition is sharp. Above the last characteristic layer there are three layers of predominately basketweave-α representing the transient layers in the as-deposited microstructure.

When coupled with the thermal model results, the position of the characteristic and transient layers, and number of thermal cycles to produce these layers is in excellent agreement with the as-deposited microstructure. The microstructure model has proven that a greater amount of colony alpha (e.g. layer band) forms during a high temperature thermal cycle into the α+β phase field resulting in the layer band formation.

Conclusion

This thesis has investigated the complex solid-state microstructure evolution during laser metal deposition of the two phase α+β titanium alloy Ti-6Al-4V through material characterization, thermal and microstructure modeling. The as-deposited macrostructure contains two distinct regions that are a direct result of the thermal cycling that occurs during the additive deposition process. A transient region of an undeveloped microstructure forms in the last three layers of the deposit. The transient region consists of fine basketweave and colony-alpha morphologies that are associated with heating into the β-phase field (T>1273K) and cooling at rates on the order of 10K/s (as observed in the baseline microstructure experiments and predicted in the thermal model). A characteristic layer develops in the fourth to last deposited layer and is repeated/retained in underlying layers.

The characteristic layer contains two regions of distinct microstructural contrast. At the bottom of the characteristic layer, fine basketweave-alpha is found. Moving in the +z direction within the characteristic layer the basketweave-alpha grains become thicker. At the top of the characteristic layer, a colony-α morphology is observed, termed the "layer band." The layer band is observed macroscopically as a periodic banding oriented parallel to the substrate.

The formation of the characteristic layer is a direct result of thermal cycling, specifically heating into the two-phase $\alpha+\beta$ field. Heating high into the two phase field dissolves a large amount of α_P and during subsequent α_S growth, large regions of colony-α_S form, e.g. the layer band. This is confirmed by thermal and microstructure modeling where periodic regions of higher amounts of colony-α_S are predicted to form.

The model-predicted microstructure is qualitatively in excellent agreement with the as-deposited microstructure. The characteristic layer is predicted and observed to form in a layer *n* due to the deposition of layer *n+3*. In addition, experimental investigations as to the effect of heating as-deposited and "traditionally processed" Ti-6Al-4V above and below the beta transus reinforced the claim that the layer band is a result of heating material high into the $\alpha+\beta$ phase field.

Future Work

In depth investigation of microstructure evolution during secondary heat treatments

In the baseline microstructure experiments, a single secondary heat treatment temperature and two different cooling rates were used. The baseline microstructure experiments were useful in that they showed the potential contrast between primary and secondary thermal treatments and their effect on primary- and secondary-alpha morphologies. The thermal model results indicate (for the processing conditions investigated) that peak temperature varies significantly with z position, while cooling rate varies much less. Therefore, peak temperature will generally have the greatest influence on microstructural evolution. Performing a series of secondary heat treatments at different temperatures in the two phase field will better illustrate the formation of colony-α_S at cooling rates observed in the microstructure model. In addition, performing secondary heat treatments followed by rapid quenching to produce α' would aid in understanding the amount of α_P dissolution that occurs during heating. Both of these experiments are similar to the work of Semiatin *et al*.[39] The difference here being the starting microstructure will consist of 100% basketweave-α_P whereas Semiatin started with a equiaxed $\alpha+\beta$ microstructure. These experiments will result in a more accurate temperature for colony-α_S formation and a better understanding of the dissolution process, which to date has not been critically investigated.

Validation of a massive transformation in Ti-6Al-4V

The work of Ahmed and Rack suggests that a massive transformation will occur in Ti-6Al-4V at moderate cooling rates between 20-410 K/s.[28] The grain boundary precipitate that they call massive alpha appears similar to very fine allotriomorphic sideplates. In Ahmed and Rack's paper, they indicate that the massive phase may also appear intragranularly, but the grains labeled as massive in their micrographs appear similar to α, whereas in other alloys, the massive phase appears very irregular, encompassing a large area of the parent grain, which is not the case here.[49,142] While bulk composition measurements were made by the authors, a much finer resolution composition measurement is needed at the interface to rule out non-partitioning local equilibrium as a mode of precipitation. To this end, further work should be performed on the baseline microstructure samples to investigate the nature of the precipitate at the prior beta grain boundary.

Thermal model improvements

Rather than beginning with a commercially available finite element code, the thermal model was developed in Mathematica in order to better understand the laser metal deposition process and associated heat transfer. Further improvements to the model will necessitate using a more flexible commercial finite element code that considers variable geometries, fluid flow, and thermal stress development. The current model assumes a new layer is rectangular in nature, not "bead" or "hemispherical cap" shaped as is in the actual deposit. This shape change will alter heat transfer at the surface via radiation and convection. Including fluid flow in the model may also correct the shape of the bead due to surface tension and gravitational forces on the molten pool. A model that considers fluid flow would also be necessary for dimensional control of the deposit. The thermal stress that develops during deposition would also be interesting to know both from a dimensional control and mechanical property standpoint.

Microstructure model improvements

While the phase fraction and morphology models are qualitatively in agreement with the as deposited microstructure, several simplifying assumptions have been made, that if corrected could lead to a more robust and quantitatively accurate model. First, the model does not consider the effect on local composition of the alpha and beta phases. Changes in the composition of

these phase will affect the kinetics of the phase transformations that take place, as well as the morphologies that form. Hemmer and Grong[120] model the dissolution and growth of austenite in a duplex stainless steel by calculating the diffusion profile during the thermal cycle. Their model could be extend to model diffusion controlled dissolution of alpha provided the assumption can be made that either vanadium or aluminum supersaturation controls the reaction.

The nucleation and growth of alpha was modeled using a single kinetic parameter that was fit to the TTT diagram describing two different nucleation sites. In reality, these nucleation sites are each described by a single JMA equation, with different $k(T)$ and n values. Jones and Bhadeshia[143,144] model the competitive formation of ferrite nucleated at austenite grain surfaces and intragranularly using the JMA approach to model simultaneous reactions. Use of a simultaneous transformation scheme for the different nucleation sites relating to colony and basketweave alpha formation would lead to a more theoretical approach to obtaining the morphology evolution during alpha growth.

Process design for microstructure and property control

The transfer of the thermal and microstructure models to industrial practice is the next major step for this research. This would involve being able to tailor microstructure during processing, leading to parts having designed or functionally graded microstructures. In order to do this, in situ process control must be realized and appropriate control and response mechanisms established for different alloys. The thermal model would need to calculate the temperature distribution in the deposit from a measured temperature in the actual deposit, the resulting microstructure calculated and compared to the desired microstructure. Then, adjustments would need to be made to the process conditions to alter microstructure.

Chapter 10: Appendices

Selected Area Diffraction Indexing Procedure

The goal of this program is to index TEM spot patterns using distances between adjacent spots in a pattern and the corresponding angles these spots make. For each set of spots, the ratio is compared with a list of generated ratios for the d-spacings and angles of the corresponding planes of the particular lattice in question. Spots matching actual planes are added to a list for further comparison with a second set of spots (R3, R1). The two lists are further refined by comparing the zone axes and the values for the R1 plane. User interpretation is needed at this point to pick the most appropriate zone index from the list of common zone axes.

The program as been used with HCP-Ti and Beta-Ti and compared with published spot patterns for BCC and HCP lattices (Edington, Carter and Williams) . It has also been compared with a Fortran based crytal program 'CRYSTAL' by H.D.H.K. Bhadeshia of Cambridge (http://www.msm.cam.ac.uk/map/crystal/programs/crystal-b.html).

User Input will appear like this.

- **06/14/2004: Added rd=Lλ to viewing results code**
- **05/5/2004: Added sterogram capability for HCP**
- **05/1/2004: Made the program general to accept any lattice (currently set-up for BCC, FCC, and HCP, $L1_0$, and $L1_2$). Previous versions good for HCP only. Can Import a Spot Pattern as an image, and picks points that are used to index the pattern.**
- **09/12/2003: Initial Code developed.**

Define Equations (no user input)

```
Clear["`*"]
Off[General::spell]
Off[General::spell1]
```

- **Generic System**

In a generic system, the metric tensor must be used

```
Clear[a, b, c]
```

CAUTION: Setting a, b=a, c=a, etc, NOW messes up G Gstar, if you do set it it now, make sure you CLEAR them before running the Indexing Procedure

```
(*a=2.950;b=a;c=4.683;α=90;β=90;γ=120;*)

(*a=1;b=a;c=1.633;α=90;β=90;γ=120;*)

(*a=a;b=a;c=c;α=90;β=90;γ=120;*)
```

```
G = {{a^2, a b Cos[γ °], a c Cos[β °]},
     {a b Cos[γ °], b^2, b c Cos[α °]},
     {a c Cos[β °], b c Cos[α °], c^2}};
Gstar = Inverse[G];
```

The angle between two planes:

```
ϕ[vec1_, vec2_] := ArcCos[vec1.Gstar.vec2 / Sqrt[(vec1.Gstar.vec1) * (vec2.Gstar.vec2)]] * 180. / π
```

The d-spacing of a plane is given by the function dis

```
dis[vec_] := (vec.Gstar.vec)^-1/2

dis[{h, k, l}];
```

The 'basisfunc' defines a basis for the particular lattice (input as a string). The user can add additional bases.
The basis is defined as a list of the atomic positions for each atom in the lattice. The first level of the list refers to different atoms and the second level refers to each atomic position of that atom.

```
basisfunc[lattice_] :=
 Which[
  lattice == "BCC", {{{0, 0, 0}, {1/2, 1/2, 1/2}}},
  lattice == "FCC", {{{0, 0, 0}, {1/2, 1/2, 0}, {1/2, 0, 1/2}, {0, 1/2, 1/2}}},
  lattice == "HCP", {{{0, 0, 0}, {1/3, 2/3, 1/2}}},
  lattice == "L10", {{{0, 0, 0}}, {{1/2, 1/2, 1/2}}},
  lattice == "L12", {{{0, 0, 0}}, {{1/2, 1/2, 0}, {1/2, 0, 1/2}, {0, 1/2, 1/2}}}
 ]
```

The intensity of the diffracting beam (structure factor). This determines whether a diffracted spot will appear based on the basis. (Eqn. 16.6, Williams and Carter).
f is arbitrary for this program. It is actually f(θ), the atomic scattering amplitude.

```
Int[{h_, k_, l_}] :=
 Sum[Sum[f[[j]] * Exp[2 π I ({h, k, l}.basis[[j, i]])], {i, 1, Length[basis[[j]]]}],
  {j, 1, Length[basis]}]
```

We need to define a list of atomic scattering amplitudes for each atom in the basis. here they are arbitrarily set to f1 and f2.

```
f = {fAl, fNi};

basis = basisfunc["L12"] (*set now to explore the 'Int' funcuntion*)
```

$$\left\{\{\{0, 0, 0\}\}, \left\{\left\{\frac{1}{2}, \frac{1}{2}, 0\right\}, \left\{\frac{1}{2}, 0, \frac{1}{2}\right\}, \left\{0, \frac{1}{2}, \frac{1}{2}\right\}\right\}\right\}$$

```
Int[{2, 2, 2}]
```

```
fAl + 3 fNi
```

■ Equations Specific to the HCP system

Typically hexagonal lattices are described using Miller-Bravais 4-index notation; however, the equations require the vectors be in the Miller three index notation. 'Hex' and UnHex' accomplish this. Hex and UnHex should be used for Planes, while 'HexAxis' and 'UnHexAxis' should be used for directions.

```
Hex[vec_] := Insert[vec, -(vec[[1]] + vec[[2]]), 3]

(*Hex[vec_]:={(2*vec[[1]]-vec[[2]]),
   (2*vec[[2]]-vec[[1]]),-(vec[[1]]+vec[[2]]),3 vec[[3]]}*)

Hex[{u, v, w}]
```

```
{u, v, -u - v, w}
```

```
Hex[{0, 0, 1}]
```

```
{0, 0, 0, 1}
```

```
UnHex[vec_] := Delete[vec, 3]

(*UnHex[vec_]:={vec[[1]]-vec[[3]],vec[[2]]-vec[[3]],vec[[4]]}*)

UnHex[{2 / 3, -1 / 3, -1 / 3, 0}]
```

$$\left\{\frac{2}{3}, -\frac{1}{3}, 0\right\}$$

```
Hex[{2, 1, 0}]
```

```
{2, 1, -3, 0}
```

```
vec = {0, 1, -1, 0};

vec == Hex[UnHex[vec]]
```

```
True
```

These equations are taken from Edington, EQ A2.8 and A2.9, they are used for going from Miller-Bravais notation to a Cartesian system and vice-versa. These are for Directions!

```
UnHexAxis[{x_, y_, z_, l_}] := {2 x + y, 2 y + x, l}
HexAxis[{x_, y_, l_}] := {(2 x - y) / 3, (2 y - x) / 3, -(y + x) / 3, l}

vec = {-2, 4, -2, 3};

vec == HexAxis[UnHexAxis[vec]]
```

```
True
```

```
UnHexAxis[vec]
```

```
{0, 6, 3}
```

■ Equations for the Zone axis

Calculating the zone axis

```
zone[vecA_, vecB_] := Cross[vecA, vecB] / (GCD @@ Cross[vecA, vecB])
```

Proper usage for HCP: HexAxis[zone[UnHex[vecA],UnHex[vecB]]]/GCD@@HexAxis[zone[UnHex[vecA],UnHex[vecB]]]

```
vecA = {0, 1, -1, 0};
vecB = {0, 1, -1, 1};
zone[UnHex[vecA], UnHex[vecB]]
HexAxis[zone[UnHex[vecA], UnHex[vecB]]]
HexAxis[zone[UnHex[vecA], UnHex[vecB]]] /
 (GCD @@ HexAxis[zone[UnHex[vecA], UnHex[vecB]]])
```

```
{1, 0, 0}
```

$$\left\{\frac{2}{3}, -\frac{1}{3}, -\frac{1}{3}, 0\right\}$$

```
{2, -1, -1, 0}
```

This test must be satisfied (True) for a plane (or diffracted spot) to have the specified zone axis (B).

```
zonetestHex[zoneplane_, zoneaxis_] := UnHex[zoneplane].UnHexAxis[zoneaxis] == 0
zonetest[zoneplane_, zoneaxis_] := zoneplane.zoneaxis == 0

zonetestHex[{2, 0, -2, -1}, {0, 1, -1, 2}]
```

```
True
```

```
UnHex[{2, 0, -2, 1}]
```

```
{2, 0, 1}
```

Proper usage for HCP is: zonetest[UnHex[zoneplane],UnHexAxis[zoneaxis]]

```
zonetest[UnHex[{2, 0, -2, -1}], UnHexAxis[{0, 1, -1, 2}]]
```

```
True
```

The weighted average zone axis using three points

$$\mathbf{B3}[\mathbf{vec1_}, \mathbf{vec2_}, \mathbf{vec3_}] := \frac{\mathbf{Cross}[\mathbf{vec2}, \mathbf{vec3}]}{\mathbf{Norm}[\mathbf{vec1}]^2} + \frac{\mathbf{Cross}[\mathbf{vec3}, \mathbf{vec1}]}{\mathbf{Norm}[\mathbf{vec2}]^2} + \frac{\mathbf{Cross}[\mathbf{vec1}, \mathbf{vec2}]}{\mathbf{Norm}[\mathbf{vec3}]^2}$$

Generic form to find the angle between two vectors in real and reciprocal space. A zone axis is in real space. UnHexAxis must be used for HCP.

```
zoneangReal[vec1_, vec2_] :=
 ArcCos[((vec1 - vec2).G.(vec1 - vec2) - (vec1.G.vec1 + vec2.G.vec2))/
     (-2 Sqrt[(vec1.G.vec1) * (vec2.G.vec2)])] / Degree // N

zoneangRecip[vec1_, vec2_] :=
 ArcCos[((vec1 - vec2).Gstar.(vec1 - vec2) - (vec1.Gstar.vec1 + vec2.Gstar.vec2)) /
     (-2 Sqrt[(vec1.Gstar.vec1) * (vec2.Gstar.vec2)])] / Degree // N
```

■ Stereogram Plot HCP

```
a = 1 ; b = 1 ; c = 1.62 ; α = 90 ; β = 90 ; γ = 120 ; (*GENERIC HCP SYSTEM*)

hcpstereo = {{1, -1, 0, 0}, {0, 0, 0, 1}, {-1, -1, 2, 0},
   {1, -1, 0, 1}, {2, -1, -1, 0}, {2, -1, -1, 2}, {1, -2, 1, 1},
   {2, -1, -1, 1}, {1, 2, -3, 1}, {-1, 2, -1, 0}, {1, -1, 0, 4}}
```

```
{{1, -1, 0, 0}, {0, 0, 0, 1}, {-1, -1, 2, 0},
 {1, -1, 0, 1}, {2, -1, -1, 0}, {2, -1, -1, 2}, {1, -2, 1, 1},
 {2, -1, -1, 1}, {1, 2, -3, 1}, {-1, 2, -1, 0}, {1, -1, 0, 4}}
```

```
hcpstereoax =
 Table[{UnHexAxis[hcpstereo[[i]]], hcpstereo[[i]]}, {i, 1, Length[hcpstereo]}]
```

```
{{{1, -1, 0}, {1, -1, 0, 0}}, {{0, 0, 1}, {0, 0, 0, 1}}, {{-3, -3, 0}, {-1, -1, 2, 0}},
 {{1, -1, 1}, {1, -1, 0, 1}}, {{3, 0, 0}, {2, -1, -1, 0}},
 {{3, 0, 2}, {2, -1, -1, 2}}, {{0, -3, 1}, {1, -2, 1, 1}}, {{3, 0, 1}, {2, -1, -1, 1}},
 {{4, 5, 1}, {1, 2, -3, 1}}, {{0, 3, 0}, {-1, 2, -1, 0}}, {{1, -1, 4}, {1, -1, 0, 4}}}
```

```
hcpstereopl =
 Table[{UnHex[hcpstereo[[i]]], hcpstereo[[i]]}, {i, 1, Length[hcpstereo]}]
```

```
{{{1, -1, 0}, {1, -1, 0, 0}}, {{0, 0, 1}, {0, 0, 0, 1}},
 {{-1, -1, 0}, {-1, -1, 2, 0}}, {{1, -1, 1}, {1, -1, 0, 1}},
 {{2, -1, 0}, {2, -1, -1, 0}}, {{2, -1, 2}, {2, -1, -1, 2}},
 {{1, -2, 1}, {1, -2, 1, 1}}, {{2, -1, 1}, {2, -1, -1, 1}},
 {{1, 2, 1}, {1, 2, -3, 1}}, {{-1, 2, 0}, {-1, 2, -1, 0}}, {{1, -1, 4}, {1, -1, 0, 4}}}
```

For Plotting DIRECTIONS on a stereogram, use G (This is in REAL space, where DIRECTIONS are points)
Directions are colored Red ('Hue[0]')
For plotting PLANES on a stereogram, use G* (This is in RECIPROCAL space, where PLANES are points)
Planes are colored Blue ('Hue[0.625]')

In addition, use 'UnHexAxis[ ]' for planes and 'UnHex[ ]' for axes. Counterintuitive, but it works this way becuase directions are in real space where 'UnHex[ ]' works and planes are in reciprocal space, where 'UnHexAxis[ ]' works.

```
ax = {-1, -1, 0}; ay = {1, -1, 0}; az = {0, 0, 1};
```

```
unitvector[pole_, mat_] := pole / Sqrt[pole.mat.pole] // N

l[pole_, mat_] :=
 unitvector[pole, mat].mat.ax /
  (Sqrt[unitvector[pole, mat].mat.unitvector[pole, mat]] * Sqrt[ax.mat.ax]) // N
m[pole_, mat_] :=
 unitvector[pole, mat].mat.ay /
  (Sqrt[unitvector[pole, mat].mat.unitvector[pole, mat]] * Sqrt[ay.mat.ay]) // N
n[pole_, mat_] :=
 unitvector[pole, mat].mat.az /
  (Sqrt[unitvector[pole, mat].mat.unitvector[pole, mat]] * Sqrt[az.mat.az]) // N
PolePlot[polelist_, labelpos_, mat_] :=
 Show[
  Graphics[
   {(*Setting up the great circle and background size*)
    GrayLevel[1],
    Point[{-2.5, -2.5}],
    Point[{2.5, 2.5}],
    GrayLevel[0],
    Circle[{0, 0}, 2],
    {(*Creating a Table of the points and their labels*)
     If[mat == G, Hue[0], Hue[0.625]], PointSize[0.01],
     Table[{Point[{2 m[polelist[[i, 1]], mat] / (1 + n[polelist[[i, 1]], mat]),
         -(2 l[polelist[[i, 1]], mat] / (1 + n[polelist[[i, 1]], mat]))}],
       Text[polelist[[i, labelpos]],
        {2 m[polelist[[i, 1]], mat] / (1 + n[polelist[[i, 1]], mat]),
         -(2 l[polelist[[i, 1]], mat] / (1 + n[polelist[[i, 1]], mat]))},
        {-1.2, 0}, {1, 0}]}, {i, 1, Length[polelist]}]},
    (*Adding Labels for the planes and directions*)
    If[mat == G, {Hue[0], Text["DIRECTIONS", {-2.4, 2.4}, {-1, 0}]},
     {Hue[0.675], Text["PLANES", {-2.4, 2.2}, {-1, 0}]}]
    }
   ],
  AspectRatio -> Automatic, TextStyle -> {FontFamily -> Arial, FontSize -> 10},
  DisplayFunction -> $DisplayFunction]

Show[PolePlot[hcpstereopl, 2, Gstar], PolePlot[hcpstereoax, 2, G]]
```

PLANES

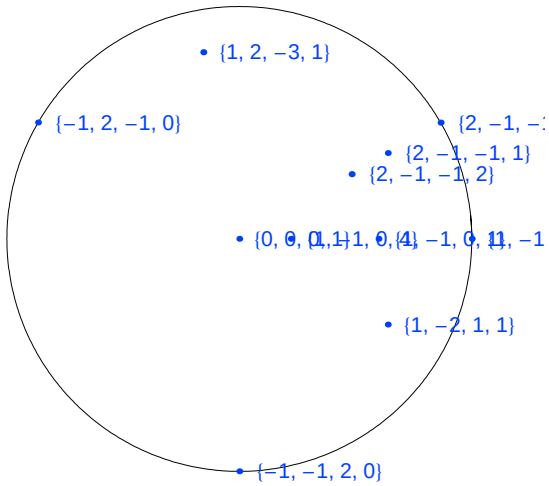

DIRECTIONS

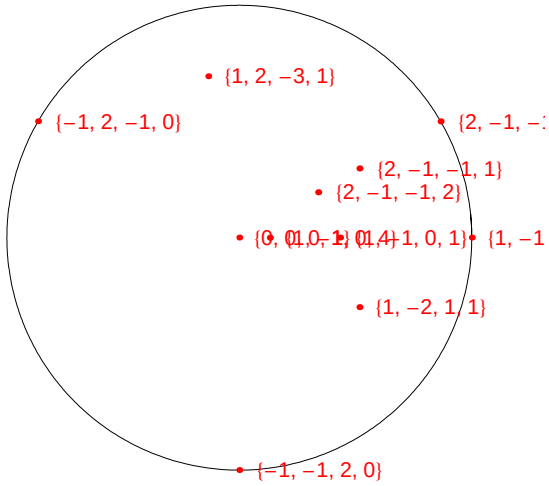

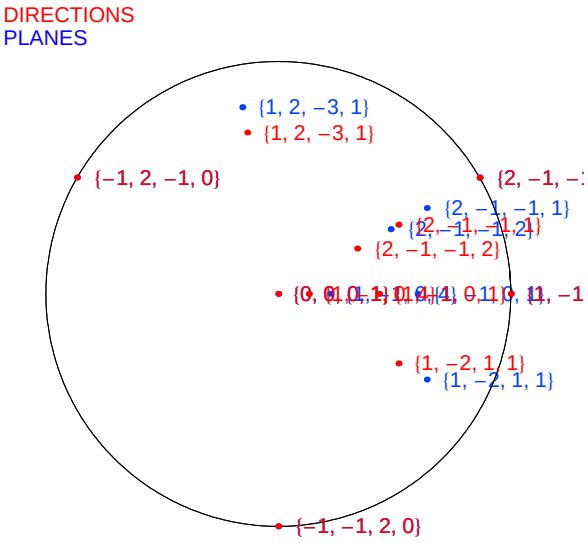

- Graphics -

Indexing Procedure

■ User Input for Lattice

User input appears in red text in a gray cell. The black text in the gray cell requires no changes.

Choose a lattice type to index. HCP, FCC, BCC, L10, L12

```
latticename = "HCP";
basis = basisfunc[latticename];
Print["The atoms in the basis are: ", basis]
```

The atoms in the basis are: $\{\{\{0, 0, 0\}, \{\frac{1}{3}, \frac{2}{3}, \frac{1}{2}\}\}\}$

If the lattice parameters are not present, add them here along with the particular lattice as needed.

```
Which[
  latticename == "HCP", {a = 2.95111; b = 2.95111;
   c = 4.68433; α = 90; β = 90; γ = 120;(*ALPHA TITANIUM*)},
  latticename == "FCC", {a = 4.45; b = 4.45; c = 4.45; α = 90;
   β = 90; γ = 90;(*TiHx Interface Phase*)},
  latticename == "BCC", {a = 3.283; b = 3.283; c = 3.283;
   α = 90; β = 90; γ = 90;(*BETA TITANIUM*)}
 ];
```

■ Set-Up

First, a list of hkl vectors is defined using 'rng'. The intensity of each of these planes is calculated and the allowable reflections (Int!=0) stored into a list 'hklallow'. The d-spacing may then be calculated, and the d-space list and the allowable hkl list reordered from the largest d-spacing to the smallest. By doing this we are starting with the low index planes first. In addition parallel planes are deleted from the list to further reduce the number of duplicate solution produced.

```
f = Table[1, {i, 1, Length[basis]}];

(*range of hkl values,
 can be changed to index higher order patterns, 3 is fine.  *)

rng = 3;
hkl = Flatten[Table[{i, j, k}, {i, -rng, rng}, {j, -rng, rng}, {k, 0, rng}], 2];
intlist = Map[Abs[Int[#]]^2 &, hkl] ;(*Intensity List*)

Length[intlist]
```

```
196
```

Allowable hkl values are defined when the Intensity or structure factor is not zero.

```
hklallow = {};
Do[If[intlist[[i]] ≠ 0, AppendTo[hklallow, hkl[[i]]],], {i, 1, Length[hkl]}]
hklallow = DeleteCases[hklallow, {0, 0, 0}];
Print["Deleted ", Length[hkl] - Length[hklallow], " forbidden reflections."]
```

```
Deleted 35 forbidden reflections.
```

Sorting from, smallest dspacing to greatest, i.e. high to low index planes

```
dspace = Map[dis[#] &, hklallow];
dspacenew = Sort[dspace, Greater];
Ordering[dspace, All, Greater];
hklallownew = Map[hklallow[[#]] &, Ordering[dspace, All, Greater]];
dspace = dspacenew
hklallow = hklallownew;
```

```
{2.55574, 2.55574, 2.55574, 2.55574, 2.55574, 2.55574, 2.34217, 2.24354,
 2.24354, 2.24354, 2.24354, 2.24354, 1.72674, 1.72674, 1.72674,
 1.72674, 1.72674, 1.72674, 1.47555, 1.47555, 1.47555, 1.47555, 1.47555,
 1.47555, 1.33244, 1.33244, 1.33244, 1.33244, 1.33244, 1.33244, 1.27787,
 1.27787, 1.27787, 1.27787, 1.27787, 1.27787, 1.24846, 1.24846, 1.24846,
 1.24846, 1.24846, 1.24846, 1.23282, 1.23282, 1.23282, 1.23282, 1.23282,
 1.23282, 1.12177, 1.12177, 1.12177, 1.12177, 1.12177, 1.12177, 0.988915,
 0.988915, 0.988915, 0.988915, 0.988915, 0.988915, 0.965977, 0.965977,
 0.965977, 0.965977, 0.965977, 0.965977, 0.965977, 0.965977, 0.965977,
 0.965977, 0.965977, 0.965977, 0.946071, 0.946071, 0.946071, 0.946071,
 0.946071, 0.946071, 0.946071, 0.946071, 0.946071, 0.946071, 0.946071,
 0.946071, 0.893009, 0.893009, 0.893009, 0.893009, 0.893009, 0.893009,
 0.893009, 0.893009, 0.893009, 0.893009, 0.893009, 0.893009, 0.851912,
 0.851912, 0.851912, 0.851912, 0.851912, 0.851912, 0.821485, 0.821485,
 0.821485, 0.821485, 0.821485, 0.821485, 0.821485, 0.821485, 0.821485,
 0.821485, 0.821485, 0.821485, 0.800598, 0.800598, 0.800598, 0.800598,
 0.800598, 0.800598, 0.737777, 0.737777, 0.708834, 0.708834, 0.708834,
 0.708834, 0.703692, 0.703692, 0.700855, 0.700855, 0.700855, 0.700855,
 0.678445, 0.678445, 0.678445, 0.678445, 0.645441, 0.645441, 0.645441,
 0.645441, 0.586326, 0.586326, 0.586326, 0.586326, 0.581786, 0.581786,
 0.581786, 0.581786, 0.568775, 0.568775, 0.568775, 0.568775, 0.548903,
 0.548903, 0.548903, 0.548903, 0.491852, 0.491852, 0.481352, 0.481352}
```

```
dis[{1, 0, 1}]
```

```
2.24354
```

```
dis[{2, -1, 0}]
```

```
1.47555
```

Further reducing duplicates from the list by deleting those planes that are parallel using the cross product. If the cross product is {0,0,0}, then parallel

```
i = 1;
len = Length[dspace];
leninit = len;
Print["The following Parallel planes [
   {h1,k1,l1}||{h2,k2,l2}] are being deleted {h2,k2,l2}:"]
While[i ≤ len,
 {
  j = 1,
  While[j ≤ len,
   {
    If[hklallow[[i]] ≠ hklallow[[j]] &&
      Cross[hklallow[[i]], hklallow[[j]]] == {0, 0, 0},
     {
      Print["Deleting ", hklallow[[j]],
       " because ", hklallow[[i]], " || ", hklallow[[j]]],
      hklallow = Drop[hklallow, {j}],
      dspace = Drop[dspace, {j}],
      len = Length[dspace]
     },
     j += 1,
     len = Length[dspace]
    ],
    len = Length[dspace],
   }
  ],
  i += 1
 }
]
Print["Deleted ", leninit - len, " parallel planes"]
Print["The list of d-spacings are: "]
dspace
Print["The list of allowable planes: "]
hklallow
```

```
The following Parallel planes [{h1,k1,l1}||{h2,k2,l2}] are being deleted {h2,k2,l2}:

Deleting {-1, 0, 0} because {1, 0, 0} || {-1, 0, 0}

Deleting {2, 0, 0} because {1, 0, 0} || {2, 0, 0}

Deleting {-2, 0, 0} because {1, 0, 0} || {-2, 0, 0}

Deleting {3, 0, 0} because {1, 0, 0} || {3, 0, 0}

Deleting {-3, 0, 0} because {1, 0, 0} || {-3, 0, 0}

Deleting {-1, 1, 0} because {1, -1, 0} || {-1, 1, 0}

Deleting {2, -2, 0} because {1, -1, 0} || {2, -2, 0}

Deleting {-2, 2, 0} because {1, -1, 0} || {-2, 2, 0}

Deleting {3, -3, 0} because {1, -1, 0} || {3, -3, 0}

Deleting {-3, 3, 0} because {1, -1, 0} || {-3, 3, 0}
```

```
Deleting {0, -1, 0} because {0, 1, 0} || {0, -1, 0}
Deleting {0, 2, 0} because {0, 1, 0} || {0, 2, 0}
Deleting {0, -2, 0} because {0, 1, 0} || {0, -2, 0}
Deleting {0, 3, 0} because {0, 1, 0} || {0, 3, 0}
Deleting {0, -3, 0} because {0, 1, 0} || {0, -3, 0}
Deleting {2, 0, 2} because {1, 0, 1} || {2, 0, 2}
Deleting {2, -2, 2} because {1, -1, 1} || {2, -2, 2}
Deleting {0, 2, 2} because {0, 1, 1} || {0, 2, 2}
Deleting {0, -2, 2} because {0, -1, 1} || {0, -2, 2}
Deleting {-2, 2, 2} because {-1, 1, 1} || {-2, 2, 2}
Deleting {-2, 0, 2} because {-1, 0, 1} || {-2, 0, 2}
Deleting {-2, 1, 0} because {2, -1, 0} || {-2, 1, 0}
Deleting {-1, -1, 0} because {1, 1, 0} || {-1, -1, 0}
Deleting {2, 2, 0} because {1, 1, 0} || {2, 2, 0}
Deleting {-2, -2, 0} because {1, 1, 0} || {-2, -2, 0}
Deleting {3, 3, 0} because {1, 1, 0} || {3, 3, 0}
Deleting {-3, -3, 0} because {1, 1, 0} || {-3, -3, 0}
Deleting {-1, 2, 0} because {1, -2, 0} || {-1, 2, 0}
Deleting {-3, 1, 0} because {3, -1, 0} || {-3, 1, 0}
Deleting {-3, 2, 0} because {3, -2, 0} || {-3, 2, 0}
Deleting {-2, -1, 0} because {2, 1, 0} || {-2, -1, 0}
Deleting {-2, 3, 0} because {2, -3, 0} || {-2, 3, 0}
Deleting {-1, -2, 0} because {1, 2, 0} || {-1, -2, 0}
Deleting {-1, 3, 0} because {1, -3, 0} || {-1, 3, 0}
Deleting {-3, -1, 0} because {3, 1, 0} || {-3, -1, 0}
Deleting {-1, -3, 0} because {1, 3, 0} || {-1, -3, 0}
Deleting {-3, -2, 0} because {3, 2, 0} || {-3, -2, 0}
Deleting {-2, -3, 0} because {2, 3, 0} || {-2, -3, 0}
Deleted 38 parallel planes
The list of d-spacings are:
```

```
{2.55574, 2.55574, 2.55574, 2.34217, 2.24354, 2.24354, 2.24354, 2.24354,
 2.24354, 2.24354, 1.72674, 1.72674, 1.72674, 1.72674, 1.72674, 1.72674,
 1.47555, 1.47555, 1.47555, 1.33244, 1.33244, 1.33244, 1.33244, 1.33244,
 1.33244, 1.24846, 1.24846, 1.24846, 1.24846, 1.24846, 1.24846, 1.23282,
 1.23282, 1.23282, 1.23282, 1.23282, 1.23282, 0.988915, 0.988915,
 0.988915, 0.988915, 0.988915, 0.988915, 0.965977, 0.965977, 0.965977,
 0.965977, 0.965977, 0.965977, 0.946071, 0.946071, 0.946071, 0.946071,
 0.946071, 0.946071, 0.946071, 0.946071, 0.946071, 0.946071, 0.946071,
 0.946071, 0.893009, 0.893009, 0.893009, 0.893009, 0.893009, 0.893009,
 0.893009, 0.893009, 0.893009, 0.893009, 0.893009, 0.893009, 0.821485,
 0.821485, 0.821485, 0.821485, 0.821485, 0.821485, 0.821485, 0.821485,
 0.821485, 0.821485, 0.821485, 0.821485, 0.800598, 0.800598, 0.800598,
 0.800598, 0.800598, 0.800598, 0.708834, 0.708834, 0.703692, 0.703692,
 0.700855, 0.700855, 0.700855, 0.700855, 0.678445, 0.678445, 0.678445,
 0.678445, 0.645441, 0.645441, 0.645441, 0.645441, 0.586326, 0.586326,
 0.581786, 0.581786, 0.581786, 0.581786, 0.568775, 0.568775, 0.568775,
 0.568775, 0.548903, 0.548903, 0.548903, 0.548903, 0.481352, 0.481352}
```

The list of allowable planes:

```
{{1, 0, 0}, {1, -1, 0}, {0, 1, 0}, {0, 0, 2}, {1, 0, 1}, {1, -1, 1}, {0, 1, 1},
 {0, -1, 1}, {-1, 1, 1}, {-1, 0, 1}, {1, 0, 2}, {1, -1, 2}, {0, 1, 2}, {0, -1, 2},
 {-1, 1, 2}, {-1, 0, 2}, {2, -1, 0}, {1, 1, 0}, {1, -2, 0}, {1, 0, 3}, {1, -1, 3},
 {0, 1, 3}, {0, -1, 3}, {-1, 1, 3}, {-1, 0, 3}, {2, -1, 2}, {1, 1, 2}, {1, -2, 2},
 {-1, 2, 2}, {-1, -1, 2}, {-2, 1, 2}, {2, 0, 1}, {2, -2, 1}, {0, 2, 1}, {0, -2, 1},
 {-2, 2, 1}, {-2, 0, 1}, {2, 0, 3}, {2, -2, 3}, {0, 2, 3}, {0, -2, 3}, {-2, 2, 3},
 {-2, 0, 3}, {3, -1, 0}, {3, -2, 0}, {2, 1, 0}, {2, -3, 0}, {1, 2, 0}, {1, -3, 0},
 {3, -1, 1}, {3, -2, 1}, {2, 1, 1}, {2, -3, 1}, {1, 2, 1}, {1, -3, 1}, {-1, 3, 1},
 {-1, -2, 1}, {-2, 3, 1}, {-2, -1, 1}, {-3, 2, 1}, {-3, 1, 1}, {3, -1, 2},
 {3, -2, 2}, {2, 1, 2}, {2, -3, 2}, {1, 2, 2}, {1, -3, 2}, {-1, 3, 2}, {-1, -2, 2},
 {-2, 3, 2}, {-2, -1, 2}, {-3, 2, 2}, {-3, 1, 2}, {3, -1, 3}, {3, -2, 3}, {2, 1, 3},
 {2, -3, 3}, {1, 2, 3}, {1, -3, 3}, {-1, 3, 3}, {-1, -2, 3}, {-2, 3, 3}, {-2, -1, 3},
 {-3, 2, 3}, {-3, 1, 3}, {3, 0, 2}, {3, -3, 2}, {0, 3, 2}, {0, -3, 2}, {-3, 3, 2},
 {-3, 0, 2}, {3, 1, 0}, {1, 3, 0}, {2, 2, 2}, {-2, -2, 2}, {3, 1, 1}, {1, 3, 1},
 {-1, -3, 1}, {-3, -1, 1}, {3, 1, 2}, {1, 3, 2}, {-1, -3, 2}, {-3, -1, 2}, {3, 1, 3},
 {1, 3, 3}, {-1, -3, 3}, {-3, -1, 3}, {3, 2, 0}, {2, 3, 0}, {3, 2, 1}, {2, 3, 1},
 {-2, -3, 1}, {-3, -2, 1}, {3, 2, 2}, {2, 3, 2}, {-2, -3, 2}, {-3, -2, 2},
 {3, 2, 3}, {2, 3, 3}, {-2, -3, 3}, {-3, -2, 3}, {3, 3, 2}, {-3, -3, 2}}
```

```
dspace
```

```
{2.55574, 2.55574, 2.55574, 2.34217, 2.24354, 2.24354, 2.24354, 2.24354,
 2.24354, 2.24354, 1.72674, 1.72674, 1.72674, 1.72674, 1.72674, 1.72674,
 1.47555, 1.47555, 1.47555, 1.33244, 1.33244, 1.33244, 1.33244, 1.33244,
 1.33244, 1.24846, 1.24846, 1.24846, 1.24846, 1.24846, 1.24846, 1.23282,
 1.23282, 1.23282, 1.23282, 1.23282, 1.23282, 0.988915, 0.988915,
 0.988915, 0.988915, 0.988915, 0.988915, 0.965977, 0.965977, 0.965977,
 0.965977, 0.965977, 0.965977, 0.946071, 0.946071, 0.946071, 0.946071,
 0.946071, 0.946071, 0.946071, 0.946071, 0.946071, 0.946071, 0.946071,
 0.946071, 0.893009, 0.893009, 0.893009, 0.893009, 0.893009, 0.893009,
 0.893009, 0.893009, 0.893009, 0.893009, 0.893009, 0.893009, 0.821485,
 0.821485, 0.821485, 0.821485, 0.821485, 0.821485, 0.821485, 0.821485,
 0.821485, 0.821485, 0.821485, 0.821485, 0.800598, 0.800598, 0.800598,
 0.800598, 0.800598, 0.800598, 0.708834, 0.708834, 0.703692, 0.703692,
 0.700855, 0.700855, 0.700855, 0.700855, 0.678445, 0.678445, 0.678445,
 0.678445, 0.645441, 0.645441, 0.645441, 0.645441, 0.586326, 0.586326,
 0.581786, 0.581786, 0.581786, 0.581786, 0.568775, 0.568775, 0.568775,
 0.568775, 0.548903, 0.548903, 0.548903, 0.548903, 0.481352, 0.481352}
```

This calulates the difference between calculated and measured values

```
err[meas_, calc_] := (calc - meas)
```

This appends a hexagonal plane or zone to the list of dspacings and 3 index notation

```
AppHexPlane[list_, pos_] :=
 If[latticename == "HCP", Append[list, Hex[list[[pos]]]], list]
AppHexAxis[list_, pos_] := If[latticename == "HCP",
  Append[list, HexAxis[list[[pos]]] / (GCD @@ HexAxis[list[[pos]]])], list]
```

■ Loading and Indexing

■ Importing an image file of the spots

Setting a "directroy string" Depending on the name of the computer I am working on, it picks different directories to get files from.

```
dirstr = Which[
   $MachineName == "ORION", "e:\Documents\Shawn
     Kelly\My Documents\Mathematica\Miscellaneous\Diffraction",
   $MachineName == "KELLYSM", "F:\Documents\KellySM\My
     Pictures\Research\Metallography\Laser Deposited
     Ti-6Al-4V\As-Received\TEM Images\\2004_05_18"
  ];
(*"F:\Documents\KellySM\My Pictures\Research\
   Metallography\Gleeble\Baseline Microstructure\TEM\\2004_05_18"*)
SetDirectory[dirstr]
```

```
F:\Documents\KellySM\My Pictures\Research\Metallography\
  Laser Deposited Ti-6Al-4V\As-Received\TEM Images\2004_05_18
```

```
FileNames[]
```

```
{A02487_G.dm3, A02487_G.tif, A02488.dm3, A02488_I.tif, A02488_IX.tif,
 A02488_KP.dm3, A02488_KP_Fire.bmp, A02488_KP_FireI.bmp, A02488_KP_FireI.tif,
 A02488_KP_Fire.tif, A02488_KP_Ice_.bmp, A02488_KP_Ice.bmp, A02488_KP.tif,
 A02489.dm3, A02489.tif, A02490.dm3, A02490_I.tif, A02490_KP.dm3,
 A02490_KP.tif, A02491.dm3, A02491_I.tif, A02491_IX.tif, A02491_KP.dm3,
 A02491_KP.tif, A02492.dm3, A02492_I.tif, A02492_IX.tif, A02492_KP.dm3,
 A02492_KP.tif, A02493.dm3, A02493_I.tif, A02493_IX.tif, A02494.dm3,
 A02494.tif, A02495.dm3, A02495.tif, A02496.dm3, A02496.tif, A02497.dm3,
 A02497.tif, A02498.dm3, A02498.tif, A02499.dm3, A02499.tif, A02500.dm3,
 A02500_G.dm3, A02500_G.tif, A02500.tif, A02501.dm3, A02501_G.dm3,
 A02501_G.tif, A02502.dm3, A02502.tif, A02503.dm3, A02503.tif, A02504.dm3,
 A02504.tif, Index_2004_05_18.doc, Thumbs.db, ~$dex_2004_05_18.doc}
```

```
fname = "A02492_I.tif";
```

```
sp = Import[fname, "TIFF"]; (*"type can also be "JPG","TIFF","BMP", etc...*)
Show[sp(*, ImageSize→72*8*)]
```

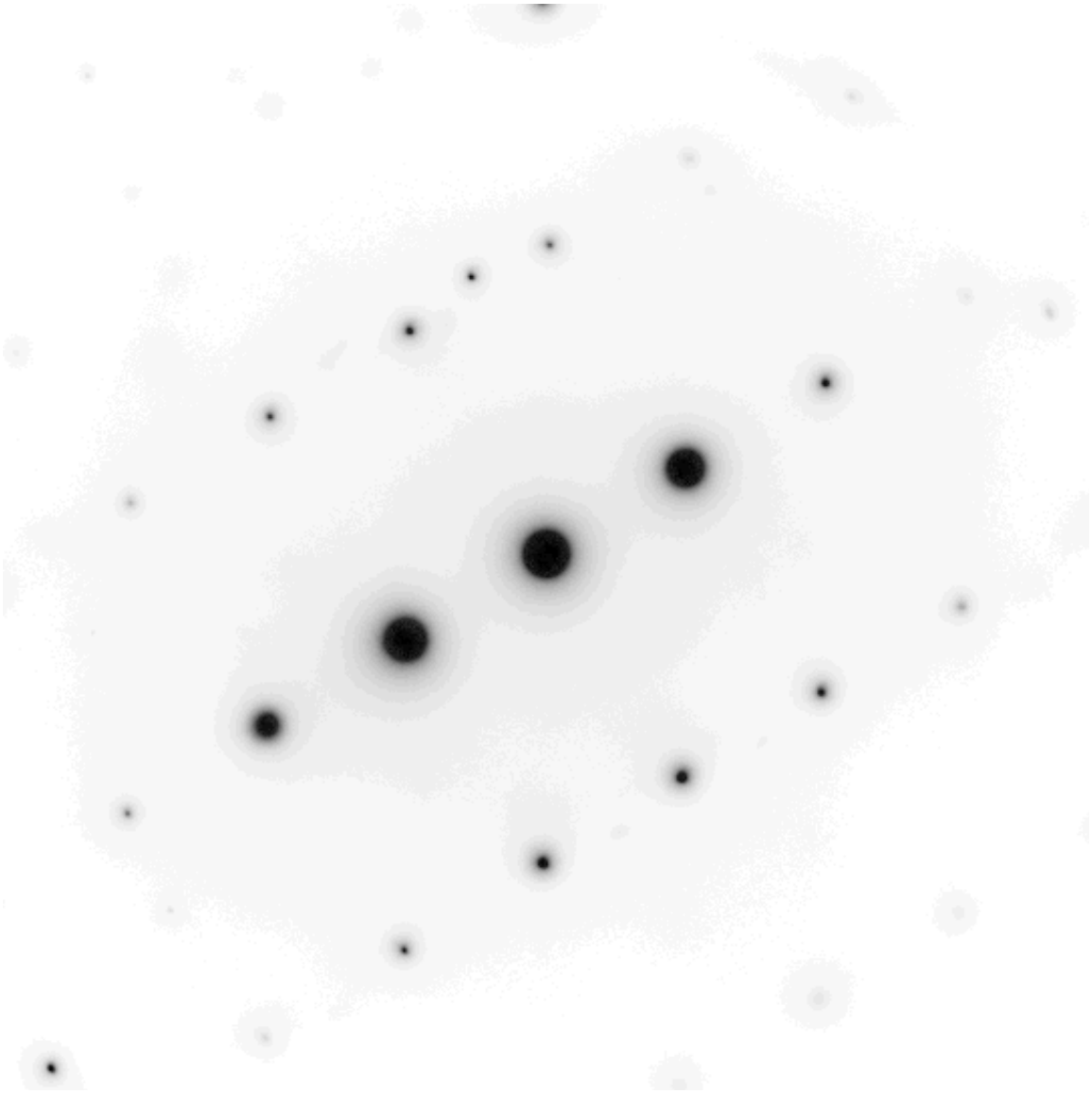

- Graphics -

R1 remains constant for both spot-pairs. R1,R2,and R3 MUST be counterclockwise,angles should be acute, but you might not always index properly with just acute angles. .

```
(*PICK SPOTS IN THE FOLLOWING ORDER: TRANSMITTED, R1, R2, R3*)
(*DO THIS BY CLICKING THE IMAGE, THEN, WHILE HOLDING <CTRL>, PICK SPOTS.*)
(*WHEN FINSISHED, COPY THE POINTS USING <CTRL>+C*)
(*PASTE THEM INTO THE LIST "spots" USING <CTRL>+V*)
spots = {{270, 268.5}, {340.001, 311.501}, {272, 422.502}, {202, 380.501}};
```

```
v1 = {spots[[2, 1]] - spots[[1, 1]], spots[[2, 2]] - spots[[1, 2]]};
v2 = {spots[[3, 1]] - spots[[1, 1]], spots[[3, 2]] - spots[[1, 2]]};
v3 = {spots[[4, 1]] - spots[[1, 1]], spots[[4, 2]] - spots[[1, 2]]};
r1 = Norm[v1];
r2 = Norm[v2];
r3 = Norm[v3];
ang21 = ArcCos[v2.v1 / (r1 * r2)] / Degree // N;
ang31 = ArcCos[v3.v1 / (r1 * r3)] / Degree // N;
Print["Lengths are in pixels"]
TableForm[{{"R3", "R2", "R1", "R3/R1", "R2/R1", "∠R3R1", "∠R2R1"},
  {r3, r2, r1, r3 / r1, r2 / r1, ang31, ang21}}, TableAlignments → Center]
```

```
Lengths are in pixels
```

R3	R2	R1	R3/R1	R2/R1	∠R3R1	∠R2R
131.028	154.015	82.1537	1.59491	1.87472	89.7015	57.69

If the camera constant is known, enter it as "CC". the table gives estimated d spacings knowing the camera constant.

```
CC = 192.0832; (*Camera Constant, if Known*)
TableForm[{{"d3", "d2", "d1", "∠R3R1", "∠R2R1"},
  {CC / r3, CC / r2, CC / r1, ang31, ang21}}, TableAlignments → Center]
```

d3	d2	d1	∠R3R1	∠R2R1
1.46598	1.24717	2.3381	89.7015	57.6939

```
(*Code could be added to search 'dspace' for matching dpsacings to each of
  these planes and then check to see if the same.   *)
```

```
dspace
```

```
{2.55574, 2.55574, 2.55574, 2.34217, 2.24354, 2.24354, 2.24354, 2.24354,
 2.24354, 2.24354, 1.72674, 1.72674, 1.72674, 1.72674, 1.72674, 1.72674,
 1.47555, 1.47555, 1.47555, 1.33244, 1.33244, 1.33244, 1.33244, 1.33244,
 1.33244, 1.24846, 1.24846, 1.24846, 1.24846, 1.24846, 1.24846, 1.23282,
 1.23282, 1.23282, 1.23282, 1.23282, 1.23282, 0.988915, 0.988915,
 0.988915, 0.988915, 0.988915, 0.988915, 0.965977, 0.965977, 0.965977,
 0.965977, 0.965977, 0.965977, 0.946071, 0.946071, 0.946071, 0.946071,
 0.946071, 0.946071, 0.946071, 0.946071, 0.946071, 0.946071, 0.946071,
 0.946071, 0.893009, 0.893009, 0.893009, 0.893009, 0.893009, 0.893009,
 0.893009, 0.893009, 0.893009, 0.893009, 0.893009, 0.893009, 0.821485,
 0.821485, 0.821485, 0.821485, 0.821485, 0.821485, 0.821485, 0.821485,
 0.821485, 0.821485, 0.821485, 0.821485, 0.800598, 0.800598, 0.800598,
 0.800598, 0.800598, 0.800598, 0.708834, 0.708834, 0.703692, 0.703692,
 0.700855, 0.700855, 0.700855, 0.700855, 0.678445, 0.678445, 0.678445,
 0.678445, 0.645441, 0.645441, 0.645441, 0.645441, 0.586326, 0.586326,
 0.581786, 0.581786, 0.581786, 0.581786, 0.568775, 0.568775, 0.568775,
 0.568775, 0.548903, 0.548903, 0.548903, 0.548903, 0.481352, 0.481352}
```

- **Manually Entering R1,R2,R3 and the angles between them**
  (IGNORE IF YOU PICKED SPOTS FROM IMAGE)

■ Solution

The solution is found by seperately indexing R2 and R1 and R3 and R1, then matching R1 and the calculated zone axes for R2R1 and R3R1.

Adjust the followiing variables "per" and "angper" to obtain more or fewer solutions. This changes the tolerance (%) of the r spot values found and the angle values. per is normally 0.03 and angper is normally 2.

```
(*THE FIRST SET OF SPOTS R1,R2*)
per = 0.03;
angper = 3;
ang = ang21;
rat = r1 / r2;
len = Length[dspace];
possible = {};
Do[
 Do[
  {
   If[
    (rat * (1 - per) ≤ dspace[[i]] / dspace[[j]] <= rat * (1 + per)) &&
     (ang - angper ≤ ϕ[hklallow[[i]], hklallow[[j]]] ≤ ang + angper) &&
     zonetest[hklallow[[j]], zone[hklallow[[i]], hklallow[[j]]]] &&
     zonetest[hklallow[[i]], zone[hklallow[[i]], hklallow[[j]]]],

    AppendTo[possible, {AppHexPlane[{dspace[[i]], hklallow[[i]]}, 2],
      AppHexPlane[{dspace[[j]], hklallow[[j]]}, 2],
      AppHexAxis[{dspace[[j]] / dspace[[i]], ϕ[hklallow[[i]], hklallow[[j]]],
        zone[hklallow[[i]], hklallow[[j]]]}, 3]}]
    ,
   ]
  },
  {j, 1, len}
 ],
 {i, 1, len}
]
{rat, 1 / rat}
posslen = Length[possible];
tab1 = Table[If[latticename == "HCP", {possible[[i, 3, 4]], possible[[i, 2, 3]]},
    {possible[[i, 3, 3]], possible[[i, 2, 2]]}], {i, 1, posslen}];
poss1 = possible; (*Map[possible[[#]]&,Ordering[Transpose[tab1][[1]]]]*)
Print["Matched ", posslen, " out of ", len,
 " possible zone axis combinations for spot R1 and R2."]
```

```
{0.533414, 1.87472}
```

```
Matched 11 out of 123 possible zone axis combinations for spot R1 and R2.
```

```
(*THE SECOND SET OF SPOTS R1,R3*)
per = 0.03;
angper = 3;
ang = ang31;
rat = r1 / r3;
len = Length[dspace];
possible = {};
Do[
 Do[
  {
   If[
    (rat * (1 - per) ≤ dspace[[i]] / dspace[[j]] <= rat * (1 + per)) &&
     (ang - angper ≤ ϕ[hklallow[[i]], hklallow[[j]]] ≤ ang + angper) &&
     zonetest[hklallow[[j]], zone[hklallow[[i]], hklallow[[j]]]] &&
     zonetest[hklallow[[j]], zone[hklallow[[i]], hklallow[[j]]]],
    AppendTo[possible, {AppHexPlane[{dspace[[i]], hklallow[[i]]}, 2],
      AppHexPlane[{dspace[[j]], hklallow[[j]]}, 2],
      AppHexAxis[{dspace[[j]] / dspace[[i]], ϕ[hklallow[[i]], hklallow[[j]]],
        zone[hklallow[[i]], hklallow[[j]]]}, 3]}]
    ,
   ]
  },
  {j, 1, len}
 ],
 {i, 1, len}
]
{rat, 1 / rat}
posslen = Length[possible];
tab2 = Table[If[latticename == "HCP", {possible[[i, 3, 4]], possible[[i, 2, 3]]},
    {possible[[i, 3, 3]], possible[[i, 2, 2]]}], {i, 1, posslen}];
poss2 = possible; (*Map[possible[[#]]&,Ordering[Transpose[tab2][[1]]]]*)
Print["Matched ", posslen, " out of ", len,
 " possible zone axis combinations for spot R1 and R3."]
```

```
{0.626995, 1.59491}
```

```
Matched 15 out of 123 possible zone axis combinations for spot R1 and R3.
```

Finding common zone axes and planes for R1 from the two groups.

```
common = {};
Do[If[MemberQ[tab2, tab1[[i]]], AppendTo[common, tab1[[i]]],
 {i, 1, Length[tab1]}]
If[
  Length[common] == 0,
  {
   Print["No Common R1 Planes and Zone Axes Found...Try Again!!!"],
   Beep[]
  },
  {
   Print[Length[common], " Common R1 planes and Zone Axes found."],
   cord = Map[common[[#]] &, Reverse[Ordering[Transpose[common][[1]]]]]
  }];
common;
```

```
3 Common R1 planes and Zone Axes found.
```

Positions of the common elements with the first pair of spots. Then generating a table of the common values (ctab)

```
p1 = {};
Do[AppendTo[p1, Position[tab1, cord[[i]]], {i, 1, Length[cord]}]
p1 = Flatten[p1];
p2 = {};
Do[AppendTo[p2, Position[tab2, cord[[i]]], {i, 1, Length[cord]}]
p2 = Flatten[p2];
ctab = Table[{poss2[[p2[[i]], 1]], poss1[[p1[[i]], 1]],
    poss1[[p1[[i]], 2]], poss1[[p1[[i]], 3]], poss2[[p2[[i]], 3]],
    If[latticename == "HCP", HexAxis[B3[poss2[[p2[[i]], 1, 2]],
       poss1[[p1[[i]], 1, 2]], poss1[[p1[[i]], 2, 2]]], B3[poss2[[p2[[i]], 1, 2]],
      poss1[[p1[[i]], 1, 2]], poss1[[p1[[i]], 2, 2]]]}, {i, 1, Length[cord]}];
```

This presents the results in a clear form

```
tabhead =
  If[latticename == "HCP", {None, {"R3: d, {hkl}, {hkil}", "R2: d, {hkl}, {hkil}",
     "R1: d, {hkl}, {hkil}", "R2/R1,  R3/R1", "B: hkl,hkil", "rd=Lλ"}},
   {None, {"R3: d, {hkl}", "R2: d, {hkl}", "R1: d, {hkl}",
     "R2/R1,  R3/R1", "B: hkl", "rd=Lλ"}}];
Print["R3/R1 = ", r3 / r1, "  ∠ = ", ang31 ]
Print["R2/R1 = ", r2 / r1, "  ∠ = ", ang21 ]
ctabclear = Table[{ctab[[i, 1]], ctab[[i, 2]], ctab[[i, 3]],
    {Drop[ctab[[i, 4]], -2], Drop[ctab[[i, 5]], -2]}, Drop[ctab[[i, 4]], 2],
    Mean[{r3 * ctab[[i, 1, 1]], r2 * ctab[[i, 2, 1]], r1 * ctab[[i, 3, 1]]}]}, {i,
    1, Length[ctab]}];
TableForm[ctabclear, TableDepth → 2, TableHeadings → tabhead,
 TableAlignments → Center]
```

```
R3/R1 = 1.59491  ∠ = 89.7015

R2/R1 = 1.87472  ∠ = 57.6939
```

R3: d, {hkl}, {hkil}	R2: d, {hkl}, {hkil}
{1.47555, {1, 1, 0}, {1, 1, -2, 0}}	{1.24846, {1, 1, 2}, {1, 1, -2, 2}}
{1.47555, {2, -1, 0}, {2, -1, -1, 0}}	{1.24846, {2, -1, 2}, {2, -1, -1, 2}}
{1.47555, {1, -2, 0}, {1, -2, 1, 0}}	{1.24846, {1, -2, 2}, {1, -2, 1, 2}}

This calculates the differences the measured and calulated ratios of spot distances and d spacings and angles. The table is order according to the sum of the absolute differences.

```
tabhead = If[latticename == "HCP",
   {None, {"d_R3/R1", "∠_R3/R1", "d_R2/R1", "∠_R2/R1", "Σ diff", "B: h k i l", "rd=Lλ"}},
   {None, {"d_R3/R1", "∠_R3/R1", "d_R2/R1", "∠_R2/R1", "Σ diff", "B: h k l", "rd=Lλ"}}];
errtab = Table[{err[r3 / r1, ctab[[i, 5, 1]]], err[ang31, ctab[[i, 5, 2]]],
    err[r2 / r1, ctab[[i, 4, 1]]], err[ang21, ctab[[i, 4, 2]]],
    Last[ctab[[i, 5]]], Last[ctabclear[[i]]]}, {i, 1, Length[ctab]}];
errsum = Table[Sum[Abs[errtab[[i, j]]], {j, 1, 4}], {i, 1, Length[errtab]}];
Do[errtab[[i]] = Insert[errtab[[i]], errsum[[i]], 5], {i, 1, Length[errtab]}]
errtab = Map[errtab[[#]] &, Ordering[errsum]];

TableForm[errtab, TableHeadings → tabhead,
 TableAlignments → Center, TableDepth → 2]
```

$d_{R3/R1}$	$\angle_{R3/R1}$	$d_{R2/R1}$	$\angle_{R2/R1}$	Σ diff	B: h k
-0.00759702	0.298536	0.00133001	0.0953196	0.402783	{1, -1,
-0.00759702	0.298536	0.00133001	0.0953196	0.402783	{0, -1,
-0.00759702	0.298536	0.00133001	0.0953196	0.402783	{-1, 0,

Checking which zone axes are parallel. Axes that are parallel are dublicates...it is up to the user to deal with this

```
parlist = {};
Do[
 Do[
  If[i ≠ j && (1 > zoneangReal[ctab[[i, 5, 3]], ctab[[j, 5, 3]]] ||
      179 < zoneangReal[ctab[[i, 5, 3]], ctab[[j, 5, 3]]]),
   AppendTo[parlist, {i, j}],
   (*Print[zoneangReal[ctab[[i,5,3]],ctab[[j,5,3]]]]*)

  ], {j, 1, Length[ctab]}
 ],
 {i, 1, Length[ctab]}
]
If[Length[parlist] == 0,
  Print["None of the zone axes are parallel...each solution is unique."],
  {
   Print["The following zone axes (positions
      {1st || axes, 2nd || axes}, in ctab) are parallel."],
   Print[parlist]
  }
 ];
```

```
None of the zone axes are parallel...each solution is unique.
```

Selecting a guess from the list

```
guess = {1, -1, 0, 0};
```

```
guessres = Map[ctab[[#]] &, Position[Transpose[cord][[1]], guess] // Flatten];
tabhead =
  If[latticename == "HCP", {None, {"R3: d, {hkl}, {hkil}", "R2: d, {hkl}, {hkil}",
     "R1: d, {hkl}, {hkil}", "R2/R1,  R3/R1", "B: hkl,hkil"}},
   {None, {"R3: d, {hkl}", "R2: d, {hkl}", "R1: d, {hkl}",
     "R2/R1,  R3/R1", "B: hkl"}}];
guesstab = TableForm[guessres, TableDepth → 2, TableHeadings → tabhead,
  TableAlignments → Center]
```

```
      R3: d, {hkl}, {hkil}                  R2: d, {hkl}, {hkil}
{1.47555, {1, 1, 0}, {1, 1, -2, 0}}      {1.24846, {1, 1, 2}, {1, 1, -2, 2}}      {2.3
```

```
g = Length[guessres]
```

```
1
```

Calculating the camera constant, Lλ, where L$\lambda = R_i\, d_{hkl}$. You need to have made a guess for the zone axes.

```
camcons =
  Table[{r3 * guessres[[i, 1, 1]], r2 * guessres[[i, 2, 1]], r1 * guessres[[i, 3, 1]],
    Mean[{r3 * guessres[[i, 1, 1]], r2 * guessres[[i, 2, 1]], r1 * guessres[[i, 3, 1]]}
   {i, 1, Length[guessres]}];
TableForm[camcons, TableHeadings → {None, {"R3", "R2", "R1", "Mean"}},
 TableAlignments → Center]
```

R3	R2	R1	Mean
193.338	192.281	192.417	192.679

```
CCScope = CC ; (*The microscope camera constant*)
```

I take the average of the three camera constants...I am not sure if this is the correct way of doing it.

```
CC = camcons[[g, 4]]
CCScope
```

```
192.679
```

```
192.083
```

```
camd = {{CC / r3, CC / r2, CC / r1},
   Table[guessres[[i, j, 1]], {j, 1, 3}, {i, 1, Length[guessres]}]};
TableForm[camd, TableHeadings → {{"Meas", "Calc"}, {"R3", "R2", "R1"}},
 TableAlignments → Center]
```

	R3	R2	R1
Meas	1.47052	1.25104	2.34535
Calc	1.47555	1.24846	2.34217

This is the final indexed image (adding the annotation was done in another program. This is for illustrative purposes only.

```
sp = Import["A02492_IX.tif", "TIFF"];
Show[sp(*, ImageSize→72*8*)]
```

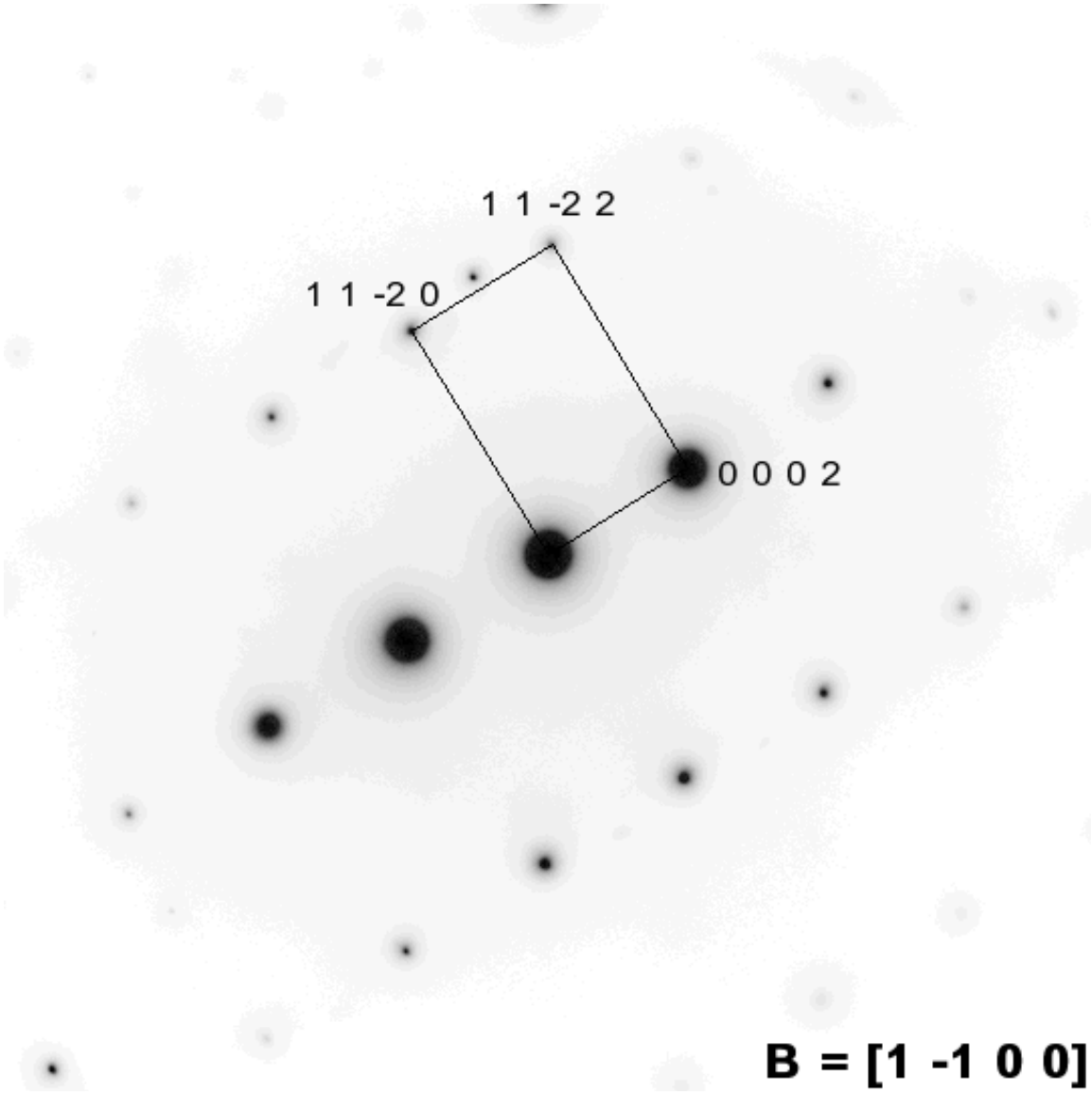


```
- Graphics -
```

Image Analysis of Last Three Layers

Several backscattered electron (BSE) micrographs were taken along the last four layers of the as-deposited material in order to better understand the microstructure morphology and to quantitatively determine the fraction of alpha and beta phases using image analysis. In Ti-6Al-4V, vanadium partitions to the beta phase making it distinguishable in BSE mode from the alpha phase which contains the lower atomic number aluminum. Thus the beta phase has a higher amount of "white" pixels in the BSE micrographs. A simple image analysis procedure is used to first convert the grayscale BSE micrograph to a binary (black/white) image. The grayscale has pixel values ranging from 0 (black) to 255 (white), while the binary image has pixel values of black or white. The technique, known as thresholding, assumes that pixels above a certain threshold value are white and those below the value are black. The total number of white pixels counted divided by the total number of pixels in the image gives an estimated phase fraction. Routines were developed in IgorPro to perform the image analysis tasks on a large number of images. The choice of the threshold value is somewhat arbitrary and the best results are obtained when each image threshold is chosen according to a user defined value (eye-balled).

Through image analysis of the BSE micrographs shown in Figure 4.10, a quantitative measure of the phase fraction distribution can be made. The image analysis results from the last four layers (L15-L18) of the as-deposited material are shown in Figure 10.1. The correlation between the grayscale and binary image and threshold value selected are shown. A correlation of 1 would indicate an exact match between the grayscale and binary images. The threshold value was "user defined" based on each image that was analyzed as opposed to an automated approach.

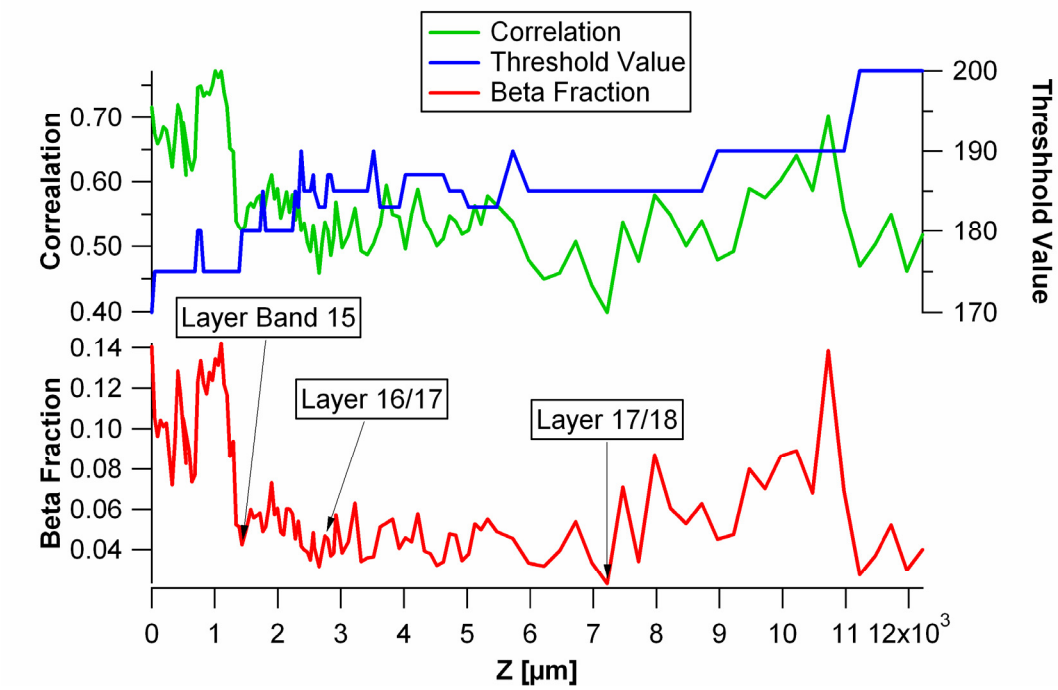

Figure 10.1: Image analysis results showing beta phase fraction, threshold correlation, and threshold value for images taken along the deposit's z-axis beginning (z=0) near the center of the 15th layer (L15) and ending at the top of the 18th layer (L18). Approximate locations of the 15th layer band and the intersection of layers 16 through 18 are indicated.

Within L15 there is approximately 10% beta present, which drops to approximately 6% at layer band 15. Thereafter, in layers 16 and 17, the beta fraction remains relatively constant around 4% before increasing in the 18th layer to a maximum of 14%. The last millimeter of layer 18 has a low beta fraction near 4%. Note that the correlation tends to follow the same trend as the phase fraction value suggesting that the image quality or morphology affects the quality of measurement made. This is illustrated in the two micrographs of Figure 10.2a and Figure 10.2b representing the best and worst correlation values in Figure 10.1. Figure 10.2a is located in the fully developed 15th layer (layer *n*) while Figure 10.2b is located at the interface of the 17th and 18th layer (*n+2* and *n+3*). Clearly, the basketweave-α morphology in Figure 10.2a has much more contrast than the fine colony-α morphology in Figure 10.2b. In the baseline microstructure results (Chapter 3) it was observed after the primary-heat treatment that lack of vanadium partitioning to the β phase resulted in a lack of image contrast as compared to the secondary-heat treated material. Other artifacts of BSE imaging such as backscattered electron channeling along preferred orientations may also lead to variance in the measured beta fraction. Thus the image analysis results do not provide enough proof to show that the β phase fraction decreases in the last three layers.

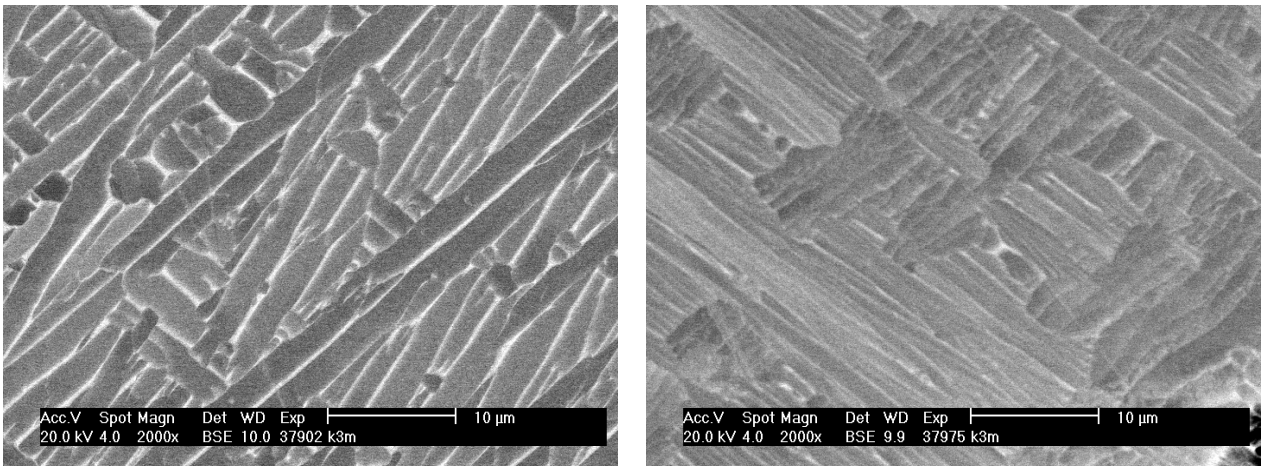

(a) **(b)**

Figure 10.2: BSE micrographs representing the (a) best and (b) worst correlation values of the plot in Figure 10.1. Alpha is dark to medium gray, while beta is white. (a) is located in the fully developed 15th layer (layer *n*) while (b) is located at the interface of the 17th and 18th layer (*n+2* and *n+3*).

Thermal Properties of Ti-6Al-4V

The thermal properties of Ti-6Al-4V are obtained from K.C. Mills.[95] The beta transus for this alloy is 1268K and the liquidus is 1923K. The data from Mills was fit to several linear equations over these different temperature ranges. Equations and plots describing the density, thermal conductivity, and specific heat as a function of temperature are shown below in Equations [10.1]-[10.3] and Figure 10.3-Figure 10.5, respectively.

$$\rho(T) = \begin{cases} 4461.1\text{-}0.1419*T & T \le 1268K \\ 4462.6\text{-}0.1425*T & 1268 < T \le 1923 \\ 5227.6 - 0.688*T & 1923 < T \le 3600 \\ 2750.8 & T > 3600 \end{cases} \quad [kg/m^3] \qquad [10.1]$$

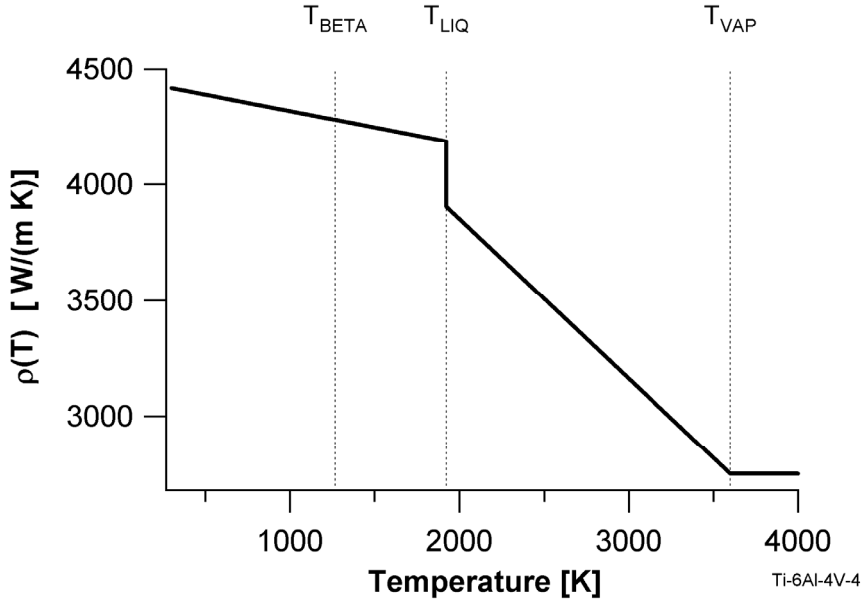

Figure 10.3: Plot of density as a function of temperature, after Eq.[10.1]; used in the thermal model.

$$k(T) = \begin{cases} 1.2595 + 0.0157*T & T \le 1268K \\ 3.5127 + 0.0127*T & 1268 < T \le 1923 \\ -12.752 + 0.024*T & T > 1923 \end{cases} \quad [W/(m \cdot K)] \qquad [10.2]$$

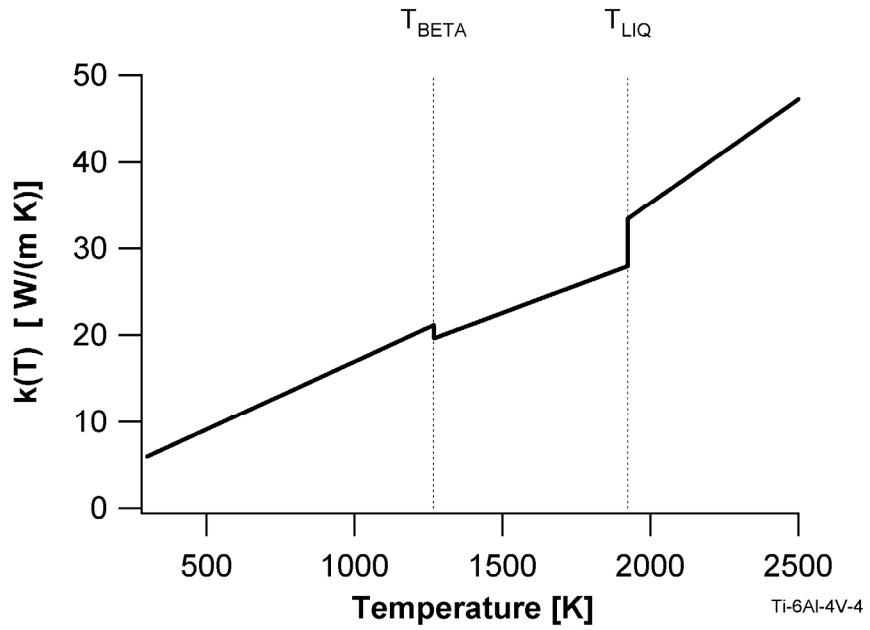

Figure 10.4: Plot of thermal conductivity as a function of temperature, after Eq.[10.2]; used in the thermal model.

$$C_p(T) = \begin{cases} 483.04 + 0.215*T & T \le 1268K \\ 412.7 + 0.1801*T & 1268 < T \le 1923 \\ 831 & T > 1923 \end{cases} \quad [J/(kg \cdot K)] \qquad [10.3]$$

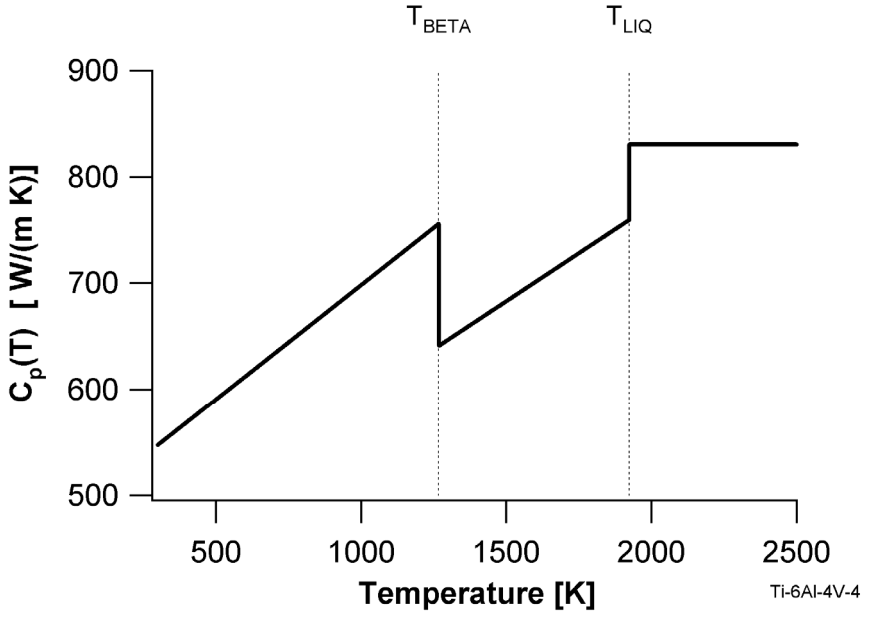

Figure 10.5: Plot of specific heat as a function of temperature, after Eq. [10.3]; used in the thermal model.

Thermal Model Finite Difference Equations

A more complete discussion of the implicit finite difference methods used in the thermal model can be found in Ref.[24]. This appendix will show the equations used in the current model for nodes having different boundary conditions.

The thermal model must solve Equation [10.4], which describes two-dimensional transient heat conduction with temperature dependent thermal properties, convection (q''), and volumetric heating (q'''). In order to accomplish this, a numerical scheme, known as implicit finite differencing is employed to approximate the derivatives in Eq.[10.4].

$$\frac{\partial}{\partial z}\left(k(T)\frac{\partial T}{\partial z}\right)+\frac{\partial}{\partial y}\left(k(T)\frac{\partial T}{\partial y}\right)+q'''-q''=\rho(T)C_p(T)\frac{\partial T}{\partial t} \qquad [10.4]$$

In order to solve Equation [10.4], the 2D area to be modeled must be discretized such that the computational domain consists of many nodes, or calculation points. The locus of these points forms a mesh. Finding a numerical solution to Eq. [10.4] may be done in a purely mathematical form using Taylor series expansions of the derivatives, as outlined by Özişik.[93] A conceptually easier to understand method, known as the control volume approach, is taken here to convert equation [10.4] into a numerical expression that can be solved for each node in the mesh. Here, the finite difference equations are developed by constraining the partial differential equation to a finite control volume and conserving energy over the volume. An energy balance, described by Eq.[10.5], is used as a starting point for the development of the finite difference equations. Equation [10.5] equates the sum of the rate of heat input (E_{in}), heat generated (E_g), and heat removed (E_{out}) to the heat stored (E_{st}) in the control volume. The inflow and outflow energy terms occur over a surface and the energy generation and storage terms occur over a volume.

$$\dot{E}_{in}+\dot{E}_g-\dot{E}_{out}=\dot{E}_{st} \qquad [10.5]$$

The control volume surrounds a central node (numbered 0) as illustrated by the box in Figure 10.6. The distance between the center node and surrounding nodes, d_i, is indicated for node 2 in the figure. The control volume has a thickness of Δx in a 2-D application; therefore, the value of A_1 is $0.5(d_4+d_2)*\Delta x$. If the nodes are spaced evenly throughout the mesh, then these distances and areas remain constant throughout the mesh. The distances and areas will change at the

surface of the mesh or when the mesh spacing is variable. Both are encountered in modeling the LMD deposit.

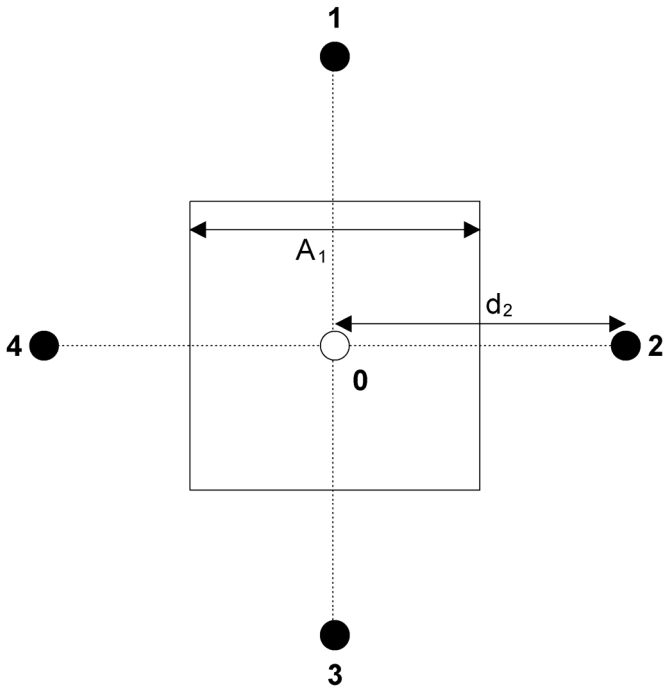

Figure 10.6: Finite difference control representation illustrating the local node numbering scheme and the location of the variables d_i and A_i. The control volume is indicated by the box.

Now each term in [10.5] will be defined for an interior node, assuming implicit finite differencing. Fourier's law describes the energy conducted into and out of opposite surfaces of the control volume according to Eq.[10.6]. Here A_i is the area normal to the direction of heat conduction.

$$\frac{\partial}{\partial y}\left(k(T)\frac{\partial T}{\partial y}\right) = E_{in,y} - E_{out,y} = q''_y - q''_{y+dy}$$
$$q''_i = -A_i k(T)\frac{dT}{dy} \qquad [10.6]$$

The energy in and out of the control volume in the y-dimension in discretized form is shown in Eq. [10.7]. Another labeling convention has been introduced here indicating the time increment that the temperatures are taken from, where p is the current time step, and $p+1$ is the time step that is currently being solved for.

$$E_{in,y} - E_{out,y} = k_4 A_4 \frac{T_4^{p+1} - T_0^{p+1}}{d_4} + k_2 A_2 \frac{T_2^{p+1} - T_0^{p+1}}{d_2} \qquad [10.7]$$

At this point the variable k_i is defined as the thermal conductivity evaluated at the midpoint of the node i and the central node, 0, as shown in Eq. [10.8]. The thermal conductivity is unknown at the $p+1$ time step because of its dependence on temperature (the unknown variable). Temperature dependent properties are incorporated into the finite difference calculation at the next time step ($p+1$) by extrapolating the thermal properties using the known temperatures from previous time steps (e.g., p, $p-1$) as shown in Eq. [10.9] for thermal conductivity, $k(T^{p+1})$.[93]

$$k_i(T) = \frac{k(T_i^{p+1}) + k(T_0^{p+1})}{2} \qquad [10.8]$$

$$k\left(T^{p+1}\right) \approx k\left(T^{p}\right) + \left(T^{p} - T^{p-1}\right) \cdot \left(\frac{dk}{dT}\right)\Bigg|_{T=T^p} \qquad [10.9]$$

The energy storage term is shown next in Eq.[10.10]. The density, ρ, and specific heat, C_p, depend on the temperature of the central node at the $p+1$ time step. The volume is determined from the d_i values and a finite thickness of the control volume, Δx, similar to that used to define A_i.

$$\begin{aligned} &\rho(T)C_p(T)\frac{\partial T}{\partial t} = E_{st} = \rho(T_0^{p+1})C_p(T_0^{p+1})V_0 \frac{T_0^{p+1} - T_0^{p}}{\Delta t} \\ &\Delta t = t^{p+1} - t^{p} \\ &V_0 = \frac{(d_4 + d_2) * (d_1 + d_3)}{4} * \Delta x \end{aligned} \qquad [10.10]$$

The energy generation term arises due to the volumetric laser heating that is used in the thermal model, as given by Eq. [10.11], with the coefficients defined in the thermal model chapter Eq. [6.10]. The values of y and z are known based on the node Eq. [10.11] is being applied to.

$$E_{gen} = Q(y,z,t)$$

$$Q(y,z,t) = \begin{cases} f_1 \dfrac{2\sigma\sqrt{\sigma}Q_{in}}{abc_1\pi^{3/2}} \exp\left(-\sigma\left(\dfrac{y^2}{a^2} + \dfrac{z^2}{b^2} + \dfrac{(c_1 - v_{laser}t)^2}{c_1^{\,2}}\right)\right) & t \le c_1 v_{laser} \\ f_2 \dfrac{2\sigma\sqrt{\sigma}Q_{in}}{abc_2\pi^{3/2}} \exp\left(-\sigma\left(\dfrac{y^2}{a^2} + \dfrac{z^2}{b^2} + \dfrac{(c_1 - v_{laser}t)^2}{c_2^{\,2}}\right)\right) & t > c_1 v_{laser} \end{cases} \qquad [10.11]$$

If we combine equations [10.8]-[10.11], a single finite difference equation describing the heat transfer at an interior node in the mesh is found, as in Eq. [10.12].

$$\sum_{i=1}^{4} \frac{k_i A_i}{d_i}(T_i^{p+1} - T_0^{p+1}) + Q(y,z,t) = \frac{\rho(T_0^{p+1})C_p(T_0^{p+1})V_0}{\Delta t}(T_0^{p+1} - T_0^{p}) \qquad [10.12]$$

A coefficient, the Fourier number, Fo_i, is now introduced Eq. [10.13]. The above equation is rearranged to obtain the $p+1$ and p terms on the right and left-hand sides of the equation.

$$Fo_i = \frac{k_i A_i}{d_i} \frac{\Delta t}{\rho(T_0^{p+1})C_p(T_0^{p+1})V_0} \qquad [10.13]$$

$$-\sum_{i=1}^{4} Fo_i T_i^{p+1} + (1 + \sum_{i=1}^{4} Fo_i)T_0^{p+1} = T_i^{p} + \frac{\Delta t}{\rho(T_0^{p+1})C_p(T_0^{p+1})V_0} Q_{in} \qquad [10.14]$$

If Eq.[10.14] is calculated for each individual node, a system of equations is attained that may be solved as in Eq. [10.15] for the vector $\{T^{p+1}\}$. The known temperature and heat input appear as $\{T^{P}\}$ and $\{Q_{in}\}$ and are often called load vectors. The coefficient matrix, $[K]$, contains the Fourier numbers for each node.

$$[K]\{T^{p+1}\} = \{T^{p}\} + \{Q_{in}\} \qquad [10.15]$$

The implicit finite difference equation for an interior node was just derived. An interior node means that the central node is surrounded by four existing nodes. Cases will exist at the surface of the geometry, where nodes will not be present due to a physical boundary. This will change the finite difference equations by adding a boundary condition such a surface heat flux due to convection or an adiabatic surface due to symmetry. Equations for different geometries and boundary conditions are now summarized in Table XVII. The convection terms introduced include the heat transfer coefficient, h, and the fluid temperature T_∞. In addition a convective surface flux can be converted into an adiabatic boundary condition (q=0) by setting h=0.

Table XVII: Summary of Implicit Finite Difference Equations for Different Geometries.

Node Type	Implicit Finite Difference Equation	Equation
Interior Node	$-\sum_{i=1}^{4} Fo_i T_i^{p+1} + (1+\sum_{i=1}^{4} Fo_i) T_0^{p+1} = T_i^{p} + Q_0$	[10.14]
Top Surface Convection	$-\sum_{i=2}^{4} Fo_i T_i^{p+1} + (1+\frac{A_1 h \Delta t}{\rho C_p V_0} + \sum_{i=2}^{4} Fo_i) T_0^{p+1} = T_i^{p} + Q_0 - \frac{A_1 h T_\infty \Delta t}{\rho C_p V_0}$	[10.16]
Right Surface Convection	$-\sum_{i=1,\neq 2}^{4} Fo_i T_i^{p+1} + (1+\frac{A_2 h \Delta t}{\rho C_p V_0} + \sum_{i=1,\neq 2}^{4} Fo_i) T_0^{p+1} = T_i^{p} + Q_0 - \frac{A_2 h T_\infty \Delta t}{\rho C_p V_0}$	[10.17]
Right Top Outside Corner Convection	$-\sum_{i=1,\neq 1,2}^{4} Fo_i T_i^{p+1} + (1+h\Delta t\left(\frac{A_1+A_2}{\rho C_p V_0}\right) + \sum_{i=1,\neq 1,2}^{4} Fo_i) T_0^{p+1} = T_i^{p} + Q_0 - hT_\infty \Delta t\left(\frac{A_1+A_2}{\rho C_p V_0}\right)$	[10.18]
Left Top Outside Corner Convection	$-\sum_{i=1,\neq 1,4}^{4} Fo_i T_i^{p+1} + (1+h\Delta t\left(\frac{A_1+A_4}{\rho C_p V_0}\right) + \sum_{i=1,\neq 1,4}^{4} Fo_i) T_0^{p+1} = T_i^{p} + Q_0 - hT_\infty \Delta t\left(\frac{A_1+A_4}{\rho C_p V_0}\right)$	[10.19]
Right Inside Corner Convection	$-\sum_{i=1}^{4} Fo_i T_i^{p+1} + (1+h\Delta t\left(\frac{A_{1,c}+A_{2,c}}{\rho C_p V_0}\right) + \sum_{i=1}^{4} Fo_i) T_0^{p+1} = T_i^{p} + Q_0 - hT_\infty \Delta t\left(\frac{A_{1,c}+A_{4,c}}{\rho C_p V_0}\right)$ $A_{1,c} = (d_4/2)\Delta x$ $A_{2,c} = (d_1/2)\Delta x$	[10.20]

Convection Heat Transfer Estimation in LMD builds

The purpose of this exercise is to estimate the heat transfer coefficient on the exterior surfaces of LMD Ti-6Al-4V builds. A similar problem is solved in Gaskell, pg. 312.

Argon is used as a shielding gas in LMD processes. The velocity and temperature of the gas, v_∞ and T_∞, are assumed to be constant at 20 m/s and 298 K, respectively. The surface temperature can range from 310 K to greater than 2000K. The length of the surface we are considering can vary from 5 mm for 1 layer to 90 mm for an 18 layer deposit. We assume a flat, horizontal plate in these calculations. The film temperature is the average of the surface and fluid temperatures and will be used in selecting the appropriate thermal properties.

```
Clear["`*"]

$TextStyle = {FontFamily -> "Verdana", FontSize → 14};

Ts = {310, 2000};
Tinf = 298;
vinf = 25;
L = {5, 90} / 1000.;
Tf = 0.5 {(Ts[[1]] + Tinf), (Ts[[2]] + Tinf)}
```

```
{304., 1149.}
```

The thermophysical properties for the gas at the lower (300K) and upper (1200K) bound film temperatures are:

```
Pr = {0.669, 0.648};
ν = {1.4 * 10^-5, 14.8 * 10^-5};  (*m^2/s*)
k = {0.0177, 0.0481};(*W/m/K*)
```

The Prandtl number is the ratio of the fluids kinematic viscosity to thermal diffusivity, Pr = $\frac{\nu}{\alpha}$.

First calculate the reynolds number at the end of the plate: $\mathrm{Re}_L = \frac{v_\infty L}{\nu}$. For Re < $5 * 10^6$, flow is laminar.

```
vinf * L[[1]] / ν[[1]]
```

```
8928.57
```

```
Table[{i, j}, {i, 1, 2}, {j, 1, 2}][[1, 1]]
```

```
{1, 1}
```

```
ReL = Map[vinf * L[[#[[1]]]] / ν[[#[[2]]]] &, Table[{i, j}, {i, 1, 2}, {j, 1, 2}], {2}]
```

```
{{8928.57, 844.595}, {160714., 15202.7}}
```

```
Position[ReL, Max[ReL]]
```

```
{{2, 1}}
```

The greatest Reynolds number is for the long plate and low temperature.

The boundary from laminar to turbulent flow occurs at $x_{trans} = \frac{500000\,\nu}{v_\infty}$

```
xtrans = Map[5 * 10^6 * ν[[#]] / vinf &, {1, 2}]
```

```
{2.8, 29.6}
```

For laminar flow, the heat transfer coefficient is $h_{x,lam} = 0.331\,k\,\mathrm{Pr}^{1/3}\,(\frac{v_\infty}{\nu})^{1/2}\,x^{-1/2}$
and for turbulent flow, $h_{x,turb} = 0.0296\,k\,\mathrm{Pr}^{1/3}\,(\frac{v_\infty}{\nu})^{4/5}\,x^{-1/5}$. The value of the heat transfer coefficient is based soley on material properties, so we only have to look at the lower and upper bound temperatures. The transition from laminar to turbulent flow is based on both, but since we are well within the realm of laminar flow, we can ignore this transition (eventhough the equation is defined tyo consider it).

```
h[i_, x_] := If[x ≤ xtrans[[i]],
  0.331 k[[i]] Pr[[i]]^1/3 (vinf / ν[[i]])^1/2 x^-1/2, 0.0296 k[[i]] Pr[[i]]^1/3 (vinf / ν[[i]])^4/5 x^-1/5]
```

```
<< Graphics`Legend`
```

```
Plot[{h[1, x], h[2, x]}, {x, 0, L[[2]]},
 PlotStyle → {{Thickness[0.01], Hue[0]}, {Thickness[0.01], Hue[0.625]}}, Frame → True,
 FrameLabel → {"x, m", "h(x), W/(m^2K)"}, PlotLegend → {"Ts = 304 K", "Ts = 1149 K"},
 LegendBorder → Automatic, LegendShadow → {0.00, -0.00}, LegendPosition → {0.1, 0}]
```

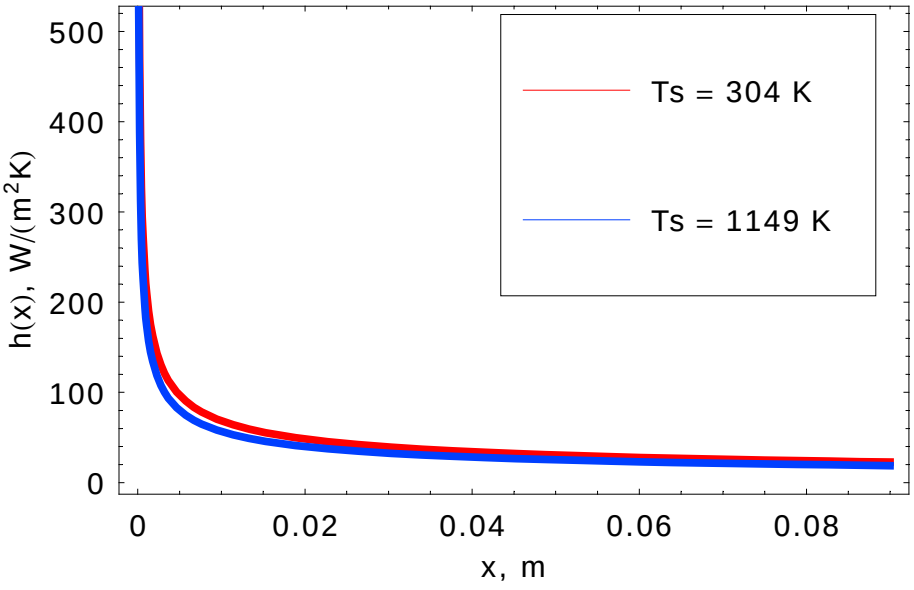


```
- Graphics -
```

The average heat transfer coefficient for the plate can be found by integrating over the lengh of the plate, the laminar and turbulent heat transfer coefficients, and dividing by the length of the plate

```
havg =
 Map[1/L[[#[[1]]]] ∫_0^L[[#[[1]]]] h[#[[2]], x] dx &, Table[{i, j}, {i, 1, 2}, {j, 1, 2}], {2}]
```

```
{{193.669, 160.158}, {45.6483, 37.7496}}
```

```
TableForm[havg,
 TableHeadings → {{"Ts = 304K", "Ts = 1149K"}, {"L = 5mm", "L = 90mm"}}]
```

	L = 5mm	L = 90mm
Ts = 304K	193.669	160.158
Ts = 1149K	45.6483	37.7496

The maximum heat transfer coeffecient arises over short distances and high low temperatures.

Thermal Model Flow Chart

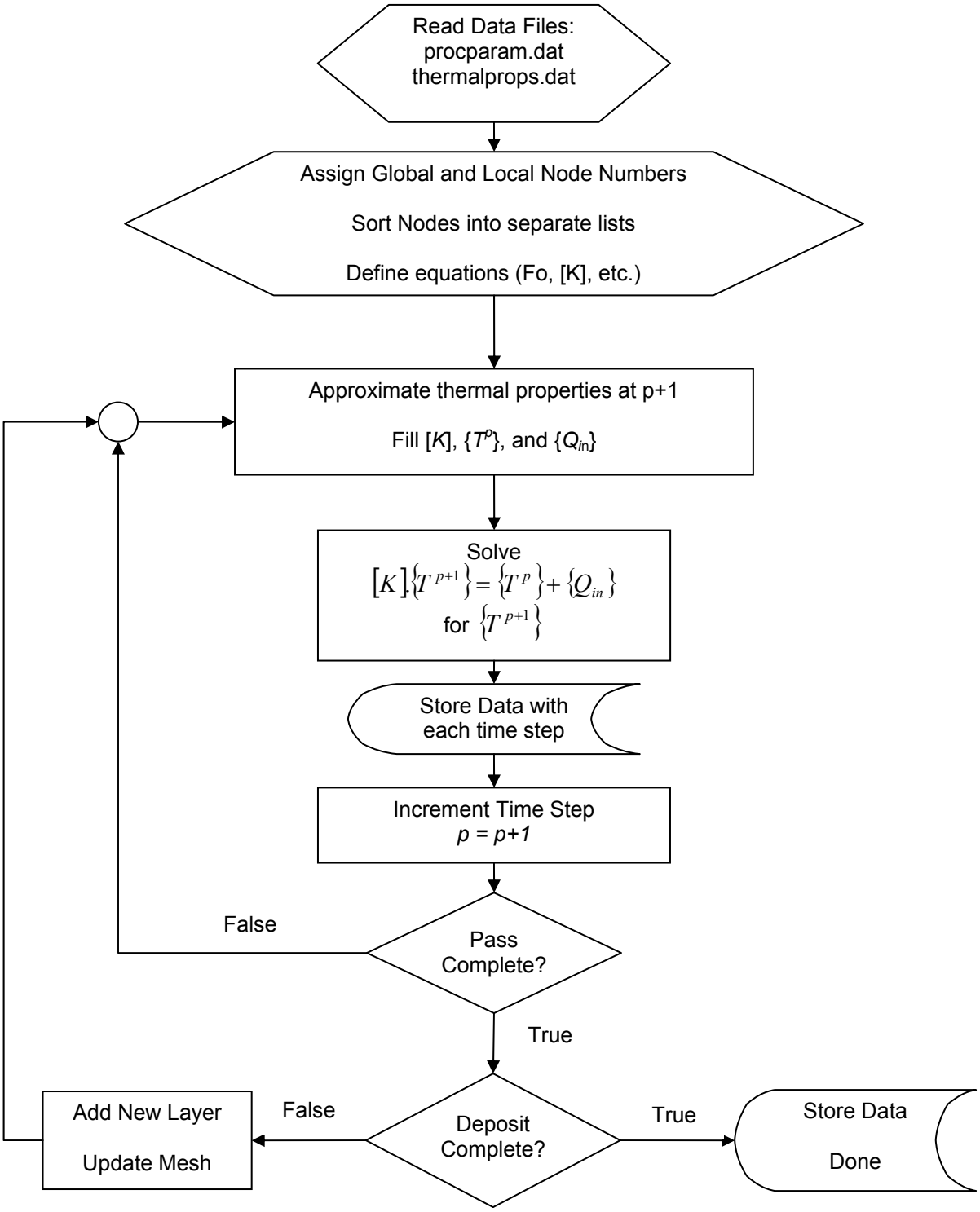

Figure 10.7: Flow chart for the thermal model.

DiCTra Simulation Macro

@@ Dictra set up macro for isothermal heating experiments.

@@ This macro sets up the simulation, runs it, then plots data and creates files for exporting into

@@ a plotting package (Mathematica, Igor, etc.)

@@ First, go to the database module to get thermodynamic data

go d-r

sw-d tidat @@Switches to the “tidat” database

def-sys Ti Al V @@Defines a system containing Ti, Al, V

rej ph * @@Reject all phases, then restore bcc and hcp, and get the data

rest ph bcc hcp

get

@@ Go to mobility database (MOB2) to append mobility of species in bcc and hcp

app mob2

def-sys Ti Al V

rej ph *

rest ph bcc hcp

get

@@ DiCTra Calculation module

go d-m

@@ First thing you do is set up geometry, defining a region of beta

ent-region beta

ent-region alpha beta yes @@ define another region alpha to the right of beta

@@ set up the grids

ent-grid beta 0.05e-6 linear 50

ent-grid alpha 0.506e-6 linear 506

```
@@ Assign phases to each region
ent-phase act beta matrix bcc
ent-phase act alpha matrix hcp
@@ Enter compositions of the phases, in weight-percent.
ent-comp beta bcc_a2 Ti w-p
Al lin 2.2 2.2
V lin 26.8 26.8
ent-comp alpha hcp_a3 Ti w-p
Al lin 6.0 6.0
V lin 2.2 2.2
s-cond glob t 0 1073; * n        @@ Set the temperature in Kelvin
s-sim-time 3600 yes 50 1e-9 1e-5      @@ Set the simulation time
save 64_1073_1 yes    @@ Begin a file to save the data
sim      @@ start the simulation
post     @@ Go to the post processor
@@ Plot beta interface position versus time
s-d-a x time
s-d-a y position beta upper
pl       @@ Plot
m-e-d 64_1073_1_t_x.exp yes          @@ Export the experimental data file
@@ Plot velocity of the beta interface versus time
s-d-a y velocity beta upper
pl
m-e-d 64_1073_1_t_vel.exp yes
@@ Plot vanadium profile versus global distance at several times.
```

```
s-p-c time .001 .1 1 10 100 1000
s-d-a x distance global
s-d-a y w-p
V
pl
m-e-d 64_1073_1_d_wpv.exp yes      @@ Export the experimental data file
@@ Plot of beta interface position versus log- time.
s-d-a x time
s-d-a y position beta upper
s-axis-type x log
s-s-s x n 1e-4 1e4
pl
set_interactive @@ Returns control to the user.
@@ The data files must then be imported into a plotting package in order to manipulate them to
@@ be plotted.  The DiCTra export file has extra lines of code other than the actual data.  A
@@  program in Mathematica has been created to condition the data for plotting in Igor.
```

Microstructure Model Code

Microstructure Model Functions

The function 'alphadis' defines the dissolution of the alpha phase. The variables and other functions not shown are described:
temp: temperature
α1H[temp]: The parabolic thickening rate, $\alpha_{1,H,SS}(T)$
βfunc[temp]: Equilibrium beta fraction
f: phase fraction
fα=phase fraction alpha

```
alphadis[temp_, Δt_] := (
  tstar = (f / (βfunc[temp] * α1H[temp]))^2;
  tcrit = (α1H[temp])^-2;
  ξ = If[Δt + tstar <= tcrit, α1H[temp] (Δt + tstar)^1/2, 1.0];
  f = βfunc[temp] * ξ;
  fα = 1 - f;
 )
```

The function 'alphappt' defines the nucleation and growth of the alpha phase.
αfunc[temp]: Equilibrium alpha fraction.
kfunc[temp]: kinetic parameter, $k(T)$

```
alphappt[temp_, Δt_] := (
  tstar = (Log[1. - f / αfunc[temp]] / -kfunc[temp])^(1/n);
  ξ = 1. - Exp[-kfunc[temp] (tstar + Δt)^n];
  f = ξ * αfunc[temp];
  fα = f;
 )
```

The function 'fraction' calculates both the alpha phase fraction and tracks alpha morphology. It contains nested 'Which' statements to select the appropriate equations based on whether dissolution or growth is occuring and for morphology, whehter the temperature is above or below $T_{IG} = 1100\,K$
fC: Fraction colony-α
fBW: Fraction basketweave-α
TIG: Start of intragranular alpha nucleation and growth. $T_{IG} = 1100\,K$
fCFG: Final amount of colony-α formed during growth.
fαS: Starting alpha fraction at dissolution
fBWFD: Final amount of basketweave-α present after dissolution.
fαFD: Final amount of α after dissolution.

slope: Determined during each time step, shows whether heating or cooling is occurring. slope =1 is positive, slope =-1 is negative.

```
fraction[temp_, Δt_] :=
 Which[
  temp == 0., (*For cases when the layer is not there*)
  {
   f = αfunc[temp],
   fα = f,
   fC = 0,
   fBW = 0
  },
  fα > αfunc[temp], (*Alpha Dissolution Required*)
  {
   f = 1 - fα, (*Converts to beta fraction*)
   alphadis[temp, Δt],
   Which[
    temp < TIG, (*TRUE: Only BW dissolution*)
    {
     fC = fCFG,
     fBW = fα - fC,
     needinit = 1
    },
    temp >= TIG, (*TRUE:  BW+C dissolution*)
    {
     If[needinit == 1,
      (*This is needed because temp may never equal TIG exactly*)
      {(*TRUE:  Set start values, BW dissolution*)
       fC = fCFG,
       fBW = fα - fC,
       fαS = fα,
       needinit = 0,
      },
     ],
     If[fαS == 0., (*This is needed becuase fα can =
        0 and the morph will still try to be calc.*)
      {fC = 0., fBW = 0.},
      {
       fC = (fCFG / fαS) * fα,
       fBW = ((fαS - fCFG) / fαS) * fα,
       fCFD = fC, (*continuously set final dissolution values*)
       fBWFD = fBW,
       fαFD = fα
      }
     ]
    }
   ],
  },
  fα < αfunc[temp], (*Alpha Growth Required*)
  {
   f = fα, (*Converts to alpha fraction*)
```

```
 If[temp ≤ Tbeta, alphappt[temp, Δt], {f = 0, fα = 0}] ,
 (*Don' t start growing until below Tbeta*)
 If[temp ≤ Tbeta,
  { (*Temp ≤ Tbeta*)
   Which[
    temp > TIG && slope <= 0, (*slope is needed because
       growth may occur during heating if non-equilibrium*)
    {
     fC = fCFD + (fα - fαFD),
     fBW = fBWFD,
     needinit = 1
    },
    temp <= TIG && slope ≤ 0,
    {
     If[needinit == 1,
      (*This is needed because temp may never equal TIG exactly*)
      {(*TRUE:  Set start values, BW dissolution*)
       fC = fC,
       fCFG = fC,
       fBW = fBWFD,
       needinit = 0
      }
     ],
     fC = fCFG,
     fBW = fα - fC
    },
    temp <= TIG && slope > 0,
    {
     fC = fCFG,
     fBW = fα - fC,
     fαFG = fα,
     needinit = 1
    },
    temp > TIG && slope > 0,
    {
     fC = fCFG + (fα - fαFG),
     fBW = fα - fC,
     needinit = 1,
     fCFG = fC,
     fαFG = fα
    }
   ]
  },
  {(*Temp > Tbeta*)
   fC = fCFD,
   fBW = fBWFD
  }
 ]
},
fα == αfunc[temp], (*At Equilibrium*)
{
```

```
 Which[
  slope == 0 || slope == 1 , (*Tt slope is positive, or horizontal,Dissolution*)
  {
   f = 1 - fα, (*Converts to beta fraction*)
   alphadis[temp, Δt]
  },
  slope == -1,              (*Ttslope is negative, Growth*)
  {
   f = fα,  (*Converts to alpha fraction*)
   If[temp ≤ Tbeta, alphappt[temp, Δt], {f = 0, fα = 0}]
   (*Don't start dissolving until below Tbeta*)
  }
 ],
 fC = fC, (*Sets the colony to the last value*)
 fBW = fBW
}
]
```

This is the calcualtion loop. The table 'data' already exists and constains the temperature data. The first column contains the time values and the data starts on row 5.

```
ftab = data; (*alpha phase fraction stored here*)
morphtabC = data; (*colony-alpha morphology stored here*)
morphtabBW = data; (*basketweave-alpha morphology stored here*)
Do[ (*Iterates over the number of nodes*)
 {
  f = αfunc[data[[5, k]]],
  (*sets the fraction f for the first time step as a alpha fraction*)
  fα = f,
  fαS = fα, (*Initialize values*)
  fαFD = fα,
  fC = 0 * fα,
  fBW = fα - fC,
  fCFD = fC,
  fCFG = fC,
  fBWFD = fBW,
  needinit = 0,
  ftab[[5, k]] = fα,
  morphtabC[[5, k]] = fC,
  morphtabBW[[5, k]] = fBW,
  Do[ (*Iterates over the number of time steps (ts)*)
   {
    Δt = data[[i, 1]] - data[[i - 1, 1]],
    slope =
     Sign[(data[[i, k]] - data[[i - 1, k]]) / (data[[i, 1]] - data[[i - 1, 1]])],
    fraction[data[[i, k]], Δt],
    ftab[[i, k]] = fα,
    morphtabC[[i, k]] = fC,
    morphtabBW[[i, k]] = fBW,
   },
   {i, 6, Length[data]}
  ],
 },
 {k, 2, nodes + 1}
]
```

Reference

[1] K. P. Cooper, *JOM* **53**, 29 (2001).

[2] M. L. Griffith, D. M. Keicher, C. L. Atwood, J. A. Romero, J. E. Smugeresky, L.D. Harwell, and D.L. Greene, in *Proceedings of the Solid Freeform Fabrication Symposium* (University of Texas, Austin, 1996), pp. 125.

[3] G. K. Lewis and E. Schlienger, *Materials and Design* **21**, 417-23 (2000).

[4] F. G. Arcella and F. H. Froes, *JOM* **52**, 28-30 (2000).

[5] F. G. Arcella, E. J. Whitney, M. A. House, P. H. Cohen, and H. B. Bomberger, in *Advances in Powder Metallurgy and Particulate Materials - 1996*, edited by T. M. Cadle and K. S. Narasimhan (Metal Powder Industries Federation, Princeton, NJ, 1997), Vol. 4(15), pp. 151-65.

[6] J. T. Schriempf, E. J. Whitney, H. B. Bomberger, and F. G. Arcella, in *Advances in Powder Metallurgy and Particulate Materials - 1997*, edited by R. Webb (Metal Powder Industries Federation, Princeton, NJ, 1997), Vol. 3-21, pp. 51-59.

[7] P. A. Kobryn, E. H. Moore, and S. L. Semiatin, *Scripta Materialia* **43**, 299-305 (2000).

[8] P. A. Kobryn and S. L. Semiatin, in *Solid Freeform Fabrication Proceedings*, edited by D. Bourell, J. Beaman, R. Crawford, H. Marcus, and J. Barlow (University of Texas, Austin, TX, 2000), pp. 58-65.

[9] P. A. Kobryn and S. L. Semiatin, *JOM* **53**, 40-42 (2001).

[10] P. A. Kobryn and S. L. Semiatin, *Journal of Materials Processing Technology* **135**, 330-39 (2003).

[11] S. M. Kelly, S. L. Kampe, and C. R. Crowe, in *Solid Freeform and Additive Fabrication - 2000*, edited by F. B. Prinz (Materials Research Society, Warrendale, PA, 2000), Vol. 625, pp. 3-8.

[12] P. S. Goodwin, C. Mitchell, J. Liang, J. Mei, and X. Wu, in *Proc. 2002 Int. Conf. on Metal Powder Deposition for Rapid Manufacturing*, edited by D. M. Keicher, J. W. Sears, and J. E. Smugeresky (Metal Powder Industries Federation, Princeton, N.J., 2002), pp. 87-95.

[13] M. L. Griffith, M. T. Ensz, J. D. Puskar, C. V. Robino, J. A. Brooks, J. A. Philliber, J. E. Smugeresky, and W. H. Hofmeister, in *Solid Freeform and Additive Fabrication - 2000*, edited by S. C. Danforth, D. Dimos, and F. B. Prinz (Materials Research Society, Warrendale, PA, 2000), Vol. 625, pp. 9-20.

[14] M. L. Griffith, E. Schlienger, L.D. Harwell, M. S. Oliver, M. D. Baldwin, M. T. Ensz, M. Essien, J. Brooks, C. V. Robino, J. E. Smugeresky, W. H. Hofmeister, M. J. Wert, and D.V. Nelson, *Materials and Design* **20**, 107-13 (1999).

[15] L. Costa, T. Reti, A.M. Deus, and R. Vilar, in *Proc. of the 2002 Int. Conf. on Metal Powder Deposition for Rapid Manufacturing*, edited by D. M. Keicher, J. W. Sears, and J. E. Smugeresky (Metal Powder Industries Federation, Princeton, NJ, 2002), pp. 172-79.

[16] W. H. Hofmeister, M. L. Griffith, M. T. Ensz, and J. E. Smugeresky, *JOM* **53**, 30-34 (2001).

[17] W. H. Hofmeister, M. J. Wert, J. E. Smugeresky, J. A. Philliber, M. L. Griffith, and M. T. Ensz, *JOM-e* **51** (1999).

[18] A. Vasinota, J. Beuth, and M. L. Griffith, in *Solid Freeform Fabrication Proceedings*, edited by D. Bourell, J. Beaman, R. Crawford, H. Marcus, and J. Barlow (University of Texas, Austin, TX, 1999), pp. 383-91.

[19] M. S. Misra, D. L. Olson, and G. R. Edwards, in *Grain Refinement in Casting and Welds: Proceedings of a Symposium*, edited by G. J. Abbaschian and S. A. David (Metallurgical Society of AIME, Warrendale, PA, 1983), pp. 259-74.

[20] J. Mazumder and W. M. Steen, *Metallurgical Transactions A* **13A**, 865-71 (1982).

[21] A. K. Shah, S. D. Kulkarni, V. Gopinathan, and R. Krishnan, *Weld J* **74**, S297-S304 (1995).

[22] A. K. Shah, S. D. Kulkarni, V. Gopinathan, and R. Krishnan, *Weld J* **74**, S325-S38 (1995).

[23] D. Rosenthal, *Transactions of the ASME*, 849-66 (1946).

[24] S. M. Kelly, M.S. Thesis, Virginia Tech (http://scholar.lib.vt.edu/theses/available/etd-05222002-223436/), 2002.

[25] S. M. Kelly and S. L. Kampe, *Metall Mater Trans A* **35A**, 1861-67 (2004).

[26] S. M. Kelly and S. L. Kampe, *Metall Mater Trans A* **35A**, 1869-79 (2004).

[27] S. Malinov, Z. Guo, W. Sha, and A. Wilson, *Metallurgical and Materials Transactions A* **32**, 879-87 (2001).

[28] T. Ahmed and H. J. Rack, *Materials Science and Engineering A* **243**, 206-11 (1998).

[29] S. Malinov, P. Markovsky, W. Sha, and Z. Guo, *Journal of Alloys and Compounds* **314**, 181-92 (2001).

[30] H. I. Aaronson, D. Eylon, C.M. Coole, M. Enomoto, and F. H. Froes, *Scripta Metallurgica* **23**, 435-40 (1989).

[31] D. Eylon, *Metallurgical Transactions* **10A**, 311-17 (1979).

[32] W. G. Burgers, *Physica* **1**, 561-86 (1934).

[33] W. A. Reinsch, in *Titanium and Titanium Alloys*, edited by M. J. Donachie (ASM, Materials Park, OH, 1982), pp. 47-49.

[34] U. Zwicker, *Titanium and Titanium Alloys*. (Springer-Verlag, Berlin, 1974).

[35] P. Shewmon, *Diffusion in Solids*. (The Minerals, Metals & Materials Society, 1989).

[36] H. Araki, T. Yamane, Y. Minamino, S. Saji, Y. Hana, and S. B. Jung, *Metall Mater Trans A* **25**, 874-76 (1994).

[37] M. P. Ginebra, F. X. Gil, J. M. Manero, and J. A. Planell, in *Titanium '95: Proceedings of the Eighth World Conference on Titanium*, edited by W. J. Blenkinsop, W. J. Evans, and H. M. Flower (IOM, London, 1996), Vol. 3, pp. 2563-70.

[38] F. J. Gil, M. P. Ginebra, J. M. Manero, and J. A. Planell, *Journal of Alloys and Compounds* **329**, 142-52 (2001).

[39] S. L. Semiatin, S. L. Knisley, P. N. Fagin, F. Zhang, and D. R. Barker, *Metall Mater Trans A* **34A**, 2377-86 (2003).

[40] R. Banerjee, D. Bhattacharyya, P. C. Collins, G. B. Viswanathan, and H. L. Fraser, *Acta Mater.* **52**, 377-85 (2004).

[41] Y. Ohmori, K. Nakai, H. Ohtsubo, and M. Tsunofuri, *Materials Transactions, JIM* **35**, 238-46 (1994).

[42] T. Furuhara, T. Makino, H. Watanabe, and T. Maki, in *Solid ->Solid Phase Transformations*, edited by W.C. Johnson, J.M. Howe, D.E. Laughlin, and W.A. Soffa (TMS, 1994), pp. 237-42.

[43] J. C. Chesnutt, C. G. Rhodes, and J. C. Williams, in *Titanium and Titanium Alloys*, edited by M. J. Donachie (ASM, Materials Park, OH, 1982), pp. 100-39.

[44] M. R. Plichta, J. C. Williams, and H. I. Aaronson, *Metallurgical and Materials Transactions A* **8A**, 1885-92 (1977).

[45] M. R. Plichta and H. I. Aaronson, *Acta Metallurgica* **26**, 1293-305 (1978).

[46] M. R. Plichta, J. H. Perepezko, H. I. Aaronson, and W. F. Lange III, *Acta Metallurgica* **28**, 1031-40 (1980).

[47] J. W. Christian, *The Theory of Transformations in Metals and Alloys*. (Pergamon, New York, 1975).

[48] T. Furuhara, K. Oishi, and T. Maki, *Metall. Mater. Trans. A-Phys. Metall. Mater. Sci.* **33**, 2327-35 (2002).

[49] T. B. Massalski, *Metall. Mater. Trans. A-Phys. Metall. Mater. Sci.* **33**, 2277-83 (2002).

[50] P. Gaunt and J. W. Christian, *Acta Metallurgica* **7**, 534-43 (1959).

[51] F. J. Gil, J. M. Manero, and J. A. Planell, in *Titanium '95: Proceedings of the Eighth World Conference on Titanium*, edited by W. J. Blenkinsop, W. J. Evans, and H. M. Flower (IOM, London, 1996), Vol. 3, pp. 2454-61.

[52] O. M. Ivasishin and R. V. Teliovich, *Materials Science and Engineering A* **263**, 142-54 (1999).

[53] W. Szkliniarz and G. Smolka, *Journal of Materials Processing Technology* **53**, 413-22 (1995).

[54] J. O. Andersson, L. Hoglund, B. Jonsson, and J. Agren, in *Fundamentals and Applications of Ternary Diffusion*, edited by G. R. Purdy (Pergammon, New York, 1990), pp. 153-63.

[55] J-O Andersson, Thomas Helander, Lars Hoglund, Pingfang Shi, and Bo Sundman, *CALPHAD* **26**, 273-312 (2002).

[56] O. M. Ivasishin and G. Lütjering, *Materials Science and Engineering A* **168**, 23-28 (1993).

[57] J. W. Elmer, T. A. Palmer, and J. Wong, *J Appl Phys* **93**, 1941-47 (2003).

[58] O. M. Ivasishin, in *Proceedings of the Sixth World Conference on Titanium*, edited by R. Lacombe, R. Tricot, and G. Beranger (Les Editions de Physique, Les Ulis Cedex, France, 1989), pp. 1535-39.

[59] H. I. Aaronson, D. Eylon, and F. H. Froes, *Scripta Metallurgica* **21**, 1241-45 (1987).

[60] E. Sarath Kumar Menon and H. I. Aaronson, *Acta Metallurgica* **35**, 549-63 (1987).

[61] W. Sha and Z. Guo, *Journal of Alloys and Compounds* **290**, L3-L7 (1999).

[62] P. A. Farrar and H. Margolin, *Transactions of the Metallurgical Society ofAIME* **221**, 1214-21 (1961).

[63] S. L. Semiatin, J. C. Soper, and I. M. Sukonnik, *Acta Materialia* **44**, 1979-86 (1996).

[64] S. L. Semiatin, P. N. Fagin, M. G. Glavicic, I. M. Sukonnik, and O. M. Ivasishin, *Materials Science and Engineering A* **299**, 225-34 (2001).

[65] G. G. E. Seward, S. Celotto, D. J. Prior, J. Wheeler, and R. C. Pond, *Acta Materialia* **52**, 821-32 (2004).

[66] A. W. Wilson and G. Spanos, *Materials Characterization* **46**, 407-18 (2001).

[67] D. Banerjee and V. S. Arunachalam, *Acta Metallurgica* **29**, 1685-94 (1981).

[68] D. Banerjee, C. G. Rhodes, and J. C. Williams, in *Titanium Science and Technology: Proceedings of the Fifth International Conference on Titanium*, edited by G. Lütjering, U. Zwicker, and W. Bunk (Deutsche Gessellschaft für Metallkunde, Munich, 1985), pp. 1597-604.

[69] D. Banerjee, C. G. Shelton, B. Ralph, and J. C. Williams, *Acta Metallurgica* **36**, 125-41 (1988).

[70] D. Banerjee and J. C. Williams, *Scripta Metallurgica* **17**, 1125-28 (1983).

[71] *OIM(TM) Analysis 3.0 User Manual v.3.0* (2000).

[72] E. J. Whitney, The Applied Research Laboratory - Penn State University, Private Communication, 2002.

[73] S. M. Kelly, S. L. Kampe, and C. R. Crowe, in *Solid Freeform and Additive Fabrication-2000*, edited by S. C. Danforth, D. Dimos, and F. B. Prinz (MATERIALS RESEARCH SOCIETY, Warrendale, 2000), Vol. 625, pp. 3-8.

[74] *ASTM B 367-93: Standard Specification for Titanium and Titanium Alloy Castings*. (ASTM, 1993).

[75] A. T. D'Annessa, *Weld J* **45**, 569s-76s (1966).

[76] K. E. Easterling, *Introduction to the Physical Metallurgy of Welding*, 1st ed. (Butterworths, Boston, 1983).

[77] N. W. Klingbeil, S. Bontha, C. J. Brown , D. R. Gaddam, P. A. Kobryn, H. L. Fraser, and J. W. Sears, in *Solid Freefrom Fabrication-2004* (2004).

[78] P. A. Kobryn, E. H. Moore, and S. L. Semiatin, *Scripta Materialia* **43**, 299-305 (2000).

[79] R. Boyer, in *Metals Handbook: Metallography and Microstructures* (American Society for Materials, Materials Park, OH, 1985), Vol. 9, pp. 458-75.

[80] W. A. Baeslack III, D. W. Becker, and F. H. Froes, *Journal of Metals* **36**, 46-58 (1984).

[81] W. A. Baeslack III, *Materials Science Letters* **1**, 229-31 (1982).

[82] W. A. Baeslack III, J. R. Davis, and C. E. Cross, in *ASM Handbook: Welding, Brazing, and Soldering* (ASM International, Materials Park, OH, 1993), Vol. 6, pp. 507-23.

[83] G. J. Davies and J. G. Garland, *International Metallurgical Reviews* **20**, 83-106 (1975).

[84] G. Lütjering, *Materials Science and Engineering A* **243**, 32-45 (1998).

[85] H. Margolin, P. A. Farrar, and M. A. Greenfield, in *The Science Technology and Application of Titanium*, edited by R. I. Jaffee and N. E. Promisel (Pergamon, New York, 1970), pp. 795-808.

[86] M. A. Greenfield, N. Kulken, and H. Margolin, *Metallurgical Transactions* **2**, 610-12 (1971).

[87] H. M. Flower, *Mater Sci Tech Ser* **6**, 1082-92 (1990).

[88] G. Lütjering, J. Albrecht, and O. M. Ivasishin, in *Microstructure/Property Relationships of Titanium Alloys*, edited by S. Ankem and J. A. Hall (The Minerals, Metals & Materials Society (TMS), Warrendale, PA, 1994), pp. 65-75.

[89] G. E. Welsch and R. R. Boyer, in *Titanium: A Technical Guide*, edited by M. J. Donachie (American Society for Materials (ASM), Materials Park, OH, 2000), pp. 1051-60.

[90] K. T. Slattery, D. H. Abbott, S. S. Fields, P. A. Kobryn, and N. Ontko, Presentation, 2003.

[91] M. T. Ensz, M. L. Griffith, and D. E. Reckaway, in *Proc. 2002 Int. Conf. on Metal Powder Deposition for Rapid Manufacturing*, edited by D. M. Keicher, J. W. Sears, and J. E. Smugeresky (Metal Powder Industries Federation, Princeton, N.J., 2002), pp. 195-202.

[92] R. R. Boyer and G. Lütjering, in *Advances in the Science and Technology of Titanium Alloy Processing*, edited by I. Weiss, R. Srinivasan, P. J. Bania, D. Eylon, and S. L. Semiatin (The Minerals, Metals & Materials Society (TMS), Warrendale, PA, 1997), pp. 349-67.

[93] M. N. Özisik, *Finite Difference Methods in Heat Transfer*. (CRC, Ann Arbor, MI, 1997).

[94] *Mathematica v.4.2* (1998-2002).

[95] K. C. Mills, *Recommended values of thermophysical properties for selected commercial alloys*. (Woodhead, Cambridge, 2002).

[96] M. Ensz and M. Griffith, 2002.

[97] J. Mazumder and W. M. Steen, *Journal of Applied Physics* **51**, 941-47 (1980).

[98] M. F. Ashby and K. E. Easterling, *Acta Metallurgica* **32**, 1935-48 (1984).

[99] J. Goldak, A. Chakravarti, and M. Bibby, *Met Trans B* **15B**, 299-305 (1984).

[100] C. Hu and T. N. Baker, *Metall Mater Trans A* **27A**, 4039-47 (1996).

[101] W. Hofmeister, M. Griffith, M. Ensz, and J. Smugeresky, *JOM* **53**, 30-34 (2001).

[102] T. J. Wieting and J. T. Schriempf, *Journal of Applied Physics* **47**, 4009-11 (1976).

[103] S. M. Kelly, S. S. Babu, S. A. David, T. Zacharia, and S. L. Kampe, in *Cost-Affordable Titanium Symposium in Honor of Professor Harvey Flower*, edited by F. H. Froes (TMS, Warrendale, 2004).

[104] B. A. B. Anderrson, *Journal of Engineering Materials and Technology* **100**, 356-62 (1978).

[105] O. Grong and H. R. Shercliff, *Progress in Materials Science* **47**, 163-282 (2002).

[106] W. A. Johnson and R. F. Mehl, *Transactions of the AIME* **135**, 416 (1939).

[107] M. Avrami, *Journal of Chemical Physics* **7**, 1103-12 (1939).

[108] M. Avrami, *Journal of Chemical Physics* **8**, 212-24 (1940).

[109] M. Avrami, *Journal of Chemical Physics* **9**, 177-84 (1941).

[110] A. N. Kolmorgorov, *Izv. Akad. Nauk. SSSR.* **3**, 355 (1937).

[111] J. W. Christian, *Theory of phase transformations in metals and alloys - Part I*. (Pergamon Press, Oxford, UK, 1975).

[112] J. W. Cahn, *Acta Metallurgica* **4**, 572-75 (1956).

[113] J. W. Cahn, *Acta Metallurgica* **4**, 449-59 (1956).

[114] M. B. Kuban, R. Jayaraman, E. B. Hawbolt, and J. K. Brimacombe, *Metallurgical Transactions* **17A**, 1493-503 (1986).

[115] Y. T. Zhu, T. C. Lowe, and R. J. Asaro, *J Appl Phys* **82**, 1129-37 (1997).

[116] Y. T. T. Zhu and T. C. Lowe, *Metallurgical and Materials Transactions B* **31**, 675-82 (2000).

[117] M. Lusk and H. J. Jou, *Metallurgical and Materials Transactions A* **28**, 287-91 (1997).

[118] T. Reti and I. Felde, *Comp Mater Sci* **15**, 466-82 (1999).

[119] O. Grong and O. R. Myhr, *Acta Mater* **48**, 445-52 (2000).

[120] H. Hemmer and Ø. Grong, *Metallurgical and Materials Transactions A* **30**, 2915-29 (1999).

[121] W. B. Li, K. E. Easterling, and M. F. Ashby, *Acta Metallurgica* **34**, 1533-43 (1986).

[122] H. Hemmer, Ø. Grong, and S. Klokkehaug, *Metallurgical and Materials Transactions A* **31**, 1035-48 (2000).

[123] J. W. Elmer, T. A. Palmer, S. S. Babu, W. Zhang, and T. DebRoy, *J Appl Phys* **95**, 8327-39 (2004).

[124] B. Sundman, B. Jansson, and J. O. Andersson, *CALPHAD* **9**, 153-90 (1985).

[125] N. Saunders, in *Titanium '95: Proceedings of the Eighth World Conference on Titanium*, edited by W. J. Blenkinsop, W. J. Evans, and H. M. Flower (IOM, London, 1996), Vol. 3, pp. 2167-77.

[126] G. N. Haidemenopoulos, *J Alloy Compd* **320**, 302-07 (2001).

[127] N. Saunders, Z. Guo, X. Li, A. P. Miodownik, and J. P. Schille, *JOM - J Min Met Mat S* **55**, 60-65 (2003).

[128] X. Li, A. P. Miodownik, and N. Saunders, *Mater. Sci. Technol.* **18**, 861-68 (2002).

[129] *JMatPro v.3.0* (2004).

[130] Thermo-Calc Software, *Thermo-Calc Classic v.P* (Stockholm, Sweden, 2002).

[131] N. Saunders and A. P. Miodownik, *CALPHAD (Calculation of Phase Diagrams): A Comprehensive Guide*. (Cambridge, 2002).

[132] R. A. Wood and R. J. Favor, in *Titanium Alloys Handbook* (Metals and Ceramics Information Center, Batelle, 1972).

[133] ThermoCalc Software, *SSOL2 - SGTE Solutions Database v.2.0* (2002).

[134] SGTE, in *The SGTE Casebook: Thermodynamics at Work*, edited by K. Hack (Inst. Materials, London, 1996), pp. 227.

[135] ThermoCalc Software, *TCS Alloys Mobility Database (MOB2) v.2.0* (1999).

[136] M. J. Whelan, *Metal Science Journal* **3**, 95-97 (1969).

[137] N. Saunders, X. Li, A. P. Miodownik, and J. P. Schille, in *Ti-2003: Proc 10th World Conference on Titanium*, edited by G. Luetjering and J. Albrecht (Wiley, Hamburg, Germany, 2003).

[138] G. F. VanderVoort, *Atlas of Time - Temperature - Transformation Diagrams for Nonferrous Alloys*. (ASM International, Materials Park, OH, 1991).

[139] S. Malinov, W. Sha, and Z. Guo, *Materials Science and Engineering A* **283**, 1-10 (2000).

[140] V. M. Majdic and G. Ziegler, *Z. Metallkunde* **64**, 751-58 (1973).

[141] S. S. Babu, J. W. Elmer, T. A. Palmer, and E. Specht, 2004.

[142] H. I. Aaronson, *Metall. Mater. Trans. A-Phys. Metall. Mater. Sci.* **33**, 2285-97 (2002).

[143] S. J. Jones and H. K. D. H. Bhadeshia, *Metall Mater Trans A* **28**, 2005-13 (1997).

[144] S. J. Jones and H. K. D. H. Bhadeshia, *Acta Mater* **45**, 2911-20 (1997).

Vita

The author, Shawn Michael Kelly, was born on September 12, 1977 in Baltimore, Maryland. He was raised in Perry Hall, a suburb of Baltimore. He attended Perry Hall High School, where he was a member and captain of the Cross Country and Track teams, and where he first stumbled across the field of Materials Science though a physics assignment on polymer matrix composite bicycle frames. Upon graduating high school in 1995, he traveled to Blacksburg, Virginia home of Virginia Tech to pursue a degree in Materials Science and Engineering. In the summers of 1997 and 1998, the author co-op'ed at NASA's Goddard Space Flight Center located in Greenbelt Maryland under the leadership of Michael Viens, Michael Barthelmy, and Brad Parker in the Materials Engineering Branch. It was through this experience that the author decided to attend graduate school. Upon graduating from Virginia Tech with a B.S. in Materials Science and Engineering, the author began working on the project documented here under Dr. Stephen Kampe. In July 2000, the author married his then fiancée Nancy Chandale Hart. During his graduate studies, the author was the recipient of the Gary Clevinger Scholarship for his participation in departmental activities and role as the Materials Engineering Professional Societies (MEPS) president. He also wrote and presented papers at the several national conferences. In June of 2004, his first peer reviewed papers were published in *Metallurgical Transactions*.

Upon completion of the requirements for the Master's of Science degree in May 2002, the author spent 6 weeks at Oak Ridge National Laboratories in Oak Ridge, Tennessee under the direction of Dr. S. Suresh Babu to further improve the thermal model and to work on computational modeling of laser surface alloying. Following the research visit to ORNL, coursework at Virginia Tech was completed and arrangements were made to return to ORNL to complete the PhD research under the added supervision of S. Suresh Babu. In June 2003, the author returned to ORNL as an employee of the University of Tennessee, made possible by the Joint Institute for Computational Sciences and sponsorship from Thomas Zacharia of ORNL. While at ORNL, the author was a member of the materials joining group, headed by Dr. Stan David.

Upon completion of the PhD work in December 2004, the author will take a research associate position with the Applied Research Laboratory – Penn State University, where he will work in the Laser Processing Division under the supervision of Dr. Rich Martukanitz.